



Trinity College Dublin

Coláiste na Tríonóide, Baile Átha Cliath

The University of Dublin

Harmonic and superparamagnetic nanoparticles for biomedical imaging and diagnostic applications

Gareth Clarke

A dissertation submitted for the degree of Doctor of Philosophy

to the School of Medicine

The University of Dublin, Trinity College – June 2020

Declaration

The University of Dublin

Trinity College – June 2019

I declare that this thesis has not been submitted as an exercise for a degree at this or any other university and it is entirely my own work.

I agree to deposit this thesis in the University's open access institutional repository or allow the library to do so on my behalf, subject to Irish Copyright Legislation and Trinity College Library conditions of use and acknowledgement.

Signed: 

Summary

Diagnosing certain diseases and tracking their progression requires the ability to “see” into the body. This is typically achieved by taking advantage of intrinsic contrast in biological tissues (such as in X-ray or magnetic resonance imaging) or by labelling structures with markers such as dyes, fluorescent tags or quantum dots. Each method has limitations – not all structures have sufficient contrast for high resolution imaging, fluorescence fades and quantum dots blink randomly. Nanomaterials were developed for *in vitro* imaging applications which can overcome the limitations of conventional imaging probes by combining harmonic nanocrystals with superparamagnetic nanoparticles in a multimodal/multifunctional diagnostic tool.

Nanocrystals of nonlinear optical bismuth ferrite were prepared by a sol-gel route. In order to enhance the purity of the nanocrystals and hence improve their nonlinear optical response, a variety of chelating agents were substituted in the sol-gel synthesis and the enhancements were quantified by Hyper Rayleigh Scattering. Stable dispersions of the nanocrystals were used as seeds for the synthesis of superparamagnetic magnetite nanoparticles by co-precipitation.

Magnetite and bismuth ferrite nanoparticles and composites were combined into silica nanowires to enhance their biocompatibility. This was achieved by incorporating silica sol-gel in which nanoparticles or composites were suspended into the pores of anodic alumina templates, annealing the silica and then dissolving the templates to release the wires.

These procedures resulted in novel nanomaterials whose physico-chemical properties such as size-distribution, morphology, colloidal stability, crystal structure and magnetic and nonlinear optical response were extensively characterised by a suite of analytical techniques, including Dynamic Light Scattering, Transmission Electron Microscopy, Zeta-potential measurements, X-ray Diffraction, Vibrating Sample Magnetometry and Second Harmonic Microscopy.

A safety assessment of the nanomaterials and composites was carried out using High Content Screening to examine cytotoxicity. Three cell lines were selected to represent different potential exposure routes: human lung cell epithelial cells, human vein endothelial cells and monocyte-derived macrophages. The response of these cell lines was evaluated with respect to cell count, cell viability and lysosomal mass/pH changes after exposure to each of the nanomaterials and composites for 24, 48 and 72 hours. Composites were functionalised to target specific markers such as epidermal growth factor receptor. The uptake, specificity and sensitivity of the probes of the functionalised nanomaterials was evaluated

using colorimetric analysis, and the targeting and localisation were assessed using Epifluorescence and Confocal Microscopy.

As proof-of-concept of their multifunctionality and multimodality, the composites were magnetically separated from biological media, and imaged using Magnetic Resonance Imaging and Second Harmonic Microscopy, which was also used to illustrate the advantages of nonlinear optical probes over conventional, fluorescent markers.

The work carried out in this thesis involved many methods to optimise the synthesis of harmonic and superparamagnetic nanomaterials and composites and demonstrated their suitability for use as multifunctional diagnostic probes in multimodal *in vitro* imaging.

Acknowledgments

I would first like to thank Dr Yannick Mugnier, Prof Ronan le Dantec, Prof Christine Galez and the team at Université de Savoie for all their help during my Erasmus placement during my undergraduate studies since that led directly to connecting with TCD and applying for this PhD. My SYMME family has been enormous support for all the long years. I would of course also like to thank my thesis supervisors Prof Yuri Volkov and Dr Adrièle Prina Mello whose help and guidance have been incalculable throughout. I am very grateful to Prof Yurii Gun'ko for the use of his lab at SNIAM, and to his research group. I especially want to thank Dr Sarah McCarthy for showing me the ropes and all TCD's amenities, for training me and letting me use her glassware – so much glassware! It was always a treat to discuss nanoscience and chemistry—physical and emotional—and everything else for good measure. I would also like to thank Prof Mike Coey at SNIAM for the use of his VSM, Dr Gemma Davies and Dr Joe McCarthy for training on nanomaterial synthesis and Dr Tania Perova for the use of her microscope.

Over the course of the thesis I benefited enormously from discussions and collaboration with scientists across Europe as part of the NAMDIATREAM project, and I am very grateful to Sandrine Gerber at EPFL and Daniel Ritz at FEE for their insights and contributions, and especially Prof Dr Luigi Bonacina at the University of Geneva. I would also like to thank Gabriel Campargue, from the GAP Biophotonics group and his predecessor Dr Andrii Rogov for carrying out Second Harmonic Microscopy studies.

For help and training throughout I would like to thank Jean-Christophe Marty and Marc Dubled at Uds; Clive Downing and Dermot Daly at the AML; Neal Leddy at CMA; Prof Mary O'Sullivan, Dr Michael Freely, Dr Anne-Marie Byrne and Dr Jennifer Conroy at the Institute of Molecular Medicine. I owe enormous gratitude to all the IMM family but especially to Tatsiana Rakovich, Dania Movia, Ciaran Maguire, Bashir Mohammed and Laura Kickham for training, cells, more training, reagents, retraining, and consumables, and to Kieran, AJ, Omar, Susie and Aidan for the sanity checks and good times.

This work would not have been possible without funding and support from the Irish Research Council, IRCSET-Égide and Campus France, EU FP7 and Science Foundation of Ireland.

Finally, I would like to thank my family for their unwavering support, patience (and my mother's proofreading skills!) and my husband Peter Hester for his love, tolerance and wicked sense of humour.

Statement of work

This work was undertaken by the author with the Nanomaterials Synthesis group at Laboratoire Systèmes et Matériaux pour la Mécatronique, Université de Savoie, France, with the Nanomedicine research group, Department of Clinical Medicine, Institute of Molecular Medicine and with the Yurii K. Gun'ko research group at the Sami Nasr Institute of Advanced Materials, The University of Dublin, Trinity College.

List of Abbreviations and Conventions

- [Core]@[shell]: a nanocomposite consisting of a core nanoparticle surrounded by a shell of nanoparticles (e.g. $\text{BiFeO}_3@Fe_3O_4$), or functionalised with a layer or linker (e.g. $\text{BiFeO}_3@APTES$)
- [Core]@[shell]@[functional coating]: a nanocomposite consisting of a core@shell nanocomposite which has been further functionalised or capped by the addition of an outer layer or shell (e.g. $\text{BiFeO}_3@Fe_3O_4@asc$)
- [Matrix]&[Embedded]: a nanocomposite consisting of a matrix in which nanoparticles or nanocomposites are embedded (e.g. $\text{SiO}_2\&\text{BiFeO}_3$)
- Ab(s): antibody(-ies)
- asc: L-Ascorbic acid
- BSA: bovine serum albumin
- DLS: Dynamic Light Scattering
- DMEM: Dulbecco's modified Eagle's medium
- EDC: N-(3-Dimethylaminopropyl)-N'-ethylcarbodiimide hydrochloride
- EGF: epidermal growth factor
- EGFR: Epidermal Growth Factor Receptor
- EtOH: ethanol
- FBS: Fetal Bovine Serum
- FSC: forward Scatter
- HNP(s): harmonic nanoparticle(s)
- HRS: Hyper Rayleigh Scattering
- (HR)TEM: (High Resolution) Transmission Electron Microscopy
- KTP: KTiOPO_4
- LMPH: Lysosomal mass/pH
- MA: mucic acid
- MDM: Monocyte-derived Macrophages
- MES: 2-(N-Morpholino)ethanesulfonic acid
- MRI: Magnetic Resonance Imaging
- NLO: Nonlinear optics
- NMR: Nuclear Magnetic Resonance

- Non-asc: not stabilised with ascorbic acid
- NP(s): nanoparticle(s)
- NT: Non-treated
- NTA: Nanoparticle Tracking Analysis
- NW(s): nanowire(s)
- PBS: phosphate buffered saline
- PFA: paraformaldehyde
- QD(s): quantum dot(s)
- SAED: Selected Area Electron Diffraction
- SEM: Scanning Electron Microscopy
- SHM: Second Harmonic Microscopy
- SSC: side scatter
- TA: tartaric acid
- TEOS: tetraethyl orthosilicate
- TMAH: tetramethylammonium hydroxide
- TMAH: tetramethylammonium hydroxide
- TTA: tartronic acid
- TXRD: Temperature-dependent X-ray diffraction
- VSM: Vibrating Sample Magnetometer
- XRD: X-ray diffraction
- Inh: Inhibited with sodium azide

TABLE OF CONTENTS

Chapter 1 Introduction	1
1.1 Aims and Research Questions	1
1.2 Nanomaterials: nanoparticles, nanowires, nanosheets, nanocomposites	2
1.2.1 Challenges	4
1.2.2 Advantages/opportunities	4
1.2.3 Harmonic nanoparticles and nonlinear materials	4
1.2.4 Magnetic materials and superparamagnetism	7
1.3 Biomedical imaging probes.....	8
1.3.1 Magnetic resonance imaging contrast agents	10
1.3.2 Targeting diagnostic markers.....	11
1.3.3 Prerequisites in the development of probes for imaging and diagnostic applications	12
1.4 Diagnostic platforms	13
1.4.1 Flow cytometry	14
1.4.2 Confocal, Two-photon and Second Harmonic Microscopy.....	14
1.4.3 Multimodal imaging	15
Chapter 2 Nanomaterial synthesis	17
2.1 Introduction	17
2.1.1 Bismuth ferrite nanoparticles: a model candidate for second harmonic microscopy	17
2.1.2 Magnetite nanoparticles: superparamagnetic applications	18
2.1.3 Silica nanowires: low-cost, low toxicity 1D nanomaterials.....	19
2.2 Materials and Methods	21
2.2.1 Reagents	45
2.2.2 Nanoparticle synthesis	21
2.2.3 Nanowire synthesis - One-pot acidic sol-gel synthesis of SiO ₂ nanowires	22

2.2.4 Nanocomposite synthesis	23
2.2.5 Physico-chemical characterisation	27
2.3 Results	33
2.3.1 Nanoparticles	33
2.3.2 Nanowires	45
2.3.3 Multimodal nanomaterials.....	46
2.4 Discussion	61
2.4.1 Additional –OH groups increase crystallinity of BiFeO ₃ at lower temperatures	62
2.4.2 Increased salt concentration enhances crystallization of BiFeO ₃	62
2.4.3 Enhanced NLO response of BiFeO ₃	63
2.4.4 One-pot synthesis is a more efficient route to obtain silica nanowires	64
2.4.5 Increased loading of magnetite and/or BiFeO ₃ in silica nanowires.....	64
2.4.6 Magnetic-harmonic nanoparticles were synthesised.....	64
2.5 Conclusion.....	65
Chapter 3 Functionalisation of nanoparticles	67
3.1 Introduction	67
3.1.1 Functionalisation	67
3.1.2 Biocompatibility	69
3.1.3 Targeting	69
3.1.4 Uptake.....	71
3.1.5 Diagnostic probes	71
3.2 Materials and Methods	72
3.2.1 Reagents	72
3.2.2 Protocols	73
3.2.3 Incubation of cells with nanomaterials.....	76
3.2.4 Equipment and Techniques.....	79

3.2.5 Techniques for characterisation.....	80
3.3 Results	82
3.3.1 Surface modification to achieve efficient coupling to selected moieties.....	82
3.3.2 Nanoparticle colloidal stability, size distribution and concentration	83
3.3.3 Bioconjugation with antibodies for targeting	92
3.3.4 Uptake of nanoparticles in A549 cells	99
3.4 Discussion	108
3.4.1 Silane layers were grown on nanoparticles to passivate their surface	108
3.4.2 BiFeO ₃ nanoparticles and BiFeO ₃ composites were conjugated to anti-EGFR antibodies	109
3.4.3 Functionalisation with anti-EGFR antibody allowed specific targeting to EGFR	109
3.5 Conclusion	109
Chapter 4 Safety assessment of nanoparticles and nanocomposites	111
4.1 Introduction	111
4.1.1 Cytotoxicity	112
4.1.2 Toxicity assessment of nanomaterials.....	112
4.1.3 High content screening for cytotoxicity screening.....	113
4.2 Materials and Methods	114
4.2.1 Reagents	114
4.2.2 Equipment and protocols	114
4.3 Results	119
4.3.1 Cytotoxicity analysis of nanomaterial interactions of A549 cells by High Content Screening.....	120
4.3.2 Cytotoxicity analysis of nanomaterial interactions of HUVEC cells by High Content Screening.....	132
4.4 Discussion	146

4.4.1 Discussion of Nanomaterial Interaction with A549 cells	146
4.4.2 SiO ₂ and BiFeO ₃ -derived NWs are not toxic to A549 cells.	148
4.4.3 BiFeO ₃ -derived NPs are highly toxic to HUVEC cells due to aggregation.....	148
4.4.4 SiO ₂ and BiFeO ₃ -derived NWs are toxic to HUVECs.....	148
4.5 Conclusions	149
Chapter 5 Multimodal applications of nanocomposites	151
5.1 Introduction	151
5.1.1 Cell separation or sorting.....	151
5.1.2 Magnetic resonance imaging (MRI).....	153
5.1.3 Nonlinear optical applications in Bioimaging.....	154
5.2 Materials and Methods	156
5.2.1 Reagents	156
5.2.2 Cell culturing and incubation	156
5.2.3 Equipment.....	157
5.2.4 Protocols for Multimodal Observation	157
5.3 Results	158
5.3.1 Magnetic separation of BiFeO ₃ @Fe ₃ O ₄ NPs from different media	158
5.3.2 Magnetic Resonance Imaging (MRI) of BiFeO ₃ @Fe ₂ O ₃ composites.....	159
5.3.3 Nonlinear Optical Imaging: Second Harmonic Microscopy	161
5.4 Discussion	164
5.4.1 BiFeO ₃ @Fe ₃ O ₄ NPs can be separated magnetically in different suspensions.....	165
5.4.2 BiFeO ₃ @Fe ₂ O ₃ nanoparticles can be used as contrast agents in Magnetic Resonance Imaging	165
5.4.3 Bismuth ferrite iron oxide nanocomposites are detectable via second harmonic microscopy.....	165
5.5 Conclusion.....	166

Chapter 6 General Discussion and Future Work	167
6.1 Application-driven optimisation	167
6.1.1 Physico-chemical tuning: size and shape refinement	168
6.1.2 Enhancement of nonlinear optical properties	168
6.1.3 Optimised end-products	169
6.2 Functionalisation and Bioconjugation	169
6.3 Multimodal imaging probes.....	170
6.4 Conclusion	170
References.....	173
Appendices.....	187
A1 High Content Screening of primary monocyte-derived macrophages (MDMs).....	187
A1.1 Summary: MDM count after exposure to each of the nanomaterials.....	187
A1.2 Summary: metabolic activity in primary monocyte-derived macrophages after exposure to each of the nanomaterials	188
A1.3 MDMs treated with BiFeO ₃ NPs	188
A1.4 MDMs treated with ascorbic acid-functionalised BiFeO ₃ NPs.....	191
A1.5 MDMs treated with BiFeO ₃ @APTES NP	194
A1.6 MDMs treated with BiFeO ₃ @Fe ₃ O ₄ @asc NPs.....	196
A1.7 MDMs treated with BiFeO ₃ @Fe ₃ O ₄ @APTES NPs.....	198
A1.8 MDMs treated with BiFeO ₃ @Fe ₂ O ₃ @asc NPs.....	201
A1.9 MDMs treated with SiO ₂ &BiFeO ₃ NWs.....	203
A1.10 MDMs treated with SiO ₂ &BiFeO ₃ @Fe ₃ O ₄ NWs	205
A1.11 MDMs treated with SiO ₂ &BiFeO ₃ @Fe ₂ O ₃ NWs	207
A2 High Content Screening of A549 cells	209
A2.1 A549 cells treated with BiFeO ₃ NPs.....	209
A2.2 A549 cells treated with ascorbic acid-functionalised BiFeO ₃ NPs (BiFeO ₃ @asc).....	214

A2.3 A549 cells treated with BiFeO ₃ @APTES NPs.....	218
A2.4 A549 cells treated with BiFeO ₃ @Fe ₃ O ₄ @asc NPs.....	223
A2.5 A549 cells treated with BiFeO ₃ @Fe ₃ O ₄ @APTES NPs	227
A2.6 A549 cells treated with BiFeO ₃ @Fe ₂ O ₃ @asc NPs.....	232
A2.7 A549 cells treated with SiO ₂ &BiFeO ₃ NWs.....	236
A2.8 A549 cells treated with SiO ₂ &BiFeO ₃ @Fe ₃ O ₄ NWs	240
A2.9 A549 cells treated with SiO ₂ &BiFeO ₃ @Fe ₂ O ₃ NWs	244
A3 High Content Screening of HUVEC cells	249
A3.1 HUVEC cells treated with BiFeO ₃ NPs	249
A3.2 HUVEC cells treated with ascorbic acid-functionalised BiFeO ₃ NPs (BiFeO ₃ @asc)....	253
A3.3 HUVEC cells treated with BiFeO ₃ @APTES NPs.....	258
A3.4 HUVEC cells treated with BiFeO ₃ @Fe ₃ O ₄ @asc NPs.....	263
A3.5 HUVEC cells treated with BiFeO ₃ @Fe ₃ O ₄ @APTES NPs.....	268
A3.6 HUVEC cells treated with BiFeO ₃ @Fe ₂ O ₃ @asc NPs.....	272
A3.7 HUVEC cells treated with SiO ₂ &BiFeO ₃ NWs.....	276
A3.8 HUVEC cells treated with SiO ₂ &BiFeO ₃ @Fe ₃ O ₄ NWs	281
A3.9 HUVEC cells treated with SiO ₂ &BiFeO ₃ @Fe ₂ O ₃ NWs	285

Index of Tables

TABLE 1.1: RESULTS SUMMARY OF A SURVEY OF THE AVERAGED SECOND HARMONIC COEFFICIENT OF WELL-KNOWN NONLINEAR OPTICAL MATERIALS	7
TABLE 1.2: MATRIX OF NANOMATERIALS, THEIR PROPERTIES AND THE NANOCOMPOSITES IN WHICH THE PROPERTIES ARE TO BE COMBINED.	16
TABLE 2.1: STRUCTURE, RATIO OF HYDROXYL GROUPS TO CARBOXYLIC ACIDS AND LOWEST ANNEALING TEMPERATURE OF EACH OF THE CHELATING AGENTS USED IN THIS STUDY	37
TABLE 2.2: SATURATION MAGNETISATION AND LOADING OF MAGNETITE AND CORRESPONDING SILICA NANOWIRES	50
TABLE 2.3: SATURATION MAGNETISATION AND LOADING OF MAGNETITE AND CORRESPONDING SILICA NANOWIRES	52
TABLE 3.1: MATRIX OF NANOMATERIALS, THEIR PROPERTIES AND THE NANOCOMPOSITES IN WHICH THE PROPERTIES ARE TO BE COMBINED.	72
TABLE 3.2: STAINS USED FOR CONFOCAL MICROSCOPY WITH EXCITATION, FILTER AND ORGANELLE DETAILS	80
TABLE 3.3: SIZE DISTRIBUTION DATA INCLUDING MEAN, D10, D50 AND D90 VALUES AND CONCENTRATION OF NANOPARTICLES PER ML OF SUSPENSION	89
TABLE 4.1: MATRIX OF NANOMATERIALS, THEIR PROPERTIES AND THE NANOCOMPOSITES IN WHICH THE PROPERTIES ARE TO BE COMBINED.	111
TABLE 4.2: FILTERS AND CORRESPONDING DETECTION WAVELENGTHS FOR EACH HCS ANALYTE	119
TABLE 5.1: APPEARANCE OF VARIOUS TISSUES IN MRI	154
TABLE 5.2: T2-WEIGHTED MR IMAGES OF NANOPARTICLES IN SUSPENSION.....	160
TABLE 5.3: T2*-WEIGHTED MR IMAGES OF NANOPARTICLES IN SUSPENSION.....	160

Index of Figures

FIGURE 1.1: SCHEMA SHOWING THE BREAKDOWN OF THE RESEARCH TASKS.....	1
FIGURE 1.2: ZERO-, ONE-, AND TWO-DIMENSIONAL NANOMATERIALS	2
FIGURE 1.3: EXPONENTIAL INCREASE IN SURFACE AREA TO VOLUME RATIO (A/V) AS A CUBE IS BROKEN INTO SMALLER CUBES	3
FIGURE 1.4: SCHEMATIC OF THE PRINCIPLE OF SECOND HARMONIC GENERATION (SHG), A NONLINEAR OPTICAL PHENOMENON	5
FIGURE 1.5: HARMONIC NANOPARTICLES AS ADVANCED BIOMEDICAL IMAGING PROBES.....	6
FIGURE 1.6: PRINCIPLE OF TARGETING	12
FIGURE 2.1: IMAGE OF TWO BiFeO_3 PRIMITIVE CELLS	17
FIGURE 2.2: SCHEMA OF SOL-GEL FORMATION.....	19
FIGURE 2.3: THE FIRST TWO STEPS OF THE SOL-GEL PROCESS WITH AN ALKOXY SILANE	20
FIGURE 2.4: SILICA NANOWIRE SYNTHESIS BY THE TEMPLATED SOL-GEL METHOD	21
FIGURE 2.5: EMBEDDING SMALL NANOPARTICLES WITHIN THE LONGER 1D NANOWIRES.	23
FIGURE 2.6: MODEL OF IRON OXIDE PARTICLES AROUND A BISMUTH FERRITE CORE.....	24
FIGURE 2.7: SCATTERING OF X-RAYS BY SUCCESSIVE CRYSTAL PLANES	28
FIGURE 2.8: OPTICAL SETUP FOR HYPER RAYLEIGH SCATTERING MEASUREMENT.....	32
FIGURE 2.9: XRD PATTERNS OF Fe_3O_4	34
FIGURE 2.10: TEM IMAGE OF AGGREGATED Fe_3O_4 NPS.....	34
FIGURE 2.11: REPRESENTATIVE SIZE DISTRIBUTION HISTOGRAM OF Fe_3O_4 NPS.....	35
FIGURE 2.12: MAGNETIC HYSTERESIS CURVE OF Fe_3O_4 NPS IN AN APPLIED FIELD FROM -1 TO 1 TESLA	36
FIGURE 2.13: XRD PATTERNS OF BiFeO_3 SYNTHESIZED WITH CHELATING AGENTS OF INCREASING LENGTH	37
FIGURE 2.14: TEMPERATURE-RESOLVED XRD PATTERNS OF POWDER PREPARED WITHOUT AND WITH GLYCEROL	38
FIGURE 2.15: XRD PATTERNS OF BiFeO_3 SAMPLES WITHOUT AND WITH NaCl AND GLYCEROL ADDED TO THE PRECURSORS	39
FIGURE 2.16: TEM, HRTEM AND SAED PATTERNS OF BiFeO_3 PREPARED WITH AND WITHOUT NaCl	40
FIGURE 2.17: VSM MEASUREMENTS OF BiFeO_3 PREPARED VIA MA, MA + NaCl + GLYCEROL, AND MA + NaCl	41
FIGURE 2.18: DLS MEASUREMENTS OF BiFeO_3 PREPARED VIA MA + NaCl , SUSPENDED IN AQUEOUS SOLUTION AT PH 11 BEFORE AND AFTER SEDIMENTATION	42
FIGURE 2.19: HRS INTENSITY AS A FUNCTION OF RELATIVE CONCENTRATION	43
FIGURE 2.20: SECOND HARMONIC MICROSCOPY IMAGES OF BiFeO_3 NANOPARTICLE AGGREGATES IMMOBILIZED IN AGAROSE, WITH THE CORRESPONDING TWO-PHOTON EMISSION SPECTRA.....	45
FIGURE 2.21: SEM IMAGE OF SILICA NANOWIRES VIA AAO TEMPLATE SYNTHESIS.	46
FIGURE 2.22: TEM IMAGES OF ULTRA-SMALL Fe_3O_4 NPS EMBEDDED IN SILICA NANOWIRES	47
FIGURE 2.23: VSM OF SiO_2 NANOWIRES EMBEDDED WITH Fe_3O_4 IN AN APPLIED FIELD FROM -1 TO 1 TESLA	48
FIGURE 2.24: TEM IMAGE SHOWING IMPROVED LOADING OF Fe_3O_4 NP IN SiO_2 NW	49
FIGURE 2.25: MAGNETIC HYSTERESIS PLOT OF BARE Fe_3O_4 AND SiO_2 NANOWIRES PREPARED BY THE ONE-POT METHOD EMBEDDED WITH Fe_3O_4 IN AN APPLIED FIELD FROM -1 TO 1 TESLA.	49

FIGURE 2.26: TRANSMITTED LIGHT MICROSCOPY IMAGES OF SiO_2 NWS EMBEDDED WITH Fe_3O_4 NPS ALIGNED IN A MAGNETIC FIELD.	50
.....	50
FIGURE 2.27: TEM IMAGE OF BiFeO_3 NPS IN SiO_2 NWS.	51
FIGURE 2.28: MAGNETIC HYSTERESIS PLOT OF BARE BiFeO_3 NPS AND SiO_2 NWS EMBEDDED WITH BiFeO_3 NPS IN AN APPLIED FIELD FROM -1 TO 1 TESLA	51
.....	51
FIGURE 2.29: PHASE CONTRAST IMAGE OF SiO_2 NWS EMBEDDED WITH BiFeO_3 AND Fe_3O_4 NPS	52
FIGURE 2.30: TWO-PHOTON MICROSCOPY IMAGE OF SiO_2 NWS EMBEDDED WITH Fe_3O_4 AND BiFeO_3 NPS	53
FIGURE 2.31: X-RAY PATTERN OF $\text{BiFeO}_3@Fe_3O_4$ NPS	54
FIGURE 2.32: TEM AND HRTEM IMAGES OF $\text{BiFeO}_3@Fe_3O_4$ NPS	55
FIGURE 2.33: VSM MEASUREMENT OF Fe_3O_4 NPS AND $\text{BiFeO}_3@Fe_3O_4$ NPS IN AN APPLIED FIELD FROM -1 TO 1 TESLA	56
FIGURE 2.34: X-RAY DIFFRACTOMETER PATTERN OF $\text{BiFeO}_3@Fe_2O_3$ NPS	58
FIGURE 2.35: TEM AND HRTEM IMAGES OF $\text{BiFeO}_3@Fe_2O_3$ NPS	59
FIGURE 2.36: VSM MEASUREMENT OF Fe_2O_3 NPS AND $\text{BiFeO}_3@Fe_2O_3$ NPS IN AN APPLIED FIELD FROM -1 TO 1 TESLA	60
FIGURE 3.1: FUNCTIONALISATION OF A NANOPARTICLE WITH A TARGETING LIGAND	67
FIGURE 3.2: SIMPLIFIED SCHEMATIC ILLUSTRATION OF EGFR STIMULATION OF CELL CYCLE PROGRESSION AND ITS EFFECTS	70
FIGURE 3.3 SCHEMATIC FOR SURFACE MODIFICATION FUNCTIONALISATION OF BiFeO_3 NP	75
FIGURE 3.4: PREPARATION OF CELL LYSATES FOR COLORIMETRIC QUANTITATION OF IRON	78
FIGURE 3.5: FTIR SPECTRA OF APTES, BiFeO_3 FUNCTIONALISED WITH APTES, AND BARE BiFeO_3 NANOPARTICLES	83
FIGURE 3.6: Z-POTENTIAL VERSUS PH CURVES OF BARE AND COATED BiFeO_3 NANOPARTICLES	84
FIGURE 3.7: SIZE DISTRIBUTION HISTOGRAM OF BARE BiFeO_3 NANOPARTICLES DISPERSED IN DI WATER	85
FIGURE 3.8: SIZE DISTRIBUTION HISTOGRAM OF ASCORBIC ACID STABILISED $\text{BiFeO}_3@ASC$ NANOPARTICLES DISPERSED IN DI WATER	86
FIGURE 3.9: SIZE DISTRIBUTION HISTOGRAM OF $\text{BiFeO}_3@APTES$ NANOPARTICLES DISPERSED IN DI WATER	86
FIGURE 3.10: SIZE DISTRIBUTION HISTOGRAM OF $\text{BiFeO}_3@Fe_2O_3@ASC$ NANOPARTICLES DISPERSED IN DI WATER	87
FIGURE 3.11: SIZE DISTRIBUTION HISTOGRAM OF $\text{BiFeO}_3@Fe_3O_4@ASC$ NANOPARTICLES DISPERSED IN DI WATER	88
FIGURE 3.12: CONCENTRATION OF NANOPARTICLES AND COMPOSITES IN DI WATER	89
FIGURE 3.13: MODE DIAMETER OF NANOPARTICLES AND COMPOSITES IN DI WATER	90
FIGURE 3.14: MODE DIAMETER OF NANOPARTICLES AND COMPOSITES IN DMEM	91
FIGURE 3.15: SIZE DISTRIBUTIONS OF 10, 50 AND 90% MASS FRACTIONS OF BiFeO_3 NANOPARTICLES AND COMPOSITES	92
FIGURE 3.16: FLOW CYTOMETRY INDICATING BINDING OF ANTI-EGFR	93
FIGURE 3.17: EPIFLUORESCENCE IMAGE OF UNTREATED A549 CELLS	94
FIGURE 3.18: EPIFLUORESCENCE IMAGE OF A549 CELLS EXPOSED TO FLUORESCENTLY TAGGED, ANTI-EGFR FUNCTIONALISED BiFeO_3 NPS	95
.....	95
FIGURE 3.19: EPIFLUORESCENCE IMAGE OF NCI-H520 CELLS EXPOSED TO FLUORESCENTLY TAGGED, ANTI-EGFR FUNCTIONALISED BiFeO_3 NPS	97
.....	97

FIGURE 3.20: EPIFLUORESCENCE IMAGE OF A549 CELLS EXPOSED TO FLUORESCENTLY TAGGED, ANTI-EGFR FUNCTIONALISED BiFeO ₃ @Fe ₃ O ₄ NPs.....	98
FIGURE 3.21: IRON QUANTITATION CALIBRATION CURVE	99
FIGURE 3.22: CONCENTRATION OF IRON IN CELL LYSATES AFTER EXPOSURE TO NANOMATERIALS.....	100
FIGURE 3.23: ABSORBANCE OF A PROTEIN STANDARD WITH A DETECTION REAGENT AT 595 NM.....	101
FIGURE 3.24: CONCENTRATION OF PROTEIN IN A549 CELL LYSATES AFTER EXPOSURE TO VARIOUS NANOPARTICLES.....	102
FIGURE 3.25: CONCENTRATION OF IRON CONTENT IN A549 CELL LYSATE PROTEIN AFTER EXPOSURE TO VARIOUS NANOPARTICLES ..	103
FIGURE 3.26: EFFECT OF INHIBITOR ON CONCENTRATION OF IRON IN A549 CELL LYSATES ON EXPOSURE TO NANOPARTICLES	104
FIGURE 3.27: CELLULAR STAINING OF A549 CELLS AND LOCALISATION OF NANOPARTICLES AND COMPOSITES BY IRON OXIDE STAINING	105
FIGURE 3.28: CELLULAR STAINING OF A549 CELLS EXPOSED TO FUNCTIONALISED BiFeO ₃ AND BiFeO ₃ @Fe ₃ O ₄ NPs IN THE PRESENCE OF AN INHIBITOR	106
FIGURE 3.29: CONFOCAL Z-STACK SLICE OF A549 CELLS LABELLED WITH FLUORESCENTLY TAGGED ANTI-EGFR BiFeO ₃ NPs	107
FIGURE 4.1: 96-WELL PLATE LAYOUT FOR EXPOSURE OF CELLS TO BiFeO ₃ NPs AND BiFeO ₃ @ASC NPs.....	116
FIGURE 4.2: 96-WELL PLATE LAYOUT FOR EXPOSURE OF CELLS TO BiFeO ₃ @APTES NPs AND BiFeO ₃ @Fe ₂ O ₃ @ASC NPs	116
FIGURE 4.3: 96-WELL PLATE LAYOUT FOR EXPOSURE OF CELLS TO BiFeO ₃ @Fe ₃ O ₄ @APTES NPs AND BiFeO ₃ @Fe ₃ O ₄ @ASC NPs	117
FIGURE 4.4: 96-WELL PLATE LAYOUT FOR EXPOSURE OF CELLS TO SiO ₂ &BiFeO ₃ NWS AND SiO ₂ &BiFeO ₃ @Fe ₂ O ₃ @ASC NWS...	117
FIGURE 4.5: 96-WELL PLATE LAYOUT FOR EXPOSURE OF CELLS TO SiO ₂ &BiFeO ₃ @Fe ₂ O ₃ @ASC NWS AND CONTROLS	118
FIGURE 4.6: A549 CELLS, CELL COUNT CONTROLS.....	120
FIGURE 4.7: OVERVIEW OF CELL COUNT OF A549 CELLS EXPOSED TO CONTROLS	121
FIGURE 4.8: OVERVIEW OF CELL VIABILITY IN A549 CELLS EXPOSED TO CONTROLS.....	122
FIGURE 4.9: OVERVIEW OF LYSOSOMAL MASS/pH CHANGES IN A549 CELLS EXPOSED TO CONTROLS	123
FIGURE 4.10: OVERVIEW OF A549 CELL COUNT AFTER EXPOSURE TO EACH OF THE NANOPARTICLES	124
FIGURE 4.11: OVERVIEW OF CELL COUNT OF A549 CELLS AFTER EXPOSURE TO EACH OF THE NANOWIRES	126
FIGURE 4.12: OVERVIEW OF CELL VIABILITY IN A549 CELLS EXPOSED TO EACH OF THE NANOPARTICLES	127
FIGURE 4.13: OVERVIEW OF CELL VIABILITY IN A549 CELLS EXPOSED TO EACH OF THE NANOWIRES	128
FIGURE 4.14: OVERVIEW OF LYSOSOMAL MASS/pH CHANGES IN A549 CELLS EXPOSED TO EACH OF THE NANOPARTICLES	130
FIGURE 4.15: OVERVIEW OF LYSOSOMAL MASS/pH CHANGES IN A549 CELLS EXPOSED TO EACH OF THE NANOWIRES	131
FIGURE 4.16: HUVEC CELLS.....	133
FIGURE 4.17: OVERVIEW OF CELL COUNT OF HUVEC CELLS EXPOSED TO ASSORTED CONTROLS.	133
FIGURE 4.18: OVERVIEW OF CELL VIABILITY IN HUVEC CELLS EXPOSED TO CONTROLS.....	135
FIGURE 4.19: OVERVIEW OF LYSOSOMAL MASS/pH CHANGES IN HUVEC CELLS EXPOSED TO CONTROLS.....	136
FIGURE 4.20: OVERVIEW OF HUVEC CELL COUNT AFTER EXPOSURE TO EACH OF THE NANOPARTICLES	138
FIGURE 4.21: OVERVIEW OF CELL COUNT OF HUVEC CELLS AFTER EXPOSURE TO EACH OF THE NANOWIRES	140

FIGURE 4.22: OVERVIEW OF CELL VIABILITY IN HUVEC CELLS EXPOSED TO EACH OF THE NANOPARTICLES.....	141
FIGURE 4.23: OVERVIEW OF CELL VIABILITY IN HUVEC CELLS EXPOSED TO EACH OF THE NANOWIRES.....	143
FIGURE 4.24: OVERVIEW OF LYSOSOMAL MASS/pH CHANGES IN HUVEC CELLS EXPOSED TO EACH OF THE NANOPARTICLES.....	144
FIGURE 4.25: OVERVIEW OF LYSOSOMAL MASS/pH CHANGES IN HUVEC CELLS EXPOSED TO EACH OF THE NANOWIRES.....	145
FIGURE 5.1: PROOF-OF-PRINCIPLE OF MAGNETIC SEPARATION OF BiFeO ₃ @Fe ₃ O ₄ NANOCOMPOSITES FROM SUSPENSION IN WATER, FBS AND PLASMA	158
FIGURE 5.2: T ₂ AND T ₂ * RELAXATION TIMES OF NANOPARTICLE SUSPENSIONS	161
FIGURE 5.3: PHOTOSTABILITY AND OPTICAL TUNABILITY OF BiFeO ₃ @Fe ₂ O ₃ NPs.....	162
FIGURE 5.4: A549 CELLS AFTER 24H EXPOSURE TO ANTI-EGFR FUNCTIONALISED BiFeO ₃ @Fe ₂ O ₃ NPs IN THE PRESENCE OF AN INHIBITOR	163
FIGURE 5.5: CONFOCAL Z-STACK SLICE OF A549 CELLS LABELLED WITH FLUORESCENTLY TAGGED ANTI-EGFR BiFeO ₃ @Fe ₂ O ₃ NPs	164
FIGURE A.1: NUMBER OF MONOCYTE-DERIVED MACROPHAGES AFTER EXPOSURE TO EACH OF THE NANOMATERIALS.	187
FIGURE A.2: REDUCTION OF RESAZURIN DYE TO RESOFURIN IN MONOCYTE-DERIVED MACROPHAGES AFTER EXPOSURE TO EACH OF THE NANOMATERIALS.	188
FIGURE A.3: REPRESENTATIVE IMAGES OF MDMs TREATED WITH BiFeO ₃ NPs AT 80 MG/ML STAINED WITH HOECHST	189
FIGURE A.4: CELL COUNT OF MDMs AFTER TREATMENT WITH BARE BiFeO ₃ NPs AND THE CORRESPONDING 95% CONFIDENCE INTERVALS, COMPUTED FROM ORDINARY ONE-WAY ANOVA DUNNET ANALYSIS.	189
FIGURE A.5: METABOLIC ACTIVITY IN MDMs AFTER EXPOSURE TO BiFeO ₃ NPs.....	190
FIGURE A.6: REPRESENTATIVE IMAGES OF MDMs TREATED WITH ASCORBIC ACID-FUNCTIONALISED BiFeO ₃ NPs AT 80 MG/ML STAINED WITH HOECHST.....	191
FIGURE A.7: CELL COUNT OF MDMs AFTER TREATMENT WITH ASCORBIC ACID-FUNCTIONALISED BiFeO ₃ NPs AND THE CORRESPONDING 95% CONFIDENCE INTERVALS, COMPUTED FROM ORDINARY ONE-WAY ANOVA DUNNETT ANALYSIS.	192
FIGURE A.8: CELL COUNT OF MDMs AFTER TREATMENT WITH ASCORBIC ACID-FUNCTIONALISED BiFeO ₃ NPs AND THE CORRESPONDING 95% CONFIDENCE INTERVALS, COMPUTED FROM ORDINARY ONE-WAY ANOVA DUNNET ANALYSIS.....	193
FIGURE A.9: METABOLIC ACTIVITY IN MDMs AFTER EXPOSURE TO BiFeO ₃ @ASC NPs	194
FIGURE A.10: REPRESENTATIVE IMAGES OF MDMs TREATED WITH APS-FUNCTIONALISED BiFeO ₃ NPs AT 80 MG/ML STAINED WITH HOECHST.....	195
FIGURE A.11: CELL COUNT OF MDMs AFTER TREATMENT WITH APTES-COATED BiFeO ₃ NPs (BiFeO ₃ @APS) AND THE CORRESPONDING 95% CONFIDENCE INTERVALS BETWEEN THE GROUPS, COMPUTED FROM ORDINARY ONE-WAY ANOVA DUNNET ANALYSIS.	195
FIGURE A.12: METABOLIC ACTIVITY IN MDMs AFTER EXPOSURE TO BiFeO ₃ @APTES NPs.....	196
FIGURE A.13: REPRESENTATIVE IMAGES OF MDMs TREATED WITH BiFeO ₃ @Fe ₃ O ₄ @ASC NPs AT 80 MG/ML STAINED WITH HOECHST.....	197
FIGURE A.14: CELL COUNT OF MDMs AFTER TREATMENT WITH BiFeO ₃ @Fe ₃ O ₄ @ASC NPs AND THE CORRESPONDING 95% CONFIDENCE INTERVALS BETWEEN THE GROUPS, COMPUTED FROM ORDINARY ONE-WAY ANOVA DUNNET ANALYSIS.	197

FIGURE A.15: METABOLIC ACTIVITY IN MDMs AFTER EXPOSURE TO $\text{BiFeO}_3@Fe_3O_4@ASC$ NPs.....	198
FIGURE A.16: REPRESENTATIVE IMAGES OF MDMs TREATED WITH $\text{BiFeO}_3@Fe_3O_4@APTES$ NPs AT 80 MG/ML STAINED WITH HOECHST	199
FIGURE A.17: CELL COUNT OF MDMs AFTER TREATMENT WITH $\text{BiFeO}_3@Fe_3O_4@APTES$ NPs AND THE CORRESPONDING 95% CONFIDENCE INTERVALS BETWEEN THE GROUPS, COMPUTED FROM ORDINARY ONE-WAY ANOVA DUNNET ANALYSIS.....	200
FIGURE A.18: METABOLIC ACTIVITY IN MDMs AFTER EXPOSURE TO $\text{BiFeO}_3@Fe_3O_4@APTES$ NPs AND THE CORRESPONDING 95% CONFIDENCE INTERVALS	201
FIGURE A.19: REPRESENTATIVE IMAGES OF MDMs TREATED WITH $\text{BiFeO}_3@Fe_2O_3@ASC$ NPs AT 80 MG/ML STAINED WITH HOECHST	202
FIGURE A.20: CELL COUNT OF MDMs AFTER TREATMENT WITH $\text{BiFeO}_3@Fe_2O_3@ASC$ NPs AND THE CORRESPONDING 95% CONFIDENCE INTERVALS BETWEEN THE GROUPS, COMPUTED FROM ORDINARY ONE-WAY ANOVA DUNNET ANALYSIS.....	202
FIGURE A.21: METABOLIC ACTIVITY IN MDMs AFTER EXPOSURE TO $\text{BiFeO}_3@Fe_2O_3@ASC$ NPs.....	203
FIGURE A.22: REPRESENTATIVE IMAGES OF MDMs TREATED WITH $\text{SiO}_2\&\text{BiFeO}_3$ NWS AT 80 MG/ML STAINED WITH HOECHST ..	204
FIGURE A.23: CELL COUNT OF MDMs AFTER TREATMENT WITH $\text{SiO}_2\&\text{BiFeO}_3$ NWS AND THE CORRESPONDING 95% CONFIDENCE INTERVALS BETWEEN THE GROUPS, COMPUTED FROM ORDINARY ONE-WAY ANOVA DUNNET ANALYSIS.....	204
FIGURE A.24: METABOLIC ACTIVITY IN MDMs AFTER EXPOSURE TO $\text{SiO}_2\&\text{BiFeO}_3$ NWS	205
FIGURE A.25: REPRESENTATIVE IMAGES OF MDMs TREATED WITH $\text{SiO}_2\&\text{BiFeO}_3@Fe_3O_4$ NWS AT 80 MG/ML STAINED WITH HOECHST	206
FIGURE A.26: CELL COUNT OF MDMs AFTER TREATMENT WITH $\text{SiO}_2\&\text{BiFeO}_3@Fe_3O_4$ NWS AND THE CORRESPONDING 95% CONFIDENCE INTERVALS BETWEEN THE GROUPS, COMPUTED FROM ORDINARY ONE-WAY ANOVA DUNNET ANALYSIS.....	206
FIGURE A.27: METABOLIC ACTIVITY IN MDMs AFTER EXPOSURE TO $\text{SiO}_2\&\text{BiFeO}_3@Fe_2O_3$ NWS.....	207
FIGURE A.28: REPRESENTATIVE IMAGES OF MDMs TREATED WITH $\text{SiO}_2\&\text{BiFeO}_3@Fe_2O_3$ NWS AT 80 MG/ML STAINED WITH HOECHST	208
FIGURE A.29: CELL COUNT OF MDMs AFTER TREATMENT WITH $\text{SiO}_2\&\text{BiFeO}_3@Fe_2O_3$ NWS AND THE CORRESPONDING 95% CONFIDENCE INTERVALS BETWEEN THE GROUPS, COMPUTED FROM ORDINARY ONE-WAY ANOVA DUNNET ANALYSIS.....	208
FIGURE A.30: METABOLIC ACTIVITY IN A549 CELLS AFTER EXPOSURE TO $\text{SiO}_2\&\text{BiFeO}_3@Fe_2O_3$ NWS	209
FIGURE A.31: HCS IMAGES OF A549 CELLS AFTER 48H EXPOSURE TO BiFeO_3 NPs AT 80 MG/ML	210
FIGURE A.32: A549 CELLS EXPOSED TO BiFeO_3 NPs, STAINED FOR DNA.....	210
FIGURE A.33: CELL COUNT OF A549 CELLS AFTER TREATMENT WITH BiFeO_3 NPs AND THE CORRESPONDING 95% CONFIDENCE INTERVALS	211
FIGURE A.34: A549 CELLS EXPOSED TO BiFeO_3 NPs, STAINED FOR CELL MEMBRANE PERMEABILITY	212
FIGURE A.35: CELL VIABILITY OF A549 CELLS AFTER TREATMENT WITH BiFeO_3 NPs AND THE CORRESPONDING 95% CONFIDENCE INTERVALS	212
FIGURE A.36: A549 CELLS EXPOSED TO BiFeO_3 NPs, STAINED FOR LYSOSOMAL MASS/PH CHANGES.....	213

FIGURE A.37: LYSOSOMAL MASS/PH CHANGES IN A549 CELLS AFTER TREATMENT WITH BiFeO ₃ NPs AND THE CORRESPONDING 95% CONFIDENCE INTERVALS	213
FIGURE A.38: HCS IMAGES OF A549 CELLS AFTER 48H EXPOSURE TO BiFeO ₃ @ASC NPs AT 80 MG/ML	214
FIGURE A.39: A549 CELLS EXPOSED TO BiFeO ₃ @ASC NPs, STAINED FOR DNA.....	215
FIGURE A.40: CELL COUNT OF A549 CELLS AFTER TREATMENT WITH BiFeO ₃ @ASC NPs AND THE CORRESPONDING 95% CONFIDENCE INTERVALS	215
FIGURE A.41: A549 CELLS EXPOSED TO BiFeO ₃ @ASC NPs, STAINED FOR CELL MEMBRANE PERMEABILITY	216
FIGURE A.42: CELL VIABILITY OF A549 CELLS AFTER TREATMENT WITH BiFeO ₃ @ASC NPs AND THE CORRESPONDING 95% CONFIDENCE INTERVALS	216
FIGURE A.43: A549 CELLS EXPOSED TO BiFeO ₃ @ASC NPs, STAINED FOR LYSOSOMAL MASS/PH CHANGES.....	217
FIGURE A.44: LYSOSOMAL MASS/PH CHANGES IN A549 CELLS AFTER TREATMENT WITH BiFeO ₃ @ASC NPs AND THE CORRESPONDING 95% CONFIDENCE INTERVALS	217
FIGURE A.45: HCS IMAGES OF A549 CELLS AFTER 48H EXPOSURE TO BiFeO ₃ @PTES NPs AT 80 MG/ML	218
FIGURE A.46: A549 CELLS EXPOSED TO BiFeO ₃ @PTES NPs, STAINED FOR DNA	219
FIGURE A.47: CELL COUNT OF A549 CELLS AFTER TREATMENT WITH BiFeO ₃ @PTES NPs AND THE CORRESPONDING 95% CONFIDENCE INTERVALS	220
FIGURE A.48: A549 CELLS EXPOSED TO BiFeO ₃ @PTES NPs, STAINED FOR CELL MEMBRANE PERMEABILITY	221
FIGURE A.49: CELL VIABILITY OF A549 CELLS AFTER TREATMENT WITH BiFeO ₃ @PTES NPs AND THE CORRESPONDING 95% CONFIDENCE INTERVALS	221
FIGURE A.50: A549 CELLS EXPOSED TO BiFeO ₃ @PTES NPs, STAINED FOR LYSOSOMAL MASS/PH CHANGES	222
FIGURE A.51: LYSOSOMAL MASS/PH CHANGES IN A549 CELLS AFTER TREATMENT WITH BiFeO ₃ @PTES NPs AND THE CORRESPONDING 95% CONFIDENCE INTERVALS.....	222
FIGURE A.52: HCS IMAGES OF A549 CELLS AFTER 48H EXPOSURE TO BiFeO ₃ @Fe ₃ O ₄ @ASC NPs AT 80 MG/ML	223
FIGURE A.53: REPRESENTATIVE CELL COUNT IMAGES OF A549 CELLS EXPOSED TO BiFeO ₃ @Fe ₃ O ₄ @ASC NPs, STAINED FOR DNA	224
FIGURE A.54: CELL COUNT OF A549 CELLS AFTER TREATMENT WITH BiFeO ₃ @Fe ₃ O ₄ @ASC NPs AND THE CORRESPONDING 95% CONFIDENCE INTERVALS	224
FIGURE A.55: A549 CELLS EXPOSED TO BiFeO ₃ @Fe ₃ O ₄ @ASC NPs, STAINED FOR CELL MEMBRANE PERMEABILITY	225
FIGURE A.56: CELL VIABILITY OF A549 CELLS AFTER TREATMENT WITH BiFeO ₃ @Fe ₃ O ₄ @ASC NPs AND THE CORRESPONDING 95% CONFIDENCE INTERVALS	226
FIGURE A.57: A549 CELLS EXPOSED TO BiFeO ₃ @Fe ₃ O ₄ @ASC NPs, STAINED FOR LYSOSOMAL MASS/PH CHANGES	226
FIGURE A.58: LYSOSOMAL MASS/PH CHANGES IN A549 CELLS AFTER TREATMENT WITH BiFeO ₃ @Fe ₃ O ₄ @ASC NPs AND THE CORRESPONDING 95% CONFIDENCE INTERVALS.....	227
FIGURE A.59: HCS IMAGES OF A549 CELLS AFTER 48H EXPOSURE TO BiFeO ₃ @Fe ₃ O ₄ @PTES NPs AT 80 MG/ML.....	228
FIGURE A.60: A549 CELLS EXPOSED TO BiFeO ₃ @Fe ₃ O ₄ @PTES NPs, STAINED FOR DNA	228

FIGURE A.61: CELL COUNT OF A549 CELLS AFTER TREATMENT WITH BiFeO ₃ @Fe ₃ O ₄ @APTES NPs AND THE CORRESPONDING 95% CONFIDENCE INTERVALS	229
FIGURE A.62: A549 CELLS EXPOSED TO BiFeO ₃ @Fe ₃ O ₄ @APTES NPs, STAINED FOR CELL MEMBRANE PERMEABILITY	229
FIGURE A.63: CELL VIABILITY OF A549 CELLS AFTER TREATMENT WITH BiFeO ₃ @Fe ₃ O ₄ @APTES NPs AND THE CORRESPONDING 95% CONFIDENCE INTERVALS	230
FIGURE A.64: A549 CELLS EXPOSED TO BiFeO ₃ @Fe ₃ O ₄ @APTES NPs, STAINED FOR LYSOSOMAL MASS/PH CHANGES	231
FIGURE A.65: LYSOSOMAL MASS/PH CHANGES IN A549 CELLS AFTER TREATMENT WITH BiFeO ₃ @Fe ₃ O ₄ @APTES NPs AND THE CORRESPONDING 95% CONFIDENCE INTERVALS.....	231
FIGURE A.66: HCS IMAGES OF A549 CELLS AFTER 48H EXPOSURE TO BiFeO ₃ @Fe ₂ O ₃ @ASC NPs AT 80 MG/ML	232
FIGURE A.67: A549 CELLS EXPOSED TO BiFeO ₃ @Fe ₂ O ₃ @ASC NPs, STAINED FOR DNA	233
FIGURE A.68: CELL COUNT OF A549 CELLS AFTER TREATMENT WITH BiFeO ₃ @Fe ₂ O ₃ @ASC NPs AND THE CORRESPONDING 95% CONFIDENCE INTERVALS	233
FIGURE A.69: A549 CELLS EXPOSED TO BiFeO ₃ @Fe ₂ O ₃ @ASC NPs, STAINED FOR CELL MEMBRANE PERMEABILITY	234
FIGURE A.70: CELL VIABILITY OF A549 CELLS AFTER TREATMENT WITH BiFeO ₃ @Fe ₂ O ₃ @ASC NPs AND THE CORRESPONDING 95% CONFIDENCE INTERVALS	234
FIGURE A.71: A549 CELLS EXPOSED TO BiFeO ₃ @Fe ₂ O ₃ @ASC NPs, STAINED FOR LYSOSOMAL MASS/PH CHANGES	235
FIGURE A.72: LYSOSOMAL MASS/PH CHANGES IN A549 CELLS AFTER TREATMENT WITH BiFeO ₃ @Fe ₂ O ₃ @ASC NPs AND THE CORRESPONDING 95% CONFIDENCE INTERVALS.....	235
FIGURE A.73: HCS IMAGES OF A549 CELLS AFTER 48H EXPOSURE TO SiO ₂ & BiFeO ₃ NWS AT 80 MG/ML	237
FIGURE A.74: A549 CELLS EXPOSED TO SiO ₂ & BiFeO ₃ NWS, STAINED FOR DNA	237
FIGURE A.75: CELL COUNT OF A549 CELLS AFTER TREATMENT WITH SiO ₂ & BiFeO ₃ NWS AND THE CORRESPONDING 95% CONFIDENCE INTERVALS	238
FIGURE A.76: A549 CELLS EXPOSED TO SiO ₂ & BiFeO ₃ NWS STAINED FOR CELL MEMBRANE PERMEABILITY	238
FIGURE A.77: CELL VIABILITY OF A549 CELLS AFTER TREATMENT WITH SiO ₂ & BiFeO ₃ NWS AND THE CORRESPONDING 95% CONFIDENCE INTERVALS	239
FIGURE A.78: A549 CELLS EXPOSED TO SiO ₂ & BiFeO ₃ NWS STAINED FOR LYSOSOMAL MASS/PH CHANGES	240
FIGURE A.79: LYSOSOMAL MASS/PH CHANGES IN A549 CELLS AFTER TREATMENT WITH SiO ₂ & BiFeO ₃ NWS AND THE CORRESPONDING 95% CONFIDENCE INTERVALS.....	240
FIGURE A.80: HCS IMAGES OF A549 CELLS AFTER 48H EXPOSURE TO SiO ₂ & BiFeO ₃ @Fe ₃ O ₄ NWS AT 80 MG/ML.....	241
FIGURE A.81: A549 CELLS EXPOSED TO SiO ₂ & BiFeO ₃ @Fe ₃ O ₄ NWS STAINED FOR DNA.....	241
FIGURE A.82: CELL COUNT OF A549 CELLS AFTER TREATMENT WITH SiO ₂ & BiFeO ₃ @Fe ₃ O ₄ NWS AND THE CORRESPONDING 95% CONFIDENCE INTERVALS	242
FIGURE A.83: A549 CELLS EXPOSED TO SiO ₂ & BiFeO ₃ @Fe ₃ O ₄ NWS STAINED FOR CELL MEMBRANE PERMEABILITY	242
FIGURE A.84: CELL VIABILITY OF A549 CELLS AFTER TREATMENT WITH SiO ₂ & BiFeO ₃ @Fe ₃ O ₄ NWS AND THE CORRESPONDING 95% CONFIDENCE INTERVALS	243

FIGURE A.85: A549 CELLS EXPOSED TO SiO ₂ & BiFeO ₃ @Fe ₃ O ₄ NWS STAINED FOR LYSOSOMAL MASS/PH CHANGES.....	243
FIGURE A.86: LYSOSOMAL MASS/PH CHANGES IN A549 CELLS AFTER TREATMENT WITH SiO ₂ & BiFeO ₃ @Fe ₃ O ₄ NWS AND THE CORRESPONDING 95% CONFIDENCE INTERVALS.....	244
FIGURE A.87: HCS IMAGES OF A549 CELLS AFTER 48H EXPOSURE TO SiO ₂ & BiFeO ₃ @Fe ₂ O ₃ NWS AT 80 MG/ML.....	245
FIGURE A.88: A549 CELLS EXPOSED TO SiO ₂ & BiFeO ₃ @Fe ₂ O ₃ NWS STAINED FOR DNA.....	245
FIGURE A.89: CELL COUNT OF A549 CELLS AFTER TREATMENT WITH SiO ₂ & BiFeO ₃ @Fe ₂ O ₃ NWS AND THE CORRESPONDING 95% CONFIDENCE INTERVALS	246
FIGURE A.90: A549 CELLS EXPOSED TO SiO ₂ & BiFeO ₃ @Fe ₂ O ₃ NWS STAINED FOR CELL MEMBRANE PERMEABILITY.....	246
FIGURE A.91: CELL VIABILITY OF A549 CELLS AFTER TREATMENT WITH SiO ₂ & BiFeO ₃ @Fe ₂ O ₃ NWS AND THE CORRESPONDING 95% CONFIDENCE INTERVALS	247
FIGURE A.92: A549 CELLS EXPOSED TO SiO ₂ & BiFeO ₃ @Fe ₂ O ₃ NWS STAINED FOR LYSOSOMAL MASS/PH CHANGES.....	247
FIGURE A.93: LYSOSOMAL MASS/PH CHANGES IN A549 CELLS AFTER TREATMENT WITH SiO ₂ & BiFeO ₃ @Fe ₂ O ₃ NWS AND THE CORRESPONDING 95% CONFIDENCE INTERVALS.....	248
FIGURE A.94: HCS IMAGES OF HUVEC CELLS AFTER 48H EXPOSURE TO BiFeO ₃ NPs AT 80 MG/ML	249
FIGURE A.95: HUVEC CELLS EXPOSED TO BiFeO ₃ NPs, STAINED FOR DNA	250
FIGURE A.96: CELL COUNT OF HUVEC CELLS AFTER TREATMENT WITH BiFeO ₃ NPs AND THE CORRESPONDING 95% CONFIDENCE INTERVALS	250
FIGURE A.97: HUVEC CELLS EXPOSED TO BiFeO ₃ NPs, STAINED FOR CELL MEMBRANE PERMEABILITY	251
FIGURE A.98: CELL VIABILITY OF HUVEC CELLS AFTER TREATMENT WITH BiFeO ₃ NPs AND THE CORRESPONDING 95% CONFIDENCE INTERVALS	251
FIGURE A.99: HUVEC CELLS EXPOSED TO BiFeO ₃ NPs, STAINED FOR LYSOSOMAL MASS/PH CHANGES	252
FIGURE A.100: LYSOSOMAL MASS/PH CHANGES IN HUVEC CELLS AFTER TREATMENT WITH BiFeO ₃ NPs AND THE CORRESPONDING 95% CONFIDENCE INTERVALS	253
FIGURE A.101: HCS IMAGES OF HUVEC CELLS AFTER 48H EXPOSURE TO BiFeO ₃ @ASC NPs AT 80 MG/ML	253
FIGURE A.102: HUVEC CELLS EXPOSED TO BiFeO ₃ @ASC NPs, STAINED FOR DNA	254
FIGURE A.103: CELL COUNT OF HUVEC CELLS AFTER TREATMENT WITH BiFeO ₃ @ASC NPs AND THE CORRESPONDING 95% CONFIDENCE INTERVALS	255
FIGURE A.104: HUVEC CELLS EXPOSED TO BiFeO ₃ @ASC NPs, STAINED FOR CELL MEMBRANE PERMEABILITY	256
FIGURE A.105: CELL VIABILITY OF HUVEC CELLS AFTER TREATMENT WITH BiFeO ₃ @ASC NPs AND THE CORRESPONDING 95% CONFIDENCE INTERVALS	256
FIGURE A.106: HUVEC CELLS EXPOSED TO BiFeO ₃ @ASC NPs, STAINED FOR LYSOSOMAL MASS/PH CHANGES	257
FIGURE A.107: LYSOSOMAL MASS/PH CHANGES IN HUVEC CELLS AFTER TREATMENT WITH BiFeO ₃ @ASC NPs AND THE CORRESPONDING 95% CONFIDENCE INTERVALS.....	258
FIGURE A.108: HCS IMAGES OF HUVEC CELLS AFTER 48H EXPOSURE TO BiFeO ₃ @APTES NPs AT 80 MG/ML	258
FIGURE A.109: HUVEC CELLS EXPOSED TO BiFeO ₃ @APTES NPs, STAINED FOR DNA	259

FIGURE A.110: CELL COUNT OF HUVEC CELLS AFTER TREATMENT WITH BiFeO ₃ @APTES NPs AND THE CORRESPONDING 95% CONFIDENCE INTERVALS	260
FIGURE A.111: HUVEC CELLS EXPOSED TO BiFeO ₃ @APTES NPs, STAINED FOR CELL MEMBRANE PERMEABILITY	260
FIGURE A.112: CELL VIABILITY OF HUVEC CELLS AFTER TREATMENT WITH BiFeO ₃ @APTES NPs AND THE CORRESPONDING 95% CONFIDENCE INTERVALS	261
FIGURE A.113: HUVEC CELLS EXPOSED TO BiFeO ₃ @APTES NPs, STAINED FOR LYSOSOMAL MASS/PH CHANGES	262
FIGURE A.114: LYSOSOMAL MASS/PH CHANGES IN HUVEC CELLS AFTER TREATMENT WITH BiFeO ₃ @APTES NPs AND THE CORRESPONDING 95% CONFIDENCE INTERVALS.....	262
FIGURE A.115: HCS IMAGES OF HUVEC CELLS AFTER 48H EXPOSURE TO BiFeO ₃ @Fe ₃ O ₄ @ASC NPs AT 80 MG/ML	263
FIGURE A.116: HUVEC CELLS EXPOSED TO BiFeO ₃ @Fe ₃ O ₄ @ASC NPs, STAINED FOR DNA	264
FIGURE A.117: CELL COUNT OF HUVEC CELLS AFTER TREATMENT WITH BiFeO ₃ @Fe ₃ O ₄ @ASC NPs AND THE CORRESPONDING 95% CONFIDENCE INTERVALS	264
FIGURE A.118: HUVEC CELLS EXPOSED TO BiFeO ₃ @Fe ₃ O ₄ @ASC NPs, STAINED FOR CELL MEMBRANE PERMEABILITY	265
FIGURE A.119: CELL VIABILITY OF HUVEC CELLS AFTER TREATMENT WITH BiFeO ₃ @Fe ₃ O ₄ @ASC NPs AND THE CORRESPONDING 95% CONFIDENCE INTERVALS	266
FIGURE A.120: HUVEC CELLS EXPOSED TO BiFeO ₃ @Fe ₃ O ₄ @ASC NPs, STAINED FOR LYSOSOMAL MASS/PH CHANGES	267
FIGURE A.121: LYSOSOMAL MASS/PH CHANGES IN HUVEC CELLS AFTER TREATMENT WITH BiFeO ₃ @Fe ₃ O ₄ @ASC NPs AND THE CORRESPONDING 95% CONFIDENCE INTERVALS.....	267
FIGURE A.122: HCS IMAGES OF HUVEC CELLS AFTER 48H EXPOSURE TO BiFeO ₃ @Fe ₃ O ₄ @APTES NPs AT 80 MG/ML.....	268
FIGURE A.123: HUVEC CELLS EXPOSED TO BiFeO ₃ @Fe ₃ O ₄ @APTES NPs, STAINED FOR DNA	269
FIGURE A.124: CELL COUNT OF HUVEC CELLS AFTER TREATMENT WITH BiFeO ₃ @Fe ₃ O ₄ @APTES NPs AND THE CORRESPONDING 95% CONFIDENCE INTERVALS	269
FIGURE A.125: HUVEC CELLS EXPOSED TO BiFeO ₃ @Fe ₃ O ₄ @APTES NPs, STAINED FOR CELL MEMBRANE PERMEABILITY	270
FIGURE A.126: CELL VIABILITY OF HUVEC CELLS AFTER TREATMENT WITH BiFeO ₃ @Fe ₃ O ₄ @APTES NPs AND THE CORRESPONDING 95% CONFIDENCE INTERVALS	270
FIGURE A.127: HUVEC CELLS EXPOSED TO BiFeO ₃ @Fe ₃ O ₄ @APTES NPs, STAINED FOR LYSOSOMAL MASS/PH CHANGES	271
FIGURE A.128: LYSOSOMAL MASS/PH CHANGES IN HUVEC CELLS AFTER TREATMENT WITH BiFeO ₃ @Fe ₃ O ₄ @APTES NPs AND THE CORRESPONDING 95% CONFIDENCE INTERVALS.....	271
FIGURE A.129: HCS IMAGES OF HUVEC CELLS AFTER 48H EXPOSURE TO BiFeO ₃ @Fe ₂ O ₃ @ASC NPs AT 80 MG/ML	272
FIGURE A.130: HUVEC CELLS EXPOSED TO BiFeO ₃ @Fe ₂ O ₃ @ASC NPs, STAINED FOR DNA	273
FIGURE A.131: CELL COUNT OF HUVEC CELLS AFTER TREATMENT WITH BiFeO ₃ @Fe ₂ O ₃ @ASC NPs AND THE CORRESPONDING 95% CONFIDENCE INTERVALS	273
FIGURE A.132: HUVEC CELLS EXPOSED TO BiFeO ₃ @Fe ₂ O ₃ @ASC NPs, STAINED FOR CELL MEMBRANE PERMEABILITY	274
FIGURE A.133: CELL VIABILITY OF HUVEC CELLS AFTER TREATMENT WITH BiFeO ₃ @Fe ₂ O ₃ @ASC NPs AND THE CORRESPONDING 95% CONFIDENCE INTERVALS	274

FIGURE A.134: HUVEC CELLS EXPOSED TO $\text{BiFeO}_3@Fe_2O_3@ASC$ NPS, STAINED FOR LYSOSOMAL MASS/PH CHANGES	275
FIGURE A.135: LYSOSOMAL MASS/PH CHANGES IN HUVEC CELLS AFTER TREATMENT WITH $\text{BiFeO}_3@Fe_2O_3@ASC$ NPS AND THE CORRESPONDING 95% CONFIDENCE INTERVALS.....	275
FIGURE A.136: HCS IMAGES OF HUVEC CELLS AFTER 48H EXPOSURE TO SiO_2 & BiFeO_3 NWS AT 80 MG/ML.....	276
FIGURE A.137: HUVEC CELLS EXPOSED TO SiO_2 & BiFeO_3 NWS STAINED FOR DNA	277
FIGURE A.138: CELL COUNT OF HUVEC CELLS AFTER TREATMENT WITH SiO_2 & BiFeO_3 NWS AND THE CORRESPONDING 95% CONFIDENCE INTERVALS	277
FIGURE A.139: HUVEC CELLS EXPOSED TO SiO_2 & BiFeO_3 NWS STAINED FOR CELL MEMBRANE PERMEABILITY	278
FIGURE A.140: CELL VIABILITY OF HUVEC CELLS AFTER TREATMENT WITH SiO_2 & BiFeO_3 NWS AND THE CORRESPONDING 95% CONFIDENCE INTERVALS	278
FIGURE A.141: HUVEC CELLS EXPOSED TO SiO_2 & BiFeO_3 NWS STAINED FOR LYSOSOMAL MASS/PH CHANGES	279
FIGURE A.142: LYSOSOMAL MASS/PH CHANGES IN HUVEC CELLS AFTER TREATMENT WITH SiO_2 & BiFeO_3 NWS AND THE CORRESPONDING 95% CONFIDENCE INTERVALS.....	280
FIGURE A.143: HCS IMAGES OF HUVEC CELLS AFTER 48H EXPOSURE TO SiO_2 & $\text{BiFeO}_3@Fe_3O_4$ NWS AT 80 MG/ML	281
FIGURE A.144: HUVEC CELLS EXPOSED TO SiO_2 & $\text{BiFeO}_3@Fe_3O_4$ NWS STAINED FOR DNA.....	281
FIGURE A.145: CELL COUNT OF HUVEC CELLS AFTER TREATMENT WITH SiO_2 & $\text{BiFeO}_3@Fe_3O_4$ NWS AND THE CORRESPONDING 95% CONFIDENCE INTERVALS	282
FIGURE A.146: HUVEC CELLS EXPOSED TO SiO_2 & $\text{BiFeO}_3@Fe_3O_4$ NWS STAINED FOR CELL MEMBRANE PERMEABILITY.....	282
FIGURE A.147: CELL VIABILITY OF HUVEC CELLS AFTER TREATMENT WITH SiO_2 & $\text{BiFeO}_3@Fe_3O_4$ NWS AND THE CORRESPONDING 95% CONFIDENCE INTERVALS	283
FIGURE A.148: HUVEC CELLS EXPOSED TO SiO_2 & $\text{BiFeO}_3@Fe_3O_4$ NWS STAINED FOR LYSOSOMAL MASS/PH CHANGES.....	283
FIGURE A.149: LYSOSOMAL MASS/PH CHANGES IN HUVEC CELLS AFTER TREATMENT WITH SiO_2 & $\text{BiFeO}_3@Fe_3O_4$ NWS AND THE CORRESPONDING 95% CONFIDENCE INTERVALS.....	284
FIGURE A.150: HCS IMAGES OF HUVEC CELLS AFTER 48H EXPOSURE TO SiO_2 & $\text{BiFeO}_3@Fe_2O_3$ NWS AT 80 MG/ML	285
FIGURE A.151: HUVEC CELLS EXPOSED TO SiO_2 & $\text{BiFeO}_3@Fe_2O_3$ NWS STAINED FOR DNA.....	286
FIGURE A.152: CELL COUNT OF HUVEC CELLS AFTER TREATMENT WITH SiO_2 & $\text{BiFeO}_3@Fe_2O_3$ NWS AND THE CORRESPONDING 95% CONFIDENCE INTERVALS	286
FIGURE A.153: HUVEC CELLS EXPOSED TO SiO_2 & $\text{BiFeO}_3@Fe_2O_3$ NWS STAINED FOR CELL MEMBRANE PERMEABILITY.....	287
FIGURE A.154: CELL VIABILITY OF HUVEC CELLS AFTER TREATMENT WITH SiO_2 & $\text{BiFeO}_3@Fe_2O_3$ NWS AND THE CORRESPONDING 95% CONFIDENCE INTERVALS	287
FIGURE A.155: HUVEC CELLS EXPOSED TO SiO_2 & $\text{BiFeO}_3@Fe_2O_3$ NWS STAINED FOR LYSOSOMAL MASS/PH CHANGES.....	288
FIGURE A.156: LYSOSOMAL MASS/PH CHANGES IN HUVEC CELLS AFTER TREATMENT WITH SiO_2 & $\text{BiFeO}_3@Fe_2O_3$ NWS AND THE CORRESPONDING 95% CONFIDENCE INTERVALS.....	288

Publications and Presentations arising from this work

- **Clarke, G.**; Rogov, A.; McCarthy, S.; Bonacina, L.; Gun'ko, Y.; Galez, C.; Dantec, R. L.; Volkov, Y.; Mugnier, Y.; Prina-Mello, A. Preparation from a Revisited Wet Chemical Route of Phase-Pure, Monocrystalline and SHG-Efficient BiFeO₃ Nanoparticles for Harmonic Bio-Imaging. *Sci. Rep.* **2018**, *8* (1), 10473. <https://doi.org/10.1038/s41598-018-28557-w>.
- **Clarke, G.**; Mugnier, Y.; Le Dantec, R.; Gunko, Y. K.; Rytz, D.; Galez, C.; M. Volkov, Y.; Prina-Mello, A. Phase Pure, Monocrystalline Bismuth Ferrite Nanoparticles for Biomedical Applications. In *European Conference on Application of Polar Dielectrics*; Vilnius, Lithuania, 2014.
- Tytus, T.; Phelan, O.; Urbain, M.; **Clarke, G.**; Riporto, J.; Le Dantec, R.; Djanta, G.; Beauquis, S.; Monnier, V.; Chevotot, Y.; et al. Preparation and Preliminary Nonlinear Optical Properties of BiFeO₃ Nanocrystal Suspensions from a Simple, Chelating Agent-Free Precipitation Route. *J. Nanomater.* **2018**, *2018*, 1–9. <https://doi.org/10.1155/2018/3019586>.
- Staedler, D.; Magouroux, T.; Hadji, R.; Joulaud, C.; Extermann, J.; Schwung, S.; Passemard, S.; Kasparian, C.; **Clarke, G.**; Gerrmann, M.; et al. Harmonic Nanocrystals for Biolabeling: A Survey of Optical Properties and Biocompatibility. *ACS Nano* **2012**, *6* (3), 2542–2549. <https://doi.org/10.1021/nn204990n>.
- Schwung, S.; Rogov, A.; **Clarke, G.**; Joulaud, C.; Magouroux, T.; Staedler, D.; Passemard, S.; Jüstel, T.; Badie, L.; Galez, C.; et al. Nonlinear Optical and Magnetic Properties of BiFeO₃ Harmonic Nanoparticles. *J. Appl. Phys.* **2014**, *116* (11), 114306. <https://doi.org/10.1063/1.4895836>.
- Baird, A.; Easty, D.; Mohamed, B. M.; Jarzabek, M.; Shiels, L.; Soltermann, A.; Raeppl, S.; McDonagh, L.; **Clarke, G.**; Crosbie-Staunton, K.; et al. Multiple RTK Targeting as a Therapeutic Option in Malignant Pleural Mesothelioma. In *Lung Cancer*; Dublin, Ireland, 2017; Vol. 103, p S26.

Chapter 1

Introduction

1.1 Aims and Research Questions

The aim of this study is to develop novel nanomaterials for *in vitro* imaging applications which can overcome the limitations of conventional imaging probes by combining harmonic nanocrystals with superparamagnetic nanoparticles (NPs) in a multimodal/multifunctional diagnostic tool.

Several sub-tasks were identified to reach this aim as outlined in Figure 1.1 and summarised below.

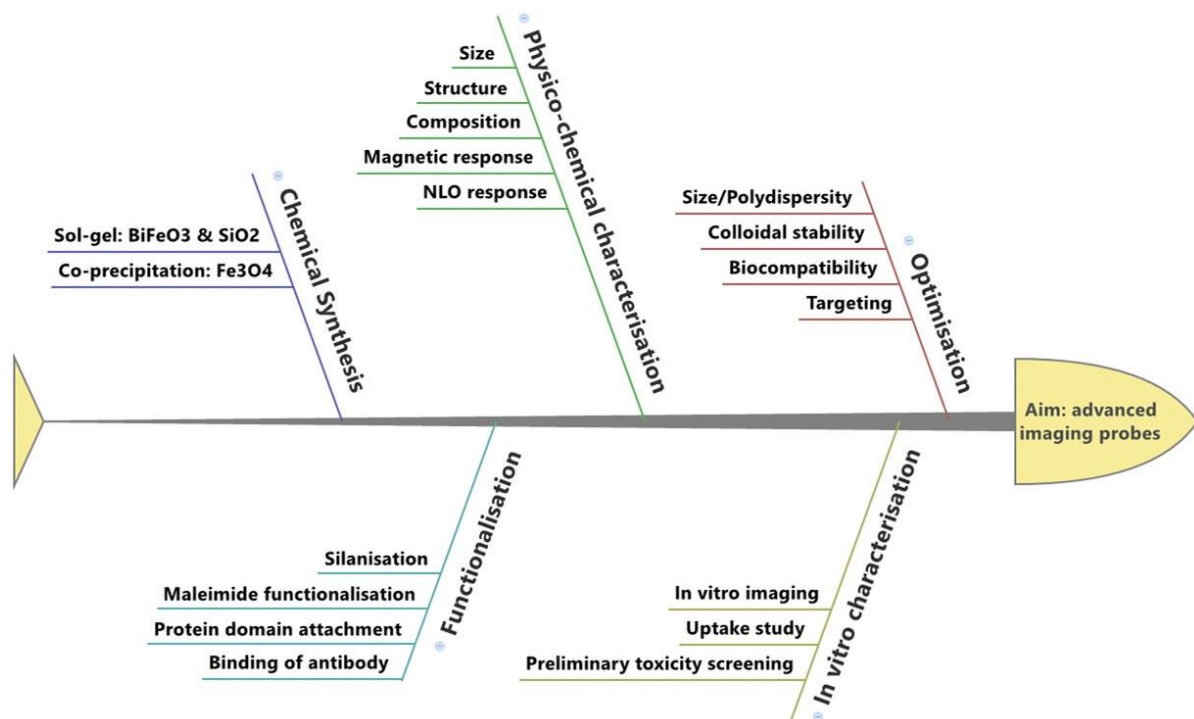


Figure 1.1: Schema showing the breakdown of the research tasks.

- ❖ Nanomaterial synthesis
- ❖ Functionalisation of BiFeO₃ NPs and composites
- ❖ Physico-chemical characterisation of ex-synthesis and functionalised nanomaterials
- ❖ *In vitro* characterisation and safety assessment
- ❖ Proof-of-concept of multimodality for clinical diagnostic application

1.2 Nanomaterials: nanoparticles, nanowires, nanosheets, nanocomposites

The prefix “nano” applies to anything with active features below 100 nm, i.e. smaller than 100 nm in at least one dimension (see Figure 1.2).

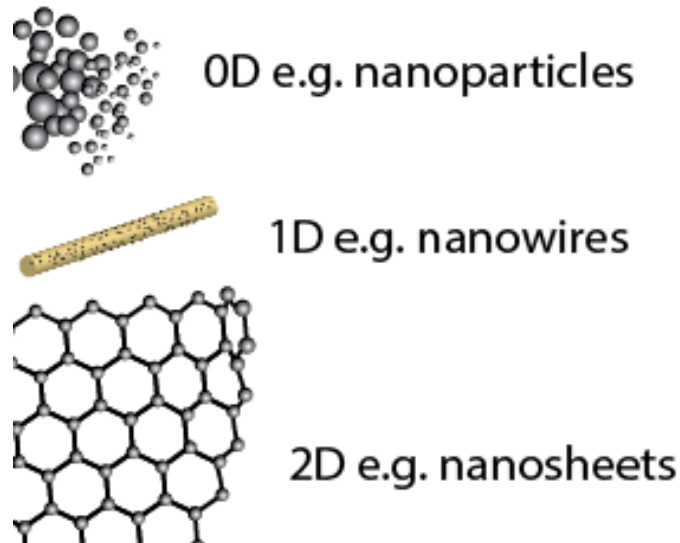


Figure 1.2: Zero-, one-, and two-dimensional nanomaterials. The definition of a nanomaterial refers to the number of dimensions of freedom. Zero-dimensional therefore means constrained in all three dimensions, 1D means constrained in two dimensions and 2D means constrained in only one dimension.

Many aspects of nanotechnology distinguish it as an active area of research; there are fundamental changes in the properties of many materials at these length scales. A highly significant parameter is the drastic change in ratio between the surface area of the material and the volume it occupies.

If a unit volume is broken up into subunits, more surface area is exposed. The unit volume remains the same, so the surface area to volume ratio increases as the subunit size decreases (see Figure 1.3).

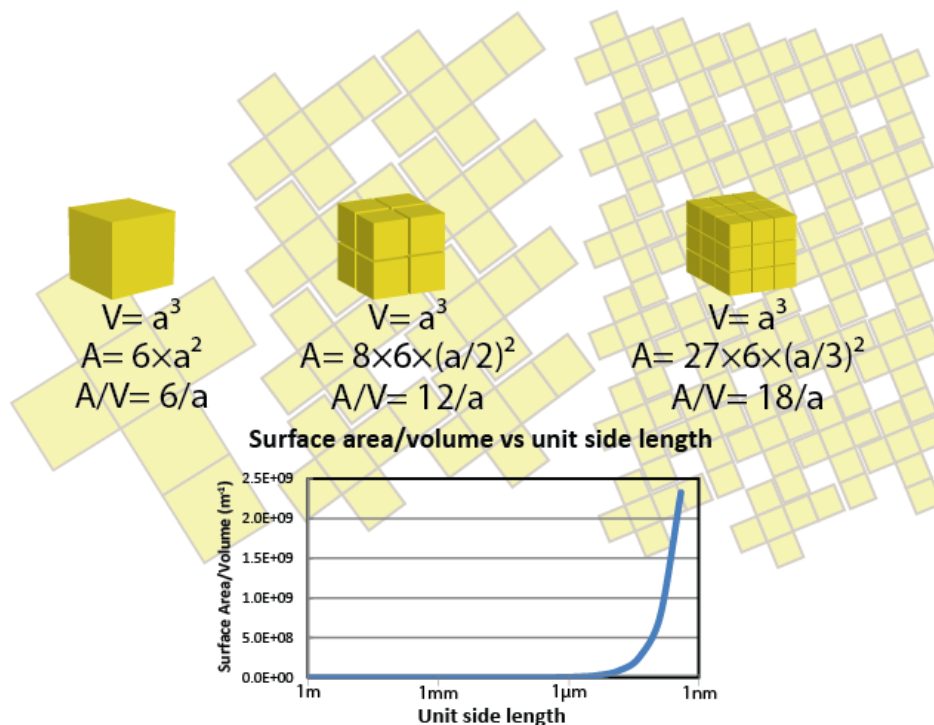


Figure 1.3: Exponential increase in surface area to volume ratio (A/V) as a cube is broken into smaller cubes. A cube of a given volume V (left) is subdivided by cutting each face once (middle) and twice (right), showing the progressive increase in A/V , with the corresponding subunit cubes unfolded in the background. Bottom, A/V as a function of unit side length, showing dramatic increase in A/V when the unit side length is below $1\mu\text{m}$.

This means that more of the material's atoms or molecules are at the surface and can therefore interact with their environment. So for a given mass of material, there is greater reactivity when the material is nanoscale.¹

This can have significant influence on the toxicity, solubility and chemical stability or reactivity of materials. Applications already exist which exploit this and are available on the market such as titanium dioxide (for cosmetic products) and zinc oxide (for cosmetics products), and silica dioxide (for food and cosmetic products) nanoparticles.²

At these scales, the traditional distinctions between chemistry, biology and physics are less well defined. For example, it is not sufficient to consider just the mass of a material in designing a chemical experiment because the size and dispersion of the material will determine the efficiency of the reaction. Nanoparticles can have such a significant portion of atoms at their surface that they do not have the same interactions as the bulk material and their increased reactivity can lead to differences in e.g. biological interactions. This is why there is a need for a multidisciplinary approach to the synthesis, development and investigation into potential applications of nanomaterials.³

1.2.1 Challenges

There are intrinsic challenges when working at this scale, such as how to manipulate structures only a few tens of atoms in size, how to characterise features much smaller than the wavelength of light, how to ensure reproducibility and how to scale up from individual nanoscale interactions to a macro-scale effect. In particular, size and shape distribution are of paramount importance in order to exploit and develop the unique physicochemical properties of nanomaterials in a commercial context.

Other challenging aspects of nanotechnology lie in the regulation of the use of engineered nanomaterials, in the assessment of the impact and the toxicity of materials, especially when the end-of-life environmental impact is considered in the life-cycle of products containing nanomaterials.⁴

1.2.2 Advantages/opportunities

Nanoscience also presents unique opportunities. Some of the opportunities are immediately apparent when we consider the implications of the rise in reactivity with decreasing particle size or increasing surface area to volume ratio. As stated above, the more atoms or molecules available at the surface of the material, the more readily the material can interact with its environment.⁵

In biomedical imaging applications, for example, it is essential that the probes are small enough to allow transport and binding at a targeted site or structure but are large enough to provide sufficient signal to be imaged.

At the nanoscale, we also encounter novel and enhanced properties such as new types of magnetic and optical behaviour.

1.2.3 Harmonic nanoparticles and nonlinear materials

At higher intensities, such as with light generated by a high-powered laser, the optical response of a material is nonlinear, resulting in nonlinear optical phenomena such as sum and difference frequency generation, in which two photons are combined in a nonlinear material and output as a single photon as shown in the schematic below (see Figure 1.4).

Second Harmonic Generation (SHG) is an example of sum frequency generation—when two photons of a given frequency are absorbed at the same time they are emitted as a single photon of exactly double that frequency.

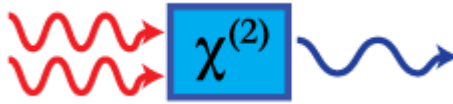


Figure 1.4: Schematic of the principle of Second Harmonic Generation (SHG), a nonlinear optical phenomenon. When two photons of a given frequency are absorbed at the same time they are emitted as a single photon of exactly double that frequency (hence the term second harmonic generation).⁶

Harmonic nanoparticles (HNPs) have been the subject of much interest because nonlinear optical effects occur more readily in nanoparticles since they are so much smaller than the wavelength of light (there is no phase-matching constraint in HNPs). The development of a next generation biomedical imaging platform, Second Harmonic Microscopy (SHM), has sought to exploit this phenomenon and its advantages over conventional imaging technologies.^{7,8}

For example, quantum dots (QDs) such as Qdot[®] Probes, blink randomly making quantitative analysis prohibitively difficult. Spectral overlap and photostability are less of an issue with QDs; they have a very narrow emission band and their emission can be tuned by synthesising QDs of different sizes.⁹ However, QDs contain toxic metals such as cadmium and concerns remain over whether surface corrosion in physiological conditions might cause the heavy metals to leach.^{10,11} Fluorescent dyes such as Hoechst, a commercially available DNA stain, require specific excitation wavelengths and also bleach over time. Indeed, different fluorescent stains must be used in order to excite at different wavelengths and to avoid channel cross-talk.

SHG is a non-resonant phenomenon so acts on any input frequency in the transparency range of the material, and the response is stable over the course of days. In contrast to conventional diagnostic techniques, HNPs do not blink or bleach and have extremely narrow emission bands as illustrated in Figure 1.5.

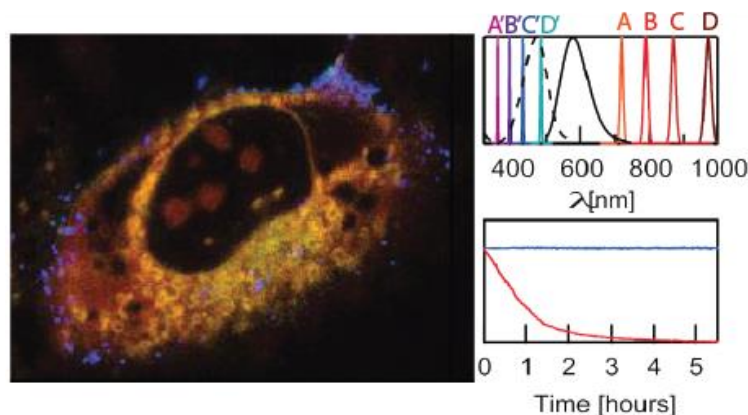


Figure 1.5: Harmonic nanoparticles as advanced biomedical imaging probes. Left, a lung epithelial cell exposed to harmonic nanoparticles. Harmonic generation is not a resonance-based phenomenon so it occurs anywhere in the transparency range of the crystal; the ability to tune the excitation wavelength (Top right panel, A-D) means energy deposition in the sample can be minimised. Unlike fluorescence, harmonic generation is stable over hours of continuous irradiation (Lower right panel)¹²

The ability to tune the excitation frequency holds great promise for the use of HNPs as labels in deep-tissue imaging. If one can select an input frequency such that neither the input nor the output is absorbed strongly by the sample, one can reduce the energy deposited in the sample and increase the penetration depth of the probe. HNPs are therefore of growing interest for use in deep tissue imaging.¹³

More importantly, static investigations of single cells, tissue sections and organs (using the well-established selective staining techniques) are so far poorly appropriate to give insight into the dynamic processes that govern interactions between cell assemblies and living tissues. Because of their long-term photostability (there is no exponential bleaching as with fluorescent imaging probes such as FITC®), HNPs have all the necessary features to better elucidate these living processes that govern metabolism and (cancer) disease mechanisms.

For these reasons, SHG is an active area of research for next generation imaging probes such as in two-photon and second harmonic imaging microscopy.¹³⁻¹⁵

Origin of Harmonic Generation

Within the volume of a bulk (or nano-) material, nonlinear optical effects such as second or higher order harmonic generation results from interactions between coherent light and valence electrons of non-centrosymmetric crystals whose unit cells contain asymmetric building blocks. Distorted motions of the electrons under the external optical field are related to different asymmetries that arise for instance from distorted octahedra of d^0 transition metal cations, such as Nb^{5+} in lithium niobite ($LiNbO_3$), lone pair cations in asymmetric coordination geometry, such as Bi^{3+} in bismuth ferrite ($BiFeO_3$), lone electron

pairs such as on iodine ions in iodate materials, or from π -conjugated planar rigid tetrahedral groups, such as PO_4^{3-} in KTiOPO_4 (KTP).

Brightness of the optical probes is another requirement in biomedical imaging. A first survey of the well-known nonlinear optical materials such as ZnO, KTP and perovskite compounds was carried out in 2012, in which the averaged nonlinear coefficient, $\langle d_{\text{HNP}} \rangle$, was measured (see Table 1.1). The nonlinear coefficient at 3 ± 2 pm/V could be readily related to that of the corresponding bulk materials thus demonstrating a volume response and the absence of any size effect for NP size above 50 nm.¹²

Table 1.1: Results summary of a survey of the averaged second harmonic coefficient of well-known nonlinear optical materials

Nanocrystal	$\langle d_{\text{HNP}} \rangle$ (pm/V)
ZnO	1.9
KTP	2.4
KNbO ₃	3.4
LiNbO ₃	3.7
BaTiO ₃	4.6

The best candidate in this survey with respect to the highest coefficient was BaTiO₃, although improvements in the synthesis of LiNbO₃ have yielded coefficients as high as 5.5 pm/V.¹⁶ Another key aspect of using nanoparticles of small size is the absence of phase matching conditions.

Because bismuth is a particularly heavy metal with a $6s^2$ lone pair electrons and distorted octahedra, BiFeO₃ is also expected to have a high hyperpolarisability relative to other perovskite materials. BiFeO₃ is thus known to have both an NLO response and room temperature antiferromagnetic ordering. For this reason, it was chosen as the model candidate for the development of HNPs as diagnostic probes in NAMDIATREAM, Nanotechnological Toolkits for Multi-Modal Disease Diagnostics and Treatment Monitoring, a large-scale EU-FP7 project coordinated by Prof Volkov and Dr Prina-Mello (as deputy).

1.2.4 Magnetic materials and superparamagnetism

Magnetic nanoparticles and probes such as Fe₃O₄ NPs have been extensively applied in biotechnology and biomedical assays for magnetic cell labelling and isolation, cell counting and cell differentiation

under common separation assay or Flow Cytometry; a significant amount of research is also focused on their use as contrast agents in Magnetic Resonance Imaging (MRI), although magnetite nanoparticles have a tendency to dissolve when unprotected from oxidation and therefore there is a need for biocompatibility shelling. One approach to preventing this corrosion is to passivate the surface layer with a coating such as a biocompatible polymer or shell such as a silane capping layer.¹⁷⁻²¹

Further applications of magnetite NPs have been explored such as magnetic hyperthermia in which NPs internalised into disease-cells are heated using an alternating external magnetic field to induce cell death.^{20,22,23}

Magnetic separation of cells from suspension is currently achieved *via* very expensive commercial solutions such as Dynabeads® or MACS® Microbeads. With these techniques, functionalised magnetic beads are incubated with cells in a suspension of primary antibodies (Abs) which target the cell type of interest. The primary Abs attach to receptors on the surface of the cells. The beads, having been functionalised with the corresponding secondary Abs, attach to the primary Abs, resulting in the magnetic beads being attached to the cells. This allows the cells to be separated from the suspension and then characterised by cleaving the antibody and analysing the cells e.g. flow cytometry.

To improve the current procedures, functionalisation of magnetic nanoparticles with antibodies which attach directly to the receptors would eliminate the need for the cocktail of primary antibodies (which is prohibitively expensive at approximately 100€ per isolation procedure). One of the aims of this study is therefore to functionalise multifunctional nanomaterials that combine magnetic and harmonic properties. To demonstrate the proof-of-principle for this application, the corresponding nanoparticles were suspended in different media to simulate physiological environments and these were separated with a magnet.

1.3 Biomedical imaging probes

An imaging probe consists of a targeting moiety which allows it to selectively bind to a structure of interest and a stain or contrast agent which acts as a label and marks its position for microscopy. Quantitative data about cellular or intracellular moieties can be derived from the intensity of accumulated labels, if the intensity is directly proportional to the concentration.

This presents a problem for conventional imaging probes such as those containing fluorescent stains or quantum dots, as mentioned earlier.

Quantum dots (QDs) are semi-conductor nanoparticles which have gained much interest due to their brightness, how readily they can be dispersed into a stable suspension and, crucially, their tunability. In semiconductors, absorption and emission are determined by the energy difference between the valence band and the conduction band. Electrons in the valence band can be excited to the conduction band by absorption of a photon whose energy is greater than the band gap energy. A photon is emitted when an excited electron drops back into the ground state. This is also true of quantum dots, but their size is so small that the number of possible energy states is constrained (quantum confinement). Adjusting the dimensions of the quantum dots allows the confinement and hence the emission to be tuned. This in turn means that a single excitation source can be used to generate a range of colours despite the fact that blinking of the probe is often observed and might be a limitation.^{24,25}

Similarly, fluorescent stains bleach over time and are therefore not suitable for long-term analysis and this complicates their use for quantitative measurements. Significant advances have been made in the development of diagnostic probes based on QDs and fluorescent stains in recent years to address these issues.²⁶⁻³⁰

An active area of research is the search for near infrared (NIR) fluorescent stains suitable for *in vivo* imaging.^{27,31-34} Biological tissue only weakly absorbs NIR radiation compared to visible or UV light, so the range of wavelengths from 650 nm to 1350 nm is known as the optical window. This means that NIR radiation has greater penetration, meaning diagnostic probes are detectable at greater depths in the tissue.

Upconversion nanoparticles have also been explored as a method of exploiting the optical window. Upconversion results from the absorption of a photon by an electron which is already in an excited state. The secondary absorption causes the electron to be promoted to an even higher energy state before dropping back to the ground state by the emission of a photon. Having been excited by two photons, for example, a single photon of approximately half the wavelength is emitted, similar to the combination of photons in Second Harmonic Generation.³⁵⁻⁴⁴

Upconversion results from transitions between real electronic energy levels, however; this means that the excited electrons undergo vibrational relaxation before collapsing to ground. This results in a spectral band of upconverted photons slightly above half the wavelength of excitation instead of a single peak at exactly half the excitation as in SHG.^{39,42,45}

As a result, the relative intensity of UCNPs, i.e. the ratio of the output intensity to that of the pump, is typically lower than that of SHG for NPs whose diameter approaches 100 nm, because intensity scales

with the square of the volume for SHG but with the volume for UCNPs. When the pump wavelength induces resonance in the UCNPs, however, the output intensity can far exceed that of SHG. Note that comparison of the efficiency of each process is so far limited to only a host material and that more spectral studies are needed with other matrices with different impurity contents to get a definitive overview⁴⁶

However, even when probes exploit the NIR optical window, the record penetration depth of deep-tissue optical imaging is approximately 1.6 mm.⁴⁷

SHG also occurs at any wavelength within the transparency range of the harmonic crystal, as opposed to requiring excitation to be within a specific band as in upconversion or other photoluminescence. As a result, SHG can be exploited further into the NIR such that both the optical pump wavelength and the generated wavelength are within the biological transparency window (pumping at 2000 nm would cause SHG at 1000 nm). Femtosecond lasers that can pump at such wavelengths are commercially available but remain prohibitively expensive. As such, throughout this study, SHG was demonstrated at lower wavelengths i.e. 750-1550 nm – using existing setups at Université de Savoie and University of Geneva. Given that the only wavelength dependence of SHG is associated with the first order susceptibility.⁴⁸

1.3.1 Magnetic resonance imaging contrast agents

For greater penetration depth, magnetic resonance imaging (MRI) is undisputedly superior for non-invasive *in vivo* imaging. Briefly, MRI involves the polarisation of hydrogen nuclei in a strong magnetic field. The polarised nuclei orient with the field. An alternating radio frequency (RF) pulse is then applied at the resonant frequency of the nuclei to excite them to a higher state and precess in phase with the pulse. As the nuclei relax to the ground state, oriented with the field, they emit RF radiation and the rate of decay is known as the longitudinal relaxation rate, T1. RF radiation is also emitted as the nuclei move out of phase with the RF pulse, at the transverse relaxation rate, T2. MRI exploits the different and characteristic rates of relaxation of tissues and structures in the body.

Paramagnetism arises due to the spin of unpaired electrons in an ion which results in a magnetic dipole moment. The dipole moments of paramagnetic materials align in the direction of an applied magnetic field but, once the field is removed, the dipoles orient randomly due to thermal motion of the ions.

By contrast, the remnance of ferromagnetic materials is much higher – their spins can remain oriented much longer after the field is removed. The magnetic moments of ions in ferromagnetic materials can

influence neighbouring ions, resulting in magnetic domains, clusters of ions whose spins orient together. Indeed, ferromagnetic materials can spontaneously magnetise due to the alignment of successive domains: each aligned domain contributes to the overall strength of the macroscale magnetic field, inducing more domains to align, until all the magnetic dipoles are oriented in the same direction.

Superparamagnetism is a phenomenon observed in ferromagnetic (and ferrimagnetic) nanoparticles, where all the magnetic ions in the particle belong to a single magnetic domain. The magnetic dipoles can randomly flip direction – only two orientations are stable, and they are antiparallel. The time between flips, the Néel relaxation time, is governed by the probability for the magnetisation to reverse and is a function of temperature, causing behaviour like paramagnetism.

To enhance contrast in MRI and to label structures, analogous to fluorescent labelling, magnetic materials are used as contrast agents. Paramagnetic materials like gadolinium(III) provide contrast for T1-weighted images, whereas superparamagnetic materials such as the iron oxide hematite provide contrast in T2-weighted images.

1.3.2 Targeting diagnostic markers

Diagnostic markers are biological indicators used to diagnose a disease. Such markers can be quantitative and used to evaluate the severity or progression of the disease (e.g. thyroid hormone levels in the blood indicate the level of thyroid activity) or qualitative, indicating the presence of a disease, such as the overexpression of HER2 (human epidermal growth factor receptor 2) in erythroblastic oncogene B-2 (ErbB-2)-positive breast and lung cancer cells.^{49,50}

HER2 belongs to a large family of membrane-bound receptor tyrosine kinases which includes epidermal growth factor receptor (EGFR) as well as ErbB-3 (HER3) and ErbB-4 (HER4), and whose over-expression is associated with many human cancers.⁵¹ Amplification of HER2 is observed in 25-30% of breast cancers,⁵² and EGFR over-expression is observed in more than 90% of head and neck cancer squamous cell carcinomas and 43% of patients with glioblastoma, for example.⁵³⁻⁵⁵

To ensure that probes ultimately label only the structures of interest or to ensure the label is transported to the site of interest, probes must be targeted to the relevant moiety or site. For instance, diagnostic markers such as HER2 and EGFR can be tagged with probes using antibodies which bind to the receptors (anti-HER2 and anti-EGFR antibodies, respectively). In this study, the label (BiFeO_3) was first coated with a linker, modified to attach a protein binding domain (protein G') which bound to an antibody (IgG). The nanocomposite is shown in the following schema (see Figure 1.6).

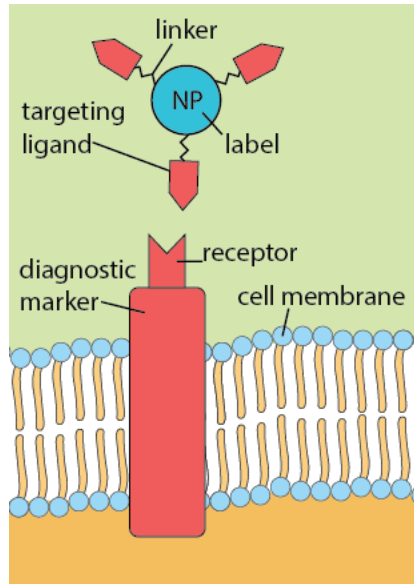


Figure 1.6: Principle of targeting. Nanoparticle labels are attached via a linker to a targeting ligand which binds specifically to a receptor on a diagnostic marker expressed on the surface of a cell.

The functionalised assembly can then be internalised into the cell or be used to indicate the presence of the receptor on the cell surface in imaging applications.

1.3.3 Size, shape and structure of nanomaterials in diagnostic imaging

The size of nanomaterials is critical to determining biological interactions: below $\sim 50\text{nm}$, it is understood that NPs might passively cross through cell membranes, i.e. without requiring active transport, below $\sim 20\text{nm}$ they could cross the blood-brain barrier. This might provide previously unattainable opportunities for imaging, however recent studies have shown that other interactions influence the uptake and transport of nanomaterials.⁵⁶ For example, high aspect ratio materials such as nanowires might be taken up into cells if the diameter is sufficiently narrow.⁵⁷

This would be desirable in imaging because of the unique appearance – a straight line contrasts well against globular or rounded cellular structures. However, a disadvantage may be in the danger posed to the cell structure; as the nanowire is taken into the cell, it might damage the cell membrane, and subcellular organelles or induce autophagy or necrotic processes.⁵⁸

1.3.4 Prerequisites in the development of probes for imaging and diagnostic applications

- For second harmonic imaging applications, nonlinear optical materials must:
 - ❖ be detectable in culture and/or tissue
 - be highly efficient at generating harmonics
 - possess high crystallinity

- ❖ be within a narrow size distribution (SHG intensity varies with the square of the volume so there is a practical lower limit on the size, and too large a size distribution would make quantitative analysis of e.g. the nonlinear optical response prohibitively difficult to model)
- For advanced imaging applications such as single-particle tracking, the materials must:
 - ❖ be suitable for quantitative characterisation
 - form single crystal particles (be monocrystalline)
 - form stable suspensions, especially in physiological conditions
- For specific targeting the materials and composites must:
 - ❖ be tailored to uptake/functionalisation
 - have uniform surfaces
 - have appropriate surface charge for the target application
 - form stable bonds with linkers and/or capping agents

For magnetic cell isolation or hyperthermia applications, the NPs or composites must have sufficiently high magnetic response to separate cells to which they are bound from suspension

- For use as MRI contrast agents, the NPs must:
 - ❖ be sufficiently small for superparamagnetism
 - stable in suspension
 - have no remnance
 - have high magnetic susceptibility

While some of the above criteria are not necessary for certain applications, the ideal candidate will satisfy these conditions.

1.4 Diagnostic platforms

Assessing whether the criteria are met requires extensive physico-chemical characterisation at each stage in the development of the materials from synthesis through functionalisation and *in vitro* testing. The characterisation equipment used in this study will be discussed in later chapters as the need arises. To put in perspective how the end-products of the study might be used, diagnostic platforms in which they have potential application are discussed below.

1.4.1 Flow cytometry

Flow cytometry measures properties of individual cells such as their fluorescence and how they scatter light. A dilute stream of cells or particles is hydrodynamically focused and passed in the path of a laser, such that single cells are illuminated. Detectors record the intensity of scattered light at different wavelengths and at right angles, measuring the forward and side scatter. The intensity and type of scattered light can be used to count and distinguish cells within a population and identify sub-populations.

Flow cytometry is often used in conjunction with fluorescent probes which label proteins or other markers expressed uniquely on a certain cell type. Where a cell type expresses no unique markers, labels can be multiplexed, and filters applied to the data to extract only information about a specific subset of the population. This is known as gating.

Flow cytometry has brought about a revolution in diagnosis and clinical analysis, not only for its ability to identify subpopulations but also for its ability to physically sort cells. Cells are passed in the path of a laser in a stream of drops. When a cell is identified, an electrostatic charge can be applied to the drop so it can be diverted from the stream and into a reservoir. This technique can be applied to sort large populations of cells into a series of reservoirs extremely rapidly ($\sim 10^6$ cells per min) and at very high purity ($\sim 99\%$).

Nonlinear optical flow cytometers are in development. The advantage in using NLO is to extend the ability to sort cells – certain cell types have intrinsic second and third generation properties. Since the probes conceived for the current study are multimodal, with non-linear optical and magnetic properties, next generation flow cytometry and cell-sorting are potential applications and might permit cells to be separated either magnetic or under flow or both.

1.4.2 Confocal, Two-photon and Second Harmonic Microscopy

Confocal microscopy is a high-resolution imaging technique in which out of focus light is blocked by directing light emitted from a sample through a pinhole before it reaches the detector. This reduces blurring, increases the signal to noise ratio and improves the resolution.

Because it allows only in-focus light to return to the detector, a scanning confocal microscope can also be used to record images in three dimensions by rasterising across a sample to form an XY section, then scanning in the Z-axis to build up a series of sections.^{59,60}

Although confocal microscopy is like two-photon microscopy in some respects – they both use a laser excitation source and a system of mirrors for scanning – two-photon microscopes achieve optical sectioning in a different manner. Because two photon excitation requires simultaneous absorption of two photons at the same time, the probability of two-photon emission is only high where the laser is most focussed.^{61,62}

This results in some of the advantages discussed earlier over conventional imaging techniques, namely reduced photobleaching (and hence lower phototoxicity), less absorption and increased penetration depth.

Second harmonic imaging is carried out on a two-photon microscope but distinguishes itself in a variety of ways, as discussed earlier. First, second harmonic generation originates from the hyperpolarisability of a material rather than electronic transitions. Second, because it is a non-resonant phenomenon, it occurs at any wavelength in the transparency range of the material rather than at a specific excitation wavelength as in two-photon excited fluorescence. Third, this means that the excitation source can be tuned such that the second harmonic is shifted to eliminate auto-fluorescence.^{8,63}

Therefore, probes which utilise second harmonic generation are highly desirable for long-term tracking of cells and deep-tissue imaging.

1.4.3 Multimodal imaging

Multimodal imaging is a target application for the multifunctional nanocomposites and particles described above. By synthesising a novel composite which has a high magnetic and nonlinear optical response, the same probe might be used for both MRI and SHM. The intensity of signal from the nanocomposites depends largely on their size distribution as outlined previously but also on the mass concentration or loading of the embedded materials and, with respect to embedded or harmonic-core composites, on the optical transparency of the matrix. For its high biocompatibility and low toxicity, silica is currently the most suitable material to be used as the matrix.⁶⁴

Similar to the procedure published by the Nanomedicine and Molecular imaging group in conjunction with the Chemistry Department, Trinity College, the University of Dublin,^{57,65} in which magnetic probes were incorporated into silica nanowires, the strategy employed in the current study was to incorporate multiple types of nanoparticles into silica wires to form composites with multimodal properties as outlined in the table below.

Table 1.2: Matrix of nanomaterials, their properties and the nanocomposites in which the properties are to be combined. Legend: ✓ known property ⊙ target property

Nanomaterial	NLO response	Magnetic response	Surface passivation	Biocompatibility	High aspect ratio	Low toxicity
BiFeO ₃ NPs	✓✓✓	✓				
Fe ₃ O ₄ NPs		✓✓✓		✓✓		✓✓
SiO ₂ NWs				✓✓	✓✓	✓
BiFeO ₃ @Fe ₃ O ₄ NPs		⊙				
BiFeO ₃ @Fe ₂ O ₃ NPs	⊙	⊙				
SiO ₂ NWs with BiFeO ₃	⊙		⊙	⊙	⊙	⊙
SiO ₂ NWs with Fe ₃ O ₄		⊙	⊙	⊙	⊙	⊙
SiO ₂ NWs with BiFeO ₃ & Fe ₂ O ₃	⊙	⊙	⊙	⊙	⊙	⊙

An immediate further advantage is the flexibility of the system and the ease with which nanoparticles of different functionalities can be combined in the silica matrix.

Chapter 2 will discuss the synthesis of the nanomaterials and composites. In Chapter 3, the functionalisation of the materials is described. Chapter 4 details the cytotoxicity and safety assessment. In Chapter 5, the multimodal applications of the materials are discussed. Chapter 6 summarises the future research which it is forecast will lead from the results reported here.

Chapter 2

Nanomaterial synthesis

2.1 Introduction

2.1.1 Bismuth ferrite nanoparticles: a model candidate for second harmonic microscopy

BiFeO_3 is a very important material in fields as diverse as energy harvesting,^{66–68} non-volatile memory,^{69,70} spintronics,^{71,72} photocatalysis^{73,74} and nonlinear optics^{12,14,75} due to its magneto-electric, piezoelectric and nonlinear optical properties.^{76–85} BiFeO_3 is a highly ferroelectric, multiferroic material with a rhombohedrally distorted perovskite structure with an $R3c$ space group. BiFeO_3 displays antiferromagnetic ordering below its Néel temperature (310 – 370°C).^{86–88}

BiFeO_3 is a rhombohedrally distorted perovskite and its noncentrosymmetry arises from the rotation of the oxygen octahedrons around the $[111]$ axis, as shown in Figure 2.1.

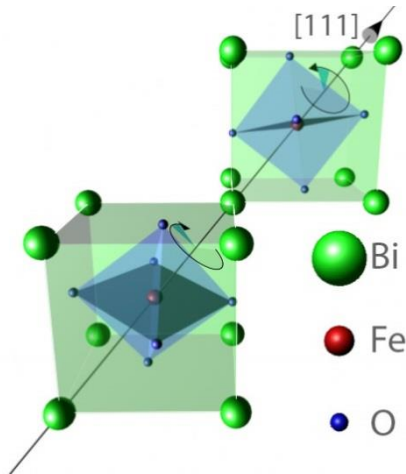


Figure 2.1: Image of two BiFeO_3 primitive cells. 3D image created with Autodesk MAYA

The non-centrosymmetric structure of BiFeO_3 enables even-order nonlinear optical responses such as second harmonic generation. As outlined in Chapter 1, SHG occurs when two photons of one frequency are combined in a crystal, resulting in a single photon of exactly double the input frequency. Because harmonic generation is a non-resonant process, the excitation can be tuned to any frequency within the crystal's transparency range.^{89–93} Harmonic generation in a nonlinear optical nanocrystal allows long term observation^{90,94,95} and the ability to tune the input frequency (and hence also the output frequency) is very significant for biomedical applications – frequencies can be tuned to avoid sample

absorbance and to prevent energy deposition in the sample. Applications in the biomedical field include deep-tissue imaging with second but also third harmonic, for instance, as an unmet clinical challenge.^{96,97} Consequently, the desirable optical and magnetic properties of BiFeO₃ combined with its low cytotoxicity⁹⁸ have motivated this work.

Applications using BiFeO₃ nanoparticles are however still limited by the difficulty in determining a facile, scalable synthesis route which yields nanoscale, monodisperse and monocrystalline nanoparticles. Conventional solid-state processing is restricted by inherent thermodynamic and kinetic aspects, as previously discussed.^{99,100}

Phase purity, size control and dispersion are also a significant challenge often mentioned in the literature for the many other existing routes that include hydrothermal, sol-gel combustion, sonochemical and microemulsion techniques.^{101–115} As preparation of monocrystalline harmonic biomarkers are here foreseen, we further develop the most promising wet chemical routes, namely Pechini's sol-gel method and Ghosh's solvent evaporation approach.¹¹⁶ Much research has been done to determine the best chelating agent for use as a template, particularly by Selbach et al.¹¹⁷ Carboxyl groups are required for complexing the Bi³⁺ and Fe³⁺ metal ions to obtain a homogeneous polyester precursor whereas hydroxyl groups are necessary for the subsequent polyesterification of the carboxyl groups.

The choice of chelating and complexation agents has however a considerable impact on the phase-purity, size distribution and crystallinity of the products for a given annealing temperature.

In the current study, we present a modification of the Ghosh's solvent evaporation method¹¹⁶ in which a chelating agent not previously reported in the synthesis of BiFeO₃ (tartronic acid) was used in place of tartaric acid. We also present a novel sol-gel combustion method in which mucic acid was used both as chelating agent and fuel. We then further investigate the interplay of key synthesis parameters which affect the nanoparticle size, polydispersity and crystallinity such as addition of extra hydroxyl groups and an excess of NaCl acting as a spacer before the crystallization step.

2.1.2 Magnetite nanoparticles: superparamagnetic applications

Due to their low toxicity and biocompatibility, iron oxides, e.g. magnetite (Fe₃O₄) and hematite (Fe₂O₃), are considered very promising candidates for biomedical applications such as biosensing, MRI contrast agents, cell isolation and manipulation, targeted drug delivery, and magnetic hyperthermia.^{118–120}

Massart's co-precipitation method is the most widely used in the synthesis of monodisperse magnetic nanoparticles due to its low cost, simplicity and narrow size distribution.¹²¹

2.1.3 Silica nanowires: low-cost, low toxicity 1D nanomaterials

Sol-gels are fundamentally synthetic glasses, organic-inorganic ceramics formed from transition metal alkoxide precursors reacted with a silane gel. The importance of sol-gels is in the compositional and microstructural control they facilitate. By adjusting the treatment of the sol or gel phases, the morphology of the end-product can be tailored to yield an assortment of shapes (fibres, films, powders and monoliths). The various microstructures have different applications in separations, filtration, insulation, sensors and antireflective surfaces.

The formation of sol-gels involves four stages: hydrolysis, condensation, gelation and aging. See Figure 2.2 for an overview of the four stages.

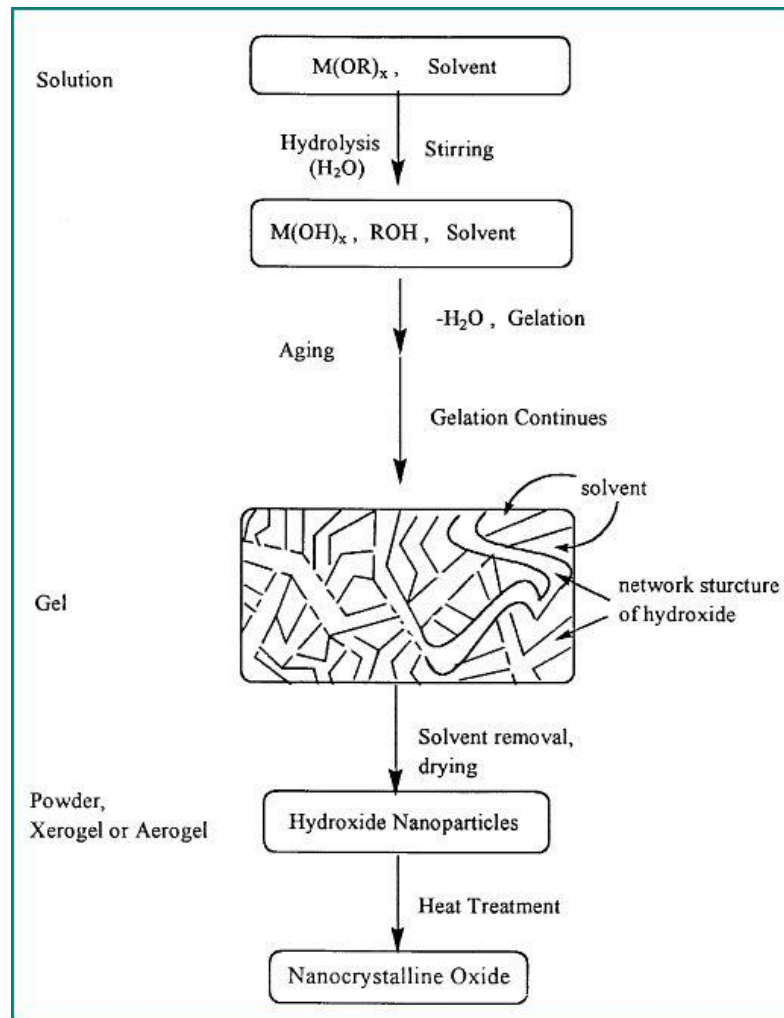


Figure 2.2: Schema of sol-gel formation. M indicates a metal ion, OR represents an alkoxide functional group, OH signifies a hydroxyl ion. Reproduced from Brinker et al ¹²²

Although many metal alkoxides can be used as precursors to form sol-gels, tetraethoxysilane (TEOS) was used exclusively in this study due to the low toxicity of the silica sol-gel that it forms.

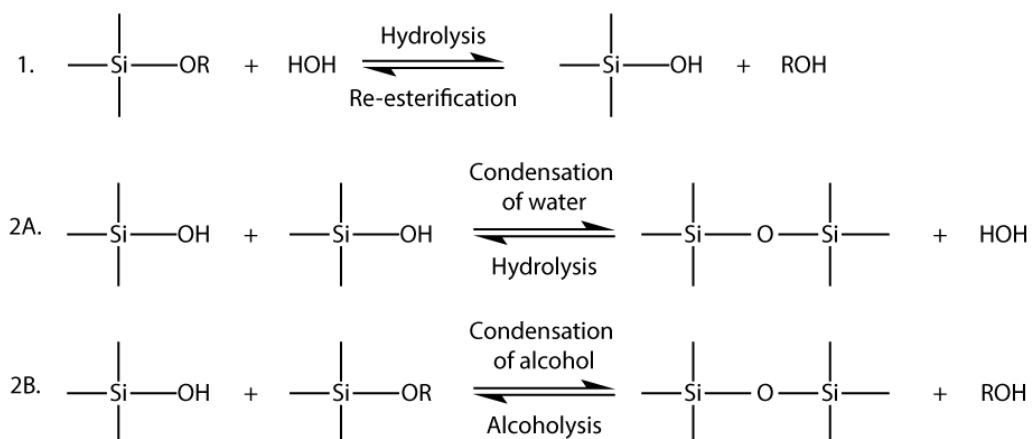


Figure 2.3: The first two steps of the sol-gel process with an alkoxysilane. 1: The alkoxysilane reacts with water. Alkoxide groups attached to the silane are replaced by hydroxyl groups, forming silanol functional groups (Si-OH) with an alcohol as a by-product. 2: Siloxane bonds (Si-O-Si) are formed as silanol groups react with other silanol groups (2A: condensation of water) or with an alkoxysilane (2B: condensation of alcohol).¹²²

With the condensation step, siloxane bonds form links between molecules. With successive links, the network of molecules grows, ultimately forming the gel. The solvents and by-products are then removed by drying.

Before gelation has completed, the sol can be drawn into a template, such as into the pores of an alumina membrane. Once the gel has hardened (either in air or by annealing) the template can be removed to leave a cast of the pores.

The synthesis of nanomaterials from the templated sol-gel method has been abundantly described in the literature,¹²³⁻¹²⁸ particularly silica nanowires, as it provides a low-cost and simple route to 1D materials which are biocompatible and exhibit very low toxicity.

A schema of the one-pot templated sol-gel synthesis of silica nanowires is shown in Figure 2.4.

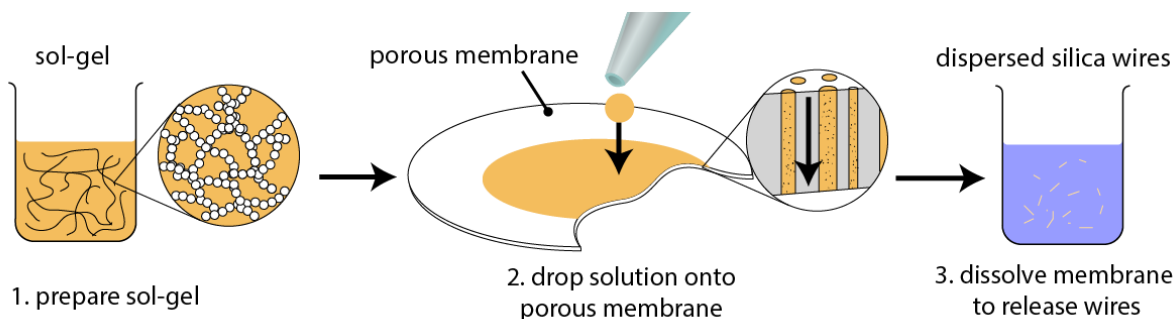


Figure 2.4: Silica Nanowire synthesis by the templated sol-gel method. Wires are formed by incorporating sols into the pores of an anodic alumina membrane, allowing the sol to dry out and form the solid gel. The gel is annealed and finally the membrane template is dissolved to release the nanowires.

Alumina membranes with pores in ranges of diameters from 20 - 400 nm are commercially available and are typically used in this synthesis. The sol is drawn into the pores with vacuum.

2.2 Materials and Methods

2.2.1 Nanoparticle synthesis

Fe₃O₄ nanoparticle synthesis

Magnetite was synthesised via the co-precipitation method.^{129–131}

In a typical synthesis, NaOH (2 g) was dispersed with vigorous stirring in 100 ml distilled and filtered water (Millipore) in a round bottom flask. The iron solution was prepared by dissolving FeCl₃•6H₂O (2.59 g, 96 mmol) and FeCl₂•4H₂O (0.95 g, 48 mmol) in 40 ml Millipore water in another round bottom flask, and both flasks were degassed under vacuum for 20-30 minutes. The NaOH solution was heated to 80°C before the iron solution was added dropwise, slowly at first. The mixture was kept at 80°C for one hour under stirring and then allowed to cool. The black powder was then separated magnetically and washed four times with Millipore water until the pH was neutral. The yield was approximately 95% (10.5 g, theoretical yield 11.1 g).

BiFeO₃ nanoparticle synthesis

BiFeO₃ nanoparticles have been prepared by modifying Ghosh et al's¹³² sol-gel method with the following improvements:

- Two new chelating agents, tartronic acid and mucic acid, were used instead of previously reported agents with a view to lowering the annealing temperature in order to inhibit Ostwald ripening and reduce the final NP size and size distribution.

- To promote crystallization and to impede particle growth, the mucic acid procedure was also carried out in the presence of salt by dissolving excess NaCl in the solution prior to evaporating the solvent.

Briefly, $\text{Bi}(\text{NO}_3)_3 \cdot 5\text{H}_2\text{O}$ (0.485 g, 1 mmol) was dissolved in 2M HNO_3 (100 ml), followed by $\text{Fe}(\text{NO}_3)_3 \cdot 9\text{H}_2\text{O}$ (0.404 g, 1 mmol). 2 mmol of chelating agent (see below) was added, then the solution was heated under stirring at 165°C for approximately one hour, until the solvent had evaporated. It is vitally important to prevent the gel from combusting if phase-pure powders are desired at lower temperatures. This was achieved by removing the beaker to a furnace at 140°C as soon as the gel began to form and allowing the remaining nitrates to evaporate for two hours. Organics were removed by baking at 350°C for a further two hours. For the temperature dependent studies, the powder was collected and then annealed at temperatures starting from 200°C for periods of 30 minutes at intervals of 50°C at 2°C per minute, with a rest of 30 minutes after each ramp before XRD diffraction patterns were recorded.

A variety of chelating agents were used: tartronic acid, tartaric acid and mucic acid, which are of increasing length with an increasing number of hydroxyl groups along their carbon chain.

Glycerol was added to determine whether the ratio of hydroxyl groups to carboxylic acid had an influence on the crystallization of BiFeO_3 . In order to establish the optimal ratio of hydroxyl groups to carboxylic acid groups, the above protocol with mucic acid was repeated, but glycerol (0.184 g, 2 mmol) was added to the solution before evaporating, yielding a final $-\text{OH}:-\text{COOH}$ ratio of 5:1.

To promote crystallization and to inhibit Ostwald ripening, the mucic acid procedure was also carried out in the presence of salt by dissolving excess NaCl (10 mmol) in the solution prior to evaporating the solvent.

After annealing, powders were washed four times in ethanol and Millipore water.

2.2.2 Nanowire synthesis - One-pot acidic sol-gel synthesis of SiO_2 nanowires

The one-pot acidic sol-gel method is similar to previously reported procedures^{57,127} with some alterations. EtOH (4.5 ml) was added to Millipore water (3.32 ml). 3 drops of concentrated HCl (30 μL , 37%) was added to the solution and stirred for two minutes. The solution was then added to TEOS (8.2 ml) and stirred for two hours. AAO membrane filters (Whatman PLC, 200 nm pores) were then placed in the solution to allow the sol to fill the pores for one hour.

The filters were removed and left to dry overnight before excess was removed from the surface by fine sanding the membranes. The membranes were then annealed at 400°C for one hour and dissolved in H_3PO_4 under stirring with mild sonication.

The resulting suspension was then centrifuged and washed until pH neutral.

2.2.3 Nanocomposite synthesis

Multimodal nanowires: embedding NPs in NWs

To incorporate NPs into the wires required only minor modification of the protocol outlined in section 2.2.2; the relevant materials were simply dispersed in the silica precursor sol by sonicating as shown in Figure 2.5.

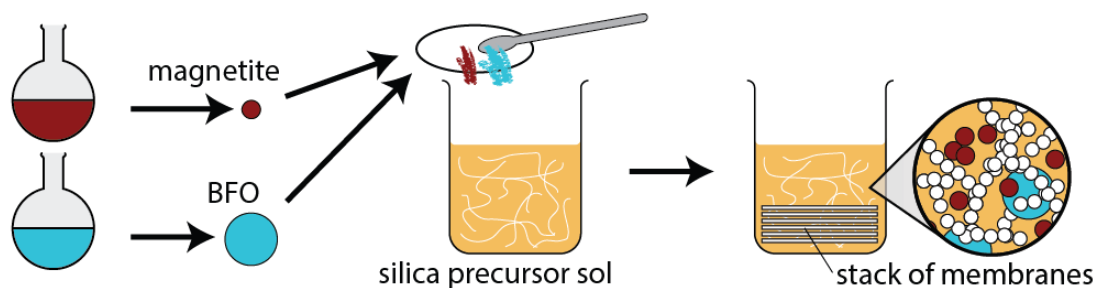


Figure 2.5: Embedding small nanoparticles within the longer 1D nanowires.

The silica precursor sol was prepared as described earlier – the acidified EtOH solution was added to TEOS and stirred for two hours. In this study, iron oxide or bismuth ferrite nanoparticles or both were added.

AAO membrane filters (Whatman PLC, 200 nm pores) were then placed in the solution to allow the sol to fill the pores for one hour.

The filters were removed and left to dry overnight before excess was removed from the surface by fine sanding the membranes. The membranes were then annealed at 350°C for one hour and dissolved in H_3PO_4 under stirring with mild sonication.

The membranes were then processed as described in section 2.2.2. Please note that “&” is used as an indication that nanoparticles have been embedded in a matrix, e.g. SiO_2 & Fe_3O_4 means that Fe_3O_4 NPs were added to a silica matrix. This is to distinguish embedded particles from those which form a core and shell, denoted by @, e.g. $BiFeO_3@Fe_3O_4$ means a $BiFeO_3$ core has a shell of Fe_3O_4).

BiFeO₃@Fe_xO_y nanocomposites

The BiFeO₃ NPs described previously were used as seeds in the co-precipitation synthesis of Fe₃O₄ to grow BiFeO₃@Fe₃O₄ core@shell NPs.

To determine the mass of BiFeO₃ to use in the synthesis, as a first order approximation, it was assumed that the Fe₃O₄ particles formed a complete monolayer on the surface of the BiFeO₃ NP seeds. It was further assumed as a first order approximation that the Fe₃O₄ NPs were spherical, with a diameter of 10 nm based on literature values,²³ and that the spheres occupied all possible sites around each BiFeO₃ core as in Figure 2.6, below. These simplifying assumptions are justified on the basis that the goal is to calculate an upper estimate of the ratio of Fe₃O₄ to BiFeO₃ NPs, in order to ensure there was an excess of Fe₃O₄. These calculations are later confirmed by Vibrating Sample Magnetometry measurements in which the ratio of the magnetic Fe₃O₄ to antiferromagnetic BiFeO₃ is measured (see section 2.3.4).

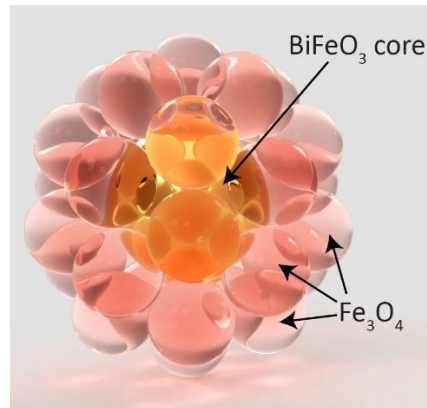


Figure 2.6: Model of iron oxide particles around a bismuth ferrite core. 3D image created with Autodesk Fusion 360

The maximum packing of 10 nm iron oxide particles around 20 nm BiFeO₃ cores resulted in a ratio of 25 Fe₃O₄ NPs to each BiFeO₃ NP.

To calculate the mass of BiFeO₃ required to add to a reaction of Fe₃O₄, the surface area of BiFeO₃ NPs is required. Assuming the BiFeO₃ NPs had a radius r of 10 nm and that the NPs are approximately spherical, the surface area, A_{NP} , and volume per NP, V_{NP} , are calculated as follows:

$$A_{NP} = 4\pi r^2 = 4\pi(10 \times 10^{-9}m)^2 \quad \text{Equation 2.1}$$

$$V_{NP} = \frac{4}{3}\pi r^3 = \frac{4}{3}\pi(10 \times 10^{-9}m)^3 \quad \text{Equation 2.2}$$

The mass per NP (m_{NP}) is given by:

$$m_{NP} = V_{NP} \times \rho$$

Equation 2.3

where V_{NP} is the volume of a single nanoparticle and ρ is the density.

The theoretical density can be calculated from the unit cell as follows¹³³:

$$\rho = \frac{n' (\Sigma A_C + \Sigma A_A)}{V_c \times N_A}$$

where n' is the number of formula units in the unit cell, ΣA_C is the sum of the atomic masses of each of the cations in the formula unit, ΣA_A is the sum of the atomic masses of the anions in the formula unit, V_c is the volume of a unit cell and N_A is Avogadro's constant.¹³⁴

Since there is only one formula unit per unit cell, $n'(\Sigma A_C + \Sigma A_A)$ is simply the molecular mass of BiFeO_3 ,

M_{BiFeO_3} .

$$\Rightarrow \rho = \frac{M_{\text{BiFeO}_3}}{V_c \times N_A}$$

Equation 2.4

BiFeO_3 's unit cell is a pseudocubic rhombohedron and its volume can be calculated from its lattice parameter and first angle ($a = 0.3965 \text{ nm}$ and $\alpha \approx 89.35^\circ$ ¹³⁵). The volume of a rhombohedron with edge length a and first angle α is given by:¹³⁶

$$V_{\text{rhom}} = a^3 * (1 - \cos(\alpha)) * \sqrt{1 + 2 \cos(\alpha)}$$

$$\Rightarrow V_{\text{BiFeO}_3 \text{ cell}} = (0.3965 \times 10^{-9} \text{ m})^3 \times (1 - \cos 89.35^\circ) \times \sqrt{1 + 2 \cos 89.35^\circ}$$

$$\Rightarrow V_{\text{BiFeO}_3 \text{ cell}} = 6.232 \times 10^{-29} \text{ m}^3$$

Equation 2.5

From Equation 2.4 and Equation 2.5:

$$\rho = \frac{M_{\text{BiFeO}_3}}{V_c \times N_A} = \frac{312.82 \text{ g} \cdot \text{mol}^{-1}}{6.232 \times 10^{-29} \text{ m}^3 \times 6.022 \times 10^{23} \text{ mol}^{-1}}$$

$$\Rightarrow \rho = 8.335 \times 10^6 \text{ g} \cdot \text{m}^{-3}$$

Equation 2.6

From Equation 2.2, Equation 2.3 and Equation 2.6, the mass of an individual nanoparticle can be derived:

$$m_{NP} = V_{NP} \times \rho = \frac{4}{3}\pi r^3 \times \rho \quad \text{Equation 2.7}$$

$$\Rightarrow m_{NP} = \frac{4}{3}\pi(10 \times 10^{-9}m)^3 \times 8.335 \times 10^6 g \cdot m^{-3}$$

$$\Rightarrow m_{NP} = 3.491 \times 10^{-17} g \quad \text{Equation 2.8}$$

Given that the density of magnetite is 5.17 g/cm^3 ,^{137,138} using Equation 2.7, the mass of a single Fe_3O_4 NP ($m_{\text{Fe}_3\text{O}_4 \text{ NP}}$) and hence the total mass of Fe_3O_4 NPs in a cluster ($m_{\text{Fe}_3\text{O}_4 \text{ cluster}}$) is therefore given by:

$$m_{NP} = \frac{4}{3}\pi r^3 \times \rho$$

$$\Rightarrow m_{\text{Fe}_3\text{O}_4 \text{ NP}} = \frac{4}{3}\pi(5 \text{ nm})^3 \times 5.17 \text{ g/cm}^{-3}$$

$$\Rightarrow m_{\text{Fe}_3\text{O}_4 \text{ NP}} = 2.707 \times 10^{-18} g$$

$$\Rightarrow m_{\text{Fe}_3\text{O}_4 \text{ cluster}} = 25 \times m_{\text{Fe}_3\text{O}_4 \text{ NP}}$$

$$\text{Equation 2.9}$$

$$\Rightarrow m_{\text{Fe}_3\text{O}_4 \text{ cluster}} = 6.768 \times 10^{-17} g$$

From Equation 2.8, the mass ratio (r_m) of BiFeO_3 to Fe_3O_4 can be calculated:

$$\Rightarrow r_m = \frac{m_{\text{BiFeO}_3 \text{ NP}}}{m_{\text{Fe}_3\text{O}_4 \text{ cluster}}} = \frac{3.491 \times 10^{-17} g}{6.768 \times 10^{-17} g} \quad \text{Equation 2.10}$$

$$\Rightarrow r_m = 0.516 \quad \text{Equation 2.11}$$

Therefore, for a synthesis with a theoretical yield ($m_{\text{Fe}_3\text{O}_4}$) of 11.1 g (see *Fe₃O₄ nanoparticle synthesis* in section 2.2.1), the mass of BiFeO_3 used to seed the synthesis of magnetite is given by:

$$\Rightarrow m_{\text{BiFeO}_3} = m_{\text{Fe}_3\text{O}_4} \times r_m = 11.1 g \times 0.516$$

$$\Rightarrow m_{\text{BiFeO}_3} = 5.73 g$$

The synthesis procedure was then followed as described in the *Fe₃O₄ nanoparticle synthesis* section (under section 2.2.1), except that BiFeO₃ NPs (5.73 g, 18.3 mmol) were dispersed in the NaOH solution with sonication and the pH adjusted to 13.5 with concentrated NaOH before heating to 80°C. The acidic iron solution was then added dropwise and the solution was kept at 80°C for one hour under stirring, allowed to cool and washed with magnetic separation. The yield was approximately 95%, similar to the synthesis of magnetite (16.0 g, theoretical yield 16.8 g).

To obtain BiFeO₃@Fe₂O₃ NPs, a sample of BiFeO₃@Fe₃O₄ NPs (200 mg) was annealed at 350°C for 1 hour.¹³⁹

This reduction of Fe³⁺ in Fe₃O₄ to Fe²⁺ on the surface of the BiFeO₃ was expected to enhance the second harmonic generation in BiFeO₃ by modifying the electric field distribution, due to work reported in the literature on enhancement of nonlinear optical effects by the reduction of metal containing nanoparticles attached to NLO materials.^{140,141}

2.2.4 Physico-chemical characterisation

Comprehensive characterisation of the probes at each development stage was necessary for their targeted applications and because the end-product properties (i.e. magnetic response and nonlinear signal strength) are size dependent. Their size and surface chemistry also determine their toxicity and biocompatibility, so it was necessary to employ a full suite of characterisation techniques including the following to determine the suitability of the probes for biomedical application development.

- Dynamic Light Scattering (DLS) and Zeta-potential (ZP): Malvern ZetaSizer Nano ZS (Malvern, UK)
- Nanoparticle Tracking Analysis: NanoSight NS500, (Malvern, UK)
- X-ray diffractometry (XRD): Philips X'pert PIW3020 using Cu K α radiation (Philips, France), and INEL CPS 120, for temperature dependent studies (TXRD), using Co K α radiation (INEL, US)
- Scanning electron microscope (SEM): Zeiss SEM Ultra (Zeiss, Germany)
- (High resolution) transmission electron microscope ([HR]TEM): FEI Titan (FEI, US)
- Magnetic hysteresis: custom-made Vibrating Sample Magnetometer (VSM)
- Nonlinear optical response by Hyper Rayleigh Scattering (HRS): custom-built optical setup (see Figure 2.8) and by Two-photon Microscopy

Crystal structure identification by X-Ray Diffractometry (XRD)

XRD was used to identify the crystal structure and determine phase purity, according to literature guidelines.¹⁴²⁻¹⁴⁴ Similarly, temperature dependent X-Ray Diffractometry (TXRD) was carried out to determine the evolution of the phase purity and structure as a function of temperature.

Scattering of x-rays from successive planes of atoms in a crystal cause constructive and destructive interference (see Figure 2.7).

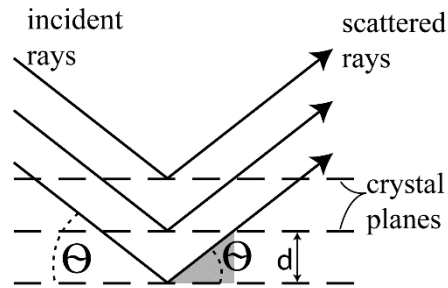


Figure 2.7: Scattering of x-rays by successive crystal planes

An x-ray detector directed at the crystal registers constructive interference as a large increase in the intensity of scattered x-rays at specific angles of incidence. The angle of incidence is related to the interplanar spacing and the x-ray wavelength by the Bragg equation:

$$n\lambda = 2d \sin\theta \quad \text{Equation 2.12}$$

where n is a whole number multiple of the wavelength (λ), d is the interplanar spacing and θ is the angle of incidence.

The interplanar spacing is equivalent to interatomic distance where the atoms of which the material is composed are ordered and repeated throughout the crystal. The angles at which peaks are observed are therefore characteristic of the crystal's unit cell and the family of peaks present identify the atoms and lattice parameters of the unit cell.

Broadening of peaks in XRD

When a crystal with small grain sizes or a powder of small crystals is placed in the path of the X-ray beam, the broadening of peaks in the XRD pattern can be related to crystallite size by the Scherrer equation:¹⁴⁵

$$d = \frac{K\lambda}{\beta \cos \theta} \quad \text{Equation 2.13}$$

where d is the average size of the crystalline domains, K is a dimensionless constant related to the shape of the crystals with a value close to 0.9; λ is the X-ray wavelength; β is the line broadening at half the maximum intensity and θ is the Bragg diffraction angle.

Particle size measurement was also carried out on SEM and TEM images (see below) to quantify nominal size distribution.

Size distribution analysis

DLS was carried out immediately after sonication and again after 3-5 days of sedimentation following established protocols.^{16,146}

DLS measures intensity fluctuations in light scattered from particles in suspension and relates the measurement to the hydrodynamic radius of the particles. Larger particles diffuse more slowly,¹⁴⁷ so the signal can be self-correlated to determine the size of the particles.

Principle of Brownian motion of molecules and particles in suspension¹⁴⁸⁻¹⁵⁰

The calculation of size from DLS measurements as described below is based on the simplifying assumption that the particles have an approximative spherical geometrical shape.

In suspension, electrostatic charges on the surface of a particle attract ions from solution. The hydrodynamic radius is the radius of the sphere of ions that surround a particle in aqueous suspension and that moves with it as the particle moves through the solution.

The velocity of spheres undergoing Brownian motion in suspension, known as their translational diffusion, is a function of temperature (molecules have more kinetic energy) and viscosity (also a function of temperature) and relates to the size of the particles by the Stokes-Einstein equation,

$$D_T = \frac{kT}{6\pi\eta r_H} \quad \text{Equation 2.14}$$

In Equation 2.14, D_T is the translational diffusion, k is Boltzmann's constant, T is the temperature in Kelvin, η is the viscosity of the fluid and r_H is the hydrodynamic radius of the sphere.

The hydrodynamic radius of a particle suspended in the fluid can be calculated from the correlation function, C :

$$C = \exp(-2\Gamma) \quad \text{Equation 2.15}$$

where Γ is the decay constant

$$\Gamma = D_T q^2 \quad \text{Equation 2.16}$$

where q is the magnitude of the scattering vector given by:

$$q = \left(\frac{4\pi n}{\lambda} \right) \sin \left(\frac{\theta}{2} \right) \quad \text{Equation 2.17}$$

where θ is the scattering angle, λ is the wavelength of the laser in vacuum and n is the refractive index of the fluid.

Hence,

$$r_H = \frac{kT}{6\pi\eta D_T} \quad \text{(from Equation 2.14)}$$

$$\Rightarrow r_H = \frac{kT q^2}{6\pi\eta \Gamma} \quad \text{(from Equation 2.16)}$$

$$\Rightarrow r_H = \frac{-kT q^2}{3\pi\eta \ln C} \quad \text{(from Equation 2.15)}$$

$$\Rightarrow r_H = \frac{-kT}{3\pi\eta \ln C} \left(\frac{4\pi n}{\lambda} \sin \left(\frac{\theta}{2} \right) \right)^2 \quad \text{(from Equation 2.17)}$$

The hydrodynamic radius of spheres suspended in a fluid can therefore be calculated from the properties of the fluid and the correlation of fluctuations of light scattered from the spheres.

$$d = \frac{K\lambda}{\beta \cos \theta} \quad \text{Equation 2.18}$$

Colloidal stability

Zeta potential (ζ) was calculated from electrophoretic mobility (μ_e) measurements as a function of pH at fixed ionic strength (I) as per IUPAC recommendations.¹⁵¹

Electrophoretic mobility is calculated by measuring particle velocity (V) in an applied electric field strength (E), using a Malvern ZetaSizer Nano from the following equation:

$$\mu_e = \frac{V}{E} \quad \text{Equation 2.19}$$

Henry's equation is used to calculate the zeta potential from the electrophoretic mobility:

$$\mu_e = \frac{2\epsilon_r \epsilon_0 \zeta \times f(K\alpha)}{3\eta} \quad \text{Equation 2.20}$$

where ϵ_r is the dielectric constant of the solution, ϵ_0 is the permittivity of free space, η is the viscosity of the fluid and $f(K\alpha)$ is Henry's function – a factor which accounts for the thickness of the electric double layer (EDL) surrounding the particle which moves with it through the suspension.

In the case of nanoparticles whose diameters are less than ≤ 100 nm in low ionic strength (10^{-5} M) this EDL is much bigger than the particle and Henry's function approaches 1 (known as the Huckel approximation), simplifying Henry's equation to the following:

$$\mu_e = \frac{2\epsilon_r\epsilon_0 \zeta}{3\eta} \quad \text{Equation 2.21}$$

$$\Rightarrow \zeta = \frac{\mu_e 3\eta}{2\epsilon_r\epsilon_0} \quad \text{Equation 2.22}$$

Surface morphology and size distribution by SEM

To image the surface morphology and carry out size distribution analysis of the nanomaterials, a drop of nanoparticle suspension was deposited on a carbon tab and scanned at low incident energy (2-5 kV) at short working distance (~ 2.5 mm), following a protocol optimised from instrumental documentation and literature.^{152,153} A minimum of 100 particles were measured using image analysis software ImageJ on three independently prepared samples.

Size distribution, surface morphology and lattice spacing measurement by TEM, STEM and HRTEM

To qualitatively and quantitatively assess the quality of the nanoparticles and nanowires synthesised a combination of techniques was used on each sample during the same recording session. These were: TEM, STEM and HRTEM and SAED which were carried out after tool calibration.

Note that care was taken to ensure that TEM samples were representative of the sample under study – dispersions were sonicated immediately before being deposited *on top* of carbon-coated TEM grids held in reversed anti-capillary tweezers. The grids were then allowed to dry in air (protocol adapted from training literature).^{152,154–156}

Crystal structure and monocrystallinity by SAED

For SAED, individual nanoparticles were identified from TEM imaging and the appropriate aperture was selected such that only the individual nanoparticle was visible, and the corresponding diffraction spot pattern was imaged. Where no individual nanoparticles could be identified sufficiently separated from

aggregates, HRTEM images were post-processed by Fast-Fourier Transform (using ImageJ) to confirm the crystal structure.^{154,157}

Magnetic response and hysteresis by VSM

Typically, ~50 µg of dried powder was analysed by a custom-made VSM within CRANN Institute, the University of Dublin. The magnetic moment of the samples was measured as a function of an externally applied magnetic field to obtain the magnetic hysteresis curve showing remanence (if any) and the saturation magnetisation of the sample.¹⁵⁸

Hyper-Rayleigh Scattering Measurement

Decanted suspensions of BiFeO₃ were placed in the path of a vertically polarized laser of wavelength 1064 nm. A photomultiplier, set at 90° to the input, was used to detect the unpolarised scattered second harmonic light using a boxcar to gate at 532 nm (see Figure 2.8).

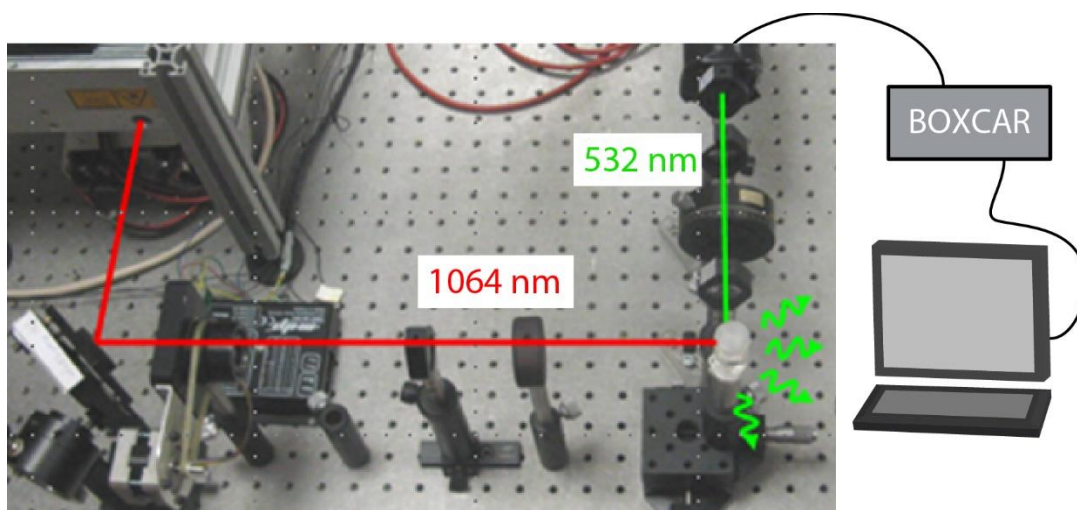


Figure 2.8: Optical Setup for Hyper Rayleigh Scattering Measurement.

Five solutions were prepared by dilution of the original concentration with 1mM aqueous solution of NaOH and, for each of the five concentrations, the intensity was measured. The HRS intensity was plotted as a function of relative concentration and the nanoparticles' effective hyperpolarisability, $\langle \beta_{np}^2 \rangle$, was calculated from the linear portion of the curve from the equation:

$$I_{2\omega} = GNT_{np} \langle \beta_{np}^2 \rangle I_{\omega}^2 \quad \text{Equation 2.23}$$

where G is an experimental constant, N is the concentration, and T_{np} is an internal field factor calculated from the solvent and nanocrystal refractive indices (here $n_{\omega} \sim 2.76$ and $n_{2\omega} \sim 3.20$ for BiFeO₃).¹⁵⁹

The nanoparticle concentration N is estimated by preparing a larger volume sample in the same way as for HRS analysis, dispersing 10mg of BiFeO_3 in 1L of 1mM NaOH and decanting over three days. 950mL of the supernatant was then evaporated in aliquots and weighed. Finally, the averaged SH coefficient $\langle d \rangle$ is calculated as follows, using V_{np} calculated from the DLS *Size by number* measurement as an estimate of the nanoparticle volume:

$$\langle \beta_{np} \rangle = \langle d \rangle V_{np} \quad \text{Equation 2.24}$$

Two-photon microscopy

Two-photon microscopy was kindly carried out by Dr Andrii Rogov, GAP Biophotonics, Université de Genève using a Nikon A1R-MultiPhoton inverted microscope coupled with a Spectra-Physics Mai-Tai tuneable oscillator (100 fs, 80 MHz, 700 - 1020 nm). Typical intensities at the focal spot were approximately 10^{11} W/cm^2 . No box car was used – the Epi detected signal was spectrally dispersed onto an array of 32 photomultipliers and the signal was not time-resolved.

2.3 Results

2.3.1 Nanoparticles

Fe_3O_4 nanoparticles

Phase-pure Fe_3O_4 nanoparticles were synthesised via the Massart co-precipitation method as can be seen in Figure 2.9. The significant peak broadening observed is mainly due to the small size of the nanoparticles. After correction of the instrumental broadening, the Scherrer equation (Equation 2.12) was used to calculate an approximate crystallite size of 15 nm from the three main peaks.

The Fe_3O_4 NPs were relatively monodisperse (see Figure 2.10), although aggregation is evident.

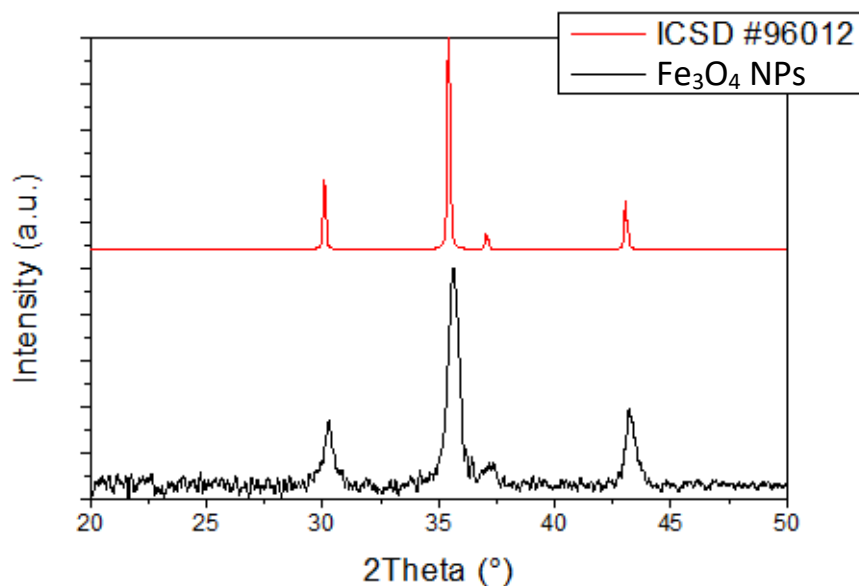


Figure 2.9: XRD patterns of Fe_3O_4 . In red above, ICSD #96012 is the literature XRD pattern for bulk Fe_3O_4 . Below, in black, the XRD pattern for the Fe_3O_4 nanoparticles. The peak broadening observed is due to the small size of the nanoparticles.

The suspension medium must be evaporated from the TEM imaging grid which induces aggregation. Pains were taken to ensure that the sample presentation on the TEM grids was representative, however. For example, the sample suspension was sonicated immediately before removing an aliquot. Second, the aliquot was deposited directly onto the TEM grid, rather than placing the grid to float on top of the sample droplet as is often done in TEM sample preparation (see Figure 2.10).

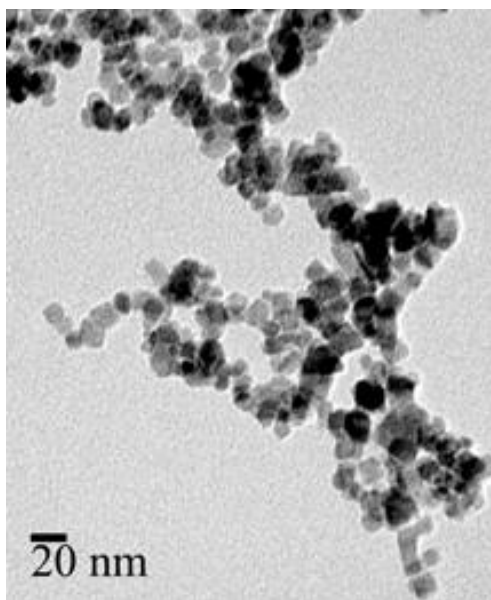


Figure 2.10: TEM image of aggregated Fe_3O_4 NPs

TEM images were analysed to determine the size – termed the physical size – of the nanoparticles. Measurements were made of 100 particles each from three independent preparations of TEM grids and the size distribution was prepared as a histogram (see Figure 2.11).

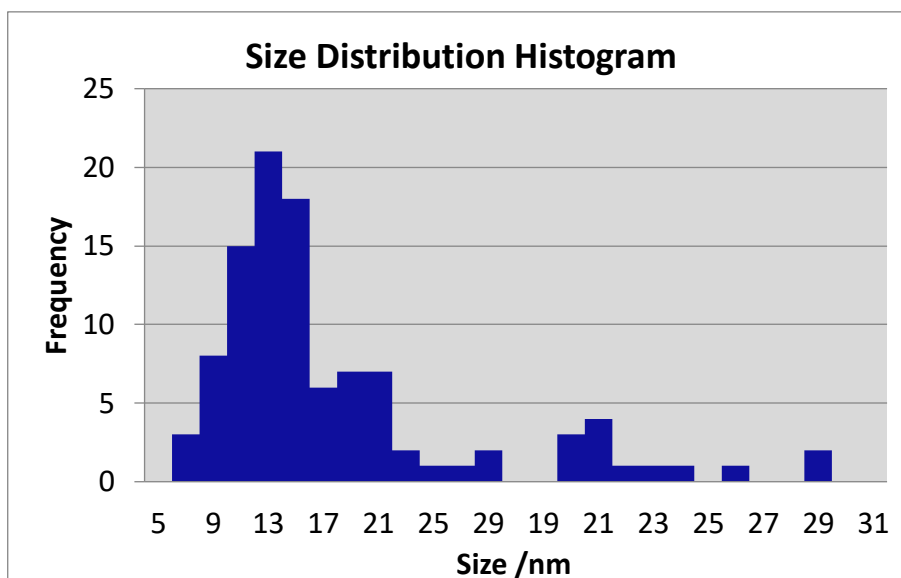


Figure 2.11: Representative size distribution histogram of Fe_3O_4 NPs. The histogram shows measurement of over 100 particles, repeated for three independent TEM grid preparations of a sample.

The average size of the Fe_3O_4 NPs was calculated from the histogram data in Figure 2.11 to be 13.5 ± 0.5 nm. This is consistent with the approximate size calculated from XRD data using the Scherrer equation.

The magnetic hysteresis curve obtained by VSM is shown in Figure 2.12 qualitatively confirms that the nanoparticles are small. As expected for such small nanoparticles, the sample displays superparamagnetic behaviour in that there is negligible remanence.

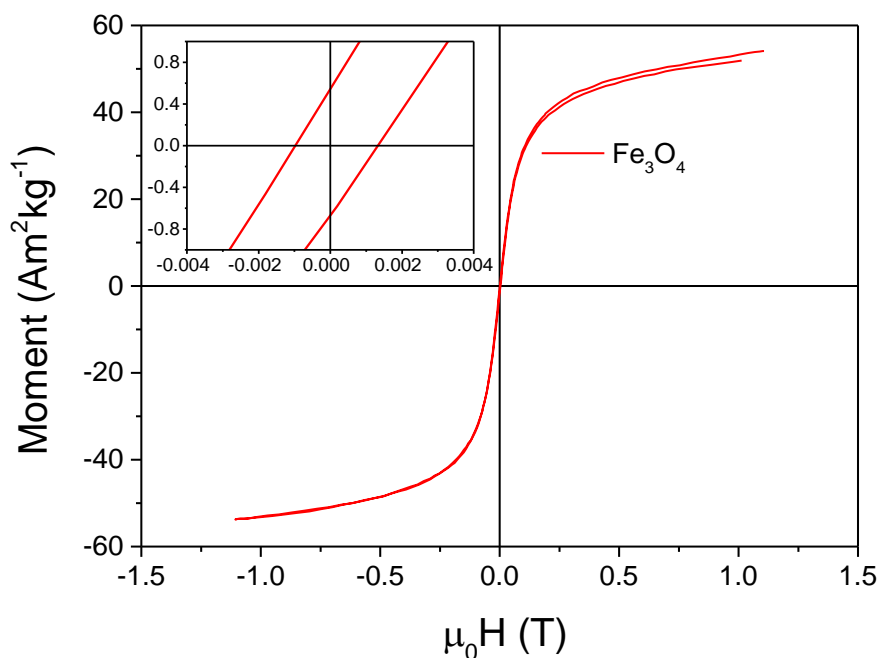


Figure 2.12: Magnetic hysteresis curve of Fe_3O_4 NPs in an applied field from -1 to 1 Tesla. Note the very low remnant magnetisation (0.001 T), indicating that the particles were superparamagnetic.

The saturation magnetisation is approximately $58 \text{ Am}^2\text{kg}^{-1}$, consistent with literature values for superparamagnetic Fe_3O_4 nanoparticles of this size at room temperature.^{121,130,137}

Next, BiFeO_3 NPs were prepared due to their advantageous nonlinear optical properties.

Bismuth ferrite nanoparticles

Alternative chelating agents toward narrower size distribution

BiFeO_3 nanoparticles were synthesized with chelating agents of increasing length and increasing ratio of hydroxyl groups to carboxylic acid groups, such as tartronic (1:2), tartaric (1:1) and mucic acid (2:1), resulting in different annealing temperatures required to form phase pure NPs as can be seen from the XRD patterns in Figure 2.13, below.

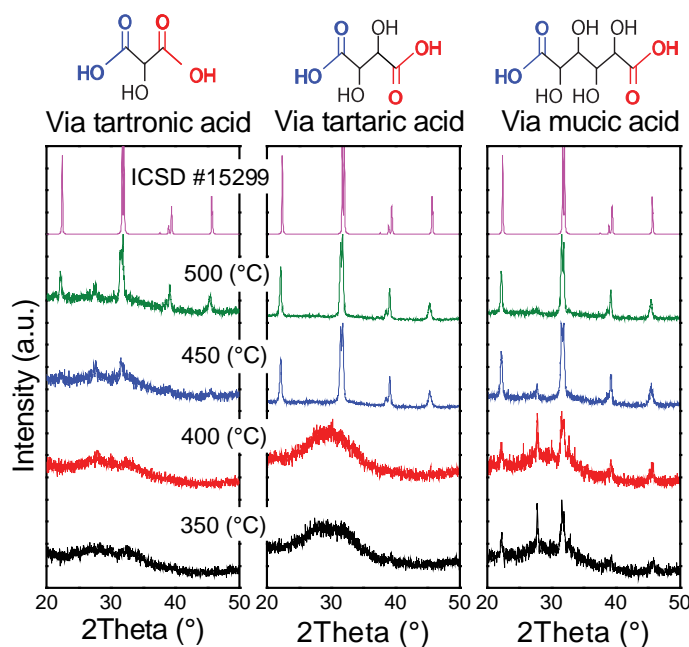


Figure 2.13: XRD patterns of BiFeO_3 synthesized with chelating agents of increasing length. Left, tartronic acid; middle, tartaric acid; right, mucic acid. The longer the carbon backbone, the lower the temperature required to form bismuth ferrite, albeit with phase impurities.

The increasing length (and the increasing $-\text{OH}:-\text{COOH}$ ratio) of the carboxylic acids and the influence on temperature is presented in Table 2.1.

Table 2.1: Structure, ratio of hydroxyl groups to carboxylic acids and lowest annealing temperature of each of the chelating agents used in this study

Chelating agent	Tartronic acid	Tartaric acid	Mucic acid
Structure			
$-\text{OH}:-\text{COOH}$	1:2	1:1	2:1
Lowest annealing temperature (30 min annealing)	>500°C	>450°C	<350°C*

* Care must be taken to inhibit combustion as suggested by Selbach¹⁶⁰ as soon as the solution has evaporated (at approximately 160°C). By removing the sample from the hotplate and transferring to a furnace at 140°C to allow nitric compounds to evaporate slowly, the sample still undergoes a colour change when the temperature is raised to 300°C to eliminate the organic compounds. However, if the nitrous compounds have been driven off, phase impurities are not introduced.

Influence of additional –OH groups on crystal formation at lower temperature

To determine whether the annealing temperature could be lowered further by increasing the concentration of –OH groups in the precursor, glycerol was added to the sol. Figure 2.14 shows the evolution of the crystal phases present as a function of temperature.

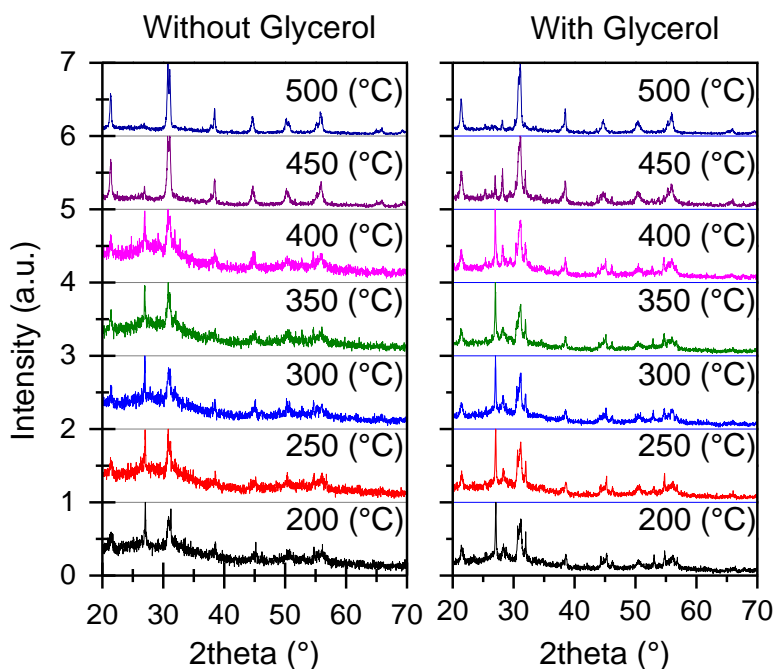


Figure 2.14: Temperature-resolved XRD patterns of powder prepared without and with glycerol. Left, without glycerol: although BiFeO_3 peaks are observed, there is a substantial amorphous background from 200 - 400°C. Right, with glycerol: temperature-resolved XRD pattern of powder prepared with glycerol: from 200 - 400°C the background is less visible and the crystal peaks more prominent. The highest peak visible at lower temperatures at $2\theta = \sim 28^\circ$ corresponds to the bismuth rich phase $\text{Bi}_{25}\text{FeO}_{39}$

Having identified that glycerol promotes the formation of the parasitic phases, the effect of salt on crystallinity was investigated next. Samples were annealed for only 30 minutes to reduce Ostwald ripening and at 450°C to ensure phase purity.

Influence of NaCl on crystal formation

To inhibit particle growth, NaCl was added to the precursor. Surprisingly, the presence of the salt resulted in phase-pure powders after annealing at lower temperatures. For comparison, Figure 2.15 shows the XRD patterns of BiFeO_3 prepared with and without NaCl and glycerol all annealed at 450°C.

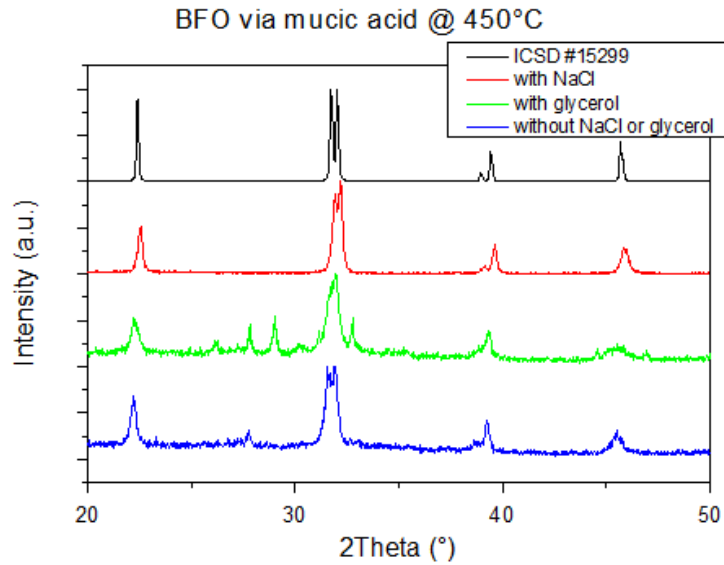


Figure 2.15: XRD patterns of BiFeO_3 samples without and with NaCl and glycerol added to the precursors. The BiFeO_3 reference spectrum corresponds to ICSD #15299.

Note from the XRD patterns in Figure 2.15 that after only 30 mins annealing at 450°C , the sample prepared with salt is entirely phase-pure and exhibits no amorphous background. By contrast, samples prepared without salt have a substantial background and small peaks of the parasitic phase $\text{Bi}_{25}\text{FeO}_{39}$ and the sample prepared with glycerol shows little background, but the parasitic phases is more obvious.

The improvement in phase-purity was confirmed by HRTEM and SAED (see Figure 2.16).

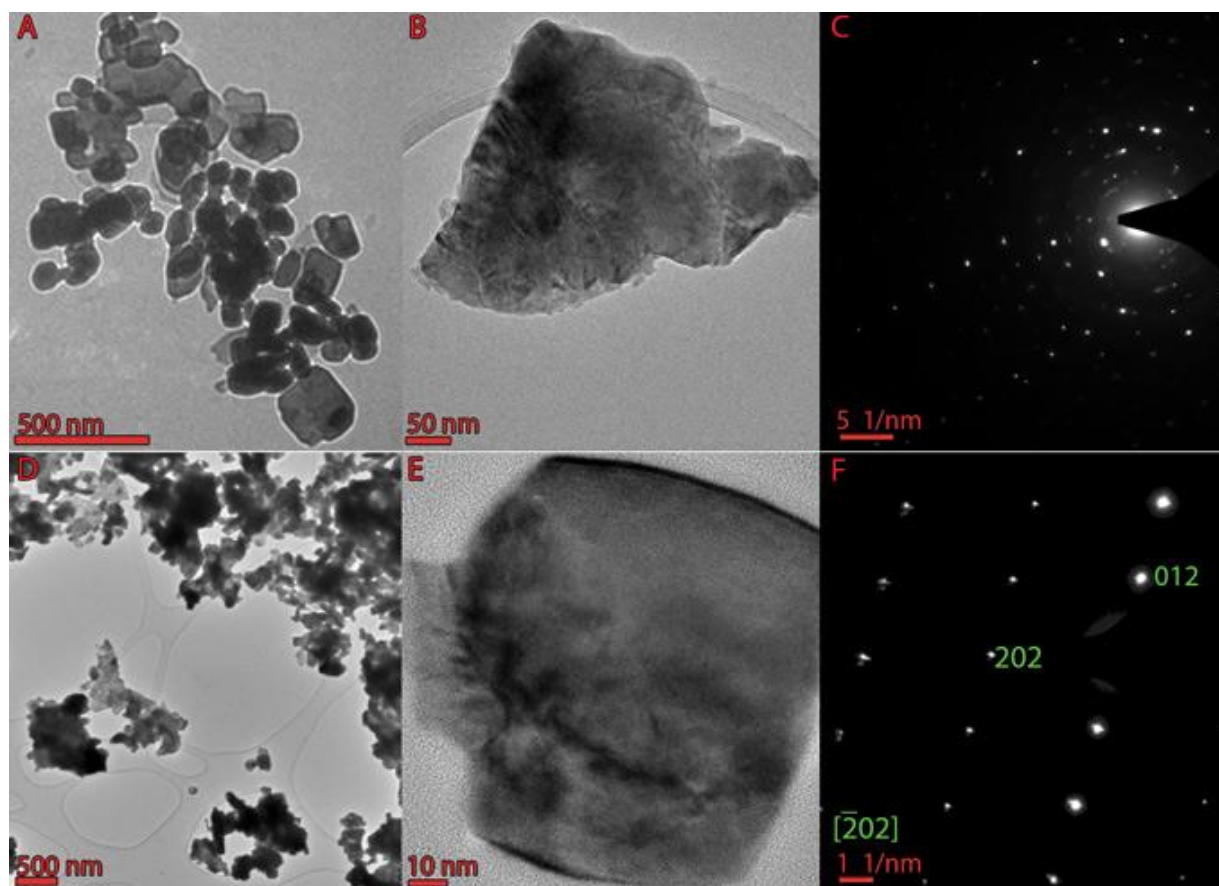


Figure 2.16: TEM, HRTEM and SAED patterns of BiFeO_3 prepared with and without NaCl. A) TEM image showing panoramic view of aggregated BiFeO_3 nanoparticles prepared without NaCl; B) HRTEM image showing amorphous surface of BiFeO_3 NPs prepared without NaCl; C) SAED pattern of the individual nanoparticle in C, showing diffraction spots of BiFeO_3 but from multiple crystal domains. D) TEM image showing panoramic view of aggregated BiFeO_3 NPs prepared with NaCl; E) HRTEM image showing the lattice spacings of well-crystallized BiFeO_3 NPs prepared with NaCl; F) SAED pattern of the individual nanoparticle in E, showing diffraction spots of BiFeO_3 , indicating that the NP is monocrystalline.

Importantly, the single, periodic array of spots in the SAED pattern (Figure 2.15, F) confirms that, not only are the NPs phase-pure BiFeO_3 , they are also monocrystalline.

The BiFeO_3 NPs prepared without and with NaCl and glycerol were probed using VSM to investigate how the improved crystallinity affected the magnetic properties (see Figure 2.17).

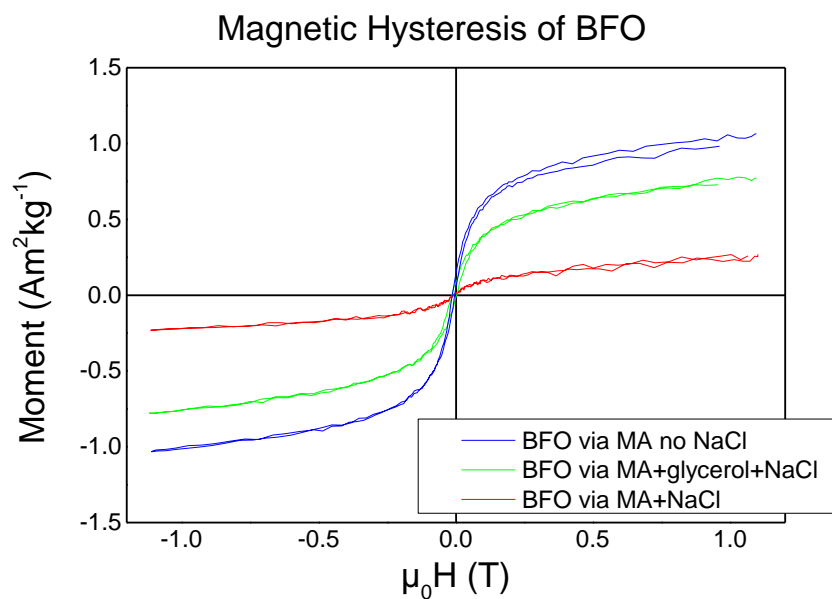


Figure 2.17: VSM measurements of BiFeO_3 prepared via MA, MA + NaCl + glycerol, and MA + NaCl.

Influence of improved crystallinity on Nonlinear Optical response

To ensure only individual NPs were probed, suspensions were prepared from pH 3 to pH 11. Sedimentation of residual aggregates was observed by time-resolved DLS, as well as by the change in the opaqueness of the sample over two days across the pH range investigated (the sample changed from yellow to transparent). Samples were therefore allowed to sediment for three days. At pH 11, the sample was still pale yellow after three days of sedimentation.

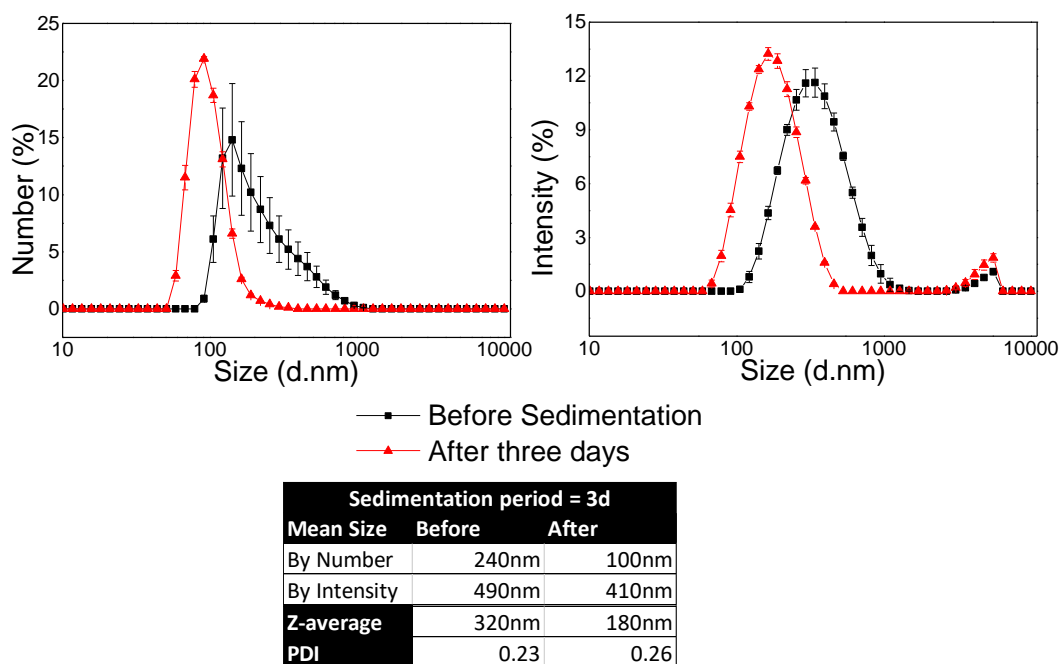


Figure 2.18: DLS measurements of BiFeO₃ prepared via MA + NaCl, suspended in aqueous solution at pH 11 before and after sedimentation. A decrease in size by number (top left), intensity (top right), mean sizes and Z-average (table) were observed.

The DLS measurements in Figure 2.18 show the dispersion of BiFeO₃ NPs in aqueous solution at pH 11 before and after the sedimentation period. These measurements were carried out to ensure that any aggregates could precipitate out of suspension, as the HRS intensity is a function of the crystallite size rather than the size of aggregates.

The presence of aggregates can be seen in the bimodal distribution observed in the DLS sizing measurement by intensity graph (top right in Figure 2.18). The relative size of the peaks in the bimodal distribution in the intensity graph might suggest there are a large number of aggregates present in the suspension. This is not the case - the scattered signal intensity scales to the sixth power of the diameter of the particle. The DLS intensity can be used to calculate the size by number of scattering particles (top left in Figure 2.18) to represent the relative numbers of particles of different sizes present.

Z-average, defined by the International Organization for Standardization (ISO) as the “harmonic intensity averaged particle diameter”, represents the hydrodynamic diameter of particles in suspension, calculated as the intensity-weighted mean size reported by DLS.¹⁶¹ However, this calculation assumes a monomodal distribution to apply cumulant analysis to the correlation curve and therefore does not accurately reflect the size of bimodal distributions.

More accurate calculations of the particles present in solution might have been resolved by adopting an orthogonal approach in particle sizing and concentration calculations.¹⁶² This would have been an interesting scientific aspect to resolve despite being secondary to the main objective presented here.

Hyper Rayleigh Scattering Measurements

Once a colloidal suspension of sufficient stability and monodispersity had been achieved, the NLO response was determined by HRS measurements (see Figure 2.19).

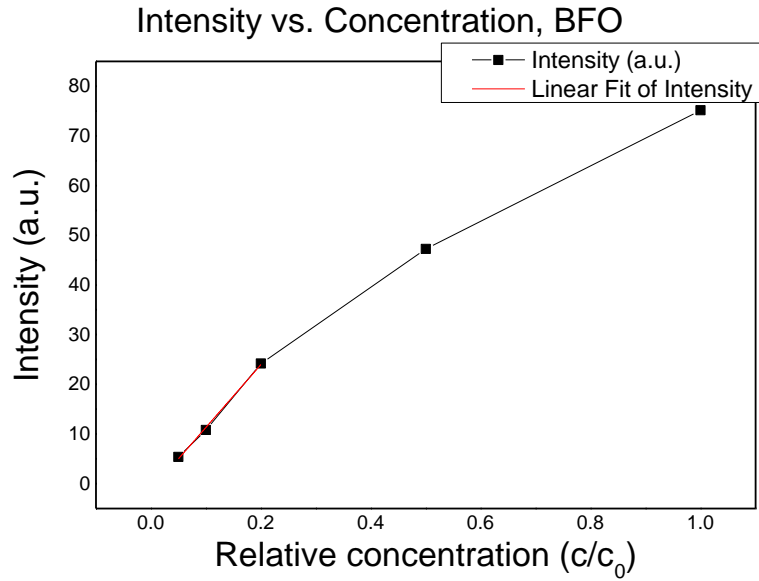


Figure 2.19: HRS intensity as a function of relative concentration. Only the lower, linear portion of the graph is used to calculate the effective hyperpolarisability (and hence the nonlinear coefficient) because the deviation from linearity is due to absorption and multiple scattering in the sample.

The slope (α) of the linear portion of the graph was compared to that of a reference (para-nitroaniline) to determine the effective hyperpolarisability $\langle \beta_{np}^2 \rangle$:

$$I_{2\omega} = GNT_{np} \langle \beta_{np}^2 \rangle I_{\omega}^2 \quad (\text{see Equation 2.23})$$

where G is an experimental constant, N is the concentration and T_{np} is an internal field factor calculated from the solvent and nanocrystal refractive indices (here $n_{\omega} \sim 2.76$ and $n_{2\omega} \sim 3.20$ for BiFeO_3).¹⁵⁹

$$\alpha = G \langle \beta^2 \rangle T I_{\omega}^2 \quad \text{Equation 2.25}$$

$$\Rightarrow \langle \beta^2 \rangle = \alpha \frac{I_{2\omega}}{N} \quad \text{Equation 2.26}$$

$$\Rightarrow \langle \beta_{np} \rangle = G \beta_{pNA} \sqrt{\frac{\alpha_{NP}}{\alpha_{pNA}}} \quad (\text{from Equation 2.24})$$

$$\Rightarrow \langle \beta_{np} \rangle = 8.53 \times 2.59 \times 10^{-29} \text{ esu} \times \sqrt{\frac{3.86 \times 10^{-9}}{2.53 \times 10^{-21}}} \quad \text{Equation 2.27}$$

$$\Rightarrow \langle \beta_{np} \rangle = 2.73 \times 10^{-22} \text{ esu} \quad \text{Equation 2.28}$$

$$\langle d \rangle = \frac{\langle \beta_{np} \rangle}{V_{np}} \quad (\text{from Equation 2.24})$$

where V_{np} is the DLS size by number of the nanoparticles after sedimentation (100 nm, see section on DLS measurements, above).

$$\Rightarrow \langle d \rangle = \frac{2.73 \times 10^{-22} \text{ esu}}{100 \times 10^{-9} \text{ m}}$$

$$\Rightarrow \langle d \rangle = 218.6 \text{ pm/V}$$

Hence the hyperpolarisability was used to calculate the averaged nonlinear coefficient, yielding a value of 220 pm/V with a typical 15% uncertainty.¹⁶

Second harmonic imaging microscopy

To demonstrate the potential for these NPs to be used as diagnostic marker labels, a sample was dispersed in saline solution and deposited in agarose to simulate *in vitro* culture conditions. Analysis was carried out using second harmonic microscopy (see Figure 2.20) which confirmed that the improved crystallinity also led to greater nonlinear optical response from individual nanoparticles.

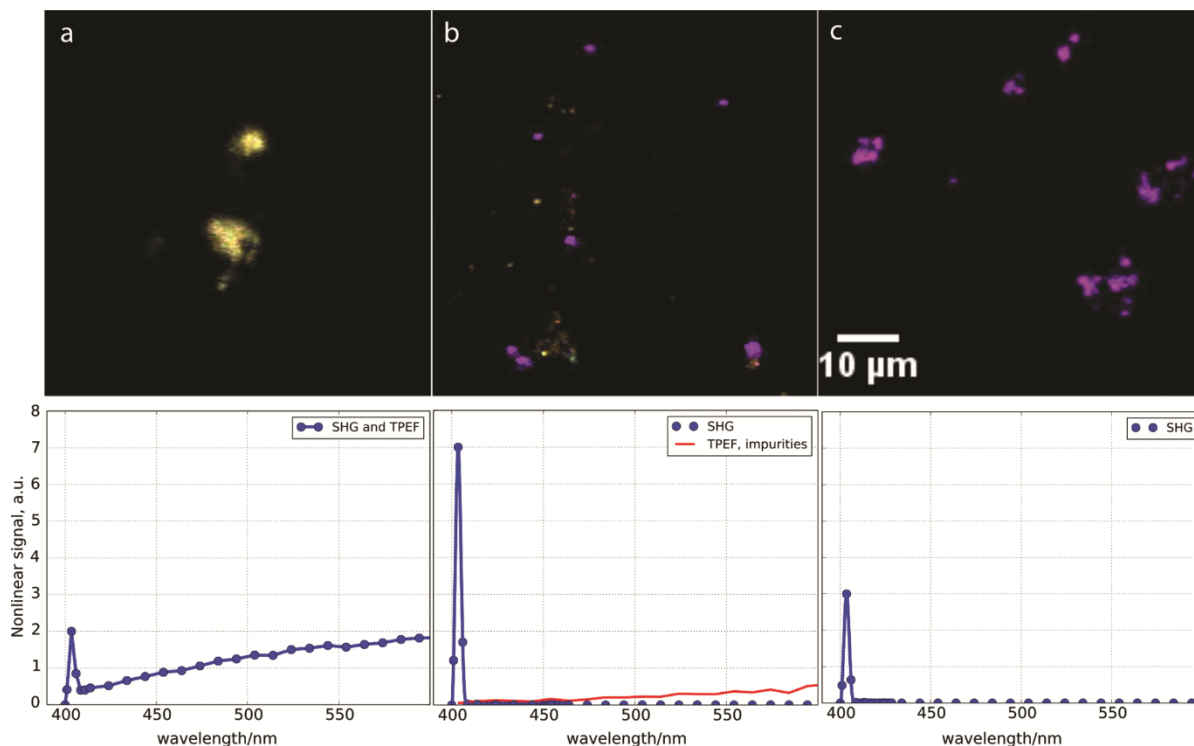


Figure 2.20: Second Harmonic Microscopy images of BiFeO_3 nanoparticle aggregates immobilized in agarose, with the corresponding two-photon emission spectra. *a*, using MA without NaCl or glycerol; *b* using MA + NaCl + glycerol; and *c*, using MA + NaCl. Each image is a composite of 32 colours (from violet to red, corresponding to 32 detection channels): excitation was at 810nm. Violet represents second harmonic (405nm), white corresponds to the mix of other colours and represents two-photon excited fluorescence. In sample *a*, in which neither NaCl nor glycerol was used, the SH signal was almost entirely occluded by two-photon excited luminescence. Typical intensity at the focal spot was 10^{11} W/cm^2

Some luminescence was observed in sample *b* where NaCl and glycerol were used, but it did not co-localize with the SH, suggesting that the phase impurities are not merely present within the BiFeO_3 nanoparticles but form particles and aggregates separately. By contrast, there was no stray two-photon excited luminescence when the sample was prepared using mucic acid and NaCl.

2.3.2 Reagents

Chemicals: $\text{FeCl}_2 \cdot 4\text{H}_2\text{O}$, $\text{FeCl}_3 \cdot 6\text{H}_2\text{O}$, $\text{Bi}(\text{NO}_3)_3 \cdot 5\text{H}_2\text{O}$, $\text{Fe}(\text{NO}_3)_3 \cdot 9\text{H}_2\text{O}$, tartronic acid (TTA), mucic acid (MA), tartaric acid (TA), NaCl, tetraethyl orthosilicate (TEOS), were obtained from Sigma (Ireland); H_3PO_4 , ethanol (EtOH), NaOH, HCl, glycerol and citric acid were obtained from Fisher Scientific (Ireland).

2.3.3 Nanowires

One-dimensional silica nanowires with diameter of $\sim 200 \text{ nm}$ and 5-25 μm in length were prepared using the AAO template synthesis (see Figure 2.21).

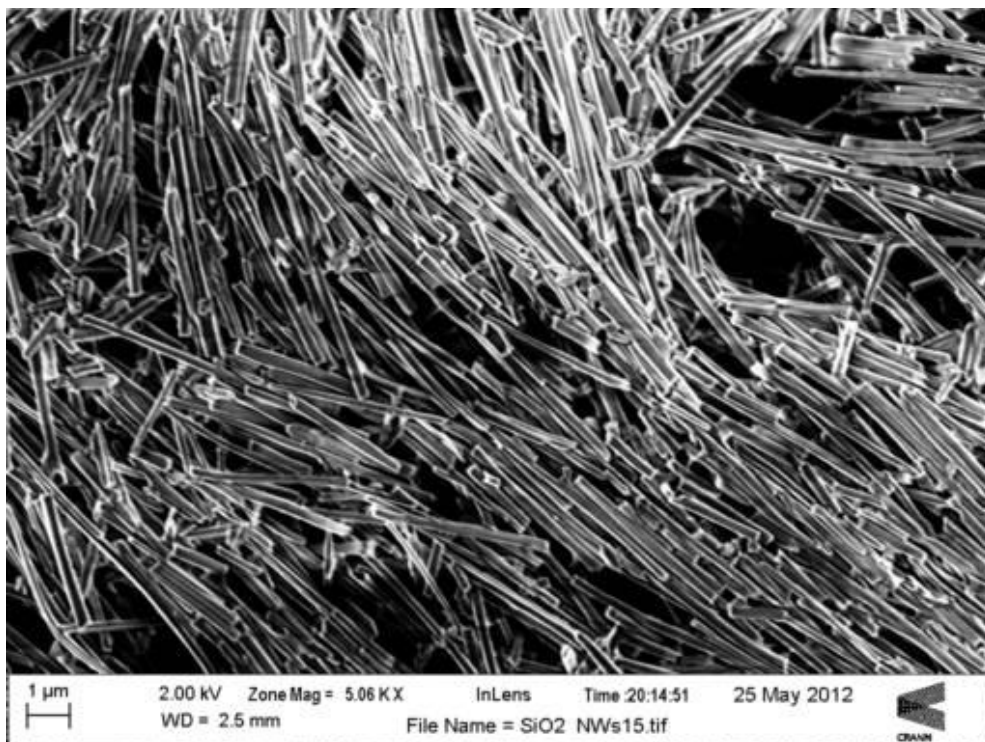


Figure 2.21: SEM image of silica nanowires via AAO template synthesis.

Much refinement was carried out on the synthesis to increase the reproducibility of the method and the uniformity of the end-products.

2.3.4 Multimodal nanomaterials

SiO₂ NWs with Fe₃O₄ NPs

Silica nanowires embedded with Fe₃O₄ NPs were prepared as described in the materials and methods section and as previously published.⁵⁷ With this method, only the smallest Fe₃O₄ NPs were incorporated into the silica wires due to the lack of stability of the NPs in the silica precursor sol, as can be seen in Figure 2.22.

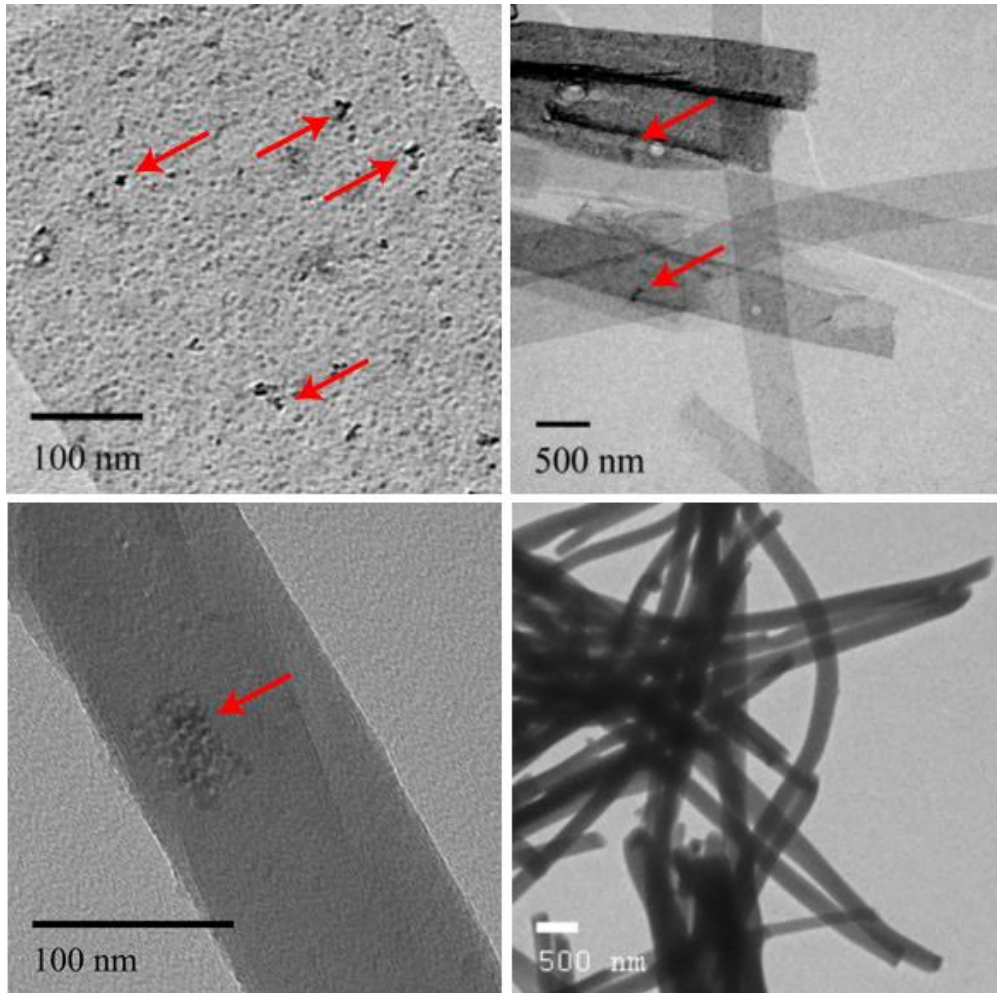


Figure 2.22: TEM images of ultra-small Fe_3O_4 NPs embedded in silica nanowires. Arrows indicate Fe_3O_4 NPs and aggregates.

The concentration of the Fe_3O_4 NPs in the SiO_2 nanowires was measured by VSM, i.e. by measuring the magnetic response of the Fe_3O_4 and that of the nanowires embedded with Fe_3O_4 , as detailed above (see Figure 2.23).

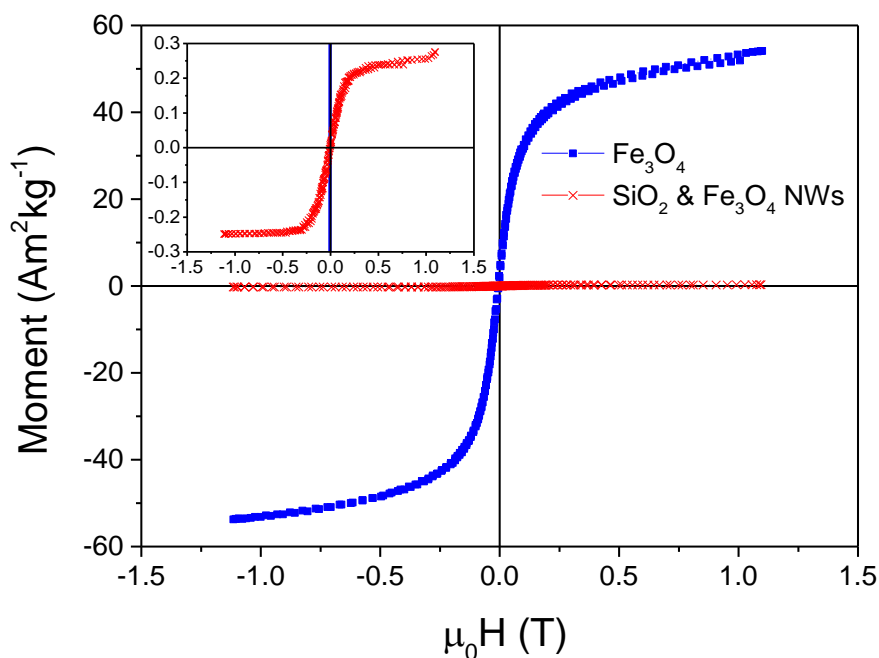


Figure 2.23: VSM of SiO₂ nanowires embedded with Fe₃O₄ in an applied field from -1 to 1 Tesla. Main panel: Magnetic susceptibility measurement of magnetite (■ Fe₃O₄) NPs and silica nanowires embedded with Fe₃O₄ (× SiO₂ & Fe₃O₄ NWs). Inset: zoom of the Y-axis.

The induced magnetic moment of the SiO₂ & Fe₃O₄ NWs was significantly lower than the induced moment of the Fe₃O₄ NPs. This supports the conclusion that the loading of Fe₃O₄ in the nanowires was low. The mass ratio of Fe₃O₄ to SiO₂ was calculated to be approximately 0.5%, much lower than the concentration required for magnetic applications.

It was therefore necessary to enhance the loading by improving the stability of the Fe₃O₄ NPs in the silica sol. By far the most successful route explored was the one-pot synthesis route; the results can be seen in Figure 2.24.

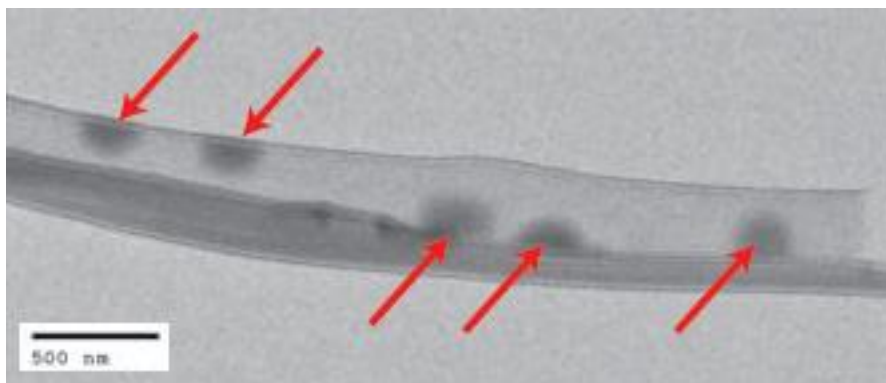


Figure 2.24: TEM image showing improved loading of Fe_3O_4 NP in SiO_2 NW. The arrows indicate aggregates of Fe_3O_4 .

The increased loading was ascribed to the change in preparation protocol. Whereas previously an aqueous suspension of magnetite NPs was prepared using citric acid which was then incorporated into the silica precursor and drawn into the membrane under vacuum, the one-pot method allowed much higher concentrations of magnetite to be added directly to the sol. The presence of much larger aggregates of Fe_3O_4 implies that sonicating the sol containing the NPs and the membranes facilitated the NPs being incorporated into the membrane pores as borne out by VSM measurements (see Figure 2.25)

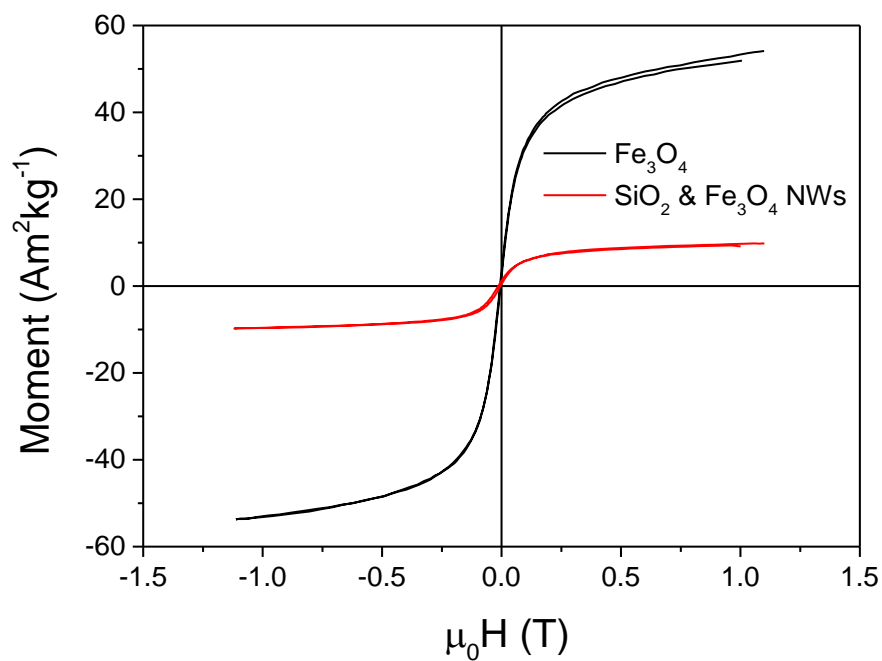


Figure 2.25: Magnetic hysteresis plot of bare Fe_3O_4 and SiO_2 nanowires prepared by the one-pot method embedded with Fe_3O_4 in an applied field from -1 to 1 Tesla.

VSM was used to confirm that the loading had increased to approximately 18%, with a final saturation magnetisation of $9.7 \pm 0.5 \text{ Am}^2\text{kg}^{-1}$ (see Table 2.2).

Table 2.2: Saturation magnetisation and loading of magnetite and corresponding silica nanowires

	Saturation magnetisation ($\text{Am}^2\text{kg}^{-1}$)	Loading
Fe_3O_4	58 ± 4	NA
SiO_2 & Fe_3O_4 via vacuum loading	0.22 ± 0.05	0.40%
SiO_2 & Fe_3O_4 via one-pot synthesis	9.7 ± 0.5	18%

This was sufficient loading to orient the wires in a magnetic field as can be seen in Figure 2.26.

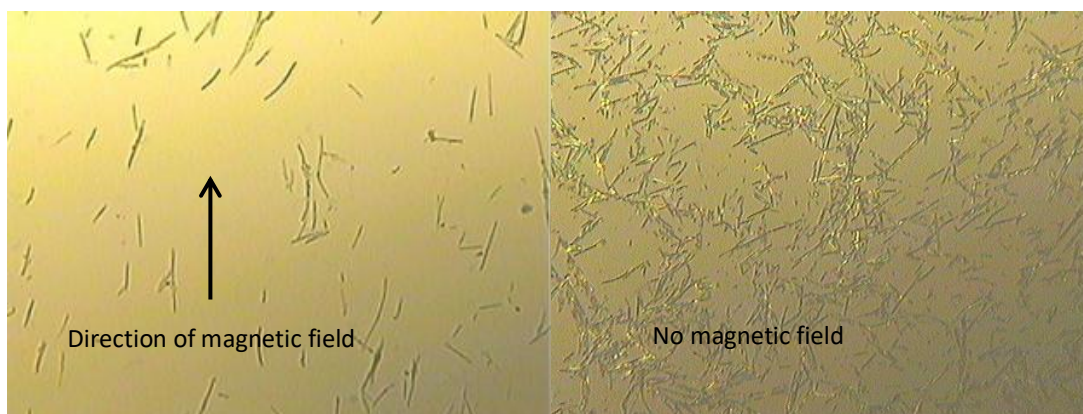


Figure 2.26: Transmitted light microscopy images of SiO_2 NWs embedded with Fe_3O_4 NPs aligned in a magnetic field. Right, control showing no preferred orientation in the absence of a magnetic field.

SiO_2 NWs with BiFeO_3 NPs

The same one-pot method was used to disperse BiFeO_3 NPs and incorporate them into silica nanowires (see Figure 2.27).

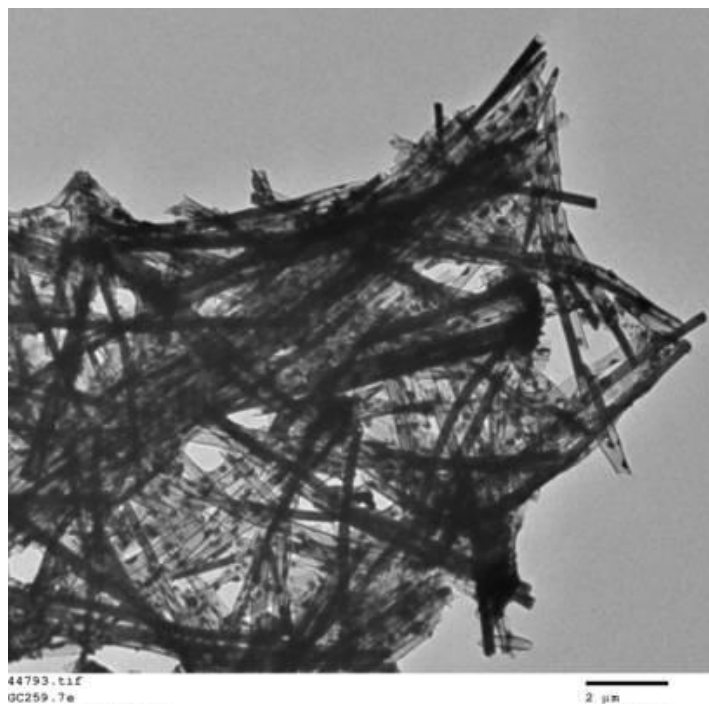


Figure 2.27: TEM image of BiFeO_3 NPs in SiO_2 NWs.

VSM was again used to determine the mass loading, yielding a final saturation magnetisation of $0.12 \text{ Am}^2\text{kg}^{-1}$ as can be seen in Figure 2.28.

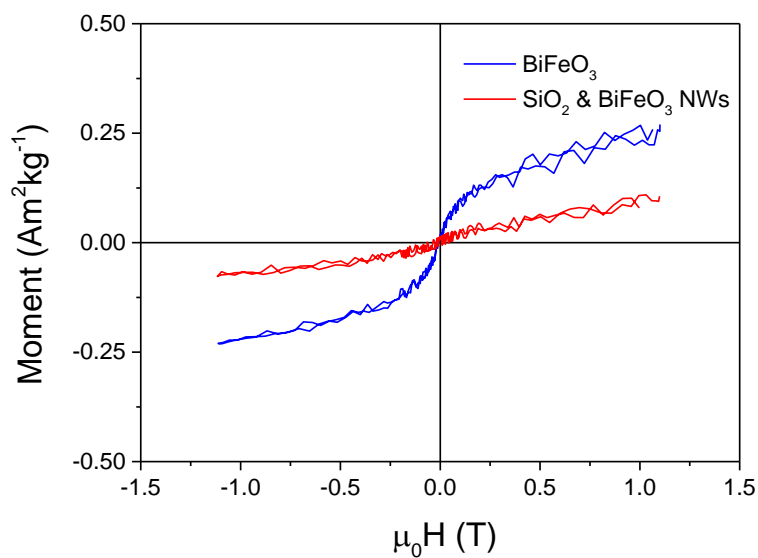


Figure 2.28: Magnetic hysteresis plot of bare BiFeO_3 NPs and SiO_2 NWs embedded with BiFeO_3 NPs in an applied field from -1 to 1 Tesla. Composite nanowires (SiO_2 & BiFeO_3 NWs) had lower induced magnetic moment than the bare BiFeO_3 NPs.

The magnetic response of the BiFeO₃-embedded wires was far lower than of those embedded with Fe₃O₄ (because the saturation magnetisation of BiFeO₃ is much lower than that of Fe₃O₄) and, even with the increased loading, the saturation magnetisation was at the noise limit of the apparatus.

This saturation magnetisation corresponds to a mass loading of approximately 33%. While this is much larger than the mass loading of Fe₃O₄ NPs in the silica wires reported above, observations from TEM indicate that the number of particles or aggregates per section is approximately the same. Not only are the BiFeO₃ NPs larger, the density of BiFeO₃ is higher than that of Fe₃O₄.

Table 2.3: Saturation magnetisation and loading of magnetite and corresponding silica nanowires

	Saturation magnetisation (Am ² kg ⁻¹)	Loading
BiFeO ₃	0.3 ± 0.1	NA
SiO ₂ & BiFeO ₃ via one-pot synthesis	0.10 ± 0.06	33%

Similarly, nanowires were prepared with Fe₃O₄ and BiFeO₃ NPs together (SiO₂ & BiFeO₃@Fe₃O₄ NWs) and Fe₂O₃ and BiFeO₃ NPs (SiO₂ & BiFeO₃@Fe₂O₃ NWs).

SiO₂ NWs with Fe₃O₄ and BiFeO₃ NPs

Fe₃O₄ and BiFeO₃ NPs were dispersed together in the silica precursor sol to incorporate both NPs in the wires by the same method. After dissolving the membrane to release the wires, the composites were imaged using phase contrast microscopy (Figure 2.29).



Figure 2.29: Phase contrast image of SiO₂ NWs embedded with BiFeO₃ and Fe₃O₄ NPs.

These wires were also imaged via two-photon microscopy to determine whether there was sufficient nonlinear optical signal for their application in diagnostic probes (see Figure 2.30).

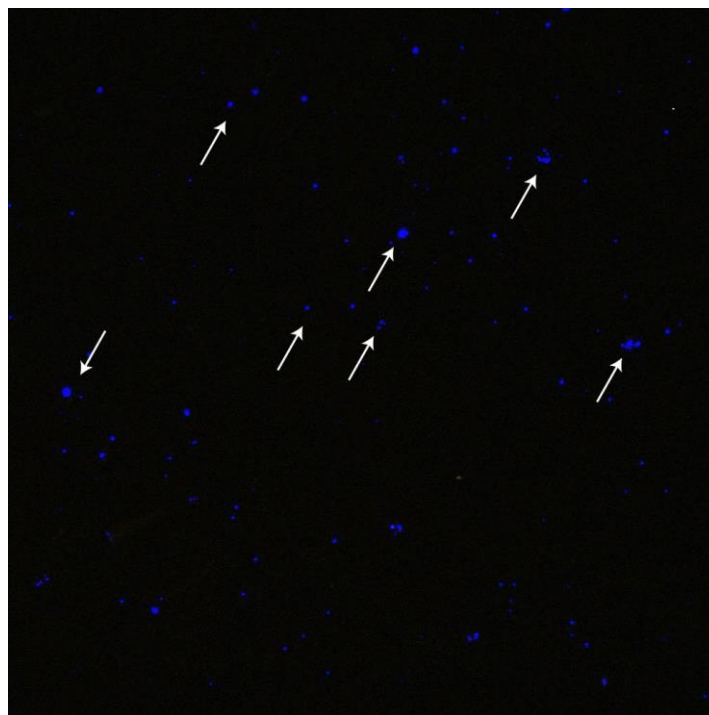


Figure 2.30: Two-photon microscopy image of SiO₂ NWs embedded with Fe₃O₄ and BiFeO₃ NPs. No stray two-photon excited fluorescence was observed (the blue dots indicated by white arrows correspond to SHG). No fluorescent signal was recorded.

BiFeO₃@Fe₃O₄ nanoparticles

Composite BiFeO₃@Fe₃O₄ nanoparticles were formed by incorporating BiFeO₃ into the co-precipitation synthesis of magnetite. Their structure was probed using XRD to determine whether the products were well crystallised (see Figure 2.31).

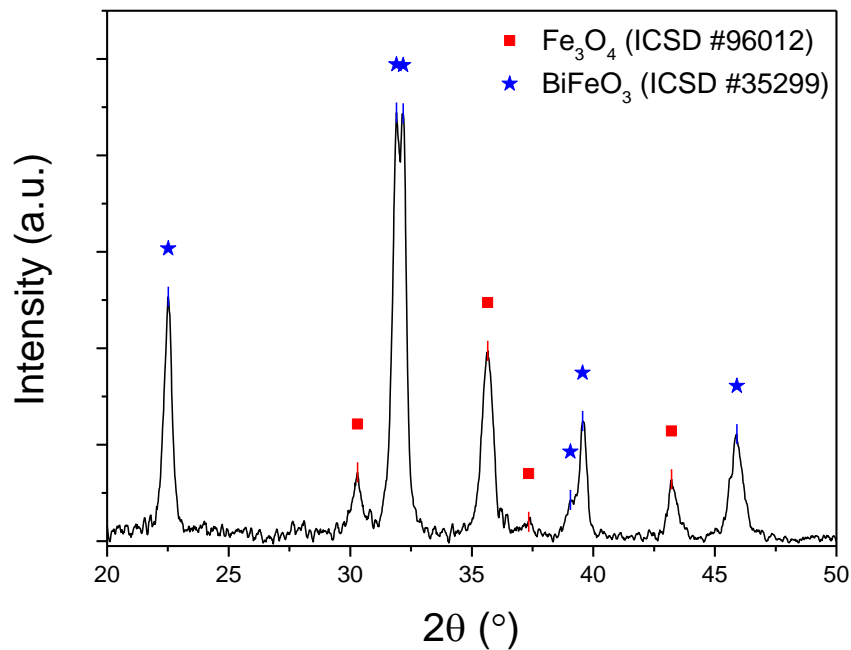


Figure 2.31: X-ray pattern of BiFeO₃@Fe₃O₄ NPs. ★ Peaks corresponding to BiFeO₃ (ICSD #15299), ■ Peaks corresponding to Fe₃O₄ (ICSD #96012)

The relative heights of the peaks in the XRD pattern suggest that there is a greater proportion of well-crystallised BiFeO₃ in the sample than of Fe₃O₄ (see Figure 2.31). The difference in peak height can be attributed to the relative sizes of the NPs, however, as the particle diameter of the BiFeO₃ NPs was approximately double that of Fe₃O₄ NPs – and broadening is more evident on the peaks ascribed to Fe₃O₄.

TEM imaging was used to determine the structure of the composite (see Figure 2.32)

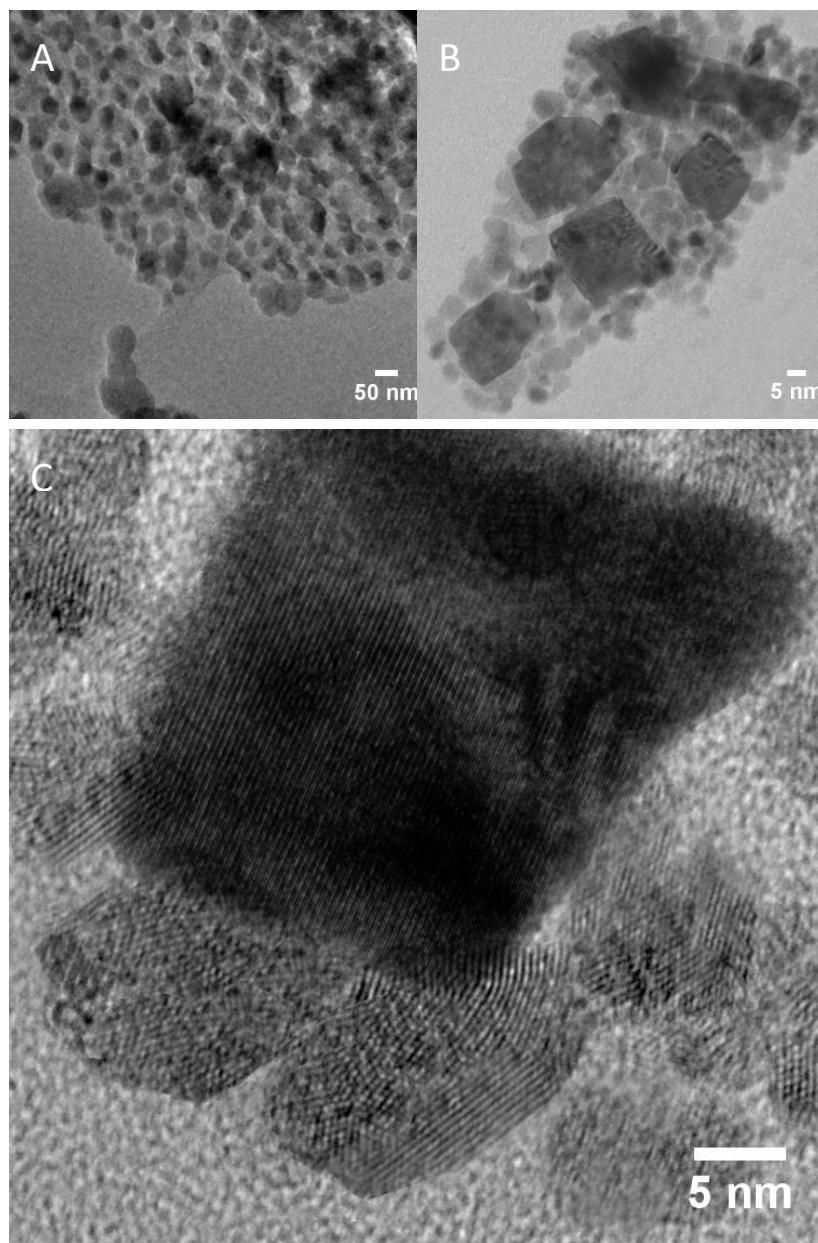


Figure 2.32: TEM and HRTEM images of $\text{BiFeO}_3@Fe_3O_4$ NPs. A, a panoramic image of an aggregate of $\text{BiFeO}_3@Fe_3O_4$ composites. B, a cluster of $\text{BiFeO}_3@Fe_3O_4$ NPs, in which larger, denser (BiFeO_3) NPs are surrounded by less electron-dense, smaller NPs. C, HRTEM showing the crystal planes of the BiFeO_3 NP core surrounded by the Fe_3O_4 NPs.

It was assumed in calculating the required amounts of reagents that the Fe_3O_4 NPs would be the same approximate size ($\sim 10\text{nm}$) whether BiFeO_3 was used as a seed or not (see the section on $\text{BiFeO}_3@Fe_xO_y$ nanocomposites synthesis, under section 2.2.3) and that the BiFeO_3 NPs would be approximately double that of Fe_3O_4 NPs. Determining the physical size of either the core BiFeO_3 or seeded Fe_3O_4 from TEM images is hampered where they overlap, especially where the electron beam transmits through clusters. As expected, panoramic images like Figure 2.32 A demonstrate that there is a distribution of

sizes in the core and seeded particles. This may have implications for the calculated mass ratios. Magnetic susceptibility measurements carried out by Vibrating Sample Magnetometry indicate that the mass ratio of BiFeO₃ is higher than that assumed above (see Figure 2.33).

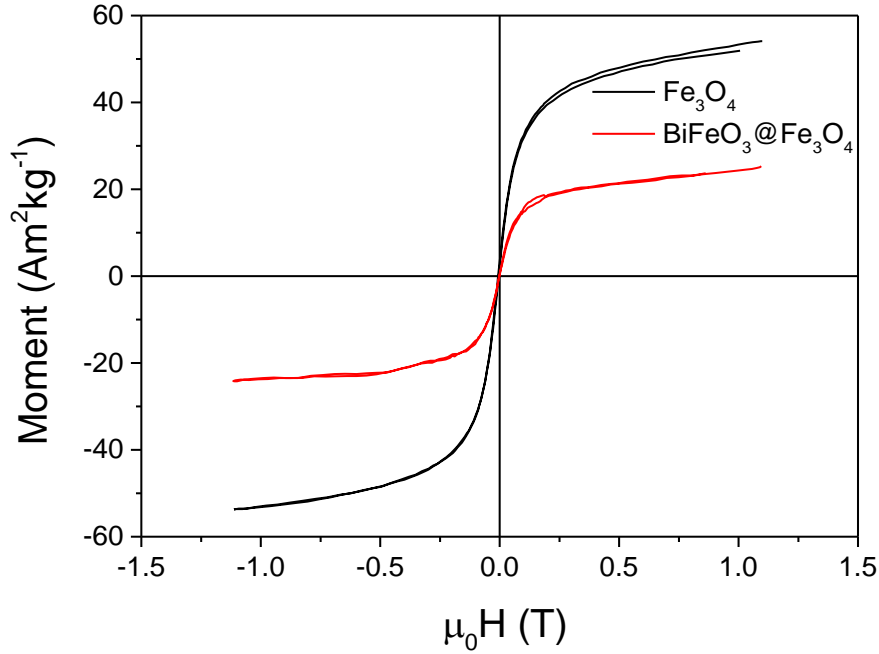


Figure 2.33: VSM measurement of Fe₃O₄ NPs and BiFeO₃@Fe₃O₄ NPs in an applied field from -1 to 1 Tesla. The remnance of both materials is very close to zero, indicating superparamagnetic particles, but the saturation magnetisation of Fe₃O₄ is more than double that of the composite.

The saturation magnetisation of the BiFeO₃@Fe₃O₄ composites was approximately 25 Am²kg⁻¹, whereas the saturation magnetisation of the Fe₃O₄ NPs was 58 Am²kg⁻¹.

Assuming the Fe₃O₄ NPs seeded onto the BiFeO₃ cores were the same size as those synthesised without BiFeO₃, the mass ratio of Fe₃O₄, $m_{r_{exp}(Fe_3O_4)}$ in the composite and hence that of BiFeO₃, $m_{r_{exp}(BiFeO_3)}$, was determined as follows:

$$m_{r_{exp}(Fe_3O_4)} = \frac{M_{satur_{composite}}}{M_{satur_{magnetite}}} \quad \text{Equation 2.29}$$

$$\Rightarrow m_{r_{exp}(BiFeO_3)} = 1 - \frac{M_{satur_{composite}}}{M_{satur_{magnetite}}}$$

$$\Rightarrow m_{r_{exp} (BiFeO_3)} = 1 - \frac{25 \text{ Am}^2\text{kg}^{-1}}{58 \text{ Am}^2\text{kg}^{-1}}$$

$$\Rightarrow m_{r_{exp} (BiFeO_3)} = 1 - \frac{25}{58}$$

$$\Rightarrow m_{r_{exp} (BiFeO_3)} = 0.57$$

where $M_{satur_{composite}}$ is the saturation magnetisation of the composite and $M_{satur_{magnetite}}$ is the saturation magnetisation of magnetite nanoparticles (see section 2.3.1).

The mass ratio of $BiFeO_3$ is higher than the estimated mass ratio (0.516, see Equation 2.11). Several factors may individually explain this discrepancy. First, the estimate assumed that the magnetite nanoparticles were 10 nm and $BiFeO_3$ nanoparticles were 20 nm in diameter whereas the synthesised particles had a size distribution. Second, the estimate assumed close packing of spherical Fe_3O_4 seeds around spherical $BiFeO_3$ cores, but it can be seen from the TEM images that the experimental results deviate from the ideal.

$BiFeO_3@Fe_2O_3$ nanoparticles

$BiFeO_3@Fe_3O_4$ composites were annealed at 350°C in air to cause the Fe^{3+} ions to be reduced to Fe^{2+} , resulting in $BiFeO_3@Fe_2O_3$ nanocomposites. Their structure was probed using XRD to determine whether the products were well crystallised (see Figure 2.34).

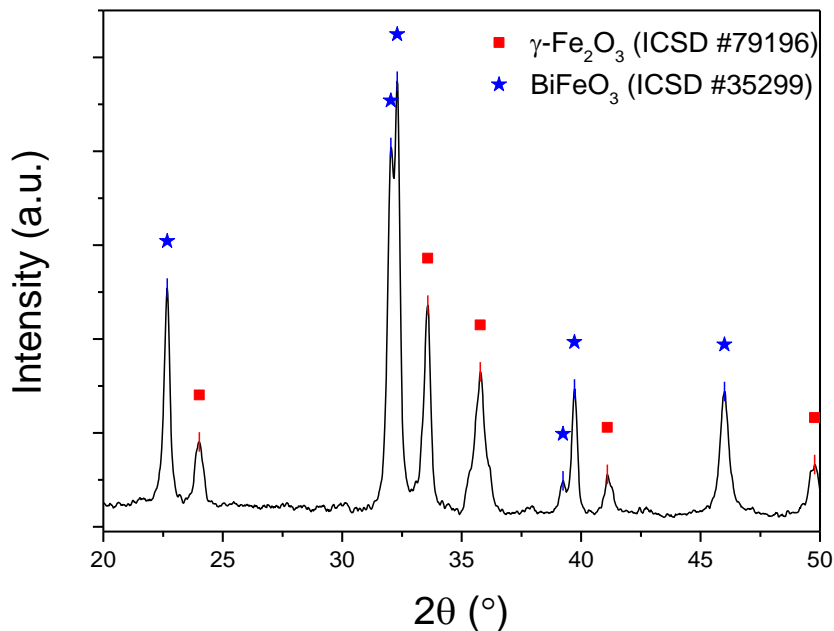


Figure 2.34: X-ray Diffractometer pattern of $\text{BiFeO}_3@Fe_2O_3$ NPs. ★ Peaks corresponding to BiFeO_3 (ICSD #15299), ■ Peaks corresponding to Fe_2O_3 (ICSD #79196)

The presence of $\gamma\text{-Fe}_2\text{O}_3$ (maghemite) was confirmed by XRD (see Figure 2.34). Other small peaks relating to iron oxides are present, but these appear in many different iron oxides such as FeO , FeOOH , and $\alpha\text{-Fe}_2\text{O}_3$, and are almost indistinguishable from the background. Superficially, the ratio of BiFeO_3 is higher than that of the maghemite, there is greater broadening in the maghemite peaks than in those ascribed to BiFeO_3 . Finally, the slightly elevated background compared to $\text{BiFeO}_3@Fe_3O_4$, suggests that some of the powder is amorphous which may be due to the presence of the iron oxide impurities.

$\text{BiFeO}_3@Fe_2O_3$ NPs formed clusters, with larger BiFeO_3 NPs being surrounded by less electron-dense, smaller NPs (see Figure 2.35).

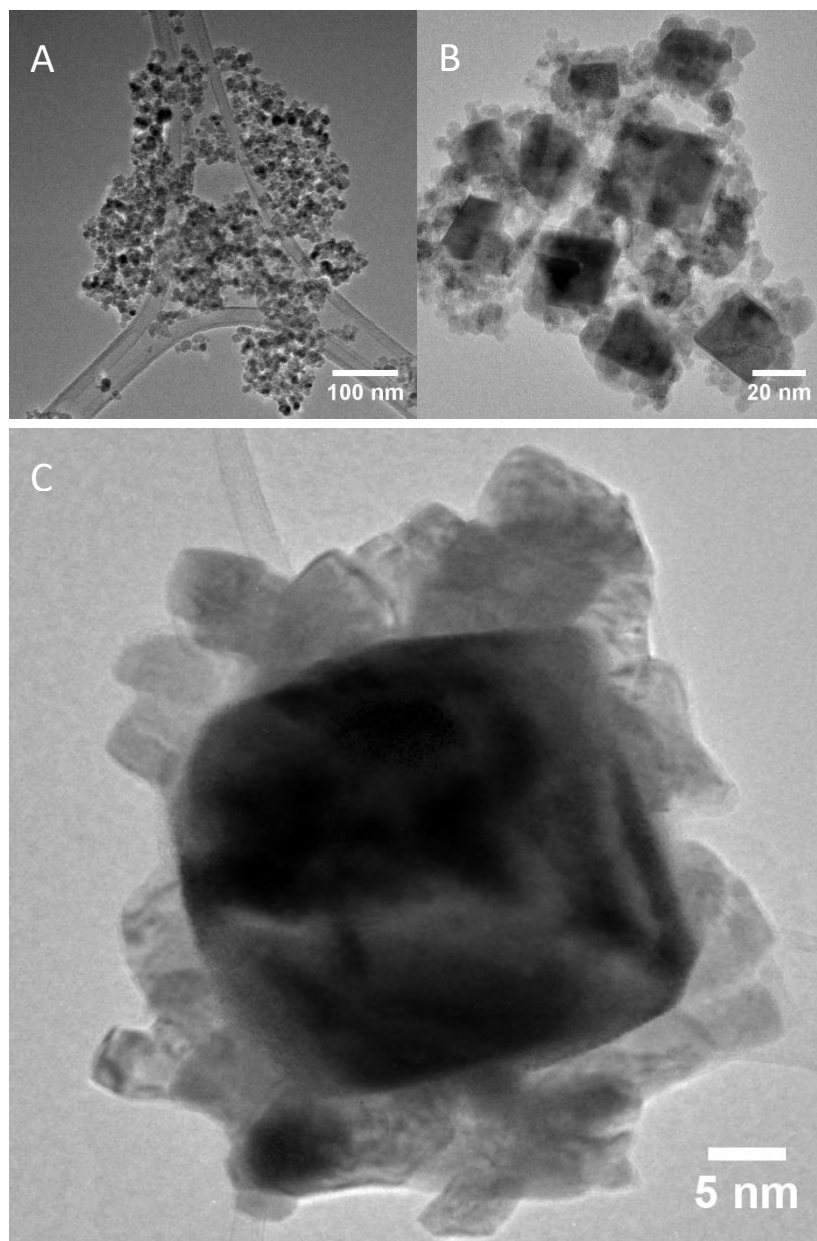


Figure 2.35: TEM and HRTEM images of $\text{BiFeO}_3@Fe_2O_3$ NPs. A, a panoramic image of an aggregate of $\text{BiFeO}_3@Fe_2O_3$ composites. B, a cluster of $\text{BiFeO}_3@Fe_2O_3$ NPs, in which larger, denser (BiFeO_3) NPs are surrounded by less electron-dense, smaller NPs. C, HRTEM showing an individual BiFeO_3 NP core surrounded by the Fe_2O_3 NPs.

The remnance of $\text{BiFeO}_3@Fe_2O_3$ composites is very close to zero indicating superparamagnetic particles (see Figure 2.36).

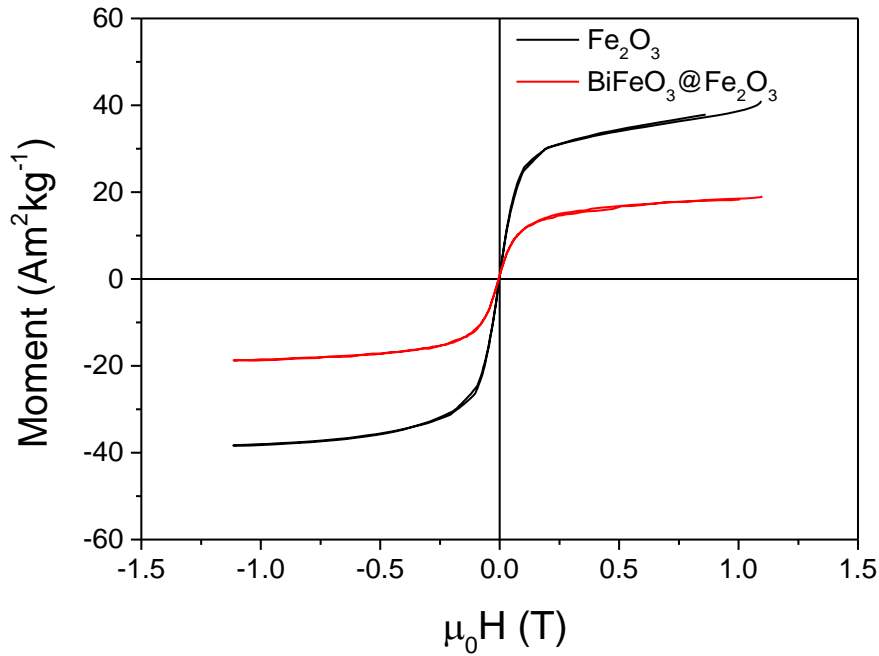


Figure 2.36: VSM measurement of Fe_2O_3 NPs and $\text{BiFeO}_3@Fe_2O_3$ NPs in an applied field from -1 to 1 Tesla. The remnance of both materials is very close to zero, indicating superparamagnetic particles, but the saturation magnetisation of Fe_2O_3 is more than double that of the composite.

In measuring the magnetic susceptibility, a control was prepared in the same way as the composite – by annealing Fe_3O_4 NPs in air at 350°C – to obtain $\gamma\text{-Fe}_2\text{O}_3$ NPs. A commercially available maghemite powder was not considered appropriate because variations in particle size can lead to large deviations in magnetic susceptibility. The saturation magnetisation of the $\text{BiFeO}_3@Fe_2O_3$ composites was approximately $19 \text{ Am}^2\text{kg}^{-1}$, whereas that of the Fe_2O_3 NPs was $41 \text{ Am}^2\text{kg}^{-1}$ (see Figure 2.36).

Using Equation 2.29, this means the mass ratio of BiFeO_3 to Fe_2O_3 NPs in the composite is given by:

$$m_{r_{exp}(\text{Fe}_2\text{O}_3)} = \frac{M_{satur_{composite}}}{M_{satur_{magnetite}}}$$

$$\Rightarrow m_{r_{exp}(\text{BiFeO}_3)} = 1 - \frac{M_{satur_{composite}}}{M_{satur_{magnetite}}}$$

$$\Rightarrow m_{r_{exp}(\text{BiFeO}_3)} = 1 - \frac{19 \text{ Am}^2\text{kg}^{-1}}{41 \text{ Am}^2\text{kg}^{-1}}$$

$$\Rightarrow m_{r_{exp}(\text{BiFeO}_3)} = 1 - \frac{19}{41}$$

$$\Rightarrow m_{r_{exp}(\text{BiFeO}_3)} = 0.54$$

The ratio of the core to seeded shell therefore decreased (from 0.57 in $\text{BiFeO}_3@Fe_3O_4$ to 0.54 in $\text{BiFeO}_3@Fe_2O_3$) on annealing at 350°C, contrary to expectation. This may be due to an increase in the size of the iron oxide particles or to surface reconstruction of the BiFeO_3 core due to interactions with the reduction of Fe_3O_4 to Fe_2O_3 .

This decrease may be evident in the high resolution TEM imaging carried out (see Figure 2.32 and Figure 2.35). However, because TEM is a transmission microscopy technique, it is prohibitively difficult to identify the edges of individual Fe_3O_4 NPs in Figure 2.32 or Fe_2O_3 NPs in Figure 2.35 or to identify where the NPs overlap, so quantitative image analysis was not justified.

2.4 Discussion

For the nanocomposites to be used in biomedical imaging applications, several prerequisites have to be met: the materials must have a sufficiently high response (magnetic or nonlinear optical response or a combination of both) and they must be suitable for quantitative characterisation and functionalisation.

Size and size distribution are of utmost importance in quantifying the response of the materials. Both colloidal stability and monocrystallinity are also crucial to the use of such materials in broader applications – the properties of monocrystalline nanomaterials are far easier to model than polycrystalline or polydisperse materials. Therefore, particle size was determined by several routes (DLS, XRD-Scherrer and TEM). The signal to noise ratio of XRD patterns also gave an initial indication of how well-crystallised the materials were and the appearance of lattice spacings in the HRTEM of BiFeO_3 NPs demonstrated improved crystallinity and the periodicity of the SAED spot patterns confirmed that the particles are monocrystalline.

While the magnetic response determined by VSM is a function of the mass of the sample rather than the particle size, the high magnetic response with minimal hysteresis of the Fe_3O_4 and BiFeO_3 confirm that the NPs are smaller than the magnetic domain size, i.e. the NPs are superparamagnetic.

It is important to note that although BiFeO_3 was present as the dominant phase in the sample at 350°C, higher temperatures were required to eliminate residual parasitic phases.

2.4.1 Additional –OH groups increase crystallinity of BiFeO₃ at lower temperatures

The addition of glycerol significantly increased the ratio of metal to hydroxyl groups. Comparing the height of the XRD peaks to the height of the amorphous background, additional –OH groups increased the crystallinity of any phases present at lower temperatures. If the size of the largest peaks relative to the amorphous background is taken as a measure of how well-crystallized the nanoparticles are, at 500°C the presence of glycerol had no significant impact on the crystallinity, whereas at 200°C, there is significant enhancement as can be seen in Figure 2.14, but parasitic phases were also promoted and even higher temperatures required to eliminate them.

To fully optimize the synthesis and to extend these results to broader applications, further research avenues include characterizing the coordination of the metal ions by the dicarboxylic acids in the precursor and the subsequent complexation by glycerol (or other alcohols). This could lead to new methods for controlling the size and morphology of the nanoparticles.

Narrower size distribution and smaller size are essential to the development of diagnostic probes. The NPs need to be on the order of 10-20 nm if they are to be used to label subcellular structures or to be internalised within cells.

It is also essential that the particles be very monodisperse (have a very narrow size distribution) for quantitative imaging applications, especially for applications including single molecule tracking to monitor cellular processes and events.¹⁶³

2.4.2 Increased salt concentration enhances crystallization of BiFeO₃

At any given temperature, the presence of salt increased the degree of crystallization and reduced the amorphous background in the XRD diffraction patterns. Again, taking the size of the largest peaks relative to the amorphous background to indicate how well-crystallized the nanoparticles are, it can be seen in Figure 2.15 that the addition of salt significantly enhances the crystallization of NPs on annealing.

Comparing these spectra with the high resolution TEM and Selected Area Diffraction (SAED) images shown in Figure 2.16, those particles prepared without salt have an amorphous surface layer (as well as trace impurities of Bi₂₅FeO₃₉). It is deduced that only the surface is amorphous because the selected area electron diffraction patterns indicate a high degree of crystallinity even in the sample whose lattice spacings could not be imaged (Figure 2.16, top row). However, it is also apparent from the rings visible and the large number of spots in the SAED that the sample is polycrystalline.

By contrast, HRTEM images and SAED patterns of individual nanoparticles prepared via NaCl showed the samples to be monocrystalline as the same crystal lattice extends throughout the particles and the spot pattern is a clean array, without amorphous rings or multiple scatterings.

By comparing the VSM results to the corresponding XRD patterns the magnetic response of the BiFeO₃ nanoparticles falls off the lower the degree of doping by parasitic iron oxide phases. Furthermore, it can be seen from Figure 2.17 that the nanoparticles are superparamagnetic, meaning that the particle size is smaller than the magnetic domain size, which is considered to be the spin cycloid length of 62 nm.¹³⁵

The precise mechanism by which the crystallinity is enhanced is not fully understood. Greater concentration of salt may permit more salt bridges to form between the hydroxyl and carboxylate groups thus promoting the formation of the polymeric precursor. On the other hand, it is possible that simply the physical separation of the nucleation sites is responsible: Ostwald ripening proceeds by the fusion of smaller nucleation sites with larger grains. If diffusion is inhibited, larger crystals form.

For imaging applications, this enhanced signal is crucial because the intensity of the signal is so heavily influenced by the size of the crystallites within the NP.⁶ Not only do these results demonstrate that the full volume of each particle is involved in generating the second harmonic, the entire NP is made up of a single crystal (as opposed to each NP being comprised of several crystals).

The presence of multiple crystals in a polycrystalline particle results in a lower intensity output due to the non-constructive interferences between signals from the different crystal domains.^{146,164} This suggests that, where the entire NP comprises an individual crystal, for a given size of NP the harmonic signal should be much brighter when imaging.

The improved crystallinity was assessed quantitatively by probing the nonlinear optical response of the NPs.

2.4.3 Enhanced NLO response of BiFeO₃

Comparing the nonlinear coefficient calculated from HRS measurements (220 pm/V) to a value of 5.5pm/V measured with LiNbO₃ NPs using the same setup,¹⁶ it is clear that BiFeO₃ is a very promising candidate for nonlinear optical applications. This also constitutes a significant improvement in the nonlinear coefficient of BiFeO₃ NPs; a previously reported study carried out on the same setup analysing BiFeO₃ NPs (synthesized via sol-gel combustion using TRIS as a starting fuel) determined the averaged $\langle d \rangle$ coefficient to be 79pm/V,¹⁶⁵ further corroborating the conclusion that the synthesis route described here leads to more monocrystalline nanoparticles. It also confirms that there is an increase

in the portion of the particles which is crystalline (since the intensity of the harmonic varies with the sixth power of the crystal diameter, $I_{2\omega} \propto d^6$). This is crucial for biomedical imaging applications – the smaller size of NP required for subcellular labelling and single molecule tracking impose a heavy cost on the signal intensity, so the enhanced NLO response of BiFeO₃ with improved crystallinity ensures that they are sufficiently bright to label the diagnostic markers of interest.

2.4.4 One-pot synthesis is a more efficient route to obtain silica nanowires

Rather than requiring separately catalysed precursors then transferring to a membrane filter which is connected to a vacuum, silica nanowires synthesised via the templated sol-gel method can be formed by simply combining all reagents in a single beaker, allowing the reaction to begin and then adding the templates.

Without the addition of a base to catalyse the condensation which results in gel formation, the reaction proceeds slowly, allowing the template to fill gradually.

This prevents the destruction of the fragile, costly templates. Furthermore, multiple templates can be immersed at once. The disadvantage is the time it takes to fill one membrane - the templates must be left immersed in the sol for one hour under sonication.

2.4.5 Increased loading of magnetite and/or BiFeO₃ in silica nanowires

A more significant advantage manifests when incorporating nanoparticles into the silica matrix. Existing methods require that the nanoparticles be stabilised in aqueous suspension, to be added during the hydrolysis step in the sol-gel reaction. The nanoparticles used in this study have low colloidal stability at the relevant pH, so loading was very limited with conventional approaches.

By incorporating the bare nanopowders directly into the sonicating sol, the loading of Fe₃O₄ nanoparticles was increased from approximately 0.5% by mass to 18% and the loading of BiFeO₃ NPs was increased to 33%. This yielded magnetic silica nanowires that oriented themselves in the direction of an applied magnetic field. This confirms that the composite nanowires synthesised have the desired physico-chemical properties.

2.4.6 Magnetic-harmonic nanoparticles were synthesised

Fe₃O₄ seeds were grown on the surface of BiFeO₃ by a simple modification of Massart's protocol, yielding the novel composite BiFeO₃@Fe₃O₄. These nanoparticles were reduced to form BiFeO₃@Fe₂O₃ nanocomposites, and both products were characterised by XRD, TEM and VSM. The increased magnetic

response of these composites is of particular interest for multimodal applications because the magnetic response of pure-phase BiFeO_3 was shown to be so low.

2.5 Conclusion

Bismuth ferrite and magnetite nanoparticles and composites were synthesised and characterised with a suite of analytical techniques to quantify their material properties. Novel, simple routes were developed to enhance their crystallinity and nonlinear optical response and to prepare them for downstream applications. To enhance their biocompatibility, BiFeO_3 and iron oxide NPs and composites were incorporated into silica nanowires.

Multimodal composites of bismuth ferrite, iron oxides and silica were also prepared and analysed by a full suite of physico-chemical characterisation.

Chapter 3

Functionalisation of nanoparticles

3.1 Introduction

This chapter presents the surface modification and properties needed to deliver multimodal probes for biomedical applications. Starting from the importance of functionalisation as a route to achieve biocompatibility, the uptake and targeting are also investigated to determine the functionalised nanomaterials' viability as diagnostic probes.

3.1.1 Functionalisation

To engineer probes that target specific cellular structures or carry out specific functions, it is necessary to modify the surface of nanoparticles. The attachment of targeting compounds can also serve to passivate the surface and to modulate the cytotoxic response.

By functionalising nanoparticles with antibodies which only bind to one specific antigen, the nanoparticles can then be targeted to sites where those antigens are expressed. Common targets are receptors expressed on the surface of cells as depicted in Figure 3.1. Targeting is discussed in further detail in section 3.1.3.

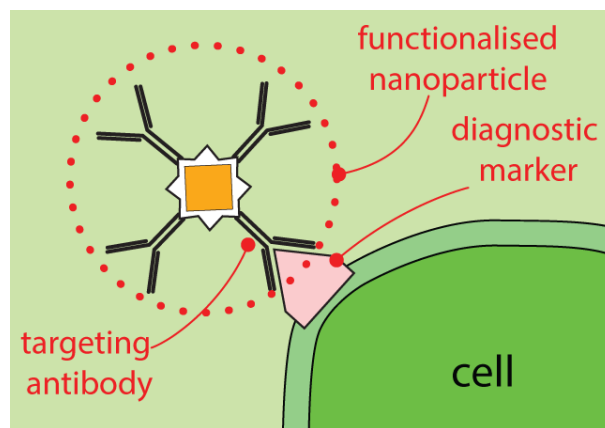


Figure 3.1: Functionalisation of a nanoparticle with a targeting ligand. The antibody binds specifically to a diagnostic marker on the surface of a cell.

Several steps are involved in functionalising nanoparticles for targeting. After synthesis of the nanoparticles, the surface must be prepared by silanisation. This procedure passivates the surface of

the nanoparticle and allows control over the surface chemistry, providing a linker between the nanoparticle and subsequent conjugation agents.

The success of functionalisation is determined by several factors such as aggregation and flocculation of the nanoparticles at each step, the degree of surface cover of functionalisation layers, and the availability of binding sites on the nanoparticle and on the antibody. Should the nanoparticles aggregate before they are silanised, for example, the silane layer will form around aggregates rather than around individual nanoparticles. This is undesirable because not only does it increase the effective size of the particles, but also raises the polydispersity in the sample.

Silanisation is an active area of research and several protocols have been developed which include the use of ultra-sonication before and during the reaction to add energy to the reaction and disperse aggregates.

The degree and nature of the surface cover are measures of adlayer formation. If ideal surface cover is achieved, with the attached molecules forming a perfect monolayer, all available sites on the surface of the nanoparticle would bind to individual silane molecules such as APTES before they polymerise. APTES molecules have an effective diameter of approximately 0.4 nm^2 once they bind to the surface, so to achieve ideal close packing, available binding sites would also have to be spaced at matching intervals, i.e. with ordered periodicity.

The reality can be far from the ideal. Dangling bonds and surface tension result in strain and defects in the lattice and cause surface reconstruction, which breaks the periodicity of the crystal at the surface.

Furthermore, APTES molecules polymerise, and may do so before bonding to the surface. Finally, rather than a closely packed single layer forming, further layers of APTES molecules can attach to those which have bound to the nanoparticle surface, which could lead to the formation of islands around the nanoparticle, rather than a uniform monolayer.

Several research groups have indicated that the above challenges can be mitigated by using sonication to disperse the nanoparticles and by reacting in the presence of an acid to inhibit polymerisation and promote attachment to the surface.^{166,167} However, lowering the pH affects the colloidal stability and, depending on the interaction between the nanoparticle's surface chemistry and the solvent, may increase aggregation and polydispersity.

Colloidal stability is also a challenge when conjugating the silanised nanoparticles – they must be re-dispersed in aqueous suspension at pH 7. Bioconjugation then involves incubation of the silanised nanoparticle with a targeting moiety such as an antibody in the presence of a crosslinker, a catalyst

which promotes binding. Here stability is even more critical as this step must be carried out without sonication, to be avoided as it would denature the biological moieties.

The advantage of functionalisation is to ensure biocompatibility or extend circulation time, control membrane internalization but also to enable coupling with biomarkers for diagnostics. The next sections provide some insight into specific markers, modifying the surface to extend the circulation time *in vivo*, increase tissue penetration and also control the cellular uptake of nanoparticles.

3.1.2 Biocompatibility

A biomaterial or diagnostic probe is biocompatible if it can enter a host, be transported and carry out its intended function without disrupting the normal processes in the recipient. The biocompatibility of a biomaterial is a measure of how well it can elicit its devised function while minimising any undesired impacts on the host.¹⁶⁸ Silane coating is biocompatible and protective to and from the core to the environment.^{169,170} A Silane layer protects the nanoparticle surface from degradation in a biological environment and inhibits the metal ions of the crystalline core from leaching into the suspension, thereby minimising unwanted interactions and increasing their biocompatibility.

3.1.3 Targeting

Targeting is the delivery of therapeutic or pharmaceutical agents to their intended site of action. This is achieved by either encapsulating with or conjugating to a ligand which binds specifically at the desired location. The purpose of targeting is to improve the efficiency and/or reduce the non-specific effects of the agent.¹⁷¹ This is particularly important for diagnostic probes, to increase their accumulation at the site of interest and maximise their efficacy and biocompatibility.

To ensure that probes ultimately label only the structures of interest or to ensure the label is transported to the site of interest, probes must be targeted to the relevant moiety or site. For instance, diagnostic markers such as HER2 and EGFR can be tagged with probes using antibodies which bind to the receptors (anti-HER2 and anti-EGFR antibodies)^{49,50} and this also induces particle uptake.

Epidermal growth factor receptor

Epidermal growth factor receptor is a transmembrane glycoprotein which exists in its inactive monomeric form until activated by growth factors which bind to specific ligand sites on its extracellular domain (see Figure 3.2). Dimerization induces tyrosine autophosphorylation at intracellular domain sites, initiating several signal transduction cascades which effect the cell's phenotype including cell proliferation, migration, adhesion, angiogenesis, and inhibition of apoptosis.¹⁷²

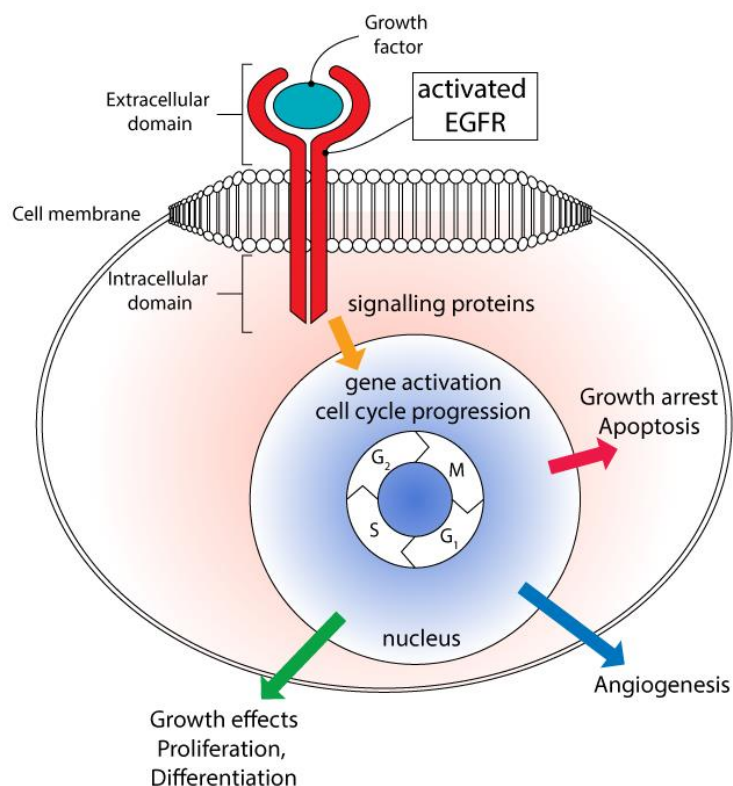


Figure 3.2: Simplified schematic illustration of EGFR stimulation of cell cycle progression and its effects. Reproduced from Harari et al.¹⁷³

It is an oncogene – several mutations associated with cancers lead to overexpression, mis-regulation and amplification of EGFR, including non-small cell carcinoma of the lungs, head and neck and glioblastoma. Consequently, EGFR is a promising target for a class of anticancer tyrosine kinase inhibitors, including erlotinib, afatinib and gefitinib.^{174–177}

Specificity and sensitivity

The performance of a probe or sensor is reported with respect to specificity and sensitivity. Specificity describes to what degree a response is triggered by untargeted moieties; sensitivity describes how accurately the response tracks changes in the target’s concentration.

Both measures are required to understand the effectiveness and accuracy of a sensor. For example, while a sensor might correctly detect the presence of EGFR in 99% of samples, a specificity of 95% will mean that many false positives will also be reported. This is especially significant where the true or background rate is low. Consider an experiment where EGFR expression is inhibited such that only 10% of cells have surface markers for EGFR. If 1,000,000 cells were plated, that will mean 100,000 express

EGFR, and the probe described above will correctly identify 99,000 of those cells. 1,000 cells are incorrectly identified as lacking EGFR (known as a false negative or Type II error).

However, because the probe only has a specificity of 95%, the probe will randomly bind to 50,000 cells—only 10% of which express EGFR. Hence, for every two cells correctly labelled as expressing HER2, there will be approximately one cell which is incorrectly labelled expressing EGFR (known as a false positive or Type I error).

Therefore, the performance of a probe is measured by its specificity and sensitivity, but its effectiveness is a function of the frequency of occurrence or concentration of the target.

3.1.4 Uptake

There are several mechanisms of endocytosis allowing chemicals or material to be internalised by cells. Phagocytosis, clathrin-mediated endocytosis, caveolae and micropinocytosis are four routes of active transport by which small molecules are moved through the cell membrane against a concentration gradient.¹⁷⁸ These pathways may all be exploited to increase the uptake of nanoparticles by cells, with a view to raising the loading at the target site.

3.1.5 Diagnostic probes

Diagnostic markers are biological indicators used to diagnose a disease. Such markers can be quantitative and used to evaluate the severity or progression of the disease (e.g. thyroid hormone levels in the blood indicate the level of thyroid activity) or qualitative, indicating the presence of a disease, such as the overexpression of EGFR in lung cancer cells.¹⁷⁹

Diagnostic markers specific to certain cells, targeted with magnetic/harmonic probes, allow those cells to be imaged by both magnetic resonance and second harmonic imaging. The magnetic properties of these probes can be further exploited by magnetic separation, cell counting and sorting, drug delivery and magnetic hyperthermia, while the harmonic-generating properties has potential application for *in vivo* imaging, flow cytometry and photodynamic therapy.

Diagnostic probes made from NLO materials therefore need to be functionalised for biocompatibility targeting and to ensure they are safe to use. Reagents, protocols and methodologies must be optimised for each different metallic nanoparticle requiring the characterisation of each intermediate product as outlined in the table below.

Table 3.1: Matrix of nanomaterials, their properties and the nanocomposites in which the properties are to be combined. Legend: ✓ known property ⊙ target property. The relative importance of each is represented by the frequency of each symbol.

Nanomaterial/composite	Optical properties	Magnetic properties	Surface properties	Geometric properties	Composite structure
BiFeO ₃ NPs	✓✓✓	✓			Metal oxide
Fe ₃ O ₄ NPs		✓✓✓			Metal oxide
SiO ₂ NWs			✓	✓✓	Dielectric material
SiO ₂ NWs with BiFeO ₃	✓		⊙	✓✓	Dielectric material embedded with metal oxide
SiO ₂ NWs with BiFeO ₃ & Fe ₂ O ₃	✓	✓	⊙	✓✓	Dielectric material embedded with two metal oxides
SiO ₂ NWs with BiFeO ₃ & Fe ₃ O ₄	✓	✓	⊙	✓✓	Dielectric material embedded with two metal oxides
BiFeO ₃ @Fe ₃ O ₄ NPs		✓✓			Core@shell composite of two metal oxides
BiFeO ₃ @Fe ₂ O ₃ NPs	✓	✓✓			Core@shell composite of two metal oxides
BiFeO ₃ @asc NPs	⊙	⊙	⊙	⊙	Metal oxide with stabilising ligand (ascorbic acid)
BiFeO ₃ @APTES NPs	⊙	⊙	⊙	⊙	Metal oxide with passivated surface (-NH ₂ from aminopropyltriethoxysilane)
BiFeO ₃ @Fe ₂ O ₃ @asc NPs	⊙	⊙	⊙	⊙	Core@shell composite of two metal oxides with stabilising ligands
BiFeO ₃ @Fe ₃ O ₄ @asc NPs	⊙	⊙	⊙	⊙	Core@shell composite of two metal oxides with stabilising ligands
BiFeO ₃ @Fe ₂ O ₃ @APTES NPs	⊙	⊙	⊙	⊙	Core@shell composite of two metal oxides with passivated surface

3.2 Materials and Methods

3.2.1 Reagents

MES Buffer, N-(3-Dimethylaminopropyl)-N'-ethylcarbodiimide hydrochloride (EDC), L-Ascorbic acid sodium salt, bovine serum albumin, 3-(2-pyridyl)-5,6-bis(phenyl sulfonic acid)-1,2,4-triazine (ferrozine),

gentamicin, streptomycin sulfate, para formaldehyde (PFA), sterile water and phosphate buffered saline (PBS), Nuclear fast red and tetramethylammonium hydroxide (TMAH) were obtained from Sigma (Ireland); H₃PO₄, ethanol (EtOH), NaOH, HCl, glycerol and citric acid were obtained from Fisher Scientific (Ireland). Recombinant goat anti-human EGFR antibody, Mix-n-Stain™ CF™, Dulbecco's modified Eagle's medium (DMEM) manufactured by Gibco were obtained from Invitrogen Ltd (Ireland). RPMI 1640 medium with 25 mM HEPES, HyClone medium, TrypLE, Fetal Bovine Serum (FBS), L-glutamine, penicillin G, epidermal growth factor (EGF), hydrocortisone, Hoechst, propium iodide, and JC-1 manufactured by Gibco were obtained from Invitrogen Ltd (Ireland). Endothelial Growth Medium 2 and Endothelial Cell Growth Medium 2 Supplement Mix were obtained from PromoCell (Ireland).

Cell culturing

Human lung epithelial carcinoma cells (A549 cells) from American Type Culture Collection (ATCC) were kindly provided by Dr Dania Movia, Trinity College Dublin.

A549 cells were cultured in Dulbecco's Modified Eagle Medium (DMEM) with 2 mM L-glutamine, supplemented with 10% fetal bovine serum and 50 µg/mL gentamicin in a 37°C incubator at 100% humidity and 5% CO₂.

3.2.2 Protocols

Stabilisation

Stabilising nanoparticles was the first step explored where ascorbic acid was selected as a chelating ligand for nanoparticles prepared via aqueous routes as the molecule is non-toxic and small relative to the size of the nanoparticle.¹⁸⁰

Large batch stabilisation

A large quantity of BiFeO₃ (200 mg) was stabilised in smaller batches by using slurry of 40 mg with NH₄OH (10M, approx. 2mL per batch) using a mortar and pestle. Aliquots of the slurry were transferred to a beaker which was topped up with NH₄OH (10M) for a final volume of 100 mL.

Ascorbic acid was added (39 mg) and the pH adjusted to 12.5 with concentrated NH₄OH and the mixture was left stirring at 80°C for 1 h.

The ascorbic acid is in vast excess (about twenty times that needed to cover the surface of the nanoparticles assuming a diameter of 20nm, calculations below). At least 5 washing steps were needed. Ethanol (5%) was used to promote precipitation.

To calculate the total mass of ascorbic acid adsorbed onto the surface of the NPs, the total surface area of all NPs in the suspension is first required.

This was achieved by calculating the mass of an individual BiFeO₃ NP which, recall from Chapter 2, resulted in the following:

$$A_{NP} = 4\pi r^2 = 4\pi(10 \times 10^{-9}m)^2 \quad \text{Equation 3.1}$$

$$V_{NP} = \frac{4}{3}\pi r^3 = \frac{4}{3}\pi(10 \times 10^{-9}m)^3 \quad \text{Equation 3.2}$$

This led to a mass of:

$$m_{NP} = V_{NP} \times \rho = \frac{4}{3}\pi r^3 \times \rho \quad \text{Equation 3.3}$$

$$\Rightarrow m_{NP} = 3.491 \times 10^{-17}g \quad \text{Equation 3.4}$$

Thus, the number of NPs (N_s) in a given mass of BiFeO₃ (m_s), and hence the total surface area of all NPs in the sample (A_s) can be calculated using Equation 3.1:

$$N_s = \frac{m_s}{m_{NP}} = \frac{0.2g}{3.491 \times 10^{-17}g}$$

$$N_s = 5.729 \times 10^{15} \text{ nanoparticles} \quad \text{Equation 3.5}$$

$$\Rightarrow A_s = N_s \times A_{NP} = N_s \times 4\pi r^2$$

$$\Rightarrow A_s = 5.729 \times 10^{15} \times 4\pi(10 \times 10^{-9}m)^2 \quad \text{Equation 3.6}$$

$$\Rightarrow A_s = 7.199 m^2$$

The topological polar surface area of ascorbic acid, asc_A , is $1.07 \times 10^{-18} m^2$, and assuming complete surface cover, the number of ascorbic acid molecules which adsorb onto the surface (N_{asc}) is therefore given by:

$$N_{AA} = \frac{A_s}{A_{AA}} = \frac{7.199 \text{ m}^2}{1.07 \times 10^{-18} \text{ m}^2}$$

$$\Rightarrow N_{AA} = 6.728 \times 10^{18} = 1.117 \times 10^{-5} \text{ mol}$$

$$\Rightarrow m_{AA} = N_{asc} \times M_{asc} = 1.117 \times 10^{-5} \text{ mol} \times 176.12 \text{ g} \cdot \text{mol}^{-1}$$

$$\Rightarrow m_{AA} = 1.96 \times 10^{-3} \text{ g}$$

This is required to achieve complete surface cover of nanoparticles with a diameter of 20nm. There are many reasons why complete monolayer formation will not occur – the binding sites on the surface of the BiFeO₃ may not be ideally presented due to the morphology or surface chemistry of the NPs, and this may vary depending from face to face on the nanocrystal; the diameter of the nanoparticles is derived from a distribution of differently sized nanoparticles; the surfaces of aggregates may also be covered, thereby reducing the number of individual nanoparticles and decreasing the total binding areas.

To prevent all mechanical and physical aggregations, sonication was used to achieve optimal stabilisation. However, the synthesis was carried out with ascorbic acid in vast excess (under sonication) to optimise the adsorption of the ascorbic acid onto the NP surface.

Functionalisation of BiFeO₃ nanoparticles

The next step was to functionalise the NP and base capping agent. Thus, the functionalisation was based in principle on encapsulation and bioconjugation of the core following literature examples and as outlined in the following schematic (see Figure 3.3).

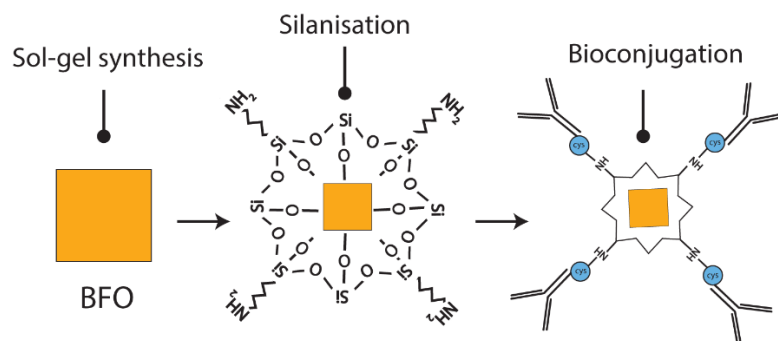


Figure 3.3 Schematic for surface modification functionalisation of BiFeO₃ NP. From Left to Right, the bare BiFeO₃ nanocrystal, silanization with APTES, followed by functionalisation with a primary antibody.

Coating of BiFeO₃ NP with APTES (BiFeO₃@APTES)

Large batches of nanoparticles (1g) were dispersed in a 1% acetic acid solution of bench EtOH (100 mL) by sonication for 30 minutes for a concentration of 10 mg/ml. Coating with APTES (6mL) was achieved and the mixture was left to sonicate at room temperature for one hour, then washed once with the 1% acetic acid EtOH solution and three times with EtOH.

BiFeO₃ nanoparticles and BiFeO₃@Fe₃O₄ nanoparticles were coated with APTES as also described above then set aside for direct conjugation with both unlabelled recombinant goat anti-human EGFR antibody (anti-hEGFR) and fluorescently labelled hEGFR.

Targeting: bioconjugation with a fluorescently labelled antibody (@anti-hEGFR)

Fluorescently labelled anti-EGFR antibodies were prepared then conjugated to nanocomposites for imaging and flow cytometry.

Fluorescent labelling of anti-EGFR antibody was achieved by using CF™ 488A (CF488). Anti-hEGFR was labelled with a fluorescent stain using Mix-n-Stain™ CF™ 488A as follows:

Vials of the staining buffers were warmed to room temperature and then centrifuged. The reaction buffer (10 µL, “10×” solution) was added to the anti-hEGFR (90 µL, 100 mg/mL in PBS), vortexed briefly and added to the CF dye. The mixture was vortexed again, covered with aluminium foil, incubated for 30 min and marked as anti-hEGFR-CF488.

Bioconjugation with anti-EGFR antibody was obtained as sterile product as outlined below:

Under sterile conditions, BiFeO₃@APTES (50 µg) was dispersed in PBS (100 µL) by agitation on a vortex/shaker with. Anti-hEGFR-CF488 (114 µL, 1 mg/mL in PBS) was added and the mixture was left overnight on a shaker at 4°C, then washed three times with PBS (2.5 mL) with centrifugation at 1400 × g, again maintaining sterile conditions. The suspension was marked BiFeO₃@anti-hEGFR-CF488 and set aside. The same procedure was carried out with unlabelled recombinant human anti-hEGFR antibody and marked BiFeO₃@anti-hEGFR, and again with BiFeO₃@Fe₃O₄ to obtain BiFeO₃@Fe₃O₄@anti-hEGFR-CF488 and BiFeO₃@Fe₃O₄@anti-hEGFR.

3.2.3 Incubation of cells with nanomaterials

To assess the uptake of BiFeO₃@Fe₃O₄ nanocomposites, ascorbic acid-stabilised nanoparticles were dispersed from sterile stock solution at a concentration of 10 mg/ml, then diluted with serum-free medium to 750 µg Fe/ml (C1), 500 µg Fe/ml (C2), and 250 µg Fe/ml (C3) with ultra-sonication for 30 min. Suspensions of ascorbic-acid (asc) stabilised BiFeO₃ nanoparticles (BiFeO₃), BiFeO₃@Fe₃O₄

nanoparticles without ascorbic acid (non-asc NP) and fluorescently labelled, functionalised nanoparticles (fNP) were prepared in the same way as C2, i.e. at 500 µg Fe/ml, as controls for the different stages of synthesis. A suspension of 9 nm Fe₃O₄ nanoparticles (MF66, 500 µg Fe/ml) were used as positive control for iron content (POS). To determine whether the uptake could be inhibited, 500 µg Fe/ml of BiFeO₃@Fe₃O₄@asc were also prepared with 1% sodium azide, as were each of the controls. To distinguish inhibited controls from the uninhibited treatments, the suffix *-Inh* was used. (C2-Inh, BiFeO₃-Inh, non-asc NP-Inh, fNP-Inh, POS-Inh respectively).

Incubation in 24-well plates for iron and protein quantitation analysis

Cells were dispensed on 24-well plates at 5×10^6 cells per mL in 2 mL of complete medium, allowed to attach and incubate for 24h before being rinsed with warmed serum-free DMEM. The complete medium was then replaced (2mL).

Treatment of cells for nanomaterial uptake analysis

A549 cells were then treated with 500 µL of either serum-free medium (untreated control, NT); BiFeO₃@Fe₃O₄@asc nanoparticles C1, C2 and C3; BiFeO₃; non-asc NP; fNP; C2-Inh; POS; BiFeO₃-Inh; non-asc NP-Inh; fNP-Inh and POS-Inh. This resulted in final concentrations of 150 µg Fe/mL, 100 µg Fe/mL, 50 µg Fe/mL for C1, C2 and C3, and of 100 µg Fe/mL for all the controls except NT.

Each of the samples was prepared in triplicate and the experiment was carried out three times.

To assess the impact of temperature and time on the uptake plates were prepared as above for treatment at 0°C and 37°C over two time-points, 1h and 24h after treatment. For the 0°C treatment, the plates were placed on melting ice in an insulated box and placed in cold storage at 4°C.

Using a protocol adapted from Riemer et al,¹⁸¹ the uptake of iron was halted by washing the plates at the desired time-points with several washes of ice-cold PBS. The first two washes contained deferoxamine (2mL per wash, 1 mM) to remove any extracellular iron.

Cells were lysed by replacing the PBS with NaOH (200 µL per well, 50 mM) and placing on a shaker for 2h at room temperature, then set aside for use in colorimetric assays for quantitation of both the iron and protein content (see below).

Colorimetric-based assay for quantitation of iron

To release the iron, the cells lysates were digested by transferring aliquots (100 µL) into Eppendorf tubes, adding aqueous HCl (solution A, 10 mM, 100 µL) and iron releasing agent (solution B, 100 µL) to each tube. Solution B consisted of equal volumes of aqueous HCl (1.4 M) and KMnO₄ (4.5%), freshly mixed.

The digested lysates were placed on a hotplate at 60°C for 2h and allowed to cool before adding iron detecting agent (solution C, 30 µL) to each tube. Solution C contained ferrozine (6.5 mM), ammonium acetate (2.5 M) and ascorbic acid (1 M) in ultrapure water. The tubes were returned to the shaker for 30 min, then aliquots (280 µL) were transferred to a 96-well plate.

See the schema in Figure 3.4, below.

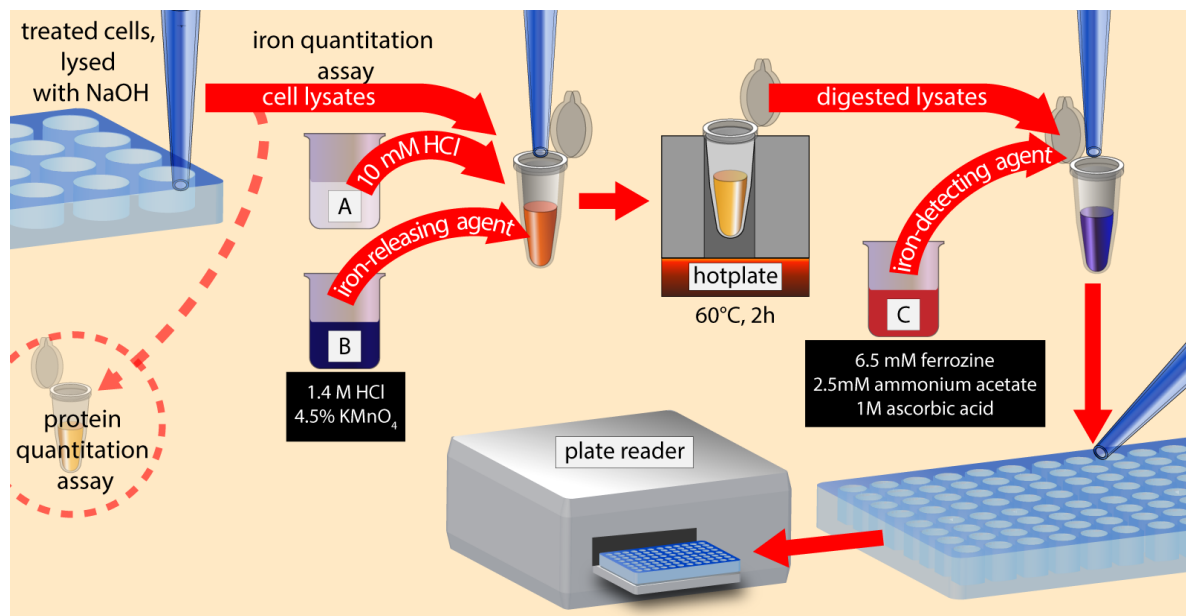


Figure 3.4: Preparation of cell lysates for colorimetric quantitation of iron. Cell lysates are digested in aqueous acidified permanganate (A+B) on a hotplate for two hours, before a ferrozine solution (C) was added, and after 30 min, transferred to a 96-well plate. The absorbance was measured by a plate reader and compared to a standard.

The iron standard FeCl_3 was prepared in a similar way to the lysates as outlined above, although the procedure differed from Riemer's protocol as follows: FeCl_3 was dissolved in ultrapure water to obtain calibration standards of known M iron content from 0 – 9 µg Fe/mL. Aliquots of the iron solutions (100 µL) were added to NaOH (50 mM, 100 µL) and digested in aqueous acidified permanganate (solutions A and B, 50 µL each) on a hotplate at 60°C for two hours. The ferrozine solution (C, 30 µL) was added once the digested iron had cooled, the tubes were placed on a shaker and an aliquot of each (280 µL) was transferred into a well of a 96-well plate to measure the absorbance at 550 nm. Each sample was prepared with two technical repeats (i.e. in triplicate) and the experiment was repeated three times.

The iron content of the digested cell lysates was determined by comparing the absorbance with that of the calibration standards.¹⁸¹

Finally, the iron content of the lysates was then normalised against the corresponding protein content, measured as described below.

Colorimetric-based assay for quantitation of protein

The protein content of the cell lysates was determined by Bio-Rad Protein Assay:

Five dilutions of bovine serum albumin in ultrapure water were prepared as a protein standard (50 – 500 µg/mL). Aliquots of each standard and cell lysate solution (160 µL) were transferred into separate microtiter plate wells, in triplicate. Dye reagent concentrate (40 µL) was added to each well with aspiration to mix the sample and reagent in the wells and the plate was incubated at room temperature for 5 min. The absorbance was then measured at 595 nm with a plate reader and the protein content of the lysate samples was determined by comparison with the calibration standards.

Incubation in 8-well chamber slides for imaging analysis of targeting specificity and uptake

To analyse the targeting specificity of the bioconjugated nanocomposites, A549 cells (which express EGFR) and NCI-H520 (which do not express EGFR) were dispensed on 24-well plates at 1.5×10^5 cells per mL in 400 µL of complete medium, allowed to attach and incubate for 24h before being rinsed with warmed serum-free DMEM. The cells were then treated with aliquots of serum-free DMEM (nontreated, denoted NT, 50 µL), the test sample BiFeO₃@Fe₃O₄@asc nanoparticle (50 µL, 500 µg Fe/mL) or the controls BiFeO₃, BiFeO₃ without ascorbic acid (non-asc NP), anti-EGFR functionalised BiFeO₃@Fe₃O₄ (fNP), Fe₃O₄@poly-acrylic acid - commercially available as MF66 used as positive control for iron oxide nanomaterial interactions - (POS), sodium azide inhibited BiFeO₃@Fe₃O₄@asc (C2-Inh), sodium azide inhibited BiFeO₃ (BiFeO₃-Inh), sodium azide inhibited and anti-EGFR functionalised BiFeO₃@Fe₃O₄ (fNP-Inh), sodium azide inhibited BiFeO₃ without ascorbic acid (non-asc NP-Inh), and sodium azide inhibited Fe₃O₄@poly-acrylic acid (POS-Inh) (50 µL, 500 µg Fe/mL) for a final concentration of 100 µg Fe/mL. The cells were incubated for 24h, washed twice with warmed PBS, fixed with warm PFA (3.7%, 200 µL per well) and washed twice more with PBS.

3.2.4 Equipment and Techniques

Localisation by Optical Microscopy

The cells were stained by immersing the slides in Perl's solution (a freshly made solution of equal parts aqueous HCl [4%] and potassium ferrocyanide [4% w/v]) for 20 minutes at room temperature. The slides were washed 4 times in ultrapure water, then immersed in Nuclear Fast Red solution (0.5% w/v) for 7 minutes to counterstain, washed twice in ultrapure water and allowed to dry in air.

The slides were then imaged under a light microscope equipped with a colour camera.

Confocal Microscopy

Cellular internalization of the functionalised nanocomposites was also evaluated by Confocal Laser Scanning Microscopy (CLSM). Live cells were stained with Hoechst for DNA and Phalloidin Red for actin were imaged under bright-field, fluorescence and reflectance mode at $\lambda_{exc} = 561$ nm using a 63× oil immersion objective on the Zeiss LSM 510 Confocal Microscope with three channels as outlined in the table below.

Table 3.2: Stains used for Confocal Microscopy with excitation, filter and organelle details

Stain	Channel	λ_{exc} (nm)	Filter range (nm)	Analyte
Hoechst	1	405	400-470	DNA
CF™488 A	2	488	470-550	Labelled, functionalised nanoparticles
Phalloidin red	3	561	550-657	Actin

3.2.5 Techniques for characterisation

Nanoparticle Tracking Analysis

Nanoparticle Tracking Analysis (NTA) was carried out using a NanoSight NS500 (Malvern, UK) to measure the size of nanoparticles. NTA records video of particles in suspension, simultaneously tracking the motion of all individual nanoparticles and aggregates within its field of view. Particles undergo Brownian motion, buffeted by the storm of intermolecular forces in a fluid. In NTA, the rate of this motion is related for each particle or aggregate to the size of its hydrodynamic radius. Although the method of measuring the motion of the particles differs from Dynamic Light Scattering, the relationship between Brownian motion and particle size, governed by the Stokes-Einstein equation, is discussed in the Physico-chemical Characterisation section of Chapter 2.

Colloidal stability

Colloids are mixtures of two or more materials, classified by the states of matter of the constituents. An emulsion is a suspension of one liquid in another, such as milk, a colloid of liquid fat in water. A foam is where gas molecules are trapped, e.g. the head of a pint of Guinness is carbon dioxide and nitrogen trapped in a cream. An aerosol, such as fog, consists of a liquid dispersed in a gas. A sol, such as paint or cytosol, is a suspension of particles in a fluid.

An unstable colloid is one where the dispersed medium tends to separate or precipitate from the dispersion medium. The stability of a colloid is a balance of the electrostatic repulsions and Van der Waals attractions and described by Derjaguin, Landau, Verwey and Overbeek (DLVO) Theory.

As discussed under size distribution analysis, electrostatic charges cause fluid ions to adhere to the particle surface. The slip plane is the bounding surface of the ions which move with the particle through the suspension.

The potential difference between the bulk suspension and the slip plane, known as the ζ potential, is a measure of a suspension's colloidal stability.

The greater the potential difference, i.e. the larger the magnitude of the ζ potential, positive or negative, the more stable the colloid. It is possible for steric interactions to contribute to a suspension's stability, but in the absence of other mechanisms, if the ζ potential magnitude is greater than 30 mV, the colloid is stable.

ζ potential was calculated from electrophoretic mobility measurements as a function of pH at fixed ionic strength as per IUPAC recommendations.¹⁵¹

Electrophoretic measurements were carried out using a Malvern ZetaSizer Nano.

Fourier Transform Infrared Spectroscopy

Fourier Transform Infrared Spectroscopy (FTIR) identifies the composition of an analyte by measuring its transmission spectrum. Light in the infrared region is absorbed by a compound when the energy of incident radiation is converted to internal energy. Energies absorbed correspond to exact changes in the molecules present – vibrational, rotational or electronic transitions. IR radiation is therefore absorbed at wavelengths characteristic of the functional groups present in the sample so analysis of a compound's transmission spectrum can indicate its chemical composition.

In FTIR, the analyte is probed by a broadband spectrum of light modified such that one wavelength at a time is filtered out using an interferometer. The interferometer steps through each wavelength in the IR range and the detected signal is recorded at each time-point as an interferogram.

A Fourier Transform is a mathematical tool which translates a time-dependent function or signal into a frequency-dependent function. This transformation allows signals which vary over time to be split into their constituent frequencies.

The interferograms recorded at each step by the FTIR are decomposed using a Fourier Transform into their constituent frequencies (expressed as wavenumbers). The wavenumber of each trough in the

resulting transmission spectrum is compared with tables of known compounds to identify the functional groups in the sample.

FTIR was used to identify the groups present on the surface of the nanoparticles after functionalisation to confirm the presence of the amide and silane functional groups after silanization.

Flow Cytometry

Flow cytometry, outlined in Chapter 1, was carried out using a BD Accuri™ C6 (BD Biosciences, USA) was used to assess the functionalisation of BiFeO₃ and BiFeO₃@Fe₃O₄ nanoparticles with fluorescently-tagged anti-hEGFR. Measurement was carried out by detecting fluorescence emission using the FL2 585/40 nm filter.

For flow cytometry, nanoparticle dispersions were diluted from stock (40 µg/mL in PBS) for a final concentration of 4 µg/mL. Samples were run until a minimum of 30000 counts were acquired under medium fluidics rate without gating, as per the BD technical notes and instrument documentation.

The efficiency (E) of fluorescent labelling was calculated as:

$$E(\%) = \frac{\text{Number of target events}}{\text{Number of events detected}} \times 100$$

3.3 Results

This section presents the results of the functionalisation of several materials with a view to quantifying uptake and assessing biocompatibility. Initially, I present results for the silanisation of metal oxide nanoparticles to then compare the size, morphology and colloidal stability of the nanoparticles and their composites. Furthermore, I present methods to achieve cell targeting via antibody coupling to the surface of the nanomaterials and composites.

3.3.1 Surface modification to achieve efficient coupling to selected moieties

Surface passivation with amine functional group (BiFeO₃@APTES)

The attachment of amine functional groups to the surface of bismuth ferrite was achieved by silanisation of the oxide surface which was confirmed by FTIR (see Figure 3.5).

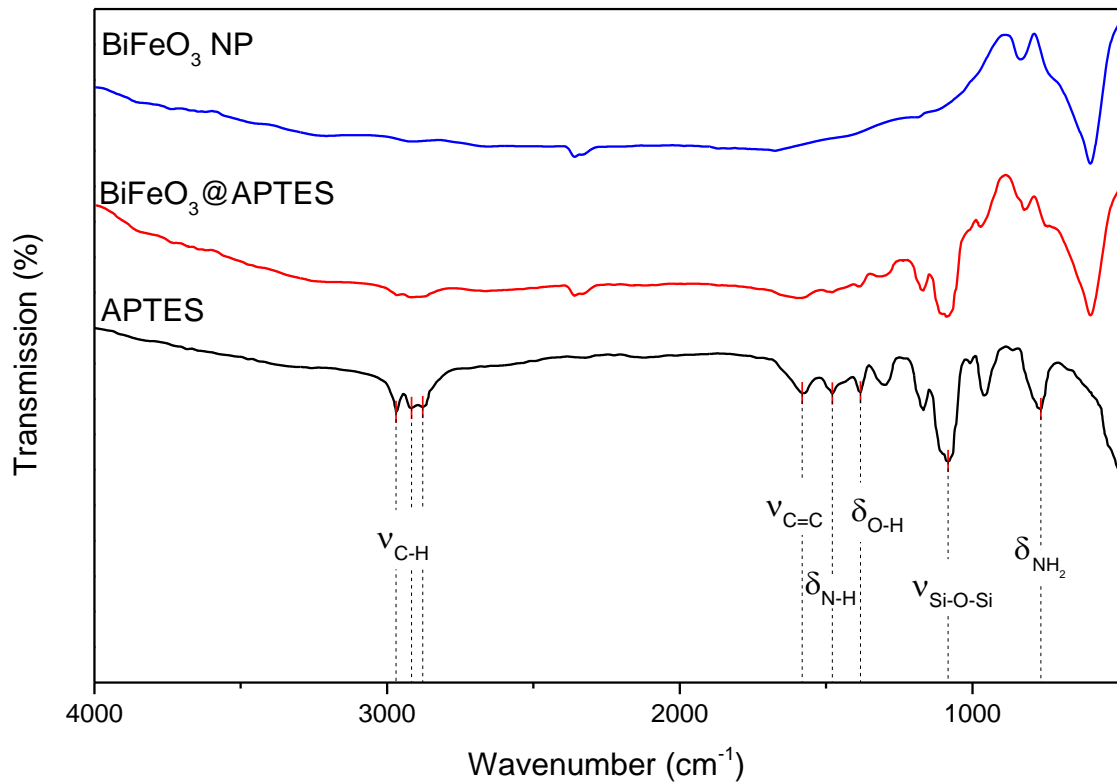


Figure 3.5: FTIR spectra of APTES, BiFeO₃ functionalised with APTES, and bare BiFeO₃ nanoparticles. Please note: ν indicates linear vibrations (i.e. stretching) whereas δ denotes deformation vibrations (bending).

Peaks at 1490 cm⁻¹ and 760 cm⁻¹ (see Figure 3.5) were assigned to the bending vibration of N–H and N–H₂. The strong absorptive peak at 500–600 cm⁻¹ in the coated and uncoated BiFeO₃ are attributed to Fe–O stretching and bending vibrations, characteristic of the octahedral O₆ groups in perovskites. The absorption band at 1075 cm⁻¹ is present in the modified sample BiFeO₃@APTES and is ascribed to asymmetric stretching vibrations of the Si–O–Si bond. These results indicate that the silane layer is absorbed on the surface of the nanoparticles.

3.3.2 Nanoparticle colloidal stability, size distribution and concentration

Colloidal stability, size distribution and concentration were assessed for all the materials under examination when dispersed in aqueous solution.

Colloidal stability

First, electrophoretic mobility was measured from which zeta potential was calculated. Because of the significance of the result, coated and uncoated BiFeO₃ are presented here to demonstrate the impact of silanisation on colloidal stability (see Figure 3.6).

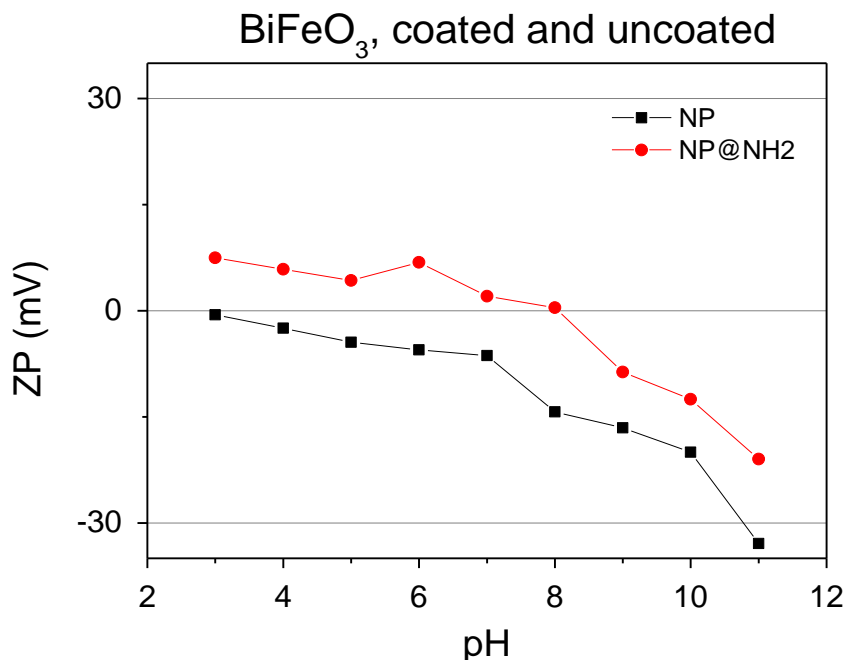


Figure 3.6: ζ -potential versus pH curves of bare and coated BiFeO_3 nanoparticles. From pH 2 to 12 it can be seen that only the bare nanoparticles reached an absolute ζ -potential greater than 30 mV and only at pH 11.

There is a large shift in the iso-electric point of the coated BiFeO_3 nanoparticles relative to the uncoated nanoparticles from approximately pH 3 to pH 8. This indicates that different surface groups are present which have altered the electrical double layer at the interface between the nanoparticle and the solution. Furthermore, only bare nanoparticles were stable at any pH. At pH 11, the absolute magnitude of the ζ -potential exceeded 30 mV, the threshold of colloidal stability according to DLVO theory as outlined in the Materials and Methods.

Size distribution and concentration

Nanoparticles and nanocomposites were dispersed in DI water and analysed using nanoparticle tracking analysis under flow. The results present a comprehensive analysis of the size distributions of the different dispersions, followed by a summary and comparison to other size measurement techniques.

BiFeO_3 nanoparticles dispersed in DI water were polydisperse: several peaks are seen in the size distribution (see Figure 3.7).

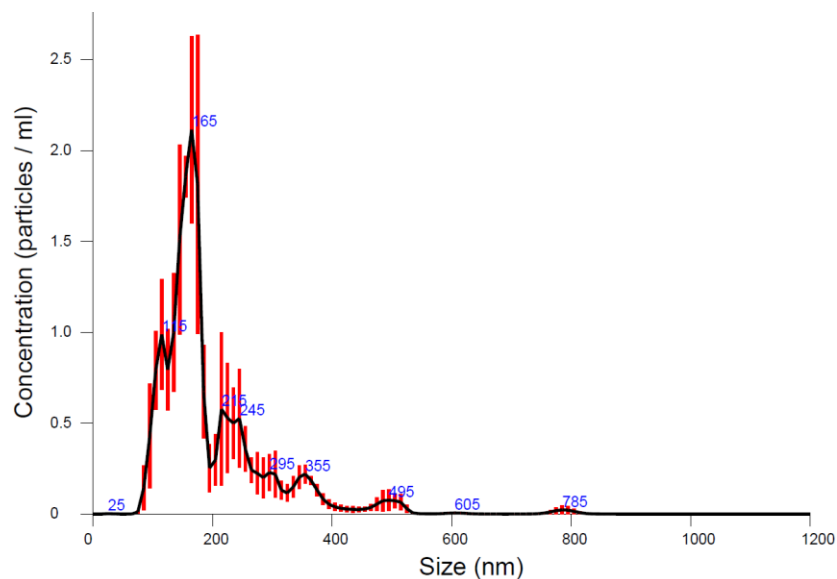


Figure 3.7: Size distribution histogram of bare BiFeO_3 nanoparticles dispersed in DI water. The graph shows the size distribution of 6 measurements of 60 seconds each: average size distribution (black line) and standard error of the mean between measurements (red plot).

Variance between successive samples resulted in large uncertainty below ~ 250 nm, as indicated by the size of the error bars. The multiple broad peaks at different sizes mean that the sample is highly polydisperse. Such variance between samples and polydispersity indicate an unstable suspension. It can be assumed that the peaks represent the polydispersity in the sample and the presence of aggregates of different sizes.

When stabilised with ascorbic acid, BiFeO_3 nanoparticles displayed far less variance between successive samples (as indicated by the size of the error bars, see Figure 3.8) and lower polydispersity

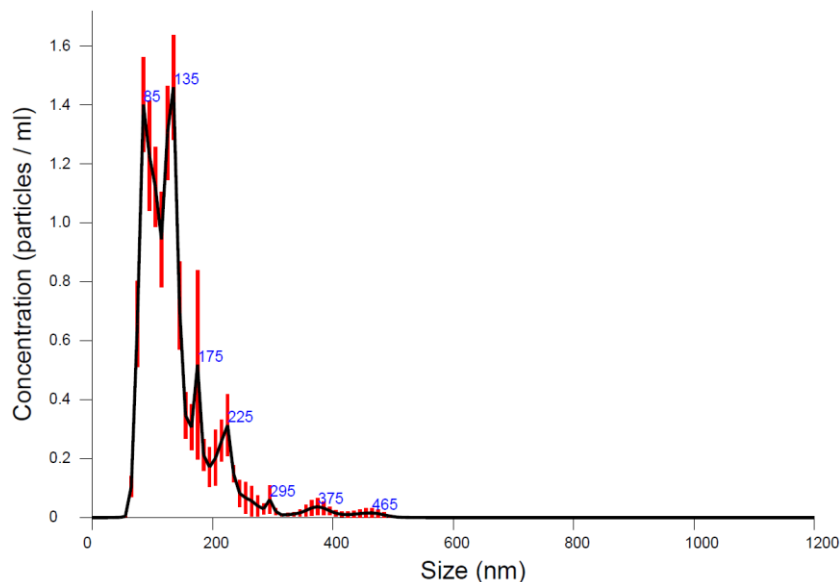


Figure 3.8: Size distribution histogram of ascorbic acid stabilised $\text{BiFeO}_3@asc$ nanoparticles dispersed in DI water. Note the aggregate size reduction and bimodal distribution between 85 and 135 nm. This graph shows the size distribution of 6 measurements of 60 seconds each: average size distribution (black line) and standard error of the mean between measurements (red plot).

The dominant, narrow double peak between 80-150nm indicate a more homogeneous dispersion of nanoparticles than that of bare BiFeO_3 nanoparticles.

Dispersions of BiFeO_3 coated with APTES were highly unstable, resulting in high polydispersity, high variance between samples and aggregates which were at the limit of NTA using the NanoSight (see Figure 3.9).

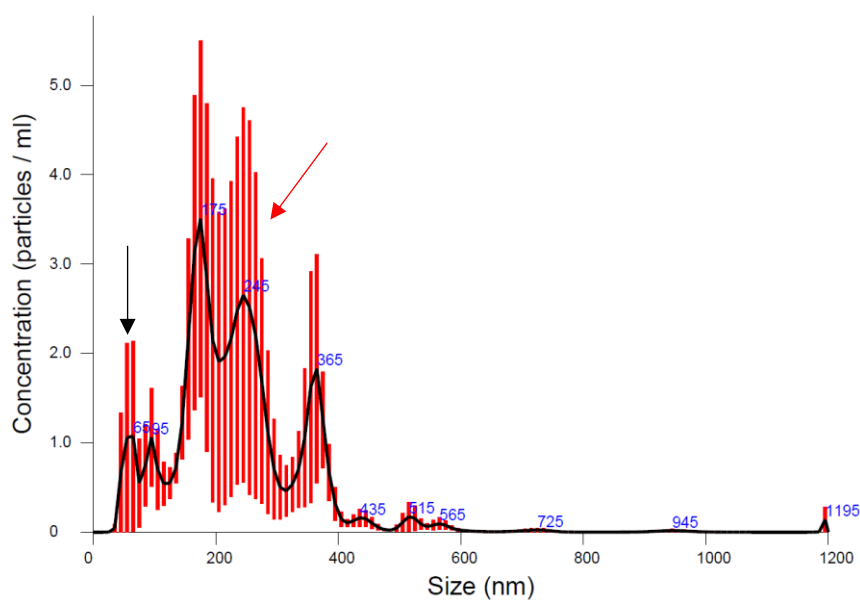


Figure 3.9: Size distribution histogram of $\text{BiFeO}_3@APTES$ nanoparticles dispersed in DI water. Note the bimodal peaks at 65-95 nm and at 175-245 nm. This graph shows the size distribution of 6 measurements of 60 seconds

each: average size distribution (black line) and standard error of the mean between measurements (red plot). There are two main populations of particles (65-95 nm, indicated by the black arrow) and aggregates (the peaks at 175, 245 and 365 nm, indicated by a red arrow).

In the case of $\text{BiFeO}_3@Fe_3O_4@APTES$ and $\text{BiFeO}_3@Fe_2O_3@APTES$ nanoparticles, the suspensions were too unstable to record measurements using NTA: the nanoparticles precipitated from suspension and only large aggregates were visible, resulting in saturation of the video.

As with BiFeO_3 nanoparticles, $\text{BiFeO}_3@Fe_2O_3$ stabilised with ascorbic acid showed improved monodispersity and stability relative to bare nanoparticles or those coated with APTES (see Figure 3.10).

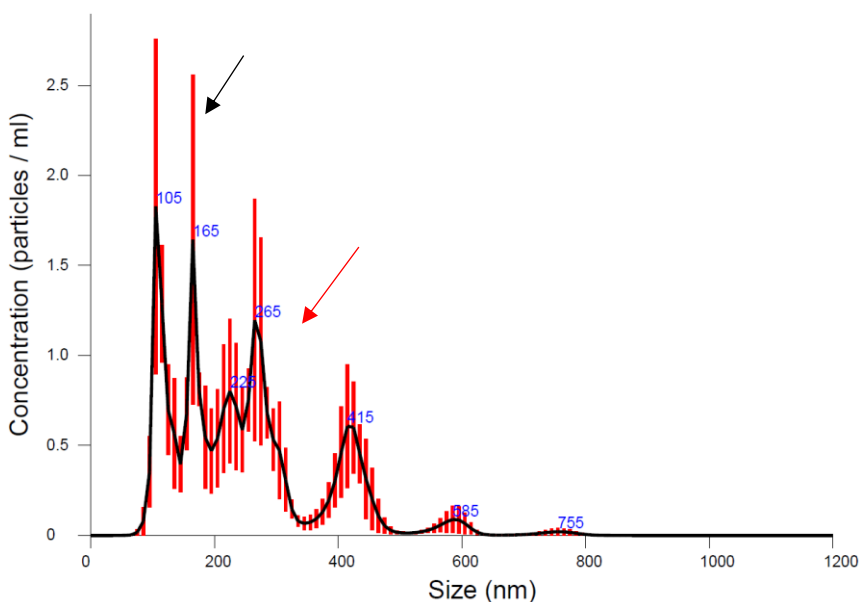


Figure 3.10: Size distribution histogram of $\text{BiFeO}_3@Fe_2O_3@asc$ nanoparticles dispersed in DI water. Note the multimodal peaks at 105, 165, 225 and 265 nm. This graph shows the size distribution of 6 measurements of 60 seconds each: average size distribution (black line) and standard error of the mean between measurements (red plot). The multimodal distribution indicates two populations: particles (two well-defined peaks at 105 and 165, indicated by the black arrow) and aggregates (the band of less-well defined peaks at 225, 265 and 415, indicated by the red arrow). The particles are larger than those of stabilised BiFeO_3 , and the size distribution is much broader.

The smallest peaks indicate a hydrodynamic diameter of 105 nm and the presence of multiple peaks indicates some polydispersity. However, the four largest peaks in the distribution (105 nm, 165 nm, 225 nm and 265 nm) are close to whole number multiples of approximately 55 nm, suggesting that the ascorbic acid has indeed stabilised aggregates. However, the absence of any peak at 55 nm or indeed below 100 nm suggests that the individual nanoparticles may have been removed from the sample. This may indeed be the case – after the stabilisation procedure, several washes are required to remove excess ascorbic acid and by-products, and only that which precipitates from suspension under centrifugation or magnetic separation can be recovered. The most stable composites are those with

the highest coverage of ascorbic acid molecules, those with the highest surface area to volume ratio, i.e. individual nanoparticles.

Similarly, $\text{BiFeO}_3@Fe_3O_4$ stabilised with ascorbic acid showed improved monodispersity and stability relative to bare nanoparticles or those coated with APTES (see Figure 3.11).

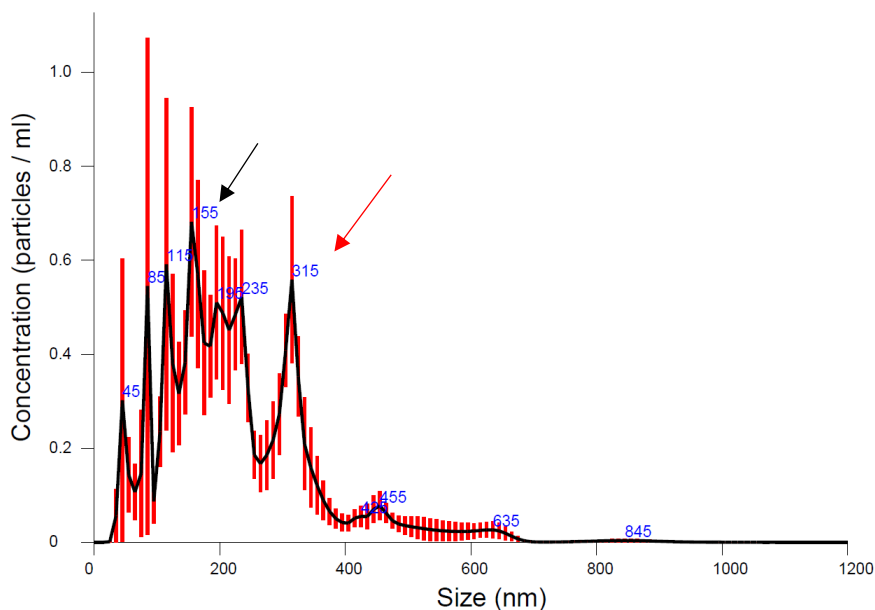


Figure 3.11: Size distribution histogram of $\text{BiFeO}_3@Fe_3O_4@asc$ nanoparticles dispersed in DI water. The graph shows the size distribution of 6 measurements of 60 seconds each: average size distribution (black line) and standard error of the mean between measurements (red plot). Note the multimodal peaks at 45, 85, 115 and 165nm (indicated by a black arrow).

The smallest peaks indicate a hydrodynamic diameter of 45 nm. Peaks in the distribution (45 nm, 85 nm, 115 nm, 155 nm, 195 nm and 235 nm) are close to whole number multiples of approximately 40 nm, suggesting that the ascorbic acid has stabilised individual nanoparticles as well as aggregates. Unlike $\text{BiFeO}_3@Fe_2O_3@asc$ nanoparticles, the individual nanoparticles are present in the sample. This may be due to the higher magnetic moment of the Fe_3O_4 nanoparticles which results in higher percentage of individual $\text{BiFeO}_3@Fe_3O_4@asc$ composites being magnetically separated, or due to greater affinity between the $\text{BiFeO}_3@Fe_2O_3$ composites and ascorbic acid.

The narrowest size distribution was observed in the BiFeO_3 nanoparticles stabilised with ascorbic acid, by mean, mode and D values (see Table 3.3).

Table 3.3: Size distribution data including mean, D10, D50 and D90 values and concentration of nanoparticles per ml of suspension \pm the corresponding standard error.

Sample	Mean (nm)	Mode (nm)	D10 (nm)	D50 (nm)	D90 (nm)	Concentration (/mL)
BiFeO ₃	197.3 \pm 6.4	161.6 \pm 4.7	105.5 \pm 5.2	156.6 \pm 2.2	310.3 \pm 18.0	(1.83 \pm 0.13) $\times 10^8$
BiFeO ₃ @asc	138.0 \pm 6.5	107.3 \pm 10.8	72.8 \pm 0.9	114.9 \pm 3.0	196.3 \pm 18.9	(1.21 \pm 0.06) $\times 10^{10}$
BiFeO ₃ @APTES	231.1 \pm 16.3	133.2 \pm 24.1	94.6 \pm 19.2	166.4 \pm 27.3	432.3 \pm 35.5	(5.34 \pm 2.73) $\times 10^8$
BiFeO ₃ @Fe ₂ O ₃ @asc	236.2 \pm 21.5	161.0 \pm 21.4	109.9 \pm 14.3	206.7 \pm 19.3	388.5 \pm 41.2	(1.23 \pm 0.23) $\times 10^8$
BiFeO ₃ @Fe ₃ O ₄ @asc	247.4 \pm 10.0	185.5 \pm 39.5	103.4 \pm 5.7	224.7 \pm 10.5	413.6 \pm 16.5	(2.24 \pm 0.07) $\times 10^8$

Note that the concentration of BiFeO₃@asc is significantly higher than that of other particles and composites. This is in part due to the smaller size of the individual particles versus that of clusters, to the increased surface area of the particles to which the stabilising ligand can attach and to the successive washing steps.

The greatly increased concentration of particles per ml support the assertion that the nanoparticles are more stable in suspension (see Figure 3.12).

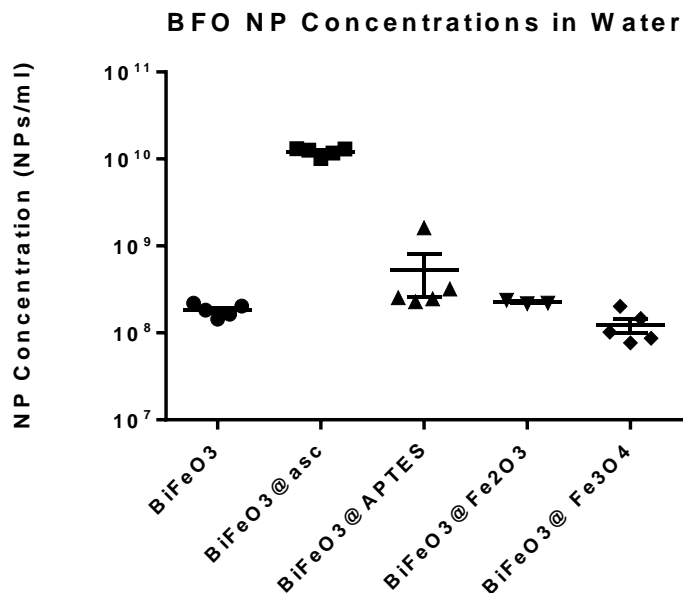


Figure 3.12: Concentration of nanoparticles and composites in DI water. The concentration of BiFeO₃ nanoparticles stabilised with ascorbic acid were two orders of magnitude greater than other particles and composites. The error bar indicates the standard error of the mean.

No single measure can be considered the “true” particle size. Each tells us something different about the size distribution: the mean is an average of all the sizes calculated from NTA, the mode is the centre of the most dominant peak in the size distribution, i.e. the most common size of particle in the sample. Although there appeared to be a large change in the mode values between the bare and ascorbic acid or iron oxide coated particles, the differences fell within the 95% confidence intervals and were therefore not significant.

By contrast, D10, D50 and D90 represent diameters of different mass fractions of the sample population (see Figure 3.13).

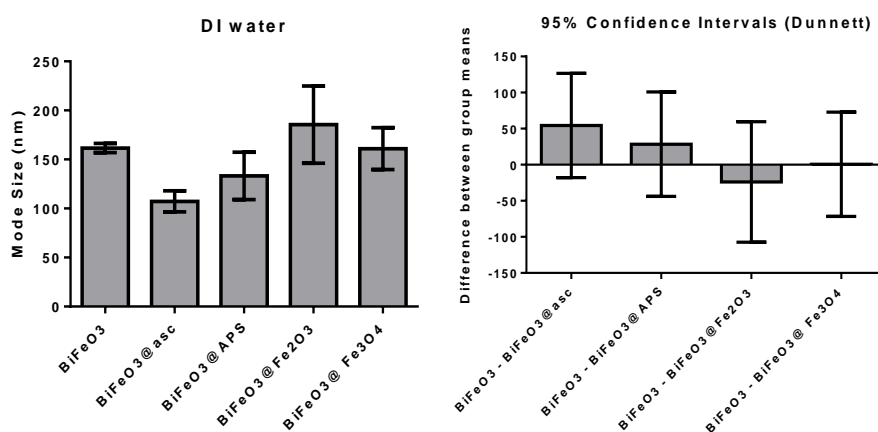


Figure 3.13: Mode diameter of nanoparticles and composites in DI water. Left, mode size of each nanoparticle with error bars representing the standard error of the mean. Right: difference between group means relative to bare BiFeO₃ nanoparticles (Dunnett’s post-test for multiple comparisons), with error bars representing the 95% confidence intervals (calculated using ordinary One-Way ANOVA).

For example, 10% of the BiFeO₃ samples’ mass consisted of nanoparticles with a diameter smaller than ~106 nm, 50% of the mass was comprised of nanoparticles whose diameter was less than ~157 nm and 90% of the sample was composed of nanoparticles with diameters less than ~310 nm (see Table 3.3). The D10, D50 and D90 are therefore more descriptive than the mean or mode in conveying the size distribution of nanoparticles.

However, the size of the nanoparticles reported by NS differs significantly from that measured by TEM or calculated from XRD measurements as seen in Chapter 2. Three factors contribute to this discrepancy. First, during the stabilisation stage, aggregates are just as likely as individual nanoparticles to be coated by ascorbic acid. Second, any nanoparticles near the lower detection threshold of NTA (i.e. stabilised individual nanoparticles) register as noise in the tracking analysis videos and are excluded from the calculation of the average particle diameter. Third, like photocorrelation spectroscopy, NTA

measures the hydrodynamic diameter, i.e. the diameter of the loosely bound cloud of counter and co-ions which travel with the particle through the dispersion medium.

Because the dispersion medium greatly influences the stability of the nanoparticles, NTA was also carried out in serum free DMEM to emulate the cell culture environment.

The mode size of ascorbic acid stabilised BiFeO₃ nanoparticles was significantly smaller than that of bare BiFeO₃ in DMEM suspension (see Figure 3.14).

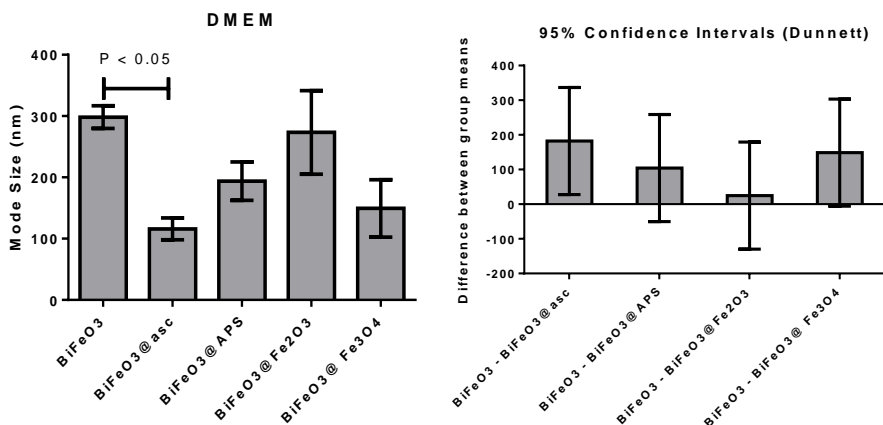


Figure 3.14: Mode diameter of nanoparticles and composites in DMEM. Left, mode size with error bars representing the standard error of the mean. Right: difference between group means relative to bare BiFeO₃ nanoparticles (Dunnett's post-test for multiple comparisons), with error bars representing the 95% confidence intervals (calculated using ordinary One-Way ANOVA).

However, mode sizes of nanoparticles or composites measured in DMEM were larger than those measured in DI water (see Figure 3.13).

Colloidal stability is determined in large part by pH, ionic strength and the presence of other moieties in a suspension. While DMEM has a pH of 7.4, DI water has a pH of approximately 6.5 due to absorption of CO₂ from the air. The ionic strength of the suspensions is very different, however, due to the presence of salts dissolved in the DMEM. The ionic strength of DMEM is 1.5×10^{-1} ,¹⁸² whereas that of DI water at pH 6.5 is approximately 6.4×10^{-6} .

Characterisation in complex media

Higher concentrations of salts increase the ionic strength of a solution resulting in a more tightly bound diffuse layer of counter and co-ions around each particle in suspension. This leads to a reduction in interparticle repulsion, resulting in increased aggregation.

For this reason, larger aggregates form in DMEM than in DI water, as can be seen in the size distribution plots below (see Figure 3.15).

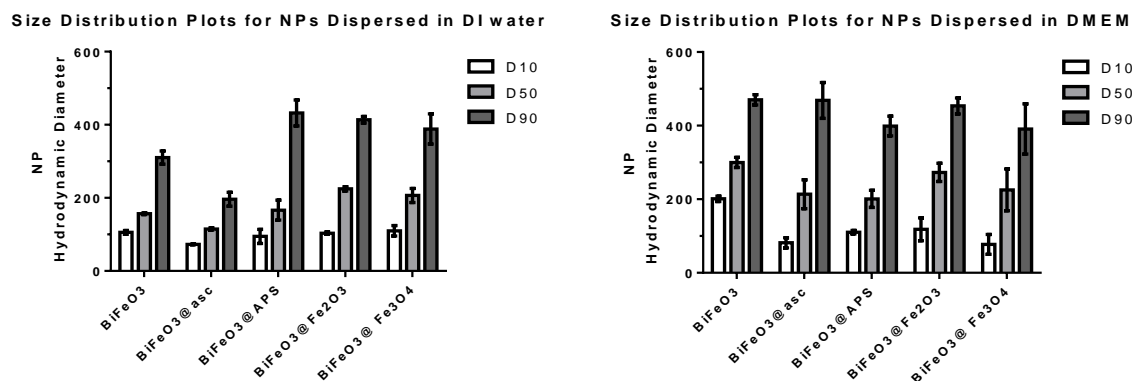


Figure 3.15: Size distributions of 10, 50 and 90% mass fractions of BiFeO₃ nanoparticles and composites. Left, nanoparticles and composites dispersed in DI water. Right, nanoparticles and composites dispersed in serum-free DMEM. The error bars indicate the standard error of the mean.

For bare BiFeO₃, the D10, D50 and D90 values were larger in DMEM than in DI water. While the D10 values of BiFeO₃@asc nanoparticles were approximately the same, the D50 and D90 values in DMEM were almost double the corresponding values in DI water.

In DI water, the narrowest size distribution was observed in the BiFeO₃ nanoparticles stabilised with ascorbic acid, but the size distribution for all particles and composites was broad in DMEM, indicating that introducing nanoparticles into medium induces aggregation.

3.3.3 Bioconjugation with antibodies for targeting

Flow cytometry

The binding of the anti-EGFR antibody to the BiFeO₃@APTES nanoparticles was assessed by flow cytometry. A qualitative study was carried out to determine whether there was a shift in the mean fluorescence intensity (i.e. due to the presence of the CF 488A fluorophore on the anti-EGFR). This shift can be seen in Figure 3.16.

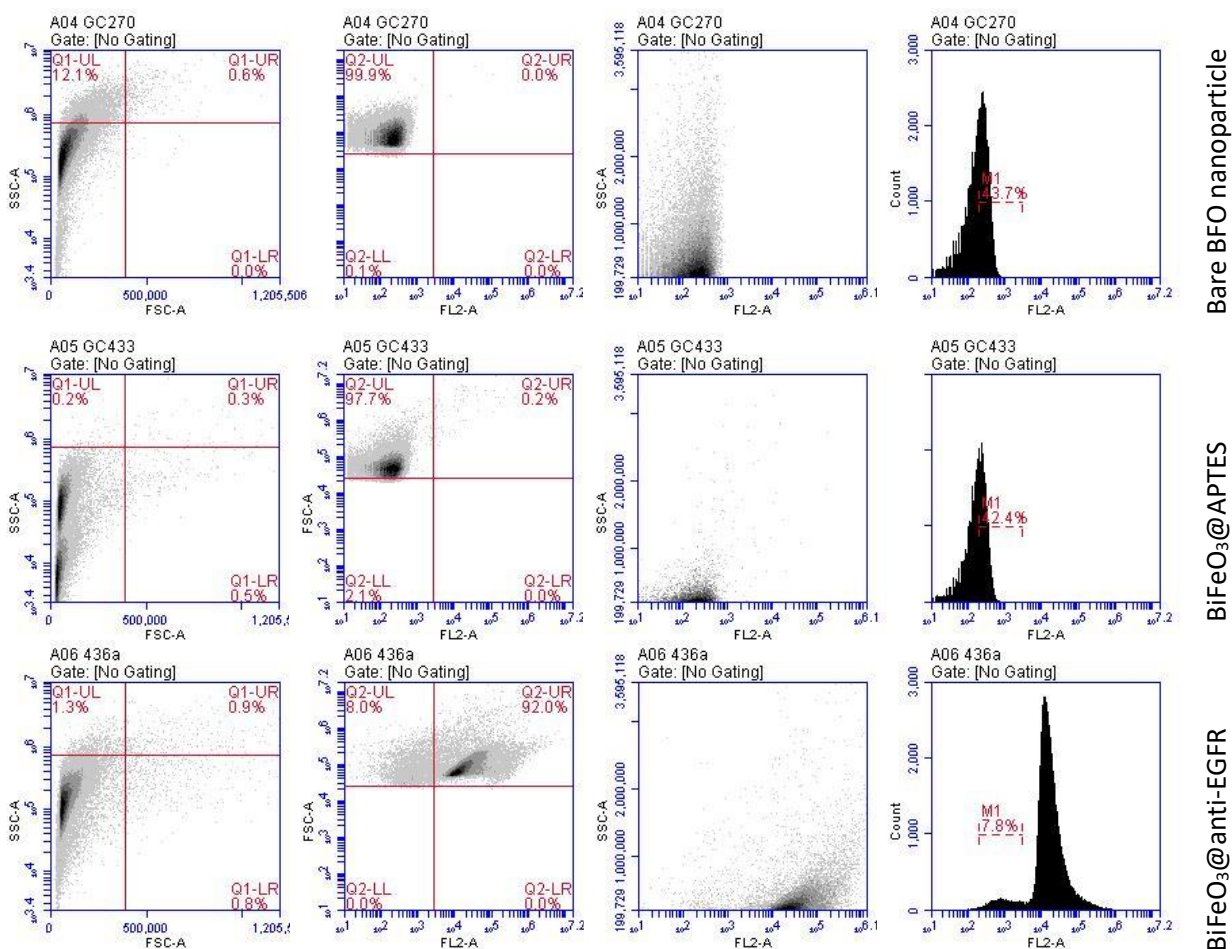


Figure 3.16: Flow Cytometry indicating binding of anti-EGFR. Top row, bare BiFeO₃ nanoparticles; middle row, BiFeO₃@APTES; bottom row, BiFeO₃@APTES bio-conjugated with anti-EGFR tagged with CF 488A. SSC: side-scatter, FSC: Forward Scatter, FL2-A: amplitude of the fluorescence in filter 2. Note that no gating was applied before measuring the shift in fluorescence/scattering in the Count vs FL2-A plots.

The shift in scattered intensity in the BiFeO₃@anti-EGFR sample indicate that the functionalisation step was successful: in Figure 3.16, in the left most column (X-axis, forward scatter, versus Y-axis, side-scatter), each of the samples has low forward scatter, consistent with small particle size. A sub-population of the samples has higher side scatter, indicating it is less optically homogeneous, consistent with a sample containing aggregates.

No shift in the mean intensity of the scattered signal was observed in the APTES-functionalised sample (BiFeO₃@APTES), whereas a significant shift was observed in the bioconjugated sample (BiFeO₃@anti-EGFR). The increase in intensity in the anti-EGFR CF488A sample indicates that the sample was successfully functionalised, with an efficiency of 92.2%, which is similar to results reported for functionalisation of other nanoparticles.¹⁸³

Epifluorescence microscopy

A549 cells were imaged using Epifluorescence Microscopy .

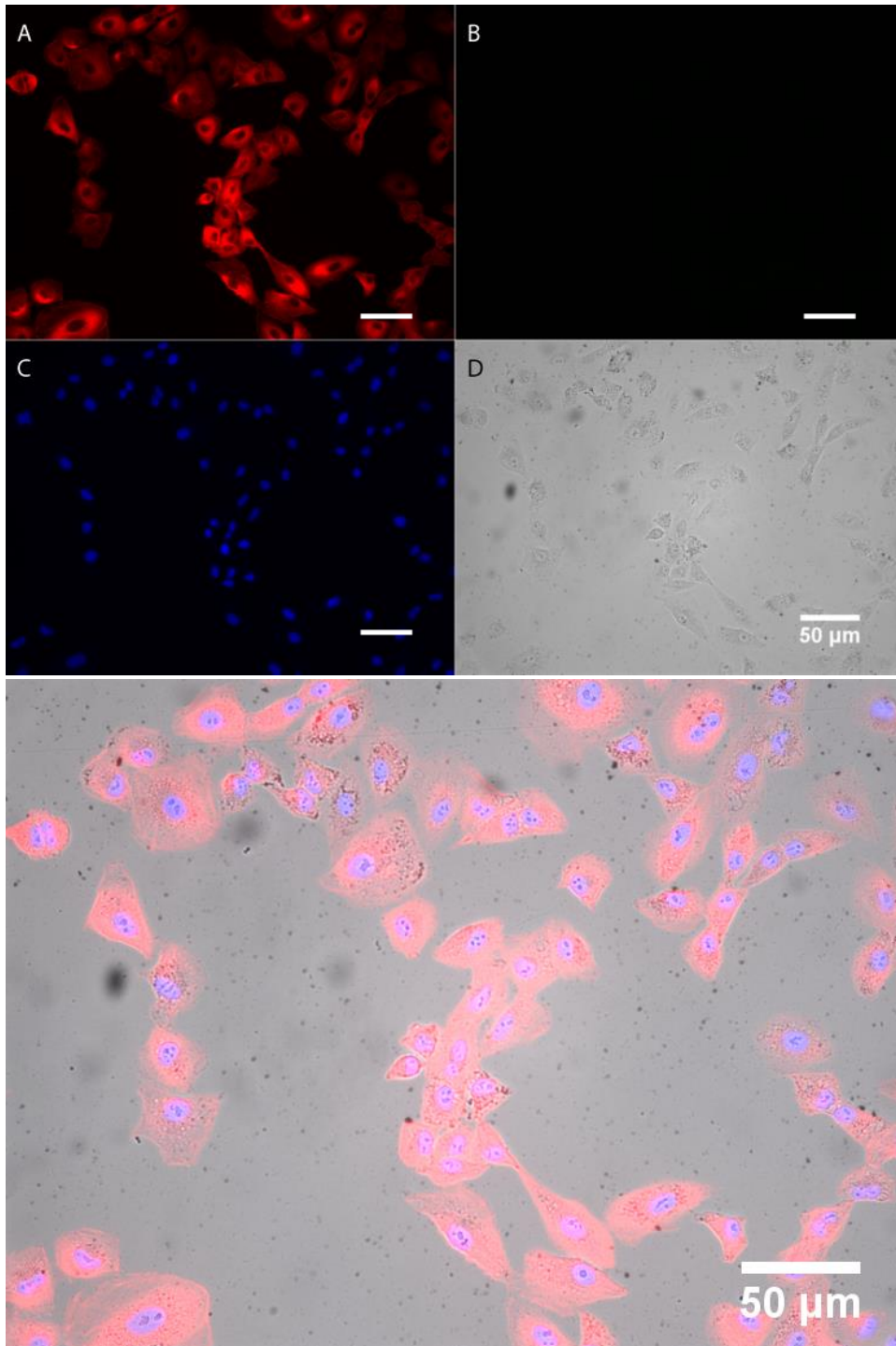


Figure 3.17: Epifluorescence image of untreated A549 cells. Actin was stained with Phalloidin Red (red channel), nuclei were stained with Hoechst (blue channel). Above, four-channel montage: A - red channel, B – green channel, C – blue channel, D – bright field, scale bar = 50 μm . Below, four-channel composite.

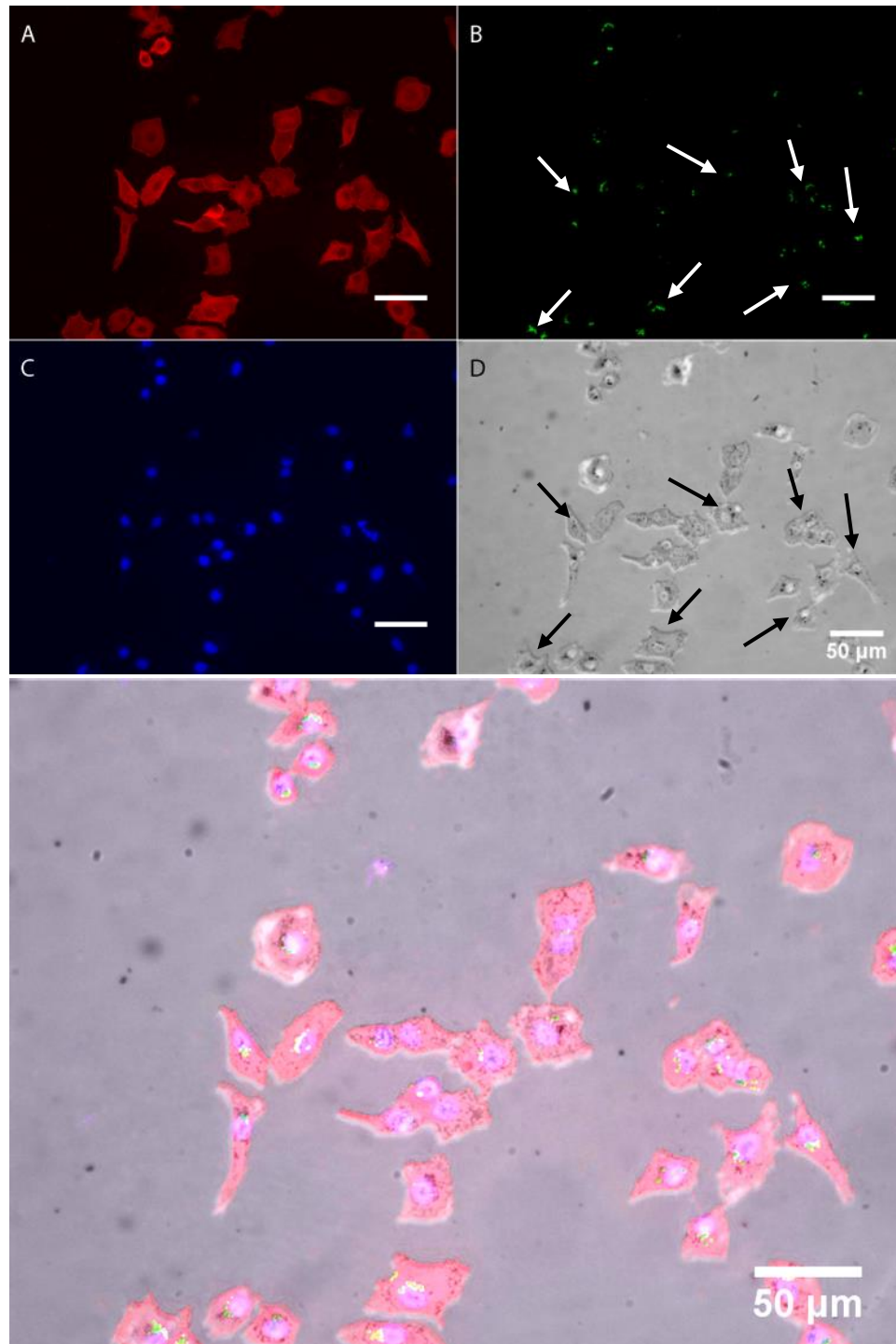


Figure 3.18: Epifluorescence image of A549 cells exposed to fluorescently tagged, anti-EGFR functionalised BiFeO_3 NPs. Actin was stained to show the cell morphology with Phalloidin Red (red channel), nuclei were stained with Hoechst (blue channel) and functionalised BiFeO_3 was labelled with CF488A (green channel). Above, four-channel montage: A - Red channel, B - green channel, C - blue channel, D - bright field, scale bar = 50 μm . Main panel, four-channel composite.

Untreated cells (see Figure 3.17) and cells exposed to fluorescently labelled BiFeO₃ NPs (see Figure 3.18) were imaged after 24h incubation at 37°C .

Because BiFeO₃ NPs are opaque, they can be identified in the bright field image (indicated by black arrows in Figure 3.18, D) and the fluorescently-tagged EGFR as corresponding bright spots in the green channel (indicated by white arrows in B).

To indicate the specificity of the anti-EGFR labelling, NCI-H520 were also exposed to the functionalised BiFeO₃ NPs. Because NCI-H520 does not express EGFR, the functionalised nanoparticles did not bind to the cells (see Figure 3.19 and Figure 3.20).

Since the binding efficiency was very high (97.2%, see the Flow Cytometry results section, above), very little non-specific binding was observed (indicated by arrows in Figure 3.19).

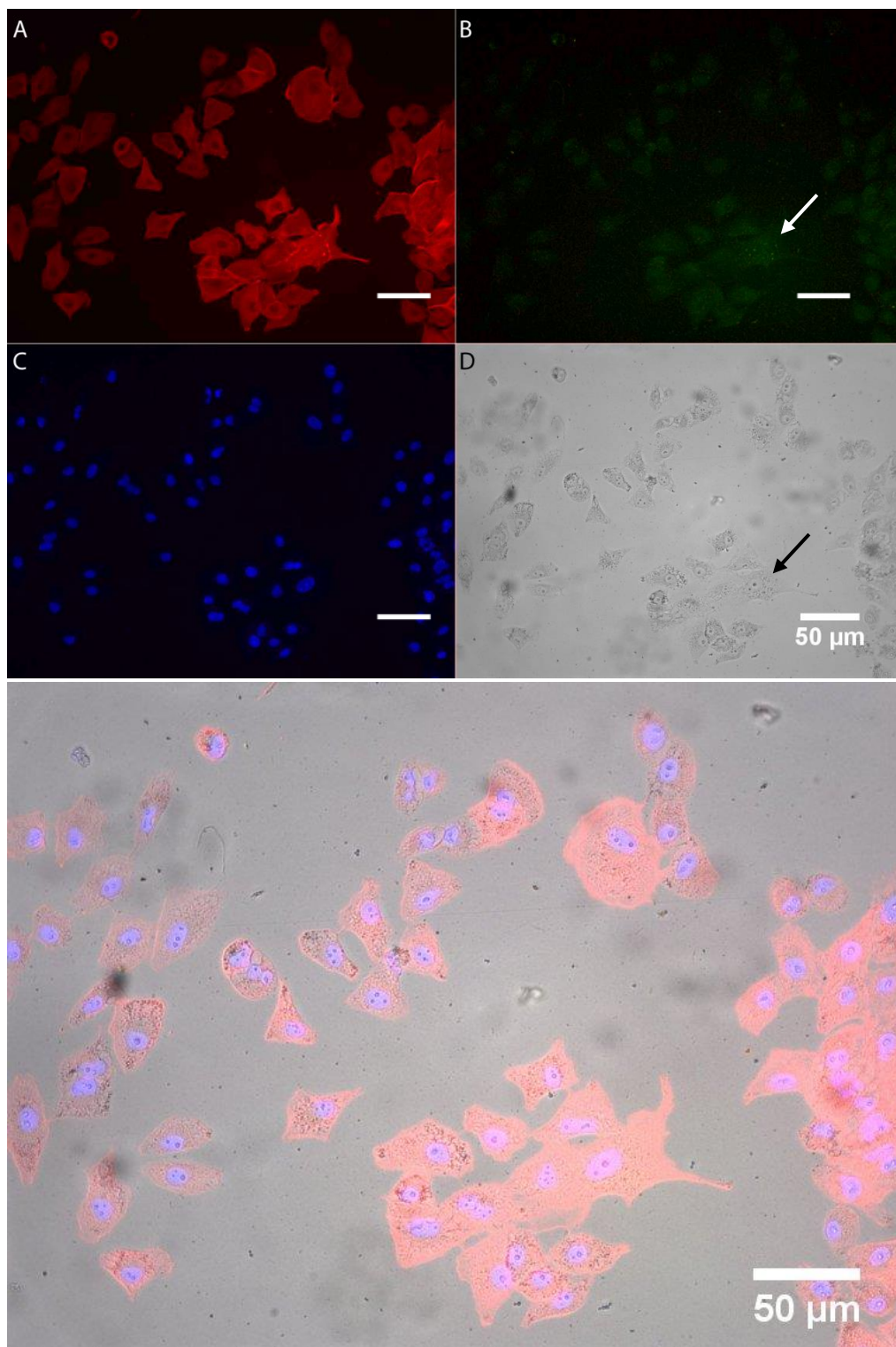


Figure 3.19: Epifluorescence image of NCI-H520 cells exposed to fluorescently tagged, anti-EGFR functionalised BiFeO₃ NPs. Actin was stained to show the cell morphology with Phalloidin Red (red channel), nuclei were stained with Hoechst (blue channel) and functionalised BiFeO₃ was labelled with CF 488A (green channel). Above, four-channel montage: A - Red channel, B - green channel, C - blue channel, D - bright field, scale bar = 50 μ m. Main panel, four-channel composite.

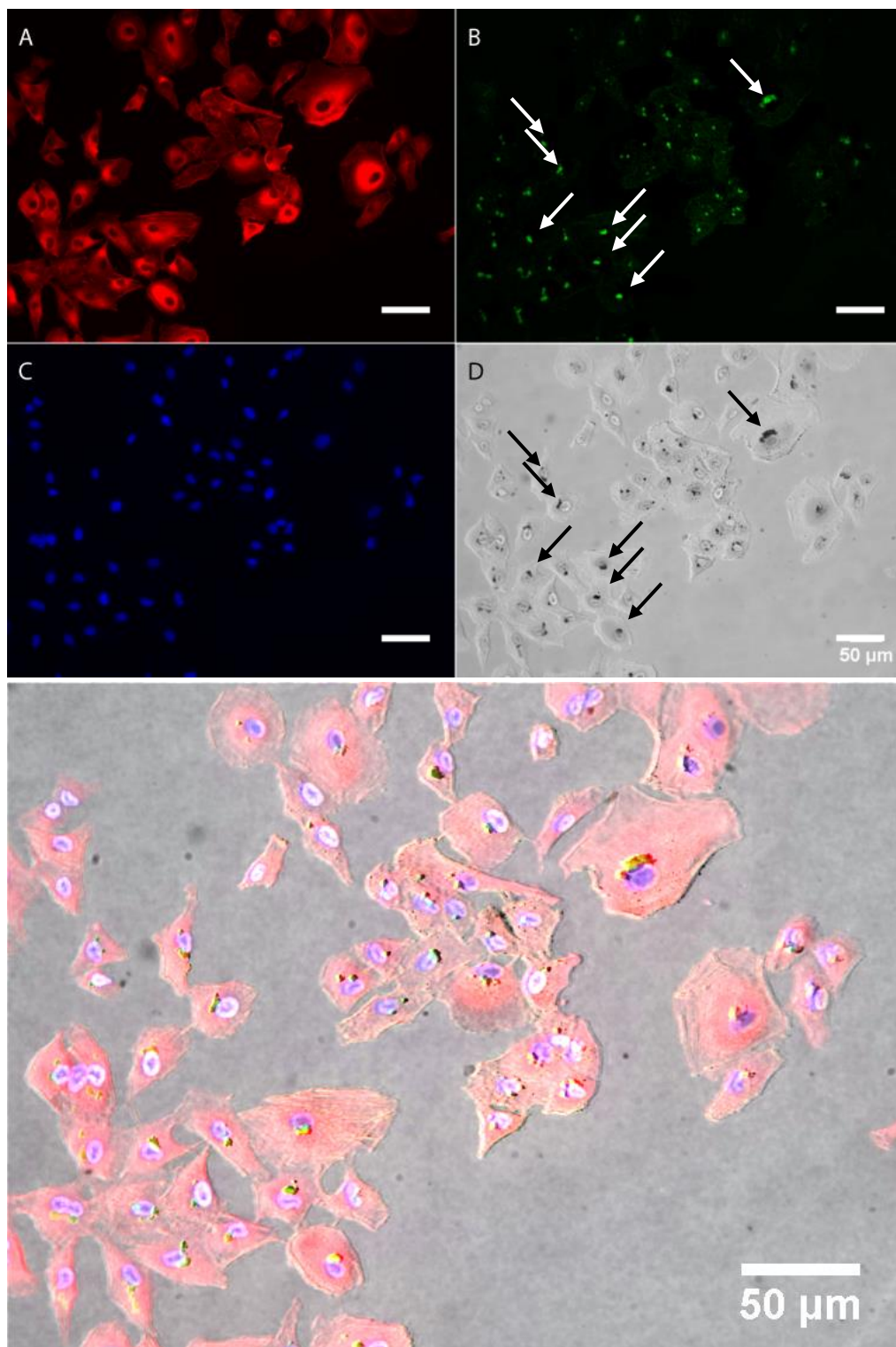


Figure 3.20: Epifluorescence image of A549 cells exposed to fluorescently tagged, anti-EGFR functionalised BiFeO₃@Fe₃O₄ NPs. Actin was stained to show the cell morphology with Phalloidin Red (red channel), nuclei were stained with Hoechst (blue channel) and functionalised BiFeO₃ was labelled with CF 488A (green channel). Above, four-channel montage: A - Red channel, B - green channel, C - blue channel, D - bright field, scale bar = 50 μm. Main panel, four-channel composite.

BiFeO₃@Fe₃O₄ NPs are also opaque, so they can be identified in the bright field image (indicated by black arrows in Figure 3.20, D) and the fluorescently-labelled EGFR as corresponding bright spots in the green channel (indicated by white arrows in B). BiFeO₃@Fe₃O₄ aggregates are more readily identifiable in the bright-field and appear larger than the BiFeO₃ NPs in Figure 3.18.

3.3.4 Uptake of nanoparticles in A549 cells

Iron quantitation

To quantify the uptake of the bare and functionalised nanoparticles, A549 lung adenocarcinoma cells were exposed to the nanoparticles for 1 and 24 hours at 0°C and 37°C, following the protocol of Riemer et al.¹⁸¹

Calibration solutions of known iron content from 0 – 9 µg Fe/mL were prepared by dissolving FeCl₃ in ultrapure water. Aliquots of the calibration solutions were digested in aqueous acidified permanganate solution on a hotplate. A solution of ferrozine was added once the digested iron had cooled. The absorbance was measured at 550 nm on a microplate reader

The absorbance of the ferrozine-iron complex was linear at the concentrations examined (see Figure 3.21).

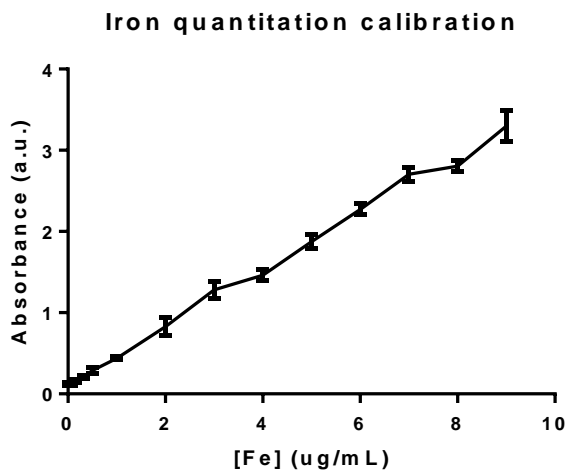


Figure 3.21: Iron quantitation calibration curve. Iron(III) chloride was used as the iron standard and prepared at concentrations from 0.02 – 9 µg Fe/mL, stained for iron with an iron detection reagent, and absorbance was measured at 550 nm. The data present the mean of triplicate samples in three independently performed experiments and the error bars represent the standard error of the mean.

A549 cells were incubated with nanoparticles and then lysed with HCl and treated in the same way as the iron calibration standards above. The iron content of the digested cell lysates was determined by comparing the absorbance with that of the calibration standards.

The concentration of iron in the lysates of cells treated with $\text{BiFeO}_3@Fe_3O_4$ nanoparticles, functionalised or stabilised with ascorbic acid, was not significantly different from that of the positive control at each time-point (see Figure 3.22).

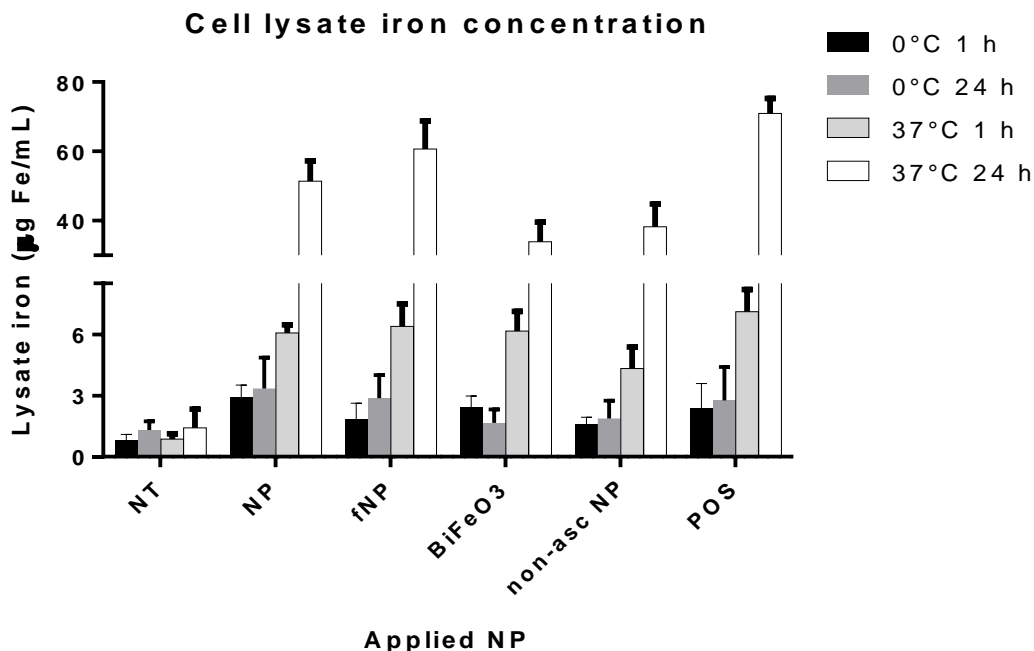


Figure 3.22: Concentration of iron in cell lysates after exposure to nanomaterials. Cells were seeded for 24h, exposed to nanoparticles for 1 or 24h, incubated on ice (0°C) or in an incubator (37°C), and then lysed with HCl. The cells were left untreated for the negative control (NT), or exposed to the following nanoparticles at 100 µg Fe/mL: $\text{BiFeO}_3@Fe_3O_4@asc$ (NP), $\text{BiFeO}_3@Fe_3O_4@anti\text{-EGFR}$ (fNP), $\text{BiFeO}_3@asc$, $\text{BiFeO}_3@Fe_3O_4$ without ascorbic acid (non-asc NP) as a control for the stabilising ligand, and $Fe_3O_4@poly\text{-acrylic acid}$ (MF66) as a positive control for iron-oxide interactions.

There was similar loading of iron via BiFeO_3 , although the content only reached 60 µg Fe/mL after 24h at 37°C. This is unsurprising as the cells were treated with the equivalent of 100 µg Fe/mL rather than 100 µg/mL of the nanoparticles. As such, to internalise the same content of iron, the cells would need to essentially double their rate of uptake.

With respect to non-asc $\text{BiFeO}_3@Fe_3O_4$, the nanoparticles aggregate rapidly and sediment out of suspension, settling on the cells in greater concentration than stabilised nanoparticles, so it is expected that the iron content of the cells should be higher. However, this requires that aggregates are as readily taken up by cells as individual nanoparticles, which is not the case; particles below ~50 nm can pass unobstructed through cell membranes but aggregates larger than 100 nm must be actively taken up into the cell. In the case of functionalised nanoparticles, the antibody can only bind to sites on the cell

surface where the antigen is expressed and there may be steric hindrance or competition for the limited number of sites.

The amount of iron in the cell lysates must be expressed as a function of the mass of protein (as a corollary of the concentration of iron per cell).

Calibration solutions of known protein content from 50 – 500 $\mu\text{g}/\text{mL}$ were prepared by dissolving albumin in ultrapure water. Aliquots of the calibration solutions were transferred to wells of a microplate with Coomassie blue dye. The absorbance was measured at 595 nm on a microplate reader. The change in absorbance of Coomassie blue as a function of albumin concentration was determined to be linear at the concentrations investigated (see Figure 3.23).

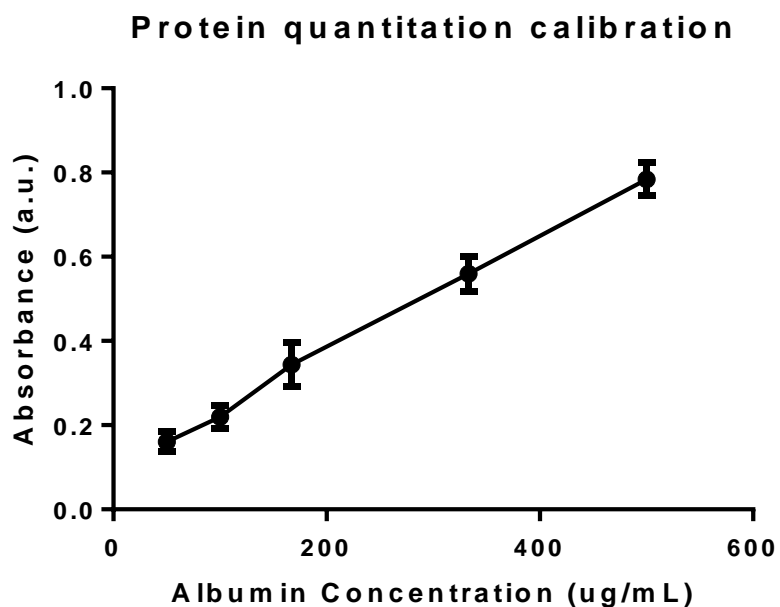


Figure 3.23: Absorbance of a protein standard with a detection reagent at 595 nm. Albumin was used as the protein standard and prepared at concentrations from 50 – 500 $\mu\text{g}/\text{mL}$, stained for protein with Bio-rad protein assay, and absorbance was measured at 595 nm. The data present the mean of triplicate samples in three independently performed experiments and the error bars represent the standard error of the mean.

Cell lysates were treated in the same way as the albumin standards.

The concentration of protein in the lysates was approximately 4 mg/ml in samples incubated at 0°C. Heterogeneity between triplicates and across the experimental repeats, as evidenced by the large standard error of the mean (see error bars, Figure 3.24), is due to the variance in cell number between repeats.

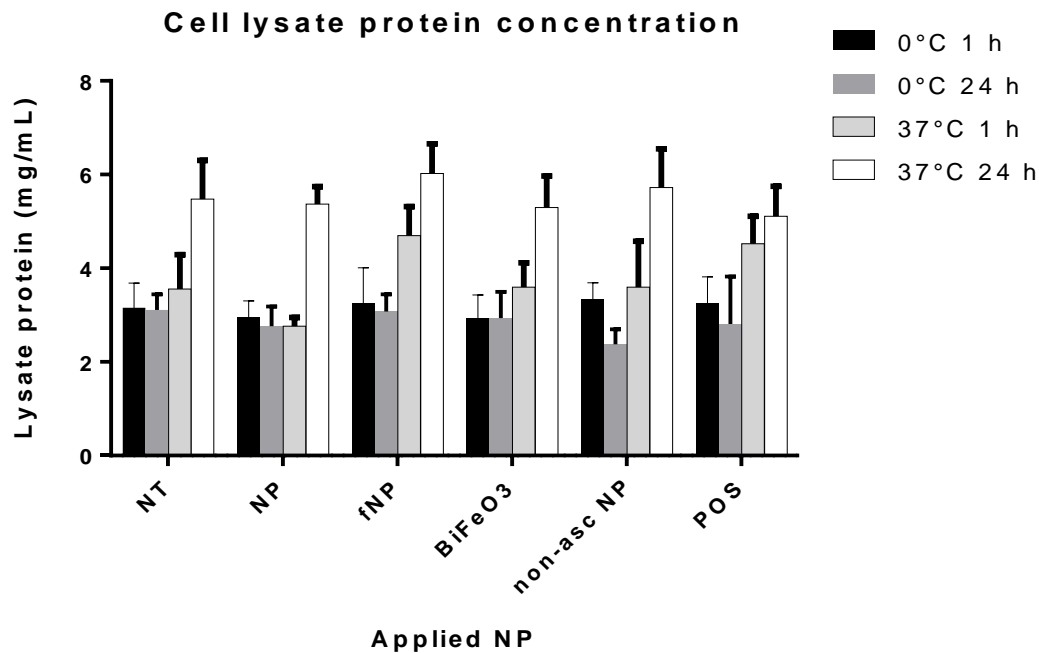


Figure 3.24: Concentration of protein in A549 cell lysates after exposure to various nanoparticles. Cells were seeded for 24h, exposed to nanoparticles for 1 or 24h, incubated on ice (0°C) or in an incubator (37°C), and then lysed with HCl. The cells were left untreated for the negative control (NT), or exposed to the following nanoparticles at 100 µg Fe/mL: BiFeO₃@Fe₃O₄@asc (NP), BiFeO₃@Fe₃O₄@anti-EGFR (fNP), BiFeO₃@asc, BiFeO₃@Fe₃O₄ without ascorbic acid (non-asc NP), and Fe₃O₄@poly-acrylic acid (MF66) as a positive control.

The lysates of the untreated control cells yielded approximately 6.5 mg/ml of protein after 24h at 37°C, significantly higher than the 0°C or 1h samples. A similar pattern was exhibited by all the cells treated with nanoparticles. This is because the doubling time of A549 cells is 23h, and cell function was halted in the 0°C samples whereas in the 37°C 1 h sample, the apparent increase in cell number was not significant.

The iron content of cells exposed to bare nanoparticles was similar to that of the positive control for magnetic nanoparticles, acid-stabilised magnetite (see Figure 3.25).

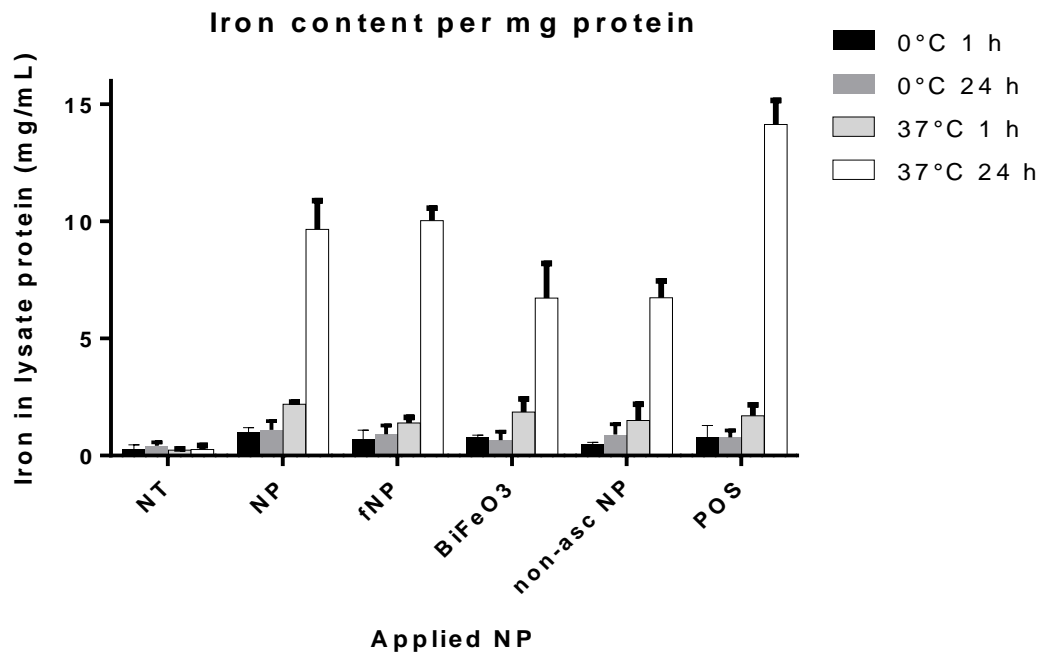


Figure 3.25: Concentration of iron content in A549 cell lysate protein after exposure to various nanoparticles. Cells were seeded for 24h, exposed to nanoparticles for 1 or 24h, incubated on ice (0°C) or in an incubator (37°C), and subsequently lysed with HCl. The cells were left untreated for the negative control (NT), or exposed to the following nanoparticles at 100 µg Fe/mL: BiFeO₃@Fe₃O₄@asc (NP), BiFeO₃@Fe₃O₄@anti-EGFR (fNP), BiFeO₃@asc, BiFeO₃@Fe₃O₄ without ascorbic acid (non-asc NP), and Fe₃O₄@poly-acrylic acid (MF66) as a positive control.

Due to the large uncertainty in the measurement of the Coomassie blue dye, similar levels were observed in cells treated with stabilised BiFeO₃ nanoparticles. This is to be expected; the dose of each of the nanoparticles was a function of the iron content – 100 mg/ml.

The iron content after 1h and 24h at 0°C was not significantly different from the untreated control for any of the samples. Slight increases were observed in the content per mass of protein in cells exposed to the functionalised nanoparticles and BiFeO₃ nanoparticles at 37°C. In the case of the functionalised nanoparticles, this suggests that the uptake of the nanoparticles is promoted by their targeting to proteins expressed on the surface of the cells. In the case of the stabilised BiFeO₃ nanoparticles, the increase in uptake may be due to their small size. However, the uptake of the bare BiFeO₃ nanoparticles was not promoted to the same degree so their stability played a significant role in their uptake: unstable nanoparticles aggregate and fall out of suspension.

Investigation of energy transport mechanism: effect of sodium azide as inhibitor

The role of sodium azide in inhibiting the uptake of the nanoparticles was investigated. The cell lysate iron concentration of cells exposed to BiFeO₃@Fe₃O₄ (nanoparticle), functionalised nanoparticles (fNP)

and MF66 as a positive control for magnetic nanoparticles (POS). Sodium azide inhibits uptake by disabling the transport of molecules across the cell membrane. Specifically, it binds to cytochrome c oxidase, an enzyme in mitochondrial electron transport. This results in the depletion of ATP in the cell, and the inhibition of oxidative phosphorylation.¹⁸⁴

The lysate iron concentration fell to the level of the untreated control when cells were treated with sodium azide and either the stabilised BiFeO₃@Fe₃O₄ nanoparticles or the positive control (see Figure 3.26).

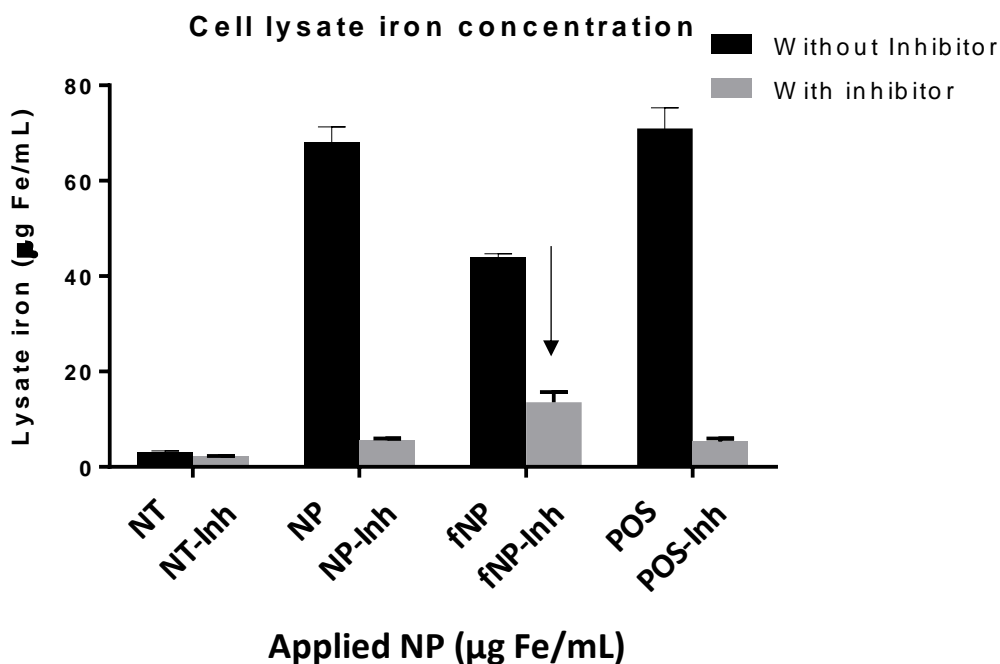


Figure 3.26: Effect of inhibitor on concentration of iron in A549 cell lysates on exposure to nanoparticles. Sodium azide (1% w/v) was used to inhibit the uptake of nanoparticles. Cells were seeded for 24h, exposed to nanoparticles for 24h, incubated at 37°C and subsequently lysed with HCl. For the negative control (NT), the cells were left untreated or treated only with sodium azide. The cells were also exposed to the following nanoparticles at 100 µg Fe/mL with sodium azide (signified by the suffix -Inh) and without sodium azide: BiFeO₃@Fe₃O₄@asc (NP), BiFeO₃@Fe₃O₄@anti-EGFR (fNP), and Fe₃O₄@poly-acrylic acid as a positive control (POS).

The iron concentration of the lysates exposed to fNP also fell, but not to the level of the positive control or the non-functionalised nanoparticles. This suggests that most nanoparticles are internalised when there is no inhibitor. It is assumed that the lysate iron content of the inhibited samples is from those nanoparticles which remained attached to the surface. The remnant iron concentration indicates greater accumulation of nanoparticles at the surface of the cell when the NPs are functionalised (indicated by an arrow in Figure 3.26).

However, the iron content of cells treated with functionalised nanoparticles was significantly lower than that of the stabilised nanoparticles (NP or POS). This is perhaps due to the tendency of the functionalised nanoparticles toward heavy aggregation. Aggregates above 100 nm in diameter cannot be as readily transported into the cell.

Localisation of nanoparticles in A549 cells

Prussian blue staining for Iron oxide quantification

A549 cells were incubated with anti-EGFR functionalised $\text{BiFeO}_3@Fe_3O_4$ and anti-EGFR functionalised $\text{BiFeO}_3@Fe_2O_3$ nanocomposites and APTES-coated $\text{BiFeO}_3@Fe_3O_4$ nanoparticles to investigate the localisation of nanoparticles. Cells treated only with serum-free medium were used as a negative control.

Anti-EGFR functionalised $\text{BiFeO}_3@Fe_3O_4$ and anti-EGFR functionalised $\text{BiFeO}_3@Fe_2O_3$ nanocomposites formed aggregates (see Figure 3.27).

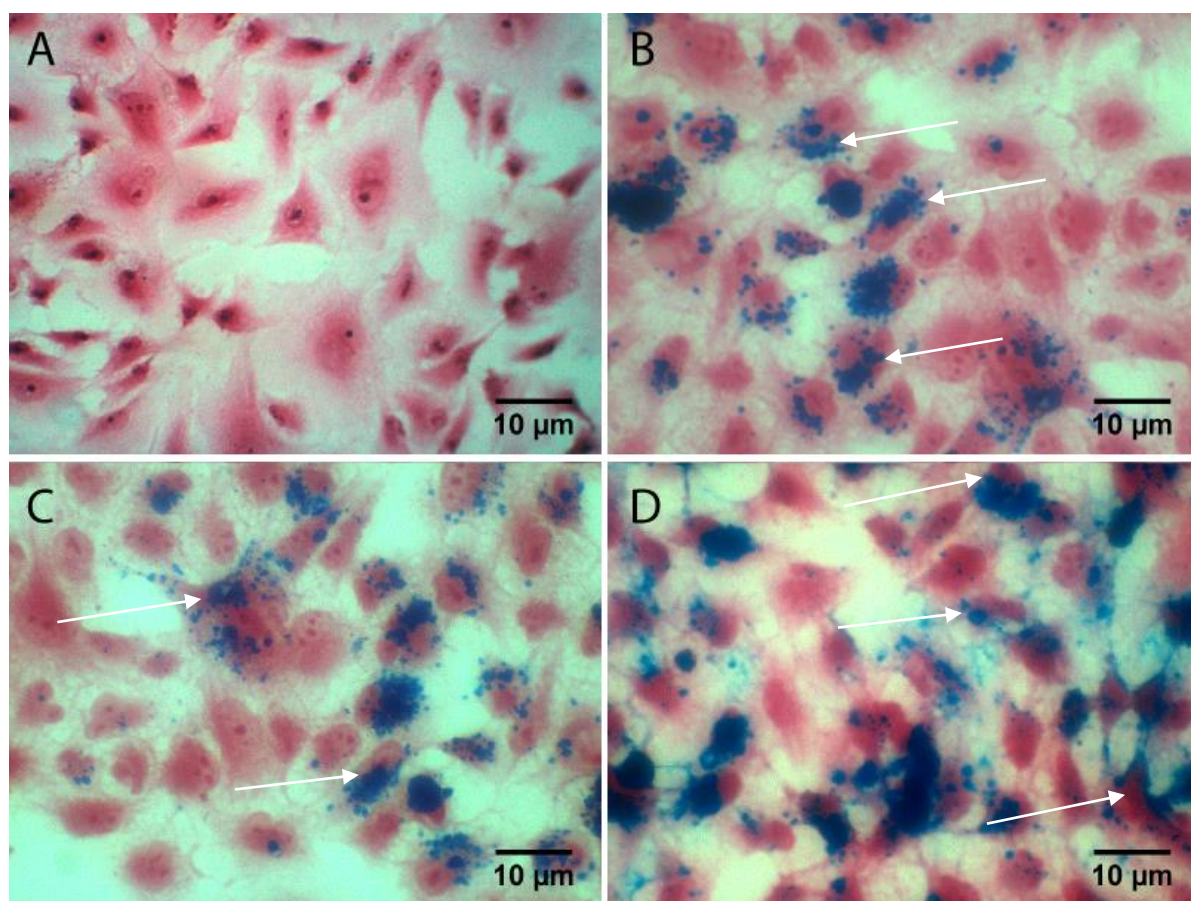


Figure 3.27: Cellular staining of A549 cells and localisation of nanoparticles and composites by iron oxide staining. A549 cells, after 24h incubation, stained with Nuclear Fast Red for cell structure and Perl's Prussian Blue for iron content. A, untreated cells (negative control); B, anti-EGFR functionalised $\text{BiFeO}_3@Fe_3O_4$; C, anti-EGFR

functionalised $\text{BiFeO}_3@Fe_2O_3$ nanoparticles; D, $\text{BiFeO}_3@Fe_3O_4@APTES$. Note that blue staining indicates the presence of any iron, whether in Fe_3O_4 , Fe_2O_3 , or in BiFeO_3 .

Regardless of their size, the aggregates clustered around the nuclei (indicated by white arrows), as in the positive control. This suggests that the NPs are localising in structures around the nucleus, perhaps on the endoplasmic reticulum, but more likely in the Golgi apparatus. APTES-coated nanoparticles appear to aggregate and cover the cells and obscuring the nuclei.

A549 cells were also incubated with anti-EGFR functionalised BiFeO_3 and anti-EGFR functionalised $\text{BiFeO}_3@Fe_3O_4$ nanoparticles, in the presence of 1% sodium azide to investigate the localisation of nanoparticles when internalisation is inhibited.

The washing steps removed did not remove all the functionalised BiFeO_3 NPs from the cells (see Figure 3.28, B).

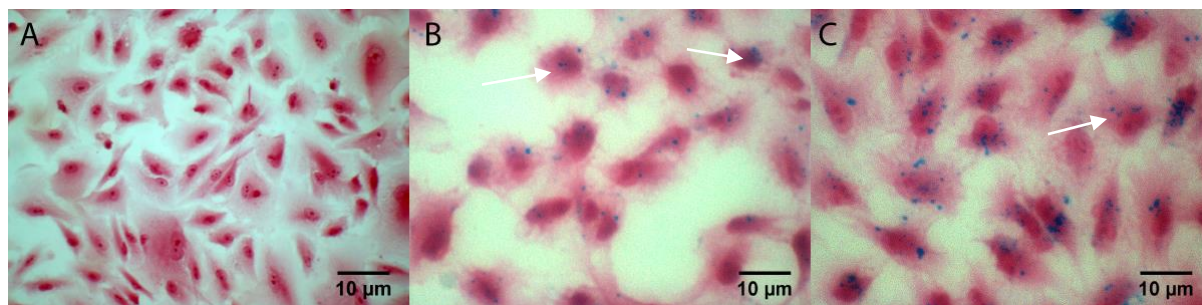


Figure 3.28: Cellular staining of A549 cells exposed to functionalised BiFeO_3 and $\text{BiFeO}_3@Fe_3O_4$ NPs in the presence of an inhibitor. Investigation of the energy transport mechanisms. A549 cells after 24 h incubation with 1% sodium azide: A – (negative control), B – exposed to anti-EGFR functionalised BiFeO_3 NPs; C – exposed to anti-EGFR functionalised $\text{BiFeO}_3@Fe_3O_4$.

Some functionalised BiFeO_3 NPs remained, indicating that the NPs had attached to the surface but had not been internalised. More of the functionalised $\text{BiFeO}_3@Fe_3O_4$ NPs remained after washing (see Figure 3.28, C). This is likely due to the lower ratio of iron in the BiFeO_3 NPs compared to the $\text{BiFeO}_3@Fe_3O_4$. While sodium azide inhibited the uptake of the functionalised particles, the anti-EGFR was still able to bind to the receptors on the surface.

Localisation was also examined by Z-stack confocal microscopy to confirm internalisation of the nanoparticles via 3D imaging. $\text{BiFeO}_3@Fe_3O_4$ nanoparticles were functionalised to target and label EGFR on A549 cells (see Figure 3.29).

Assessment of intracellular localisation of NP by confocal microscopy

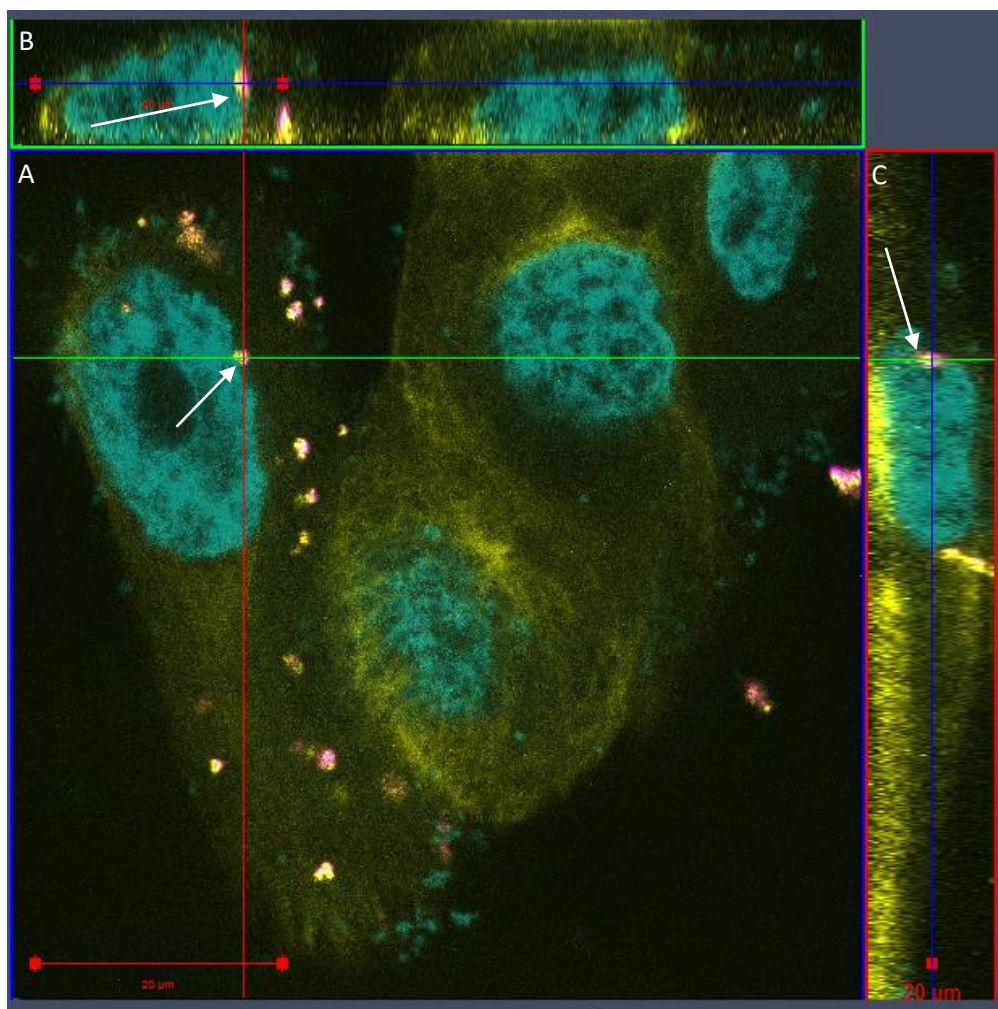


Figure 3.29: Confocal Z-stack slice of A549 cells labelled with fluorescently tagged anti-EGFR BiFeO₃ NPs. Clockwise from main panel: Panel A shows the top down view of a Z-stack slice of the cells after 24h incubation with nanoparticles, represented in blue in the orthogonal slice views B and C. Panel B shows a side view whose slice is represented in green in Panels A and C). Panel C shows the orthogonal view whose slice is represented in red in Panels A and B. DNA was stained with Hoechst to show nuclei (cyan), actin was stained with Phalloidin Red to show cell structure (yellow). The anti-EGFR antibody was tagged with CF 488A and is indicated in magenta.

Some nanoparticles were localised near the nucleus (indicated by white arrows in each of the orthogonal views). The side view labelled A shows that the nanoparticles may be embedded in the cell membrane, although they penetrate to the same depth within the cell as the nucleus does. Although EGFR is a transmembrane protein, the presence of the inhibitor cuts off the supply of ATP the cell required to internalise the functionalised nanoparticle.

3.4 Discussion

From the results presented above, it is evident that the materials functionalised were suitable for use as diagnostic probes.

For the nanocomposites to be used in biomedical imaging applications, several prerequisites had to be met: the surface of the materials had to be passivated to increase biocompatibility and enable efficient coupling, labelling, and bioconjugation appropriate to the intended target which, in this study, was for imaging and targeting accumulation quantification.

3.4.1 Silane layers were grown on nanoparticles to passivate their surface

FTIR analysis indicated the presence of silane and amine groups on BiFeO₃. Nanoparticles coated with APTES were markedly less stable in aqueous suspension, resulting in aggregation and particle growth as well as precipitation of particle agglomerates from suspension.

APTES coating is most efficient at pH 4, so the ζ -potential of bare nanoparticles at this pH is important. However, the absolute magnitude of the ζ -potential of the nanoparticles in aqueous suspension at pH 4 was less than 5 mV (see Figure 3.6), indicating that the nanoparticles were extremely unstable. Aggregation and flocculation were induced, which led to rapid precipitation of the powder.

Silanisation was carried out in 85% EtOH with acetic acid (1 mM) to achieve an approximate pH_{EtOH} of 4. BiFeO₃ nanoparticles were also unstable at this pH in EtOH – borne out by the images inset in Figure 3.6 showing the nanoparticle suspension immediately after sonication and 20 min later. This results in both particles and aggregates being coated with a silane layer, which is undesirable. Ideally, the nanoparticle suspension would be stable, with individual particles well separated and electrostatically repulsive to one another. This would result in the greatest surface area available for binding with APTES molecules and lead to individual nanoparticles being coated with a silane layer. Because silanisation must be carried out at pH 4, the suspension is unstable, and the nanoparticles aggregate and quickly sediment from the solution.

Of vital interest for biological applications is the colloidal stability, as indicated by the ζ -potential, at pH 7, particularly after coating with APTES. The behaviour of the silanised nanoparticles was not ideal: at physiological pH, the ζ -potential of the BiFeO₃@APTES nanoparticles was less than 5 mV, indicating very low colloidal stability.

Aggregation inhibits uniform attachment of antibodies. Ideally, antibodies will attach to all available binding sites on each nanoparticle. Where aggregates form, antibodies may attach to the cluster as

well as to individual nanoparticles. The issue is confounded further because aggregation induces sedimentation.

3.4.2 BiFeO₃ nanoparticles and BiFeO₃ composites were conjugated to anti-EGFR antibodies

Anti-EGFR antibodies were fluorescently tagged with CF 488A. BiFeO₃@APTES and BiFeO₃@APTES NPs (and aggregates) were functionalised with the CF 488A antibodies. This was confirmed to be successful by flow cytometry and epifluorescence microscopy. It also demonstrated the ability to target the multimodal nanoparticles to specific markers and establishes that the functionalised composites can be used as diagnostic probes.

Conjugation protocols are used in practice to functionalise nanomaterials with a library of primary and secondary antibodies for targeting specific diagnostic markers.^{65,123,185}

3.4.3 Functionalisation with anti-EGFR antibody allowed specific targeting to EGFR

Because the bare nanoparticles are smaller than 50 nm in diameter, they can pass through pores in the cell membrane into the cytosol of cells. Greater concentrations of iron were detected in cells that had been exposed to non-functionalised nanoparticles and composites than in those exposed to functionalised nanoparticles. This may be due to increased size as a result of aggregation during the functionalisation steps.

However, when transport was inhibited with sodium azide, the amount of iron associated with the cells was higher for functionalised nanoparticles, confirmed by cytochemical staining. Z-stack confocal imaging showed that functionalised nanoparticles are embedded in or near the surface of the cell. This suggests that bioconjugation with anti-EGFR antibodies increases the targeting of nanoparticles to the EGFR, even when internalisation is inhibited.

3.5 Conclusion

The work outlined in this chapter demonstrated variety of nanoparticles and composites were functionalised with unlabelled or fluorescently labelled antibodies to target EGFR on the surface of A549 cells. The preparation of targeted multifunctional nanocomposites was a major milestone for this thesis which required considerable effort since the synthesis work is novel and the literature available is very limited or inconsistent.

The methods employed can also be extended: nanoparticles and composites can be functionalised with a library of targeting antibodies using the same techniques – for example, the anti-EGFR antibody used in this study is one of a family of antibodies which can be used to deliver nanoparticles for diagnostic and therapeutic applications.

The uptake of labelled, functionalised nanoparticles was confirmed via advanced fluorescence microscopy and the localisation of the composites was visualised via histochemical staining as well as by confocal microscopy. This indicates that the composites can be targeted to diagnostic markers and that the functionalised probes can label structures of interest and confirms the preparation of multifunctional diagnostic probes for advanced biomedical imaging.

The safety of the functionalised composites is assessed in the next chapter to determine at what concentrations the materials can be used as diagnostic probes and understand what exposure routes might pose most risk.

Chapter 4 Safety assessment of nanoparticles and nanocomposites

4.1 Introduction

This chapter presents the safety assessment of functionalised nanoparticles and composites prepared as multimodal probes for biomedical applications. The results of cytotoxicity assays carried out on various cell lines are examined to demonstrate the suitability of the functionalised nanomaterials for use as diagnostic probes according to the following table.

Table 4.1: Matrix of nanomaterials, their properties and the nanocomposites in which the properties are to be combined. Legend: ✓ known property ⊙ target property. The relative importance of each is represented by the frequency of each symbol.

Nanomaterial/composite	Optical properties	Magnetic properties	Surface properties	Geometric properties	Composite structure
BiFeO ₃ NPs	✓✓✓	✓			Metal oxide
Fe ₃ O ₄ NPs		✓✓✓			Metal oxide
SiO ₂ NWs			✓	✓✓	Dielectric material
SiO ₂ NWs with BiFeO ₃	✓		⊙	✓✓	Dielectric material embedded with metal oxide
SiO ₂ NWs with BiFeO ₃ & Fe ₂ O ₃	✓	✓	⊙	✓✓	Dielectric material embedded with two metal oxides
SiO ₂ NWs with BiFeO ₃ & Fe ₃ O ₄	✓	✓	⊙	✓✓	Dielectric material embedded with two metal oxides
BiFeO ₃ @Fe ₃ O ₄ NPs		✓✓			Core@shell composite of two metal oxides
BiFeO ₃ @Fe ₂ O ₃ NPs	✓	✓✓			Core@shell composite of two metal oxides
BiFeO ₃ @asc NPs	⊙	⊙	⊙	⊙	Metal oxide with stabilising ligand (ascorbic acid)
BiFeO ₃ @APTES NPs	⊙	⊙	⊙	⊙	Metal oxide with passivated surface (-NH ₂ from aminopropyltriethoxysilane)
BiFeO ₃ @Fe ₂ O ₃ @asc NPs	⊙	⊙	⊙	⊙	Core@shell composite of two metal oxides with stabilising ligands
BiFeO ₃ @Fe ₃ O ₄ @asc NPs	⊙	⊙	⊙	⊙	Core@shell composite of two metal oxides with stabilising ligands
BiFeO ₃ @Fe ₂ O ₃ @APTES NPs	⊙	⊙	⊙	⊙	Core@shell composite of two metal oxides with passivated surface

4.1.1 Cytotoxicity

Toxic effects of reagents and compounds on whole animals can be predicted to some extent by the effect of those reagents and compounds on cells in culture. Several factors indicate the health of cells after exposure to potentially toxic or foreign materials, including the levels of adenosine triphosphate (ATP), cell proliferation and metabolism. Among these, the mechanism of cell death is associated with toxicity. For example, cells may become necrotic, in which the cell membrane becomes permeable and the cells lyse rapidly, or apoptotic, in which cells undergo controlled cell death. The rates of apoptosis and necrosis is affected by the presence of a toxic compound. For example, the release of heavy metals such as cadmium or the surface charge on metal oxide nanoparticles has been shown to induce oxidative stress and mitochondrial damage, resulting in increased apoptosis.¹⁸⁶

Cytotoxicity is determined by exposing cells to a certain mass of a substance: knowing the number of cells and measuring the effects on cell health by means of count and proliferation, starting from a statistically significant cell number. However, the definition of toxicity in terms of exposure of cells to a mass of material, is inaccurate for application to nanomaterials because material properties change as the ratio of surface area to volume increases. For example, 10 mg of bulk silver has only minimal toxic effects on a whole animal, whereas 10 mg of nanoscale silver has been shown to have size-dependent deleterious effects in a variety of human cell types.^{187,188}

4.1.2 Toxicity assessment of nanomaterials

Because of their small size, nanomaterials can pass easily through many biological membranes that act as a barrier for larger particles.^{189–193} This means they can more readily interact with cellular and subcellular structures.¹⁹⁴ While their pervasiveness means a greater array of toxicological end points,¹⁹⁵ it also means they have potential application in labelling or in targeting such structures.

Much research has focussed on superparamagnetic iron oxide nanoparticles (SPIONs) for use in magnetic resonance imaging (MRI),^{196–199} drug delivery^{20,200–202} and magnetic hyperthermia, yet there are outstanding challenges for each application.^{203–207}

For example, to obtain sufficient contrast in MRI, very high concentrations of intracellular SPIONs are needed.^{208–210} Non-invasive delivery of such high concentrations remains prohibitive, yet the main advantage of MRI is that it is non-invasive. Recent studies have shown that there are also issues with

the safety of such high doses of intracellular SPIONs and their impact on cell function, proliferation and homeostasis.^{211–213}

There are also outstanding and more fundamental challenges in assessing the safety of such materials.^{189,191,214} Nanotoxicology is a new field and definitions and standards are still in preparation.^{215,216} At present, there is no consensus on what constitutes an appropriate control for nanoparticle interaction, or which cell lines are most appropriate to examine.^{217,218}

This lack of standard operating procedures results in different research groups reporting data that is disparate, incomplete and/or incompatible. Several platforms have been established to set out new definitions, procedures and standards to overcome this challenge.

In this study, cell lines were chosen on their relevance to potential exposure routes. A human lung epithelial cell line (A549) was chosen to represent exposure to nanoparticles through inhalation and a human umbilical vein endothelial cell line (HUVEC) to represent the exposure of an endothelial cell monolayer. Macrophage-like cells were differentiated from monocytes to investigate a general immune response; however, cytotoxicity results from the macrophage-like cells were so heterogeneous that the data was inconclusive. For further details, see Appendix A1.

4.1.3 High content screening for cytotoxicity screening

In recent years, cytotoxicity assays have been revolutionised by automated imaging. Previously, cell cultures were stained and individually imaged using, for example, a confocal microscope, and the images were analysed for cell viability and other indicators of toxicity. High content screening (HCS) involves the use of an automated imaging system to permit very high numbers of assays to be carried out in parallel in which multiple parameters are measured on a cell-by cell basis to obtain quantitative information for the population.²¹⁹

The preparation of the cell culture is as follows:

- Cells are typically seeded in 96-well plates, allowed to attach, then exposed to the analyte in fresh media.
- The culture is incubated with the compound of interest for a set period.
- The cells are stained, fixed and then imaged.

The 96-well plate is placed on an automated imaging stage, one of the wells is used to set the focus for the plate and multiple fields from each of the wells can be selected for imaging. The stage is then controlled by software and images are recorded at each position, using lasers like those used in confocal

microscopy to excite fluorescence. Often, a set of images from each field consists of a bright-field image and red, green and blue images, acquired by applying filters appropriate to the staining.

The power of HCS results from the image analysis software which processes each image to return quantitative data on a cell-by-cell basis. This is then used to determine field-by-field data, which is used in turn to assess well-by-well information and finally overall population results for a given experiment. Automated imaging analysis can count the number of cells in a given field by identifying the number of contiguous, simple, elliptical areas greater than $10 \mu\text{m}^2$, for example, when a filter is applied which isolates the nuclear stain. Cell membranes can be identified by the software by overlaying known positions of nuclei with contiguous regions larger than $10 \mu\text{m}^2$ but less than $100 \mu\text{m}^2$ in the channel which corresponds to cell membrane or cytoskeletal staining. Then for each cell identified, the relative intensity and spatial distribution of each stain is recorded and, importantly, the same analysis is carried out over the entire population. Manual filters can also be subsequently applied to identify subpopulations.

Depending on the assay and staining, multiple parameters like cell and organelle physiology (i.e. size and morphology) and metabolic activity can be assessed for approximately one million individual cells in a single assay.

4.2 Materials and Methods

4.2.1 Reagents

RPMI 1640 medium with 25 mM HEPES, HyClone medium, TrypLE, fetal bovine serum, L-glutamine, penicillin G, streptomycin, epidermal growth factor (EGF), hydrocortisone, Hoechst 33342 (referred to below as Hoechst), propidium iodide, and JC-1 from Gibco (Invitrogen Ltd, Ireland); para formaldehyde (PFA), sterile water and phosphate buffered saline (PBS) were obtained from Sigma (Ireland). Endothelial Growth Medium 2 and Endothelial Cell Growth Medium 2 Supplement Mix were obtained from PromoCell.

4.2.2 Equipment and protocols

The broad expertise of the Nanomedicine and Molecular Imaging Group was an invaluable resource in the development of protocols and training in the following characterisation techniques. ^{49,50,57,220-224}

Cell culture

Human lung epithelial carcinoma cells (A549 cells) from American Type Culture Collection ATCC were kindly provided by Dr Dania Movia, as part of the Nanomedicine Laboratory work under the NANOREG FP7 project at Trinity College Dublin and cultured as described in Chapter 3.

Human umbilical vein endothelial cells (HUVECs) from American Type Culture Collection ATCC were generously supplied by Dr Toby Paul, Cellix Ltd, Ireland.

HUVECs were cultured in Endothelial Growth Medium 2 supplemented with 5% foetal calf serum, epidermal growth factor (recombinant human) (5 ng/ml), basic fibroblast growth factor (recombinant human) (10 ng/ml), insulin-like growth factor (long R3 IGF-1) (20 ng/ml), vascular Endothelial Growth Factor 165 (recombinant human) (0.5 ng/ml), ascorbic acid (1 µg/ml), heparin (22.5 µg/ml) and hydrocortisone (0.2 µg/ml).

Human monocyte-derived macrophages (MDMs) were prepared by isolating peripheral blood monocytes from blood (single-donor buffy coat). Buffy coats were kindly supplied by the Irish Haematology Centre.

Treatment with nanoparticles

Cells were seeded at 5000 cells per well in a 96-well plate, allowed to attach and incubate for 24h before being rinsed with warmed serum-free medium and treated with nanomaterials.

For the treatment, the nanoparticles were dispersed from sterile stock solution at a concentration of 10 mg/ml by sonication for 30 min, then diluted with medium to 960 µg/ml (c1), followed by successive dilution to 480 µg/ml (c2), 240 µg/ml (c3), 120 µg/ml (c4), 80 µg/ml (c5), 40 µg/ml (c6), 20 µg/ml (c7), 10 µg/ml (c8) and 5 µg/ml (c9).

For cell cycle analysis and high content screening, cells were treated after rinsing with PBS by overlaying them with an aliquot of the NP suspensions c1 – c9 and allowed to incubate for three time points: 24 h, 48 h and 72 h. Valinomycin (120 µM) was used as positive control for cell death, tacrine (100 µM) as the positive control for changes in lysosomal mass or pH, zinc oxide nanoparticles (100 µg/ml) and magnetite nanoparticles (100 µg/ml) were used to control for the effects of toxic and non-toxic nanoparticles, while silica nanowires were used as a control for the influence of nanowires on the cells.

Experimental Design

For HCS analysis the following plate layouts were used (see Figure 4.1-Figure 4.5).

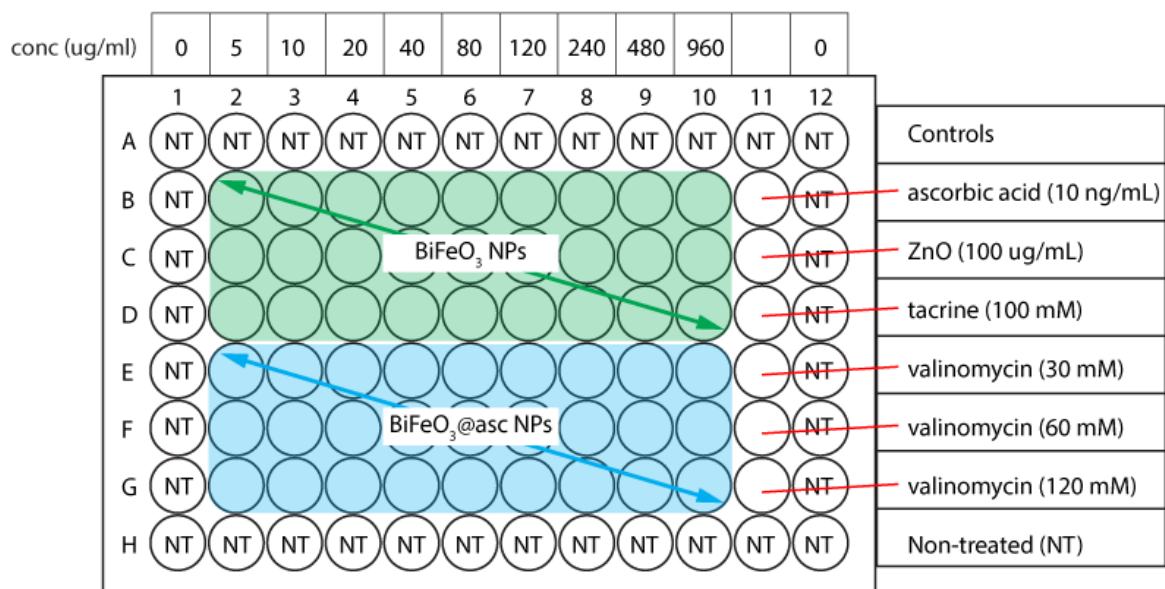


Figure 4.1: 96-well plate layout for exposure of cells to BiFeO₃ NPs and BiFeO₃@asc NPs

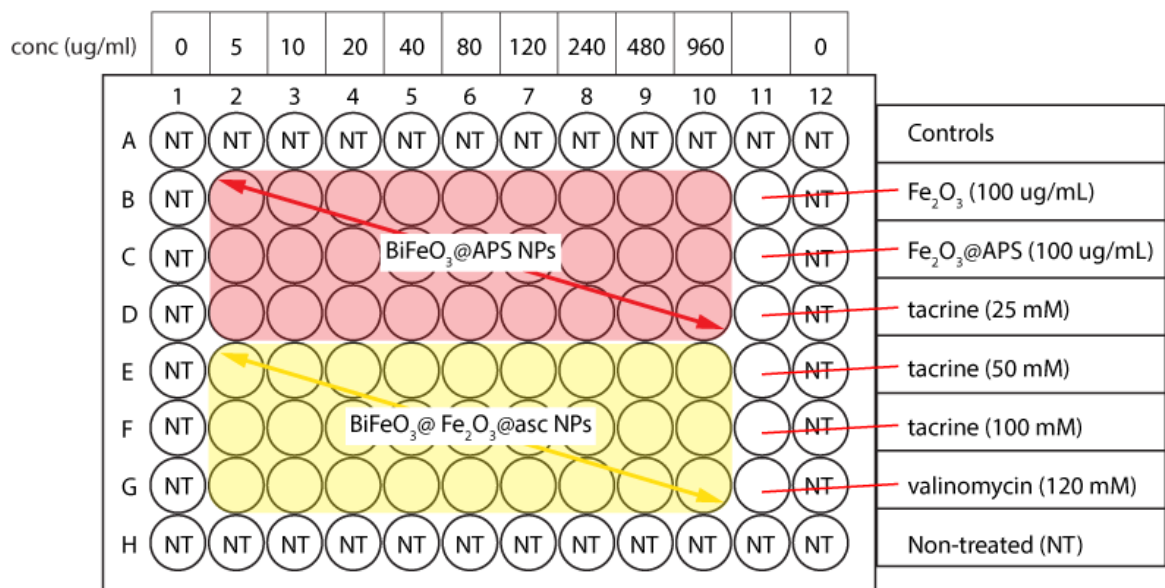


Figure 4.2: 96-well plate layout for exposure of cells to BiFeO₃@APTES NPs and BiFeO₃@Fe₂O₃@asc NPs

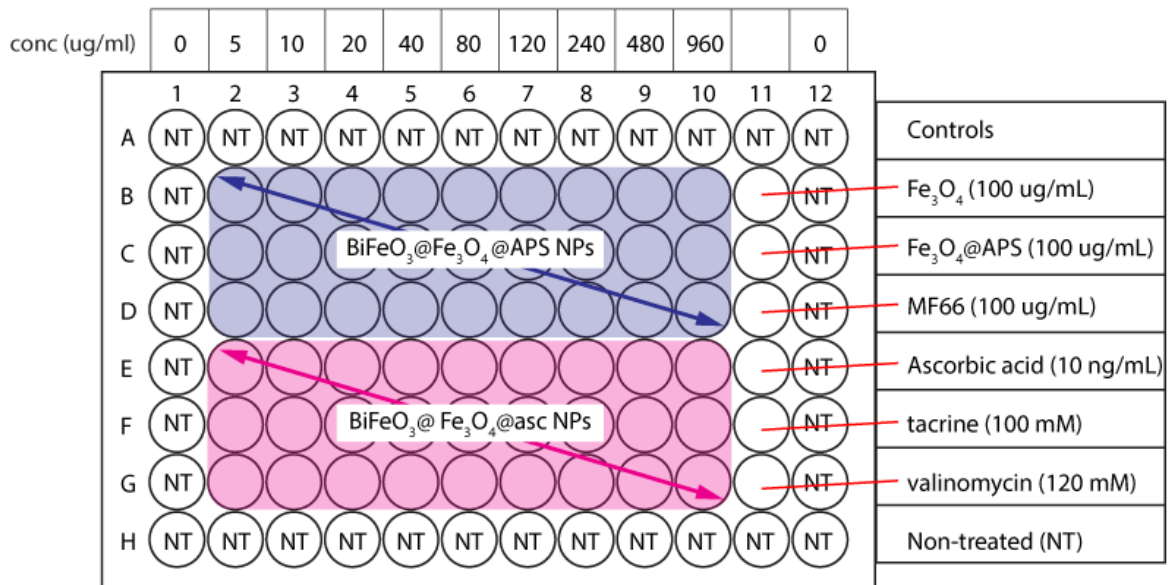


Figure 4.3: 96-well plate layout for exposure of cells to BiFeO₃@Fe₃O₄@APTES NPs and BiFeO₃@Fe₃O₄@asc NPs

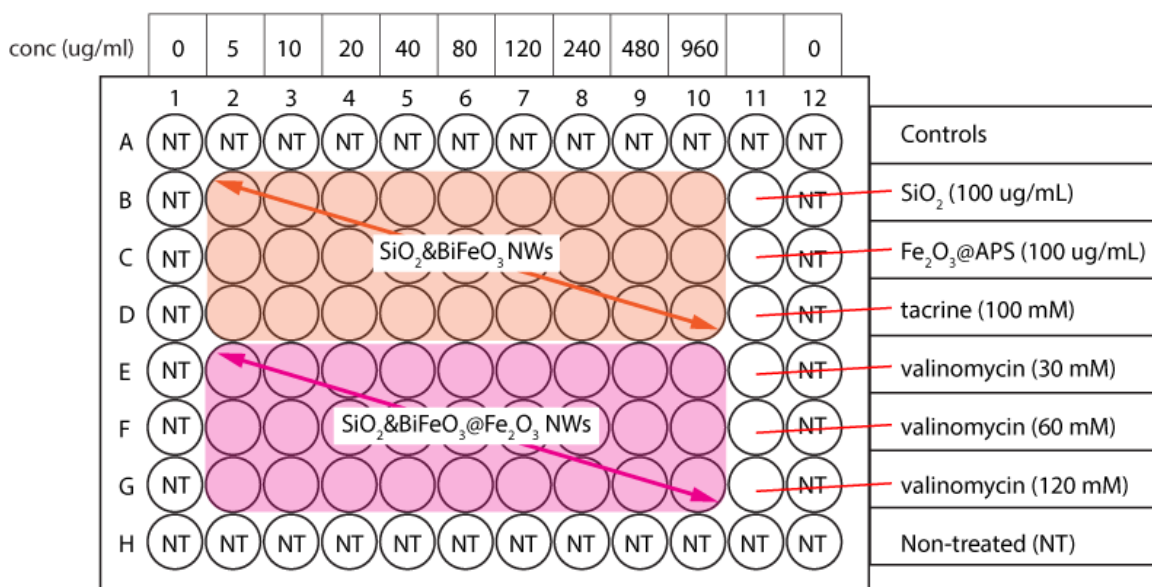


Figure 4.4: 96-well plate layout for exposure of cells to SiO₂&BiFeO₃ NWs and SiO₂&BiFeO₃@Fe₂O₃@asc NWs

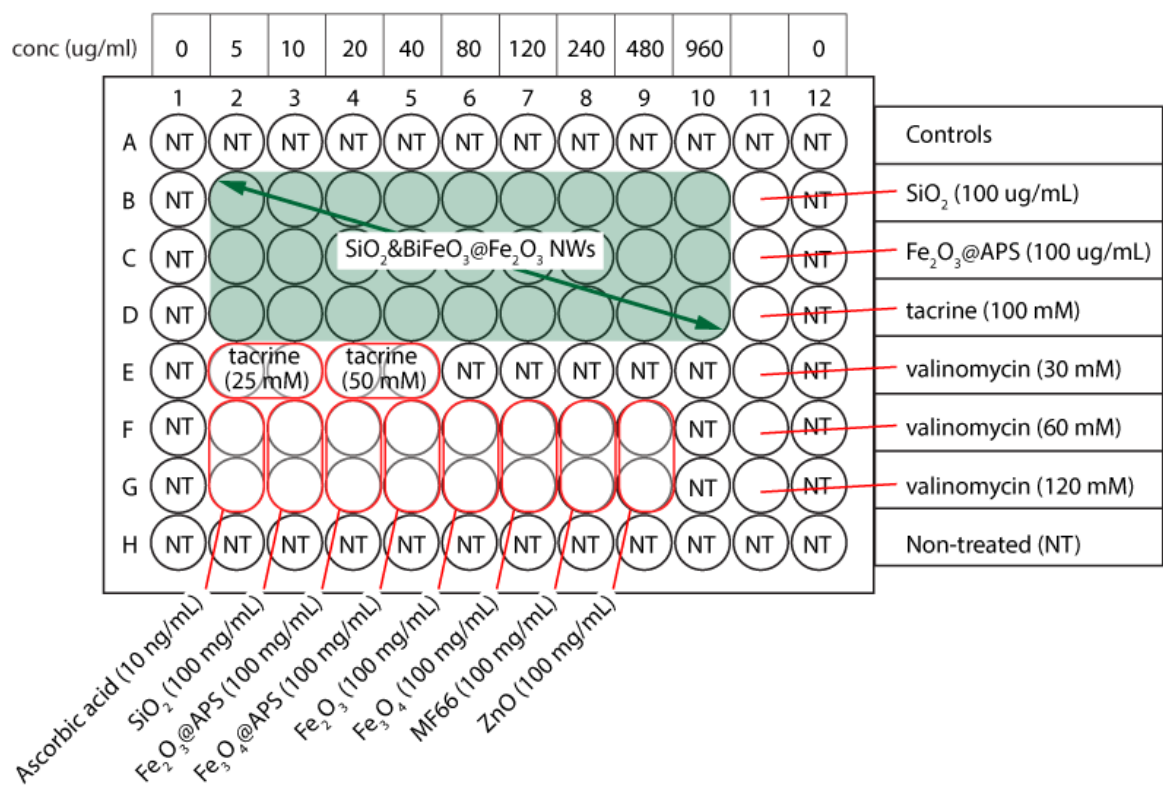


Figure 4.5: 96-well plate layout for exposure of cells to $\text{SiO}_2\&\text{BiFeO}_3\&\text{Fe}_2\text{O}_3\&\text{asc}$ NWs and controls

Staining

Live cells were stained with Hoechst (1 $\mu\text{g}/\text{ml}$), cell-membrane permeability dye (propidium iodide, 1 $\mu\text{g}/\text{ml}$) and mitochondrial membrane potential dye (JC-1, 5 $\mu\text{g}/\text{ml}$), allowed to incubate for 20-30 min, rinsed with warmed PBS and then fixed with warmed paraformaldehyde (3.7%) for 10-15 min before being rinsed twice with PBS and stored at 4°C until ready to image.

High Content Screening

BiFeO_3 and a suite of derivative nanomaterials were analysed for cytotoxicity by HCS. HCS imaging and analysis were carried out with a GE Healthcare InCell 1000 and Cytell Analyzer. Cells were seeded in 96-well plates, with a final concentration of 4000 cells per well. BiFeO_3 -treated cells were imaged using three channels in the imaging system as outlined in the table below.

Table 4.2: Filters and corresponding detection wavelengths for each HCS analyte

Stain	Filter	Channel	Detection Wavelength (nm)	Analyte
Hoechst	DAPI	1	461	DNA/nuclear intensity
Cell membrane permeability stain	FITC	2	509	Cell membrane permeability
LysoTracker™ Red	TRITC/Cy5	3	599	Lysosomal mass/pH

To elucidate the cytotoxic response of the full range of materials, A549, HUVEC and monocyte-derived macrophage cells were treated with the assorted nanomaterials at three-time points (24 h, 48 h, 72 h), imaged and analysed by High Content Screening and colorimetric staining techniques. Controls included ZnO at 100 µg/mL (to control for induction of cell death from nanomaterials of similar size), APS (to control for cytotoxic effects from silane terminal groups), and ascorbic acid (to control for cytotoxic effects from unbound ascorbic acid). Valinomycin (Val) at 120 µM was used as positive control (POS) to induce cell death and then compared to the equivalent untreated control or negative control (NT).

Images of the treated and untreated cells were recorded with the InCell Analyzer 1000 (GE Healthcare) and Cytell Imaging systems and were analysed with the InCell Analyzer software.

4.3 Results

This section presents the results of the cytotoxicity analysis carried out to determine the biological interactions of the functionalised nanoparticles and their composites. The cytotoxicity results elucidate the safety of the multifunctional nanomaterials and their constituents and evaluate their suitability for application as diagnostic probes.

The results of cytotoxicity analysis of each of the nanomaterials is elaborated fully in the Appendix. In this section, the results of the cytotoxicity analysis are summarised. To facilitate ease of comparison, the results are grouped according to cell type, then by the indicator of toxicity (cell count, cell viability and lysosomal/pH changes), and further according to nanomaterial type (nanoparticle and nanowire).

4.3.1 Cytotoxicity analysis of nanomaterial interactions of A549 cells by High Content Screening

In the following section, the response of A549 cells to each of the nanomaterials is presented with respect to three parameters: cell count, cell membrane permeability (as a measure of cell viability), and lysosomal mass/pH changes. After presenting the materials individually, a summary of the data is then provided and the response of cells to the different nanomaterials is compared.

A549 cells exposed to valinomycin (120 $\mu\text{g}/\text{mL}$) was a positive control for cell count in this study and showed no surviving cells after 24h. By contrast, A549 cells which were left untreated (NT) continued to proliferate after 72h (see Figure 4.6 and Figure 4.7)

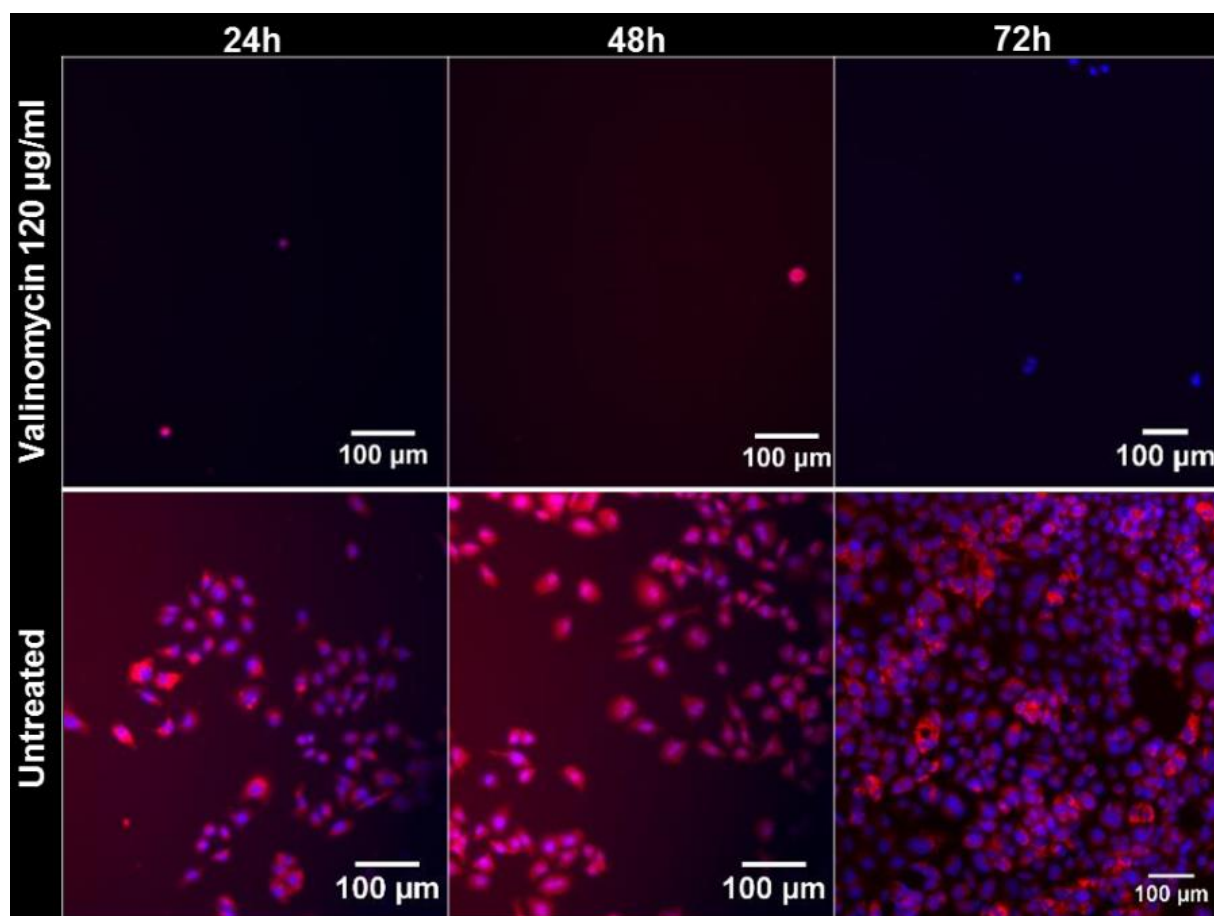


Figure 4.6: A549 cells, cell count controls. Top Row, cells treated with 120 μM valinomycin; bottom row, untreated cells. Left, 24h exposure; middle, 48h exposure, right, 72h exposure. Blue: Hoechst nuclear stain, red: lysosomal stain.

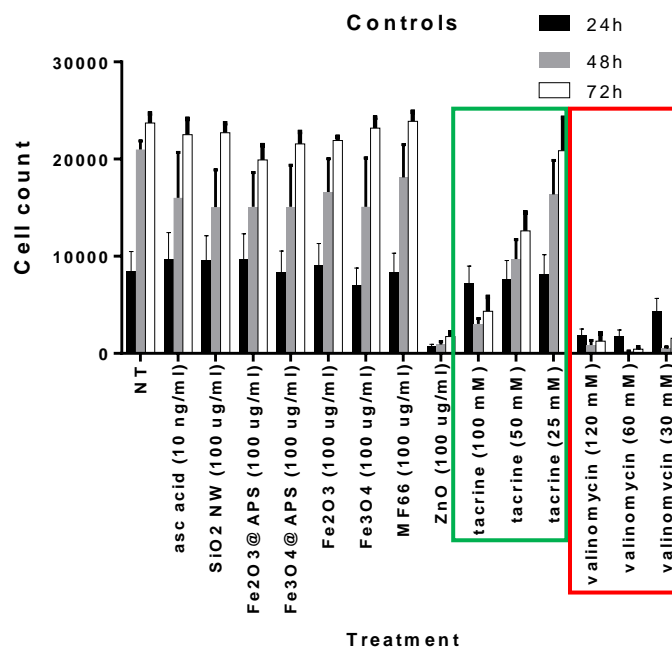


Figure 4.7: Overview of cell count of A549 cells exposed to controls. The error bars represent the standard error of the mean between three independent studies.

The controls used in this study (see Figure 4.7) were the negative control (NT, cells cultured without the addition of nanomaterials); ascorbic acid to control for the influence of the stabilising ligand; SiO₂ NWs to control for the influence of SiO₂ with high aspect ratio; 30 nm Fe₂O₃ and 15 nm Fe₃O₄, bare and silanised, were used as controls for NP interactions and as controls for the components of the composites; MF66 as a form of Fe₃O₄ stabilised with polyacrylic acid to compare to a commercially available standard; ZnO as a positive control for NP toxicity; tacrine as positive control for lysosomal mass or pH changes (see the green box in Figure 4.7) and valinomycin as positive control for cell death (see the red box in Figure 4.7).

Notably, there was no significant difference between the negative control and any of the controls for the components of the nanomaterials (ascorbic acid, silica, magnetite or hematite).

There are inherent challenges relating to the use of stains for quantitative analysis of cell viability,²²⁵ a primary challenge being that dead cells lose their adherence, since viability is calculated as a percentage of all those counted. This is especially evident from the viability of cells exposed to the positive control (POS), valinomycin (see the box, Figure 4.8).

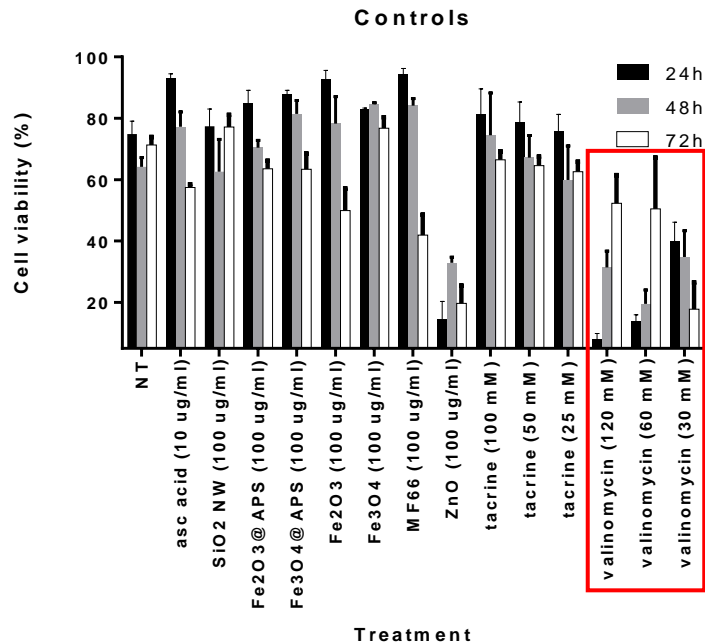


Figure 4.8: Overview of cell viability in A549 cells exposed to controls. The error bars represent the standard error of the mean between three independent studies.

Viability was calculated as a percentage of the total surviving cells in each field imaged and determined by analysing the co-localisation of cell membrane permeability with cell nuclei; when a cell membrane becomes permeable and permits the membrane permeability stain to reach the nucleus, the cell is no longer viable. Once the cell membrane becomes permeable and the cell dies, the cell's nuclear material and contents may remain in the wells and lead to false detection and thus erroneous results.

Where there is a dense population of cells, the impact of these erroneous results is negligible, but where the cell count is low, as in the positive control for cell death and NP toxicity, these results have greater significance, particularly where the parameter being analysed is a percentage of the surviving cells. For example, if all but 500 cells in a well have been killed by the positive control and 20% of those remaining are viable, 100 false positives would result in a calculated viability of 40%, whereas in a well containing 25000 cells with 20% viability, the same number of false positives would result in a calculated viability of 20.4%.

This leads to heterogeneity between samples or experimental repeats and often to cell viability being grossly over-estimated at low cell counts, but results are more robust with respect to false positives at higher cell number.

It must also be noted that the viability of the cells was also affected by other controls, most notably the reduction in viability after 72h exposure to MF66 NPs.

Challenges relating to the quantitative analysis of fluorescent staining also apply to the interpretation of the lysosomal mass/pH data. Because the intensity of staining is normalised on a plate by plate basis and because the intensity is calculated by normalising to cell number, the calculated lysosomal mass/pH values are often heterogeneous (see Figure 4.9).

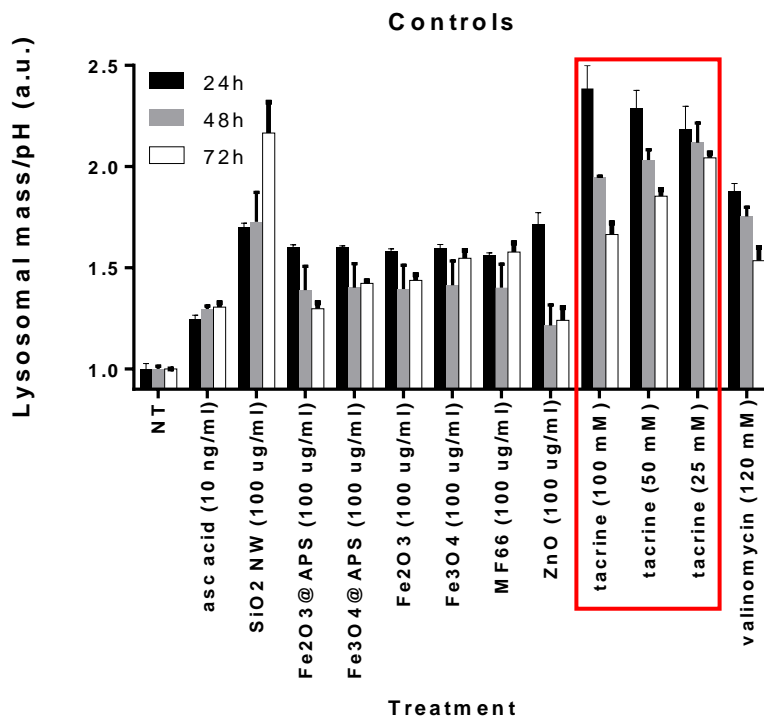


Figure 4.9: Overview of lysosomal mass/pH changes in A549 cells exposed to controls. The error bars represent the standard error of the mean between three independent studies.

This is similar to the determination of viability of cells exposed to the positive control, valinomycin (see Figure 4.8).

A549 Cell count

The response in A549 cell count to different nanoparticles is presented below (see Figure 4.10). See Appendix sections A.2.1.1, A.2.2.1, A.2.3.1, A.2.4.1, A.2.5.1 and A.2.6.1 for further details.

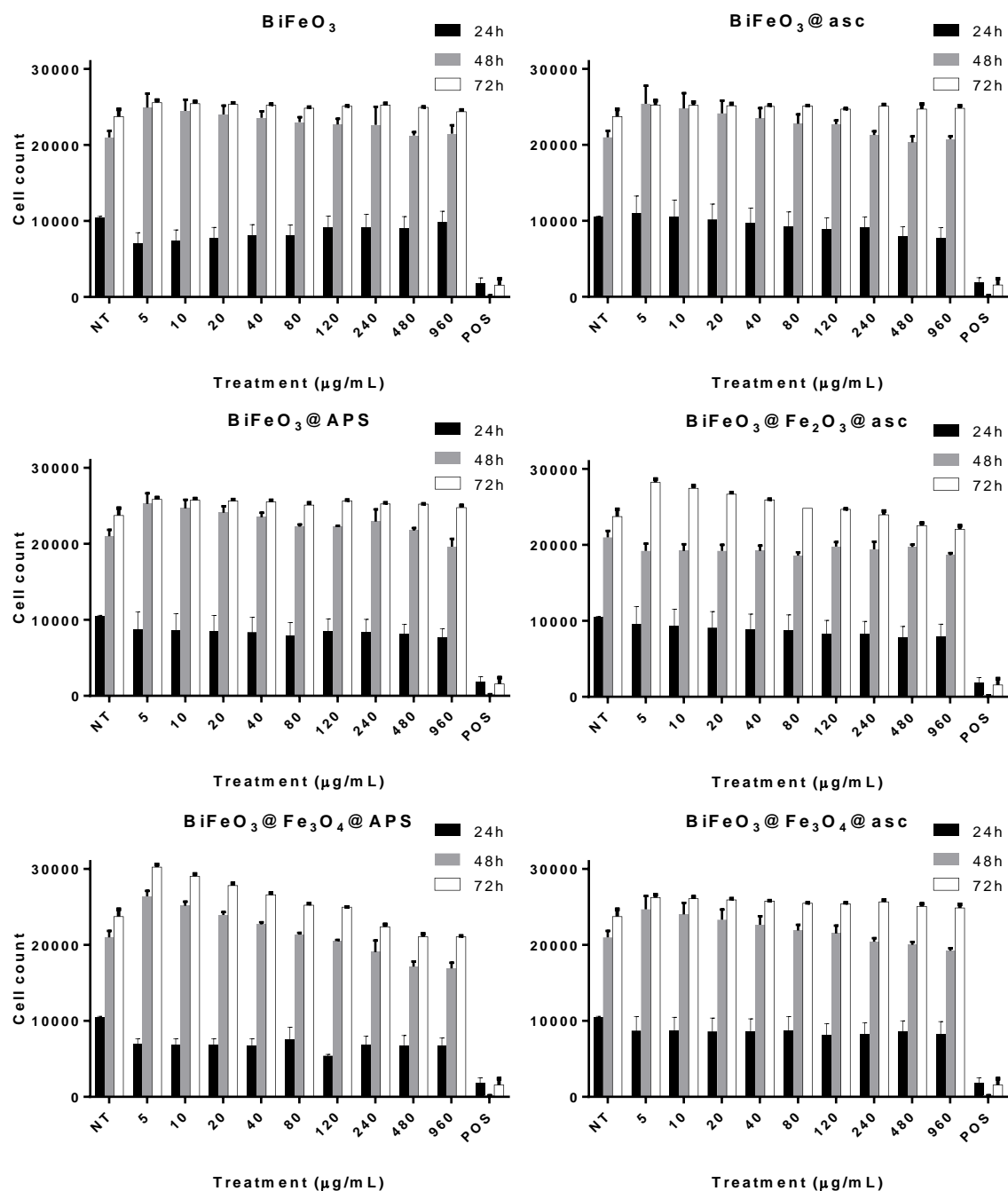


Figure 4.10: Overview of A549 cell count after exposure to each of the nanoparticles. NT signifies the negative control (cells cultured without the addition of nanomaterials) and POS represents the positive control for cell death (valinomycin 120 µM). The error bars represent the standard error of the mean between three independent studies.

Overall, the cell count data indicates that NPs derived from BiFeO₃ do not adversely affect A549 cell proliferation over the concentration range examined, and that the response of the cells does not

strongly depend on the surface chemistry of these NPs (see Figure 4.10). Such minimal impact across such a broad range of concentration has been reported for few nanomaterials.

However, the response of the cells to $\text{BiFeO}_3@APTES$, $\text{BiFeO}_3@Fe_3O_4@asc$, $\text{BiFeO}_3@Fe_3O_4@APTES$, and $\text{BiFeO}_3@Fe_2O_3@asc$ NPs suggests that this interpretation may be somewhat simplistic and that there may be confounding interactions. Particularly, small but significant increases in cell count at lower concentrations in response to treatment with these NPs (accompanied by a reduction in cell number at higher concentrations of $\text{BiFeO}_3@Fe_3O_4@APTES$ NPs) suggest that the NPs promote cell growth, yet the overall dose-dependence of the response indicates that the NPs are toxic at higher doses. Nevertheless, only in the case of $\text{BiFeO}_3@Fe_3O_4@APTES$ NPs did the cell count fall below the level of the untreated control.

This biphasic response is characteristic of a hormetic mechanism. See the discussion section for further details.

The response of A549 cell count to different nanowires is presented below (see Figure 4.11). See Appendix sections A.2.7.1, A.2.8.1 and A.2.9.1 for further details.

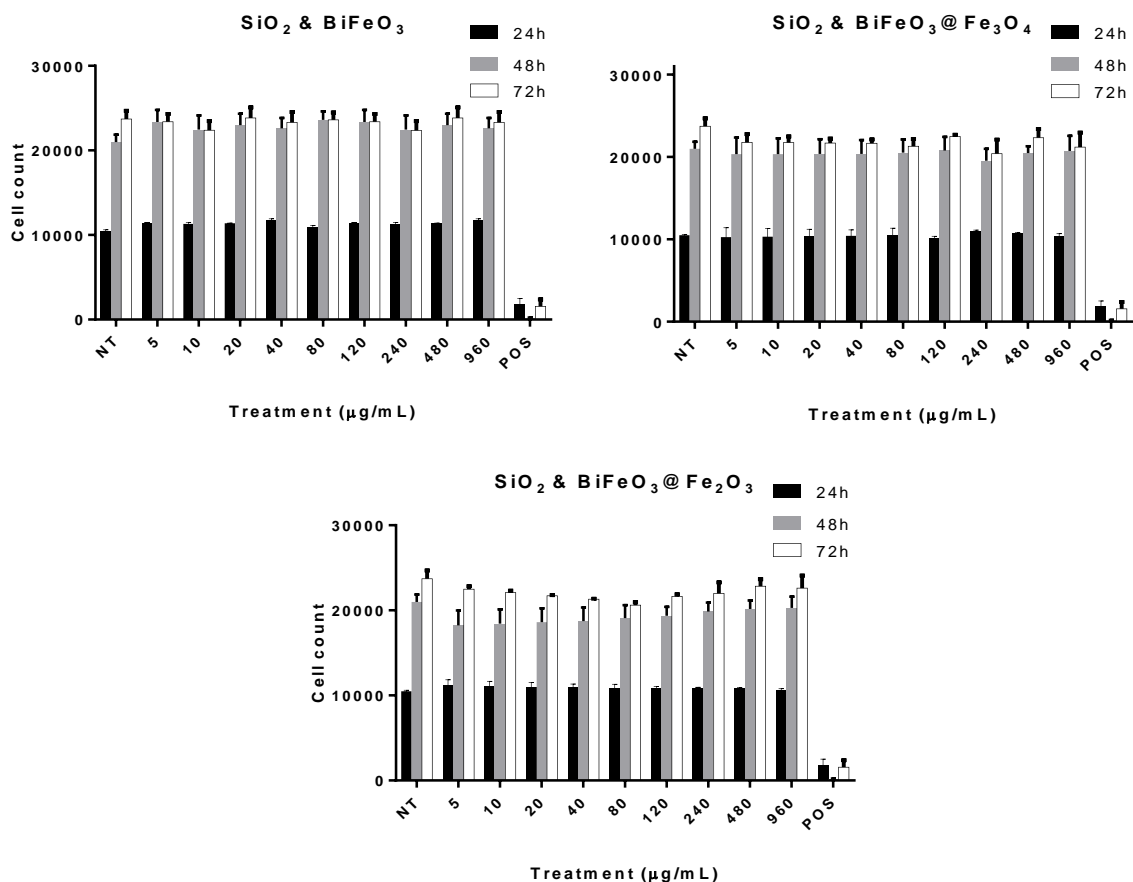


Figure 4.11: Overview of cell count of A549 cells after exposure to each of the nanowires. NT signifies the negative control (cells cultured without the addition of nanomaterials) and POS represents the positive control for cell death (valinomycin 120 µM). The error bars represent the standard error of the mean between three independent studies.

SiO₂ nanowire-based BiFeO₃ composites do not accelerate cell death in A549 cells at the concentrations analysed (see Figure 4.11). This suggests that embedding the NPs in silica nanowires passivates the surface of the NPs and also that A549 cells are not sensitive to high aspect ratio morphologies. This represents a significant development in the preparation of diagnostic probes – high aspect ratio nanocomposites extend the range of potential applications of the individual materials. The lack of toxic response implies that the composites have increased biocompatibility and could be used for longer circulation times.

A549 Cell viability

The response in A549 cell viability to different nanoparticles is presented below (see Figure 4.12). See Appendix sections A.2.1.2, A.2.2.2, A.2.3.2, A.2.4.2, A.2.5.2 and A.2.6.2 for further details.

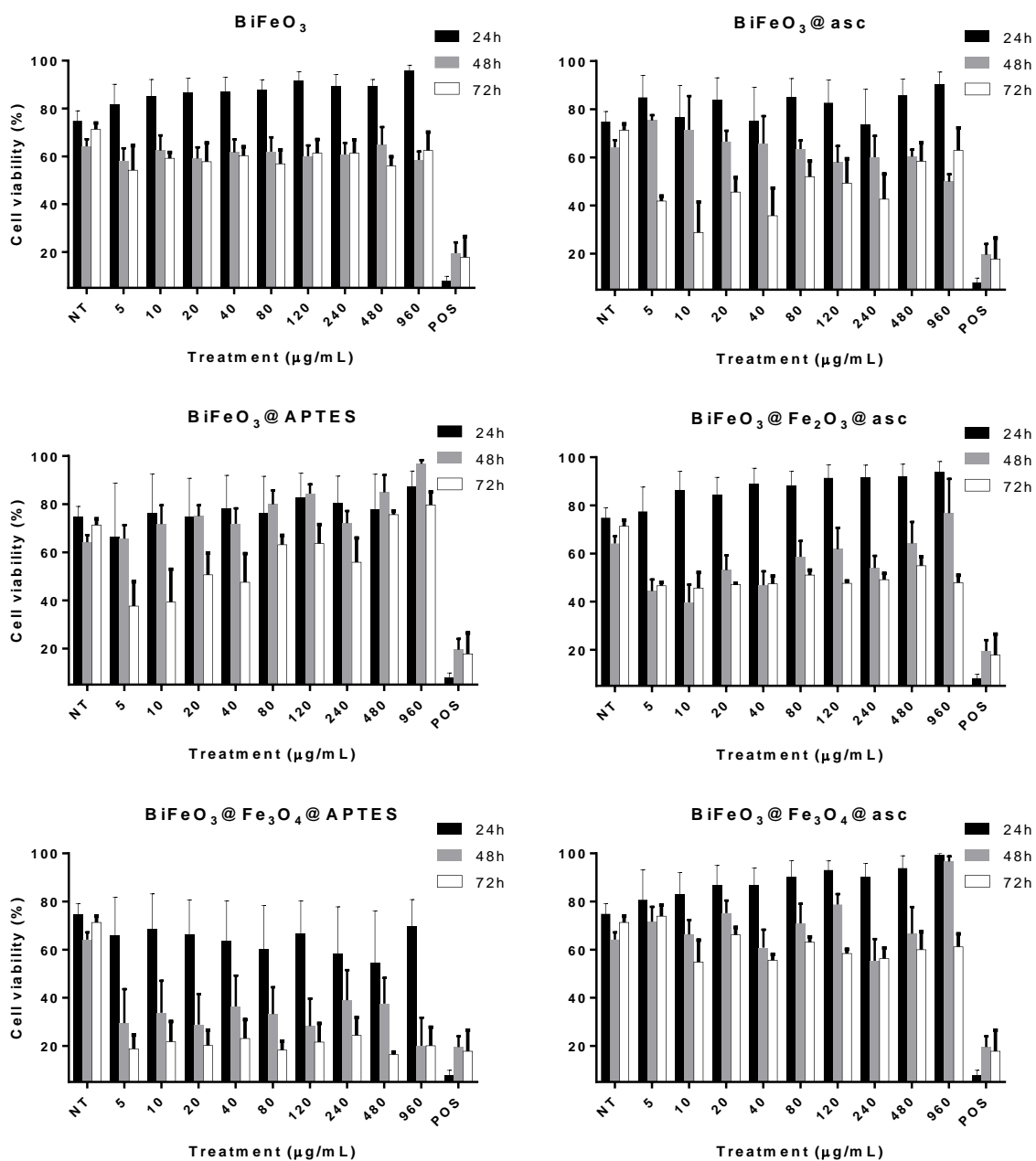


Figure 4.12: Overview of cell viability in A549 cells exposed to each of the nanoparticles. NT signifies the negative control (cells cultured without the addition of nanomaterials) and POS represents the positive control for cell death (valinomycin 120 µM). The error bars represent the standard error of the mean between three independent studies.

Comparing the influence of the different nanoparticles on A549 cells, there is appreciable heterogeneity in the viabilities (i.e. between triplicate samples or between repeated experiments) as demonstrated by the size of the standard errors of the mean at each time-point (see Figure 4.12). Where materials induced significant change in viability relative to the negative control, the response

did not seem to be determined by surface chemistry. For example, $\text{BiFeO}_3@asc$ and $\text{BiFeO}_3@APTES$ exhibited a low dose inhibition/high dose promotion of cell viability, whereas $\text{BiFeO}_3@Fe_3O_4@APTES$ exposure reduced the cell viability to near the level of the positive control.

The response of A549 cells to $\text{BiFeO}_3@Fe_3O_4@APTES$ NPs was unique in that the significant increase in cell count at lower concentrations and decrease at higher concentrations were accompanied by decreases in cell viability at all concentrations. This suggests that these $\text{BiFeO}_3@Fe_3O_4@APTES$ NPs are somewhat toxic and would therefore require modification for use in longer term *in vitro* studies.

The response in A549 cell viability to different nanowires is presented below (see Figure 4.13). See Appendix sections A.2.7.2, A.2.8.2 and A.2.9.2 for details.

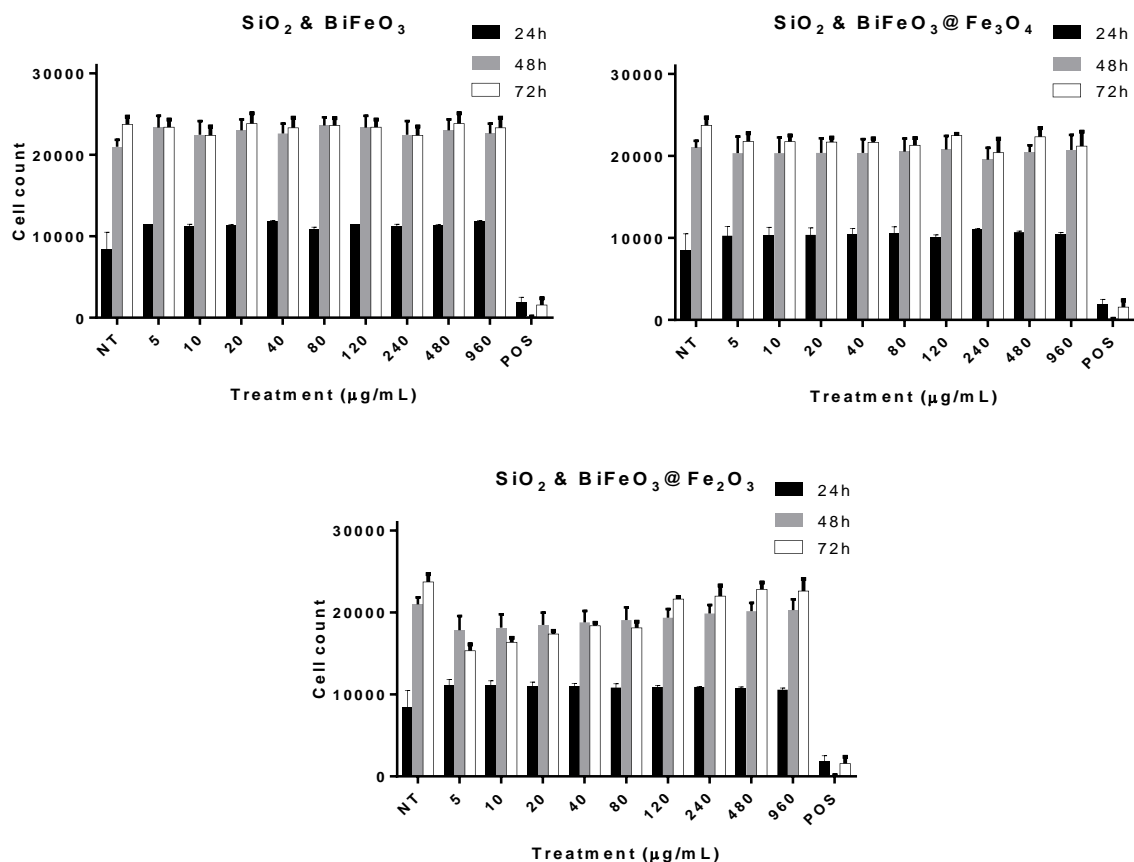


Figure 4.13: Overview of cell viability in A549 cells exposed to each of the nanowires. NT signifies the negative control (cells cultured without the addition of nanomaterials) and POS represents the positive control for cell death (valinomycin, 120 µM). The error bars represent the standard error of the mean between three independent studies.

SiO₂ nanowire-based BiFeO₃ composites do not reduce cell viability in A549 cells at the concentrations analysed with the exception of high concentrations of SiO₂ & BiFeO₃@Fe₃O₄ NWs after 72h exposure (see Figure 4.13).

The mitigation of the toxic effect supports the conclusions that embedding the NPs in silica nanowires passivates the surface of the NPs, that A549 cells are not sensitive to high aspect ratio morphologies and that the composites have increased biocompatibility.

A549 lysosomal mass/pH changes

The response of A549 cell viability to different nanoparticles is presented below (see Figure 4.14). See Appendix sections A.2.1.3, A.2.2.3, A.2.3.3, A.2.4.3, A.2.5.3 and A.2.6.3 for details.

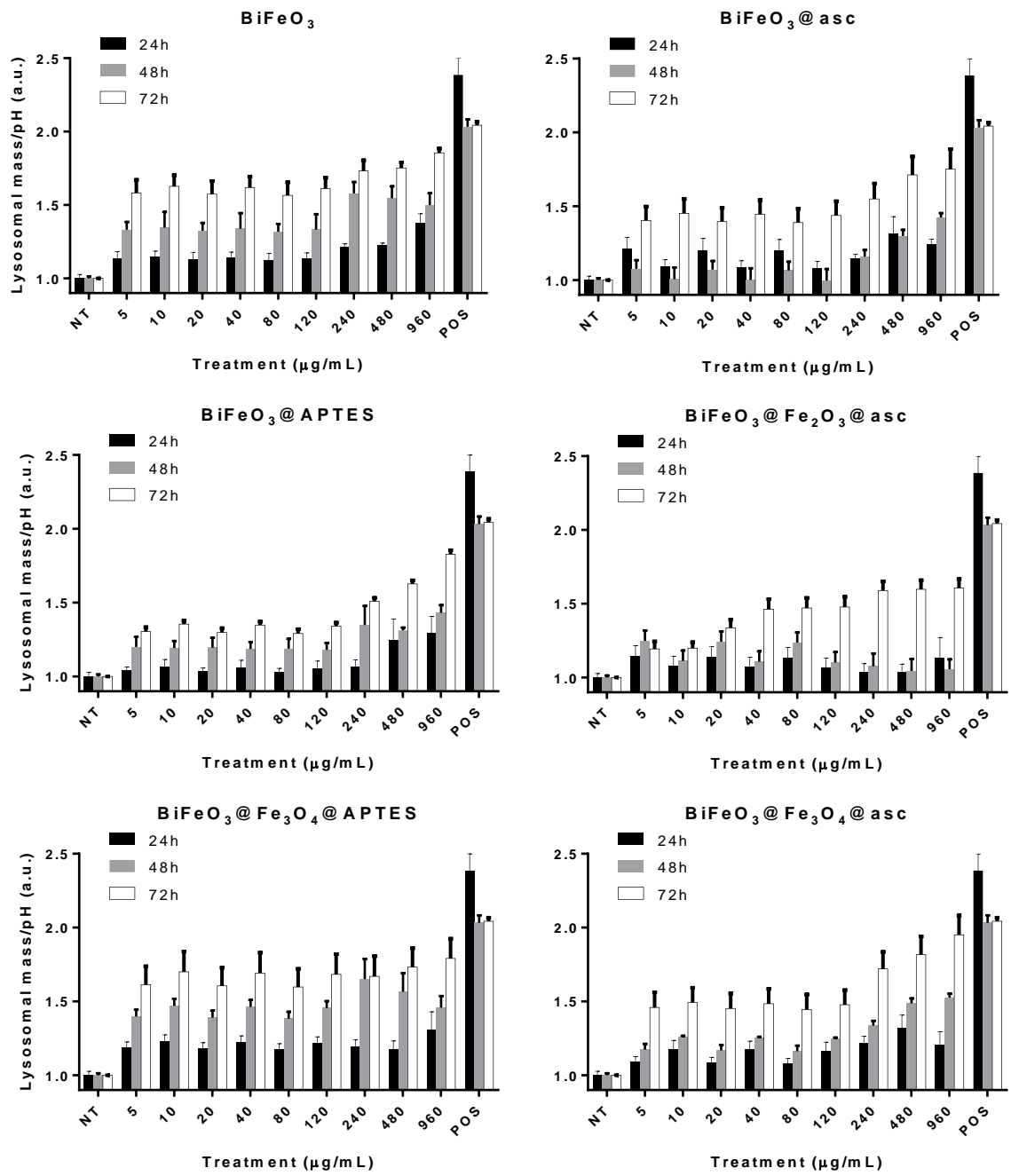


Figure 4.14: Overview of lysosomal mass/pH changes in A549 cells exposed to each of the nanoparticles. NT signifies the negative control (cells cultured without the addition of nanomaterials) and POS represents the positive control for lysosomal mass/pH changes (tacrine, 100 µM). The error bars represent the standard error of the mean between three independent studies.

Concentration-dependent increases in lysosomal mass/pH (LMPH) were observed for each of the BiFeO₃-derived NPs after 72h, some even after 48h or even 42h in the case of BiFeO₃ and BiFeO₃@APTES (see Figure 4.14). The NPs with the lowest increases of this indicator for the first two

days were those coated with ascorbic acid, indicating that the stabilisation of the NPs inhibited uptake. This is likely because, being more stable in suspension, fewer NPs settled onto the cells and could not therefore be internalised.

The response in A549 cell count to different nanowires is presented below (see Figure 4.15). See Appendix sections A.2.7.3, A.2.8.3 and A.2.9.3 for further details.

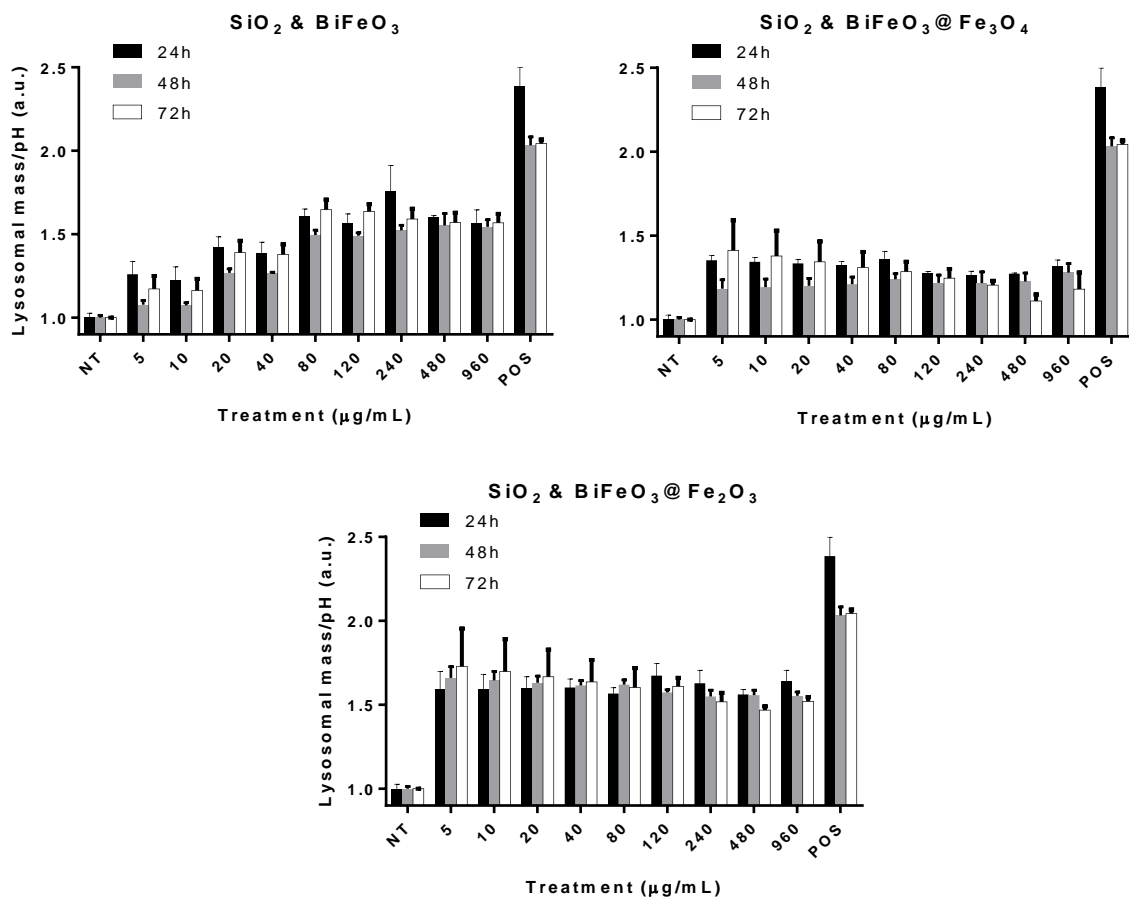


Figure 4.15: Overview of lysosomal mass/pH changes in A549 cells exposed to each of the nanowires. NT signifies the negative control (cells cultured without the addition of nanomaterials) and POS represents the positive control for lysosomal mass/pH changes (tacrine, 100 μ M). The error bars represent the standard error of the mean between three independent studies.

For each of the nanowires, common behaviours were observed (see Figure 4.15):

- The reduction of the dye at all concentrations was approximately 50% of the untreated control after 24h.
- After 48h the reduction of the dye in treated samples had fallen further to maximum of 10% of NT, and showed some concentration dependence, with the reduction falling off at larger concentrations

similar to a dose-response curve.

- After 72h the same dose-response pattern was observed.

Interestingly, the BiFeO₃ sample coated with an Fe₃O₄ shell (BiFeO₃@Fe₃O₄@asc) also showed the same response, whereas when the shell was capped with APS (BiFeO₃@Fe₃O₄@APTES), replaced with Fe₂O₃ (BiFeO₃@Fe₂O₃@asc) or when the NPs were embedded in silica, higher levels of reduction were observed after 24h that persisted after 48h and 72h.

4.3.2 Cytotoxicity analysis of nanomaterial interactions of HUVEC cells by High Content Screening

As with the discussion of A549 cells in the previous segment, the response of HUVEC cells to each of the nanomaterials is presented in the following sections (A3.1-A3.9) with respect to three parameters: cell count, cell membrane permeability (as a measure of cell viability), and lysosomal mass/pH changes. After presenting the materials individually, a summary of the data is then provided and the reaction of cells to the different nanomaterials is compared.

HUVEC cells exposed to valinomycin (120 µg/mL) was the positive control for cell count in this study and showed no surviving cells after 24h. By contrast, HUVEC cells which were left untreated (NT) continued to proliferate after 72h (see Figure 4.16 and Figure 4.17).

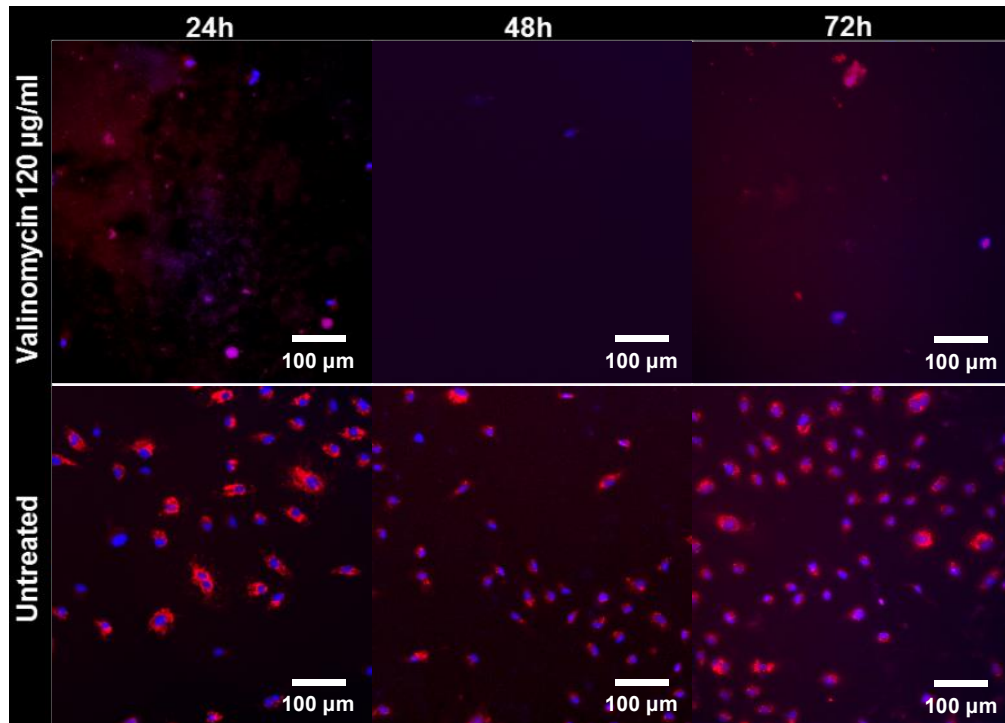


Figure 4.16: HUVEC cells. Top Row, cells treated with 120 µM valinomycin; bottom row, untreated cells. Left, 24h exposure; middle, 48h exposure, right, 72h exposure. Blue: Hoechst nuclear stain, red: lysosomal stain.

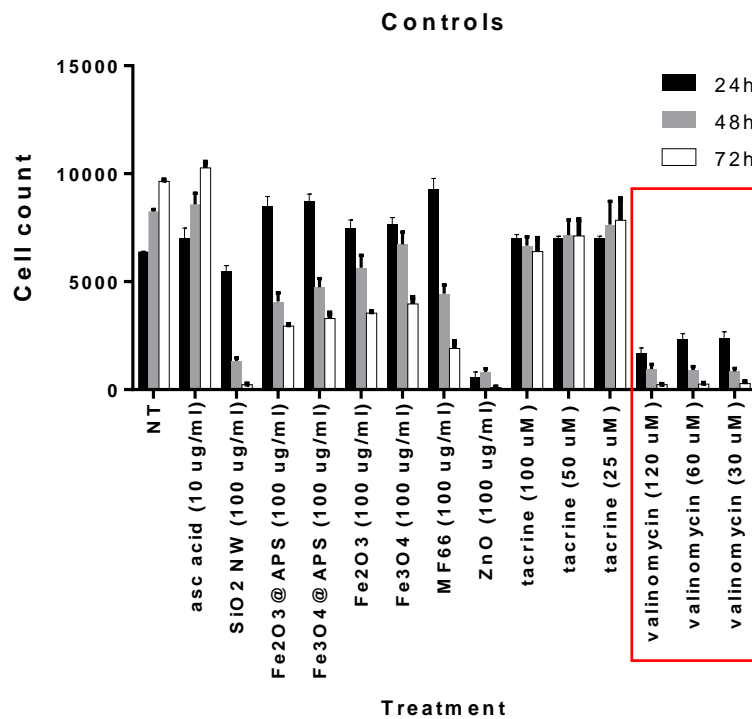


Figure 4.17: Overview of cell count of HUVEC cells exposed to assorted controls.

The controls used in this study included an untreated negative control (NT, cells cultured without the addition of nanomaterials), ascorbic acid to control for the influence of the stabilising ligand, SiO₂ NWs to control for the influence of SiO₂ with high aspect ratio, 30 nm Fe₂O₃ and 15 nm Fe₃O₄, bare and silanised, were used as controls for NP interactions and as controls for the components of the composites, MF66 as a stabilised form of Fe₃O₄ to compare to a commercially available standard, ZnO as a positive control for NP toxicity, tacrine as positive control for lysosomal mass or pH changes (see the green box in Figure 4.17) and valinomycin as positive control for cell death (see the box in Figure 4.17).

Unlike the response of A549 cells to the various controls, there were significant differences between the negative control and the controls for the components of the nanomaterials (ascorbic acid, SiO₂, Fe₃O₄ or Fe₂O₃).

While, ascorbic acid induced a very slight increase in cell count at each time point, SiO₂ nanowires induced a small decrease at 24h, followed by a steep decline to ~1000 cells at 48h. At 72h the SiO₂ nanowires had reduced the count to that of the positive control, valinomycin.

Hormesis was observed in bare and APTES-coated Fe₂O₃ and Fe₃O₄ NPs including the commercially available polyacrylic acid-stabilised magnetite, MF66. In general, the greater the initial increase relative to the untreated control, the lower the final count.

By contrast, the control for nanoparticle toxicity, ZnO, resulted in cell count of less than 500 cells at each time point and was therefore more toxic than the positive control.

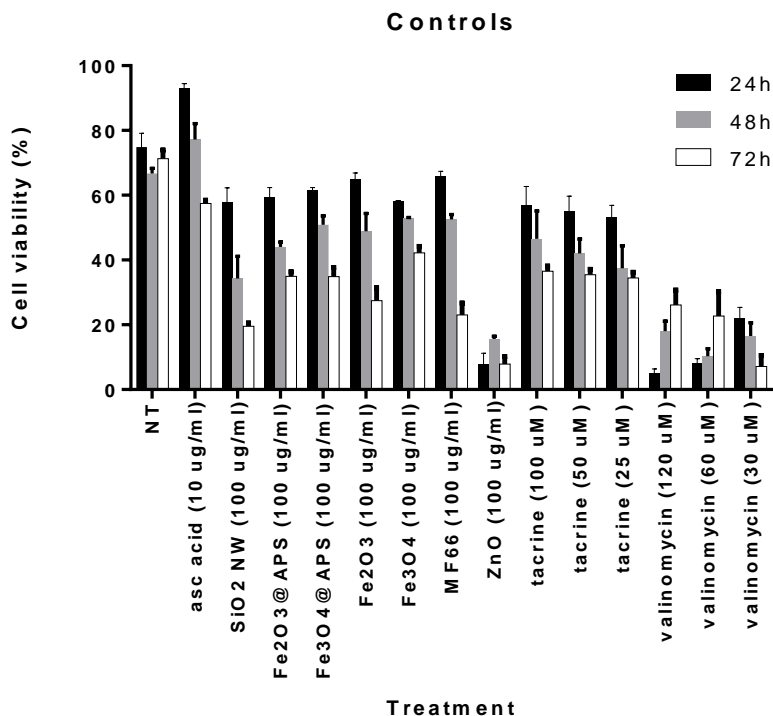


Figure 4.18: Overview of cell viability in HUVEC cells exposed to controls.

The same controls were used for cell viability as described above. It must be noted, however, that viability is calculated as a function of the total number of cells in the population remaining after a given time. Thus, although the cell count of the untreated control rose, the percentage of viable cells was approximately equal at 24h, 48h and 72h (see Figure 4.18). Furthermore, because cell viability is calculated from the intensity of the cell membrane stain, cell debris can result in some false positives. Where there is a high proportion of cell debris and few cells, even low numbers of false positives result in artefacts. The increases in cell viability which occur where the lowest cell counts were recorded are therefore considered artefacts.

120 mM valinomycin was the positive control for 24h exposure, 60 mM for 48h exposure and 30 mM for 72h.

Overall, the percentage viability ranged from about 90% in the ascorbic acid treated NPs to 5-20% in the positive controls. The positive control for nanoparticle cytotoxicity, ZnO, induced a similar reduction in viability to valinomycin.

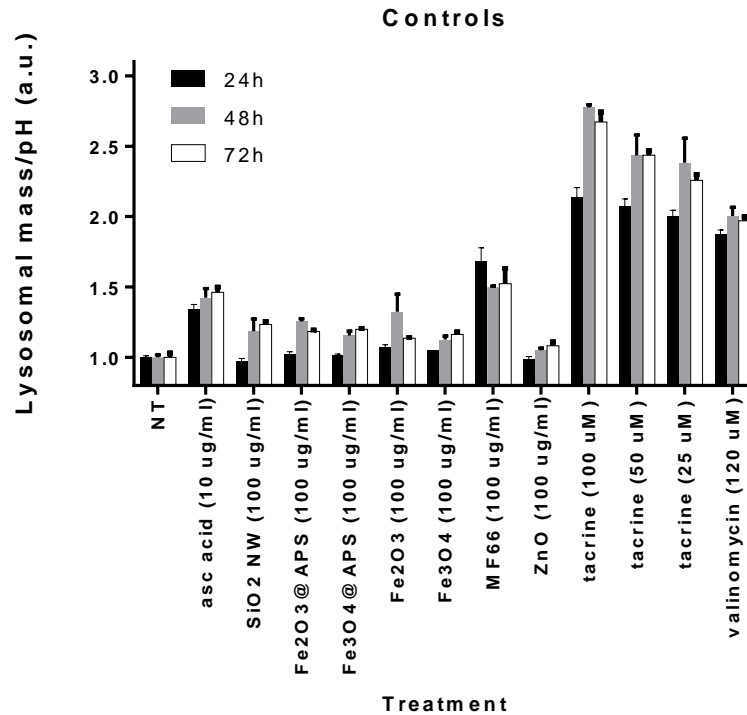


Figure 4.19: Overview of lysosomal mass/pH changes in HUVEC cells exposed to controls.

The same controls were used for lysosomal mass/pH as those described above except the positive control for changes in LMPH: 100 mM tacrine was the positive control for 24h exposure, 50 mM for 48h and 25 mM for 72h (see Figure 4.19). LMPH values are calculated from the intensity of the LMPH stain in each well, normalised to the number of cells in the well. Finally, the values are normalised to the intensity-per-cell of the negative control (NT) cells cultured without the addition of nanomaterials for each of the timepoints.

This means that LMPH, like cell viability, is calculated as a function of the total number of cells in the population remaining after a given time. Thus, cell debris can result in some false positives and the lower the cell count, where there is a high proportion of cell debris and few cells, the greater the artefacts. The increases in cell viability which occur where the lowest cell counts were recorded are therefore considered artefacts.

Many of the controls for NP interactions induced increases in the LMPH over time, with slight increases at each timepoint. This suggests that the NPs are being taken up by HUVECs and accumulating in lysosomes.

One notable exception was the MF66 sample, where the LMPH increased to ~1.5 times that of NT after 24h and remained at that level. This sample was a commercially available magnetite stabilised in excess

polyacrylic acid. Similar increases in LMPH were observed when cells were exposed to ascorbic acid, after a delay of 24h. The LMPH of the positive control was much higher, however (2-2.5 times that of NT).

HUVEC Cell count

The response in HUVEC cell count to different nanoparticles is presented below. See Appendix sections A.3.1.1, A.3.2.1, A.3.3.1, A.3.4.1, A.3.5.1 and A.3.6.1 for further details.

In general, nanoparticles induced cell death in HUVECs (see Figure 4.20).

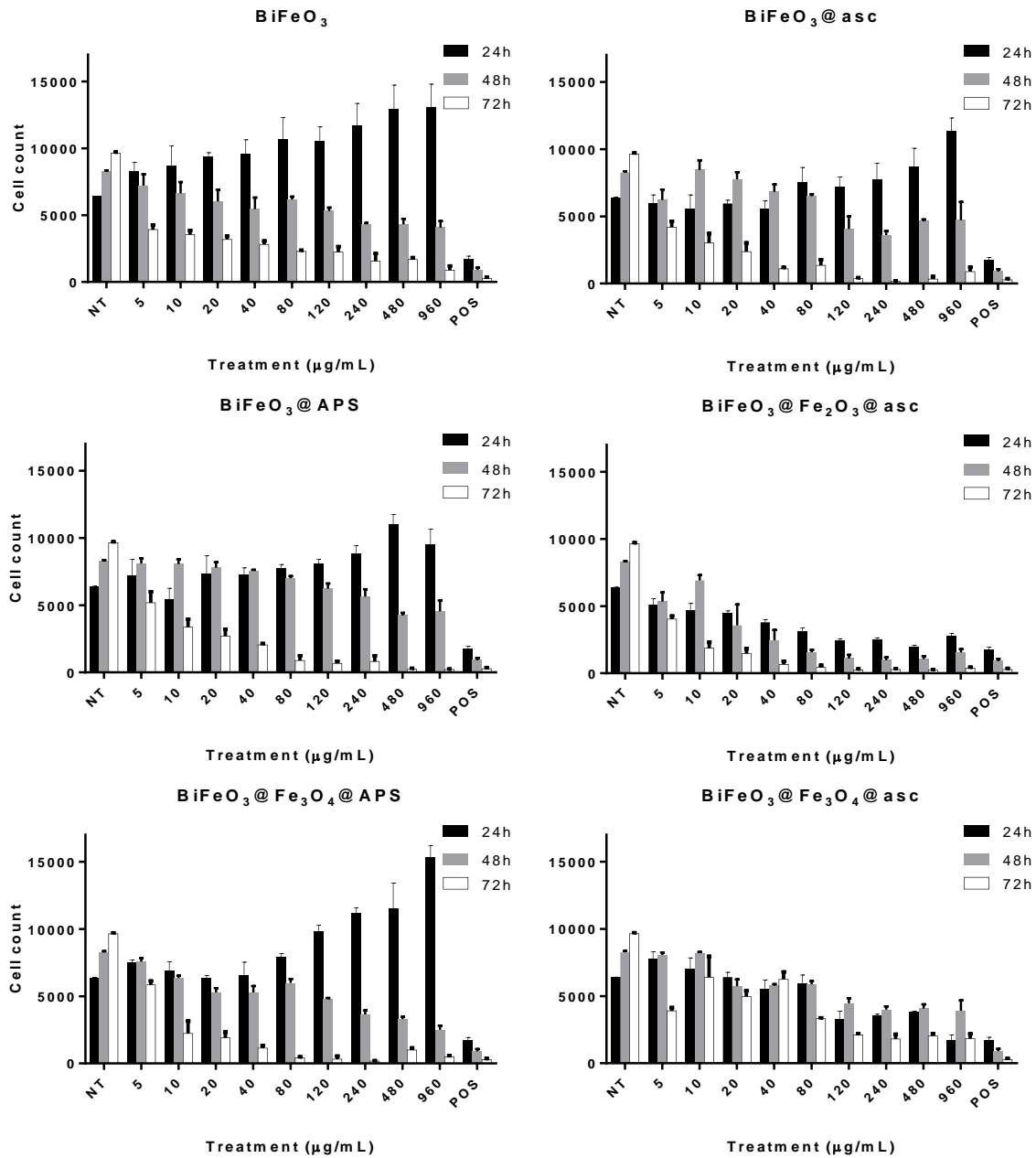


Figure 4.20: Overview of HUVEC cell count after exposure to each of the nanoparticles. NT signifies the negative control (cells cultured without the addition of nanomaterials) and POS represents the positive control for cell death (valinomycin 120 µM). The error bars represent the standard error of the mean between three independent studies.

Hormesis was observed when the cells were exposed to bare BiFeO₃, ascorbic acid-coated or APTES-coated BiFeO₃ and in APTES-coated BiFeO₃@Fe₃O₄, similar to the response of the cells to the controls for coated and uncoated iron oxides. In each case, higher doses led to increased cell count after 24h, followed by a decrease in cell number at higher concentrations after 48h, particularly when exposed to

80 µg/ml or more. Cell counts in these samples fell further after 72h, falling with increasing NP concentration. High Content Screening indicated aggregation was more prevalent in three of these samples, so it may be that when NPs are unstable in suspension and sedimentation occurs, they induce a stress response in the cells by depositing in much higher concentrations on the cell surface.

No hormesis was observed in BiFeO₃@Fe₂O₃@asc or BiFeO₃@Fe₃O₄@asc, and the cells exhibited a typical dose-response with cell counts dropping with rising mass of NPs per unit.

Taken together, this suggests that NP aggregation influences cell count by inducing a hormetic stress response. Whether the NPs underwent sedimentation or remained suspended, whether uncoated, coated with ascorbic acid or with APTES, the nanoparticles induced a concentration-dependent toxic response after 72h. Furthermore, both ascorbic acid-coated samples exhibited a reduction in cell count which increased with the dose at each time point. Finally, coating with APTES did not eliminate the toxic response of the NPs but merely delayed it.

The response in HUVEC cell count to different nanowires is presented below. See Appendix sections A.3.7.1, A.3.8.1 and A.3.9.1 for further details.

HUVECs exposed to silica nanowires exhibit similar behaviour at 24h exposure regardless of what NP was imbedded in the silica matrix: there was no significant difference from the untreated control up to approximately 40 µg/mL (see Figure 4.21). Each of the nanowires induced a reduction in cell count that was more pronounced with rising concentration, after 48 and 72h.

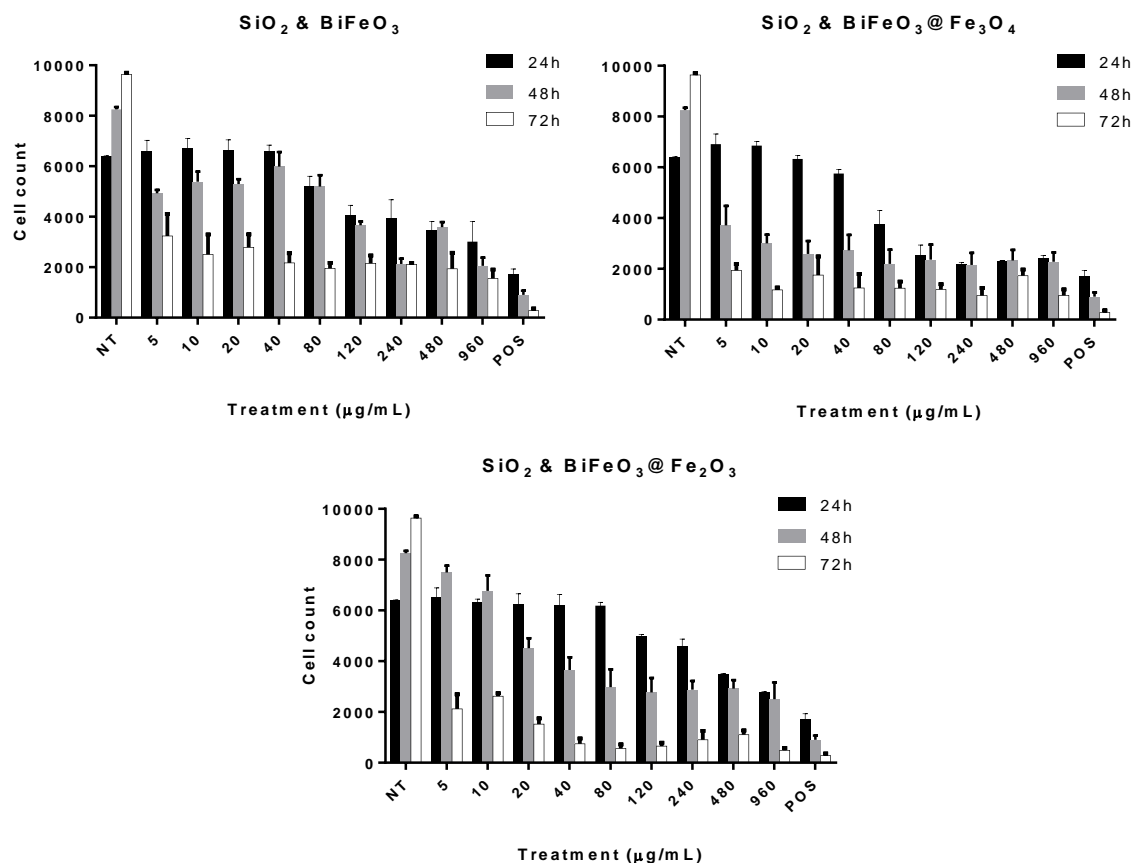


Figure 4.21: Overview of cell count of HUVEC cells after exposure to each of the nanowires. NT signifies the negative control (cells cultured without the addition of nanomaterials) and POS represents the positive control for cell death (valinomycin 120 µM). The error bars represent the standard error of the mean between three independent studies.

HUVEC cell viability

The response in HUVEC cell viability to different nanoparticles is presented below. See Appendix sections A.3.1.2, A.3.2.2, A.3.3.2, A.3.4.2, A.3.5.2 and A.3.6.2 for further details. In general, exposure to nanoparticles induced a concentration-dependent reduction in the viability of HUVECs which became more pronounced over time (see Figure 4.22).

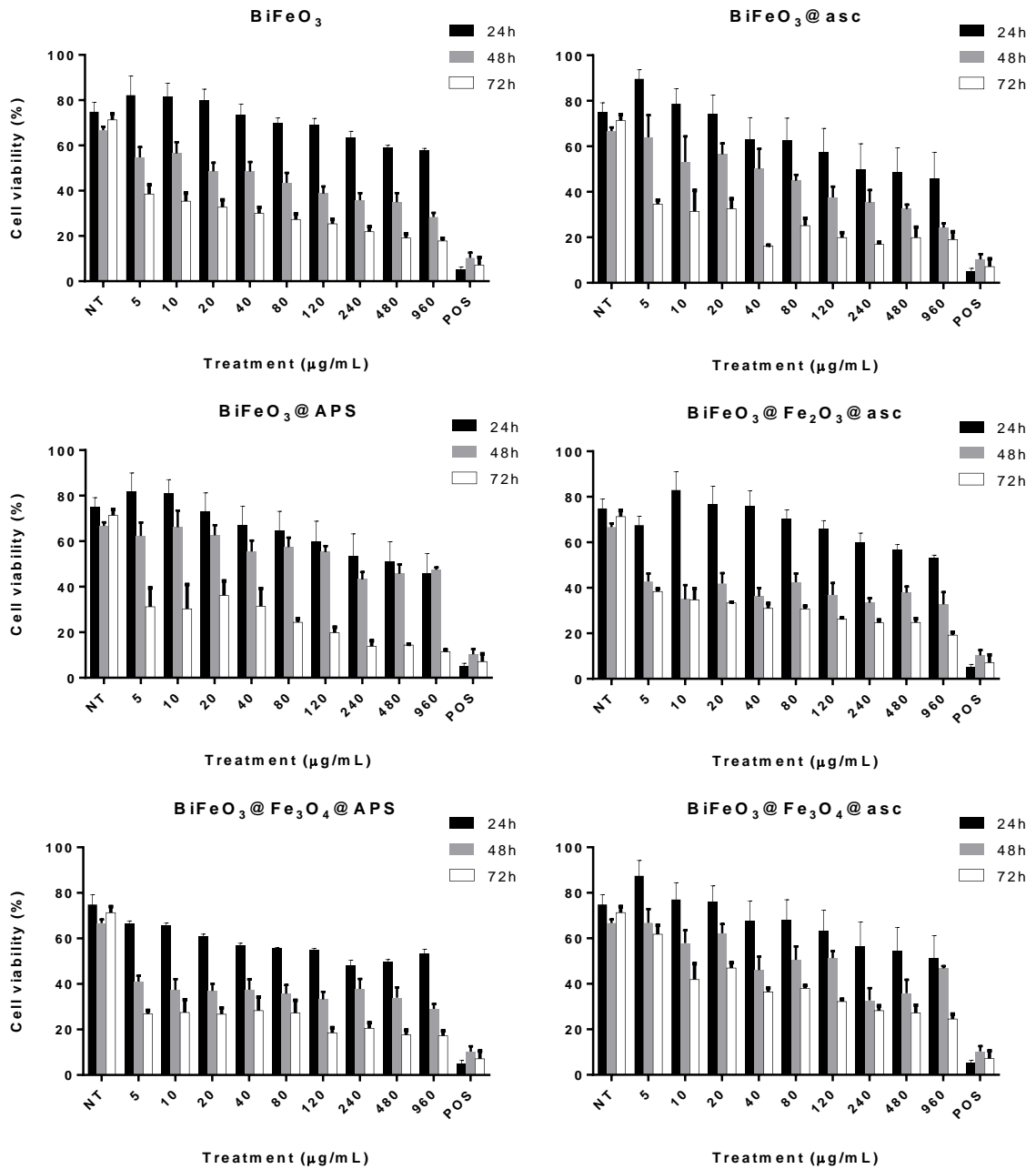


Figure 4.22: Overview of cell viability in HUVEC cells exposed to each of the nanoparticles. NT signifies the negative control (cells cultured without the addition of nanomaterials) and POS represents the positive control for cell death (valinomycin 120 µM). The error bars represent the standard error of the mean between three independent studies.

At doses below 120 µg/mL with 24h exposure, cell viability was above 50%, suggesting that the materials might be suitable for short-term *in vitro* applications.

We see that there is more variability in the viability data than in the cell counts. Several patterns are apparent, however. For example, after 72h, the viability of HUVECs exposed to each of the nanoparticles except BiFeO₃@Fe₃O₄@asc had fallen to approximately 30% at the lowest concentration, dropping to ~20% at the highest dose.

BiFeO₃@Fe₃O₄@asc stands out with viability of ~60% after 72h exposure at 5 µg/mL dropping to ~25% at 960 µg/mL. Treatment with this NP also resulted in the highest cell counts after 72h.

This supports the conclusion that the presence of NPs induces cell death in HUVECs and that modifying the surface with Fe₃O₄ and stabilising ligands may somewhat mitigate the response.

However, the reduction in cell viabilities and cell counts observed at higher concentrations over time suggest that there is an upper limit on the concentration or duration of *in vitro* applications of these NPs with HUVECs.

The response in HUVEC cell viability to different nanowires is presented below. See Appendix sections A.3.7.2, A.3.8.2 and A.3.9.2 for further details. The viability of HUVECs exposed to silica nanowires embedded with various NPs exhibit very similar trends – there was a dose-dependent drop in viability at each time point, falling from approximately 75% at 5µg/mL to 40% at 960 µg/mL after 24h exposure (see Figure 4.23).

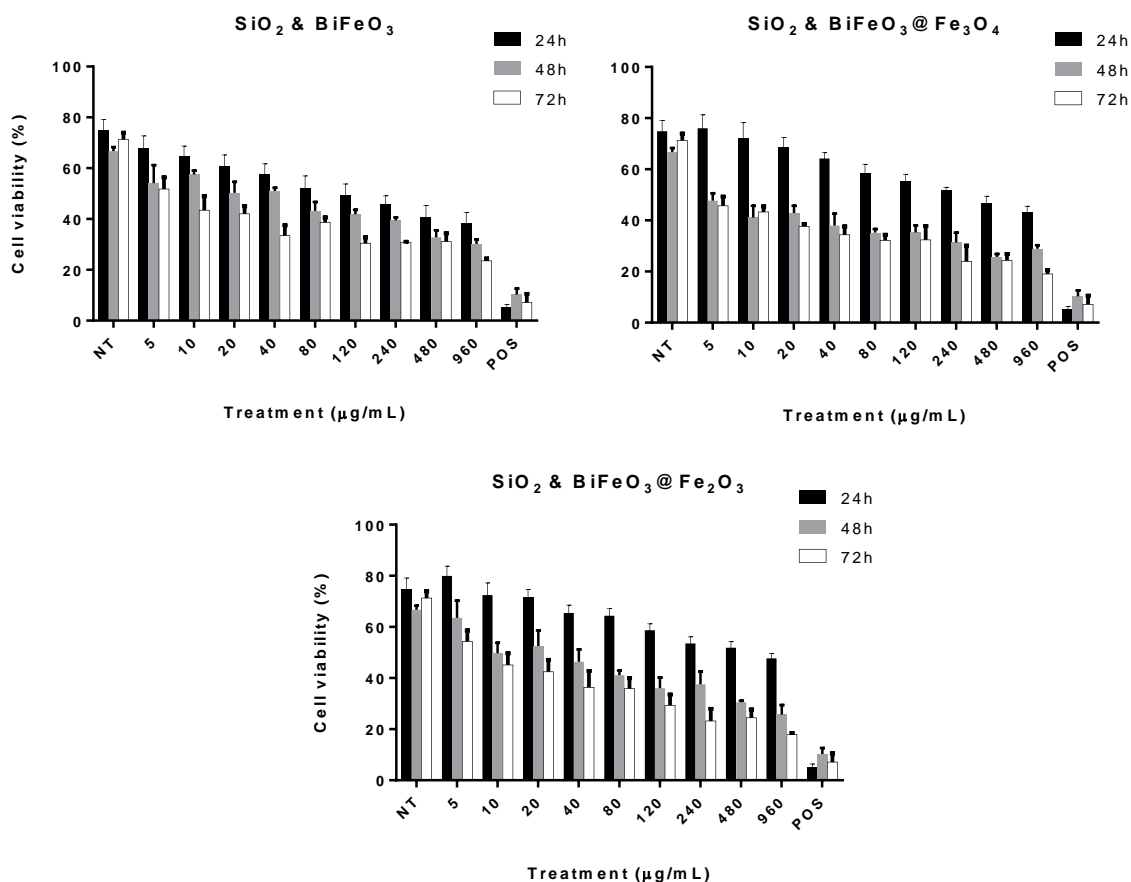


Figure 4.23: Overview of cell viability in HUVEC cells exposed to each of the nanowires. NT signifies the negative control (cells cultured without the addition of nanomaterials) and POS represents the positive control for cell death (valinomycin, 120 µM). The error bars represent the standard error of the mean between three independent studies.

Like the cell count data, the largest drop at 48h was observed in cells exposed to nanowires embedded with $\text{BiFeO}_3 @ \text{Fe}_3\text{O}_4$ NPs whereas cells treated with nanowires embedded with BiFeO_3 or $\text{BiFeO}_3 @ \text{Fe}_2\text{O}_3$ NPs had viabilities of approximately 50% up to doses of 40 µg/mL.

These values and trends are also similar to the response of HUVECs to the SiO_2 nanowires (used as control for nanomaterial morphology); this supports the conclusion that exposure to NWs reduces cell viability and induces a toxic response, but the morphology (aspect ratio) is not the most critical factor in determining the extent of cell death.

HUVEC lysosomal mass/pH changes

The response in HUVEC lysosomal mass/pH to different nanoparticles is presented below (see Figure 4.24). See Appendix sections A.3.1.3, A.3.2.3, A.3.3.3, A.3.4.3, A.3.5.3 and A.3.6.3 for further details.

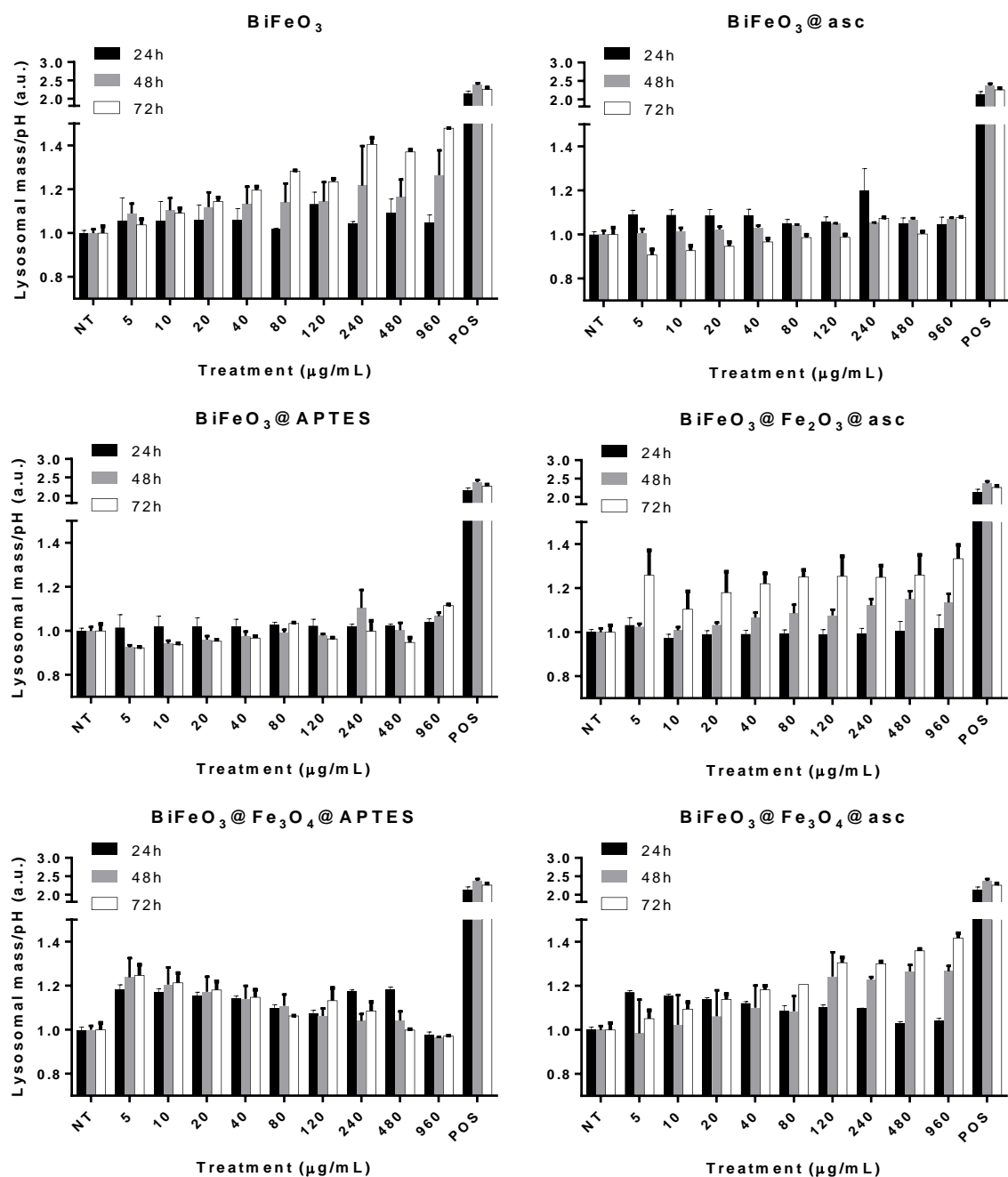


Figure 4.24: Overview of lysosomal mass/pH changes in HUVEC cells exposed to each of the nanoparticles. NT signifies the negative control (cells cultured without the addition of nanomaterials) and POS represents the positive control for lysosomal mass/pH changes (tacrine, 100 µM). The error bars represent the standard error of the mean between three independent studies.

BiFeO₃, BiFeO₃@Fe₂O₃@asc and BiFeO₃@Fe₃O₄@asc induced a dose-dependent increase in Lysosomal mass/pH (LMPH) which become more pronounced after 48h and 72h (see Figure 4.24). BiFeO₃ coated with either ascorbic acid or APTES induced no significant response at any concentration even after 72h.

Uniquely, exposure to $\text{BiFeO}_3@Fe_3O_4@APTES$ resulted in the highest increases at lower temperature and a dose -dependent decrease in LMPH at each time point.

Therefore, the changes in LMPH are not solely due to differences in surface chemistry. For example, coating with APTES, used to passivate the surface, reduces colloidal stability at pH 7, whereas coating with ascorbic acid increases the stability. Because LMPH increases where there is increased lysosomal mass or reduced pH, modification of surface chemistry affects the functional groups present on the surface and consequently alters the colloidal stability.

The response in HUVEC cell count to different nanowires is presented below (see Figure 4.25). See Appendix sections A.3.7.3, A.3.8.3 and A.3.9.3 for further details.

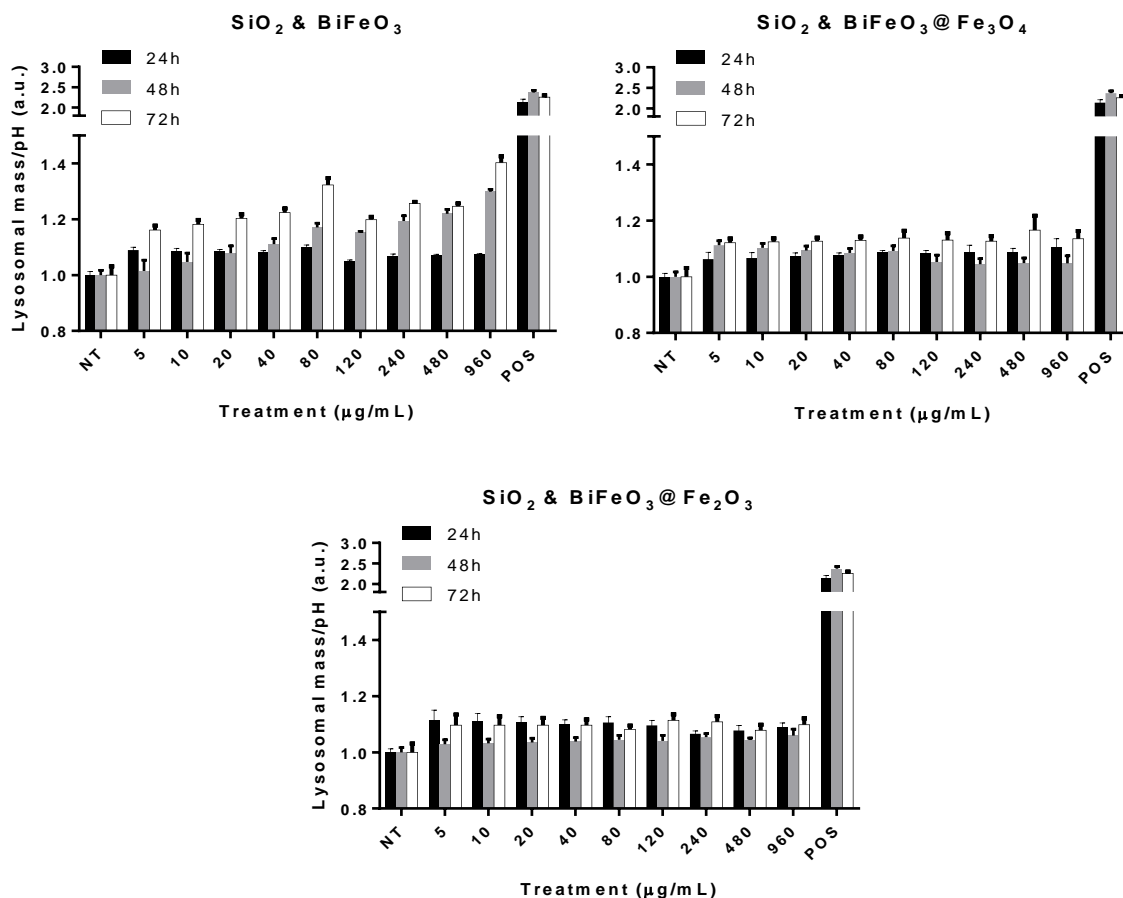


Figure 4.25: Overview of lysosomal mass/pH changes in HUVEC cells exposed to each of the nanowires. NT signifies the negative control (cells cultured without the addition of nanomaterials) and POS represents the positive control for lysosomal mass/pH changes (tacrine, 100 µM). The error bars represent the standard error of the mean between three independent studies.

While SiO₂ nanowires embedded with BiFeO₃ induced concentration-dependent increases in LMPH, nanowires embedded with BiFeO₃@Fe₂O₃ or BiFeO₃@Fe₃O₄ NPs resulted in no significant trend (see Figure 4.25). The response of the HUVECs to SiO₂ & BiFeO₃ nanowires most closely matched the interaction of the cells with bare SiO₂ nanowires.

Where there was no significant change in the LMPH, it suggests that NPs were not internalised, perhaps due to the morphology of the material. However, the concentration-dependent decreases in cell count and cell viability indicate a toxic response. This means that either the presence of the nanomaterials on the surface of the HUVECs induces stress and interferes with cell proliferation or there are multiple factors at play which confound the interpretation of the LMPH data.

4.4 Discussion

The results presented here indicate that the functionalised nanomaterials are suitable for use as diagnostic probes but also that certain exposure routes represent a significant risk when the aggregation of the nanomaterials is not mitigated.

4.4.1 Discussion of Nanomaterial Interaction with A549 cells

In order to achieve comparability between experiments and results, good experimental design is essential to ensure experiments are reproducible and that the results are repeatable. With this in mind, A549 cells were chosen to represent exposure to NPs through inhalation and HUVEC were selected to represent the exposure of an endothelial cell monolayer after a systemic administration route.

BiFeO₃-derived NPs exhibit low toxicity in A549 cells

NPs derived from BiFeO₃ did not adversely affect A549 cell counts over the concentration range examined and the response did not strongly depend on the surface chemistry of the nanoparticles. This suggests that despite differences in NP surface charge which would elicit different interactions with the cell surface, the concentration, composition or aggregation state of the NPs did not determine the cytotoxicity. Unlike HUVECs, A549 cells are a cancerous cell line and their viability is not dependent on the formation of a monolayer. Such minimal impact across a broad range of concentration has been reported for few nanomaterials.²²⁶

Although there was a concentration-dependent increase in the viability of cells exposed to BiFeO₃@asc and BiFeO₃@APTES, the cell counts exhibited hormesis. This may be evidence of the mechanism by which hormesis acts: increased cell number at lower doses coincided with lower viability, indicative of

a stress response. No interference was observed between the nanoparticles or aggregates and the stains used (refer to the epifluorescence imaging in section 3.2.3 and the section on uptake in Chapter 3). At higher concentrations, the rise in cell number was lower but viability was higher, which suggests that the higher doses may have activated adaptive stress response pathways.

Hormesis

With a toxicological endpoint such as cell proliferation, hormesis is characterised by stimulation in response to a low dose, followed by inhibition at higher concentrations.²²⁷ Hormesis has been attributed to adaptive stress response signalling pathways being activated by changes in hormones, ion availability or energy availability.²²⁸

In response, adaptive stress response pathways may be activated in cells involving kinases, deacetylases and transcription factors²²⁹ resulting in the production of proteins that protect cells against more severe stress.²³⁰

Examples of cyto-protective agents include antioxidants, growth factors, proteins involved in the regulation of energy metabolism and protein chaperones.^{231–233}

Hormesis has been observed previously in toxicological studies of other nanomaterials: in the length of murine neuroblastoma cells exposed to thioglycolic acid-capped cadmium telluride quantum dots,²²² in the cell viability of PBMCs in response to silver NPs,²³⁴ and in the cell viability of A549 cells exposed to carbon nanotubes.²³⁵ However, with quantum dots, toxic effects are often attributed to the heavy metals,¹⁰ while silver NPs toxic effects have been ascribed to the leaching of silver ions from the NP core²³⁶ and the aspect ratio of carbon nanotubes is thought to contribute to their toxicity.²³⁷

In each case, there are significant distinctions to the nanomaterials analysed in this study, so direct extrapolation is not justified.

The stress response was not solely determined by functional groups present on the surface of the NPs. Cells exhibited a stress response in response to each of the nanomaterials where aggregation was observed, whether at the surface of the cells or internalised. It has been suggested that accumulation of aggregates on the cell surface may interfere with cell signalling and surface charge is known to affect the interaction between nanoparticles and the cell surface, modulating the internalisation of nanoparticles. Where large aggregates are present, their size may inhibit internalisation.

4.4.2 SiO₂ and BiFeO₃-derived NWs are not toxic to A549 cells.

Despite significant differences in morphology, silica nanowires embedded with BiFeO₃-derived NPs did not adversely affect A549 cell counts over the concentration range examined. Again, the response did not depend on the chemical composition of the embedded materials as can be seen in Figure 4.11, Figure 4.13 and Figure 4.15. This supports the suggestion that aggregation state plays more of a role in determining the cytotoxicity of these materials than the chemical composition, since the proliferation of A549 cells does not require monolayer formation.

While one of the advantages of embedding the NPs in silica nanowires was in forming a composite with high aspect ratio, another expected benefit was in surface passivation. However, due to the low toxicity of the embedded materials, any reduction in cell - NP interaction was not obvious from the cell count or viability data. Importantly though, differences were observed in the lysosomal mass/pH changes of A549 cells in response to the various nanowires, suggesting that the nanowires were at least affecting the cells differently.

This may be because SiO₂ nanowires are mesoporous, with pores large enough to permit unbound embedded NPs to be released from the silica matrix.²³⁸ Indeed, there was similarity between the LMPH response of A549 cells to bare BiFeO₃ NPs and SiO₂ embedded with BiFeO₃.

4.4.3 BiFeO₃-derived NPs are highly toxic to HUVEC cells due to aggregation

In stark contrast with the response of A549 cells, BiFeO₃-derived NPs were extremely toxic to HUVECs, although aggregation state seemed to be the primary factor in inducing toxicity in the cells. Samples showing substantial aggregation exhibited significant hormesis, with initial concentration-dependent increases in cell count, accompanied by drops in viability, then followed by dose-dependent decreases in cell numbers.

Crucially, aggregation seemed to play a more important role than surface chemistry, with similar responses observed in cells exposed to bare BiFeO₃ NPs, those coated with ascorbic acid, APTES or with Fe₃O₄ and capped with APTES. Further support for this conclusion can be seen in the difference in the response of the cells to BiFeO₃@asc in comparison to BiFeO₃@Fe₂O₃@asc or BiFeO₃@Fe₃O₄@asc nanoparticles (see section 3.3.2 Nanoparticle colloidal stability, size distribution and concentration).

4.4.4 SiO₂ and BiFeO₃-derived NWs are toxic to HUVECs.

Although silica nanowires embedded with BiFeO₃-derived NPs did not initially induce cell death in HUVECs at low doses, higher concentrations were toxic. After 72h, cell viability and cell numbers had

fallen significantly, indicating that the silica served to partially mitigate the toxic effects of the nanoparticles. Coating the NPs with a silane layer (i.e. using APTES) did not reduce the toxic effects but embedding the NPs in nanowires somewhat postponed the cell death. This supports the conclusion that the size or morphology of the materials influenced the response of the cells.

As discussed previously, SiO₂ nanowires are mesoporous, with pores large enough to permit unbound embedded NPs to be released from the silica matrix. The data suggest that NPs are released from the pores of the wires over the course of 48h.

4.5 Conclusions

The work outlined in this chapter provided extensive evidence on the biological interactions of functionalised nanoparticles and composites with two relevant *in vitro* models. The cytotoxicity and safety assessment of targeted multifunctional nanocomposites is very important for industrial translation of new nanomaterials for biomedical applications and therefore it was a key milestone for this thesis.

A549 cells showed a hormetic stress response from the NPs and nanocomposites, but without significant reduction in cell number after 72h except for BiFeO₃@Fe₃O₄@APTES NPs. This represents comprehensive evidence that there is minimal intrinsic toxicity. By contrast, all the nanomaterials induced cell death in HUVECs, but both coating and embedding the composites postponed the toxic effects. Overall, this means that the materials investigated are suitable for use for *in vitro* imaging applications where aggregation is mitigated.

The next chapter describes several proofs of concept to illustrate how the materials can be applied to different imaging modalities.

Chapter 5

Multimodal applications of nanocomposites

5.1 Introduction

This chapter will provide proof of concept evidence and demonstrate the multifunctional applicability of the non-linear optical nanomaterials presented in this thesis, and results of the synthesis, functionalisation and characterisation, as presented in detail in the previous chapters.

As presented, the potential uses for the nanomaterials summarised in Table 2.1 (Ch. 2) and Table 3.1 (Ch. 3) to be used in biomedical applications are diverse and according to their specific physico-chemical properties - magnetic, optical and magneto/optical.

Currently these properties are exploited in several applications:

- 1) Magnetic cell sorting and separation based on the intrinsic magnetic properties, surface functionalised biomarkers and their hydrodynamic profile.
- 2) Magnetic Resonance Imaging capability as viable probes for advanced labelling or functional imaging.
- 3) Optical microscopy based on the non-linear optical properties of the probes (e.g. SHG).
- 4) Magneto/optical for combined magnetics separation and flow cytometry.

5.1.1 Cell separation or sorting

Magnetic Separation

Current methods of cell sorting involve attachment of antibodies to magnetic beads. In positive selection sorting, functionalised magnetic beads are incubated with a suspension of mixed cells, some of which express proteins to which the antibodies are targeted. The suspension is then placed in a magnetic field and the antibody-bound cells are drawn out of suspension and washed in the magnetic field to remove unbound cells.

Positive selection requires that the cell of interest expresses protein markers unique to that cell line. This means that the antibodies attached to the magnetic beads can only bind with the target cells, allowing them to be drawn from suspension leaving all other cells.

Negative selection is an alternative cell sorting technique in which antibodies are attached to magnetic microbeads to allow all cells except the target cells to be drawn from the suspension. This requires that a cocktail of antibodies on the magnetic beads bind to proteins expressed on the surface of all other cells in suspension, allowing them to be drawn toward the magnet, leaving the cell of interest in suspension.

Care must be taken in the choice of antibody to ensure that, in the case of positive selection, the antibody specifically targets the cell of interest, i.e. that it selectively binds to proteins only expressed on those cells.

Magneto-optical: sorting by flow cytometry

This application avails of the probes' multimodalities to achieve a strong separation yield (e.g. positive/negative), followed by flow cytometry. In flow cytometry, the emission and scattering of cells and their markers can be used to separate and sort a heterogeneous mixture. A stream of dilute mixed cells is directed past a laser such that the cells pass one at a time. A cell's emission profile is then measured by a detector, correlated to cell size and fluorescent signal from any staining applied, and sorted into a fraction with cells of similar properties. This method is extremely fast and can yield greater than 99% purity.

Unlike magnetic sorting, which requires that cells be bound to magnetically tagged markers for the cells to be sorted from the mixture, both in the manner in which light scatters from moieties in the fluid stream and their fluorescent properties can convey information about the cell and hence be used to automatically sort cells.

Larger cells such as monocytes scatter light differently to smaller cells such as lymphocytes, meaning that a heterogeneous population of cells can be sorted by analysis of their scattering properties.

Light scatter can be measured along the path of the laser (forward scatter, FSC) or perpendicular to the path (side scatter, SSC). Typically, the intensity of FSC is determined by the size of the cell, whereas the intensity of SSC is a measure of the degree of granularity within the cell.

Cells can be sorted according to their fluorescent properties by tagging surface or intracellular proteins or structures with fluorophores. Tagged cells can then be diverted from the fluid stream by charging individual droplets in which the cell of interest is suspended and using electrostatic separation to collect homogeneous fractions.

5.1.2 Magnetic resonance imaging (MRI)

MRI is a non-invasive technique used primarily to image soft-tissue and is based on nuclear magnetic resonance (NMR) of hydrogen nuclei. NMR determines the molecular structure of organic compounds containing nuclei with odd atomic or mass numbers (e.g. ^1H , ^{13}C , ^{15}N , ^{19}F , ^{31}P) by measuring the response of the materials to changes in an applied magnetic field.

Charges moving in a circular path induce a magnetic moment. Similarly, the total angular momentum or “spin” of a nucleus results in a magnetic moment. The protons in NMR-active nuclei align with an applied field and precess around the axis of the field at a resonance frequency proportional to the strength of the field (the Larmor frequency).

If an alternating radiofrequency (RF) electromagnetic pulse is then applied at the Larmor frequency, the energy is absorbed by the protons (and they are promoted to higher energy states). Turning off the RF pulse allows the excited protons to return to their resting alignment through relaxation. Excited spins return to their original orientation with the applied field (known as the longitudinal relaxation rate, T_1) and the protons which had been precessing in phase with the applied RF pulse begin to go out of phase (transverse relaxation rate, T_2 and T_2^* , where T_2 is the rate of transverse magnetization decay due to spin-spin relaxation, and T_2^* is a combined measure of transverse magnetization decay and magnetic field inhomogeneity).²³⁹ Relaxation results in the emission of RF radiation which is detected by coils in the MRI scanner. A Fourier Transform is applied to the frequency data to obtain intensity information for each voxel, resulting in a 3D model of the subject.

MRI probes the hydrogen nuclei present in water and fats, the two main constituents of the body. Because the environment of the protons influences the rates of relaxation, different intensities correspond to different tissue types. Certain tissues such as bone produce very low contrast in MRI due to their low hydrogen content (see Table 5.1).

Table 5.1: Appearance of various tissues in MRI (adapted from Jackson et al.²⁴⁰)

TISSUE	T1-WEIGHTED	T2-WEIGHTED
FAT	Bright	Light
MUSCLE	Grey	Dark Grey
BONE	Grey	Bright
AIR	Very Dark	Very Dark
CSF	Dark	Bright
WHITE MATTER	Light	Dark Grey
CORTEX	Grey	Light Grey
SPINAL CORD	Grey	Light Grey
INFLAMMATION (Oedema, infarction, infection, demyelination)	Dark	Bright

Distinguishing between normal tissue and a tumour, for example, can be aided by the use of a contrast agent. As discussed in Chapter 1, superparamagnetic nanoparticles have advantages as contrast agents over other magnetic materials, as they avoid aggregation of magnetic contrast agents, as their magnetic moment only arises in response to an applied field.

5.1.3 Nonlinear optical applications in Bioimaging

Harmonic nanoparticles (HNPs) have been the subject of much interest because nonlinear optical effects occur more readily in nanoparticles since they are so much smaller than the wavelength of light. The development of a next generation biomedical imaging platform, Second Harmonic Microscopy (SHM), has sought to exploit this phenomenon and its advantages over conventional imaging technologies.^{7,8}

For example, quantum dots (QDs) such as Qdot[®] Probes, blink randomly making quantitative analysis prohibitively difficult. Spectral overlap and photostability are less of an issue with QDs; they have a very narrow emission band and their emission can be tuned by synthesising QDs of different sizes.⁹ However, QDs contain toxic metals such as cadmium and concerns remain over whether surface corrosion in physiological conditions might cause the heavy metals to leach.^{10,11} Fluorescent dyes such as Hoechst, a commercially available DNA stain, require specific excitation wavelengths and also bleach over time. Indeed, different fluorescent stains must be used in order to excite at different wavelengths and to avoid channel cross-talk.

As discussed in Chapter 1, unlike with upconversion nanoparticles (UCNPs), SHG occurs across the transparency range of the nanoparticles. However, when the pump wavelength induces resonance in UCNPs, the output intensity can far exceed that of SHG.⁴⁶ It may be that the large nonlinear coefficient of bismuth ferrite nanoparticles reported here (220 pm/V, see Chapter 2) might result in harmonic efficiencies that compete with the resonance-enhanced conversion efficiency of lanthanide-doped nanocrystals. However, direct comparison requires further studies involving for instance the successful doping of BFO with NIR luminescent ions.

More importantly, static investigations of single cells, tissue sections and organs (using the well-established selective staining techniques) are so far inappropriate to give insight of the dynamic processes that govern interactions between cell assemblies and living tissues. Because of their long-term photostability (there is no exponential bleaching as with fluorescent imaging probes such as FITC®), HNPs have all the necessary features to better elucidate these living processes that govern metabolism and disease mechanisms, including those of cancer.

For these reasons, SHG is an active area of research for next generation imaging probes such as in two-photon and second harmonic imaging microscopy.¹³⁻¹⁵

Second harmonic microscopes work in the same way as conventional microscopes except they have an extra filter in the optical path to exclude the fundamental mode of the excitation laser. They therefore produce an image of two-photon excited fluorescence and second and third harmonics generated in the sample. Some tissues produce endogenous harmonics: fat and collagen produce second harmonics whereas intra and extracellular membranes and the extracellular matrix generate third harmonics, allowing selective imaging of these structures.

A major advantage of second (and higher order) harmonic imaging is wavelength tunability: the same sample can be probed with any excitation beam across the transparency range of the harmonic material, allowing the excitation to be selected such that absorption of the input beam and the generated harmonic can be minimised.

As described in Chapter 1, SHG is a non-resonant phenomenon so acts on any input frequency in the transparency range of the material, and the response is stable over the course of a number of days.

Research has been carried to eliminate all possible interference in one step by recording second and third harmonics at the same time, convoluting the signals to eliminate stray fluorescence. This is of particular significance in deep tissue imaging where some tissues exhibit intrinsic second harmonic generation. HNPs are therefore of growing interest for use in deep tissue imaging.¹³

5.2 Materials and Methods

5.2.1 Reagents

BiFeO₃, BiFeO₃@Fe₂O₃, BiFeO₃@Fe₃O₄, Fe₂O₃ and Fe₃O₄ NPs were prepared as described in Chapter 2. NPs were modified with APTES as described in Chapter 3 to form a silane layer and act as a linker. Functionalisation was carried out as described in Chapter 3 to target EGFR, which is expressed on the surface of Human lung epithelial carcinoma cells (A549 cells).

5.2.2 Cell culturing and incubation

A549 cells were cultured and incubated as described in Chapters 3 and 4. Briefly, A549 cells were cultured in Dulbecco's Modified Eagle Medium (DMEM) with 2 mM L-glutamine, supplemented with 10% fetal bovine serum and 50 µg/mL gentamicin in a 37°C incubator at 100% humidity and 5% CO₂.

To assess the second harmonic response of BiFeO₃@Fe₂O₃ nanocomposites, ascorbic acid-stabilised nanoparticles were dispersed from sterile stock solution at a concentration of 10 mg/ml, then diluted with serum-free medium to 500 µg Fe/ml with ultra-sonication for 30 min. Suspensions of ascorbic-acid stabilised BiFeO₃ NPs (BiFeO₃), bare BiFeO₃@Fe₂O₃ NPs (non-asc NP) and fluorescently labelled, functionalised nanoparticles (fNP) were prepared in the same way, i.e. at 500 µg Fe/ml, as controls for the different stages of synthesis.

Incubation in 8-well chamber slides for second harmonic imaging

Cells were dispensed on 8-well chamber slides at 5×10^6 cells per mL in 1 mL of complete medium, allowed to attach and incubate for 24h before being rinsed with warmed serum-free DMEM. The complete medium was then replaced (1mL).

Incubation of cells with nanomaterials

A549 cells were then treated with 500 µL of either serum-free medium (untreated control, NT); BiFeO₃@Fe₂O₃@asc NPs; BiFeO₃; bare BiFeO₃@Fe₂O₃ NPs (non-asc NP); or fluorescently labelled, functionalised nanoparticles (fNP). This resulted in final concentrations of 100 µg Fe/mL for all the controls except NT.

Each of the samples was prepared in triplicate and the experiment was carried out three times.

Cell Staining

Live cells were stained with Hoechst for DNA and Phalloidin Red for cytoskeletal actin filaments as described in Chapter 3.

5.2.3 Equipment

Magnetic resonance imaging and measurements (T2 and T2*) were kindly carried out by Dr Andrew Fagan, School of Medicine, TCD.

Second harmonic microscopy was carried out at the University of Geneva by Gabriel Campargue, GAP Biophotonics group.

5.2.4 Protocols for Multimodal Observation

Magnetic separation

Stabilised BiFeO₃@Fe₃O₄ NPs were dispersed in water, fetal bovine serum (FBS) and plasma at a concentration of 1 mg/mL using sonication. The suspensions were then placed in a magnetic field and images taken at intervals of 5 seconds to examine whether the NPs could be separated from the suspension as a proof-of-principle illustrating their potential use in cell sorting.

MRI

NPs were dispersed in 1.5 mL ultrapure water at concentrations from 1-5 µg/mL in micro-centrifuge tubes. The following controls were prepared in the same way: 15 nm Fe₂O₃ NPs 1-5 µg/mL (positive control for magnetic response), 100 nm polystyrene NPs at 5 µg/mL (negative control: no magnetic response), and 30 nm BiFeO₃ NPs at 5 µg/mL (positive control: core NP, antiferromagnetic response).

Second Harmonic Microscopy

To demonstrate the wavelength tunability of the NPs' harmonic response, A549 cells were seeded into 8-well chamber slides, allowed to attach over 24 hours and were then exposed to the optimised composite nanomaterials, BiFeO₃@Fe₂O₃ NPs. Samples were excited at 820nm, at 3.1 mW. Tunability measurements were carried out by varying the output wavelength of a tunable laser such that the output power was constant (20±1 mW).

5.3 Results

This section presents the proof-of-concept use of the multifunctional nanomaterials in diagnostic applications, namely cell sorting and separation, magnetic resonance imaging and second harmonic imaging.

To demonstrate application in cell separation, $\text{BiFeO}_3@Fe_3O_4$ NPs were magnetically separated from different media including water, fetal bovine serum and plasma. As proof of concept of their multimodality, their use as magnetic contrast agents and in nonlinear optical applications was demonstrated by imaging $\text{BiFeO}_3@Fe_2O_3$ NPs with both Magnetic Resonance Imaging and Nonlinear Optical Imaging, in this case, Second Harmonic Microscopy.

5.3.1 Magnetic separation of $\text{BiFeO}_3@Fe_3O_4$ NPs from different media

Stabilised $\text{BiFeO}_3@Fe_3O_4$ NPs were dispersed in water, fetal bovine serum (FBS) and plasma at a concentration of 1 mg/mL using sonication. The suspensions were then placed in a magnetic field and images taken at intervals of 5 seconds to examine whether the NPs could be separated from the suspension as a proof-of-principle illustrating their potential use in cell sorting (see Figure 5.1).

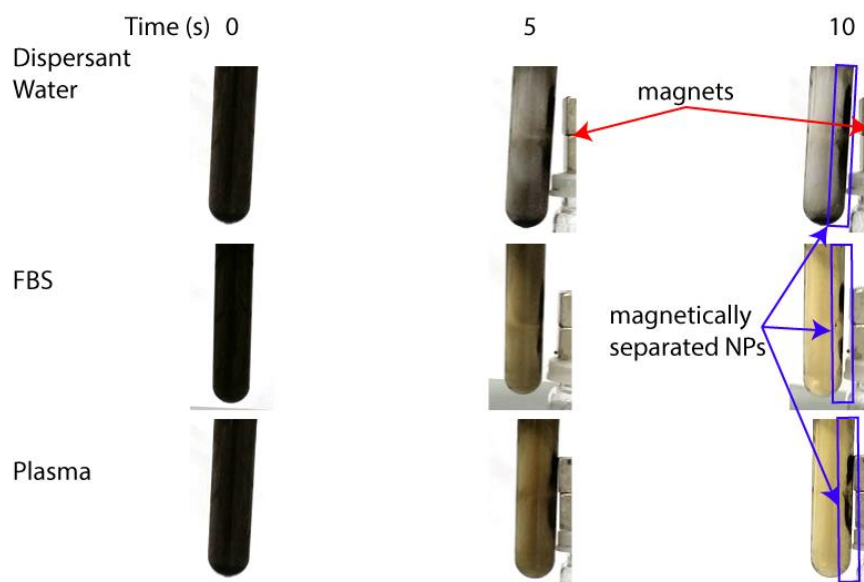


Figure 5.1: Proof-of-principle of magnetic separation of $\text{BiFeO}_3@Fe_3O_4$ nanocomposites from suspension in water, FBS and plasma. Red arrows indicate the position of the magnets next to the sample tubes, blue arrows and boxes show the separated NPs.

With all three dispersants, the NPs were pulled from suspension. In each case, the NPs had been separated by the magnet from the solution within 10 seconds, and that the separation progressed more quickly in the FBS and plasma than in water (see Figure 5.1).

This illustrates the principle that the multifunctional NPs can be separated magnetically and have potential use in bio-applications exploiting the magnetic properties of nanomaterials. Given the existence of commercial products which are capable of cost-effective, high throughput magnetic separation and cell sorting, e.g. as Dynabeads[®] or MACS[®] microbeads, the advantage of these composites stands in their combined imaging modality which is explained in the next section with respect to the applications. In fact, the speed of separation demonstrated here compares favourably to these commercially available solutions, which can take two minutes to separate cells from suspension (human blood or buffy coat).²⁴¹











5.3.2 Magnetic Resonance Imaging (MRI) of BiFeO₃@Fe₂O₃ composites

In order to demonstrate that the developed composites can be used as magnetic probes for MRI, images were obtained in a clinical setup and compared to controls.

Images were recorded at varying echo times to determine the T2 and T2* decay rates. To visually demonstrate the varying rates of transverse relaxation, the following tables contain a subset of the corresponding MR images. Each table represents a snapshot before the signal from any of the samples had dropped to zero, to illustrate the decay rates at different concentrations.











Qualitatively, there was a concentration-dependent decrease in the intensity of T2 weighted signal of BiFeO₃@Fe₂O₃ NPs (see Table 5.2). At lower concentrations, the intensity of the BiFeO₃@Fe₂O₃ NPs was lower than that of the control, Fe₂O₃, most notably at 1.5 µg Fe/mL (see third row of Table 5.2, highlighted in red).

Table 5.2: T2-weighted MR images of nanoparticles in suspension. The first of eight MRI echoes recorded at short echo time – before decay of the T2-weighted signal. Maghemite (Fe_2O_3) and BiFeO_3 NPs were used as positive controls, and polystyrene spheres were used as negative controls.

$\mu\text{g}_{\text{Fe}}/\text{mL}$	$\text{BiFeO}_3@Fe_2O_3$	Fe_2O_3	BiFeO_3	Polystyrene
5				
2.5				
1.5				
1.0				

Similarly, there was a concentration-dependent decrease in the intensity of T2* weighted signal of $\text{BiFeO}_3@Fe_2O_3$ NPs (see Table 5.3). Again, at lower concentrations the intensity of the $\text{BiFeO}_3@Fe_2O_3$ NPs was lower than that of the control, Fe_2O_3 . This is also most notable at 1.5 $\mu\text{g Fe/mL}$ (see third row of Table 5.3, highlighted in red).

Table 5.3: T2*-weighted MR images of nanoparticles in suspension. The third of 32 MRI echoes recorded at short echo time – before decay of the T2* signal. Maghemite (Fe_2O_3) and BiFeO_3 NPs were used as positive controls, and polystyrene spheres were used as negative controls.

$\mu\text{g}_{\text{Fe}}/\text{mL}$	$\text{BiFeO}_3@Fe_2O_3$	Fe_2O_3	BiFeO_3	Polystyrene
5				
2.5				
1.5				
1.0				

Quantitatively, the T2 and T2* relaxation times decreased as the concentration of $\text{BiFeO}_3@Fe_2O_3$ NPS increased (see Figure 5.2). At lower concentrations, the T2 relaxation time of $\text{BiFeO}_3@Fe_2O_3$ NPs appeared lower than that of the control, Fe_2O_3 , but all differences fell within the 95% confidence interval and were therefore not significant.

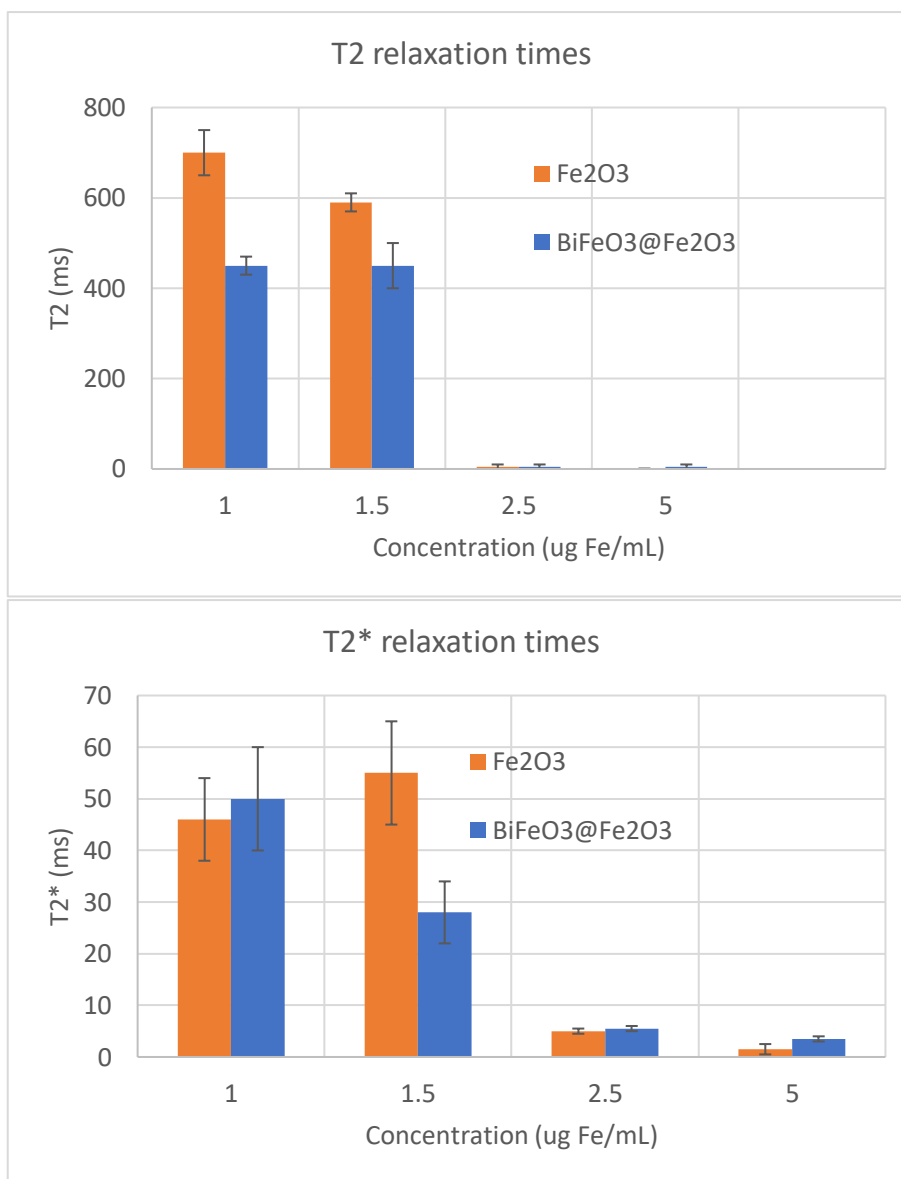


Figure 5.2: T2 and T2* relaxation times of nanoparticle suspensions. The T2 signal of BiFeO₃@Fe₂O₃ NPs decayed more rapidly than that of commercially available Fe₂O₃ NPs at a given concentration. The T2* relaxation times were not significantly different at any concentration.

This demonstrates the multimodal potential of this family of composites and shows that the presence of the second harmonic generating BiFeO₃ does not interfere with the T2* signal from the Fe₂O₃. This also suggests that the BiFeO₃@Fe₂O₃ NPs are sufficiently magnetic for use as MRI contrast agents, with or without the magnetic separation described above.

5.3.3 Nonlinear Optical Imaging: Second Harmonic Microscopy

To demonstrate the application of the NPs and composites in Second Harmonic Microscopy as nonlinear optical probes, the following conditions had to be met:

- Optical stability and multiplexing capabilities
- Specificity to EGFR

Photostability and optical tunability

To demonstrate the utility of SHG NPs over conventional fluorescent stains, A549 cells were treated with $\text{BiFeO}_3@Fe_2O_3$ NPs, as described in Chapter 3, to investigate their photostability and optical tunability (see Figure 5.3).

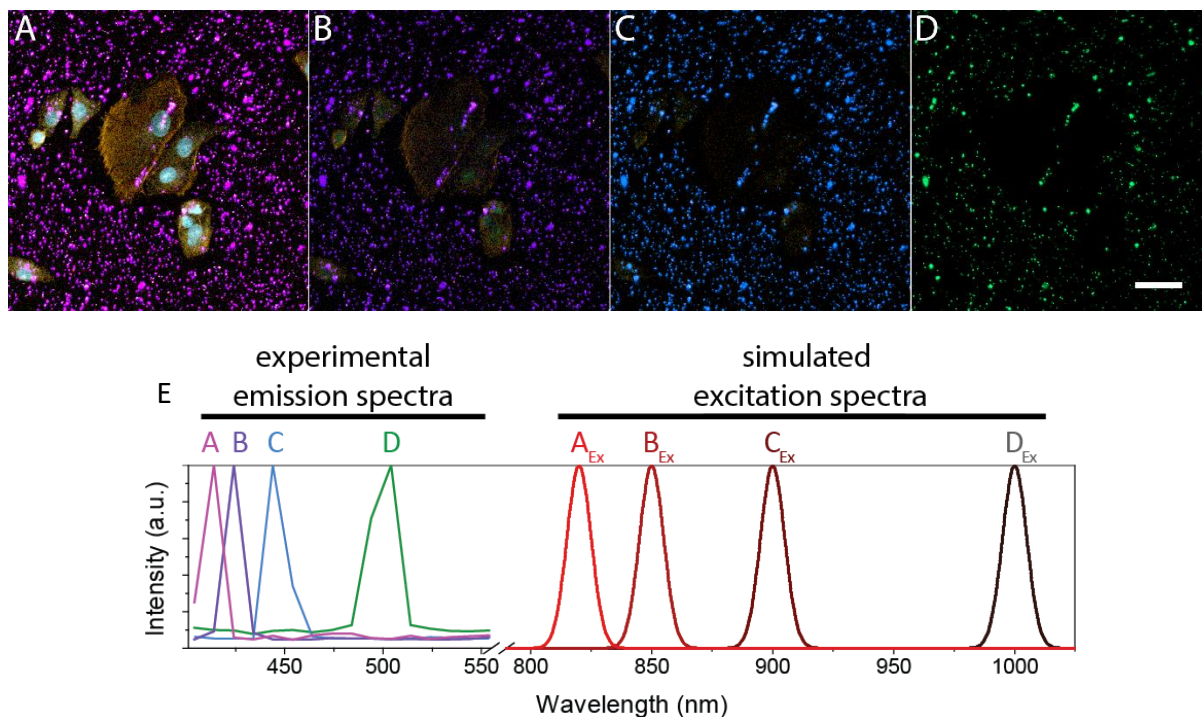


Figure 5.3: Photostability and optical tunability of $\text{BiFeO}_3@Fe_2O_3$ NPs. Panels A-D show the same cells excited with a laser tuned to different wavelengths: excitation A 820 nm, B - excitation = 850 nm, C - excitation = 900 nm, D - excitation = 1000 nm. Image A549 cells were treated with 100 $\mu\text{g}/\text{mL}$ $\text{BiFeO}_3@Fe_2O_3$ NPs and stained for DNA (cyan) and actin (yellow). The first image A was taken after 15 min irradiation at 20 mW, as soon as photo-bleaching was observed in the sample, and images B-D were taken at intervals of two minutes. The scale bar is 50 μm . E: simulated excitation spectra (A_{Ex} , B_{Ex} , C_{Ex} , D_{Ex}) and the corresponding experimental data from spectrally resolved imaging measured for each excitation from 400 nm – 650 nm (A-D). The peak in each case is centred at the second harmonic: i.e. excitation at A_{Ex} (820 nm) generated the second harmonic at A (410 nm). The experimental data was extracted by spectrally resolved analysis of the images in the top row A-D.

Results here are shown as a comparison of commercially available intracellular fluorescent dyes vs. the developed composites. To achieve this, once photo-bleaching was observed in the fluorescent stains, the sample was imaged for nonlinear optical imaging (e.g. SHG) at four different excitation wavelengths. While the two-photon excitation of the Phalloidin and Hoechst stains are still visible in panel A, they are no longer visible in panel D and only the composites (HNPs) can be seen. This

illustrates both the optical tunability of the second harmonic generation and the time-resolved photostability of the HNPs.

Specificity

To demonstrate that functionalised composites can be specifically targeted to A549 cell surface receptors, these were incubated for 24h and imaged after inhibiting non-specific uptake with sodium azide.

EGFR-targeted surface receptors became the preferred site for active binding of the functionalised composites as shown in Figure 5.4.

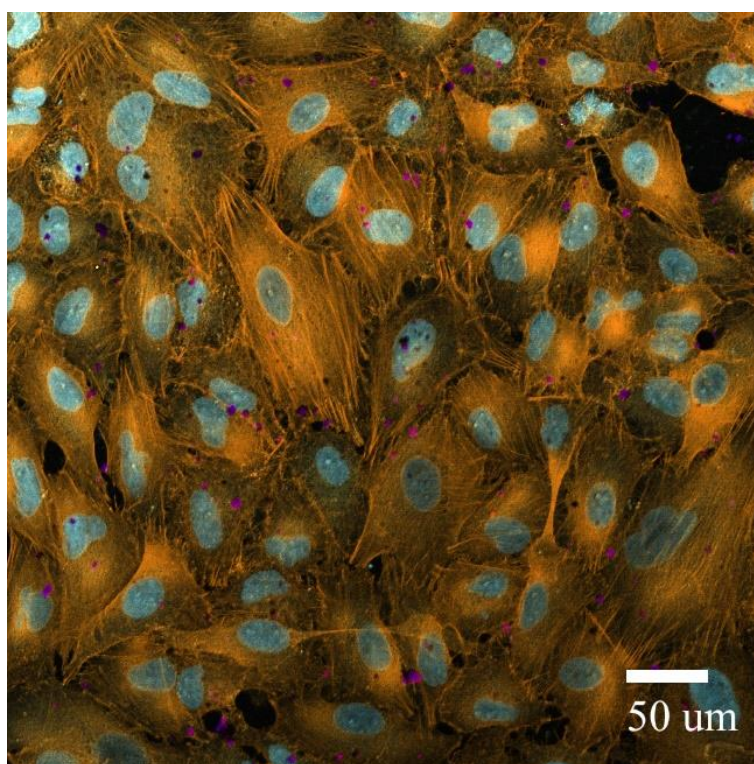


Figure 5.4: A549 cells after 24h exposure to anti-EGFR functionalised BiFeO₃@Fe₂O₃ NPs in the presence of an inhibitor. Nuclei were stained with Hoechst (shown in cyan) and actin was stained with Phalloidin (shown in yellow). The second harmonic response from the BiFeO₃@Fe₂O₃ NPs is false coloured with magenta.

This could be associated with the sodium azide inhibiting the available ATP required for the dimer formation and conformational changes in EGFR which allow binding with the targeting antibody on the composites as hypothesised in Chapter 3.

To further corroborate the localisation, confocal imaging was used to determine the binding location of the composite.

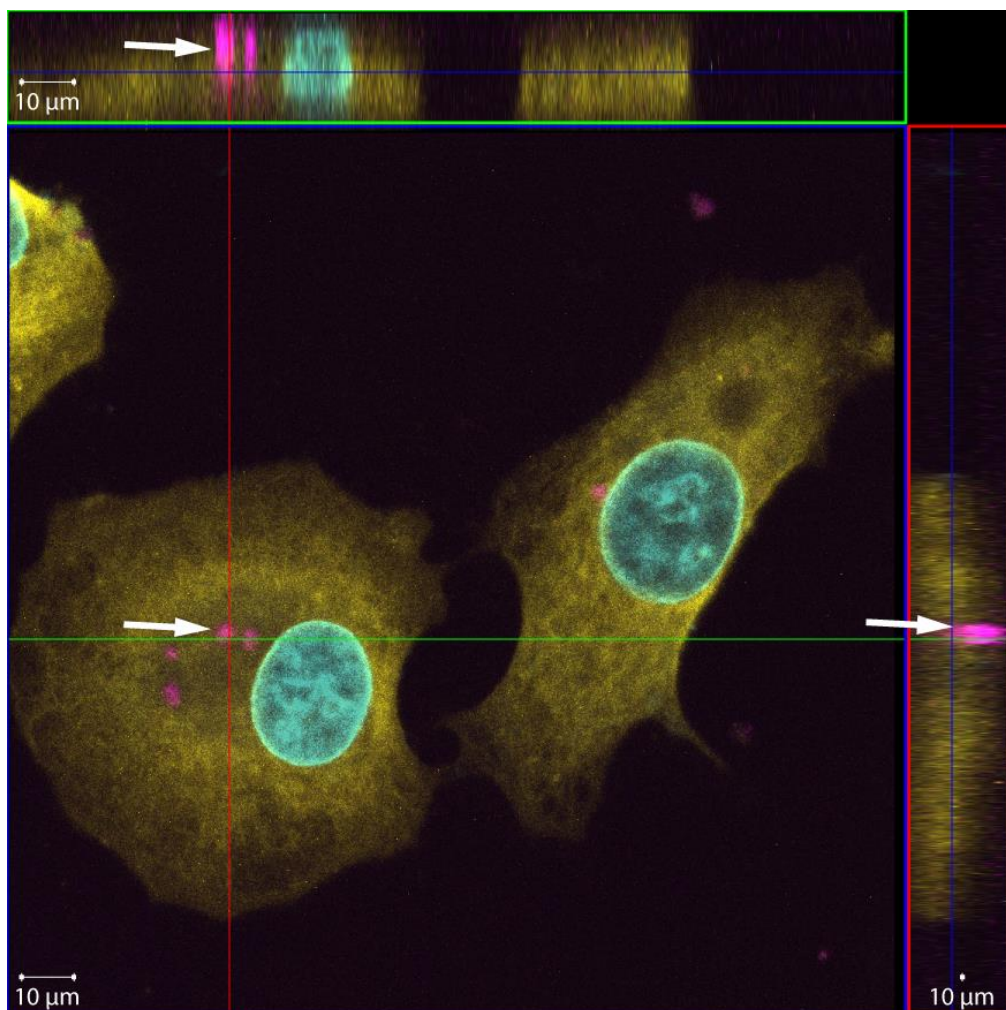


Figure 5.5: Confocal Z-stack slice of A549 cells labelled with fluorescently tagged anti-EGFR $\text{BiFeO}_3@Fe_2O_3$ NPs. DNA was stained with Hoechst to show nuclei (cyan), actin was stained with Phalloidin Red to show cell structure (yellow). The anti-EGFR antibody was tagged with CF 488A and is indicated in magenta.

This is in agreement with what was presented in Chapter 3 section 3.3.4, where a single imaging modality (i.e. confocal imaging) was exploited for the SHG material (see Figure 3.29 in Chapter 3). In this instance, we confirm the application to imaging but further expand on the multimodality aspect at the centre of this chapter – superparamagnetic and nonlinear optical nanocomposites can also be labelled with fluorescent stains for Confocal or Epifluorescence Microscopy.

5.4 Discussion

From the results presented above, it emerges that the functionalised materials have application as multifunctional and multimodal probes.

5.4.1 BiFeO₃@Fe₃O₄ NPs can be separated magnetically in different suspensions

Magnetic separation was demonstrated in water, FBS and plasma to simulate physiological conditions (Figure 5.1). Qualitatively, the NPs separated quickly from the different suspensions, each of which became transparent after approximately 10 s. The FBS and plasma samples cleared more quickly than the aqueous dispersion.

This suggests that the multimodal NPs possess sufficient magnetic response to be pulled from suspension.

This serves to demonstrate that the magnetic/harmonic NPs could be used for cell isolation applications by means of positive or negative magnetic separation, similar to commercially available products such as Dynabeads® or MACS® microbeads. By functionalising the NPs to target specific markers expressed on cells of interest, the composites could be used in cell isolation, as described previously, or in other applications. With the accelerating developments in Theranostics, multimodal composites are becoming the norm. In the biomedical field in particular, applications such as diagnostics and imaging are becoming essential tools for accelerating and reducing costs in clinical laboratory practice. Thus, the use of the composites presented here could potentially lead to more rapid, personalised diagnosis and treatment.

5.4.2 BiFeO₃@Fe₂O₃ nanoparticles can be used as contrast agents in Magnetic Resonance Imaging

Within the theranostic field, the use of composite magnetic material has already been established as a suitable replacement for gadolinium-based contrast agents. This is the case for iron oxide alloys e.g. gold-iron and gadolinium. To the best of our knowledge the composites developed in this work is the first example of linear/nonlinear optical material with associated magnetic properties for bioimaging and potential clinical diagnostic applications.

To further advance this research, the multimodality was pushed one step further where appropriate functionalisation was used to target moieties of interest.

5.4.3 Bismuth ferrite iron oxide nanocomposites are detectable via second harmonic microscopy

Nonlinear optical properties were shown via Second Harmonic Microscopy images to confirm that the signal from the magnetic-harmonic composites is detectable and sufficiently bright for nonlinear optical applications and shown to have distinct advantages over conventional fluorophores and

metallic nanoparticles. Limitations still exist relating to colloidal stability which could be an aspect to be addressed in the future.^{6,146}

Qualitatively, functionalised $\text{BiFeO}_3@Fe_2O_3$ opens up opportunities to investigate trimodal applications (e.g. fluorescence, refractance and SHG) in which linear as well as nonlinear optics are exploited.

This implies that the multimodal probes are suitable for diagnostic imaging.

5.5 Conclusion

Bismuth ferrite and magnetite nanoparticles and composites were characterised with a suite of analytical techniques to quantify their suitability for use as multifunctional probes for diagnostics and biomedical imaging.

The applications of multimodal nanocomposites were demonstrated by measuring their magnetic separation potential combined with their nonlinear optical properties in Magnetic Resonance Imaging and Second Harmonic Microscopy without and with functionalised moieties, respectively.

The following chapter summarises the outputs of this study and discusses the future outlook.

Chapter 6

General Discussion and Future Work

6.1 Application-driven optimisation

The aim of the study was to develop novel nanomaterials for *in vitro* imaging applications which can overcome the limitations of conventional imaging by combining harmonic nanocrystals with superparamagnetic nanoparticles in multimodal imaging probes.

Overall, the physico-chemical properties showed that the nanoparticles defined in this work satisfy the above aim. The nanoparticles:

- formed single crystal particles (and are monocrystalline)
- fell within a narrow size range to achieve colloidal stability
- bare BiFeO₃ nanoparticles induced internalisation in A549 cells
- can be used for multimodal imaging *in vitro* when functionalised

A simple approach was followed: well-established superparamagnetic nanoparticles were combined with nonlinear optical BiFeO₃ nanoparticles which were synthesised via new synthetic routes, in novel nanoparticle and nanowire composites. Uptake studies and Second Harmonic Microscopy demonstrated that the nanomaterials are detectable *in vitro*. This means these nanocomposites will be suitable for future biomedical imaging applications.

Beyond the applications demonstrated in this study, namely magnetic separation in physiological media, *in vitro* cell uptake tagging and cell-specific targeting, each of the properties enables distinct applications:

- the photostability of the harmonic nanoparticles means they are ideal for use in long term cell tracking²⁴²
- the wavelength tunability means that they have potential use in deep tissue including *in vivo* imaging (the excitation wavelength can be selected to minimise absorption in the tissue and hence minimise energy deposition)
- the magnetic response means they can be used as contrast agents in MRI and, given sufficient loading, to manipulate cells for cell counting or cell sorting in advanced flow cytometry analysis and

for theranostic applications which combine cell targeting and treatment.

6.1.1 Physico-chemical tuning: size and shape refinement

The ability to influence the crystallinity and size distribution of the harmonic nanoparticles is of paramount importance so it is evident that further work should be done to characterise and ultimately quantify these interactions.

One route to achieving this with respect to BiFeO_3 may be to reduce further the temperature at which the BiFeO_3 precursor is annealed. In ongoing work, the ignition of the precursor powder in the mucic acid method was prevented by extending the drying phase until the sol-gel forms an aerogel. Current efforts explore the use of other complexation agents to further raise the hydroxyl-carboxylic acid ratio and recently published work has led to the development of chelation-agent free synthesis.²⁴³ The use of other salts is also under investigation to determine whether the nature of counter- and co-ions might preferentially lower the surface tension of certain crystal faces. This would promote crystal growth in the direction of those faces, which might facilitate control over the aspect ratio of the nanoparticles. Initial results suggest that the impact of changing the salt and salt types (i.e. the use of chlorides vs. sulphates vs. carbonates etc.) will both provide greater control over the size and shape of the harmonic nanoparticles.

6.1.2 Enhancement of nonlinear optical properties

It has been demonstrated recently that the surface plasmon resonance of a gold layer grown on the surface will boost the harmonic signal; simple simulations indicate that coating the nanoparticles with gold will allow increases in the second harmonic generation by several orders of magnitude. However, the initial studies on BiFeO_3 nanoparticles with gold seeds attached, reported here, suggest that the real gains are more modest. The discrepancy between the model and experimental data has been ascribed to variability in size distributions and shell thickness.^{244,245} Nevertheless, even modest gains will serve to enhance the utility of the end-product materials so further studies are underway to improve the attachment of gold seeds to the surface of BiFeO_3 nanoparticles and to characterise the enhancement of the second harmonic generation.

An alternative approach to such modification has been published recently²⁴⁶ and is being applied to the current work. This work suggests that by coating harmonic nanoparticles with a neutral species e.g. Fe_3O_4 and annealing in the presence of a reducing agent, it may be possible to achieve a similar enhancement which is not dependent on resonance. The synthesis route presented in this study,

forming the novel composites $\text{BiFeO}_3@Fe_3O_4$ and $\text{BiFeO}_3@Fe_2O_3$, already constitute the first steps in this direction. Analysis of whether the desired increase in second harmonic signal was achieved is an immediate next step in this research.

6.1.3 Optimised end-products

The enhanced materials above were incorporated into silica nanowires to obtain optimised end-products such as SiO_2 nanowires with Fe_3O_4 and BiFeO_3 nanoparticles and SiO_2 nanowires with $\text{BiFeO}_3@Fe_3O_4$ or with $\text{BiFeO}_3@Fe_2O_3$ nanoparticles. By increasing the nanoparticle loading, end-products which possess all the advantages demonstrated through this study are obtained. This can allow multimodal, biocompatible and high aspect ratio probes to be prepared for biomedical applications. One such application is the magnetic separation of cells from suspension while being probed for second harmonic generation.

Specifically, magnetic cell separation combined with second harmonic generation measurement would constitute a significant advance over the conventional approach which comprises several steps: i) cells must be first suspended with a cocktail of fluorescent primary antibodies, ii) magnetic beads functionalised with secondary antibodies such as Dynabeads[®] are introduced and the cells are incubated, iii) magnetically separated for ten minutes and then iv) characterised using a two-step flow cytometry analysis. This is a time-consuming and expensive process which it is envisaged to be simplified by the proof of concept provided in this work.

Using a setup like that used for Hyper Rayleigh Scattering detection, the change in SH response could be measured when the blood sample is placed in a magnetic field, by choosing the probe wavelength such that the input and output are within the optical window of blood. Quantitative information could be potentially acquired, given a full characterisation of the functionalisation and targeting potential of the composites is established.

6.2 Functionalisation and Bioconjugation

The anti-EGFR antibodies used in the current work were used as a model system to demonstrate whether bioconjugation of the nanoparticles could be achieved and to apply the functionalisation to targeting. Additional functionality can be obtained by selecting different antibodies to target other markers. The protocol used to attach the primary conjugation agent to the maleimide group could also be modified to covalently bind primary antibodies²⁴⁷ (for longer term storage and to permit more vigorous post-synthesis processing).

Quantification of specific EGFR surface binding using Western Blot with and without uptake inhibition would provide insight on the exact molecular targeting. TEM imaging would complement the molecular medicine approach.

6.3 Multimodal imaging probes

As stated previously, the advantages of these probes over conventional modalities is their multiplexed properties: the photostability and wavelength tunability of the harmonic nanoparticles and the magnetic contrast of the Fe_3O_4 nanoparticles and the passivation of their surfaces by the SiO_2 matrix.

This creates opportunities to investigate advanced imaging techniques such as by using both linear and nonlinear optical properties simultaneously. To the best of our knowledge, such opportunity has not been developed before or previously explored using other metallic composites.

6.4 Conclusion

Well-established superparamagnetic nanoparticles were combined with nonlinear optical BiFeO_3 nanoparticles which were synthesised via new synthetic routes, in novel nanoparticle and nanowire composites. Uptake studies and Second Harmonic Microscopy demonstrated that the nanomaterials are detectable *in vitro*. This means these nanocomposites might be suitable for biomedical applications once the biocompatibility is assessed for their end use.

Each of the properties enables distinct applications including long term cell tracking, deep tissue *in vivo* imaging, as contrast agents in MRI and cell manipulation, counting or sorting, high throughput and theranostics.

In this work, the following outcomes were achieved:

- ❖ Nanomaterials synthesis
 - Fe_3O_4 nanoparticles
 - BiFeO_3 nanoparticles
 - Nanoparticle composites of BiFeO_3 nanoparticles coated with Fe_3O_4 or with Fe_2O_3
 - SiO_2 nanowires
 - Multimodal nanowire composites of the nanoparticles embedded in the silica nanowire matrix to combine their properties and to passivate the surfaces of the BiFeO_3 and Fe_3O_4 nanoparticles
- ❖ Functionalisation of BiFeO_3 nanoparticles and composites

- ❖ Physico-chemical characterisation of ex-synthesis and functionalised nanomaterials
- ❖ In vitro characterisation and safety assessment
- ❖ Proof-of-concept of multimodality for a clinical application

Thus, the composite materials presented in this study (i.e. BiFeO_3 , $\text{BiFeO}_3@Fe_2O_3$, $\text{BiFeO}_3@Fe_3O_4$ nanoparticles, and SiO_2 nanowires with BiFeO_3 or with BiFeO_3 and Fe_3O_4 or Fe_2O_3) represent a step forward in the development of probes for biomedical imaging and combined diagnostic and treatment applications. It is expected that this array of advanced nanocomposites will lead to enhanced clinical diagnostic and treatment techniques and ultimately to improved patient outcomes.

References

- (1) Wolf, E. L. *Nanophysics and Nanotechnology: An Introduction to Modern Concepts in Nanoscience*, 2nd, updated and enl. ed ed.; Physics textbook; Wiley-VCH: Weinheim, 2006.
- (2) Nanotechnology - Project on Emerging Nanotechnologies <http://www.nanotechproject.org/> (accessed Aug 10, 2015).
- (3) Hornyak, G. L.; Moore, J. J.; Tibbals, H. F.; Dutta, J. *Fundamentals of Nanotechnology*; CRC Press, 2008.
- (4) *Characterization of Nanomaterials in Complex Environmental and Biological Media*; Elsevier, 2015.
- (5) Cui, Z. *Nanofabrication: Principles, Capabilities and Limits*; Springer, 2009.
- (6) Boyd, R. W. *Nonlinear Optics*; Academic press, 2003.
- (7) Campagnola, P. J.; Clark, H. A.; Mohler, W. A.; Lewis, A.; Loew, L. M. Second-Harmonic Imaging Microscopy of Living Cells. *J. Biomed. Opt.* **2001**, *6* (3), 277–286.
- (8) Campagnola, P. J.; Loew, L. M. Second-Harmonic Imaging Microscopy for Visualizing Biomolecular Arrays in Cells, Tissues and Organisms. *Nat. Biotechnol.* **2003**, *21* (11), 1356–1360. <https://doi.org/10.1038/nbt894>.
- (9) Clift, M. J. D.; Stone, V. Quantum Dots: An Insight and Perspective of Their Biological Interaction and How This Relates to Their Relevance for Clinical Use. *Theranostics* **2012**, *2* (7), 668–680. <https://doi.org/10.7150/thno.4545>.
- (10) Derfus, A. M.; Chan, W. C. W.; Bhatia, S. N. Probing the Cytotoxicity of Semiconductor Quantum Dots. *Nano Lett.* **2004**, *4* (1), 11–18. <https://doi.org/10.1021/nl0347334>.
- (11) Hardman, R. A Toxicologic Review of Quantum Dots: Toxicity Depends on Physicochemical and Environmental Factors. *Environ. Health Perspect.* **2006**, *114* (2), 165–172. <https://doi.org/10.1289/ehp.8284>.
- (12) Staedler, D.; Magouroux, T.; Hadji, R.; Joulaud, C.; Extermann, J.; Schwung, S.; Passemard, S.; Kasparian, C.; Clarke, G.; Germann, M.; et al. Harmonic Nanocrystals for Biolabeling: A Survey of Optical Properties and Biocompatibility. *ACS Nano* **2012**, *6* (3), 2542–2549. <https://doi.org/10.1021/nn204990n>.
- (13) Bonacina, L. Nonlinear Nanomedicine: Harmonic Nanoparticles toward Targeted Diagnosis and Therapy. *Mol. Pharm.* **2013**, *10* (3), 783–792. <https://doi.org/10.1021/mp300523e>.
- (14) Dempsey, W. P.; Fraser, S. E.; Pantazis, P. SHG Nanoprobes: Advancing Harmonic Imaging in Biology. *BioEssays* **2012**, *34* (5), 351–360. <https://doi.org/10.1002/bies.201100106>.
- (15) Brown, D. J.; Morishige, N.; Neekhra, A.; Minckler, D. S.; Jester, J. V. Application of Second Harmonic Imaging Microscopy to Assess Structural Changes in Optic Nerve Head Structure Ex Vivo. *J. Biomed. Opt.* **2007**, *12* (2), 024029. <https://doi.org/10.1117/1.2717540>.
- (16) Joulaud, C.; Mugnier, Y.; Djanta, G.; Dubled, M.; Marty, J.-C.; Galez, C.; Wolf, J.-P.; Bonacina, L.; Le Dantec, R. Characterization of the Nonlinear Optical Properties of Nanocrystals by Hyper Rayleigh Scattering. *J. Nanobiotechnology* **2013**, *11* (Suppl 1), S8.
- (17) Liu, J.; Sun, Z.; Deng, Y.; Zou, Y.; Li, C.; Guo, X.; Xiong, L.; Gao, Y.; Li, F.; Zhao, D. Highly Water-Dispersible Biocompatible Magnetite Particles with Low Cytotoxicity Stabilized by Citrate Groups. *Angew. Chem. Int. Ed.* **2009**, *48* (32), 5875–5879. <https://doi.org/10.1002/anie.200901566>.
- (18) Reddy, L. H.; Arias, J. L.; Nicolas, J.; Couvreur, P. Magnetic Nanoparticles: Design and Characterization, Toxicity and Biocompatibility, Pharmaceutical and Biomedical Applications. *Chem. Rev.* **2012**, *112* (11), 5818–5878. <https://doi.org/10.1021/cr300068p>.
- (19) Colombo, M.; Carregal-Romero, S.; Casula, M. F.; Gutiérrez, L.; Morales, M. P.; Böhm, I. B.; Heverhagen, J. T.; Prospero, D.; Parak, Wolfgang. J. Biological Applications of Magnetic Nanoparticles. *Chem. Soc. Rev.* **2012**, *41* (11), 4306. <https://doi.org/10.1039/c2cs15337h>.

- (20) Mahmoudi, M.; Sant, S.; Wang, B.; Laurent, S.; Sen, T. Superparamagnetic Iron Oxide Nanoparticles (SPIONs): Development, Surface Modification and Applications in Chemotherapy. *Adv. Drug Deliv. Rev.* **January**, 63 (1–2), 24–46. <https://doi.org/10.1016/j.addr.2010.05.006>.
- (21) Pauluhn, J. Subchronic Inhalation Toxicity of Iron Oxide (Magnetite, Fe₃O₄) in Rats: Pulmonary Toxicity Is Determined by the Particle Kinetics Typical of Poorly Soluble Particles. *J. Appl. Toxicol. JAT* **2012**, 32 (7), 488–504. <https://doi.org/10.1002/jat.1668>.
- (22) Cuadro, C. B. Stable Colloidal Dispersions of Magnetic Nanoparticles in Aqueous Media and Polymer Melts, University of Puerto Rico, 2009.
- (23) Kim, D. K.; Zhang, Y.; Voit, W.; Rao, K. V.; Kehr, J.; Bjelke, B.; Muhammed, M. Superparamagnetic Iron Oxide Nanoparticles for Bio-Medical Applications. *Scr. Mater.* **2001**, 44 (8–9), 1713–1718.
- (24) Efros, A. L.; Nesbitt, D. J. Origin and Control of Blinking in Quantum Dots. *Nat. Nanotechnol.* **2016**, 11 (8), 661–671. <https://doi.org/10.1038/nnano.2016.140>.
- (25) Yuan, G.; Gómez, D. E.; Kirkwood, N.; Boldt, K.; Mulvaney, P. Two Mechanisms Determine Quantum Dot Blinking. *ACS Nano* **2018**, 12 (4), 3397–3405. <https://doi.org/10.1021/acsnano.7b09052>.
- (26) Eggeling, C.; Widengren, J.; Rigler, R.; Seidel, C. a. M. Photostability of Fluorescent Dyes for Single-Molecule Spectroscopy: Mechanisms and Experimental Methods for Estimating Photobleaching in Aqueous Solution. In *Applied Fluorescence in Chemistry, Biology and Medicine*; Springer Berlin Heidelberg, 1999; pp 193–240. https://doi.org/10.1007/978-3-642-59903-3_10.
- (27) Jokic, T.; Borisov, S. M.; Saf, R.; Nielsen, D. A.; Kühl, M.; Klimant, I. Highly Photostable Near-Infrared Fluorescent PH Indicators and Sensors Based on BF₂-Chelated Tetraarylazadipyrromethene Dyes. *Anal. Chem.* **2012**, 84 (15), 6723–6730. <https://doi.org/10.1021/ac3011796>.
- (28) Panchuk-Voloshina, N.; Haugland, R. P.; Bishop-Stewart, J.; Bhalgat, M. K.; Millard, P. J.; Mao, F.; Leung, W. Y.; Haugland, R. P. Alexa Dyes, a Series of New Fluorescent Dyes That Yield Exceptionally Bright, Photostable Conjugates. *J. Histochem. Cytochem.* **1999**, 47 (9), 1179–1188.
- (29) Medintz, I. L.; Uyeda, H. T.; Goldman, E. R.; Mattoussi, H. Quantum Dot Bioconjugates for Imaging, Labelling and Sensing. *Nat. Mater.* **2005**, 4 (6), 435–446. <https://doi.org/10.1038/nmat1390>.
- (30) Resch-Genger, U.; Grabolle, M.; Cavaliere-Jaricot, S.; Nitschke, R.; Nann, T. Quantum Dots versus Organic Dyes as Fluorescent Labels. *Nat. Methods* **2008**, 5 (9), 763–775. <https://doi.org/10.1038/nmeth.1248>.
- (31) Ajayaghosh, A. Chemistry of Squaraine-Derived Materials: Near-IR Dyes, Low Band Gap Systems, and Cation Sensors. *Acc. Chem. Res.* **2005**, 38 (6), 449–459. <https://doi.org/10.1021/ar0401000>.
- (32) Arunkumar, E.; Forbes, C. C.; Noll, B. C.; Smith, B. D. Squaraine-Derived Rotaxanes: Sterically Protected Fluorescent near-IR Dyes. *J. Am. Chem. Soc.* **2005**, 127 (10), 3288–3289. <https://doi.org/10.1021/ja042404n>.
- (33) Song, J. L.; Mao, J. G. New Types of Blue, Red or near IR Luminescent Phosphonate-Decorated Lanthanide Oxalates. *Chem.-Eur. J.* **2005**, 11 (5), 1417–1424. <https://doi.org/10.1002/chem.200400889>.
- (34) Yu, F.; Li, P.; Li, G.; Zhao, G.; Chu, T.; Han, K. A Near-IR Reversible Fluorescent Probe Modulated by Selenium for Monitoring Peroxynitrite and Imaging in Living Cells. *J. Am. Chem. Soc.* **2011**, 133 (29), 11030–11033. <https://doi.org/10.1021/ja202582x>.
- (35) Chatterjee, D. K.; Rufalhah, A. J.; Zhang, Y. Upconversion Fluorescence Imaging of Cells and Small Animals Using Lanthanide Doped Nanocrystals. *Biomaterials* **2008**, 29 (7), 937–943. <https://doi.org/10.1016/j.biomaterials.2007.10.051>.
- (36) Heer, S.; Kompe, K.; Gudel, H. U.; Haase, M. Highly Efficient Multicolour Upconversion Emission in Transparent Colloids of Lanthanide-Doped NaYF₄ Nanocrystals. *Adv. Mater.* **2004**, 16 (23–24), 2102–+. <https://doi.org/10.1002/adma.200400772>.
- (37) Li, Z.; Zhang, Y.; Jiang, S. Multicolor Core/Shell-Structured Upconversion Fluorescent Nanoparticles. *Adv. Mater.* **2008**, 20 (24), 4765–+. <https://doi.org/10.1002/adma.200801056>.

- (38) Wang, C.; Cheng, L.; Liu, Z. Drug Delivery with Upconversion Nanoparticles for Multi-Functional Targeted Cancer Cell Imaging and Therapy. *Biomaterials* **2011**, *32* (4), 1110–1120. <https://doi.org/10.1016/j.biomaterials.2010.09.069>.
- (39) Wang, F.; Han, Y.; Lim, C. S.; Lu, Y.; Wang, J.; Xu, J.; Chen, H.; Zhang, C.; Hong, M.; Liu, X. Simultaneous Phase and Size Control of Upconversion Nanocrystals through Lanthanide Doping. *Nature* **2010**, *463* (7284), 1061–1065. <https://doi.org/10.1038/nature08777>.
- (40) Wang, F.; Banerjee, D.; Liu, Y.; Chen, X.; Liu, X. Upconversion Nanoparticles in Biological Labeling, Imaging, and Therapy. *Analyst* **2010**, *135* (8), 1839–1854. <https://doi.org/10.1039/c0an00144a>.
- (41) Wang, F.; Liu, X. Upconversion Multicolor Fine-Tuning: Visible to near-Infrared Emission from Lanthanide-Doped NaYF₄ Nanoparticles. *J. Am. Chem. Soc.* **2008**, *130* (17), 5642–+. <https://doi.org/10.1021/ja800868a>.
- (42) Wang, F.; Liu, X. Recent Advances in the Chemistry of Lanthanide-Doped Upconversion Nanocrystals. *Chem. Soc. Rev.* **2009**, *38* (4), 976–989. <https://doi.org/10.1039/b809132n>.
- (43) Wang, L. Y.; Yan, R. X.; Hao, Z. Y.; Wang, L.; Zeng, J. H.; Bao, J.; Wang, X.; Peng, Q.; Li, Y. D. Fluorescence Resonant Energy Transfer Biosensor Based on Upconversion-Luminescent Nanoparticles. *Angew. Chem.-Int. Ed.* **2005**, *44* (37), 6054–6057. <https://doi.org/10.1002/anie.200501907>.
- (44) Zhou, J.; Liu, Z.; Li, F. Upconversion Nanophosphors for Small-Animal Imaging. *Chem. Soc. Rev.* **2012**, *41* (3), 1323–1349. <https://doi.org/10.1039/c1cs15187h>.
- (45) Chen, G.; Qiu, H.; Prasad, P. N.; Chen, X. Upconversion Nanoparticles: Design, Nanochemistry, and Applications in Theranostics. *Chem. Rev.* **2014**, *114* (10), 5161–5214. <https://doi.org/10.1021/cr400425h>.
- (46) Regny, S.; Riporto, J.; Mugnier, Y.; Le Dantec, R.; Kodjikian, S.; Pairis, S.; Gautier-Luneau, I.; Dantelle, G. Microwave Synthesis and Up-Conversion Properties of SHG-Active α -(La, Er)(IO₃)₃ Nanocrystals. *Inorg. Chem.* **2019**, *58* (2), 1647–1656. <https://doi.org/10.1021/acs.inorgchem.8b03208>.
- (47) Kobat, D.; Horton, N. G.; Xu, C. In Vivo Two-Photon Microscopy to 1.6-Mm Depth in Mouse Cortex. *J. Biomed. Opt.* **2011**, *16* (10), 106014–106014.
- (48) Riporto, J.; Urbain, M.; Mugnier, Y.; Multian, V.; Riporto, F.; Bredillet, K.; Beauquis, S.; Galez, C.; Monnier, V.; Chevolut, Y.; et al. Second Harmonic Spectroscopy of ZnO, BiFeO₃ and LiNbO₃ Nanocrystals. *Opt. Mater. Express* **2019**, *9* (4), 1955. <https://doi.org/10.1364/OME.9.001955>.
- (49) Rakovich, T. Y.; Mahfoud, O. K.; Mohamed, B. M.; Prina-Mello, A.; Crosbie-Staunton, K.; Van Den Broeck, T.; De Kimpe, L.; Sukhanova, A.; Baty, D.; Rakovich, A.; et al. Highly Sensitive Single Domain Antibody-Quantum Dot Conjugates for Detection of HER2 Biomarker in Lung and Breast Cancer Cells. *ACS Nano* **2014**, *8* (6), 5682–5695. <https://doi.org/10.1021/nn500212h>.
- (50) Mahfoud, O. K.; Rakovich, T. Y.; Prina-Mello, A.; Movia, D.; Alves, F.; Volkov, Y. Detection of ErbB2: Nanotechnological Solutions for Clinical Diagnostics. *RSC Adv.* **2013**, *4* (7), 3422–3442. <https://doi.org/10.1039/C3RA45401K>.
- (51) Zhang, H.; Berezov, A.; Wang, Q.; Zhang, G.; Drebin, J.; Murali, R.; Greene, M. I. ErbB Receptors: From Oncogenes to Targeted Cancer Therapies. *J. Clin. Invest.* **2007**, *117* (8), 2051–2058. <https://doi.org/10.1172/JCI32278>.
- (52) Mendes, D.; Alves, C.; Afonso, N.; Cardoso, F.; Passos-Coelho, J. L.; Costa, L.; Andrade, S.; Batel-Marques, F. The Benefit of HER2-Targeted Therapies on Overall Survival of Patients with Metastatic HER2-Positive Breast Cancer – a Systematic Review. *Breast Cancer Res.* **2015**, *17* (1), 140. <https://doi.org/10.1186/s13058-015-0648-2>.
- (53) Herbst, R. S. Review of Epidermal Growth Factor Receptor Biology. *Int. J. Radiat. Oncol.* **2004**, *59* (2), S21–S26. <https://doi.org/10.1016/j.ijrobp.2003.11.041>.
- (54) Kalyankrishna, S.; Grandis, J. R. Epidermal Growth Factor Receptor Biology in Head and Neck Cancer. *J. Clin. Oncol.* **2006**, *24* (17), 2666–2672. <https://doi.org/10.1200/JCO.2005.04.8306>.

- (55) Libermann, T. A.; Nusbaum, H. R.; Razon, N.; Kris, R.; Lax, I.; Soreq, H.; Whittle, N.; Waterfield, M. D.; Ullrich, A.; Schlessinger, J. Amplification, Enhanced Expression and Possible Rearrangement of EGF Receptor Gene in Primary Human Brain Tumours of Glial Origin. *Nature* **1985**, *313* (5998), 144–147. <https://doi.org/10.1038/313144a0>.
- (56) Kreuter, J. Influence of the Surface Properties on Nanoparticle-Mediated Transport of Drugs to the Brain. *J. Nanosci. Nanotechnol.* **2004**, *4* (5), 484–488. <https://doi.org/10.1166/jnn.2003.077>.
- (57) Prina-Mello, A.; Whelan, A. M.; Atzberger, A.; McCarthy, J. E.; Byrne, F.; Davies, G.; Coey, J. M. D.; Volkov, Y.; Gun'ko, Y. K. Comparative Flow Cytometric Analysis of Immunofunctionalized Nanowire and Nanoparticle Signatures. *Small* **2010**, *6* (2), 247–255. <https://doi.org/10.1002/smll.200901014>.
- (58) Verma, N. K.; Conroy, J.; Lyons, P. E.; Coleman, J.; O'Sullivan, M. P.; Kornfeld, H.; Kelleher, D.; Volkov, Y. Autophagy Induction by Silver Nanowires: A New Aspect in the Biocompatibility Assessment of Nanocomposite Thin Films. *Toxicol. Appl. Pharmacol.* **2012**, *264* (3), 451–461. <https://doi.org/10.1016/j.taap.2012.08.023>.
- (59) Claxton, N. S.; Fellers, T. J.; Davidson, M. W. Laser Scanning Confocal Microscopy. *Dep. Opt. Microsc. Digit. Imaging Fla. State Univ. Tallahass. Httpwww Olymp. ComtheoryLSCMIntro Pdf* **2006**.
- (60) Pawley, J. *Handbook of Biological Confocal Microscopy*; Springer Science & Business Media, 2006.
- (61) Denk, W.; Strickler, J. H.; Webb, W. W.; others. Two-Photon Laser Scanning Fluorescence Microscopy. *Science* **1990**, *248* (4951), 73–76.
- (62) Helmchen, F.; Denk, W. Deep Tissue Two-Photon Microscopy. *Nat. Methods* **2005**, *2* (12), 932–940. <https://doi.org/10.1038/nmeth818>.
- (63) Dubreil, L.; Leroux, I.; Ledevin, M.; Schleder, C.; Lagalice, L.; Lovo, C.; Fleurisson, R.; Passemard, S.; Kilin, V.; Gerber-Lemaire, S.; et al. Multi-Harmonic Imaging in the Second Near-Infrared Window of Nanoparticle-Labeled Stem Cells as a Monitoring Tool in Tissue Depth. *ACS Nano* **2017**. <https://doi.org/10.1021/acsnano.7b00773>.
- (64) Soenen, S. J.; Manshian, B.; Doak, S. H.; De Smedt, S. C.; Braeckmans, K. Fluorescent Non-Porous Silica Nanoparticles for Long-Term Cell Monitoring: Cytotoxicity and Particle Functionality. *Acta Biomater.* **2013**, *9* (11), 9183–9193. <https://doi.org/10.1016/j.actbio.2013.04.026>.
- (65) Corr, S. A.; O'Byrne, A.; Gun'ko, Y. K.; Ghosh, S.; Brougham, D. F.; Mitchell, S.; Volkov, Y.; Prina-Mello, A. Magnetic-Fluorescent Nanocomposites for Biomedical Multitasking. *Chem. Commun.* **2006**, No. 43, 4474. <https://doi.org/10.1039/b610746j>.
- (66) Fei, L.; Hu, Y.; Li, X.; Song, R.; Sun, L.; Huang, H.; Gu, H.; Chan, H. L. W.; Wang, Y. Electro-Spun Bismuth Ferrite Nanofibers for Potential Applications in Ferroelectric Photovoltaic Devices. *ACS Appl. Mater. Interfaces* **2015**, 150126130508002. <https://doi.org/10.1021/acsnano.7b00773>.
- (67) Moubah, R.; Rousseau, O.; Colson, D.; Artemenko, A.; Maglione, M.; Viret, M. Photoelectric Effects in Single Domain BiFeO₃ Crystals. *Adv. Funct. Mater.* **2012**, *22* (22), 4814–4818. <https://doi.org/10.1002/adfm.201201150>.
- (68) Rivera, R.; Safari, A. Fabrication of Bismuth Ferrite Nanofibers via Electrospinning. In *Applications of Ferroelectric and Workshop on the Piezoresponse Force Microscopy (ISAF/PFM), 2013 IEEE International Symposium on the*; 2013; pp 156–158. <https://doi.org/10.1109/ISAF.2013.6748682>.
- (69) Yamada, H.; Garcia, V.; Fusil, S.; Boyn, S.; Marinova, M.; Gloter, A.; Xavier, S.; Grollier, J.; Jacquet, E.; Carrétéro, C.; et al. Giant Electroresistance of Super-Tetragonal BiFeO₃-Based Ferroelectric Tunnel Junctions. *ACS Nano* **2013**, *7* (6), 5385–5390. <https://doi.org/10.1021/nn401378t>.
- (70) Heron, J. T.; Bosse, J. L.; He, Q.; Gao, Y.; Trassin, M.; Ye, L.; Clarkson, J. D.; Wang, C.; Liu, J.; Salahuddin, S.; et al. Deterministic Switching of Ferromagnetism at Room Temperature Using an Electric Field. *Nature* **2014**, *516* (7531), 370–373. <https://doi.org/10.1038/nature14004>.
- (71) Sando, D.; Agbelele, A.; Rahmedov, D.; Liu, J.; Rovillain, P.; Toulouse, C.; Infante, I. C.; Pyatakov, A. P.; Fusil, S.; Jacquet, E.; et al. Crafting the Magnonic and Spintronic Response of BiFeO₃ Films by Epitaxial Strain. *Nat. Mater.* **2013**, *12* (7), 641–646. <https://doi.org/10.1038/nmat3629>.

- (72) Balke, N.; Choudhury, S.; Jesse, S.; Huijben, M.; Chu, Y. H.; Baddorf, A. P.; Chen, L. Q.; Ramesh, R.; Kalinin, S. V. Deterministic Control of Ferroelastic Switching in Multiferroic Materials. *Nat. Nanotechnol.* **2009**, *4* (12), 868–875. <https://doi.org/10.1038/nnano.2009.293>.
- (73) Li, S.; Lin, Y.-H.; Zhang, B.-P.; Nan, C.-W.; Wang, Y. Photocatalytic and Magnetic Behaviors Observed in Nanostructured BiFeO₃ Particles. *J. Appl. Phys.* **2009**, *105* (5), 056105-056105–3. <https://doi.org/doi:10.1063/1.3080131>.
- (74) Wang, X.; Lin, Y.; Zhang, Z. C.; Bian, J. Y. Photocatalytic Activities of Multiferroic Bismuth Ferrite Nanoparticles Prepared by Glycol-Based Sol-Gel Process. *J. Sol-Gel Sci. Technol.* **2011**, *60* (1), 1–5. <https://doi.org/10.1007/s10971-011-2542-4>.
- (75) Bonacina, L.; Mugnier, Y.; Courvoisier, F.; Dantec, R. L.; Extermann, J.; Lambert, Y.; Boutou, V.; Galez, C.; Wolf, J.-P. Polar Fe(IO₃)₃ Nanocrystals as Local Probes for Nonlinear Microscopy. *Appl. Phys. B* **2007**, *87* (3), 399–403. <https://doi.org/10.1007/s00340-007-2612-z>.
- (76) Michel, C.; Moreau, J.-M.; Achenbach, G. D.; Gerson, R.; James, W. J. The Atomic Structure of BiFeO₃. *Solid State Commun.* **1969**, *7* (9), 701–704. [https://doi.org/10.1016/0038-1098\(69\)90597-3](https://doi.org/10.1016/0038-1098(69)90597-3).
- (77) Sosnowska, I.; Neumaier, T. P.; Steichele, E. Spiral Magnetic Ordering in Bismuth Ferrite. *J. Phys. C Solid State Phys.* **1982**, *15* (23), 4835. <https://doi.org/10.1088/0022-3719/15/23/020>.
- (78) Popov, Yu. F.; Kadomtseva, A. M.; Vorob'ev, G. P.; Zvezdin, A. K. Discovery of the Linear Magnetoelectric Effect in Magnetic Ferroelectric BiFeO₃ in a Strong Magnetic Field. *Ferroelectrics* **1994**, *162* (1), 135–140. <https://doi.org/10.1080/00150199408245098>.
- (79) Hill, N. A. Density Functional Studies of Multiferroic Magnetoelectrics. *Annu. Rev. Mater. Res.* **2002**, *32*, 1–37. <https://doi.org/10.1146/annurev.matsci.32.101901.152309>.
- (80) Li, J. F.; Wang, J. L.; Wuttig, M.; Ramesh, R.; Wang, N.; Ruetter, B.; Pyatakov, A. P.; Zvezdin, A. K.; Viehland, D. Dramatically Enhanced Polarization in (001), (101), and (111) BiFeO₃ Thin Films Due to Epitaxial-Induced Transitions. *Appl. Phys. Lett.* **2004**, *84* (25), 5261–5263. <https://doi.org/10.1063/1.1764944>.
- (81) Jiang, Q.; Qiu, J. H. The Thickness Dependence of Ferroelectric and Magnetic Properties in Epitaxial BiFeO₃ Thin Films. *J. Appl. Phys.* **2006**, *99* (10). <https://doi.org/10.1063/1.2196238>.
- (82) Kadomtseva, A. M.; Popov, Y. F.; Pyatakov, A. P.; Vorob'ev, G. P.; Zvezdin, A. K.; Viehland, D. Phase Transitions in Multiferroic BiFeO₃ Crystals, Thin-Layers, and Ceramics: Enduring Potential for a Single Phase, Room-Temperature Magnetoelectric “Holy Grail.” *Phase Transit.* **2006**, *79* (12), 1019–1042. <https://doi.org/10.1080/01411590601067235>.
- (83) Bea, H.; Gajek, M.; Bibes, M.; Barthelemy, A. Spintronics with Multiferroics. *J. Phys.-Condens. Matter* **2008**, *20* (43). <https://doi.org/10.1088/0953-8984/20/43/434221>.
- (84) Skorikov, V. M.; Kalinkin, A. N.; Polyakov, A. E. Magnetic and Electrical Properties of Multiferroic BiFeO₃, Its Synthesis and Applications. *Inorg. Mater.* **2012**, *48* (13), 1210–1225. <https://doi.org/10.1134/S0020168512130043>.
- (85) Kumar, A.; Rai, R. C.; Podraza, N. J.; Denev, S.; Ramirez, M.; Chu, Y.-H.; Martin, L. W.; Ihlefeld, J.; Heeg, T.; Schubert, J.; et al. Linear and Nonlinear Optical Properties of BiFeO₃. *Appl. Phys. Lett.* **2008**, *92* (12), 121915. <https://doi.org/doi:10.1063/1.2901168>.
- (86) Catalan, G.; Scott, J. F. Physics and Applications of Bismuth Ferrite. *Adv. Mater.* **2009**, *21* (24), 2463–2485. <https://doi.org/10.1002/adma.200802849>.
- (87) Haumont, R.; Kreisel, J.; Bouvier, P.; Hippert, F. Phonon Anomalies and the Ferroelectric Phase Transition in Multiferroic BiFeO₃. *Phys. Rev. B* **2006**, *73* (13), 132101.
- (88) Selbach, S. M.; Tybell, T.; Einarsrud, M.; Grande, T. Size-Dependent Properties of Multiferroic BiFeO₃ Nanoparticles. *Chem Mater* **2007**, No. 13, 6478–6484.
- (89) Bonacina, L.; Mugnier, Y.; Courvoisier, F.; Le Dantec, R.; Extermann, J.; Lambert, Y.; Boutou, V.; Galez, C.; Wolf, J.-P. Polar Fe(IO₃)₃ Nanocrystals as Local Probes for Nonlinear Microscopy. *Appl. Phys. B* **2007**, *87* (3), 399–403. <https://doi.org/10.1007/s00340-007-2612-z>.

- (90) Staedler, D.; Magouroux, T.; Hadji, R.; Joulaud, C.; Extermann, J.; Schwung, S.; Passemard, S.; Kasparian, C.; Clarke, G.; Germann, M.; et al. Harmonic Nanocrystals for Bio-Labeling: A Survey of Optical Properties and Biocompatibility. *ACS Nano* **2012**, *6*(3), 2542–2549.
- (91) Dempsey, W. P.; Fraser, S. E.; Pantazis, P. SHG Nanoprobes: Advancing Harmonic Imaging in Biology. *BioEssays* **2012**, *34* (5), 351–360. <https://doi.org/10.1002/bies.201100106>.
- (92) Pantazis, P.; Maloney, J.; Wu, D.; Fraser, S. E. Second Harmonic Generating (SHG) Nanoprobes for in Vivo Imaging. *Proc. Natl. Acad. Sci. U. S. A.* **2010**, *107* (33), 14535–14540. <https://doi.org/10.1073/pnas.1004748107>.
- (93) Bonacina, L. Nonlinear Nanomedicine: Harmonic Nanoparticles toward Targeted Diagnosis and Therapy. *Mol. Pharm.* **2013**, *10*, 783–792. <https://doi.org/10.1021/mp300523e>.
- (94) Le Xuan, L.; Zhou, C.; Slablab, A.; Chauvat, D.; Tard, C.; Perruchas, S.; Gacoin, T.; Villeval, P.; Roch, J.-F.; Le, X. L. Photostable Second-Harmonic Generation from a Single KTiOPO₄ Nanocrystal for Nonlinear Microscopy. *Small* **2008**, *4* (9), 1332–1336. <https://doi.org/10.1002/smll.200701093>.
- (95) Magouroux, T.; Extermann, J.; Hoffmann, P.; Mugnier, Y.; Le Dantec, R.; Jaconi, M. E.; Kasparian, C.; Ciepielewski, D.; Bonacina, L.; Wolf, J.-P. High-Speed Tracking of Murine Cardiac Stem Cells by Harmonic Nanodoublers. *Small* **2012**, *8* (17), 2752–2756. <https://doi.org/10.1002/smll.201200366>.
- (96) Extermann, J.; Bonacina, L.; Cuña, E.; Kasparian, C.; Mugnier, Y.; Feurer, T.; Wolf, J.-P. Nanodoublers as Deep Imaging Markers for Multi-Photon Microscopy. *Opt. Express* **2009**, *17* (17), 15342–15349.
- (97) Rogov, A.; Irondelle, M.; Ramos Gomes, F.; Bode, J.; Staedler, D.; Passemard, S.; Courvoisier, S.; Yamamoto, Y.; Waharte, F.; Ciepielewski, D.; et al. Simultaneous Multiharmonic Imaging of Nanoparticles in Tissues for Increased Selectivity. *ACS Photonics* **2015**, *2* (10), 1416–1422.
- (98) Staedler, D.; Passemard, S.; Magouroux, T.; Rogov, A.; Maguire, C. M.; Mohamed, B. M.; Schwung, S.; Rytz, D.; Jüstel, T.; Hwu, S.; et al. Cellular Uptake and Biocompatibility of Bismuth Ferrite Harmonic Advanced Nanoparticles. *Nanomedicine Nanotechnol. Biol. Med.* **2015**, *11* (4), 815–824.
- (99) Selbach, S. M.; Einarsrud, M.; Grande, T. On the Thermodynamic Stability of BiFeO₃. *Chem Mater* **2009**, *21*, 169–173.
- (100) Rojac, T.; Bencan, A.; Malic, B.; Tutunçu, G.; Jones, J. L.; Daniels, J. E.; Damjanovic, D. BiFeO₃ Ceramics: Processing, Electrical, and Electromechanical Properties. *J. Am. Ceram. Soc.* **2014**, *97* (7), 1993–2011.
- (101) Mao, Y.; Park, T.-J.; Wong, S. S. Synthesis of Classes of Ternary Metal Oxide Nanostructures. *Chem. Commun.* **2005**, No. 46, 5721–5735.
- (102) Popa, M.; Crespo, D.; Calderon-Moreno, J. M.; Preda, S.; Fruth, V. Synthesis and Structural Characterization of Single-Phase BiFeO₃ Powders from a Polymeric Precursor. *J. Am. Ceram. Soc.* **2007**, *90* (9), 2723–2727.
- (103) Yang, H.; Xian, T.; Wei, Z. Q.; Dai, J. F.; Jiang, J. L.; Feng, W. J. Size-Controlled Synthesis of BiFeO₃ Nanoparticles by a Soft-Chemistry Route. *J. Sol-Gel Sci. Technol.* **2011**, *58* (1), 238–243.
- (104) Das, N.; Majumdar, R.; Sen, A.; Maiti, H. S. Nanosized Bismuth Ferrite Powder Prepared through Sonochemical and Microemulsion Techniques. *Mater. Lett.* **2007**, *61*, 2100–2104. <https://doi.org/10.1016/j.matlet.2006.08.026>.
- (105) Prado-Gonjal, J.; Villafuerte-Castrejón, M. E.; Fuentes, L.; Moran, E. Microwave–Hydrothermal Synthesis of the Multiferroic BiFeO₃. *Mater. Res. Bull.* **2009**, *44* (8), 1734–1737.
- (106) Zhang, H.; Kajiyoshi, K. Hydrothermal Synthesis and Size-Dependent Properties of Multiferroic Bismuth Ferrite Crystallites. *J. Am. Ceram. Soc.* **2010**, *93* (11), 3842–3849.
- (107) Yang, J.; Li, X.; Zhou, J.; Tang, Y.; Zhang, Y.; Li, Y. Factors Controlling Pure-Phase Magnetic BiFeO₃ Powders Synthesized by Solution Combustion Synthesis. *J. Alloys Compd.* **2011**, *509* (37), 9271–9277.
- (108) Han, J.-T.; Huang, Y.-H.; Wu, X.-J.; Wu, C.-L.; Wei, W.; Peng, B.; Huang, W.; Goodenough, J. B. Tunable Synthesis of Bismuth Ferrites with Various Morphologies. *Adv. Mater.* **2006**, *18* (16), 2145–2148.

- (109) Teng, C.; Xie, D.; Sun, M.; Xu, J.; Zhao, C. Sucrose-Templated Nanoporous BiFeO₃ for Promising Magnetically Recoverable Multifunctional Environment-Purifying Applications: Adsorption and Photocatalysis. *RSC Adv.* **2016**, *6*, 67550–67555. <https://doi.org/10.1039/C6RA12413E>.
- (110) Chen, C.; Ā, J. C.; Yu, S.; Che, L.; Meng, Z. Hydrothermal Synthesis of Perovskite Bismuth Ferrite Crystallites. *J. Cryst. Growth* **2006**, *291*, 135–139. <https://doi.org/10.1016/j.jcrysgro.2006.02.048>.
- (111) Farhadi, S.; Zaidi, M. Bismuth Ferrite (BiFeO₃) Nanopowder Prepared by Sucrose-Assisted Combustion Method: A Novel and Reusable Heterogeneous Catalyst for Acetylation of Amines, Alcohols and Phenols under Solvent-Free Conditions. *J. Mol. Catal. Chem.* **2009**, *299* (1), 18–25.
- (112) Han, S. H.; Kim, K. S.; Kim, H. G.; Lee, H.-G.; Kang, H.-W.; Kim, J. S.; Cheon, C. II. Synthesis and Characterization of Multiferroic BiFeO₃ Powders Fabricated by Hydrothermal Method. *Ceram. Int.* **2010**, *36* (4), 1365–1372.
- (113) Wang, Y.; Xu, G.; Ren, Z.; Wei, X.; Weng, W.; Du, P.; Shen, G.; Han, G. Low Temperature Polymer Assisted Hydrothermal Synthesis of Bismuth Ferrite Nanoparticles. *Ceram. Int.* **2008**, *34* (6), 1569–1571.
- (114) Rashad, M. M. Effect of Synthesis Conditions on the Preparation of BiFeO₃ Nanopowders Using Two Different Methods. *J. Mater. Sci. Mater. Electron.* **2012**, *23* (4), 882–888.
- (115) Aguiar, E. C.; Ramirez, M. A.; Moura, F.; Varela, J. A.; Longo, E.; Simoes, A. Z. Low-Temperature Synthesis of Nanosized Bismuth Ferrite by the Soft Chemical Method. *Ceram. Int.* **2013**, *39* (1), 13–20.
- (116) Ghosh, S.; Dasgupta, S.; Sen, A.; Sekhar Maiti, H. Low-Temperature Synthesis of Nanosized Bismuth Ferrite by Soft Chemical Route. *J. Am. Ceram. Soc.* **2005**, *88* (5), 1349–1352.
- (117) Selbach, S. M.; Einarsrud, M.-A.; Tybell, T.; Grande, T. Synthesis of BiFeO₃ by Wet Chemical Methods. *J. Am. Ceram. Soc.* **2007**, *90* (11), 3430–3434.
- (118) Prasad, P. N. *Introduction to Nanomedicine and Nanobioengineering*; Wiley series in biomedical engineering and multidisciplinary integrated systems; John Wiley & Sons: Hoboken, N.J, 2012.
- (119) Bloemen, M.; Brullot, W.; Luong, T. T.; Geukens, N.; Gils, A.; Verbiest, T. Improved Functionalization of Oleic Acid-Coated Iron Oxide Nanoparticles for Biomedical Applications. *J. Nanoparticle Res.* **2012**, *14* (9), 1–10. <https://doi.org/10.1007/s11051-012-1100-5>.
- (120) Ito, A.; Shinkai, M.; Honda, H.; Kobayashi, T. Medical Application of Functionalized Magnetic Nanoparticles. *J. Biosci. Bioeng.* **2005**, *100* (1), 1–11. <https://doi.org/10.1263/jbb.100.1>.
- (121) Laurent, S.; Forge, D.; Port, M.; Roch, A.; Robic, C.; Vander Elst, L.; Muller, R. N. Magnetic Iron Oxide Nanoparticles: Synthesis, Stabilization, Vectorization, Physicochemical Characterizations, and Biological Applications. *Chem. Rev.* **2008**, *108* (6), 2064–2110. <https://doi.org/10.1021/cr068445e>.
- (122) Brinker, C. J.; Scherer, G. W. *Sol-Gel Science: The Physics and Chemistry of Sol-Gel Processing*; Academic Press: Boston, 1990.
- (123) Chen, C. -c; Liu, Y. -c; Wu, C. -h; Yeh, C. -c; Su, M. -t; Wu, Y. -c. Preparation of Fluorescent Silica Nanotubes and Their Application in Gene Delivery. *Adv. Mater.* **2005**, *17* (4), 404–407. <https://doi.org/10.1002/adma.200400966>.
- (124) McCarthy, S. A.; Davies, G.-L.; Gun'ko, Y. K. Preparation of Multifunctional Nanoparticles and Their Assemblies. *Nat. Protoc.* **2012**, *7* (9), 1677–1693. <https://doi.org/10.1038/nprot.2012.082>.
- (125) Coleman, N. R. B.; O'Sullivan, N.; Ryan, K. M.; Crowley, T. A.; Morris, M. A.; Spalding, T. R.; Steytler, D. C.; Holmes, J. D. Synthesis and Characterization of Dimensionally Ordered Semiconductor Nanowires within Mesoporous Silica. *J Am Chem Soc* **2001**, *123* (29), 7010–7016. <https://doi.org/10.1021/ja015833j>.
- (126) Crowley, T. A.; Ziegler, K. J.; Lyons, D. M.; Erts, D.; Olin, H.; Morris, M. A.; Holmes, J. D. Synthesis of Metal and Metal Oxide Nanowire and Nanotube Arrays within a Mesoporous Silica Template. *Chem Mater* **2003**, *15* (18), 3518–3522. <https://doi.org/10.1021/cm034139v>.

- (127) Wu, Y.; Livneh, T.; Zhang, Y. X.; Cheng, G.; Wang, J.; Tang, J.; Moskovits, M.; Stucky, G. D. Templated Synthesis of Highly Ordered Mesosstructured Nanowires and Nanowire Arrays. *Nano Lett* **2004**, *4* (12), 2337–2342. <https://doi.org/10.1021/nl048653r>.
- (128) Yang, Z.; Niu, Z.; Cao, X.; Yang, Z.; Lu, Y.; Hu, Z.; Han, C. C. Template Synthesis of Uniform 1D Mesosstructured Silica Materials and Their Arrays in Anodic Alumina Membranes. *Angew. Chem. Int. Ed.* **2003**, *42* (35), 4201–4203. <https://doi.org/10.1002/anie.200250808>.
- (129) Massart, R.; Cabuil, V. Effect of Some Parameters on the Formation of Colloidal Magnetite in Alkaline-Medium - Yield and Particle-Size Control. *J. Chim. Phys. Phys.-Chim. Biol.* **1987**, *84* (7–8), 967–973.
- (130) Baumgartner, J.; Dey, A.; Bomans, P. H. H.; Le Coadou, C.; Fratzl, P.; Sommerdijk, N. A. J. M.; Faivre, D. Nucleation and Growth of Magnetite from Solution. *Nat. Mater.* **2013**, *12* (4), 310–314. <https://doi.org/10.1038/nmat3558>.
- (131) Li, Z.; Chen, H.; Bao, H.; Gao, M. One-Pot Reaction to Synthesize Water-Soluble Magnetite Nanocrystals. *Chem. Mater.* **2004**, *16* (8), 1391–1393. <https://doi.org/10.1021/cm035346y>.
- (132) Ghosh, S.; Dasgupta, S.; Sen, A.; Sekhar Maiti, H. Low-Temperature Synthesis of Nanosized Bismuth Ferrite by Soft Chemical Route. *J. Am. Ceram. Soc.* **2005**, *88* (5), 1349–1352. <https://doi.org/10.1111/j.1551-2916.2005.00306.x>.
- (133) Barsoum, M. W. *Fundamentals of Ceramics*, 2. print.; Series in materials science and engineering; IOP: Bristol, 2003.
- (134) West, A. R. *Solid State Chemistry and Its Applications*; John Wiley and Sons: Chichester, 2004.
- (135) Catalan, G.; Scott, J. F. Physics and Applications of Bismuth Ferrite. *Adv. Mater.* **2009**, *21* (24), 2463–2485. <https://doi.org/10.1002/adma.200802849>.
- (136) Kreyszig, E. *Advanced Engineering Mathematics*; John Wiley & Sons, 2010.
- (137) Blaney, L. Magnetite (Fe₃O₄): Properties, Synthesis, and Applications. **2007**.
- (138) Cornell, R. M.; Schwertmann, U. *The Iron Oxides Structure, Properties, Reactions, Occurrences and Uses*; Wiley-VCH: Weinheim, 2006.
- (139) Jafari, A.; Farjami Shayesteh, S.; Salouti, M.; Boustani, K. Effect of Annealing Temperature on Magnetic Phase Transition in Fe₃O₄ Nanoparticles. *J. Magn. Magn. Mater.* **2015**, *379*, 305–312. <https://doi.org/10.1016/j.jmmm.2014.12.050>.
- (140) Yue, M.; Si, J.; Yan, L.; Yu, Y.; Hou, X. Enhanced Nonlinear Optical Properties of Reduced Graphene Oxide Decorated with Silver Nanoparticles. *Opt. Mater. Express* **2018**, *8* (3), 698. <https://doi.org/10.1364/OME.8.000698>.
- (141) Koudoumas, E.; Konstantaki, M.; Mavromanolakis, A.; Couris, S.; Fanti, M.; Zerbetto, F.; Kordatos, K.; Prato, M. Large Enhancement of the Nonlinear Optical Response of Reduced Fullerene Derivatives. *Chem. - Eur. J.* **2003**, *9* (7), 1529–1534. <https://doi.org/10.1002/chem.200390175>.
- (142) Ismailzade, I. G. X-Ray Diffraction Study of Phase Transitions in Bismuth Ferrite. *Dokl. Akad. Nauk Sssr* **1966**, *170* (1), 85-.
- (143) Klug, H. P.; Alexander, L. E. *X-Ray Diffraction Procedures for Polycrystalline and Amorphous Materials*, 2d ed.; Wiley: New York, 1974.
- (144) Cullity, B. D. *Elements Of X Ray Diffraction*; Addison-Wesley Publishing Company, Inc., 1956.
- (145) Patterson, A. L. The Scherrer Formula for X-Ray Particle Size Determination. *Phys. Rev.* **1939**, *56* (10), 978–982. <https://doi.org/10.1103/PhysRev.56.978>.
- (146) Le Dantec, R.; Mugnier, Y.; Djanta, G.; Bonacina, L.; Extermann, J.; Badie, L.; Joulaud, C.; Germann, M.; Rytz, D.; Wolf, J. P.; et al. Ensemble and Individual Characterization of the Nonlinear Optical Properties of ZnO and BaTiO₃ Nanocrystals. *J. Phys. Chem. C* **2011**, *115* (31), 15140–15146. <https://doi.org/10.1021/jp200579x>.

- (147) Einstein, A. Theorie Der Opaleszenz von Homogenen Flüssigkeiten Und Flüssigkeitsgemischen in Der Nähe Des Kritischen Zustandes. *Ann. Phys.* **1910**, 338 (16), 1275–1298. <https://doi.org/10.1002/andp.19103381612>.
- (148) Tscharnuter, W. Photon Correlation Spectroscopy in Particle Sizing. *Encycl. Anal. Chem.* **2000**.
- (149) Hiemenz, P. C.; Rajagopalan, R. *Principles of Colloid and Surface Chemistry*; Marcel Dekker, 1997.
- (150) Hackley, V. A. *Measuring the Size of Nanoparticles in Aqueous Media Using Batch-Mode Dynamic Light Scattering*; NIST SP 1200-6; National Institute of Standards and Technology, 2015.
- (151) Delgado, A. V.; González-Caballero, F.; Hunter, R. J.; Koopal, L. K.; Lyklema, J. Measurement and Interpretation of Electrokinetic Phenomena (IUPAC Technical Report). *Pure Appl. Chem.* **2005**, 77 (10), 1753–1805. <https://doi.org/10.1351/pac200577101753>.
- (152) Echlin, P. *Handbook of Sample Preparation for Scanning Electron Microscopy and X-Ray Microanalysis*; Springer Science & Business Media, 2011.
- (153) Shimizu, K.; Mitani, T. *New Horizons of Applied Scanning Electron Microscopy*; Springer Science & Business Media, 2009.
- (154) Ayache, J.; Beaunier, L.; Boumendil, J.; Ehret, G.; Laub, D. *Sample Preparation Handbook for Transmission Electron Microscopy: Methodology*; Springer Science & Business Media, 2010.
- (155) Kole, F.; Guan, Y.; Konicek, P. Measurement of Silica Particles by Transmission Electron Microscope.
- (156) Williams, D. B.; Carter, C. B. *Transmission Electron Microscopy: A Textbook for Materials Science*; Springer Science & Business Media, 2009.
- (157) Goodhew, P. J.; Humphreys, F. J. *Electron Microscopy And Analysis*; CRC Press, 1988.
- (158) Smith, D. O. Development of a Vibrating-Coil Magnetometer. *Rev. Sci. Instrum.* **1956**, 27 (5), 261–268. <https://doi.org/10.1063/1.1715538>.
- (159) Kumar, A.; Rai, R. C.; Podraza, N. J.; Denev, S.; Ramirez, M.; Chu, Y.-H.; Martin, L. W.; Ihlefeld, J.; Heeg, T.; Schubert, J.; et al. Linear and Nonlinear Optical Properties of BiFeO₃. *Appl. Phys. Lett.* **2008**, 92 (12), 121915. <https://doi.org/10.1063/1.2901168>.
- (160) Selbach, S. M.; Einarsrud, M.-A.; Tybell, T.; Grande, T. Synthesis of BiFeO₃ by Wet Chemical Methods. *J. Am. Ceram. Soc.* **2007**, 90 (11), 3430–3434. <https://doi.org/10.1111/j.1551-2916.2007.01937.x>.
- (161) ISO/TC 24/SC 4, P. characterization. ISO 22412 Particle Size Analysis — Dynamic Light Scattering (DLS). International Organization for Standardization 2017.
- (162) Caputo, F.; Clogston, J.; Calzolari, L.; Rösslein, M.; Prina-Mello, A. Measuring Particle Size Distribution of Nanoparticle Enabled Medicinal Products, the Joint View of EUNCL and NCI-NCL. A Step by Step Approach Combining Orthogonal Measurements with Increasing Complexity. *J. Controlled Release* **2019**, 299, 31–43. <https://doi.org/10.1016/j.jconrel.2019.02.030>.
- (163) Baba, K.; Nishida, K. Single-Molecule Tracking in Living Cells Using Single Quantum Dot Applications. *Theranostics* **2012**, 2 (7), 655–667. <https://doi.org/10.7150/thno.3890>.
- (164) Kumar, A.; Murari, N. M.; Katiyar, R. S. Probing the Ferroelectric Phase Transition in Sol-Gel-Derived Polycrystalline Bismuth Ferrite Thin Films. *J. Raman Spectrosc.* **2008**, 39 (9), 1262–1267. <https://doi.org/10.1002/jrs.1984>.
- (165) Schwung, S.; Rogov, A.; Clarke, G.; Joulaud, C.; Magouroux, T.; Staedler, D.; Passemard, S.; Jüstel, T.; Badie, L.; Galez, C.; et al. Nonlinear Optical and Magnetic Properties of BiFeO₃ Harmonic Nanoparticles. *J. Appl. Phys.* **2014**, 116 (11), 114306. <https://doi.org/10.1063/1.4895836>.
- (166) Liu, Y.; Li, Y.; Li, X.-M.; He, T. Kinetics of (3-Aminopropyl)Triethoxysilane (APTES) Silanization of Superparamagnetic Iron Oxide Nanoparticles. *Langmuir* **2013**, 29 (49), 15275–15282. <https://doi.org/10.1021/la403269u>.
- (167) Chong, A. S. M.; Zhao, X. S. Functionalization of SBA-15 with APTES and Characterization of Functionalized Materials. *J. Phys. Chem. B* **2003**, 107 (46), 12650–12657.

- (168) Williams, D. F. On the Mechanisms of Biocompatibility. *Biomaterials* **2008**, *29* (20), 2941–2953. <https://doi.org/10.1016/j.biomaterials.2008.04.023>.
- (169) Dupraz, A. M. P.; Meer, S. A. T. v d; Wijn, J. R. D.; Goedemoed, J. H. Biocompatibility Screening of Silane-Treated Hydroxyapatite Powders, for Use as Filler in Resorbable Composites. *J. Mater. Sci. Mater. Med.* **1996**, *7* (12), 731–738. <https://doi.org/10.1007/BF00121408>.
- (170) Malvindi, M. A.; De Matteis, V.; Galeone, A.; Brunetti, V.; Anyfantis, G. C.; Athanassiou, A.; Cingolani, R.; Pompa, P. P. Toxicity Assessment of Silica Coated Iron Oxide Nanoparticles and Biocompatibility Improvement by Surface Engineering. *PLoS ONE* **2014**, *9* (1), e85835. <https://doi.org/10.1371/journal.pone.0085835>.
- (171) Brannon-Peppas, L.; Blanchette, J. O. Nanoparticle and Targeted Systems for Cancer Therapy. *Adv. Drug Deliv. Rev.* **2004**, *56* (11), 1649–1659. <https://doi.org/10.1016/j.addr.2004.02.014>.
- (172) *Robbins Basic Pathology*, 9th ed.; Kumar, V., Abbas, A. K., Aster, J. C., Robbins, S. L., Eds.; Elsevier/Saunders: Philadelphia, PA, 2013.
- (173) Harari, P. M.; Huang, S.-M. *Modulation of Molecular Targets to Enhance Radiation*; AACR, 2000.
- (174) Minkovsky, N.; Berezov, A. BIBW-2992, a Dual Receptor Tyrosine Kinase Inhibitor for the Treatment of Solid Tumors. *Curr. Opin. Investig. Drugs Lond. Engl.* **2008**, *9* (12), 1336–1346.
- (175) Riely, G. J. Second-Generation Epidermal Growth Factor Receptor Tyrosine Kinase Inhibitors in Non-Small Cell Lung Cancer. *J. Thorac. Oncol. Off. Publ. Int. Assoc. Study Lung Cancer* **2008**, *3* (6 Suppl 2), S146-149. <https://doi.org/10.1097/JTO.0b013e318174e96e>.
- (176) Lucas, L.; Chen, X. K.; Smith, A. J.; Korbelik, M.; Zeng, H.; Lee, P. W. K.; Hewitt, K. C. Aggregation of Nanoparticles in Endosomes and Lysosomes Produces Surface-Enhanced Raman Spectroscopy. *J. Nanophotonics* **2015**, *9* (1), 093094. <https://doi.org/10.1117/1.JNP.9.093094>.
- (177) Bocharov, E. V.; Bragin, P. E.; Pavlov, K. V.; Bocharova, O. V.; Mineev, K. S.; Polyansky, A. A.; Volynsky, P. E.; Efremov, R. G.; Arseniev, A. S. The Conformation of the Epidermal Growth Factor Receptor Transmembrane Domain Dimer Dynamically Adapts to the Local Membrane Environment. *Biochemistry* **2017**, *56* (12), 1697–1705. <https://doi.org/10.1021/acs.biochem.6b01085>.
- (178) Calero, M.; Chiappi, M.; Lazaro-Carrillo, A.; Rodríguez, M. J.; Chichón, F. J.; Crosbie-Staunton, K.; Prina-Mello, A.; Volkov, Y.; Villanueva, A.; Carrascosa, J. L. Characterization of Interaction of Magnetic Nanoparticles with Breast Cancer Cells. *J. Nanobiotechnology* **2015**, *13* (1), 16.
- (179) Kobayashi, K.; Hagiwara, K. Epidermal Growth Factor Receptor (EGFR) Mutation and Personalized Therapy in Advanced Nonsmall Cell Lung Cancer (NSCLC). *Target. Oncol.* **2013**, *8* (1), 27–33. <https://doi.org/10.1007/s11523-013-0258-9>.
- (180) Sreeja, V.; Jayaprabha, K. N.; Joy, P. A. Water-Dispersible Ascorbic-Acid-Coated Magnetite Nanoparticles for Contrast Enhancement in MRI. *Appl. Nanosci.* **2014**, *5* (4), 435–441. <https://doi.org/10.1007/s13204-014-0335-0>.
- (181) Riemer, J.; Hoepken, H. H.; Czerwinska, H.; Robinson, S. R.; Dringen, R. Colorimetric Ferrozine-Based Assay for the Quantitation of Iron in Cultured Cells. *Anal. Biochem.* **2004**, *331* (2), 370–375. <https://doi.org/10.1016/j.ab.2004.03.049>.
- (182) Thompson, G. L.; Reukov, V. V.; Nikiforov, M. P.; Jesse, S.; Kalinin, S. V.; Vertegel, A. A. Electromechanical and Elastic Probing of Bacteria in a Cell Culture Medium. *Nanotechnology* **2012**, *23* (24), 245705. <https://doi.org/10.1088/0957-4484/23/24/245705>.
- (183) Tripathi, K.; Driskell, J. D. Quantifying Bound and Active Antibodies Conjugated to Gold Nanoparticles: A Comprehensive and Robust Approach To Evaluate Immobilization Chemistry. *ACS Omega* **2018**, *3* (7), 8253–8259. <https://doi.org/10.1021/acsomega.8b00591>.
- (184) Tsubaki, M. Fourier-Transform Infrared Study of Azide Binding to the Fea3-CuB Binuclear Site of Bovine Heart Cytochrome c Oxidase: New Evidence for a Redox-Linked Conformational Change at the Binuclear Site. *Biochemistry* **1993**, *32* (1), 174–182.

- (185) Burns, A. Development and Applications of Fluorescent Core-Shell Silica Nanoparticles for Bioimaging and Sensing. **2008**.
- (186) Seabra, A.; Durán, N. Nanotoxicology of Metal Oxide Nanoparticles. *Metals* **2015**, *5* (2), 934–975. <https://doi.org/10.3390/met5020934>.
- (187) AshaRani, P. V.; Low Kah Mun, G.; Hande, M. P.; Valiyaveetil, S. Cytotoxicity and Genotoxicity of Silver Nanoparticles in Human Cells. *ACS Nano* **2009**, *3* (2), 279–290. <https://doi.org/10.1021/nn800596w>.
- (188) Park, M. V. D. Z.; Neigh, A. M.; Vermeulen, J. P.; de la Fonteyne, L. J. J.; Verharen, H. W.; Briedé, J. J.; van Loveren, H.; de Jong, W. H. The Effect of Particle Size on the Cytotoxicity, Inflammation, Developmental Toxicity and Genotoxicity of Silver Nanoparticles. *Biomaterials* **2011**, *32* (36), 9810–9817. <https://doi.org/10.1016/j.biomaterials.2011.08.085>.
- (189) Buzea, C.; Pacheco, I. I.; Robbie, K. Nanomaterials and Nanoparticles: Sources and Toxicity. *Biointerphases* **2007**, *2* (4), MR17–MR71. <https://doi.org/10.1116/1.2815690>.
- (190) Johnston, H. J.; Hutchison, G.; Christensen, F. M.; Peters, S.; Hankin, S.; Stone, V. A Review of the in Vivo and in Vitro Toxicity of Silver and Gold Particulates: Particle Attributes and Biological Mechanisms Responsible for the Observed Toxicity. *Crit. Rev. Toxicol.* **2010**, *40* (4), 328–346. <https://doi.org/10.3109/10408440903453074>.
- (191) Lewinski, N.; Colvin, V.; Drezek, R. Cytotoxicity of Nanoparticles. *Small* **2008**, *4* (1), 26–49. <https://doi.org/10.1002/smll.200700595>.
- (192) Pan, Y.; Neuss, S.; Leifert, A.; Fischler, M.; Wen, F.; Simon, U.; Schmid, G.; Brandau, W.; Jahnke-Dechent, W. Size-Dependent Cytotoxicity of Gold Nanoparticles. *Small* **2007**, *3* (11), 1941–1949. <https://doi.org/10.1002/smll.200700378>.
- (193) Blanco, E.; Shen, H.; Ferrari, M. Principles of Nanoparticle Design for Overcoming Biological Barriers to Drug Delivery. *Nat. Biotechnol.* **2015**, *33* (9), 941–951. <https://doi.org/10.1038/nbt.3330>.
- (194) Rocks, L.; Dawson, K. A. The Interaction between Nanoparticles and Biological Barriers. *Eur. J. Nanomedicine* **2014**, *6* (3), 121–122. <https://doi.org/10.1515/ejnm-2014-0029>.
- (195) Hong, T.-K.; Tripathy, N.; Son, H.-J.; Ha, K.-T.; Jeong, H.-S.; Hahn, Y.-B. A Comprehensive in Vitro and in Vivo Study of ZnO Nanoparticles Toxicity. *J. Mater. Chem. B* **2013**, *1* (23), 2985. <https://doi.org/10.1039/c3tb20251h>.
- (196) Jasmin; Torres, A. L. M.; Jelicks, L.; de Carvalho, A. C. C.; Spray, D. C.; Mendez-Otero, R. Labeling Stem Cells with Superparamagnetic Iron Oxide Nanoparticles: Analysis of the Labeling Efficacy by Microscopy and Magnetic Resonance Imaging. *Methods Mol. Biol. Clifton NJ* **2012**, *906*, 239–252. https://doi.org/10.1007/978-1-61779-953-2_18.
- (197) Calder, S.; Boies, A.; Lei, P.; Girshick, S. Synthesis of Silica-Coated Iron Oxide Nanoparticles for Magnetic Resonance Contrast Enhancement and Thermal Therapies. *J. Med. Devices* **2011**, *5* (2), 027534–1. <https://doi.org/10.1115/1.3591376>.
- (198) Jun, Y.; Lee, J.; Cheon, J. Chemical Design of Nanoparticle Probes for High-Performance Magnetic Resonance Imaging. *Angew. Chem. Int. Ed.* **2008**, *47* (28), 5122–5135. <https://doi.org/10.1002/anie.200701674>.
- (199) Kim, J.; Kim, H. S.; Lee, N.; Kim, T.; Kim, H.; Yu, T.; Song, I. C.; Moon, W. K.; Hyeon, T. Multifunctional Uniform Nanoparticles Composed of a Magnetite Nanocrystal Core and a Mesoporous Silica Shell for Magnetic Resonance and Fluorescence Imaging and for Drug Delivery. *Angew. Chem. Int. Ed.* **2008**, *47* (44), 8438–8441. <https://doi.org/10.1002/anie.200802469>.
- (200) Gupta, A. K.; Wells, S. Surface-Modified Superparamagnetic Nanoparticles for Drug Delivery: Preparation, Characterization, and Cytotoxicity Studies. *IEEE Trans. NanoBioscience* **2004**, *3* (1), 66–73. <https://doi.org/10.1109/TNB.2003.820277>.
- (201) Sun, C.; Lee, J. S. H.; Zhang, M. Magnetic Nanoparticles in MR Imaging and Drug Delivery. *Adv. Drug Deliv. Rev.* **2008**, *60* (11), 1252–1265. <https://doi.org/10.1016/j.addr.2008.03.018>.

- (202) Veiseh, O.; Gunn, J. W.; Zhang, M. Design and Fabrication of Magnetic Nanoparticles for Targeted Drug Delivery and Imaging. *Adv. Drug Deliv. Rev.* **2010**, *62* (3), 284–304. <https://doi.org/10.1016/j.addr.2009.11.002>.
- (203) Ho, D.; Sun, X.; Sun, S. Monodisperse Magnetic Nanoparticles for Theranostic Applications. *Acc. Chem. Res.* **2011**, *44* (10), 875–882. <https://doi.org/10.1021/ar200090c>.
- (204) Kossatz, S.; Grandke, J.; Couleaud, P.; Latorre, A.; Aires, A.; Crosbie-Staunton, K.; Ludwig, R.; Dähling, H.; Ettelt, V.; Lazaro-Carrillo, A.; et al. Efficient Treatment of Breast Cancer Xenografts with Multifunctionalized Iron Oxide Nanoparticles Combining Magnetic Hyperthermia and Anti-Cancer Drug Delivery. *Breast Cancer Res. BCR* **2015**, *17* (1). <https://doi.org/10.1186/s13058-015-0576-1>.
- (205) Kumar, C. S. S. R.; Mohammad, F. Magnetic Nanomaterials for Hyperthermia-Based Therapy and Controlled Drug Delivery. *Adv. Drug Deliv. Rev.* **2011**, *63* (9), 789–808. <https://doi.org/10.1016/j.addr.2011.03.008>.
- (206) Grüttner, C.; Müller, K.; Teller, J.; Westphal, F. Synthesis and Functionalisation of Magnetic Nanoparticles for Hyperthermia Applications. *Int. J. Hyperthermia* **2013**, *29* (8), 777–789. <https://doi.org/10.3109/02656736.2013.835876>.
- (207) Sadhukha, T.; Wiedmann, T. S.; Panyam, J. Inhalable Magnetic Nanoparticles for Targeted Hyperthermia in Lung Cancer Therapy. *Biomaterials* **2013**, *34* (21), 5163–5171. <https://doi.org/10.1016/j.biomaterials.2013.03.061>.
- (208) Di Corato, R.; Espinosa, A.; Lartigue, L.; Tharaud, M.; Chat, S.; Pellegrino, T.; Ménager, C.; Gazeau, F.; Wilhelm, C. Magnetic Hyperthermia Efficiency in the Cellular Environment for Different Nanoparticle Designs. *Biomaterials* **2014**, *35* (24), 6400–6411. <https://doi.org/10.1016/j.biomaterials.2014.04.036>.
- (209) Deatsch, A. E.; Evans, B. A. Heating Efficiency in Magnetic Nanoparticle Hyperthermia. *J. Magn. Magn. Mater.* **2014**, *354*, 163–172. <https://doi.org/10.1016/j.jmmm.2013.11.006>.
- (210) Jordan, A.; Scholz, R.; Wust, P.; Fähling, H.; Felix, R. Magnetic Fluid Hyperthermia (MFH): Cancer Treatment with AC Magnetic Field Induced Excitation of Biocompatible Superparamagnetic Nanoparticles. *J. Magn. Magn. Mater.* **1999**, *201* (1–3), 413–419. [https://doi.org/10.1016/S0304-8853\(99\)00088-8](https://doi.org/10.1016/S0304-8853(99)00088-8).
- (211) Gupta, A. K.; Gupta, M. Cytotoxicity Suppression and Cellular Uptake Enhancement of Surface Modified Magnetic Nanoparticles. *Biomaterials* **2005**, *26* (13), 1565–1573. <https://doi.org/10.1016/j.biomaterials.2004.05.022>.
- (212) Könczöl, M.; Ebeling, S.; Goldenberg, E.; Treude, F.; Gminski, R.; Gieré, R.; Grobéty, B.; Rothen-Rutishauser, B.; Merfort, I.; Mersch-Sundermann, V. Cytotoxicity and Genotoxicity of Size-Fractionated Iron Oxide (Magnetite) in A549 Human Lung Epithelial Cells: Role of ROS, JNK, and NF- κ B. *Chem. Res. Toxicol.* **2011**, *24* (9), 1460–1475. <https://doi.org/10.1021/tx200051s>.
- (213) Li, L.; Mak, K. Y.; Shi, J.; Koon, H. K.; Leung, C. H.; Wong, C. M.; Leung, C. W.; Mak, C. S. K.; Chan, N. M. M.; Zhong, W.; et al. Comparative In Vitro Cytotoxicity Study on Uncoated Magnetic Nanoparticles: Effects on Cell Viability, Cell Morphology, and Cellular Uptake. *J. Nanosci. Nanotechnol.* **2012**, *12* (12), 9010–9017. <https://doi.org/10.1166/jnn.2012.6755>.
- (214) Wohlleben, W.; Kuhlbusch, T. A. J.; Schneidenburger, J.; Lehr, C.-M. *Safety of Nanomaterials along Their Lifecycle: Release, Exposure, and Human Hazards*; CRC Press, 2014.
- (215) Oberdörster, G.; Oberdörster, E.; Oberdörster, J. Nanotoxicology: An Emerging Discipline Evolving from Studies of Ultrafine Particles. *Environ. Health Perspect.* **2005**, *113* (7), 823. <https://doi.org/10.1289/ehp.7339>.
- (216) *Nanotoxicity: From in Vivo and in Vitro Models to Health Risks*; Sahu, S. C., Casciano, D., Eds.; John Wiley: Chichester, West Sussex, UK, 2009.
- (217) Laurent, S.; Burtea, C.; Thirifays, C.; Häfeli, U. O.; Mahmoudi, M. Crucial Ignored Parameters on Nanotoxicology: The Importance of Toxicity Assay Modifications and “Cell Vision.” *PLoS ONE* **2012**, *7* (1), e29997. <https://doi.org/10.1371/journal.pone.0029997>.

- (218) Warheit, D. B. How Meaningful Are the Results of Nanotoxicity Studies in the Absence of Adequate Material Characterization? *Toxicol. Sci.* **2008**, *101* (2), 183–185. <https://doi.org/10.1093/toxsci/kfm279>.
- (219) Prina-Mello, A.; Mohamed, B.; Verma, N.; Jain, N.; Volkov, Y. Advanced Methodologies and Techniques for Assessing Nanomaterials Toxicity: From Manufacturing to Nanomedicine Screening. In *Nanotoxicology: Progress Towards Nanomedicine*; CRC Press, 2014; pp 156–173.
- (220) Staedler, D.; Passemar, S.; Magouroux, T.; Rogov, A.; Maguire, C. M.; Mohamed, B. M.; Schwung, S.; Rytz, D.; Jüstel, T.; Hwu, S.; et al. Cellular Uptake and Biocompatibility of Bismuth Ferrite Harmonic Advanced Nanoparticles. *ArXiv14102068 Phys. Q-Bio* **2014**.
- (221) Nabiev, I.; Mitchell, S.; Davies, A.; Williams, Y.; Kelleher, D.; Moore, R.; Gun'ko, Y. K.; Byrne, S.; Rakovich, Y. P.; Donegan, J. F.; et al. Nonfunctionalized Nanocrystals Can Exploit a Cell's Active Transport Machinery Delivering Them to Specific Nuclear and Cytoplasmic Compartments. *Nano Lett.* **2007**, *7* (11), 3452–3461. <https://doi.org/10.1021/nl0719832>.
- (222) Jan, E.; Byrne, S. J.; Cuddihy, M.; Davies, A. M.; Volkov, Y.; Gun'ko, Y. K.; Kotov, N. A. High-Content Screening as a Universal Tool for Fingerprinting of Cytotoxicity of Nanoparticles. *ACS Nano* **2008**, *2* (5), 928–938. <https://doi.org/10.1021/nn7004393>.
- (223) Mittar, D.; Paramban, R.; McIntyre, C. Flow Cytometry and High-Content Imaging to Identify Markers of Monocyte-Macrophage Differentiation. *BD Biosci.* **2011**, *1*, 1–18.
- (224) Buchser, W.; Collins, M.; Garyantes, T.; Guha, R.; Haney, S.; Lemmon, V.; Li, Z.; Trask, O. J. Assay Development Guidelines for Image-Based High Content Screening, High Content Analysis and High Content Imaging. In *Assay Guidance Manual*; Sittampalam, G. S., Coussens, N. P., Nelson, H., Arkin, M., Auld, D., Austin, C., Bejcek, B., Glicksman, M., Inglese, J., Lemmon, V., et al., Eds.; Eli Lilly & Company and the National Center for Advancing Translational Sciences: Bethesda (MD), 2004.
- (225) Jones, K. H.; Senft, J. A. An Improved Method to Determine Cell Viability by Simultaneous Staining with Fluorescein Diacetate-Propidium Iodide. *J. Histochem. Cytochem.* **1985**, *33* (1), 77–79. <https://doi.org/10.1177/33.1.2578146>.
- (226) Sharifi, S.; Behzadi, S.; Laurent, S.; Forrest, M. L.; Stroeve, P.; Mahmoudi, M. Toxicity of Nanomaterials. *Chem. Soc. Rev.* **2012**, *41* (6), 2323–2343. <https://doi.org/10.1039/C1CS15188F>.
- (227) Klaassen, C. D. *Casarett & Doull's Toxicology: The Basic Science of Poisons, Seventh Edition*; McGraw Hill Professional, 2007.
- (228) Nascarella, M. A.; Calabrese, E. J. A Method to Evaluate Hormesis in Nanoparticle Dose-Responses. *Dose-Response* **2012**, *10* (3), 344–354. <https://doi.org/10.2203/dose-response.10-025.Nascarella>.
- (229) Frescas, D.; Valenti, L.; Accili, D. Nuclear Trapping of the Forkhead Transcription Factor FoxO1 via Sirt-Dependent Deacetylation Promotes Expression of Glucogenetic Genes. *J. Biol. Chem.* **2005**, *280* (21), 20589–20595. <https://doi.org/10.1074/jbc.M412357200>.
- (230) Mattson, M. P.; Cheng, A. Neurohormetic Phytochemicals: Low-Dose Toxins That Induce Adaptive Neuronal Stress Responses. *Trends Neurosci.* **2006**, *29* (11), 632–639. <https://doi.org/10.1016/j.tins.2006.09.001>.
- (231) Mattson, M. P. Hormesis Defined. *Ageing Res. Rev.* **2008**, *7* (1), 1–7. <https://doi.org/10.1016/j.arr.2007.08.007>.
- (232) Mattson, M. P. Dietary Factors, Hormesis and Health. *Ageing Res. Rev.* **2008**, *7* (1), 43–48. <https://doi.org/10.1016/j.arr.2007.08.004>.
- (233) Calabrese, E. J.; Bachmann, K. A.; Bailer, A. J.; Bolger, P. M.; Borak, J.; Cai, L.; Cedergreen, N.; Cherian, M. G.; Chiueh, C. C.; Clarkson, T. W.; et al. Biological Stress Response Terminology: Integrating the Concepts of Adaptive Response and Preconditioning Stress within a Hormetic Dose–Response Framework. *Toxicol. Appl. Pharmacol.* **2007**, *222* (1), 122–128. <https://doi.org/10.1016/j.taap.2007.02.015>.
- (234) Shin, S.-H.; Ye, M.-K.; Kim, H.-S.; Kang, H.-S. The Effects of Nano-Silver on the Proliferation and Cytokine Expression by Peripheral Blood Mononuclear Cells. *Int. Immunopharmacol.* **2007**, *7* (13), 1813–1818. <https://doi.org/10.1016/j.intimp.2007.08.025>.

- (235) Pulskamp, K.; Wörle-Knirsch, J. M.; Hennrich, F.; Kern, K.; Krug, H. F. Human Lung Epithelial Cells Show Biphasic Oxidative Burst after Single-Walled Carbon Nanotube Contact. *Carbon* **2007**, *45* (11), 2241–2249. <https://doi.org/10.1016/j.carbon.2007.06.054>.
- (236) Dobias, J.; Bernier-Latmani, R. Silver Release from Silver Nanoparticles in Natural Waters. *Environ. Sci. Technol.* **2013**, *47* (9), 4140–4146. <https://doi.org/10.1021/es304023p>.
- (237) Ji, S.; Liu, C.; Zhang, B.; Yang, F.; Xu, J.; Long, J.; Jin, C.; Fu, D.; Ni, Q.; Yu, X. Carbon Nanotubes in Cancer Diagnosis and Therapy. *Biochim. Biophys. Acta BBA - Rev. Cancer* **2010**, *1806* (1), 29–35. <https://doi.org/10.1016/j.bbcan.2010.02.004>.
- (238) He, Q.; Shi, J. Mesoporous Silica Nanoparticle Based Nano Drug Delivery Systems: Synthesis, Controlled Drug Release and Delivery, Pharmacokinetics and Biocompatibility. *J. Mater. Chem.* **2011**, *21* (16), 5845–5855. <https://doi.org/10.1039/C0JM03851B>.
- (239) Chavhan, G. B.; Babyn, P. S.; Thomas, B.; Shroff, M. M.; Haacke, E. M. Principles, Techniques, and Applications of T2*-Based MR Imaging and Its Special Applications. *RadioGraphics* **2009**, *29* (5), 1433–1449. <https://doi.org/10.1148/rg.295095034>.
- (240) Jackson, E. F.; Ginsberg, L. E.; Schomer, D. F.; Leeds, N. E. A Review of MRI Pulse Sequences and Techniques in Neuroimaging. *Surg. Neurol.* **1997**, *47* (2), 185–199. [https://doi.org/10.1016/S0090-3019\(96\)00375-8](https://doi.org/10.1016/S0090-3019(96)00375-8).
- (241) Neurauter, A. A.; Bonyhadi, M.; Lien, E.; Nøkleby, L.; Ruud, E.; Camacho, S.; Aarvak, T. Cell Isolation and Expansion Using Dynabeads®. In *Cell Separation*; Kumar, A., Galaev, I. Y., Mattiasson, B., Eds.; Springer Berlin Heidelberg: Berlin, Heidelberg, 2008; Vol. 106, pp 41–73. https://doi.org/10.1007/10_2007_072.
- (242) Magouroux, T.; Extermann, J.; Hoffmann, P.; Mugnier, Y.; Le Dantec, R.; Jaconi, M. E.; Kasparian, C.; Ciepielewski, D.; Bonacina, L.; Wolf, J.-P. High-Speed Tracking of Murine Cardiac Stem Cells by Harmonic Nanodoublers. *Small* **2012**, *8* (17), 2752–2756. <https://doi.org/10.1002/sml.201200366>.
- (243) Tytus, T.; Phelan, O.; Urbain, M.; Clarke, G.; Riporto, J.; Le Dantec, R.; Djanta, G.; Beauquis, S.; Monnier, V.; Chevolut, Y.; et al. Preparation and Preliminary Nonlinear Optical Properties of BiFeO₃ Nanocrystal Suspensions from a Simple, Chelating Agent-Free Precipitation Route <https://www.hindawi.com/journals/jnm/2018/3019586/abs/> (accessed Jun 20, 2019). <https://doi.org/10.1155/2018/3019586>.
- (244) Ding, S.-J.; Nan, F.; Yang, D.-J.; Zhong, Y.-T.; Hao, Z.-H.; Wang, Q.-Q. Tunable Plasmon Resonance and Enhanced Second Harmonic Generation and Upconverted Fluorescence of Hemispheric-like Silver Core/Shell Islands. *Nanoscale* **2015**. <https://doi.org/10.1039/C5NR03627E>.
- (245) Pu, Y.; Grange, R.; Hsieh, C.-L.; Psaltis, D. Nonlinear Optical Properties of Core-Shell Nanocavities for Enhanced Second-Harmonic Generation. *Phys. Rev. Lett.* **2010**, *104*. <https://doi.org/10.1103/PhysRevLett.104.207402>.
- (246) Gayvoronsky, V. Y.; Kopylovsky, M. A.; Brodyn, M. S.; Pritula, I. M.; Kolybaeva, M. I.; Puzikov, V. M. Impact of Incorporated Anatase Nanoparticles on the Second Harmonic Generation in KDP Single Crystals. *Laser Phys. Lett.* **2013**, *10* (3), 035401. <https://doi.org/10.1088/1612-2011/10/3/035401>.
- (247) Hermanson, G. T. *Bioconjugate Techniques*, Third edition.; Elsevier/AP: London ; Waltham, MA, 2013.

Appendices

A1 High Content Screening of primary monocyte-derived macrophages (MDMs)

A1.1 Summary: MDM count after exposure to each of the nanomaterials

The response in MDM cell count to different nanomaterials is presented below (see A 1). See Appendix sections A.1.3.1, A.1.4.1, A.1.5.1, A.1.6.1, A.1.7.1 and A.1.8.1, A.1.9.1, A.1.10.1 and A.1.11.1 for further details.

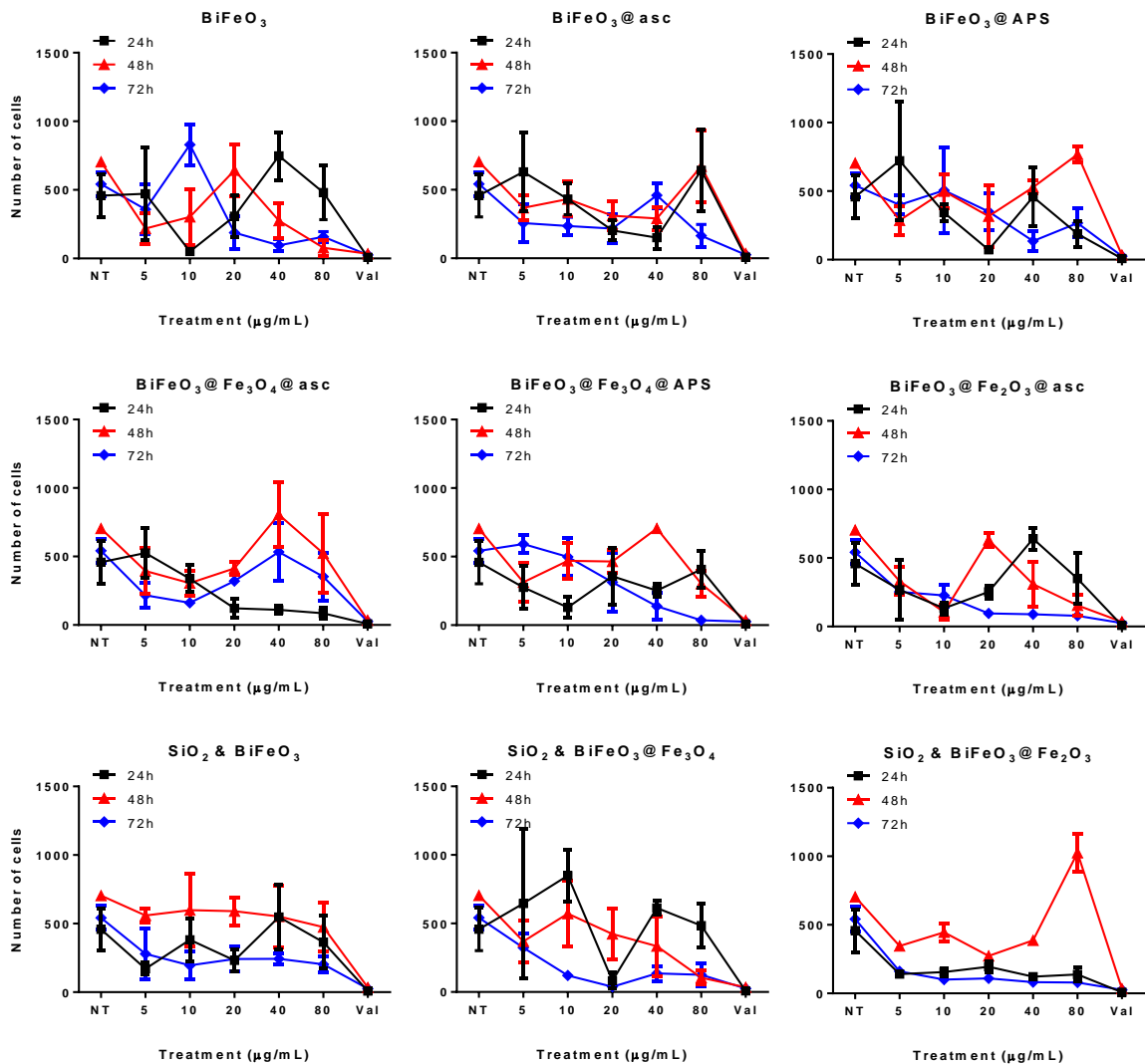


Figure A.1: Number of monocyte-derived macrophages after exposure to each of the nanomaterials.

A1.2 Summary: metabolic activity in primary monocyte-derived macrophages after exposure to each of the nanomaterials

The reduction of resazurin dye to resofurin in MDM in response to different nanomaterials is presented below (see Figure A 2). See Appendix sections A.1.3.2, A.1.4.2, A.1.5.2, A.1.6.2, A.1.7.1 and A.1.8.2, A.1.9.2, A.1.10.2 and A.1.11.2 for further details.

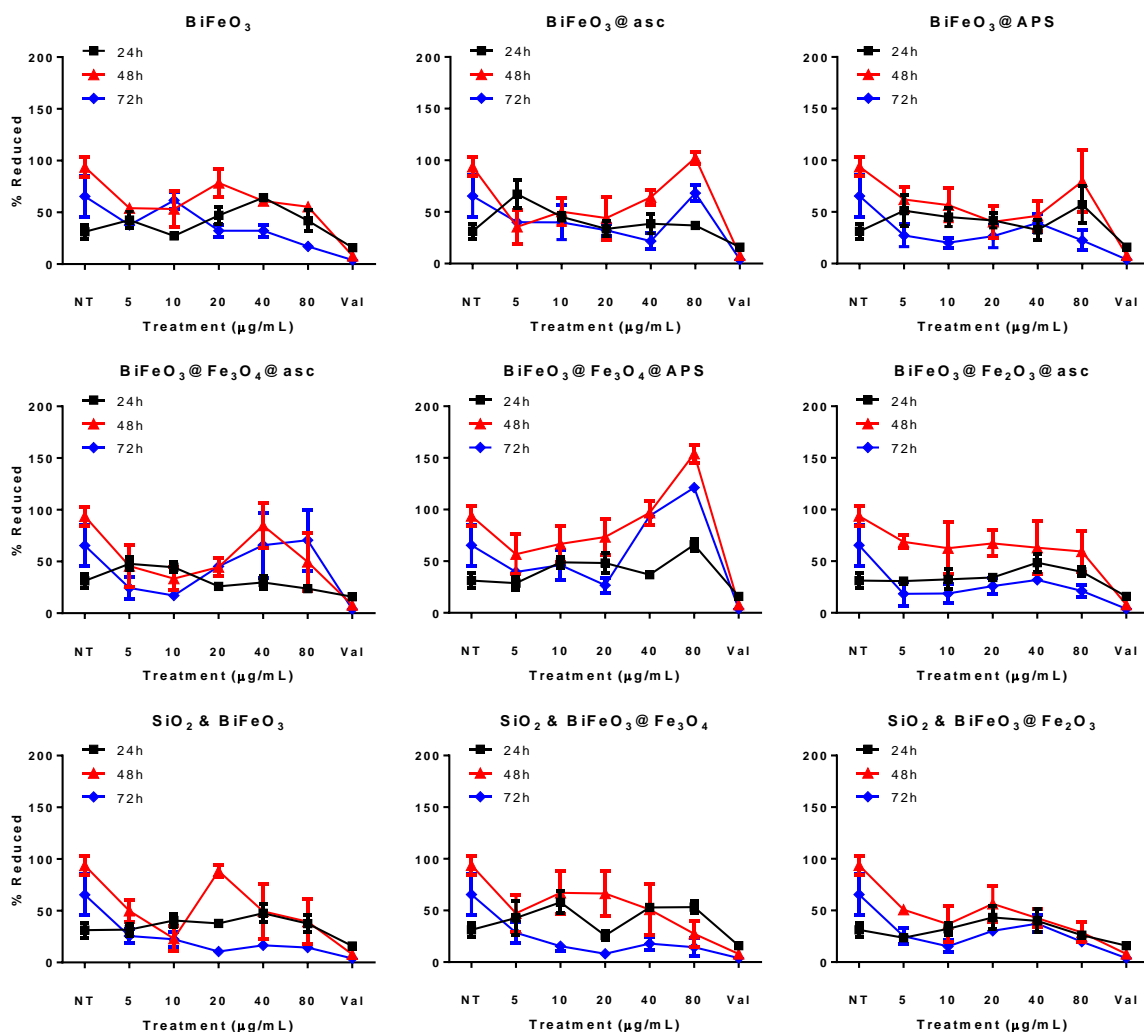


Figure A.2: Reduction of resazurin dye to resofurin in monocyte-derived macrophages after exposure to each of the nanomaterials.

A1.3 MDMs treated with BiFeO_3 NPs

A1.3.1 Cell count

MDMs were treated with BiFeO_3 NPs at 80 µg/mL and stained with Hoechst and imaged with a blue filter (see Figure A.3 and Figure A.4). Cells treated with the positive control (valinomycin, 120 µg/mL)

had lysed and no longer adhered to the plate after 48h. By contrast, untreated cells (NT) proliferated, as did the cells exposed to BiFeO₃ NPs for 24, 48 and 72h.

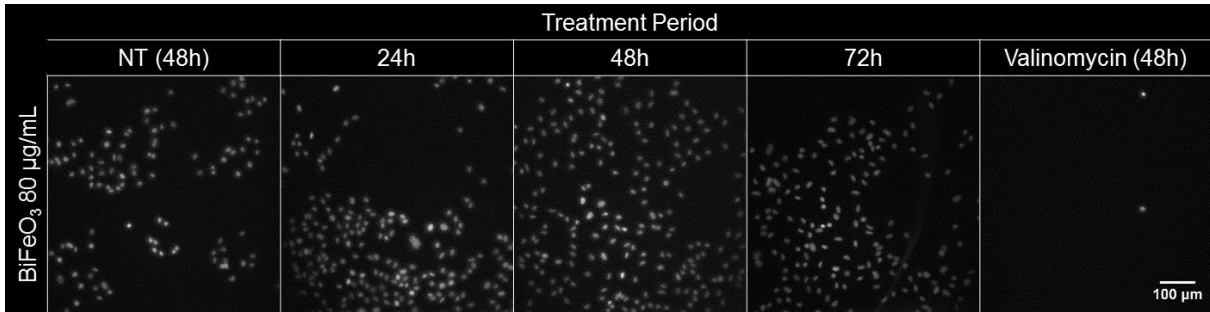


Figure A.3: Representative images of MDMs treated with BiFeO₃ NPs at 80 µg/mL stained with Hoechst. From left: untreated cells after 48h; cells treated with BiFeO₃ for 24h, 48h and 72h; right, cells treated with valinomycin for 48h.

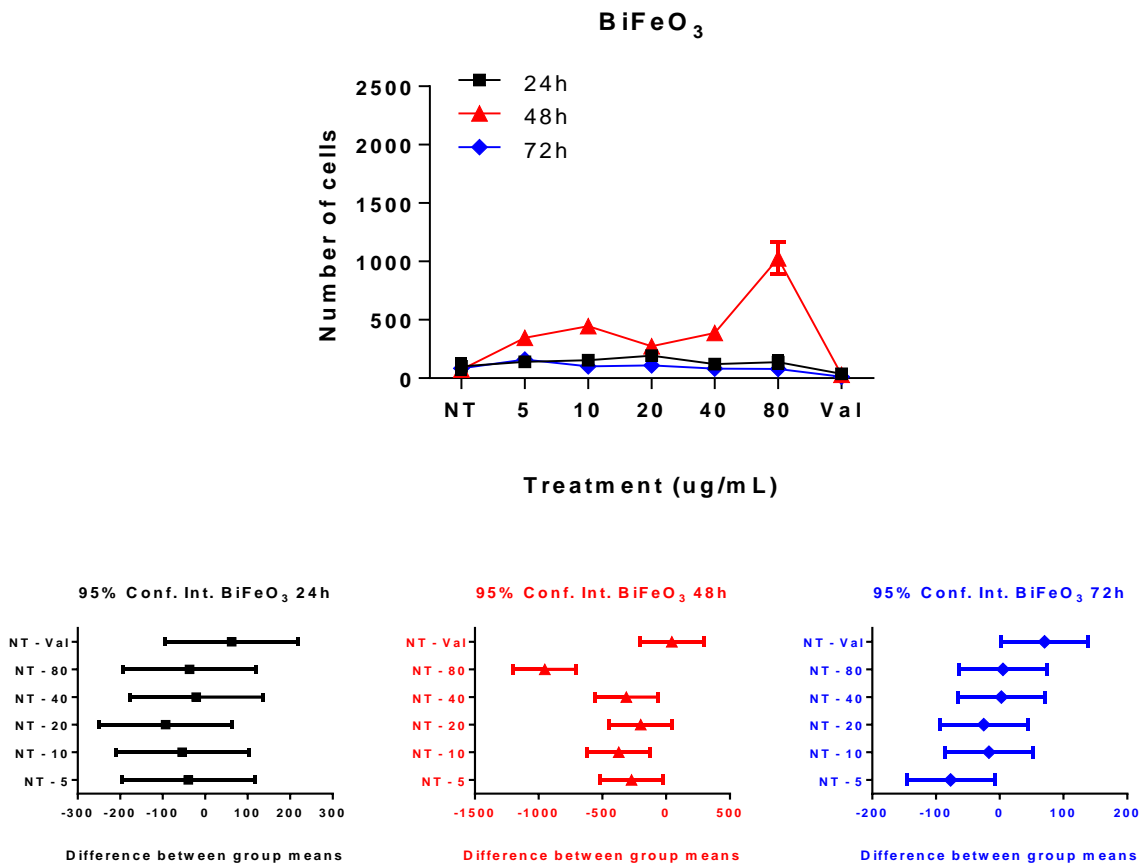


Figure A.4: Cell count of MDMs after treatment with bare BiFeO₃ NPs and the corresponding 95% confidence intervals, computed from ordinary one-way Anova Dunnet analysis.

As can be seen from Figure A.4:

- Samples exposed to BiFeO₃ had approximately the same cell count as the untreated controls after

24h and slightly lower cell counts were observed at higher concentrations.

The number of cells increased significantly after 48h but fell again to approximately the level of the untreated control after 72h, with the largest increase in cell count observed at the highest concentration after 48h.

A1.3.2 Metabolic Activity

Metabolic activity dropped significantly after 24h and continued to fall after 48h and 72h (see Figure A.5).

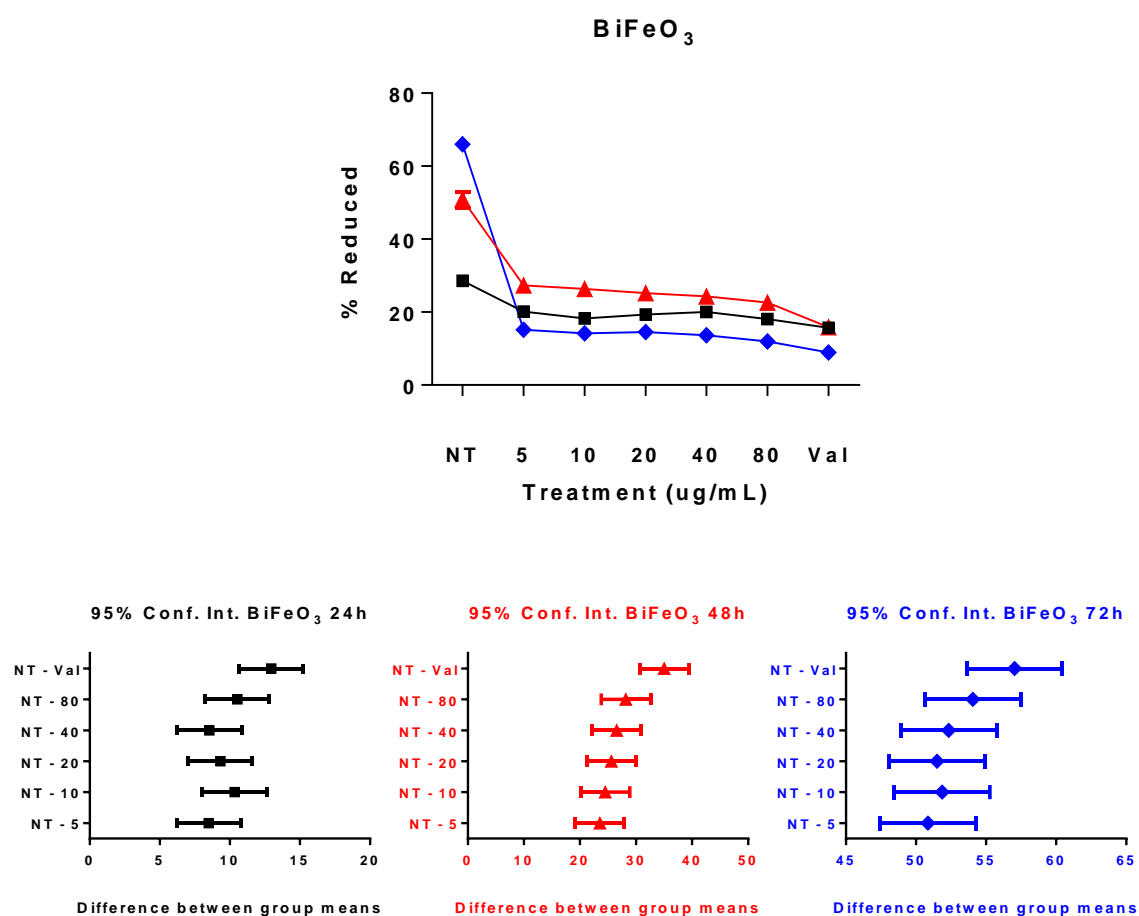


Figure A.5: Metabolic activity in MDMs after exposure to BiFeO₃ NPs. Top: Number of cells vs concentration of nanomaterial; bottom row: 95% confidence intervals between group means after 24h (left), after 48h (middle) and 72h (right). Note: the confidence interval plots show the difference between group means (X-axis) for each of the groups (Y-axis) relative to the untreated control NT.

A1.4 MDMs treated with ascorbic acid-functionalised BiFeO₃ NPs

A1.4.1 Cell count

MDMs were treated with ascorbic acid-functionalised BiFeO₃ (BiFeO₃@asc) NPs at 80 µg/mL, stained with Hoechst and imaged with a blue filter (see Figure A.6 and Figure A.7). Cells treated with the positive control (valinomycin, 120 µg/mL) had lysed and no longer adhered to the plate after 48h. By contrast, untreated cells (NT) proliferated, as did the cells exposed to BiFeO₃ NPs for 24, 48 and 72h.

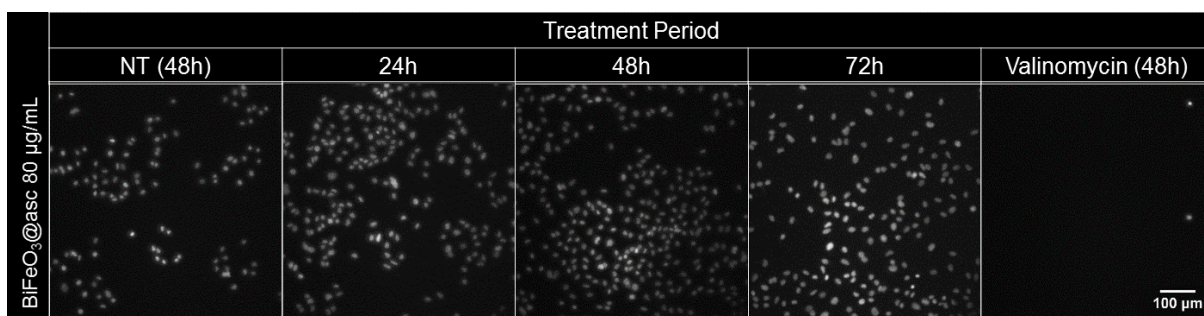


Figure A.6: Representative images of MDMs treated with ascorbic acid-functionalised BiFeO₃ NPs at 80 µg/mL stained with Hoechst. From left: untreated cells after 48h; cells treated with BiFeO₃@asc NPs for 24h, 48h and 72h; right, cells treated with valinomycin for 48h.

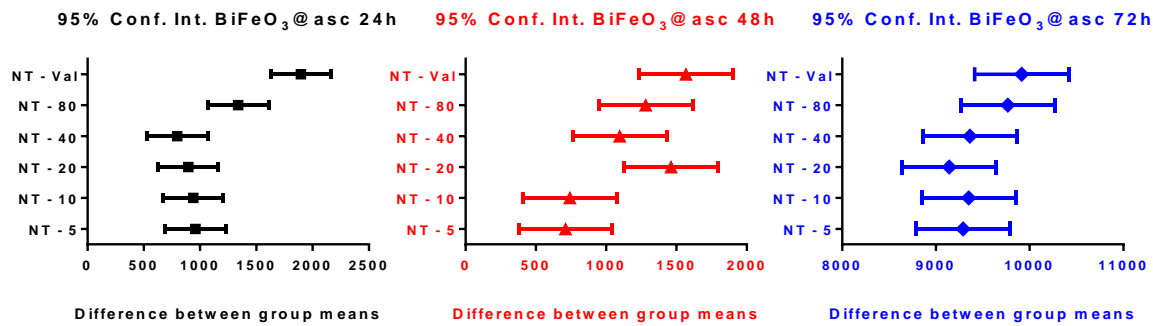
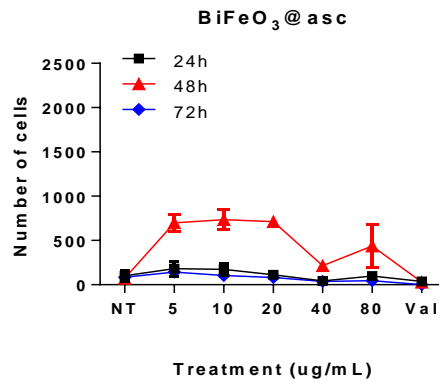


Figure A.7: Cell count of MDMs after treatment with ascorbic acid-functionalised BiFeO_3 NPs and the corresponding 95% confidence intervals, computed from ordinary one-way ANOVA Dunnett analysis.

As can be seen from Figure A.7, cells exposed to $\text{BiFeO}_3@asc$ behaved similarly to those exposed to BiFeO_3 :

- Samples exposed to $\text{BiFeO}_3@asc$ had approximately the same cell count as the untreated controls after 24h and slightly lower cell counts were observed at higher concentrations.
- The number of cells increased significantly after 48h but fell again to approximately the level of the untreated control after 72h, with the largest increase in cell count observed at the highest concentration after 48h.

Cells exposed to $\text{BiFeO}_3@asc$ behaved similarly to those exposed to BiFeO_3 (see Figure A.8).

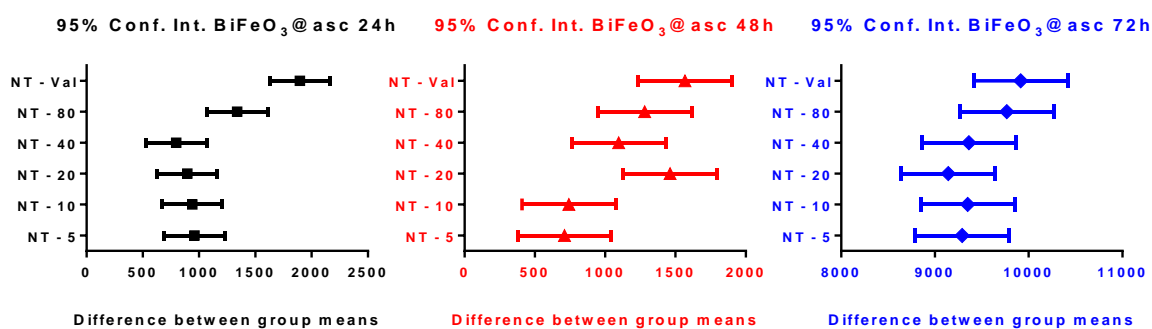
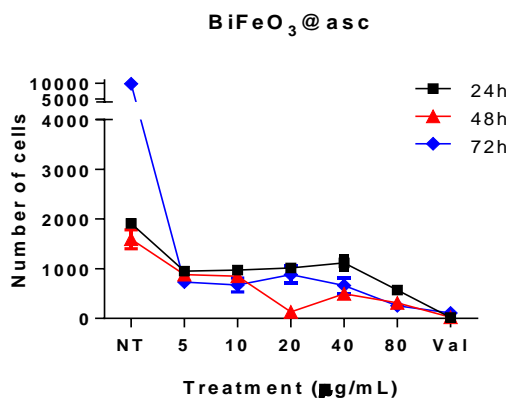


Figure A.8: Cell count of MDMs after treatment with ascorbic acid-functionalised BiFeO_3 NPs and the corresponding 95% confidence intervals, computed from ordinary one-way Anova Dunnet analysis.

As can be seen from Figure A.8:

- Samples exposed to $\text{BiFeO}_3@asc$ had lower cell count relative to the untreated controls after 24, 48h and 72h, especially at higher concentrations.
- The number of cells decreased slightly after 48h and again after 72h. This contrasts strongly with the large increase in cell count observed with the untreated sample as described above.

A1.4.2 Metabolic Activity

Metabolic activity dropped significantly after 24h and continued to fall after 48h and 72h (see Figure A.9).

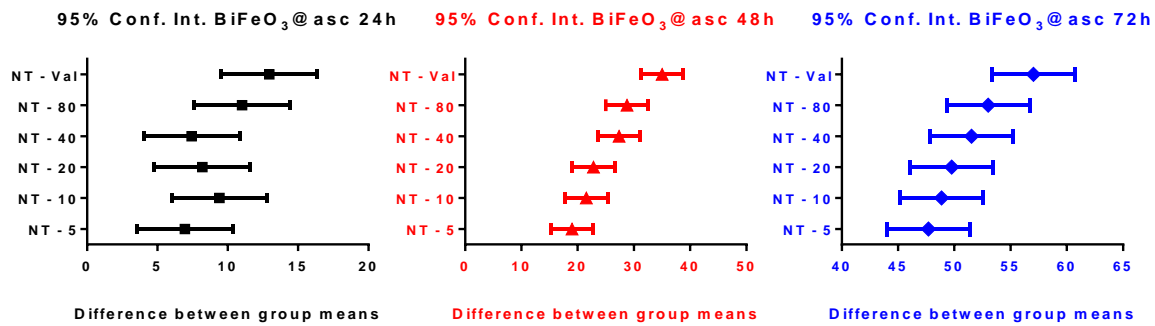
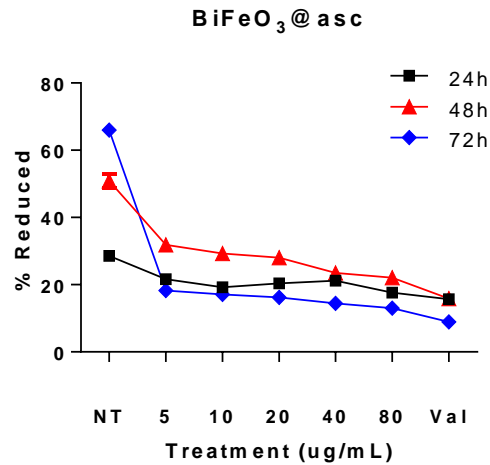


Figure A.9: Metabolic activity in MDMs after exposure to BiFeO₃@asc NPs. Top: Number of cells vs concentration of nanomaterial; bottom row: 95% confidence intervals between group means after 24h (left), after 48h (middle) and 72h (right). Note: the confidence interval plots show the difference between group means (X-axis) for each of the groups (Y-axis) relative to the untreated control NT.

A1.5 MDMs treated with BiFeO₃@APTES NP

A1.5.1 Cell count

MDMs were treated with APS-functionalised BiFeO₃ (BiFeO₃@APTES) NPs at 80 µg/mL, stained with Hoechst and imaged with a blue filter (see Figure A.11 and Figure A.12). Cells treated with the positive control (valinomycin, 120 µg/mL) had lysed and no longer adhered to the plate after 48h. By contrast, untreated cells (NT) proliferated, as did the cells exposed to BiFeO₃ NPs for 24, 48 and 72h.

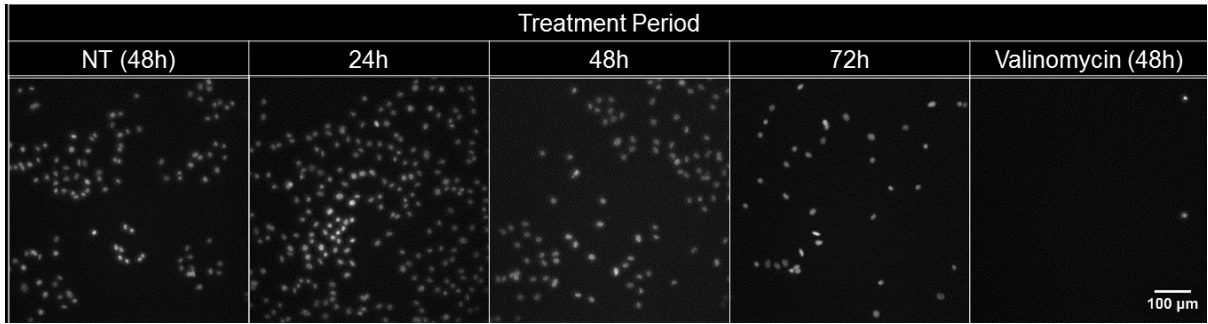


Figure A.10: Representative images of MDMs treated with APS-functionalised BiFeO_3 NPs at $80 \mu\text{g/mL}$ stained with Hoechst. From left: untreated cells after 48h; cells treated with $\text{BiFeO}_3\text{@APTES}$ NPs for 24h, 48h and 72h; right, cells treated with valinomycin for 48h.

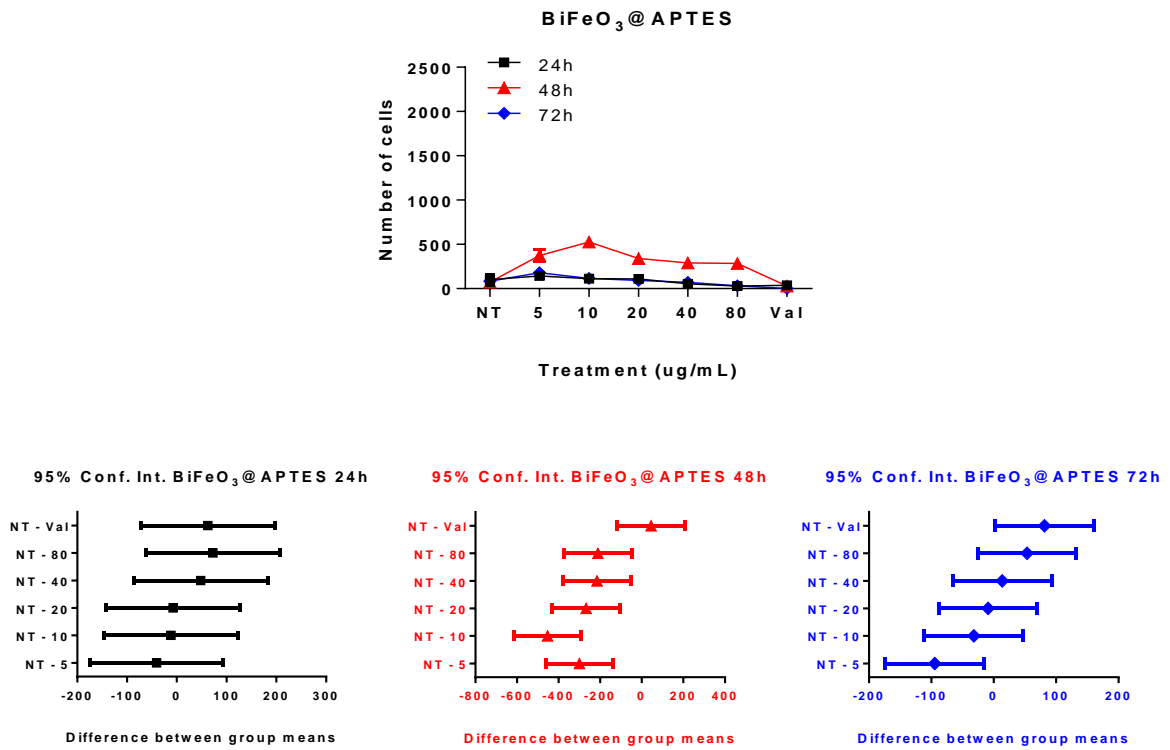


Figure A.11: Cell count of MDMs after treatment with APTES-coated BiFeO_3 NPs ($\text{BiFeO}_3\text{@APS}$) and the corresponding 95% confidence intervals between the groups, computed from ordinary one-way Anova Dunnet analysis.

As can be seen from A.11, cells exposed to $\text{BiFeO}_3\text{@APTES}$ NPs behaved similarly to those exposed to BiFeO_3 and those coated with ascorbic acid:

- Samples exposed to $\text{BiFeO}_3\text{@APTES}$ had approximately the same cell count as the untreated controls after 24h and slightly lower cell counts fell with increasing concentrations.
- The number of cells rose significantly after 48h but fell again to approximately the level of the

untreated control after 72h, with the largest increase in cell count observed at the highest concentration after 48h.

A1.5.2 Metabolic Activity

Metabolic activity in MDMs dropped significantly after 24h and continued to fall after 48h and 72h (see Figure A.12).

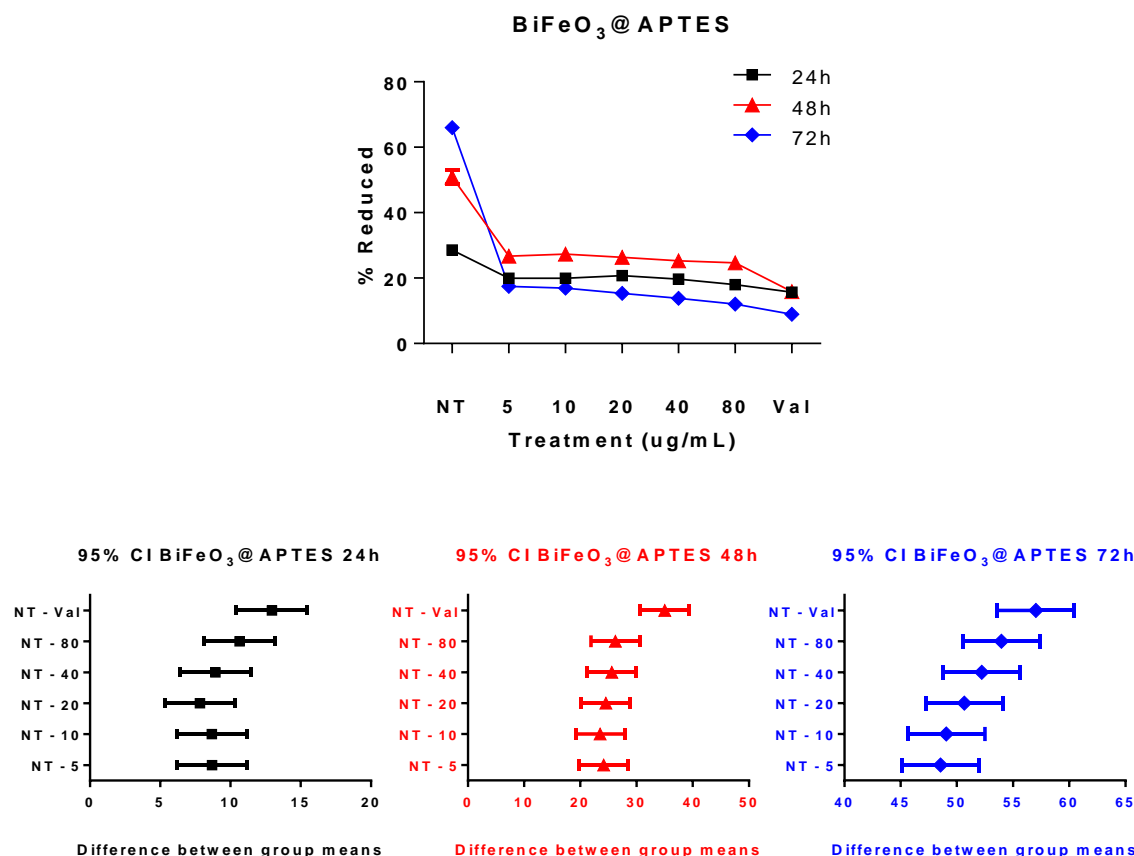


Figure A.12: Metabolic activity in MDMs after exposure to BiFeO₃@APTES NPs. Top: Number of cells vs concentration of nanomaterial; bottom row: 95% confidence intervals between group means after 24h (left), after 48h (middle) and 72h (right). Note: the confidence interval plots show the difference between group means (X-axis) for each of the groups (Y-axis) relative to the untreated control NT.

A1.6 MDMs treated with BiFeO₃@Fe₃O₄@asc NPs

A1.6.1 Cell count

MDMs were treated with (core@shell@[functional coating]) BiFeO₃@Fe₃O₄@asc NPs at 80 µg/mL and stained with Hoechst and imaged with a blue filter (see Figure A.16 and). Cells treated with the positive

control (valinomycin, 120 µg/mL) had lysed and no longer adhered to the plate after 48h. By contrast, untreated cells (NT) proliferated, as did the cells exposed to BiFeO₃ NPs for 24, 48 and 72h.

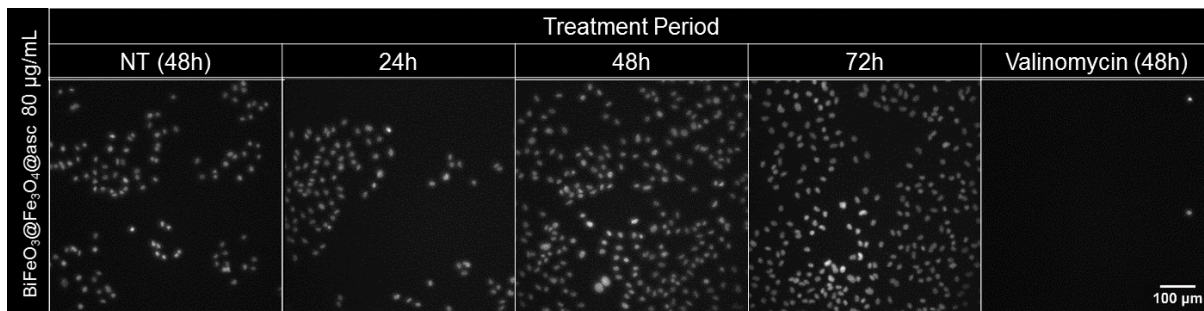


Figure A.13: Representative images of MDMs treated with BiFeO₃@Fe₃O₄@asc NPs at 80 µg/mL stained with Hoechst. From left: untreated cells after 48h; cells treated with BiFeO₃@Fe₃O₄@asc NPs for 24h, 48h and 72h; right, cells treated with valinomycin for 48h.

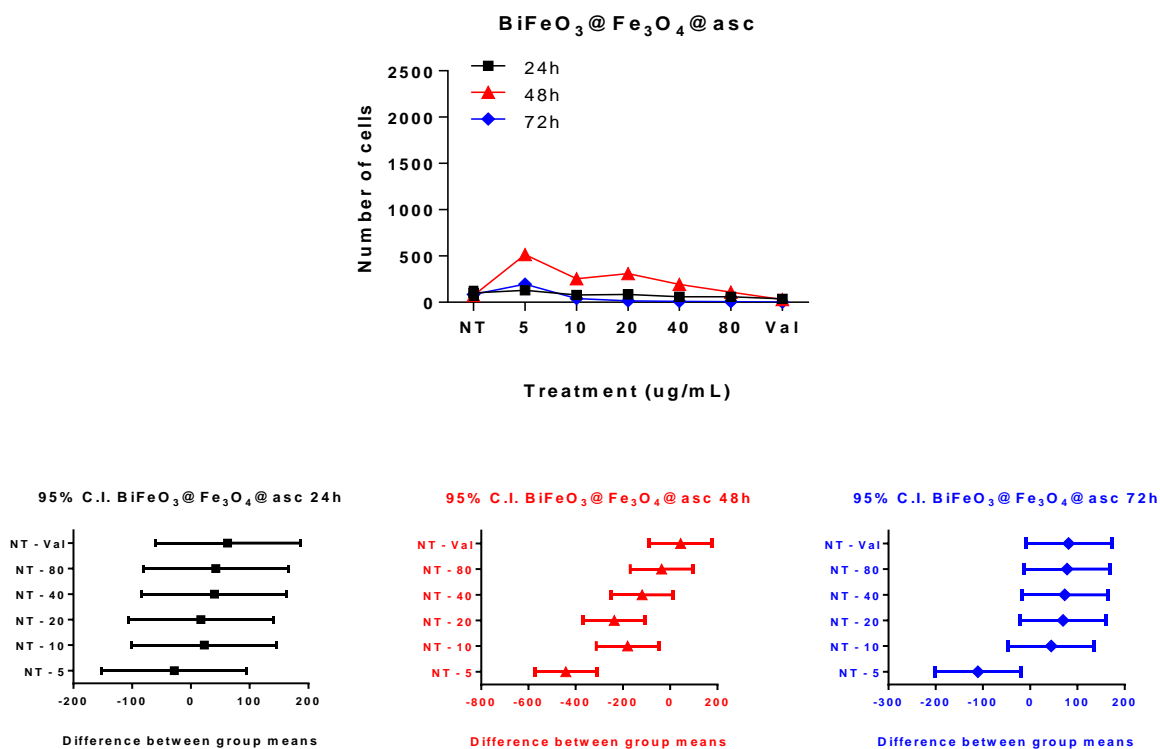


Figure A.14: Cell count of MDMs after treatment with BiFeO₃@Fe₃O₄@asc NPs and the corresponding 95% confidence intervals between the groups, computed from ordinary one-way Anova Dunnet analysis.

As can be seen from A.17, cells exposed to BiFeO₃@Fe₃O₄@asc NPs behaved similarly to those exposed to BiFeO₃, BiFeO₃@asc and BiFeO₃@APTES:

- Samples exposed to BiFeO₃@APTES had approximately the same cell count as the untreated controls after 24h and slightly lower cell counts fell with increasing concentrations.

- The number of cells rose significantly after 48h but fell again to approximately the level of the untreated control after 72h, with the largest increase in cell count observed at the highest concentration after 48h.

A1.6.2 Metabolic Activity

Metabolic activity dropped significantly after 24h and continued to fall after 48h and 72h (see Figure A.15).

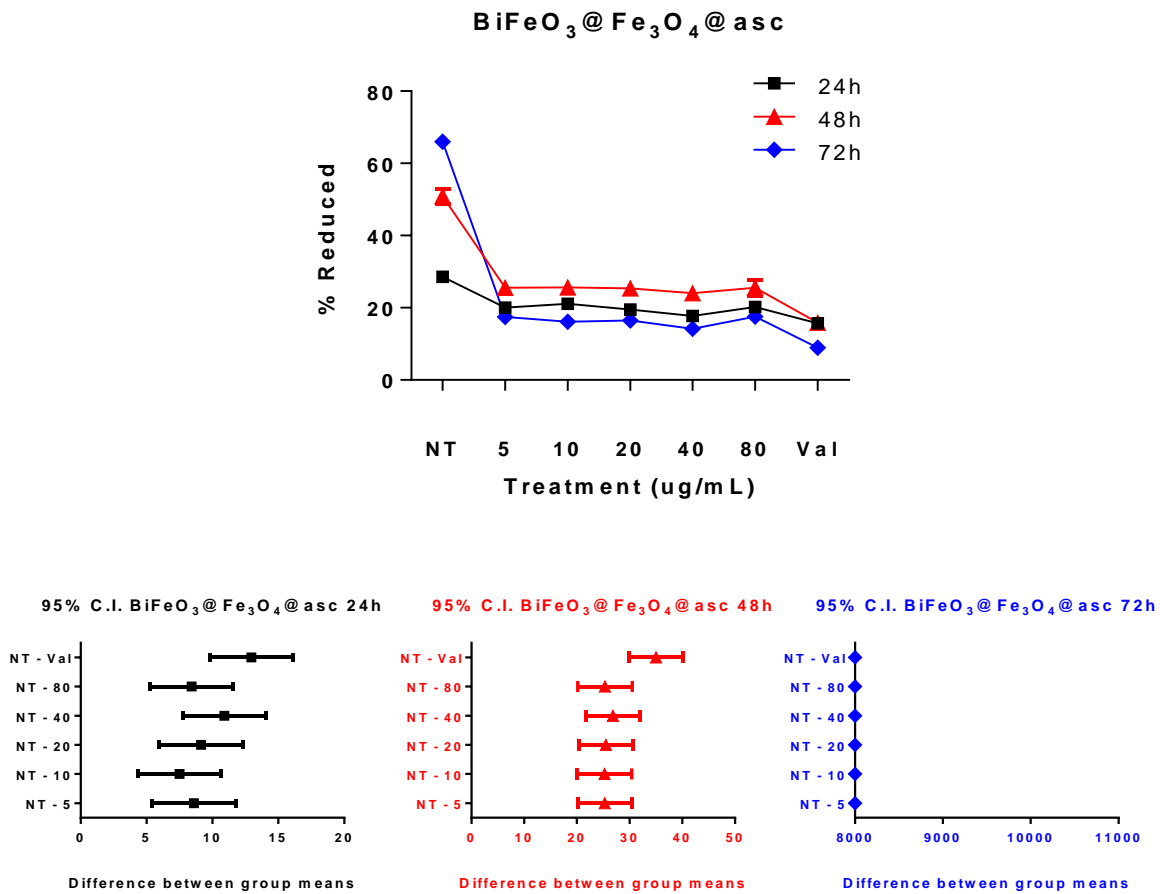


Figure A.15: Metabolic activity in MDMs after exposure to BiFeO₃@Fe₃O₄@asc NPs. Top: Number of cells vs concentration of nanomaterial; bottom row: 95% confidence intervals between group means after 24h (left), after 48h (middle) and 72h (right). Note: the confidence interval plots show the difference between group means (X-axis) for each of the groups (Y-axis) relative to the untreated control NT.

A1.7 MDMs treated with BiFeO₃@Fe₃O₄@APTES NPs

A1.7.1 Cell count

MDMs were treated with core@shell@[functional coating] BiFeO₃@Fe₃O₄@APTES NPs at 80 µg/mL and stained with Hoechst and imaged with a blue filter (see Figure A.16 and Figure A.17). Cells treated

with the positive control (valinomycin, 120 $\mu\text{g}/\text{mL}$) had lysed and no longer adhered to the plate after 48h. By contrast, untreated cells (NT) proliferated, as did the cells exposed to BiFeO_3 NPs for 24, 48 and 72h.

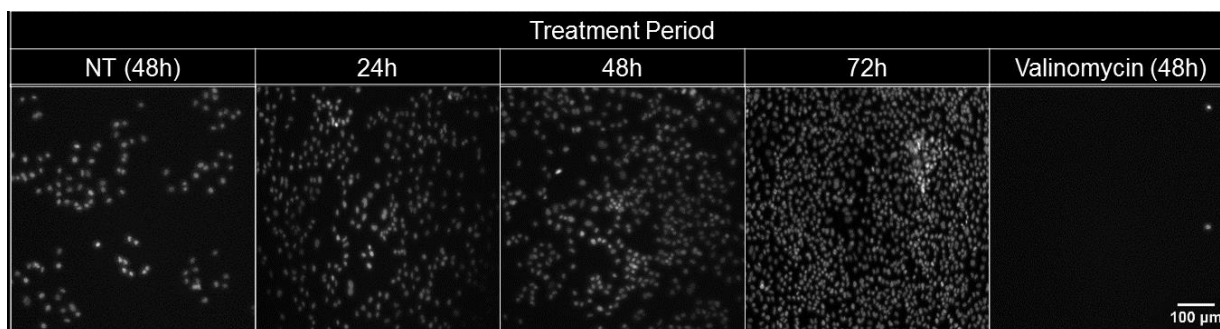


Figure A.16: Representative images of MDMs treated with $\text{BiFeO}_3@Fe_3O_4@APTES$ NPs at 80 $\mu\text{g}/\text{mL}$ stained with Hoechst. From left: untreated cells after 48h; cells treated with $\text{BiFeO}_3@Fe_3O_4@APTES$ NPs for 24h, 48h and 72h; right, cells treated with valinomycin for 48h.

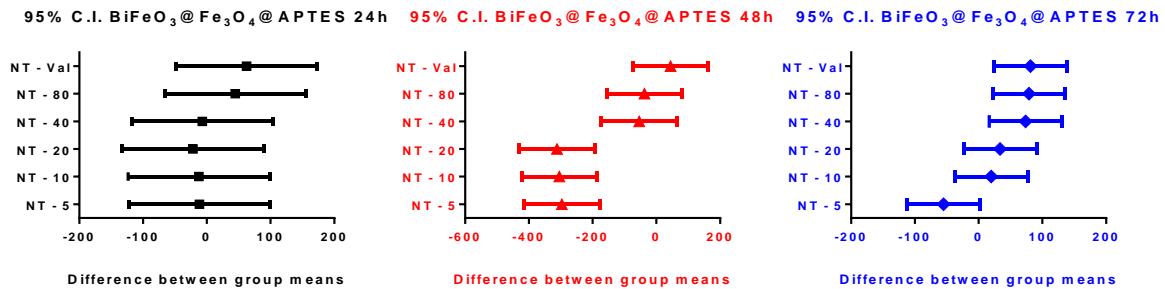
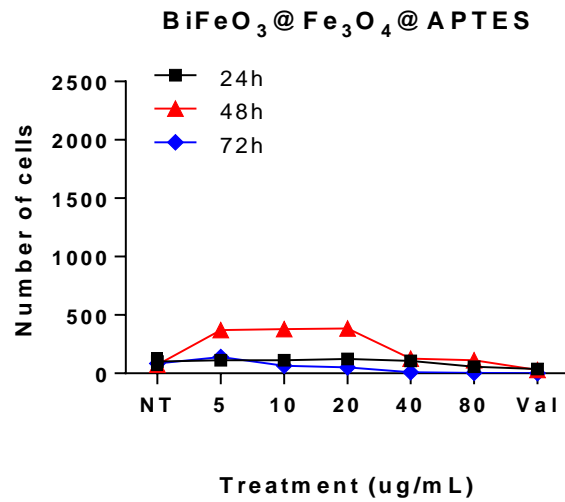


Figure A.17: Cell count of MDMs after treatment with BiFeO₃@Fe₃O₄@APTES NPs and the corresponding 95% confidence intervals between the groups, computed from ordinary one-way Anova Dunnet analysis.

As can be seen from Figure A.17, samples treated with BiFeO₃@Fe₃O₄@APTES NPs responded similarly to those exposed to BiFeO₃, BiFeO₃@asc, BiFeO₃@APTES and BiFeO₃@Fe₃O₄@asc NPs, showing a significant increase from the control at the 48h time-point.

A1.7.2 Metabolic Activity

Metabolic activity in MDMs dropped significantly after 24h and continued to fall after 48h and 72h (see Figure A.18) on exposure to BiFeO₃@Fe₃O₄@APTES NPs.

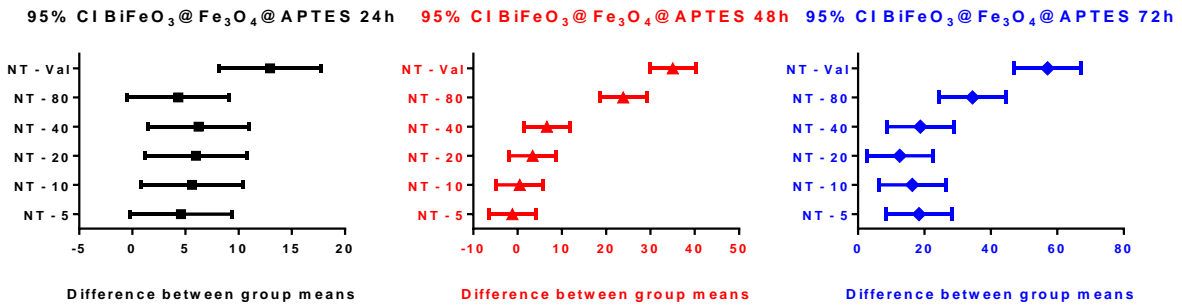
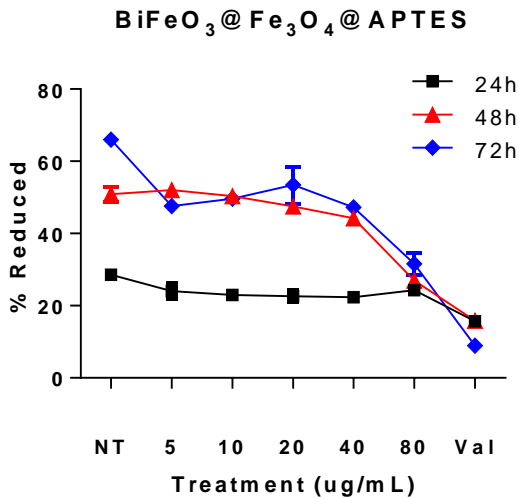


Figure A.18: Metabolic activity in MDMs after exposure to BiFeO₃@Fe₃O₄@APTES NPs and the corresponding 95% confidence intervals. Top: Number of cells vs concentration of nanomaterial; bottom row: 95% confidence intervals between group means after 24h (left), after 48h (middle) and 72h (right). Note: the confidence interval plots, computed from ordinary one-way Anova using Dunnett's post-test for multiple comparisons, show the difference between group means (X-axis) for each of the groups (Y-axis) relative to the untreated control NT.

A1.8 MDMs treated with BiFeO₃@Fe₂O₃@asc NPs

A1.8.1 Cell count

MDMs were treated with BiFeO₃@Fe₂O₃@asc NPs at 80 µg/mL and stained with Hoechst and imaged with a blue filter (see Figure A.19). Cells treated with the positive control (valinomycin, 120 µg/mL) had lysed and no longer adhered to the plate after 48h. By contrast, untreated cells (NT) proliferated, as did the cells exposed to BiFeO₃ NPs for 24, 48 and 72h.

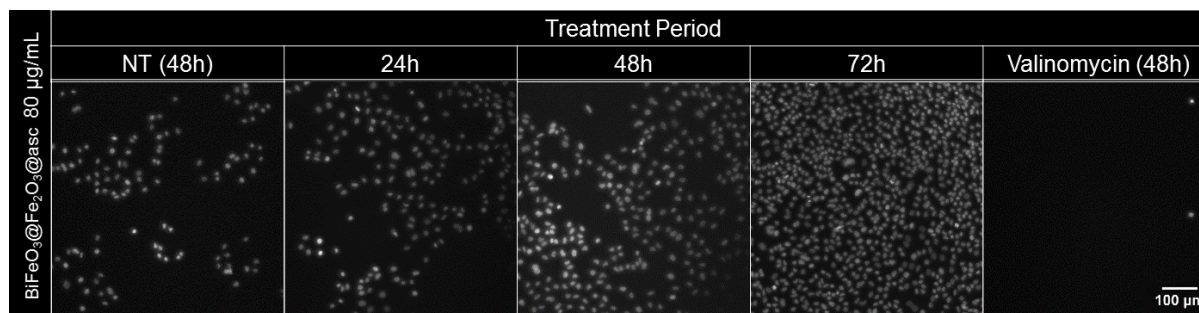


Figure A.19: Representative images of MDMs treated with $\text{BiFeO}_3@Fe_2O_3@asc$ NPs at $80 \mu\text{g/mL}$ stained with Hoechst. From left: untreated cells after 48h; cells treated with $\text{BiFeO}_3@Fe_2O_3@asc$ for 24h, 48h and 72h; right, cells treated with valinomycin for 48h.

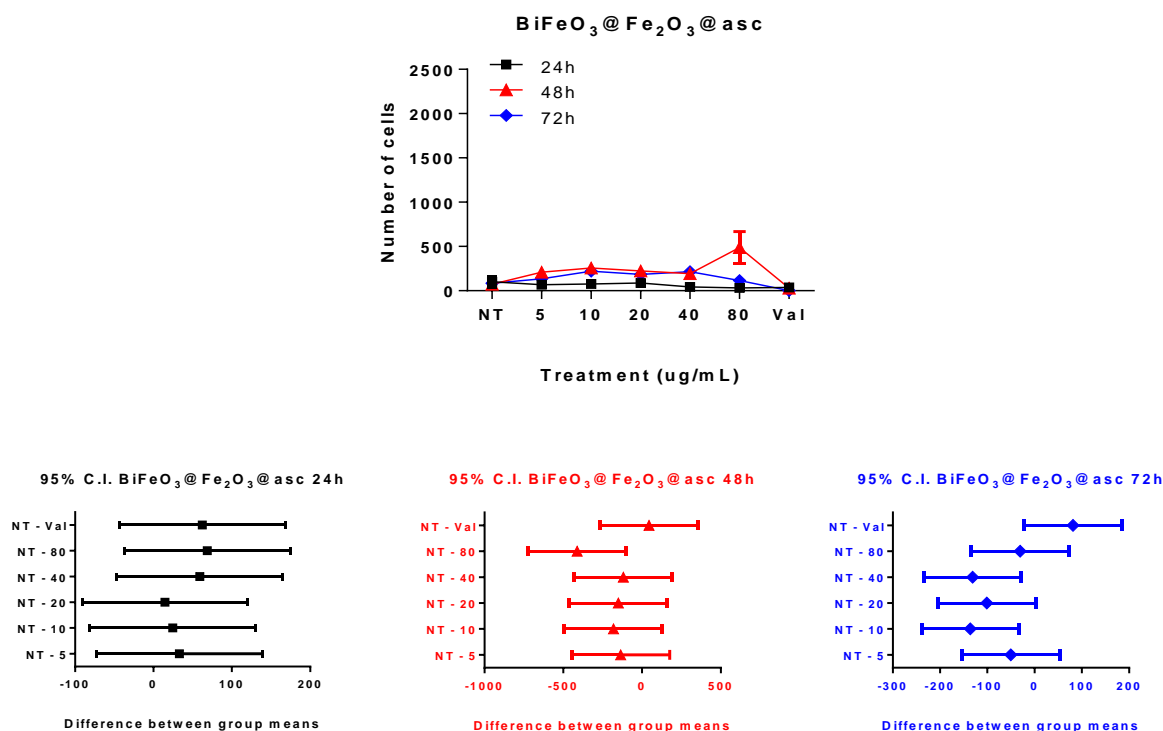


Figure A.20: Cell count of MDMs after treatment with $\text{BiFeO}_3@Fe_2O_3@asc$ NPs and the corresponding 95% confidence intervals between the groups, computed from ordinary one-way Anova Dunnet analysis.

As can be seen from Figure A.25, the cell count fell slightly after 24h exposure, with the count decreasing with increasing concentrations. After 48h the cell count rose relative to the control at all concentrations and remained at that level after 72h.

A1.8.2 Metabolic Activity

Metabolic activity dropped significantly after 24h and continued to fall after 48h and 72h (see Figure A.21) on exposure to $\text{BiFeO}_3@Fe_2O_3@asc$.

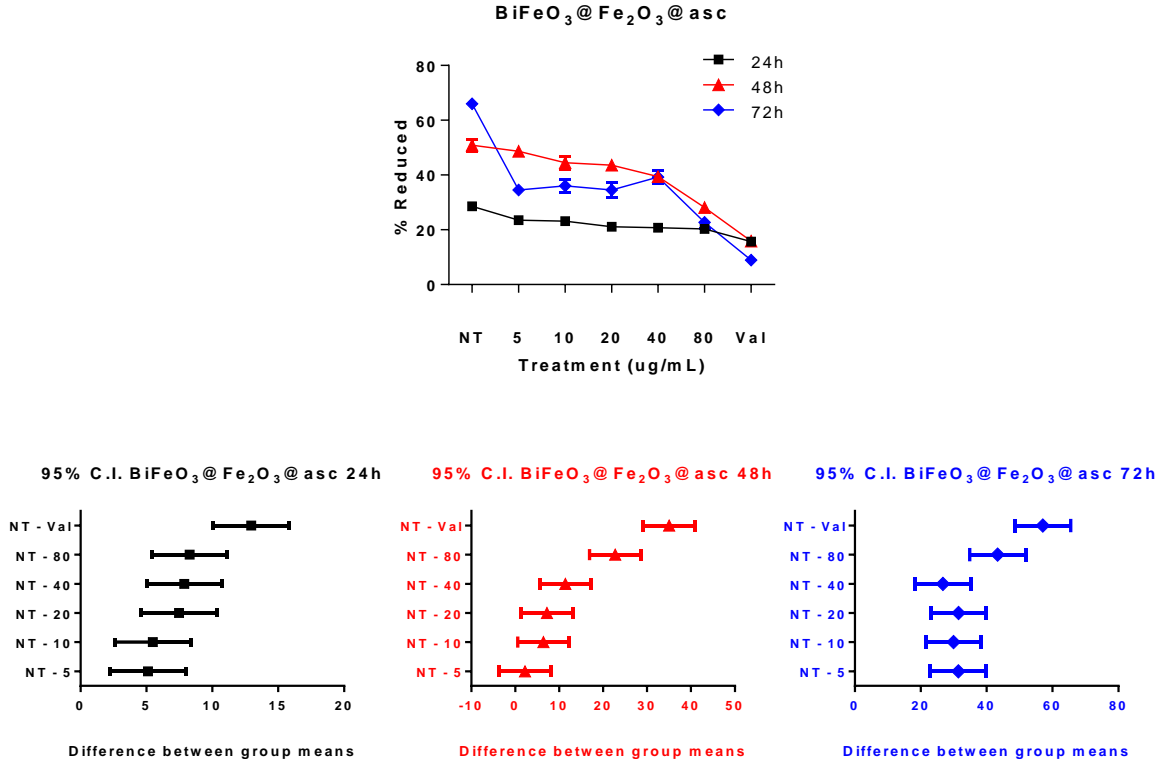


Figure A.21: Metabolic activity in MDMs after exposure to $\text{BiFeO}_3@Fe_2O_3@asc$ NPs. Top: Number of cells vs concentration of nanomaterial; bottom row: 95% confidence intervals between group means after 24h (left), after 48h (middle) and 72h (right). Note: the confidence interval plots show the difference between group means (X-axis) for each of the groups (Y-axis) relative to the untreated control NT.

A1.9 MDMs treated with $\text{SiO}_2@BiFeO_3$ NWs

A1.9.1 Cell count

MDMs treated with $\text{SiO}_2@BiFeO_3$ NWs at 80 $\mu\text{g}/\text{mL}$ and stained with Hoechst and imaged with a blue filter (see Figure A.22). Cells treated with the positive control (valinomycin, 120 $\mu\text{g}/\text{mL}$) had lysed and no longer adhered to the plate after 48h. By contrast, untreated cells (NT) proliferated, as did the cells exposed to BiFeO_3 NPs for 24, 48 and 72h.

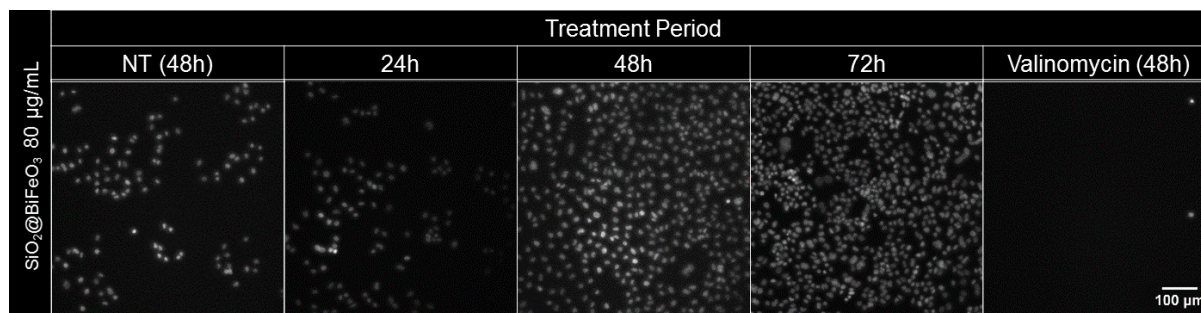


Figure A.22: Representative images of MDMs treated with $\text{SiO}_2\&\text{BiFeO}_3$ NWs at $80\ \mu\text{g/mL}$ stained with Hoechst. From left: untreated cells after 48h; cells treated with BiFeO_3 for 24h, 48h and 72h; right, cells treated with valinomycin for 48h.

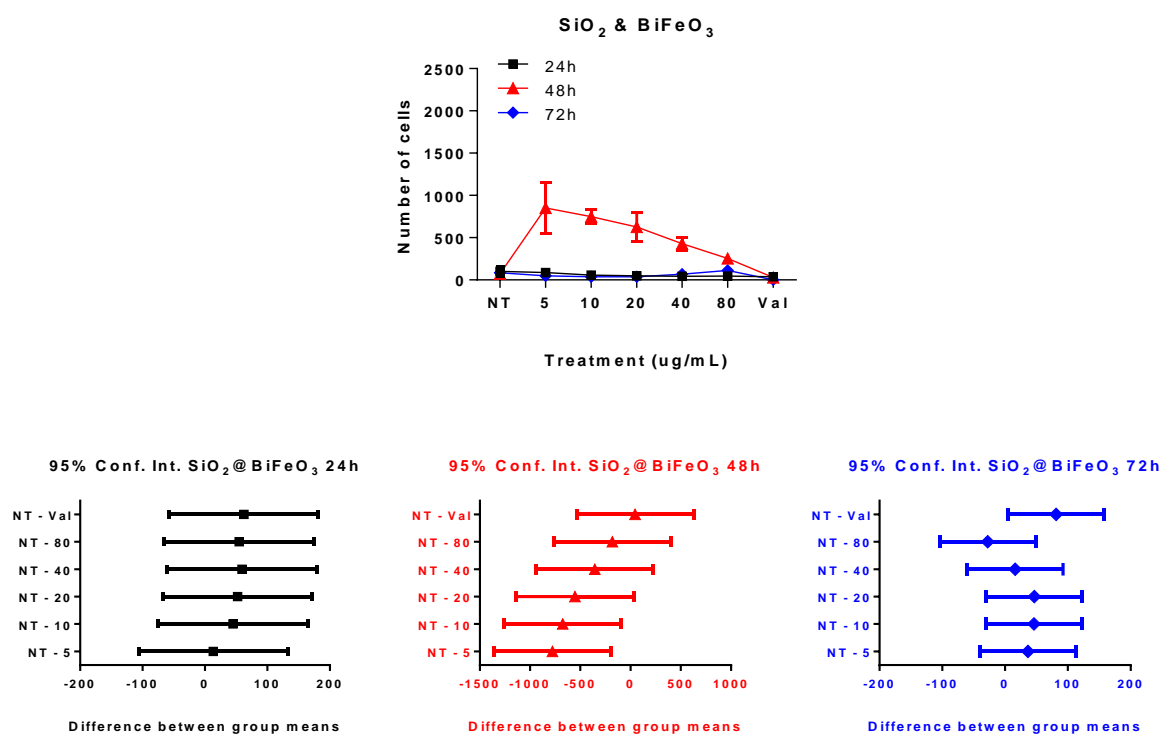


Figure A.23: Cell count of MDMs after treatment with $\text{SiO}_2\&\text{BiFeO}_3$ NWs and the corresponding 95% confidence intervals between the groups, computed from ordinary one-way Anova Dunnet analysis.

As can be seen from Figure A.29, samples treated with $\text{SiO}_2\&\text{BiFeO}_3$ NWs responded similarly to those exposed to BiFeO_3 , $\text{BiFeO}_3\&\text{asc}$, $\text{BiFeO}_3\&\text{APTES}$, $\text{BiFeO}_3\&\text{Fe}_3\text{O}_4\&\text{asc}$ and $\text{BiFeO}_3\&\text{Fe}_3\text{O}_4\&\text{APTES}$ NPs, showing a significant increase from the control at the 48h time-point followed by a return to the same level as that of the untreated control.

A1.9.2 Metabolic Activity

Metabolic activity dropped significantly after 24h and continued to fall after 48h and 72h (see Figure A.24) on exposure to SiO_2 & BiFeO_3

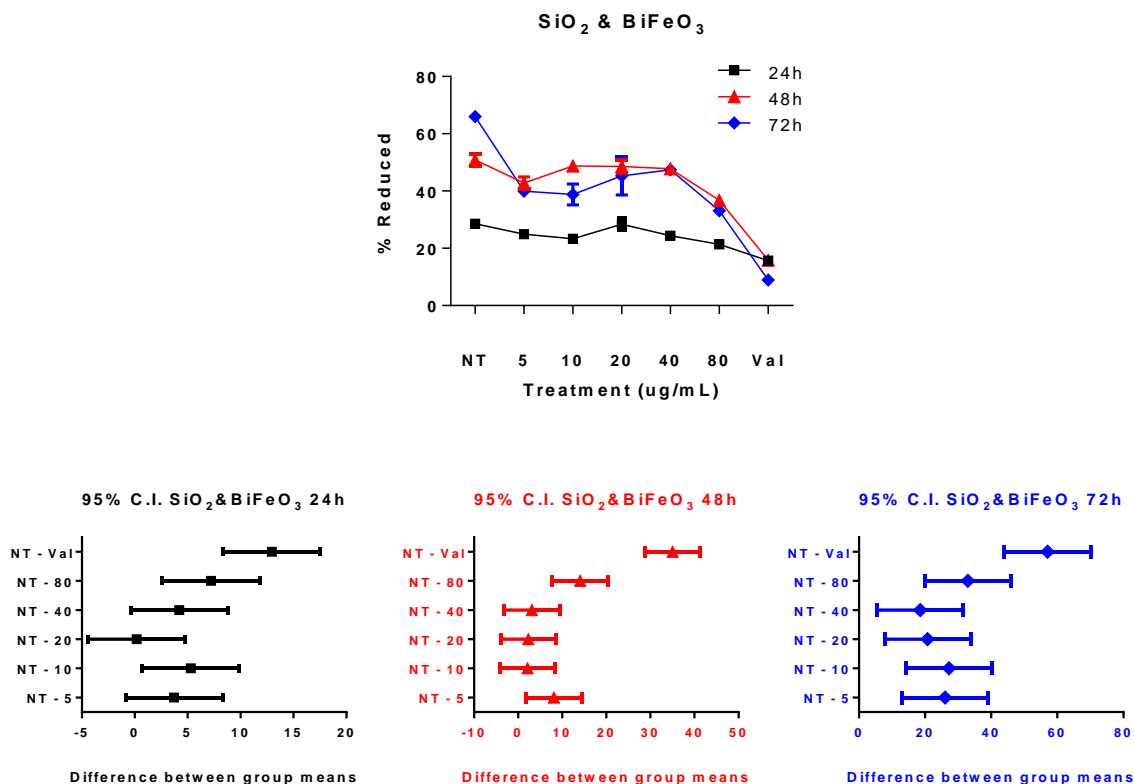


Figure A.24: Metabolic activity in MDMs after exposure to SiO_2 & BiFeO_3 NWs. Top: Number of cells vs concentration of nanomaterial; bottom row: 95% confidence intervals between group means after 24h (left), after 48h (middle) and 72h (right). Note: the confidence interval plots show the difference between group means (X-axis) for each of the groups (Y-axis) relative to the untreated control NT.

A1.10 MDMs treated with SiO_2 & BiFeO_3 @ Fe_3O_4 NWs

A1.10.1 Cell count

MDMs were treated with SiO_2 & BiFeO_3 @ Fe_3O_4 NWs at 80 $\mu\text{g}/\text{mL}$ and stained with Hoechst and imaged with a blue filter (see Figure A.25). Cells treated with the positive control (valinomycin, 120 $\mu\text{g}/\text{mL}$) had lysed and no longer adhered to the plate after 48h. By contrast, untreated cells (NT) proliferated, as did the cells exposed to BiFeO_3 NPs for 24, 48 and 72h.

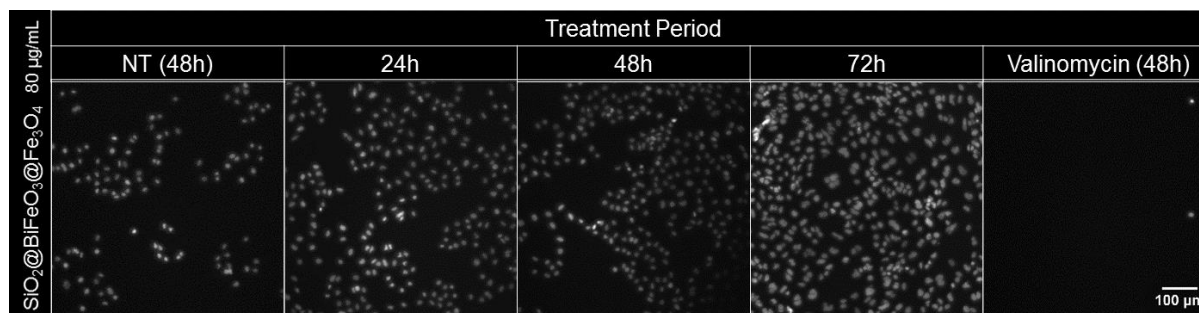


Figure A.25: Representative images of MDMs treated with $\text{SiO}_2\&\text{BiFeO}_3\text{@Fe}_3\text{O}_4$ NWs at $80\ \mu\text{g/mL}$ stained with Hoechst. From left: untreated cells after 48h; cells treated with $\text{SiO}_2\&\text{BiFeO}_3\text{@Fe}_3\text{O}_4$ NWs for 24h, 48h and 72h; right, cells treated with valinomycin for 48h.

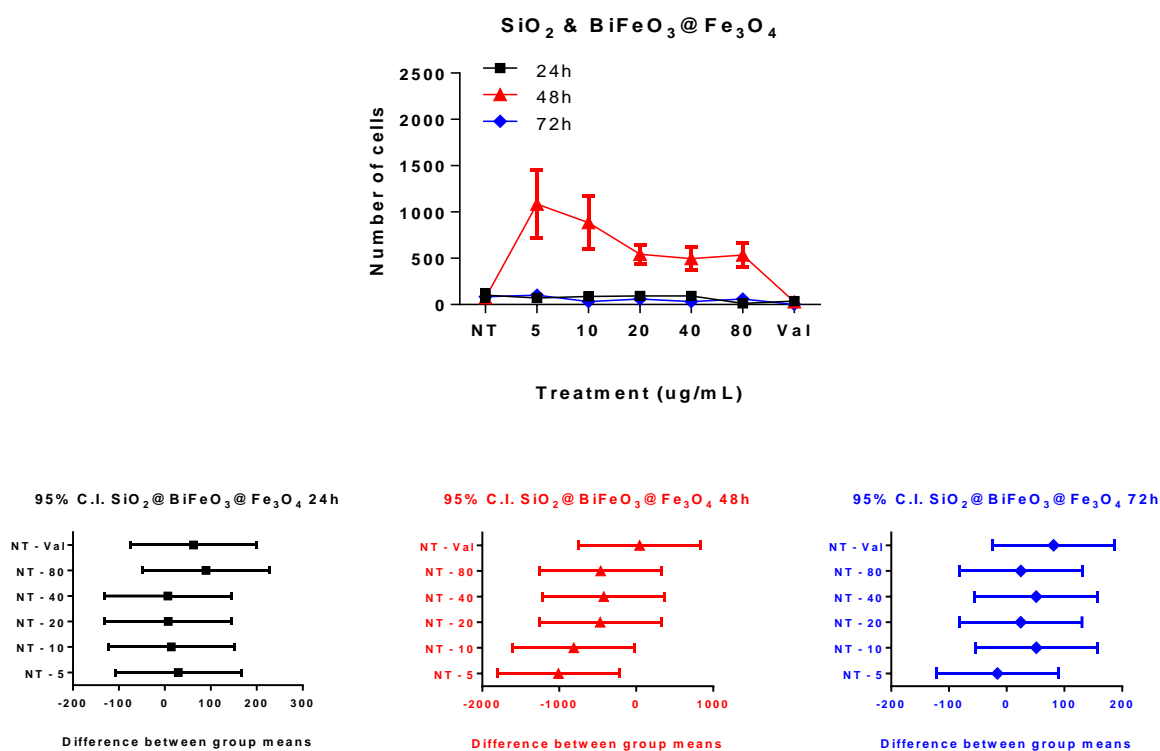


Figure A.26: Cell count of MDMs after treatment with $\text{SiO}_2\&\text{BiFeO}_3\text{@Fe}_3\text{O}_4$ NWs and the corresponding 95% confidence intervals between the groups, computed from ordinary one-way Anova Dunnet analysis.

As can be seen from Figure A.26, samples treated with $\text{SiO}_2\&\text{BiFeO}_3\text{@Fe}_3\text{O}_4$ NWs responded similarly to those exposed to BiFeO_3 , $\text{BiFeO}_3\text{@asc}$, $\text{BiFeO}_3\text{@APTES}$, $\text{BiFeO}_3\text{@Fe}_3\text{O}_4\text{@asc}$ and $\text{BiFeO}_3\text{@Fe}_3\text{O}_4\text{@APTES}$ NPs and $\text{SiO}_2\&\text{BiFeO}_3$ NWs, showing a significant increase from the control at the 48h time-point followed by a return to the same level as that of the untreated control after 72h. There was also a concentration-dependent response – cell count fell as concentrations rose at each time point.

A1.10.2 Metabolic Activity

Metabolic activity dropped significantly after 24h and continued to fall after 48h and 72h (see Figure A.27) on exposure to $\text{SiO}_2\&\text{BiFeO}_3\text{@Fe}_3\text{O}_4$ NWs.

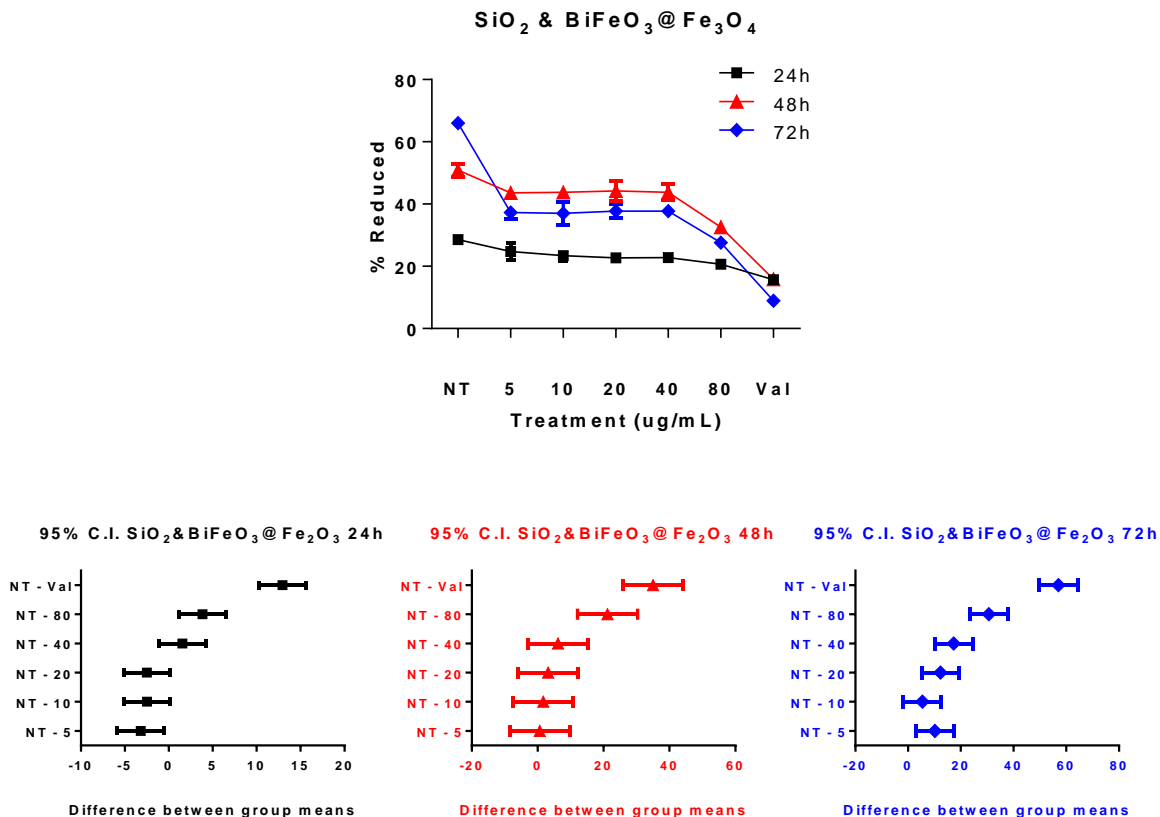


Figure A.27: Metabolic activity in MDMs after exposure to $\text{SiO}_2\&\text{BiFeO}_3\text{@Fe}_2\text{O}_3$ NWs. Top: Number of cells vs concentration of nanomaterial; bottom row: 95% confidence intervals between group means after 24h (left), after 48h (middle) and 72h (right). Note: the confidence interval plots show the difference between group means (X-axis) for each of the groups (Y-axis) relative to the untreated control NT.

A1.11 MDMs treated with $\text{SiO}_2\&\text{BiFeO}_3\text{@Fe}_2\text{O}_3$ NWs

A1.11.1 Cell count

MDMs were treated with $\text{SiO}_2\&\text{BiFeO}_3\text{@Fe}_2\text{O}_3$ NWs at 80 $\mu\text{g}/\text{mL}$ and stained with Hoechst and imaged with a blue filter (see Figure A.28 and Figure A.29). Cells treated with the positive control (valinomycin, 120 $\mu\text{g}/\text{mL}$) had lysed and no longer adhered to the plate after 48h. By contrast, untreated cells (NT) proliferated, as did the cells exposed to BiFeO_3 NPs for 24, 48 and 72h.

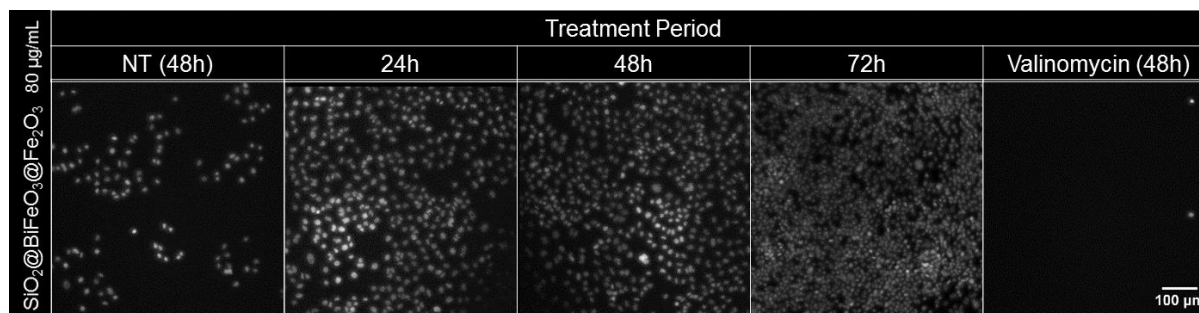


Figure A.28: Representative images of MDMs treated with $\text{SiO}_2\&\text{BiFeO}_3\text{@Fe}_2\text{O}_3$ NWs at $80\ \mu\text{g/mL}$ stained with Hoechst. From left: untreated cells after 48h; cells treated with $\text{SiO}_2\&\text{BiFeO}_3\text{@Fe}_2\text{O}_3$ NWs for 24h, 48h and 72h; right, cells treated with valinomycin for 48h.

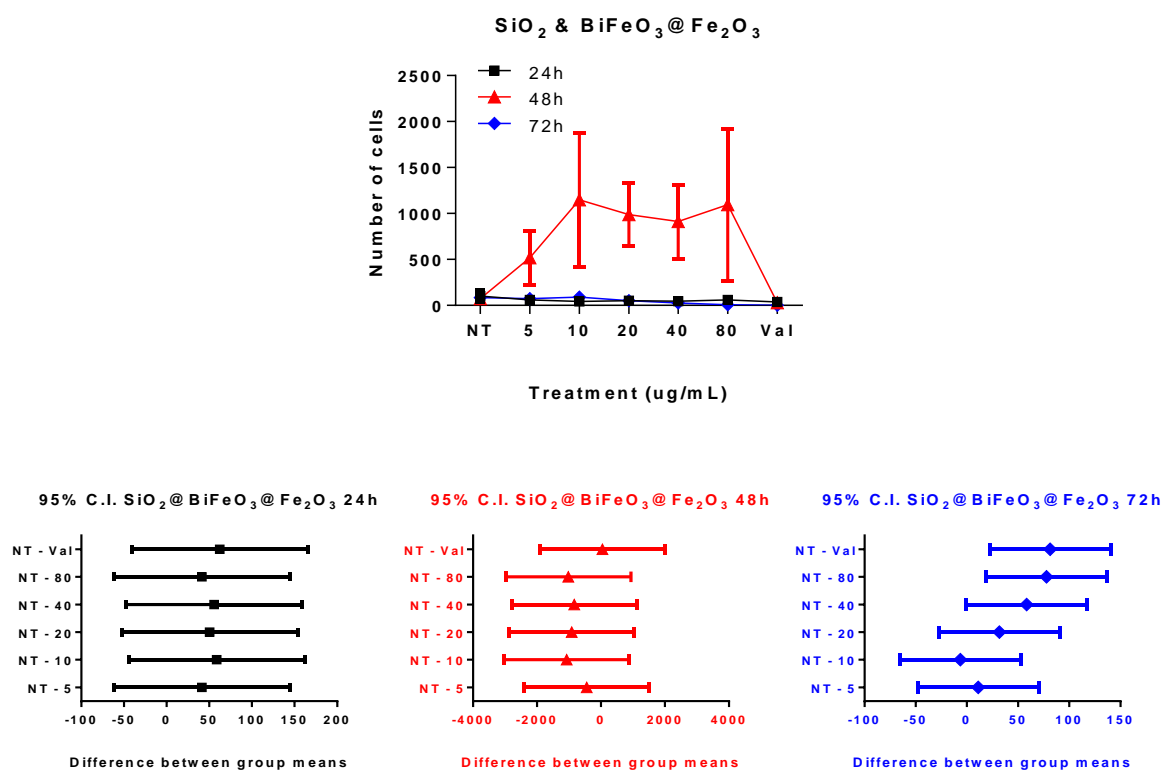


Figure A.29: Cell count of MDMs after treatment with $\text{SiO}_2\&\text{BiFeO}_3\text{@Fe}_2\text{O}_3$ NWs and the corresponding 95% confidence intervals between the groups, computed from ordinary one-way Anova Dunnet analysis.

As can be seen from Figure A.29, samples treated with $\text{SiO}_2\&\text{BiFeO}_3\text{@Fe}_2\text{O}_3$ NWs responded similarly to those exposed to BiFeO_3 , $\text{BiFeO}_3\text{@asc}$, $\text{BiFeO}_3\text{@APTES}$, $\text{BiFeO}_3\text{@Fe}_3\text{O}_4\text{@asc}$ and $\text{BiFeO}_3\text{@Fe}_3\text{O}_4\text{@APTES}$ NPs and $\text{SiO}_2\&\text{BiFeO}_3$ and $\text{SiO}_2\&\text{BiFeO}_3\text{@Fe}_3\text{O}_4$ NWs, showing a significant increase from the control at the 48h time-point followed by a return to the same level as that of the untreated control after 72h. There was also a concentration-dependent response – cell count fell as concentrations rose at each time point.

A1.11.2 Metabolic Activity

Metabolic activity dropped significantly after 24h and continued to fall after 48h and 72h (see Figure A.30) on exposure to $\text{SiO}_2\&\text{BiFeO}_3\text{@Fe}_2\text{O}_3$ NWS.

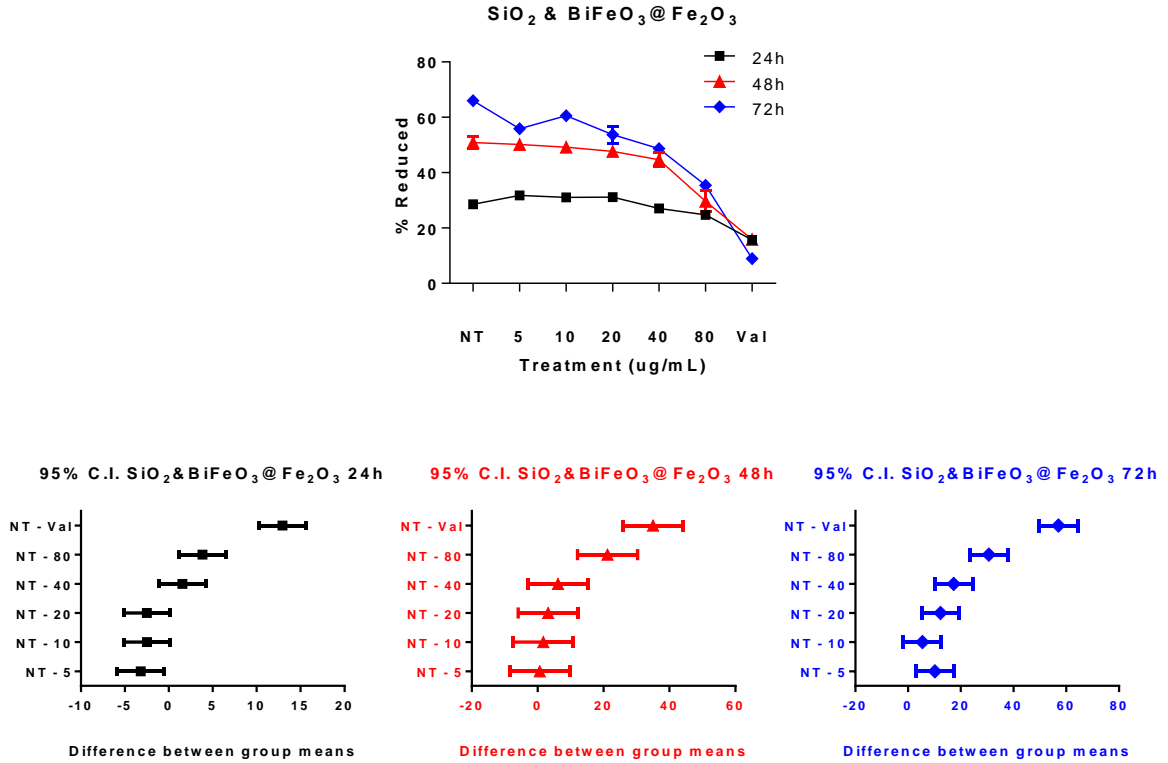


Figure A.30: Metabolic activity in A549 cells after exposure to $\text{SiO}_2\&\text{BiFeO}_3\text{@Fe}_2\text{O}_3$ NWS. Top: Number of cells vs concentration of nanomaterial; bottom row: 95% confidence intervals between group means after 24h (left), after 48h (middle) and 72h (right). Note: the confidence interval plots show the difference between group means (X-axis) for each of the groups (Y-axis) relative to the untreated control NT.

A2 High Content Screening of A549 cells

A2.1 A549 cells treated with BiFeO₃ NPs

A549 cells were exposed to BiFeO₃ NPs at 80 $\mu\text{g}/\text{mL}$ for HCS (see Figure A.31), fixed after 48h and stained for DNA (blue channels), cell morphology and membrane permeability (green channels) and lysosomal mass/pH changes (red channels).

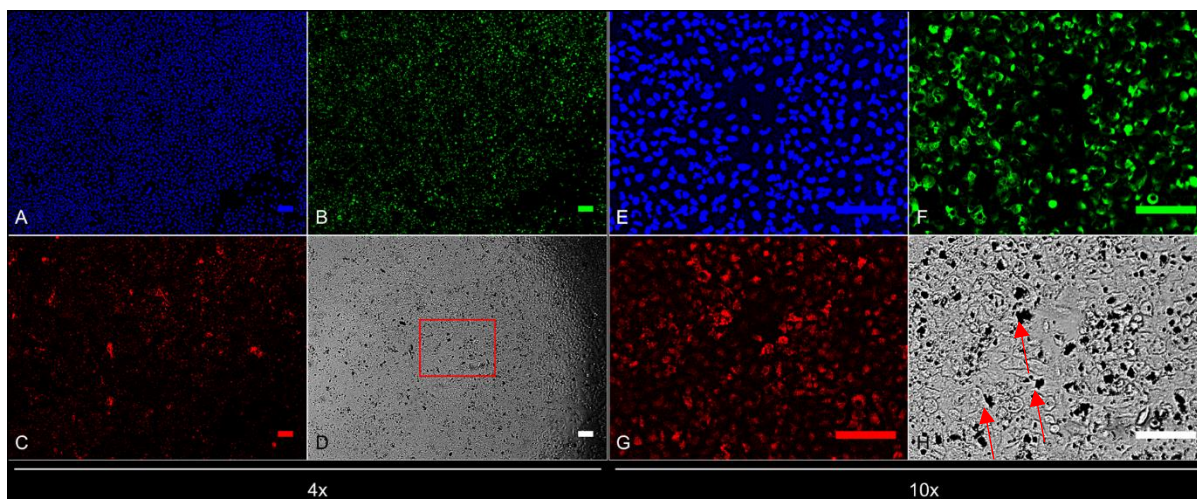


Figure A.31: HCS images of A549 cells after 48h exposure to BiFeO_3 NPs at $80 \mu\text{g/mL}$. Panels A and E (blue channels): nuclear staining with Hoechst; Panels B and F (green channels): cell membrane permeability staining; Panels C and G (red channels): lysosomal mass/pH staining; Panels D and H (transmitted light channels). Left (A-D): 4x objective images. The region highlighted in the Transmitted Light Channel (D) is the area magnified in the right panels (E-H): 10x objective images. The scale bars are $100 \mu\text{m}$.

The aggregation and localisation of the BiFeO_3 NPs can be seen in the transmitted light panels (grey channels). As can be seen, after 48h the cells had reached confluency despite the presence of the NPs, and the particles had aggregated inside the cells (Panels D and H, aggregates indicated by arrows in H).

A2.1.1 Cell count

A549 cells were exposed to BiFeO_3 NPs at three time points and stained for DNA to determine cell count (Figure A.32).

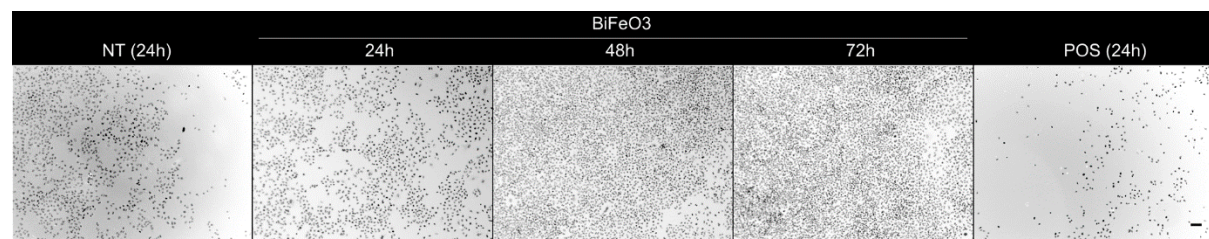


Figure A.32: A549 cells exposed to BiFeO_3 NPs, stained for DNA. From left: representative images of untreated cells after 24h, cells exposed to BiFeO_3 NPs at $80 \mu\text{g/mL}$ for 24h, 48h, 72h, and cells treated with the positive control (valinomycin, $120 \mu\text{M}$) for 24h. Only the Hoechst channel is shown, inverted. The scale bar is $100 \mu\text{m}$ and is the same for all the images.

Again, it can be seen that the cells reached confluency after 48h and this is borne out by the HCS data below.

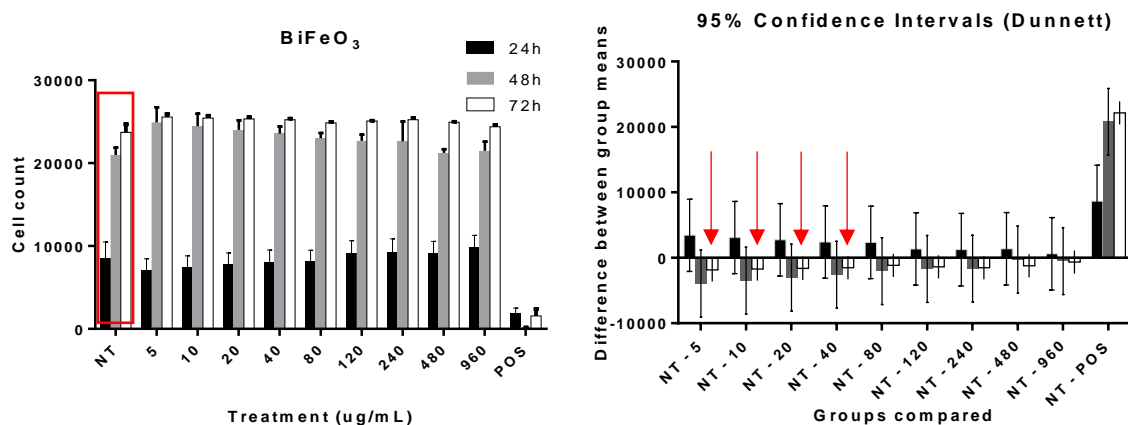


Figure A.33: Cell count of A549 cells after treatment with BiFeO_3 NPs and the corresponding 95% confidence intervals. Left: Number of cells vs concentration of nanomaterial. Valinomycin was used as positive control. The error bars represent the standard error of the mean of triplicates in three independent experiments. Right: difference between group means relative to the untreated control NT (Dunnett's test for multiple comparisons). The error bars represent the 95% confidence intervals (calculated using ordinary One-Way ANOVA).

After 24h, the untreated cell count was ~ 8500 cells (see the rectangular region of Figure A.33, left panel). After 48h, the cell count had reached ~ 20500 , corresponding to a doubling time of 19 hours, estimated using ... Equation A.0.1.

$$\text{Doubling Time} = \frac{\text{duration} * \log 2}{\log(\text{Final Concentration}) - \log(\text{Initial Concentration})} \quad \dots \text{Equation A.0.1}$$

The doubling time reported here is an approximation and varies from the literature value of 22 hours for the following reasons: the estimate is based only on a small sample size and over one generation, and when the cells are seeded the population of cells is not all at the same stage of the cell cycle as is necessary when determining the doubling time. The approximation here is intended merely for comparison between the time points.

After 72h, the cell count reached approximately 24000, indicating that the cells had reached confluency shortly after the 48h time-point.

While there are some apparent trends in the variation of cell count with concentration (Figure A.33, left panel), only after 72h were the counts significantly different from the untreated control, and only at concentrations below $80 \mu\text{g/mL}$, as can be seen from the 95% confidence intervals (indicated by arrows in the right panel of Figure A.33).

This means that the BiFeO_3 NPs did not adversely affect cell proliferation over the concentration range examined.

A2.1.2 Cell Membrane Permeability

Cell membrane permeability was used to indicate cell viability (see Figure A.34).

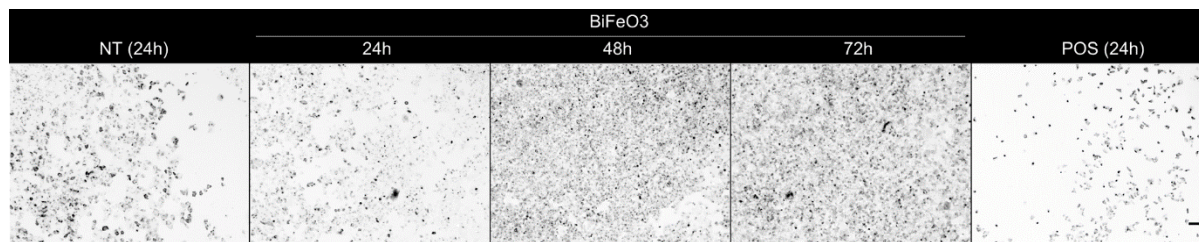


Figure A.34: A549 cells exposed to BiFeO_3 NPs, stained for cell membrane permeability. From left: representative images of untreated cells after 24h, cells exposed to BiFeO_3 NPs at $80 \mu\text{g/mL}$ for 24h, 48h, 72h, and cells treated with the positive control (valinomycin, $120 \mu\text{M}$) for 24h. Only the CMP (green) channels are shown, inverted. The scale bar is $100 \mu\text{m}$ and is the same for all the images.

Because the images in Figure A.34 are inverted, the darkest spots correspond to areas in which there was a high concentration of the CMP stain. If the intensity of the stain in the region around a nucleus exceeds a certain threshold, the cell membrane is permeable, and the cell is therefore no longer viable. The number of viable cells in each image is therefore the number of cells in which the intensity of CMP stain surrounding and overlapping the nucleus is below that threshold. The data are displayed below (see Figure A.36).

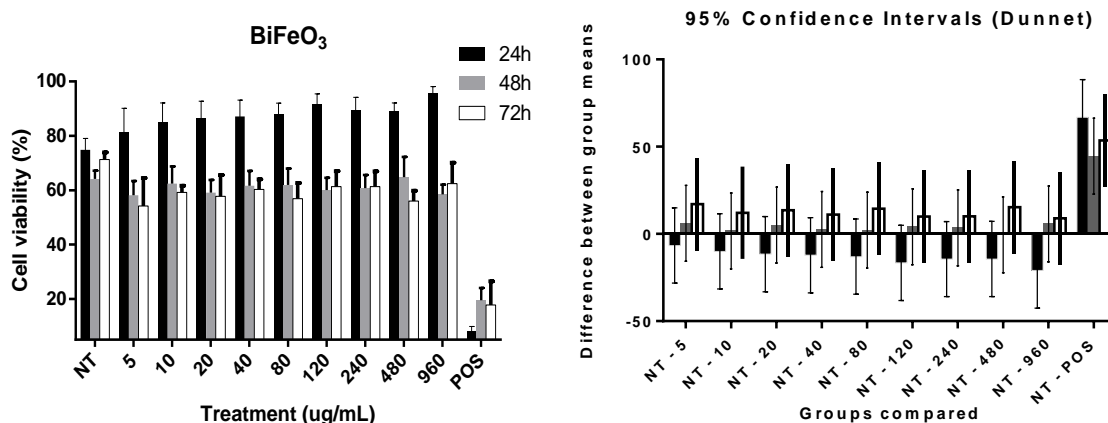


Figure A.35: Cell viability of A549 cells after treatment with BiFeO_3 NPs and the corresponding 95% confidence intervals. Left: cell viability vs concentration of nanomaterial. Valinomycin was used as positive control. The error bars represent the standard error of the mean of triplicates in three independent experiments. Right: difference between group means relative to the untreated control NT (Dunnett's test for multiple comparisons). The error bars represent the 95% confidence intervals (calculated using ordinary One-Way ANOVA).

As with the cell count, there are apparent trends in the concentration-dependent response of the cells to the NM, especially at 24h (see left panel, Figure A.35). However, the variations all fall within the 95% confidence intervals and are therefore not statistically significant (Figure A.35, right panel).

This supports the conclusion that the BiFeO₃ NPs do not heavily impact cell viability in A549 cells at the concentration range analysed.

The cells were also examined for changes in lysosomal mass/pH as a final indicator of cytotoxicity.

A2.1.3 Lysosomal mass/pH

LysoTracker™ Red was used to stain for changes in lysosomal mass or pH (see Figure A.36).

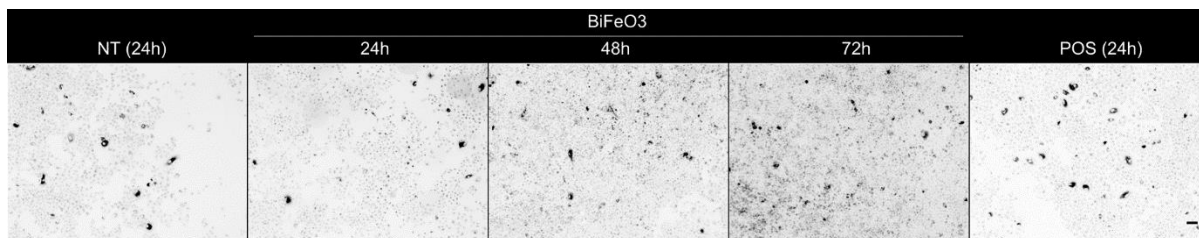


Figure A.36: A549 cells exposed to BiFeO₃ NPs, stained for lysosomal mass/pH changes. From left: representative images of untreated cells after 24h, cells exposed to BiFeO₃ NPs at 80 µg/mL for 24h, 48h, 72h, and cells treated with the positive control (tacrine, 100 µM) for 24h. Only the LysoTracker (red) channels are shown, inverted. The scale bar is 100 µm and is the same for all the images.

LysoTracker™ Red was used to stain for changes in lysosomal mass or pH. Because the images in Figure A.36 are inverted, the darkest spots correspond to areas in which there was a high concentration of the LysoTracker stain. Unlike the CMP stain, the intensity of the stain is recorded for each cell, averaged over the number of cells in each image field. The mean intensity per cell is computed for each well and then normalised to the mean intensity of untreated control wells.

An increase in the intensity therefore corresponds to a larger mass of lysosomes or decrease in pH, indicating a toxic response to the analyte. These data are displayed below (see Figure A.37).

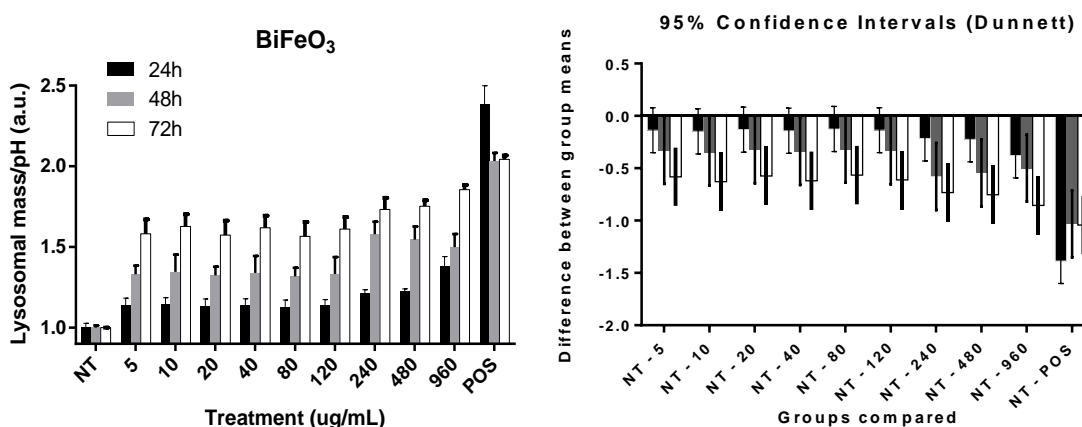


Figure A.37: Lysosomal mass/pH changes in A549 cells after treatment with BiFeO₃ NPs and the corresponding 95% confidence intervals. Left: Lysosomal mass/pH vs concentration of nanomaterial. Tacrine was used as positive control. The error bars represent the standard error of the mean of triplicates in three independent experiments.

Right: difference between group means relative to the untreated control NT (Dunnett's test for multiple comparisons). The error bars represent the 95% confidence intervals (calculated using ordinary One-Way ANOVA).

There is a dose-dependent response in the lysosomal mass/pH as a function of concentration of BiFeO₃ NPs as can be seen in Figure A.37, left panel. After 24h only the highest concentrations (i.e. from 240 µg/mL) induced a significant increase in lysosomal mass/pH. After 48h and 72h all of the variations fell outside of the respective 95% confidence intervals and are hence (right panel, Figure A.37).

The rise in lysosomal mass/pH can be attributed to the internalisation of NPs by the cells (see the section on uptake in Chapter 3 for further discussion).

A2.2 A549 cells treated with ascorbic acid-functionalised BiFeO₃ NPs (BiFeO₃@asc)

A549 cells were exposed to BiFeO₃ NPs at 80 µg/mL for HCS (see Figure A.38), fixed after 48h and stained for DNA (blue channels), cell morphology and membrane permeability (green channels) and lysosomal mass/pH changes (red channels).

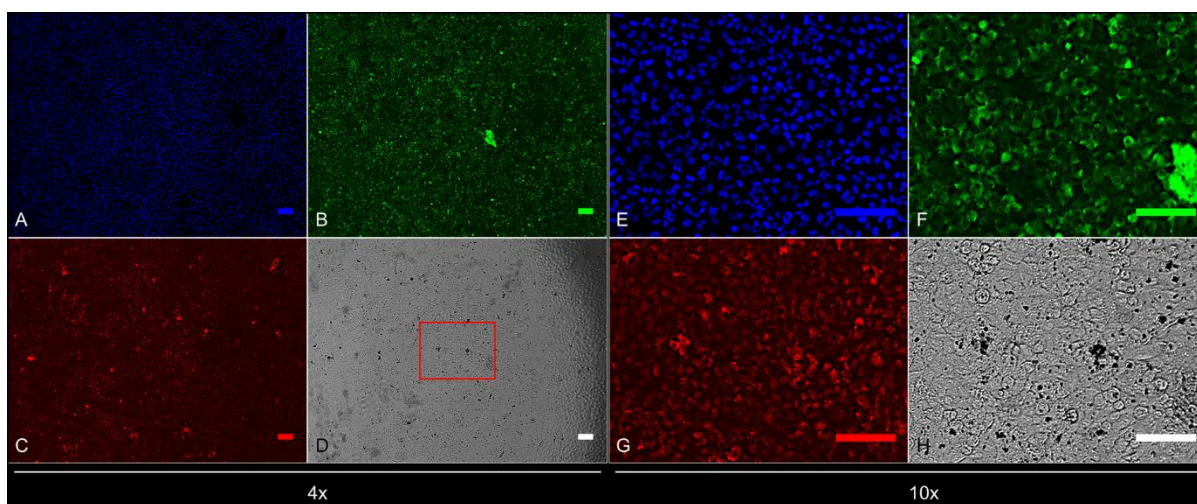


Figure A.38: HCS images of A549 cells after 48h exposure to BiFeO₃@asc NPs at 80 µg/mL. Panels A and E (blue channels): nuclear staining with Hoechst; Panels B and F (green channels): cell membrane permeability staining; Panels C and G (red channels): lysosomal mass/pH staining; Panels D and H (transmitted light channels). Left (A-D): 4x objective images. The region highlighted in the Transmitted Light Channel (D) is the area magnified in the right panels (E-H): 10x objective images. The scale bars are 100 µm.

Figure A.38 shows A549 cells after 48h of exposure to BiFeO₃@asc NPs at 80 µg/mL, stained for DNA (blue channels), cell morphology and membrane permeability (green channels) and lysosomal mass/pH changes (red channels). The aggregation and localisation of the BiFeO₃@asc NPs can be seen in the transmitted light panels (grey channels). As can be seen, after 48h the cells had reached confluency despite the presence of the NPs and the particles had aggregated inside the cells (Panels D and H).

A2.2.1 Cell count

A549 cells were exposed to BiFeO₃@asc NPs at three time points and stained for DNA to determine cell count (see Figure A.39).

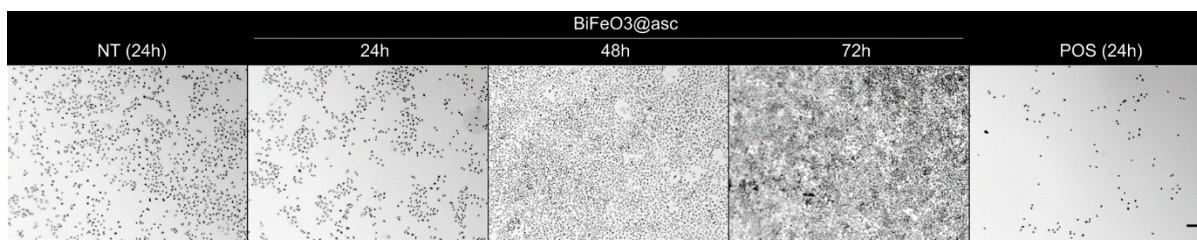


Figure A.39: A549 cells exposed to BiFeO₃@asc NPs, stained for DNA. From left: representative images of untreated cells after 24h, cells exposed to BiFeO₃@asc NPs at 80 µg/mL for 24h, 48h, 72h, and cells treated with the positive control (valinomycin, 120 µM) for 24h. Only the Hoechst channel is shown, inverted. The scale bar is 100 µm and is the same for all the images.

As can be seen, the cells reached confluency after 48h as borne out by the HCS data below.

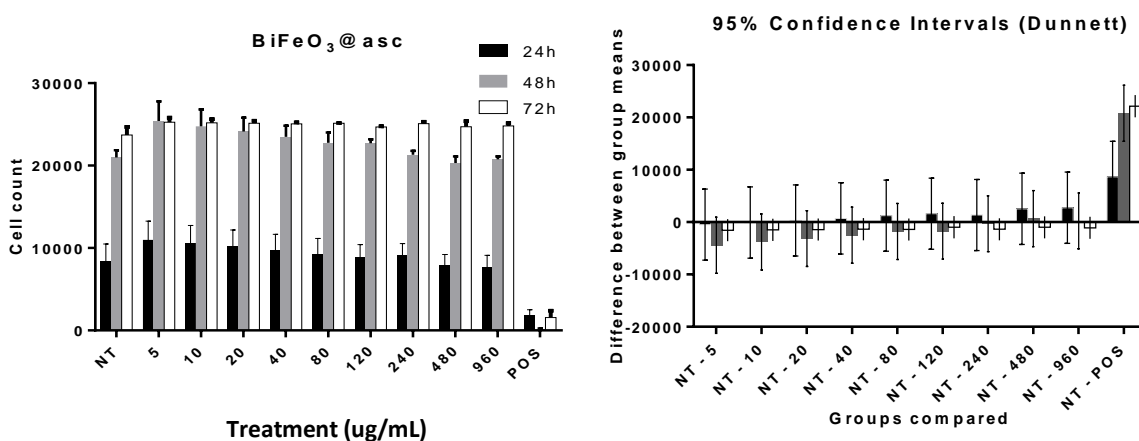


Figure A.40: Cell count of A549 cells after treatment with BiFeO₃@asc NPs and the corresponding 95% confidence intervals. Left: Number of cells vs concentration of nanomaterial. Valinomycin was used as positive control. The error bars represent the standard error of the mean of triplicates in three independent experiments. Right: difference between group means relative to the untreated control NT (Dunnett's test for multiple comparisons). The error bars represent the 95% confidence intervals (calculated using ordinary One-Way ANOVA).

As with A549 cells treated with BiFeO₃ NPs, while there are some apparent trends in the variation of cell count with concentration after 24 and 48 h (Figure A.40, left panel), the counts were not significantly different from the untreated control as can be seen from the 95% confidence intervals (Figure A.40, right panel).

This means that the BiFeO₃@asc NPs did not adversely affect cell proliferation over the concentration range examined.

A2.2.2 Cell Membrane Permeability

Cell membrane permeability was used to indicate cell viability (see Figure A.41).

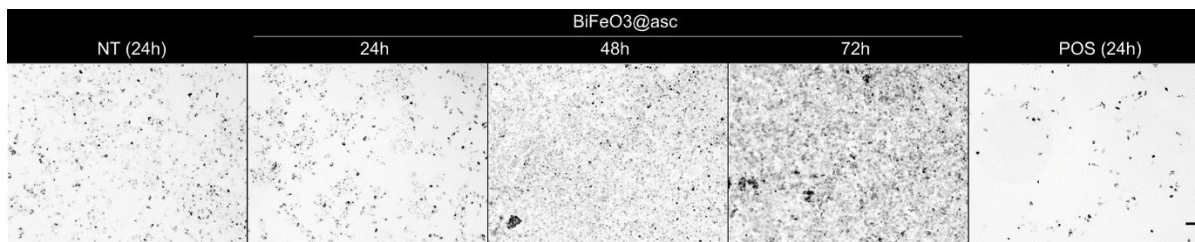


Figure A.41: A549 cells exposed to $\text{BiFeO}_3@asc$ NPs, stained for cell membrane permeability. From left: representative images of untreated cells after 24h, cells exposed to $\text{BiFeO}_3@asc$ NPs at $80 \mu\text{g}/\text{mL}$ for 24h, 48h, 72h, and cells treated with the positive control (valinomycin, $120 \mu\text{M}$) for 24h. Only the CMP (green) channels are shown, inverted. The scale bar is $100 \mu\text{m}$ and is the same for all the images.

Again, the darkest spots correspond to areas in which there was a high concentration of the CMP stain. If the intensity of the stain in the region around a nucleus exceeds a certain threshold, the cell membrane is permeable, and the cell is therefore no longer viable.

The number of viable cells in each image is therefore the number of cells in which the intensity of CMP stain surrounding and overlapping the nucleus is below that threshold. The data are displayed below (see Figure A.42).

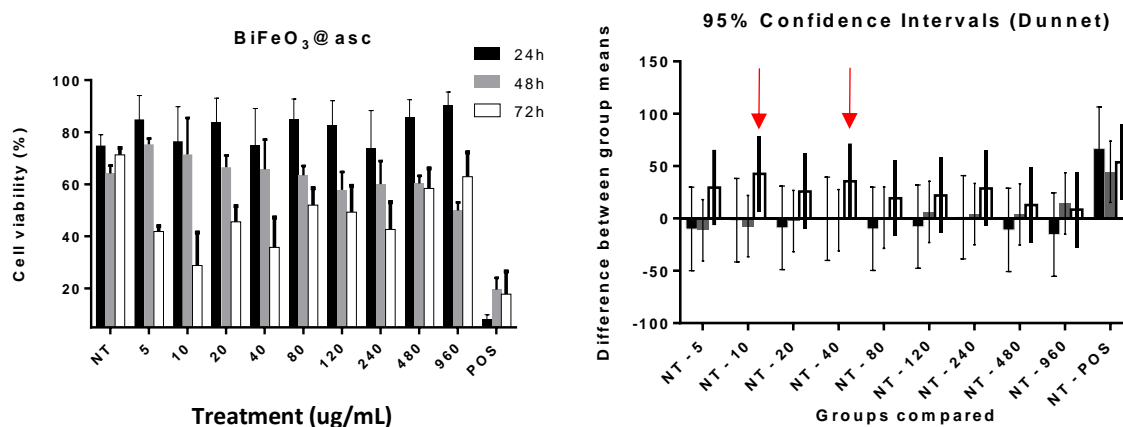


Figure A.42: Cell viability of A549 cells after treatment with $\text{BiFeO}_3@asc$ NPs and the corresponding 95% confidence intervals. Left: cell viability vs concentration of nanomaterial. Valinomycin was used as positive control. The error bars represent the standard error of the mean of triplicates in three independent experiments. Right: difference between group means relative to the untreated control NT (Dunnett's post-test for multiple comparisons). The error bars represent the 95% confidence intervals (calculated using ordinary One-Way ANOVA).

Unlike with the cell count, there are apparent trends in the concentration-dependent response of the cells to the NM (see left panel, Figure A.42). With the exception of two measurements, the variations fall within the 95% confidence intervals according to the Dunnett post-test analysis (see right panel,

Figure A.42) and are therefore not statistically significant. The viability after exposure to BiFeO₃@asc NPs was significantly lower than the untreated control at 10 and 40 µg/mL (indicated by arrows in Figure A.42, right panel), trending toward higher viability at higher concentrations, contrary to a typical dose-response curve for a toxic compound.

This supports the conclusion that the BiFeO₃@asc NPs do not lower cell viability in A549 cells at the highest concentrations analysed but the variability and heterogeneity of the response of the cells at different doses suggests that the interaction is not straightforward.

A2.2.3 Lysosomal mass/pH

The cells were also examined for changes in lysosomal mass/pH as a final indicator of cytotoxicity (see Figure A.43).

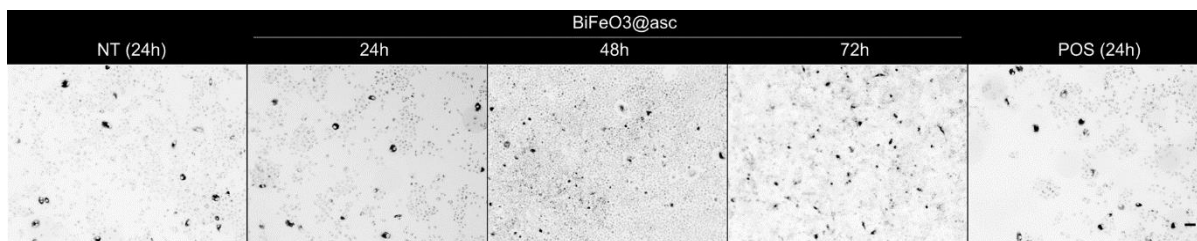


Figure A.43: A549 cells exposed to BiFeO₃@asc NPs, stained for lysosomal mass/pH changes. From left: representative images of untreated cells after 24h, cells exposed to BiFeO₃@asc NPs at 80 µg/mL for 24h, 48h, 72h, and cells treated with the positive control (tacrine, 100 µM) for 24h. Only the LysoTracker (red) channels are shown, inverted. The scale bar is 100 µm and is the same for all the images.

Because the images in Figure A.43 are inverted, an increase in the intensity therefore corresponds to a larger mass of lysosomes or decrease in pH, indicating a toxic response to the BiFeO₃@asc NP. The data from the imaging analysis are displayed below (see Figure A.44).

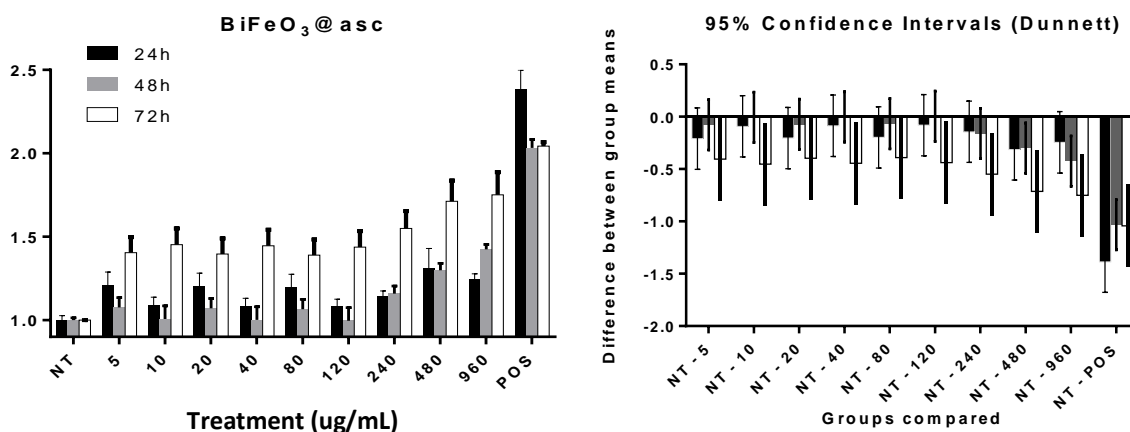


Figure A.44: Lysosomal mass/pH changes in A549 cells after treatment with BiFeO₃@asc NPs and the corresponding 95% confidence intervals. Left: Lysosomal mass/pH vs concentration of nanomaterial. Tacrine was

used as positive control. The error bars represent the standard error of the mean of triplicates in three independent experiments. Right: difference between group means relative to the untreated control NT (Dunnett's test for multiple comparisons). The error bars represent the 95% confidence intervals (calculated using ordinary One-Way ANOVA).

As with the BiFeO₃ NPs treated cells, there is a distinct dose-dependent response in the lysosomal mass/pH (LMPH) as a function of concentration of BiFeO₃@asc NPs (see Figure A.44, left panel). However, after 24h and 48h exposure to NPs at concentrations at 240 µg/mL and below resulted in the LMPH values that fall within the respective 95% confidence intervals and are hence not significant (right panel, Figure A.44). After 72h, there is a significant trend of increasing LMPH with rising concentration. The rise in lysosomal mass/pH can be attributed to the internalisation of NPs by the cells. We might expect that the stabilising ligand, ascorbic acid, would desorb from the surface of the NPs, lowering the pH and increasing the intensity of the stain. It is surprising that the increase is somewhat lower than that observed on exposure to BiFeO₃, but the presence of ascorbic acid does more than simply lower the pH. The adsorption of ascorbic acid on the NPs' surface dramatically increases their colloidal stability, reducing the mass of NPs available for internalisation. See the section on colloidal stability (section 3.3.2) and the summary below for details on the relevant controls.

A2.3 A549 cells treated with BiFeO₃@APTES NPs

A549 cells were exposed to BiFeO₃@APTES NPs at 80 µg/mL for HCS (see Figure A.45), fixed after 48h and stained for DNA (blue channels), cell morphology and membrane permeability (green channels) and lysosomal mass/pH changes (red channels).

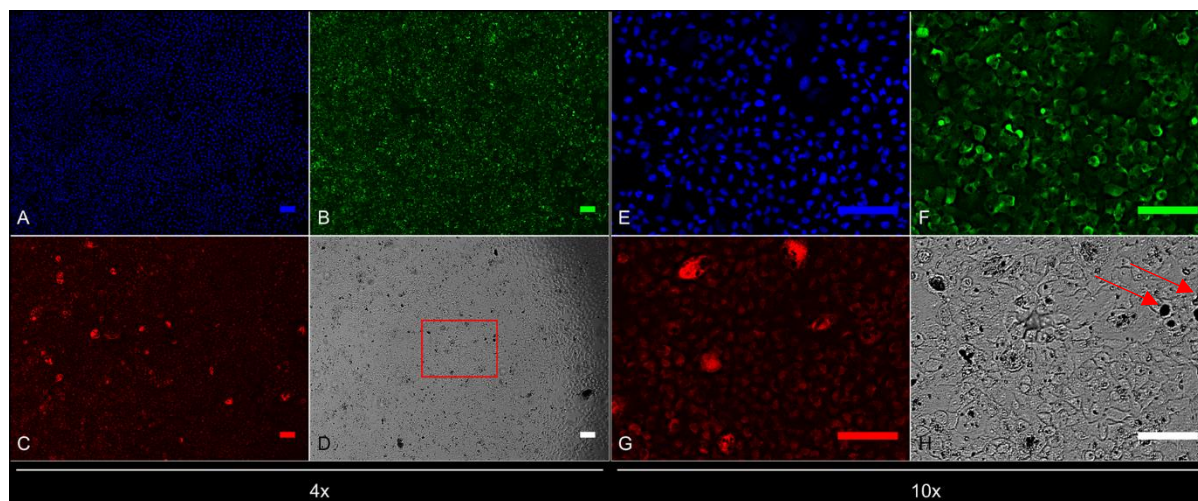


Figure A.45: HCS images of A549 cells after 48h exposure to BiFeO₃@APTES NPs at 80 µg/mL. Panels A and E (blue channels): nuclear staining with Hoechst; Panels B and F (green channels): cell membrane permeability staining; Panels C and G (red channels): lysosomal mass/pH staining; Panels D and H (transmitted light channels).

Left (A-D): 4x objective images. The region highlighted in the Transmitted Light Channel (D) is the area magnified in the right panels (E-H): 10x objective images. The scale bars are 100 μm .

Figure A.45 shows A549 cells after 48h of exposure to $\text{BiFeO}_3@APTES$ NPs at 80 $\mu\text{g}/\text{mL}$, stained for DNA (blue channels), cell morphology and membrane permeability (green channels) and lysosomal mass/pH changes (red channels). The aggregation and localisation of the $\text{BiFeO}_3@APTES$ NPs can be seen in the transmitted light panels (grey channels). As can be seen, after 48h the cells had reached confluency despite the presence of the NPs and the particles had aggregated inside the cells (Panels D and H). Large aggregates in these images are indicated by arrows in Panel H. The lighter halo surrounding these larger aggregates suggest they lie on a different focal plane to the cells (confirmed by Confocal imaging, see section 3.3.4). We conclude that aggregates of APS-coated NPs form when they are dispersed in media and the largest of these cannot be taken up by A549 cells.

A2.3.1 Cell count

A549 cells were exposed to $\text{BiFeO}_3@APTES$ NPs at three time points and stained for DNA to determine cell count (see Figure A.46).

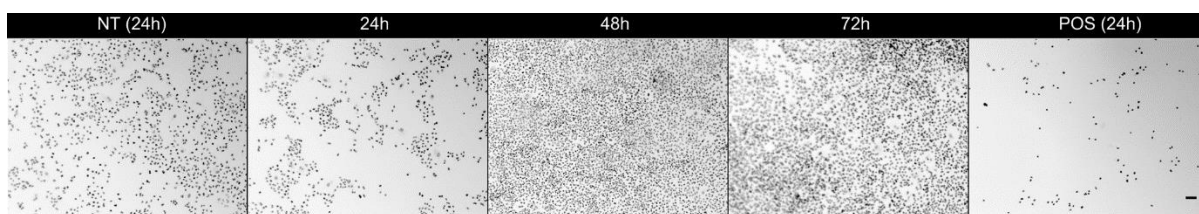


Figure A.46: A549 cells exposed to $\text{BiFeO}_3@APTES$ NPs, stained for DNA. From left: representative images of untreated cells after 24h, cells exposed to $\text{BiFeO}_3@APTES$ NPs at 80 $\mu\text{g}/\text{mL}$ for 24h, 48h, 72h, and cells treated with the positive control (valinomycin, 120 μM) for 24h. Only the Hoechst channel is shown, inverted. The scale bar is 100 μm and is the same for all the images.

As can be seen, the cells reached confluency after 48h. This is borne out by the HCS data below.

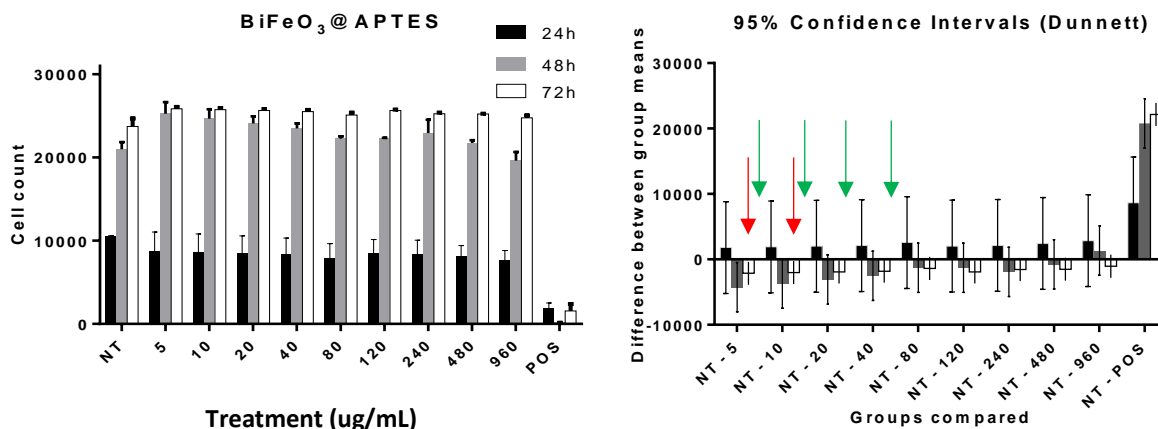


Figure A.47: Cell count of A549 cells after treatment with BiFeO₃@APTES NPs and the corresponding 95% confidence intervals. Left: Number of cells vs concentration of nanomaterial. Valinomycin was used as positive control. The error bars represent the standard error of the mean of triplicates in three independent experiments. Right: difference between group means relative to the untreated control NT (Dunnett's test for multiple comparisons). The error bars represent the 95% confidence intervals (calculated using ordinary One-Way ANOVA).

After 72h, the cell count reached approximately 24000, indicating that the cells had reached confluency shortly after the 48h time-point, as was the case with A549 cells exposed to BiFeO₃ and BiFeO₃@asc NPs.

There are some trends in the variation of cell count with concentration (Figure A.47, left panel):

- After 48h, cell counts are significantly higher than the untreated control at concentrations below 20 µg/mL, as can be seen from the 95% confidence intervals (indicated by red arrows in the right panel of Figure A.47).
- The count drops as the concentration of the treatment rises such that the values lie within the 95% CI, and the trend resembles the familiar dose-response curve. There is a notable distinction here – generally cell count does not exceed that of the untreated control at lower concentrations of analyte. Such behaviour suggests that the size, morphology or even surface chemistry may be promoting the proliferation of the A549 cells. For further detail, see the discussion on Hormesis in the summary at the end of this section.
- After 72h the counts are significantly higher than the untreated control at concentrations below 80 µg/mL, as they fall outside the 95% confidence intervals (indicated by green arrows in the right panel of Figure A.47).

Overall, we can conclude that the BiFeO₃@APTES NPs did not adversely affect cell proliferation over the concentration range examined.

A2.3.2 Cell Membrane Permeability

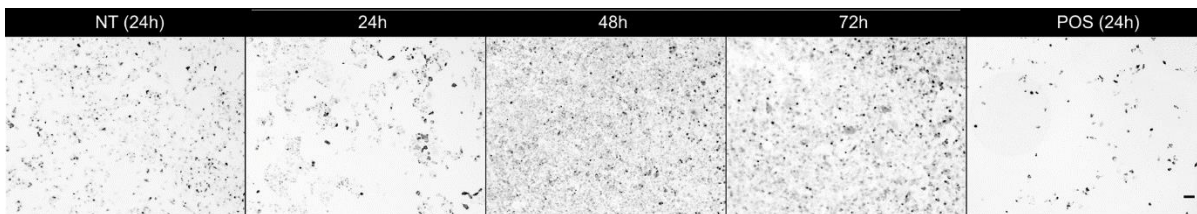


Figure A.48: A549 cells exposed to $\text{BiFeO}_3\text{@APTES}$ NPs, stained for cell membrane permeability. From left: representative images of untreated cells after 24h, cells exposed to $\text{BiFeO}_3\text{@APTES}$ NPs at $80\ \mu\text{g/mL}$ for 24h, 48h, 72h, and cells treated with the positive control (valinomycin, $120\ \mu\text{M}$) for 24h. Only the CMP (green) channels are shown, inverted. The scale bar is $100\ \mu\text{m}$ and is the same for all the images.

Cell membrane permeability was used to indicate cell viability. Because the images in Figure A.48 are inverted, the number of viable cells in each image is therefore the number of cells in which the intensity of CMP stain surrounding and overlapping the nucleus is below the threshold determined for each plate analysed as described above (see A2.2.2). The corresponding data are displayed below (see Figure A.49).

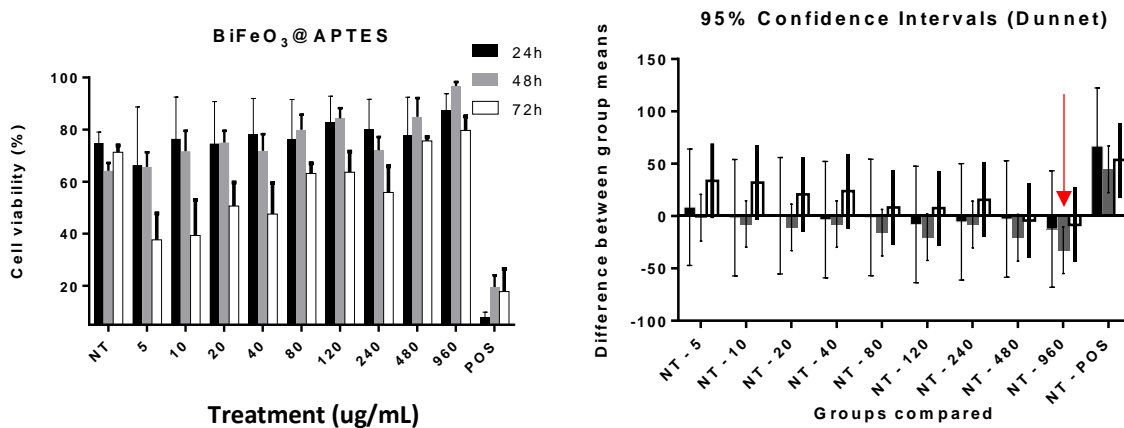


Figure A.49: Cell viability of A549 cells after treatment with $\text{BiFeO}_3\text{@APTES}$ NPs and the corresponding 95% confidence intervals. Left: cell viability vs concentration of nanomaterial. Valinomycin was used as positive control. The error bars represent the standard error of the mean of triplicates in three independent experiments. Right: difference between group means relative to the untreated control NT (Dunnett's test for multiple comparisons). The error bars represent the 95% confidence intervals (calculated using ordinary One-Way ANOVA).

As with cells treated with BiFeO_3 and $\text{BiFeO}_3\text{@asc}$ NPs, there are apparent trends in the concentration-dependent response of the cells to the NM, especially after 72h (see left panel, Figure A.49). It is notable that the same trend toward higher viability at higher doses is observed at each time point. Due to heterogeneity across the repeated experiments, however, the variations all fall within the 95%

confidence intervals and are therefore not statistically significant, except at the highest concentration after 48h where the viability has increased relative to the untreated control.

This supports the conclusion that the BiFeO₃@APTES NPs do not increase the cell membrane permeability, which would result in a decrease in viability of A549 cells at the concentrations analysed.

The cells were also examined for changes in lysosomal mass/pH as a final indicator of cytotoxicity.

A2.3.3 Lysosomal mass/pH

LysoTracker™ Red was used to stain for changes in lysosomal mass or pH (see Figure A.50). Because the images in Figure A.50 are inverted, an increase in the intensity therefore corresponds to a larger mass of lysosomes or decrease in pH, indicating a toxic response to the analyte.

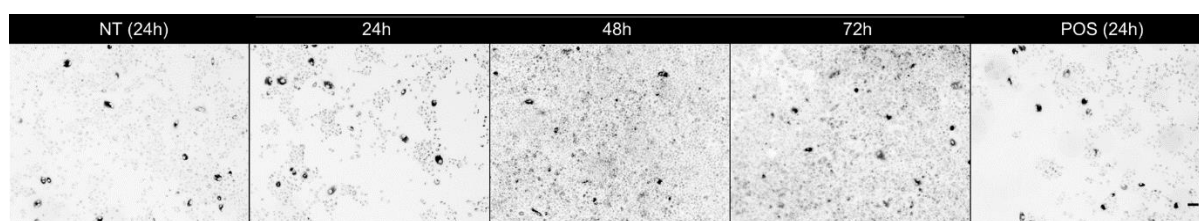


Figure A.50: A549 cells exposed to BiFeO₃@APTES NPs, stained for lysosomal mass/pH changes. From left: representative images of untreated cells after 24h, cells exposed to BiFeO₃@APTES NPs at 80 µg/mL for 24h, 48h, 72h, and cells treated with the positive control (tacrine, 100 µM) for 24h. Only the LysoTracker (red) channels are shown, inverted. The scale bar is 100 µm and is the same for all the images.

The corresponding HCS data are displayed below (see Figure A.51).

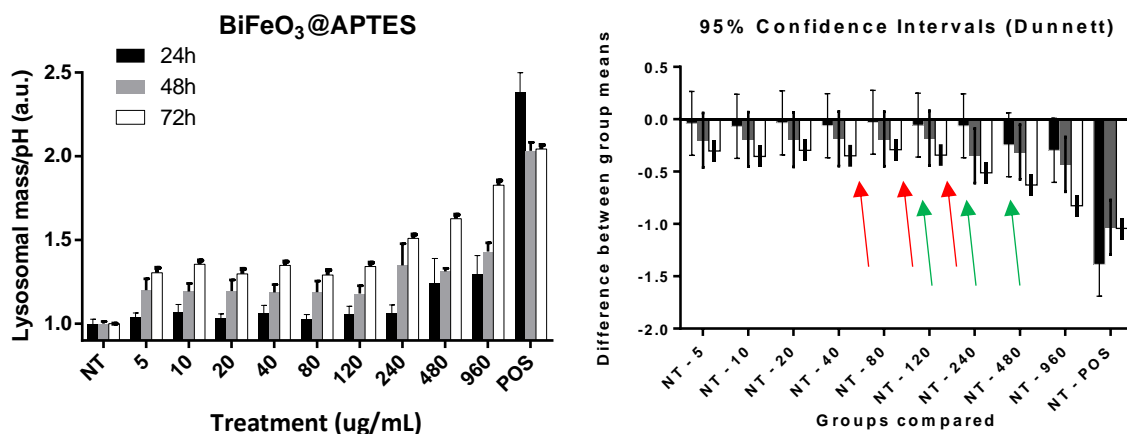


Figure A.51: Lysosomal mass/pH changes in A549 cells after treatment with BiFeO₃@APTES NPs and the corresponding 95% confidence intervals. Left: Lysosomal mass/pH vs concentration of nanomaterial. Tacrine was used as positive control. The error bars represent the standard error of the mean of triplicates in three independent experiments. Right: difference between group means relative to the untreated control NT (Dunnett's test for multiple comparisons). The error bars represent the 95% confidence intervals (calculated using ordinary One-Way ANOVA).

There is a dose-dependent response in the lysosomal mass/pH as a function of concentration of BiFeO₃@APTES NPs as can be seen in Figure A.51, left panel. The increases in LMPH on exposure to concentrations below 960 µg/mL after 24h (indicated by a green arrow in Figure A.51, right panel) and below 240 µg/mL after 48h (indicated by red arrows in Figure A.51, right panel) fell within the 95% confidence interval and were therefore not significant. In contrast, there was a significant trend of increasing LMPH with rising NP concentration after 72h.

The rise in LMPH can be attributed to the internalisation of NPs by the cells (see the section on uptake for further information).

A2.4 A549 cells treated with BiFeO₃@Fe₃O₄@asc NPs

A549 cells were exposed to BiFeO₃@Fe₃O₄@asc NPs at 80 µg/mL for HCS (see Figure A.52), fixed after 48h and stained for DNA (blue channels), cell morphology and membrane permeability (green channels) and lysosomal mass/pH changes (red channels).

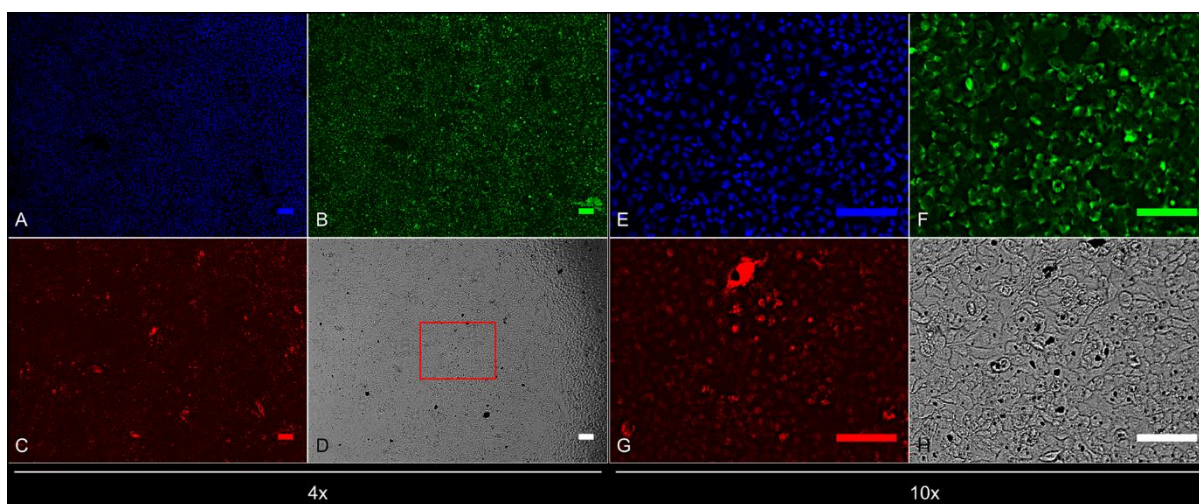


Figure A.52: HCS images of A549 cells after 48h exposure to BiFeO₃@Fe₃O₄@asc NPs at 80 µg/mL. Panels A and E (blue channels): nuclear staining with Hoechst; Panels B and F (green channels): cell membrane permeability staining; Panels C and G (red channels): lysosomal mass/pH staining; Panels D and H (transmitted light channels). Left (A-D): 4x objective images. The region highlighted in the Transmitted Light Channel (D) is the area magnified in the right panels (E-H): 10x objective images. The scale bars are 100 µm.

A549 cells after 48h of exposure to BiFeO₃@Fe₃O₄@asc NPs at 80 µg/mL are shown in Figure A.52, for stained DNA (blue channels), cell morphology and membrane permeability (green channels) and lysosomal mass/pH changes (red channels). The aggregation and localisation of the BiFeO₃@Fe₃O₄@asc NPs can be seen in the transmitted light panels (grey channels). As can be seen, after 48h the cells had reached confluency despite the presence of the NPs and the particles had aggregated inside the cells (Panels D and H). In comparison to the APS-coated BiFeO₃ NPs (see Figure A.46), the aggregates are

smaller and co-localise with the cells suggesting that the NPs and any aggregates are taken up by the cells.

A2.4.1 Cell count

A549 cells were exposed to $\text{BiFeO}_3@Fe_3O_4@asc$ NPs at three time points and stained for DNA to determine cell count (Figure A.53). The cells reached confluency after 48h.

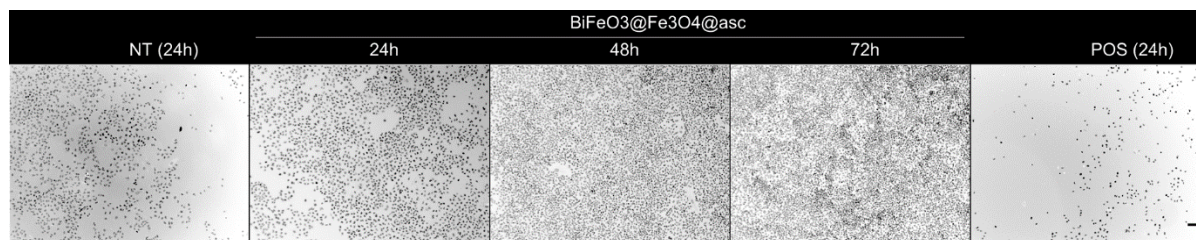


Figure A.53: Representative cell count images of A549 cells exposed to $\text{BiFeO}_3@Fe_3O_4@asc$ NPs, stained for DNA. From left: representative images of untreated cells after 24h, cells exposed to $\text{BiFeO}_3@Fe_3O_4@asc$ at $80 \mu\text{g/mL}$ NPs at $80 \mu\text{g/mL}$ for 24h, 48h, 72h, and cells treated with the positive control (valinomycin, $120 \mu\text{M}$) for 24h. Only the Hoechst channel is shown, inverted. The scale bar is $100 \mu\text{m}$ and is the same for all the images.

This is borne out by the HCS data below.

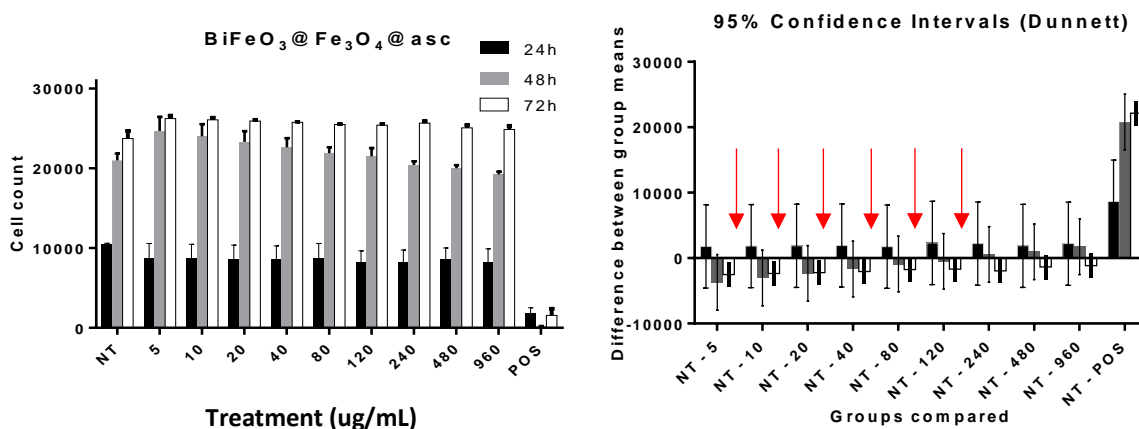


Figure A.54: Cell count of A549 cells after treatment with $\text{BiFeO}_3@Fe_3O_4@asc$ NPs and the corresponding 95% confidence intervals. Left: Number of cells vs concentration of nanomaterial. Valinomycin was used as positive control. The error bars represent the standard error of the mean of triplicates in three independent experiments. Right: difference between group means relative to the untreated control NT (Dunnett's test for multiple comparisons). The error bars represent the 95% confidence intervals (calculated using ordinary One-Way ANOVA).

On treating A549 cells with $\text{BiFeO}_3@Fe_3O_4@asc$ NPs, the following observations can be made:

- There is no significant growth in cell count after 24h at any concentration (see Figure A.54, left panel).
- After 48h we observe an elevated count at $5 \mu\text{g/mL}$ trending lower with increasing concentration, but these values fall within the 95% confidence interval (Figure A.54, right panel).

- There is a small but significant increase relative to the untreated control after 72h especially at concentrations below 120 $\mu\text{g}/\text{mL}$, with a slight dose-dependent response.
- The count drops as the concentration of the treatment rises such that the values lie within the 95% CI, and the trend resembles the familiar dose-response curve. There is a notable distinction here – generally cell count does not exceed that of the untreated control at lower concentrations of analyte when analysing cytotoxicity. Such behaviour suggests that the size, morphology or even surface chemistry may be promoting the proliferation of the A549 cells.

This means that the $\text{BiFeO}_3@Fe_3O_4@asc$ NPs did not adversely affect cell proliferation over the concentration range examined. The similarity of this data with the cell count of A549 cells exposed to BiFeO_3 , $\text{BiFeO}_3@asc$ or $\text{BiFeO}_3@APTES$ suggests also that the response of the cells does not strongly depend on the surface chemistry of these NPs.

A2.4.2 Cell Membrane Permeability

Cell membrane permeability was used to support the cell viability (see Figure A.55).

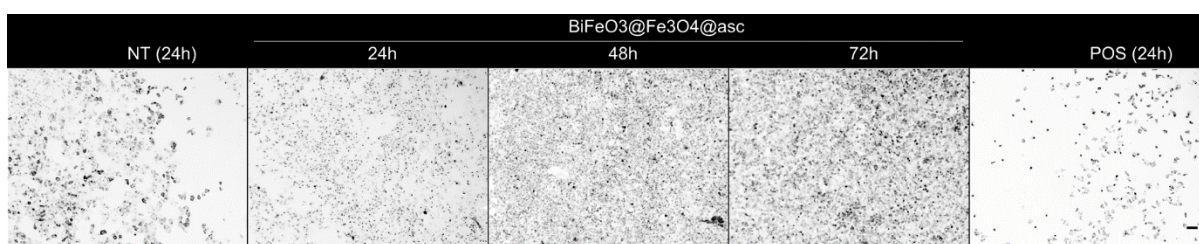


Figure A.55: A549 cells exposed to $\text{BiFeO}_3@Fe_3O_4@asc$ NPs, stained for cell membrane permeability. From left: representative images of untreated cells after 24h, cells exposed to $\text{BiFeO}_3@Fe_3O_4@asc$ NPs at 80 $\mu\text{g}/\text{mL}$ for 24h, 48h, 72h, and cells treated with the positive control (valinomycin, 120 μM) for 24h. Only the CMP (green) channels are shown, inverted. The scale bar is 100 μm and is the same for all the images.

Because the images in Figure A.55 are inverted, the number of viable cells in each image is therefore the number of cells in which the intensity of CMP stain surrounding and overlapping the nucleus is below the threshold determined for each plate analysed as described above (see A2.2.2).

Histogram plots of the HCS corresponding HCS data are displayed below (see Figure A.56).

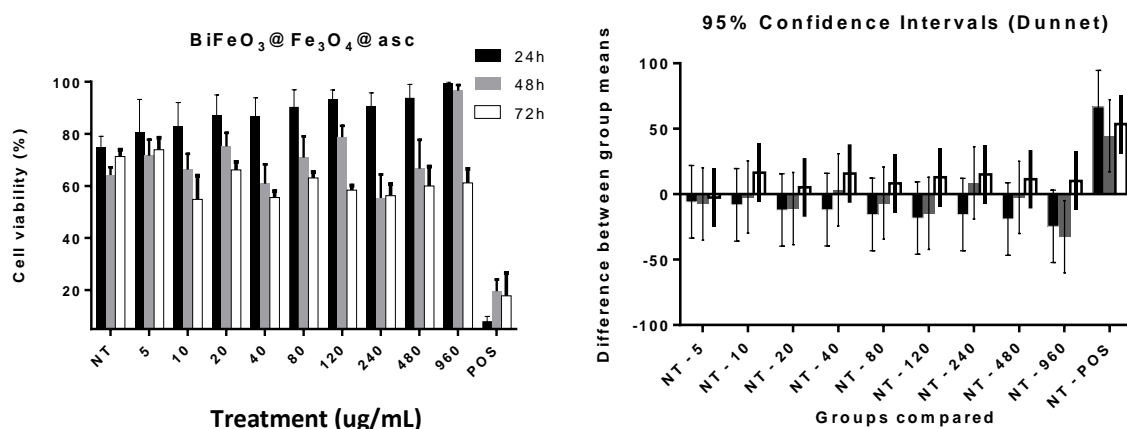


Figure A.56: Cell viability of A549 cells after treatment with BiFeO₃@Fe₃O₄@asc NPs and the corresponding 95% confidence intervals. Left: cell viability vs concentration of nanomaterial. Valinomycin was used as positive control. The error bars represent the standard error of the mean of triplicates in three independent experiments. Right: difference between group means relative to the untreated control NT (Dunnett's test for multiple comparisons). The error bars represent the 95% confidence intervals (calculated using ordinary One-Way ANOVA).

Similar to the NPs discussed above, there are apparent trends in the concentration-dependent response of the cells to the NM (see left panel, Figure A.56). However, the variations all fall within the 95% confidence intervals and are therefore not statistically significant (right panel, Figure A.56).

This supports the conclusion that the BiFeO₃@Fe₃O₄@asc NPs do not accelerate cell death in A549 cells at the concentrations analysed.

A2.4.3 Lysosomal mass/pH

The cells were then examined for changes in lysosomal mass/pH as a final indicator of cytotoxicity (see Figure A.57).

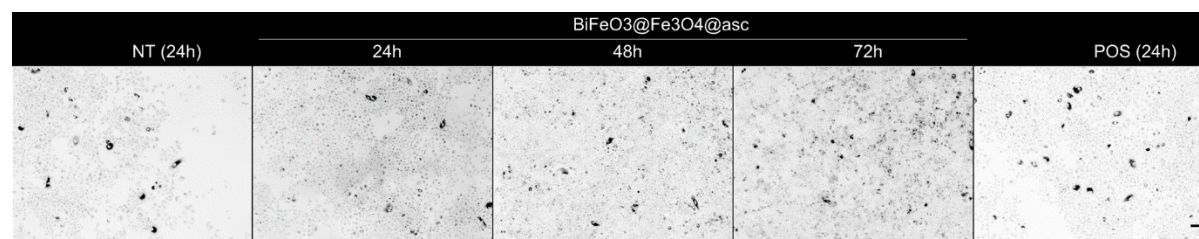


Figure A.57: A549 cells exposed to BiFeO₃@Fe₃O₄@asc NPs, stained for lysosomal mass/pH changes. From left: representative images of untreated cells after 24h, cells exposed to BiFeO₃@Fe₃O₄@asc NPs at 80 μg/mL for 24h, 48h, 72h, and cells treated with the positive control (tacrine, 100 μM) for 24h. Only the LysoTracker (red) channels are shown, inverted. The scale bar is 100 μm and is the same for all the images.

LysoTracker™ Red was used to stain for changes in lysosomal mass or pH. Because the images in Figure A.57 are inverted, an increase in the intensity therefore corresponds to a larger mass of lysosomes or

decrease in pH, indicating a toxic response to the analyte. Corresponding histogram plots of the data are displayed below (see Figure A.58).

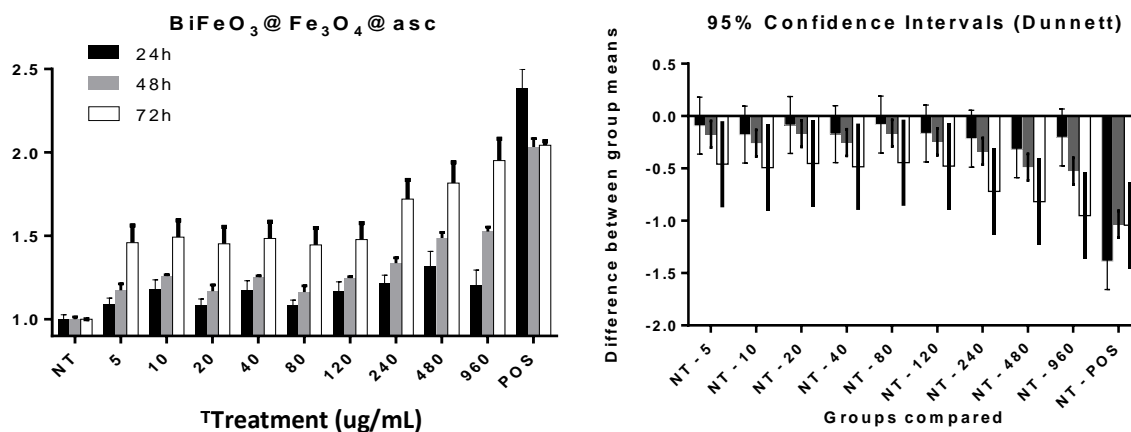


Figure A.58: Lysosomal mass/pH changes in A549 cells after treatment with BiFeO₃@Fe₃O₄@asc NPs and the corresponding 95% confidence intervals. Left: Lysosomal mass/pH vs concentration of nanomaterial. Tacrine was used as positive control. The error bars represent the standard error of the mean of triplicates in three independent experiments. Right: difference between group means relative to the untreated control NT (Dunnett's test for multiple comparisons). The error bars represent the 95% confidence intervals (calculated using ordinary One-Way ANOVA).

Several features distinguish the response of A549 cells to BiFeO₃@Fe₃O₄@asc NPs in comparison to the NPs previously discussed. Here, there is a dose-dependent increase in LMPH after 48h which rises further after 72h, with the LMPH significantly higher than the negative control at all concentrations (see Figure A.58, left panel). A similar trend (lysosomal mass/pH increasing with rising concentration) is apparent after 24h but the variations fall within the 95% confidence intervals and are hence not significant (see Figure A.58, right panel).

The rise in lysosomal mass/pH can be attributed to the internalisation of NPs by the cells (see the section on uptake in Chapter 3 for further information).

A2.5 A549 cells treated with BiFeO₃@Fe₃O₄@APTES NPs

A549 cells were exposed to BiFeO₃@Fe₃O₄@APTES NPs at 80 µg/mL were processed by HCS (see Figure A.59), fixed and stained for DNA (blue channels), cell morphology and membrane permeability (green channels) and lysosomal mass/pH changes (red channels).

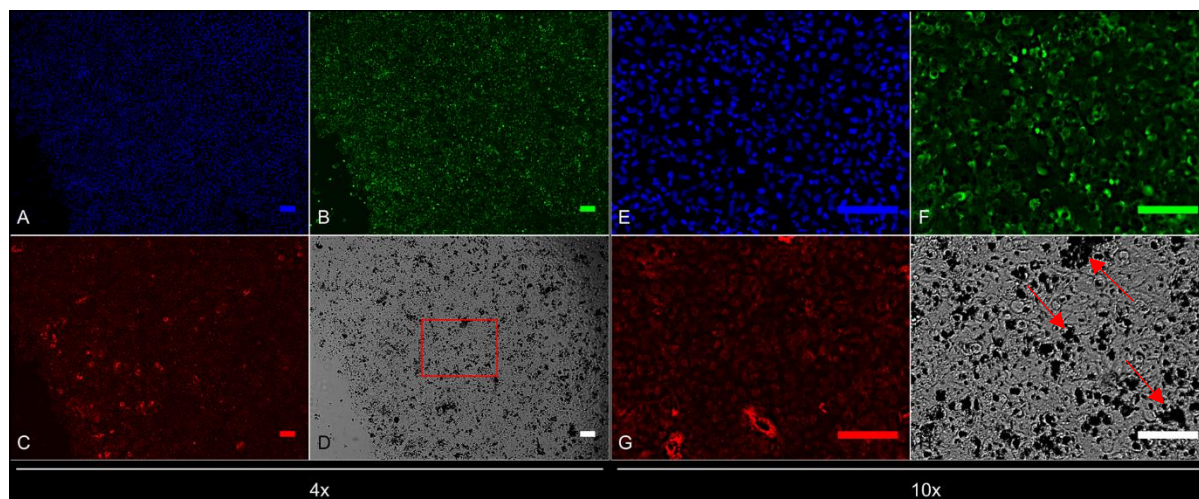


Figure A.59: HCS images of A549 cells after 48h exposure to $\text{BiFeO}_3@Fe_3O_4@APTES$ NPs at $80 \mu\text{g/mL}$. Panels A and E (blue channels): nuclear staining with Hoechst; Panels B and F (green channels): cell membrane permeability staining; Panels C and G (red channels): lysosomal mass/pH staining; Panels D and H (transmitted light channels). Left (A-D): 4x objective images. The region highlighted in the Transmitted Light Channel (D) is the area magnified in the right panels (E-H): 10x objective images. The scale bars are $100 \mu\text{m}$.

The aggregation and localisation of the $\text{BiFeO}_3@Fe_3O_4@APTES$ NPs can be seen in the transmitted light panels (grey channels). After 48h the cells had reached confluency despite the presence of the NPs and the particles had aggregated around or inside the cells (Panels D and H). Particularly in Panel H, we can see that the NPs have formed very large aggregates, many larger than the diameter of the cells, suggesting that the aggregates also form in suspension, and that capping the surface of the NPs with APS accelerates aggregation, supporting the conclusions drawn from the DLS/NS analysis in Chapter 2.

A2.5.1 Cell count

A549 cells were exposed to $\text{BiFeO}_3@Fe_3O_4@APTES$ NPs at three time points and stained for DNA to determine cell count (Figure A.60).

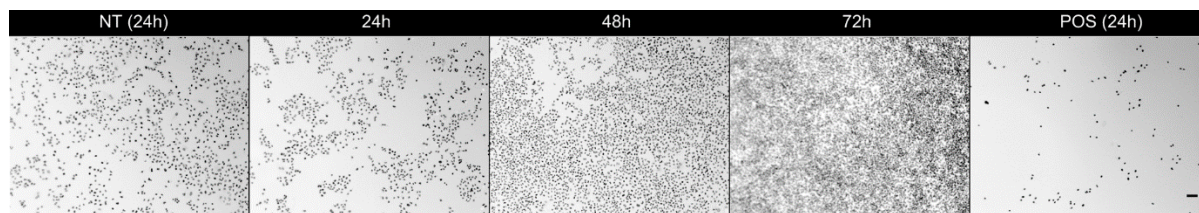


Figure A.60: A549 cells exposed to $\text{BiFeO}_3@Fe_3O_4@APTES$ NPs, stained for DNA. From left: representative images of untreated cells after 24h, cells exposed to $\text{BiFeO}_3@Fe_3O_4@APTES$ NPs at $80 \mu\text{g/mL}$ for 24h, 48h, 72h, and cells treated with the positive control (valinomycin, $120 \mu\text{M}$) for 24h. Only the Hoechst channel is shown, inverted. The scale bar is $100 \mu\text{m}$ and is the same for all the images.

As previously, the cells reached confluency after 48h. This is borne out by the HCS data below.

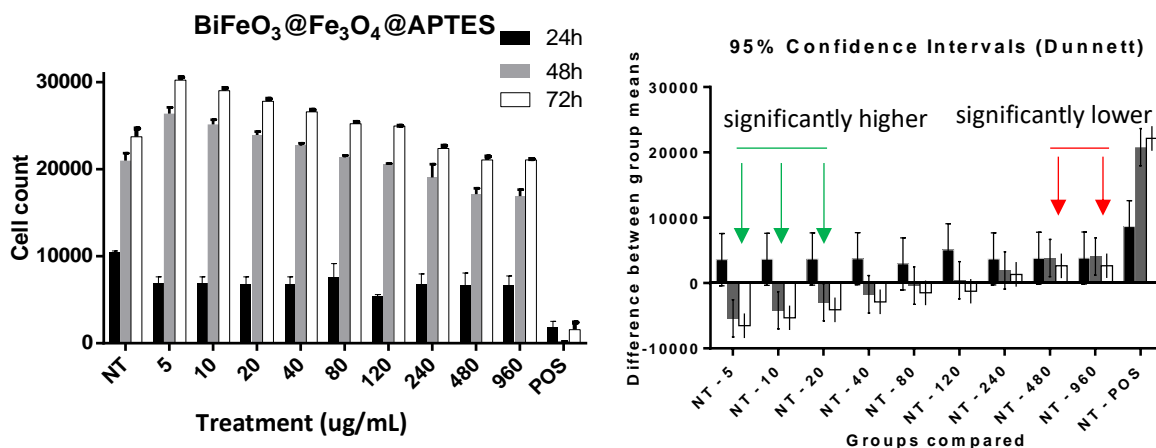


Figure A.61: Cell count of A549 cells after treatment with $\text{BiFeO}_3@Fe_3O_4@APTES$ NPs and the corresponding 95% confidence intervals. Left: Number of cells vs concentration of nanomaterial. Valinomycin was used as positive control. The error bars represent the standard error of the mean of triplicates in three independent experiments. Right: difference between group means relative to the untreated control NT (Dunnett's test for multiple comparisons). The error bars represent the 95% confidence intervals (calculated using ordinary One-Way ANOVA).

Unlike the NPs discussed above, there are significant trends in the variation of the cell count for all the concentrations after both 48 and 72h exposure (Figure A.61, left panel). After 48h the counts were significantly higher than the untreated control's count at NP concentrations below 40 $\mu\text{g}/\text{mL}$, but falling as the concentration rose such that from 480 $\mu\text{g}/\text{mL}$ the count was significantly lower than the NT count and the pattern persisted after 72h, as can be seen from the 95% confidence intervals (indicated by arrows in the right panel of Figure A.61).

This means that the $\text{BiFeO}_3@Fe_3O_4@APTES$ NPs reduced cell proliferation at higher concentrations, despite promoting cell growth at lower concentrations.

A2.5.2 Cell Membrane Permeability

Cell membrane permeability was used to indicate cell viability (see Figure A.62).

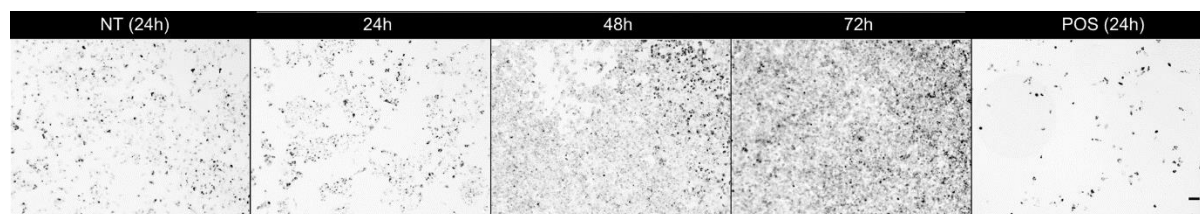


Figure A.62: A549 cells exposed to $\text{BiFeO}_3@Fe_3O_4@APTES$ NPs, stained for cell membrane permeability. From left: representative images of untreated cells after 24h, cells exposed to $\text{BiFeO}_3@Fe_3O_4@APTES$ NPs at 80 $\mu\text{g}/\text{mL}$ for 24h, 48h, 72h, and cells treated with the positive control (valinomycin, 120 μM) for 24h. Only the CMP (green) channels are shown, inverted. The scale bar is 100 μm and is the same for all the images.

Cell membrane permeability was used to indicate cell viability. Because the images in Figure A.62 are inverted, the number of viable cells in each image is therefore the number of cells in which the intensity of CMP stain surrounding and overlapping the nucleus is below the threshold determined for each plate analysed as described above (see A2.2.2). The data are displayed below (see Figure A.63).

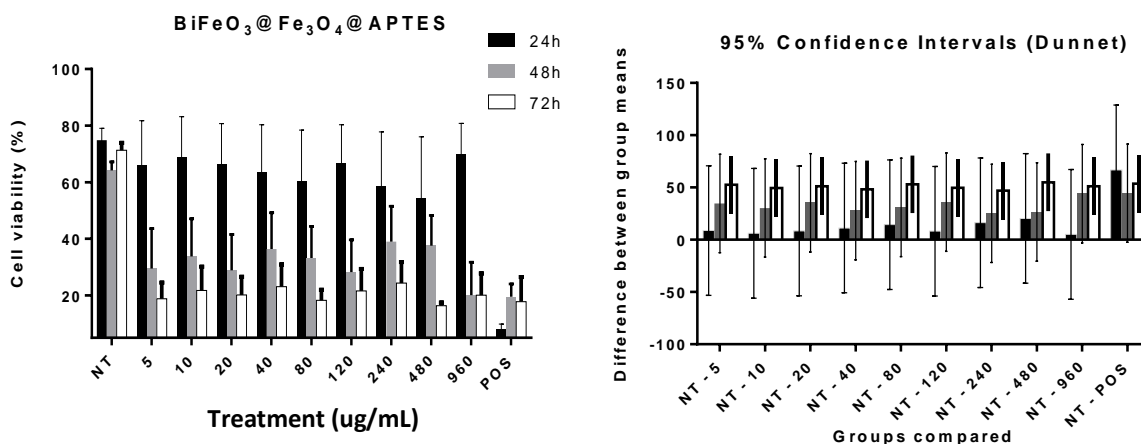


Figure A.63: Cell viability of A549 cells after treatment with BiFeO₃@Fe₃O₄@APTES NPs and the corresponding 95% confidence intervals. Left: cell viability vs concentration of nanomaterial. Valinomycin was used as positive control. The error bars represent the standard error of the mean of triplicates in three independent experiments. Right: difference between group means relative to the untreated control NT (Dunnett's test for multiple comparisons). The error bars represent the 95% confidence intervals (calculated using ordinary One-Way ANOVA).

With respect to cell viability on exposure to BiFeO₃@Fe₃O₄@APTES, as with other NPs, there is appreciable heterogeneity within each group (i.e. between triplicate samples or between repeated experiments) as demonstrated by the considerable size of the standard error of the mean at each time-point (see left panel, Figure A.63).

For this reason, the variations after 24 and 48h all fall within the 95% confidence intervals and therefore the data are not statistically significant (see Figure A.63, right panel).

After 72h the cell viability dropped from approximately 70% to approximately 20% (see left panel, Figure A.63) but there is no clear dependency on the dose; the viability had fallen to approximately the same level at all concentrations. Furthermore, this is the same viability as in cells exposed to the positive control, valinomycin.

This demonstrates the toxicity profile of the BiFeO₃@Fe₃O₄@APTES NPs where, with increasing cell permeability, there was an associated lower cell viability in A549 cells at the concentrations analysed after two days' incubation.

A2.5.3 Lysosomal mass/pH

The cells were also examined for changes in lysosomal mass/pH as a final indicator of cytotoxicity (see Figure A.64).

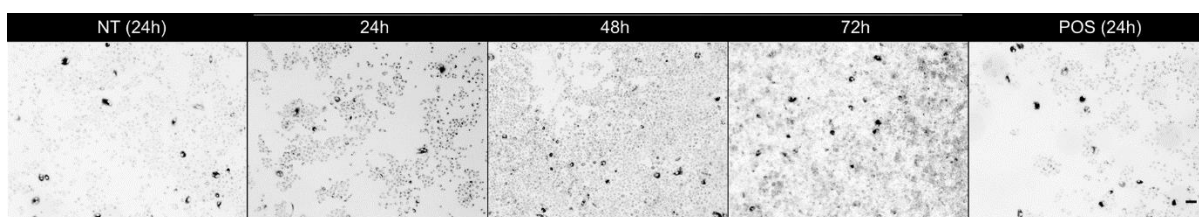


Figure A.64: A549 cells exposed to $\text{BiFeO}_3@Fe_3O_4@APTES$ NPs, stained for lysosomal mass/pH changes. From left: representative images of untreated cells after 24h, cells exposed to $\text{BiFeO}_3@Fe_3O_4@APTES$ NPs at $80 \mu\text{g/mL}$ for 24h, 48h, 72h, and cells treated with the positive control (tacrine, $100 \mu\text{M}$) for 24h. Only the LysoTracker (red) channels are shown, inverted. The scale bar is $100 \mu\text{m}$ and is the same for all the images.

LysoTracker™ Red was used to stain for changes in lysosomal mass or pH. Because the images in Figure A.64 are inverted, an increase in the intensity therefore corresponds to a larger mass of lysosomes or decrease in pH, indicating a toxic response to the analyte. The corresponding data are displayed below (see Figure A.65).

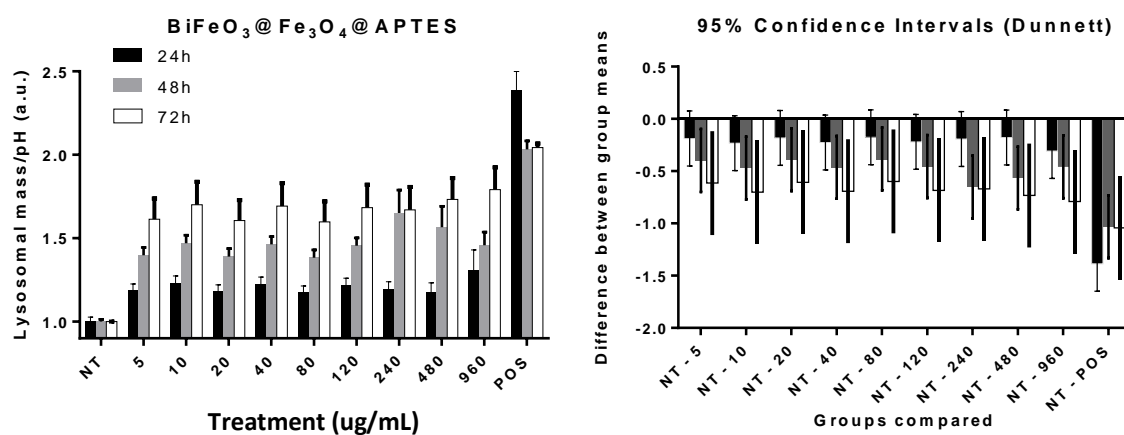


Figure A.65: Lysosomal mass/pH changes in A549 cells after treatment with $\text{BiFeO}_3@Fe_3O_4@APTES$ NPs and the corresponding 95% confidence intervals. Left: Lysosomal mass/pH vs concentration of nanomaterial. Tacrine was used as positive control. The error bars represent the standard error of the mean of triplicates in three independent experiments. Right: difference between group means relative to the untreated control NT (Dunnett's test for multiple comparisons). The error bars represent the 95% confidence intervals (calculated using ordinary One-Way ANOVA).

The response of A549 cells exposed to $\text{BiFeO}_3@Fe_3O_4@APTES$ NPs very closely mirror that observed on exposure to $\text{BiFeO}_3@Fe_3O_4@asc$:

- There is a dose-dependent increase in LMPH after 48h which rises further after 72h, with the LMPH significantly higher than the negative control at all concentrations (see Figure A.65, left panel).

- LMPH also appears to increase with rising concentration after 24h but the variations fall within the 95% confidence intervals and are hence not significant (see Figure A.65, right panel).

There was greater deviation across samples and experiments on exposure to APS coated NPs, however this can be seen in the difference in bars representing the SEM, for example. This heterogeneity may be partially attributed to the aggregation observed in Figure A.59.

Coating with APS, on the other hand, reduces colloidal stability in aqueous suspension and biological media. This resulted in increased aggregation, precipitation and accumulation of NPs on top of cells, raising the mass of NPs internalised as indicated by the increased LMPH.

A2.6 A549 cells treated with BiFeO₃@Fe₂O₃@asc NPs

A549 cells were exposed to BiFeO₃@Fe₂O₃@APTES NPs at 80 µg/mL were processed by HCS (see Figure A.66), fixed and stained for DNA (blue channels), cell morphology and membrane permeability (green channels) and lysosomal mass/pH changes (red channels).

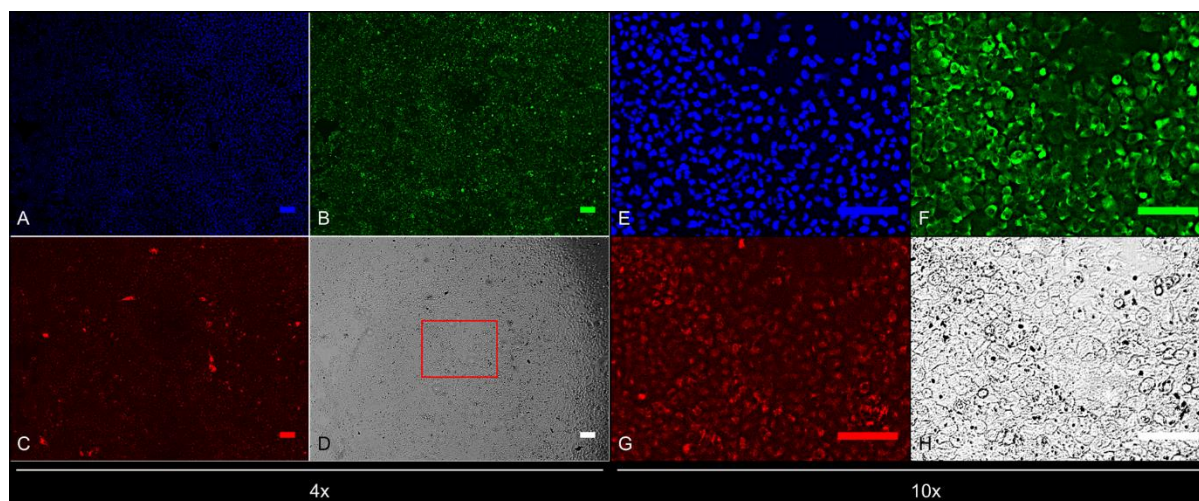


Figure A.66: HCS images of A549 cells after 48h exposure to BiFeO₃@Fe₂O₃@asc NPs at 80 µg/mL. Panels A and E (blue channels): nuclear staining with Hoechst; Panels B and F (green channels): cell membrane permeability staining; Panels C and G (red channels): lysosomal mass/pH staining; Panels D and H (transmitted light channels). Left (A-D): 4x objective images. The region highlighted in the Transmitted Light Channel (D) is the area magnified in the right panels (E-H): 10x objective images. The scale bars are 100 µm.

The aggregation and localisation of the BiFeO₃@Fe₂O₃@asc NPs can be seen in the transmitted light panels (grey channels). As can be seen, after 48h the cells had reached confluency despite the presence of the NPs and the particles had aggregated inside the cells (Panels D and H).

A2.6.1 Cell count

A549 cells were exposed to BiFeO₃@Fe₂O₃@asc NPs at three time points and stained for DNA to determine cell count (Figure A.67).

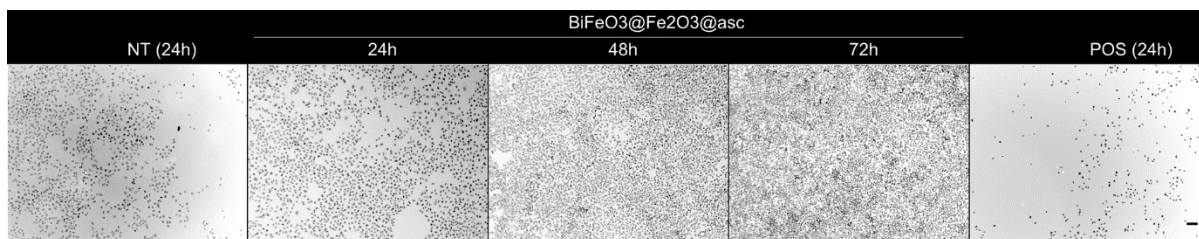


Figure A.67: A549 cells exposed to $\text{BiFeO}_3@Fe_2O_3@asc$ NPs, stained for DNA. From left: representative images of untreated cells after 24h, cells exposed to $\text{BiFeO}_3@Fe_2O_3@asc$ NPs at $80 \mu\text{g/mL}$ for 24h, 48h, 72h, and cells treated with the positive control (valinomycin, $120 \mu\text{M}$) for 24h. Only the Hoechst channel is shown, inverted. The scale bar is $100 \mu\text{m}$ and is the same for all the images.

The graphical data below report on the cells' confluency after 48h. This is borne out by the HCS data below.

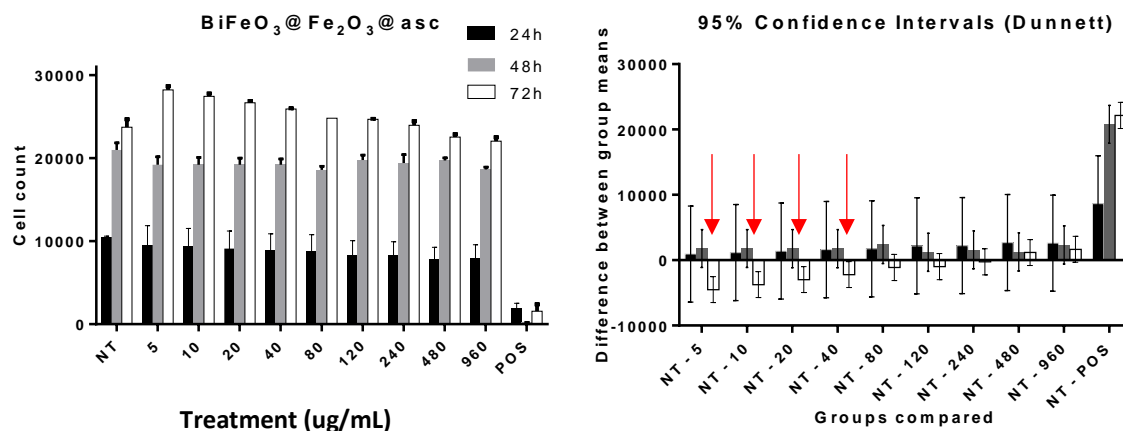


Figure A.68: Cell count of A549 cells after treatment with $\text{BiFeO}_3@Fe_2O_3@asc$ NPs and the corresponding 95% confidence intervals. Left: Number of cells vs concentration of nanomaterial. Valinomycin was used as positive control. The error bars represent the standard error of the mean of triplicates in three independent experiments. Right: difference between group means relative to the untreated control NT (Dunnett's test for multiple comparisons). The error bars represent the 95% confidence intervals (calculated using ordinary One-Way ANOVA).

The cells had reached confluency shortly after the 48h time-point.

While there are some apparent trends in the variation of cell count with concentration (Figure A.68, left panel), only after 72h were the counts significantly different from the untreated control, and only at concentrations below $80 \mu\text{g/mL}$, as can be seen from the 95% confidence intervals (indicated by arrows in the right panel of Figure A.68).

This means that the $\text{BiFeO}_3@Fe_2O_3@asc$ NPs did not adversely affect cell proliferation over the concentration range examined. In fact, the small but significant concentration-dependent increase in cell growth at lower concentrations after 72h further support the conclusion that there are complex

interactions at play as suggested by the responses of the cells to $\text{BiFeO}_3@APTES$, $\text{BiFeO}_3@Fe_3O_4@asc$, $\text{BiFeO}_3@Fe_3O_4@APTES$ and $\text{BiFeO}_3@Fe_2O_3$ NPs.

A2.6.2 Cell Membrane Permeability

Cell membrane permeability was used to indicate cell viability (see Figure A.69).

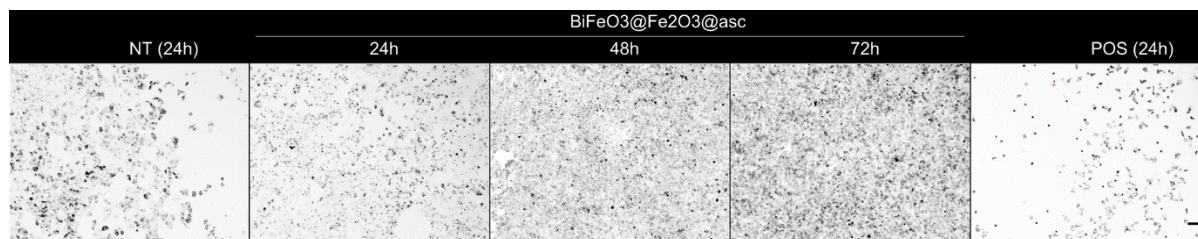


Figure A.69: A549 cells exposed to $\text{BiFeO}_3@Fe_2O_3@asc$ NPs, stained for cell membrane permeability. From left: representative images of untreated cells after 24h, cells exposed to $\text{BiFeO}_3@Fe_2O_3@asc$ NPs at $80 \mu\text{g/mL}$ for 24h, 48h, 72h, and cells treated with the positive control (valinomycin, $120 \mu\text{M}$) for 24h. Only the CMP (green) channels are shown, inverted. The scale bar is $100 \mu\text{m}$ and is the same for all the images.

Because the images in Figure A.69 are inverted, the number of viable cells in each image is therefore the number of cells in which the intensity of CMP stain surrounding and overlapping the nucleus is below the threshold determined for each plate analysed as described above (see A2.2.2). The data are displayed below (see Figure A.70).

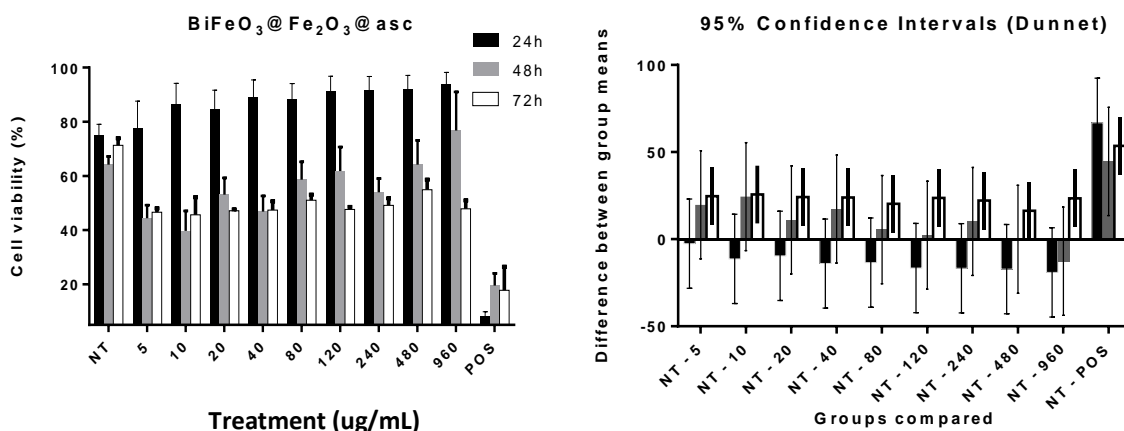


Figure A.70: Cell viability of A549 cells after treatment with $\text{BiFeO}_3@Fe_2O_3@asc$ NPs and the corresponding 95% confidence intervals. Left: cell viability vs concentration of nanomaterial. Valinomycin was used as positive control. The error bars represent the standard error of the mean of triplicates in three independent experiments. Right: difference between group means relative to the untreated control NT (Dunnett's test for multiple comparisons). The error bars represent the 95% confidence intervals (calculated using ordinary One-Way ANOVA).

As with the cell count, there are apparent trends in the concentration-dependent response of the cells to the NM, especially at 24h and 48h (see left panel, Figure A.70). However, the 24h and 48h variations all fall within the 95% confidence intervals and are therefore not statistically significant.

Cell viability fell below 50% after 72h at all concentrations, with no discernible concentration dependence. This is in contrast with the increase in cell count discussed above. The rise in cell number accompanied by a reduction in viability supports the conclusion that the $\text{BiFeO}_3@Fe_2O_3@asc$ NPs induce stress in A549 cells.

The cells were also examined for changes in lysosomal mass/pH as a final indicator of cytotoxicity.

A2.6.3 Lysosomal mass/pH

LysoTracker™ Red was used to stain for changes in lysosomal mass or pH (see Figure A.71).

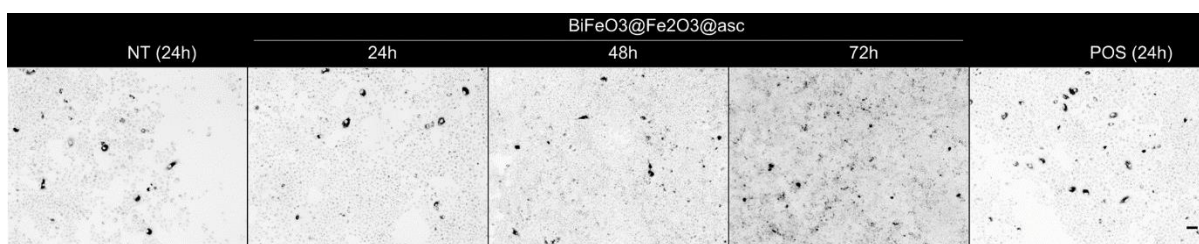


Figure A.71: A549 cells exposed to $\text{BiFeO}_3@Fe_2O_3@asc$ NPs, stained for lysosomal mass/pH changes. From left: representative images of untreated cells after 24h, cells exposed to $\text{BiFeO}_3@Fe_2O_3@asc$ NPs at 80 $\mu\text{g}/\text{mL}$ for 24h, 48h, 72h, and cells treated with the positive control (tacrine, 100 μM) for 24h. Only the LysoTracker (red) channels are shown, inverted. The scale bar is 100 μm and is the same for all the images.

Because the images in Figure A.71 are inverted, an increase in the intensity therefore corresponds to a larger mass of lysosomes or decrease in pH, indicating a toxic response to the analyte. These data are displayed below (see Figure A.72).

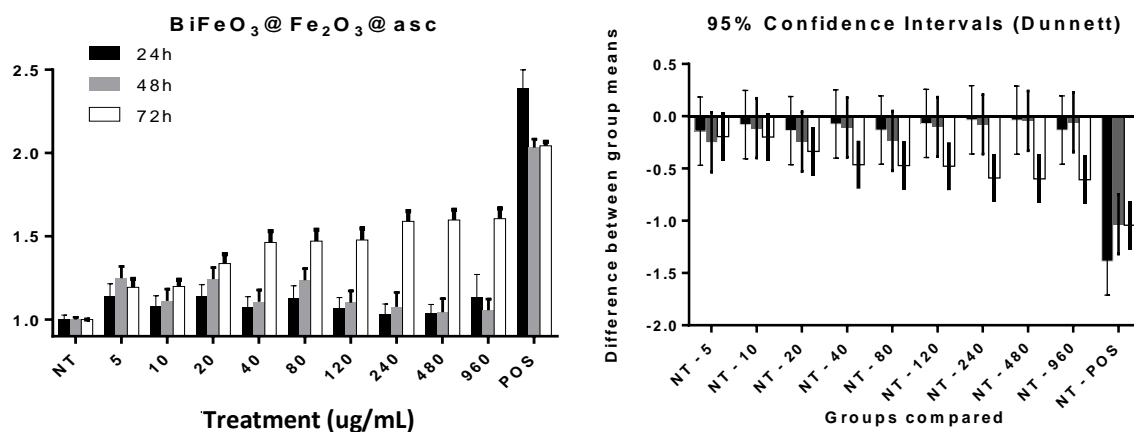


Figure A.72: Lysosomal mass/pH changes in A549 cells after treatment with $\text{BiFeO}_3@Fe_2O_3@asc$ NPs and the corresponding 95% confidence intervals. Left: Lysosomal mass/pH vs concentration of nanomaterial. Tacrine was

used as positive control. The error bars represent the standard error of the mean of triplicates in three independent experiments. Right: difference between group means relative to the untreated control NT (Dunnett's test for multiple comparisons). The error bars represent the 95% confidence intervals (calculated using ordinary One-Way ANOVA).

On exposure to $\text{BiFeO}_3@Fe_2O_3@asc$, increases in A549 cells' lysosomal mass/pH were only significant after 72h and only above 20 $\mu\text{g}/\text{mL}$ (see Figure A.72). After 24h and 48h, the LMPH values fell within the respective 95% confidence intervals and are hence not significant (right panel, Figure A.72).

The dose-dependent rise in lysosomal mass/pH observed after 72h can again be attributed to the internalisation of NPs by the cells. As discussed previously, we might expect that ascorbic acid to desorb from the surface of the NPs, lowering the pH and increasing the intensity of the stain. Yet, the LMPH of A549 cells exposed to $\text{BiFeO}_3@Fe_2O_3@asc$ is somewhat lower than with any other NP. This may be due to greater affinity of the adsorbed ascorbic acid to the surface groups available on $\text{BiFeO}_3@Fe_2O_3$ composite resulting in increased immobilisation of ascorbic acid. Furthermore, increased adsorption of ascorbic acid may result in greater surface charge which would draw more counterions from suspension reducing the pH and decreasing the intensity of the LMPH further.

It is evident that the aggregates are smaller for $\text{BiFeO}_3@Fe_2O_3@asc$ NPs than for any other, as shown in Figure A.66. This supports the conclusion that improved colloidal stability results in reduced internalisation.

A2.7 A549 cells treated with $\text{SiO}_2@BiFeO_3$ NWs

A549 cells were prepared for HCS processing after exposure to SiO_2 & BiFeO_3 NWs at 80 $\mu\text{g}/\text{mL}$, stained for DNA (blue channels), cell morphology and membrane permeability (green channels) and lysosomal mass/pH changes (red channels), as shown in Figure A.73.

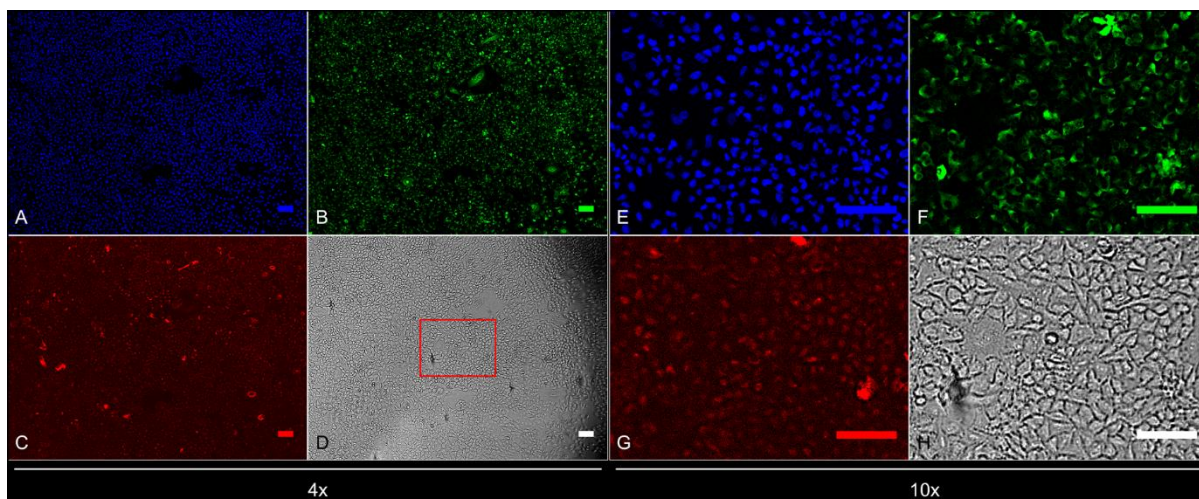


Figure A.73: HCS images of A549 cells after 48h exposure to SiO_2 & BiFeO_3 NWs at $80 \mu\text{g/mL}$. Panels A and E (blue channels): nuclear staining with Hoechst; Panels B and F (green channels): cell membrane permeability staining; Panels C and G (red channels): lysosomal mass/pH staining; Panels D and H (transmitted light channels). Left (A-D): 4x objective images. The region highlighted in the Transmitted Light Channel (D) is the area magnified in the right panels (E-H): 10x objective images. The scale bars are $100 \mu\text{m}$.

The aggregation and localisation of the SiO_2 & BiFeO_3 NWs can be seen in the transmitted light panels (grey channels). After 48h the cells had reached confluency despite the presence of the NWs and the particles had aggregated inside the cells (Panels D and H).

A2.7.1 Cell count

A549 cells were exposed to SiO_2 & BiFeO_3 NWs at three time points and stained for DNA to determine cell count (Figure A.74).

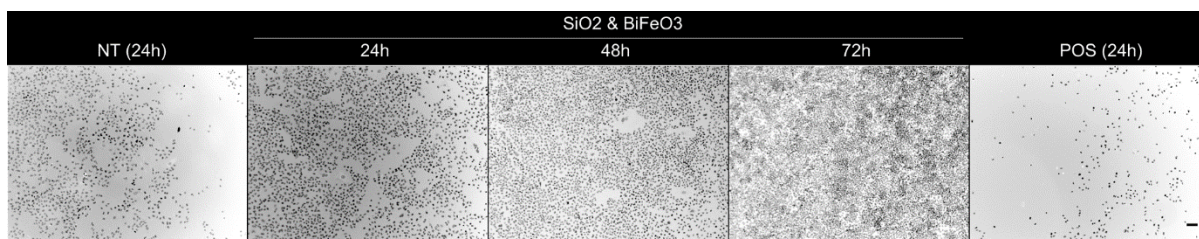


Figure A.74: A549 cells exposed to SiO_2 & BiFeO_3 NWs, stained for DNA. From left: representative images of untreated cells after 24h, cells exposed to SiO_2 & BiFeO_3 NWs at $80 \mu\text{g/mL}$ for 24h, 48h, 72h, and cells treated with the positive control (valinomycin, $120 \mu\text{M}$) for 24h. Only the Hoechst channel is shown, inverted. The scale bar is $100 \mu\text{m}$ and is the same for all the images.

As can be seen, the cells reached confluency after 48h. This is borne out by the HCS data below.

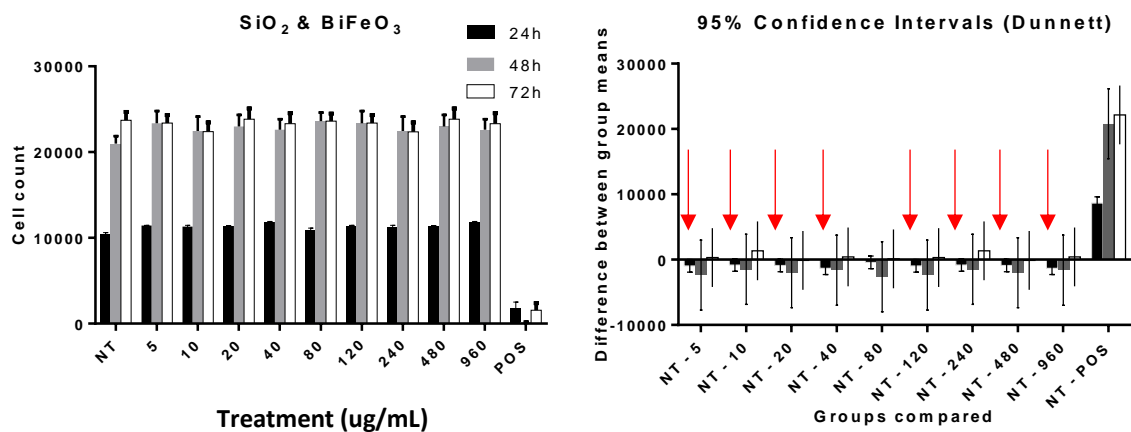


Figure A.75: Cell count of A549 cells after treatment with SiO₂ & BiFeO₃ NWs and the corresponding 95% confidence intervals. Left: Number of cells vs concentration of nanomaterial. Valinomycin was used as positive control. The error bars represent the standard error of the mean of triplicates in three independent experiments. Right: difference between group means relative to the untreated control NT (Dunnett's test for multiple comparisons). The error bars represent the 95% confidence intervals (calculated using ordinary One-Way ANOVA).

Only the cell counts after 24h were significantly different from the untreated control as can be seen from the 95% confidence intervals (indicated by arrows in the right panel of Figure A.75). With the exception of where treated with SiO₂ & BiFeO₃ NWs, there was a small but significant increase in A549 cell count after 24h (Figure A.75, left panel), but this increase was not concentration dependent and had disappeared after 48h.

After 72h, the cell count reached approximately 24000, indicating that the cells had reached confluency shortly after the 48h time-point.

This means that the SiO₂ & BiFeO₃ NWs did not adversely affect cell proliferation over the concentration range examined.

A2.7.2 Cell Membrane Permeability

Cell membrane permeability was used to indicate cell viability (see Figure A.76).

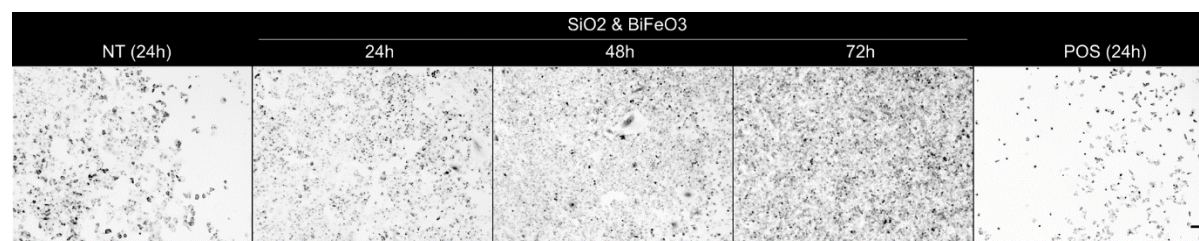


Figure A.76: A549 cells exposed to SiO₂ & BiFeO₃ NWs stained for cell membrane permeability. From left: representative images of untreated cells after 24h, cells exposed to SiO₂ & BiFeO₃ NWs at 80 µg/mL for 24h, 48h, 72h, and cells treated with the positive control (valinomycin, 120 µM) for 24h. Only the CMP (green) channels are shown, inverted. The scale bar is 100 µm and is the same for all the images.

Cell membrane permeability was used to indicate cell viability. Because the images in Figure A.76 are inverted, the number of viable cells in each image is therefore the number of cells in which the intensity of CMP stain surrounding and overlapping the nucleus is below the threshold determined for each plate analysed as described above (see A2.2.2). The data are displayed below (see Figure A.77).

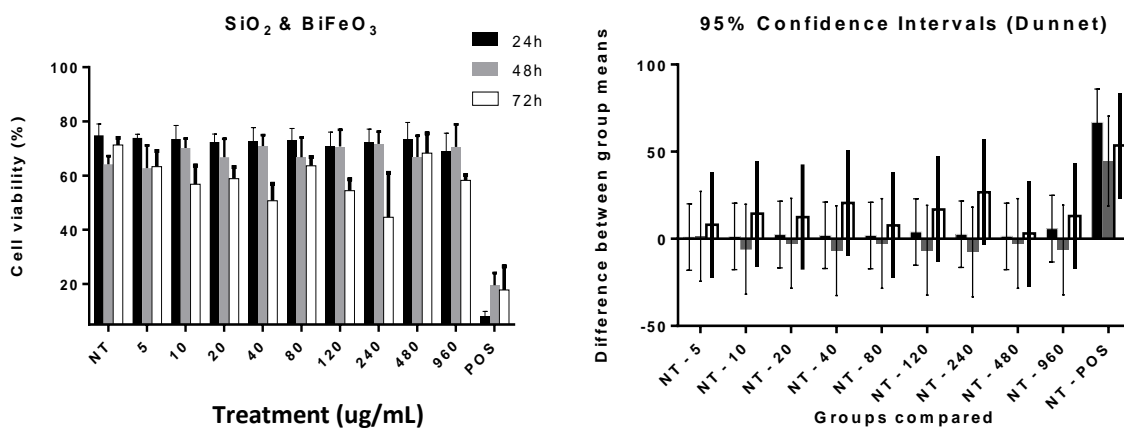


Figure A.77: Cell viability of A549 cells after treatment with SiO₂ & BiFeO₃ NWs and the corresponding 95% confidence intervals. Left: cell viability vs concentration of nanomaterial. Valinomycin was used as positive control. The error bars represent the standard error of the mean of triplicates in three independent experiments. Right: difference between group means relative to the untreated control NT (Dunnett's test for multiple comparisons). The error bars represent the 95% confidence intervals (calculated using ordinary One-Way ANOVA).

As with the cell count, there are apparent trends in the concentration-dependent response of the cells to the NM, especially at 24h (see left panel, Figure A.77). However, the variations all fall within the 95% confidence intervals and are therefore not statistically significant.

This supports the conclusion that the SiO₂ & BiFeO₃ NWs do not lower cell viability in A549 cells at the concentrations analysed.

A2.7.3 Lysosomal mass/pH

The cells were also examined for changes in lysosomal mass/pH as a final indicator of cytotoxicity (Figure A.78).

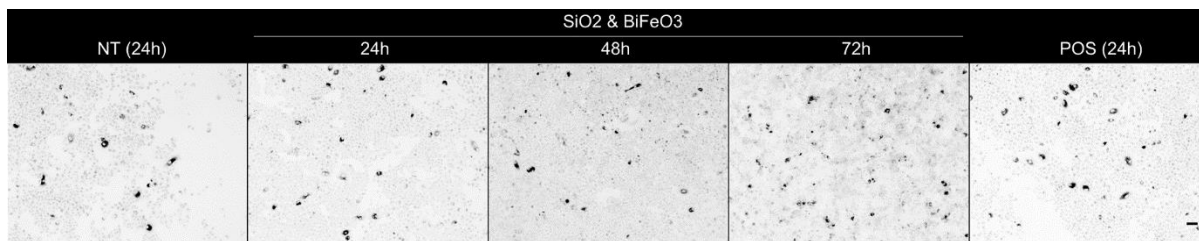


Figure A.78: A549 cells exposed to SiO₂ & BiFeO₃ NWs stained for lysosomal mass/pH changes. From left: representative images of untreated cells after 24h, cells exposed to SiO₂ & BiFeO₃ NWs at 80 µg/mL for 24h, 48h, 72h, and cells treated with the positive control (tacrine, 100 µM) for 24h. Only the LysoTracker (red) channels are shown, inverted. The scale bar is 100 µm and is the same for all the images.

LysoTracker™ Red was used to stain for changes in lysosomal mass or pH. Because the images in Figure A.78 are inverted, an increase in the intensity therefore corresponds to a larger mass of lysosomes or decrease in pH, indicating a toxic response to the analyte. These data are displayed below (see Figure A.79).

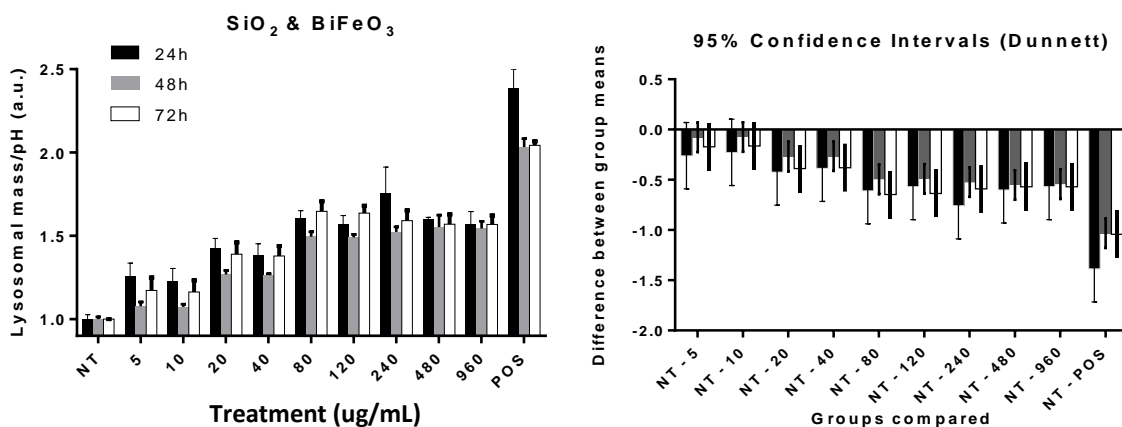


Figure A.79: Lysosomal mass/pH changes in A549 cells after treatment with SiO₂ & BiFeO₃ NWs and the corresponding 95% confidence intervals. Left: Lysosomal mass/pH vs concentration of nanomaterial. Tacrine was used as positive control. The error bars represent the standard error of the mean of triplicates in three independent experiments. Right: difference between group means relative to the untreated control NT (Dunnett's test for multiple comparisons). The error bars represent the 95% confidence intervals (calculated using ordinary One-Way ANOVA).

There is a distinct dose-dependent response in the lysosomal mass/pH as a function of concentration of SiO₂ & BiFeO₃ NWs after 24h as can be seen in Figure A.79, left panel. A similar trend of increasing lysosomal mass/pH with rising concentration is observed after 48h and 72h but the variations fall within the respective 95% confidence intervals and are hence not significant except at the highest concentration after 72h (indicated by an arrow, right panel, Figure A.79).

The rise in lysosomal mass/pH can be attributed to the internalisation of NWs by the cells (see the section on uptake for further information).

A2.8 A549 cells treated with SiO₂&BiFeO₃@Fe₃O₄ NWs

A549 cells were prepared for HCS processing after exposure to SiO₂ & BiFeO₃@Fe₃O₄ NWs at 80 µg/mL (see Figure A.80).

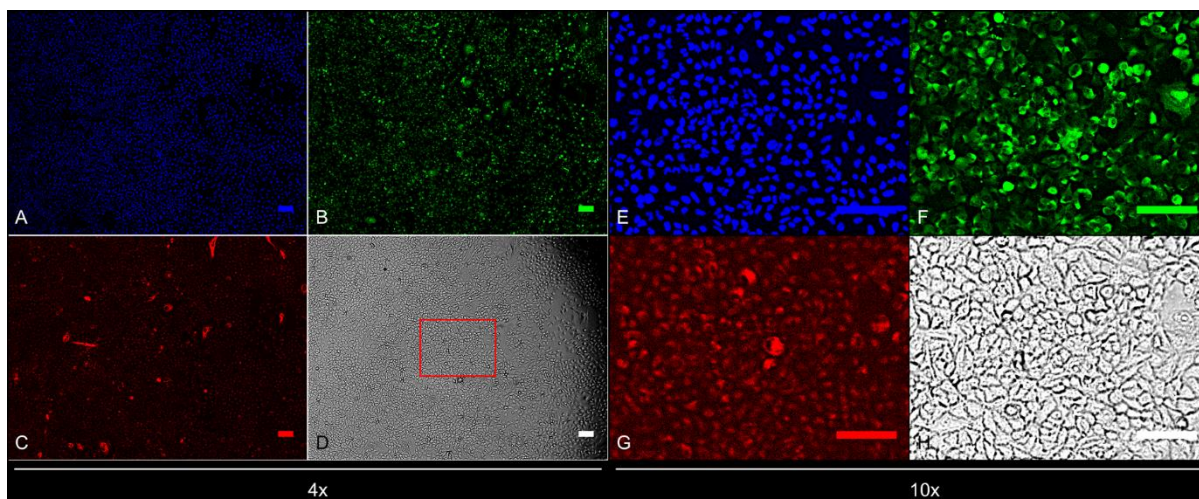


Figure A.80: HCS images of A549 cells after 48h exposure to SiO_2 & $\text{BiFeO}_3@Fe_3O_4$ NWs at $80 \mu\text{g/mL}$. Panels A and E (blue channels): nuclear staining with Hoechst; Panels B and F (green channels): cell membrane permeability staining; Panels C and G (red channels): lysosomal mass/pH staining; Panels D and H (transmitted light channels). Left (A-D): 4x objective images. The region highlighted in the Transmitted Light Channel (D) is the area magnified in the right panels (E-H): 10x objective images. The scale bars are $100 \mu\text{m}$.

A549 cells, after 48h of exposure to SiO_2 & $\text{BiFeO}_3@Fe_3O_4$ NWs at $80 \mu\text{g/mL}$, stained for DNA (blue channels), cell morphology and membrane permeability (green channels) and lysosomal mass/pH changes (red channels), are shown in Figure A.80. The aggregation and localisation of the SiO_2 & $\text{BiFeO}_3@Fe_3O_4$ NWs can be seen in the transmitted light panels (grey channels). As can be seen, after 48h the cells had reached confluency despite the presence of the NWs and the particles had aggregated inside the cells (Panels D and H).

A2.8.1 Cell count

A549 cells were exposed to SiO_2 & $\text{BiFeO}_3@Fe_3O_4$ NWs at three time points and stained for DNA to determine cell count (Figure A.81).

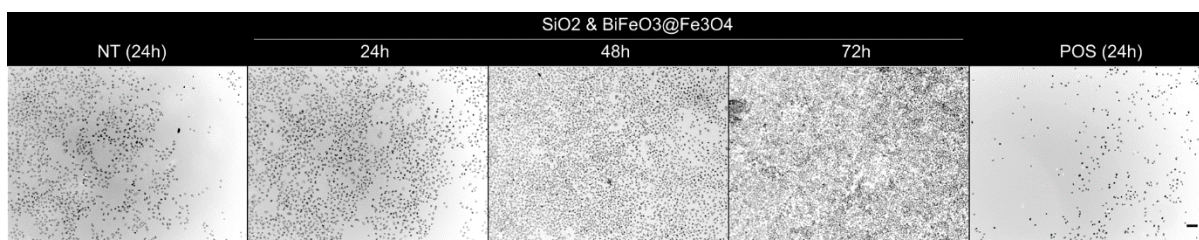


Figure A.81: A549 cells exposed to SiO_2 & $\text{BiFeO}_3@Fe_3O_4$ NWs stained for DNA. From left: representative images of untreated cells after 24h, cells exposed to SiO_2 & $\text{BiFeO}_3@Fe_3O_4$ NWs at $80 \mu\text{g/mL}$ for 24h, 48h, 72h, and cells treated with the positive control (valinomycin, $120 \mu\text{M}$) for 24h. Only the Hoechst channel is shown, inverted. The scale bar is $100 \mu\text{m}$ and is the same for all the images.

As can be seen, the cells reached confluency after 48h. This is borne out by the HCS data below.

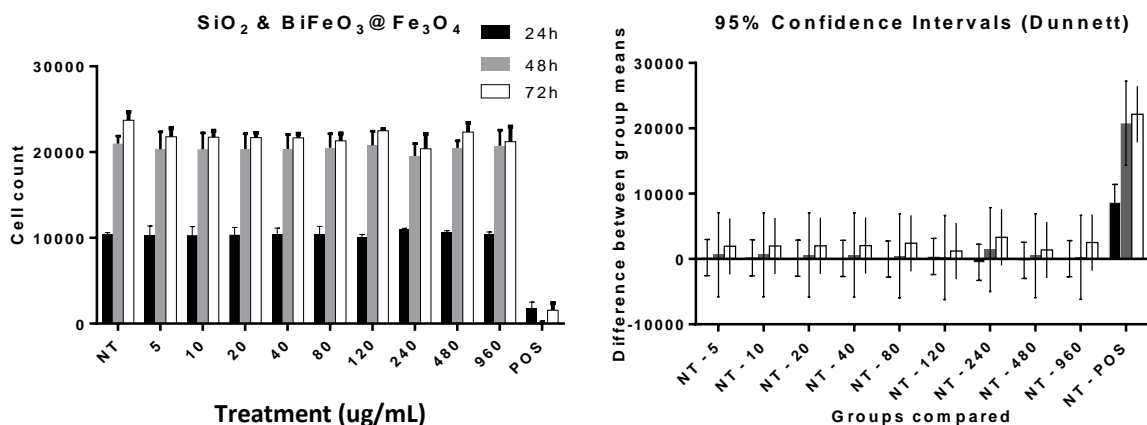


Figure A.82: Cell count of A549 cells after treatment with SiO₂ & BiFeO₃@Fe₃O₄ NWs and the corresponding 95% confidence intervals. Left: Number of cells vs concentration of nanomaterial. Valinomycin was used as positive control. The error bars represent the standard error of the mean of triplicates in three independent experiments. Right: difference between group means relative to the untreated control NT (Dunnett's test for multiple comparisons). The error bars represent the 95% confidence intervals (calculated using ordinary One-Way ANOVA).

The cells reached confluency shortly after the 48h time-point.

While there are some apparent trends in the variation of cell count with concentration (Figure A.82, left panel), the counts were not significantly different from the untreated control (see Figure A.82).

This means that the SiO₂ & BiFeO₃@Fe₃O₄ NWs did not adversely affect cell proliferation over the concentration range examined.

A2.8.2 Cell Membrane Permeability

Cell membrane permeability was used to indicate cell viability (see Figure A.83).

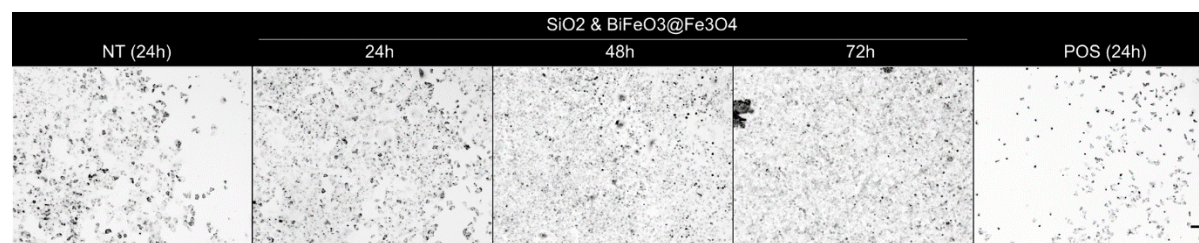


Figure A.83: A549 cells exposed to SiO₂ & BiFeO₃@Fe₃O₄ NWs stained for cell membrane permeability. From left: representative images of untreated cells after 24h, cells exposed to SiO₂ & BiFeO₃@Fe₃O₄ NWs at 80 μ g/mL for 24h, 48h, 72h, and cells treated with the positive control (valinomycin, 120 μ M) for 24h. Only the CMP (green) channels are shown, inverted. The scale bar is 100 μ m and is the same for all the images.

Because the images in Figure A.83 are inverted, the number of viable cells in each image is therefore the number of cells in which the intensity of CMP stain surrounding and overlapping the nucleus is below the threshold determined for each plate analysed as described above (see A2.2.2). The data are displayed below (see Figure A.84).

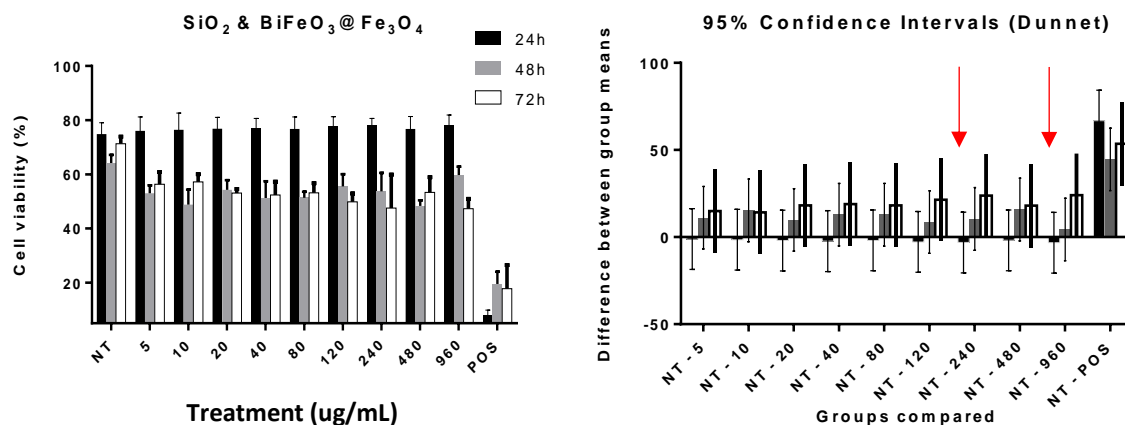


Figure A.84: Cell viability of A549 cells after treatment with SiO₂ & BiFeO₃@Fe₃O₄ NWs and the corresponding 95% confidence intervals. Left: cell viability vs concentration of nanomaterial. Valinomycin was used as positive control. The error bars represent the standard error of the mean of triplicates in three independent experiments. Right: difference between group means relative to the untreated control NT (Dunnett's test for multiple comparisons). The error bars represent the 95% confidence intervals (calculated using ordinary One-Way ANOVA).

As with the cell count, there are apparent trends in the concentration-dependent response of the cells to the NM, especially at 24h (see left panel, Figure A.84). However, the variations all fall within the 95% confidence intervals and are therefore not statistically significant, except for after exposure to very high doses after 72h (indicated by an arrow in Figure A.84, right panel).

SiO₂ & BiFeO₃@Fe₃O₄ NWs therefore cause a small but significant decrease in cell viability in A549 cells at high concentrations after 72h exposure.

A2.8.3 Lysosomal mass/pH

The cells were also examined for changes in lysosomal mass/pH as a final indicator of cytotoxicity (see Figure A.85).

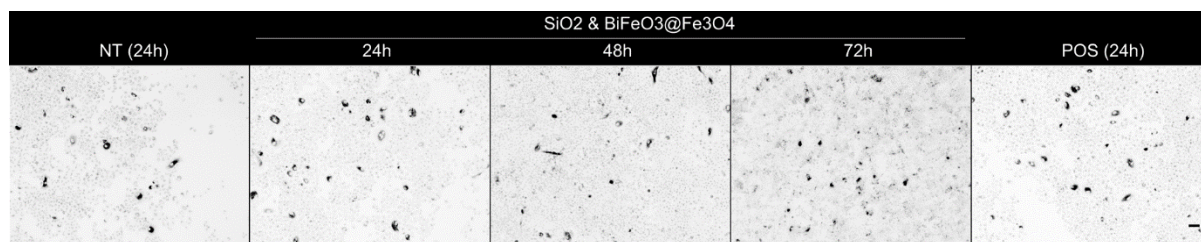


Figure A.85: A549 cells exposed to SiO₂ & BiFeO₃@Fe₃O₄ NWs stained for lysosomal mass/pH changes. From left: representative images of untreated cells after 24h, cells exposed to SiO₂ & BiFeO₃@Fe₃O₄ NWs at 80 μg/mL for 24h, 48h, 72h, and cells treated with the positive control (tacrine, 100 μM) for 24h. Only the LysoTracker (red) channels are shown, inverted. The scale bar is 100 μm and is the same for all the images.

LysoTracker™ Red was used to stain for changes in lysosomal mass or pH. Because the images in Figure A.85 are inverted, an increase in the intensity therefore corresponds to a larger mass of lysosomes or decrease in pH, indicating a toxic response to the analyte. These data are displayed below (see Figure A.86).

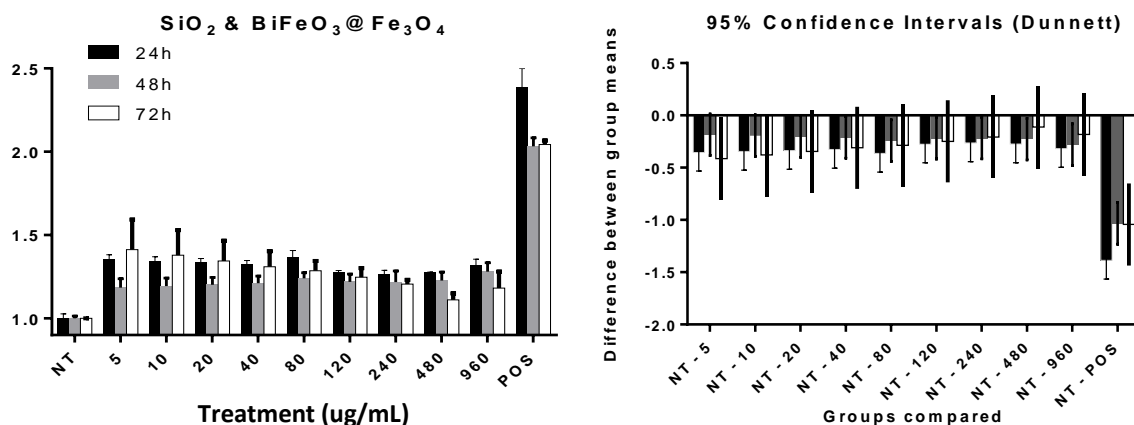


Figure A.86: Lysosomal mass/pH changes in A549 cells after treatment with SiO₂ & BiFeO₃@Fe₃O₄ NWs and the corresponding 95% confidence intervals. Left: Lysosomal mass/pH vs concentration of nanomaterial. Tacrine was used as positive control. The error bars represent the standard error of the mean of triplicates in three independent experiments. Right: difference between group means relative to the untreated control NT (Dunnett's test for multiple comparisons). The error bars represent the 95% confidence intervals (calculated using ordinary One-Way ANOVA).

Exposing A549 cells to SiO₂ & BiFeO₃@Fe₃O₄ NWs results in a significant increase in lysosomal mass/pH after 24h and 48h at all concentrations and the rise does not appear to be dose-dependent.

There is a distinct dose-dependent response in the lysosomal mass/pH as a function of concentration of SiO₂ & BiFeO₃@Fe₃O₄ NWs after 24h as can be seen in Figure A.86, left panel. A similar trend of increasing lysosomal mass/pH with rising concentration is observed after 48h and 72h but the variations fall within the respective 95% confidence intervals and are hence not significant except at the highest concentration after 72h (indicated by an arrow, right panel, Figure A.86).

The rise in lysosomal mass/pH can be attributed to the internalisation of NWs by the cells (see the section on uptake for further information).

A2.9 A549 cells treated with SiO₂&BiFeO₃@Fe₂O₃ NWs

A549 cells were prepared for HCS after exposure to SiO₂ & BiFeO₃@Fe₂O₃ NWs at 80 µg/mL, stained for DNA (blue channels), cell morphology and membrane permeability (green channels) and lysosomal mass/pH changes (red channels) (see Figure A.87).

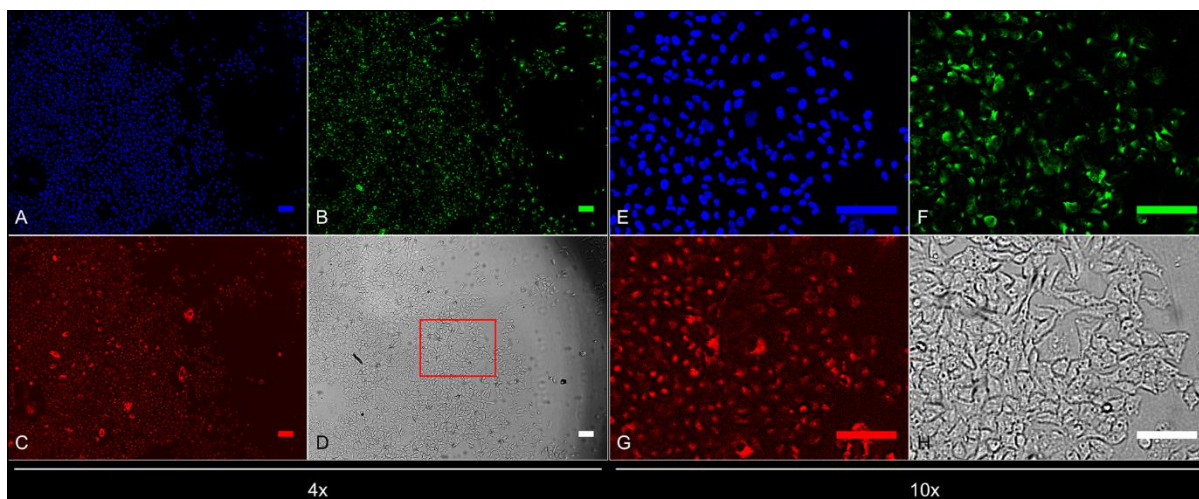


Figure A.87: HCS images of A549 cells after 48h exposure to SiO_2 & $\text{BiFeO}_3@Fe_2O_3$ NWs at $80 \mu\text{g/mL}$. Panels A and E (blue channels): nuclear staining with Hoechst; Panels B and F (green channels): cell membrane permeability staining; Panels C and G (red channels): lysosomal mass/pH staining; Panels D and H (transmitted light channels). Left (A-D): 4x objective images. The region highlighted in the Transmitted Light Channel (D) is the area magnified in the right panels (E-H): 10x objective images. The scale bars are $100 \mu\text{m}$.

A549 cells after 48h of exposure to SiO_2 & $\text{BiFeO}_3@Fe_2O_3$ NWs at $80 \mu\text{g/mL}$, stained for DNA (blue channels), cell morphology and membrane permeability (green channels) and lysosomal mass/pH changes (red channels), as in Figure A.87. The aggregation and localisation of the SiO_2 & $\text{BiFeO}_3@Fe_2O_3$ NWs can be seen in the transmitted light panels (grey channels). As can be seen, after 48h the cells had reached confluency despite the presence of the NWs and the particles had aggregated inside the cells (Panels D and H).

A2.9.1 Cell count

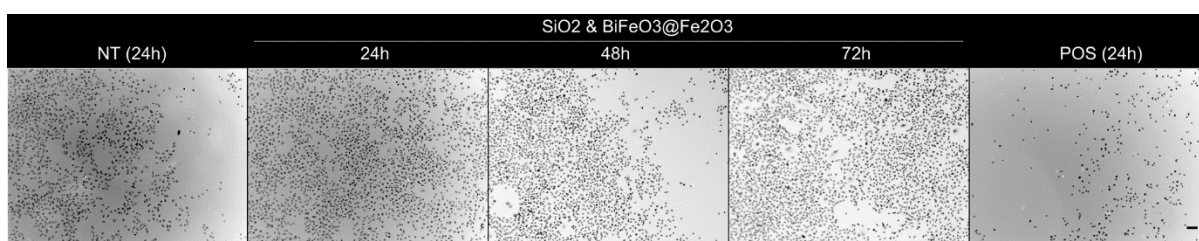


Figure A.88: A549 cells exposed to SiO_2 & $\text{BiFeO}_3@Fe_2O_3$ NWs stained for DNA. From left: representative images of untreated cells after 24h, cells exposed to SiO_2 & $\text{BiFeO}_3@Fe_2O_3$ NWs at $80 \mu\text{g/mL}$ for 24h, 48h, 72h, and cells treated with the positive control (valinomycin, $120 \mu\text{M}$) for 24h. Only the Hoechst channel is shown, inverted. The scale bar is $100 \mu\text{m}$ and is the same for all the images.

A549 cells were exposed to SiO_2 & $\text{BiFeO}_3@Fe_2O_3$ NWs at three time points and stained for DNA to determine cell count (Figure A.88). As can be seen, the cells reached confluency after 48h. This is borne out by the HCS data below.

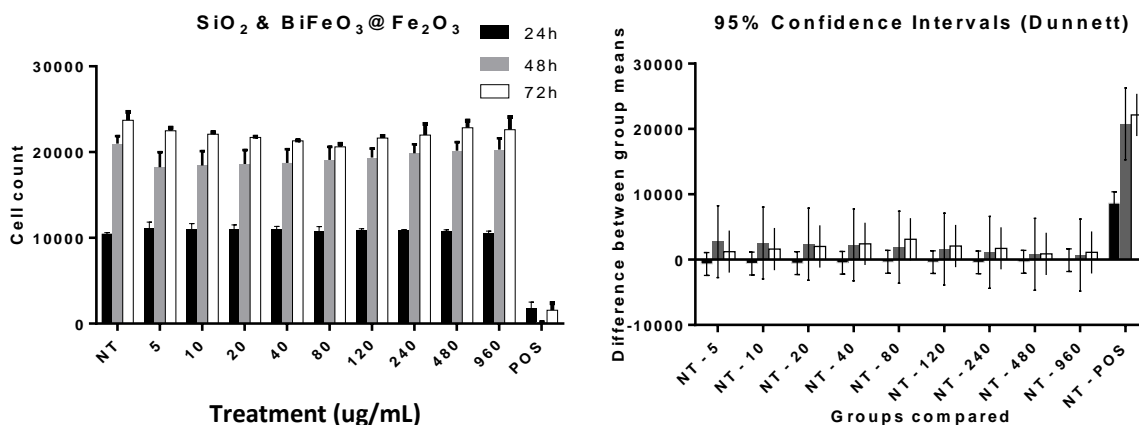


Figure A.89: Cell count of A549 cells after treatment with SiO₂ & BiFeO₃@Fe₂O₃ NWs and the corresponding 95% confidence intervals. Left: Number of cells vs concentration of nanomaterial. Valinomycin was used as positive control. The error bars represent the standard error of the mean of triplicates in three independent experiments. Right: difference between group means relative to the untreated control NT (Dunnett's test for multiple comparisons). The error bars represent the 95% confidence intervals (calculated using ordinary One-Way ANOVA).

The cells had reached confluency shortly after the 48h time-point, at approximately 24000 cells (Figure A.89, left panel).

While there are some apparent trends in the variation of cell count with concentration, the variations all lie within the 95% confidence intervals (Figure A.89, right panel) and are therefore not statistically significant.

This means that the SiO₂ & BiFeO₃@Fe₂O₃ NWs did not adversely affect cell proliferation at the concentrations investigated.

A2.9.2 Cell Membrane Permeability

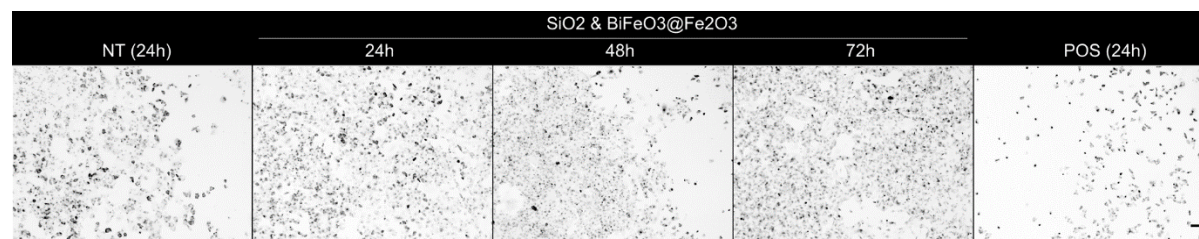


Figure A.90: A549 cells exposed to SiO₂ & BiFeO₃@Fe₂O₃ NWs stained for cell membrane permeability. From left: representative images of untreated cells after 24h, cells exposed to SiO₂ & BiFeO₃@Fe₂O₃ NWs at 80 μg/mL for 24h, 48h, 72h, and cells treated with the positive control (valinomycin, 120 μM) for 24h. Only the CMP (green) channels are shown, inverted. The scale bar is 100 μm and is the same for all the images.

Cell membrane permeability was used to indicate cell viability. Because the images in Figure A.90 are inverted, the number of viable cells in each image is therefore the number of cells in which the intensity

of CMP stain surrounding and overlapping the nucleus is below the threshold determined for each plate analysed as described above (see A2.2.2). The data are displayed below (see Figure A.91).

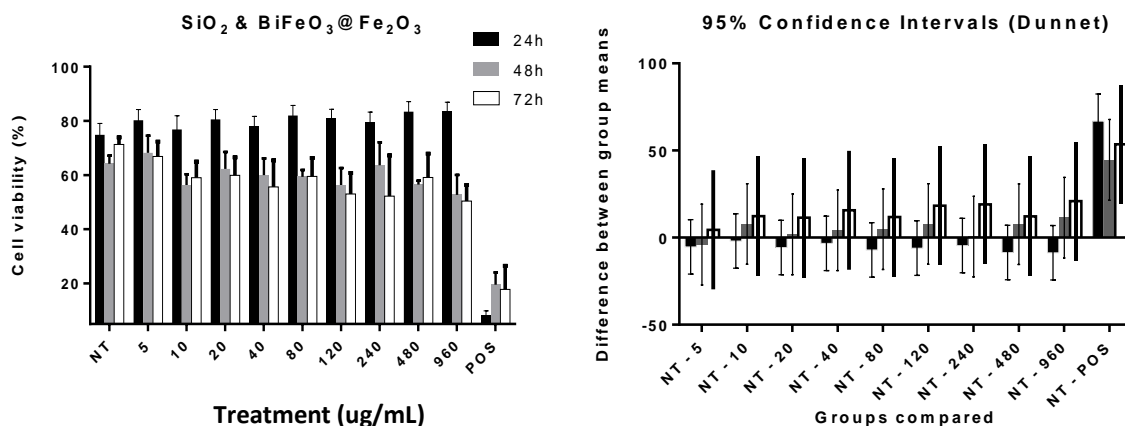


Figure A.91: Cell viability of A549 cells after treatment with SiO₂ & BiFeO₃@Fe₂O₃ NWs and the corresponding 95% confidence intervals. Left: cell viability vs concentration of nanomaterial. Valinomycin was used as positive control. The error bars represent the standard error of the mean of triplicates in three independent experiments. Right: difference between group means relative to the untreated control NT (Dunnett's test for multiple comparisons). The error bars represent the 95% confidence intervals (calculated using ordinary One-Way ANOVA).

As with the cell count, there are apparent trends in the concentration-dependent response of the cells to the NM, especially at 24h (see left panel, Figure A.91). However, the variations all fall within the 95% confidence intervals and are therefore not statistically significant.

This supports the conclusion that the SiO₂ & BiFeO₃@Fe₂O₃ NWs do not decrease cell viability in A549 cells at the concentrations analysed.

The cells were also examined for changes in lysosomal mass/pH as a final indicator of cytotoxicity.

A2.9.3 Lysosomal mass/pH

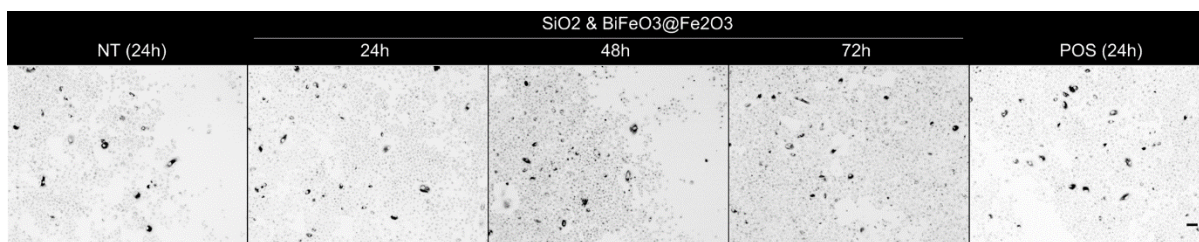


Figure A.92: A549 cells exposed to SiO₂ & BiFeO₃@Fe₂O₃ NWs stained for lysosomal mass/pH changes. From left: representative images of untreated cells after 24h, cells exposed to SiO₂ & BiFeO₃@Fe₂O₃ NWs at 80 µg/mL for 24h, 48h, 72h, and cells treated with the positive control (tacrine, 100 µM) for 24h. Only the LysoTracker (red) channels are shown, inverted. The scale bar is 100 µm and is the same for all the images.

LysoTracker™ Red was used to stain for changes in lysosomal mass or pH. Because the images in Figure A.72 are inverted, an increase in the intensity therefore corresponds to a larger mass of lysosomes or

decrease in pH, indicating a toxic response to the analyte. These data are displayed below (see Figure A.93).

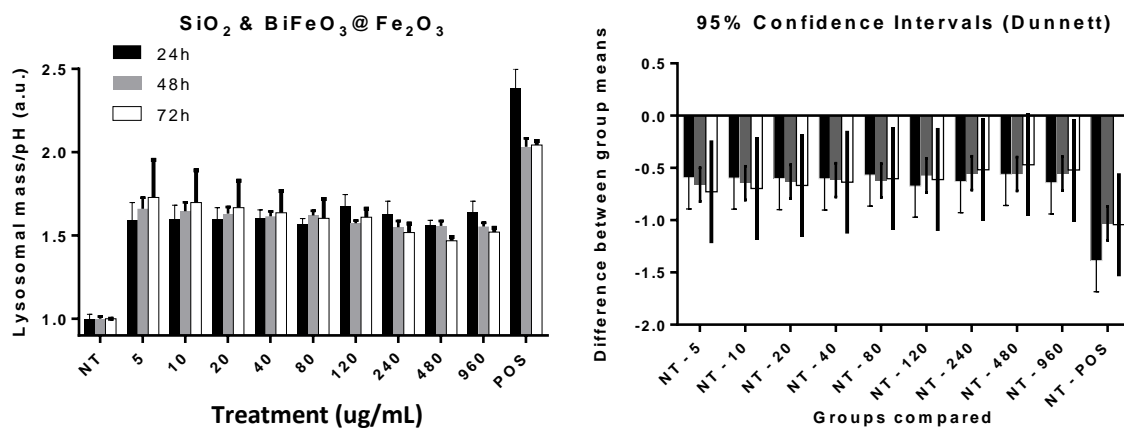


Figure A.93: Lysosomal mass/pH changes in A549 cells after treatment with SiO₂ & BiFeO₃@Fe₂O₃ NWs and the corresponding 95% confidence intervals. Left: Lysosomal mass/pH vs concentration of nanomaterial. Tacrine was used as positive control. The error bars represent the standard error of the mean of triplicates in three independent experiments. Right: difference between group means relative to the untreated control NT (Dunnett's test for multiple comparisons). The error bars represent the 95% confidence intervals (calculated using ordinary One-Way ANOVA).

There was a slight dose-dependent response in the lysosomal mass/pH as a function of concentration of SiO₂ & BiFeO₃@Fe₂O₃ NWs after 24h as can be seen in Figure A.93, left panel. A similar trend of increasing lysosomal mass/pH with rising concentration is observed after 48h and 72h (see right panel, Figure A.93).

The rise in lysosomal mass/pH can be attributed to the internalisation of NWs by the cells (see the section on uptake in Chapter 3 for further information).

A3 High Content Screening of HUVEC cells

A3.1 HUVEC cells treated with BiFeO₃ NPs

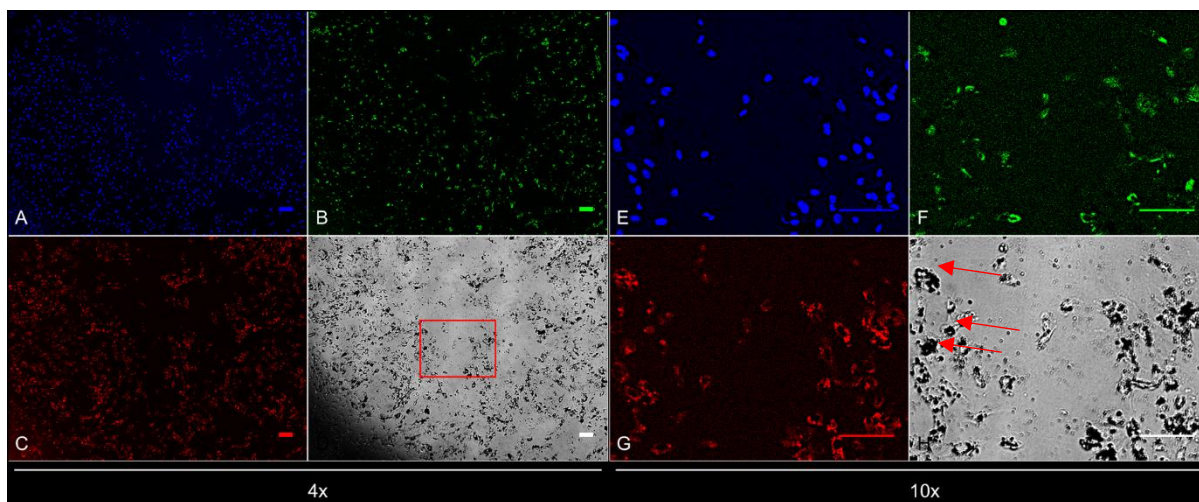


Figure A.94: HCS images of HUVEC cells after 48h exposure to BiFeO₃ NPs at 80 µg/mL. Panels A and E (blue channels): nuclear staining with Hoechst; Panels B and F (green channels): cell membrane permeability staining; Panels C and G (red channels): lysosomal mass/pH staining; Panels D and H (transmitted light channels). Left (A-D): 4x objective images. The region highlighted in the Transmitted Light Channel (D) is the area magnified in the right panels (E-H): 10x objective images. The scale bars are 100 µm.

Figure A.94 shows HUVEC cells after 48h of exposure to BiFeO₃ NPs at 80 µg/mL, stained for DNA (blue channels), cell morphology and membrane permeability (green channels) and lysosomal mass/pH changes (red channels). The aggregation and localisation of the BiFeO₃ NPs can be seen in the transmitted light panels (grey channels). As can be seen, after 48h the cells were not confluent, and the particles had aggregated inside the cells (Panels D and H, aggregates are indicated by arrows in H). Furthermore, the aggregates are very large and demonstrate that the bare BiFeO₃ NPs are not stable in biological media.

In comparison to A549 cells treated in the same way, it is evident that both the CMP and lysosomal mass/pH staining is more intense and that almost every cell is distinctly stained in HUVECs exposed to BiFeO₃ NPs.

A3.1.1 Cell count

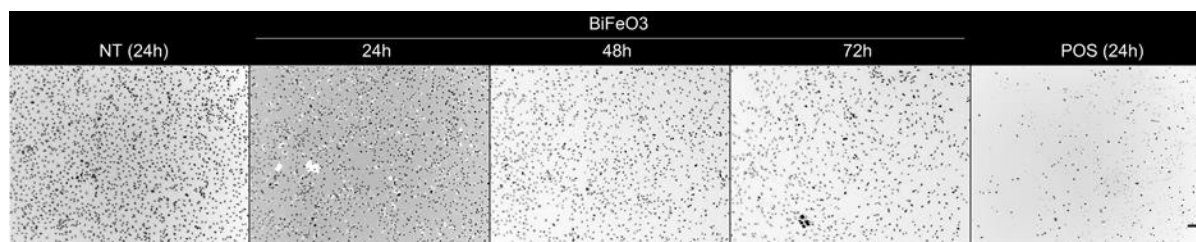


Figure A.95: HUVEC cells exposed to BiFeO_3 NPs, stained for DNA. From left: representative images of untreated cells after 24h, cells exposed to BiFeO_3 NPs at $80 \mu\text{g/mL}$ for 24h, 48h, 72h, and cells treated with the positive control (valinomycin, $120 \mu\text{M}$) for 24h. Only the Hoechst channel is shown, inverted. The scale bar is $100 \mu\text{m}$ and is the same for all the images.

HUVEC cells were exposed to BiFeO_3 NPs over three time-points and stained for DNA to determine cell count (see Figure A.95). The cells did not reach confluency and the cell counts dropped after 24h. This is borne out by the HCS data below.

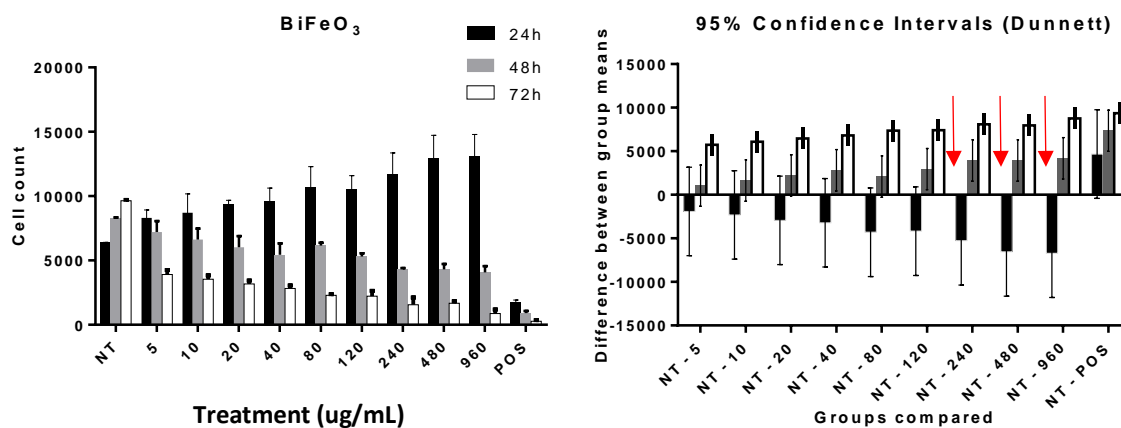


Figure A.96: Cell count of HUVEC cells after treatment with BiFeO_3 NPs and the corresponding 95% confidence intervals. Left: Number of cells vs concentration of nanomaterial. Valinomycin was used as positive control. The error bars represent the standard error of the mean of triplicates in three independent experiments. Right: difference between group means relative to the untreated control NT (Dunnett's test for multiple comparisons). The error bars represent the 95% confidence intervals (calculated using ordinary One-Way ANOVA).

Cell count varied significantly with concentration (Figure A.96, left panel). Contrary to the typical dose-response curve, the cell number rose with increasing concentration over 24h, although the counts were only significant when the concentration was at least $240 \mu\text{g/mL}$ (indicated by arrows in the right panel of Figure A.96). Cell proliferation increased relative to the control and ever more so when exposed to higher concentrations of the NPs.

After 48h the trend had reversed; the greater the dose of NPs, the lower the cell number. This concentration-dependent response is expected for a toxic material and can be used to determine the

half maximal inhibitory concentration (IC_{50}). Since the cell count did not fall to the same value as the positive control after 48h, even at the highest dose of NPs, the IC_{50} can be more accurately determined using the data from the 72h time-point.

The reversal in trend observed between 24h and 48h may be attributed to a stress response in the cells in which the HUVECs undergo a period of rapid division, like the behaviour seen in A549 cells reported above. A typical dose-response curve was observed after 48 and 72h.

A3.1.2 Cell Membrane Permeability

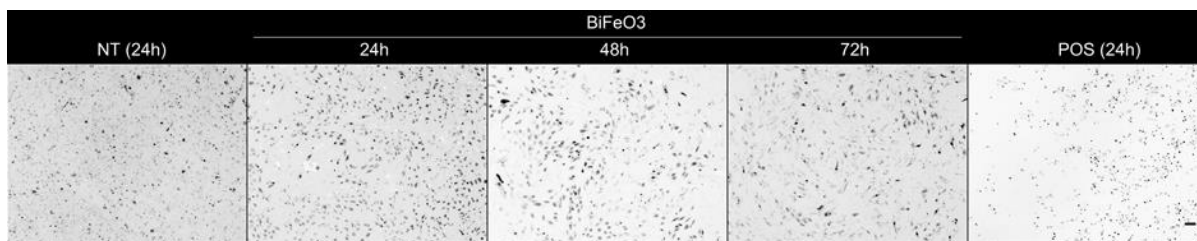


Figure A.97: HUVEC cells exposed to $BiFeO_3$ NPs, stained for cell membrane permeability. From left: representative images of untreated cells after 24h, cells exposed to $BiFeO_3$ NPs at $80 \mu\text{g/mL}$ for 24h, 48h, 72h, and cells treated with the positive control (valinomycin, $120 \mu\text{M}$) for 24h. Only the CMP (green) channels are shown, inverted. The scale bar is $100 \mu\text{m}$ and is the same for all the images.

Cell membrane permeability was used to indicate cell viability. Because the images in Figure A.97 are inverted, the number of viable cells in each image is therefore the number of cells in which the intensity of CMP stain surrounding and overlapping the nucleus is below the threshold determined for each plate as described above (see A2.2.2). The corresponding data are displayed below (see Figure A.98).

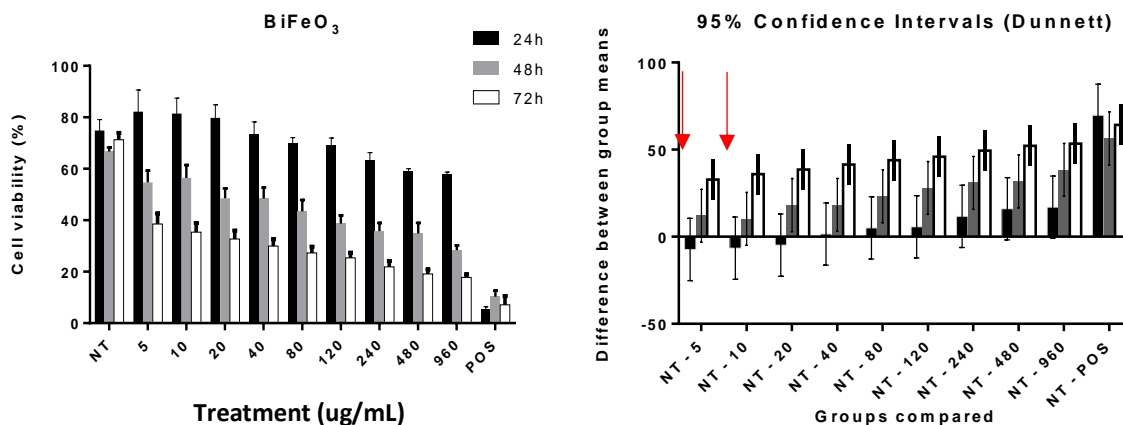


Figure A.98: Cell viability of HUVEC cells after treatment with $BiFeO_3$ NPs and the corresponding 95% confidence intervals. Left: cell viability vs concentration of nanomaterial. Valinomycin was used as positive control. The error bars represent the standard error of the mean of triplicates in three independent experiments. Right: difference

between group means relative to the untreated control NT (Dunnett's test for multiple comparisons). The error bars represent the 95% confidence intervals (calculated using ordinary One-Way ANOVA).

There is an apparent concentration-dependent trend in the response of the HUVECs to the BiFeO₃ NPs at 24 (see left panel, Figure A.98). At 24h, the average viability was higher than the untreated control at 5 µg/mL and trended lower with increasing concentration, however the variations all fell within the 95% CI and were therefore not significant (see Figure A.98, right panel).

At 48h and 72h, cell viability decreased significantly and in a dose-dependent manner. While the falls in viability at 5 and 10 µg/mL were within the 95% CI at 48h, indicated by red arrows in Figure A.98, right panel, the values dropped with increasing concentration to approximately 30% at 960 µg/mL.

At 72h, the decrease was significant at all doses, falling from 40% viability at 5 µg/mL to approximately 20% at 960 µg/mL.

The increase in cell count at 24h (see Figure A.96) did not coincide with a rise in viability. This serves to support the conclusion that the presence of nanoparticles raises cell proliferation initially, perhaps by stressing the cells.

Due to the reduction in viability and in cell number with increasing concentration, we can conclude that the BiFeO₃ NPs increase cell permeability and therefore lower the viability of HUVECs at the concentrations analysed.

The cells were also examined for changes in lysosomal mass/pH as a final indicator of cytotoxicity.

A3.1.3 Lysosomal mass/pH

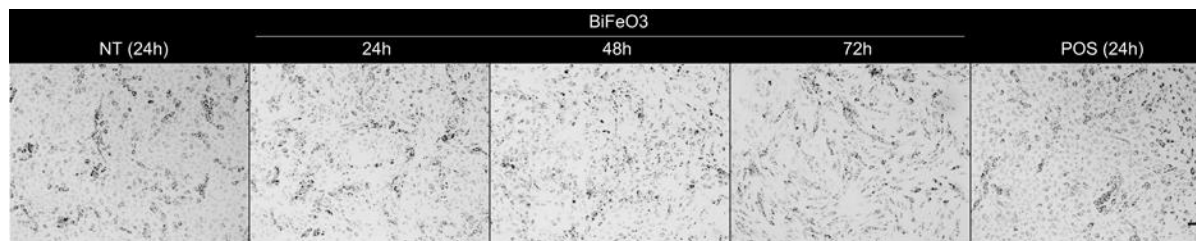


Figure A.99: HUVEC cells exposed to BiFeO₃ NPs, stained for lysosomal mass/pH changes. From left: representative images of untreated cells after 24h, cells exposed to BiFeO₃ NPs at 80 µg/mL for 24h, 48h, 72h, and cells treated with the positive control (tacrine, 100 µM) for 24h. Only the LysoTracker (red) channels are shown, inverted. The scale bar is 100 µm and is the same for all the images.

LysoTracker™ Red was used to stain for changes in lysosomal mass or pH. Because the images in Figure A.99 are inverted, an increase in the intensity therefore corresponds to a larger mass of lysosomes or decrease in pH, indicating a toxic response to the analyte. These data are displayed below (see Figure A.100).

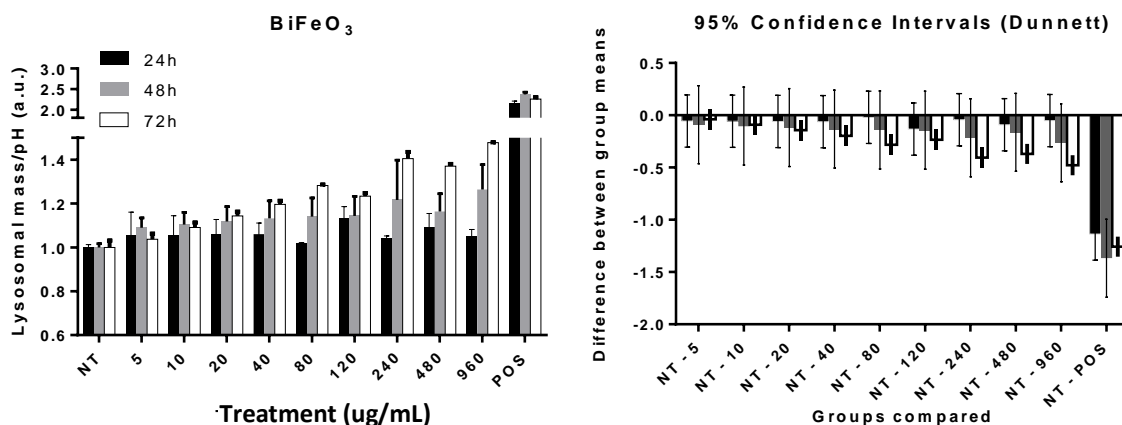


Figure A.100: Lysosomal mass/pH changes in HUVEC cells after treatment with BiFeO₃ NPs and the corresponding 95% confidence intervals. Left: Lysosomal mass/pH vs concentration of nanomaterial. Tacrine was used as positive control. The error bars represent the standard error of the mean of triplicates in three independent experiments. Right: difference between group means relative to the untreated control NT (Dunnett's test for multiple comparisons). The error bars represent the 95% confidence intervals (calculated using ordinary One-Way ANOVA).

There is a small but significant dose-dependent response in the lysosomal mass/pH as a function of concentration of BiFeO₃ NPs after 72h as can be seen in Figure A.100, left panel. Although the same trend appears after 48h, the variations fall within the 95% confidence intervals and are hence not significant (right panel, Figure A.100) as are all the variations observed after 24h.

The rise in lysosomal mass/pH as a function of concentration can be attributed to the internalisation of NPs by the cells (see the section on uptake 3.3.2 for further discussion).

A3.2 HUVEC cells treated with ascorbic acid-functionalised BiFeO₃ NPs (BiFeO₃@asc)

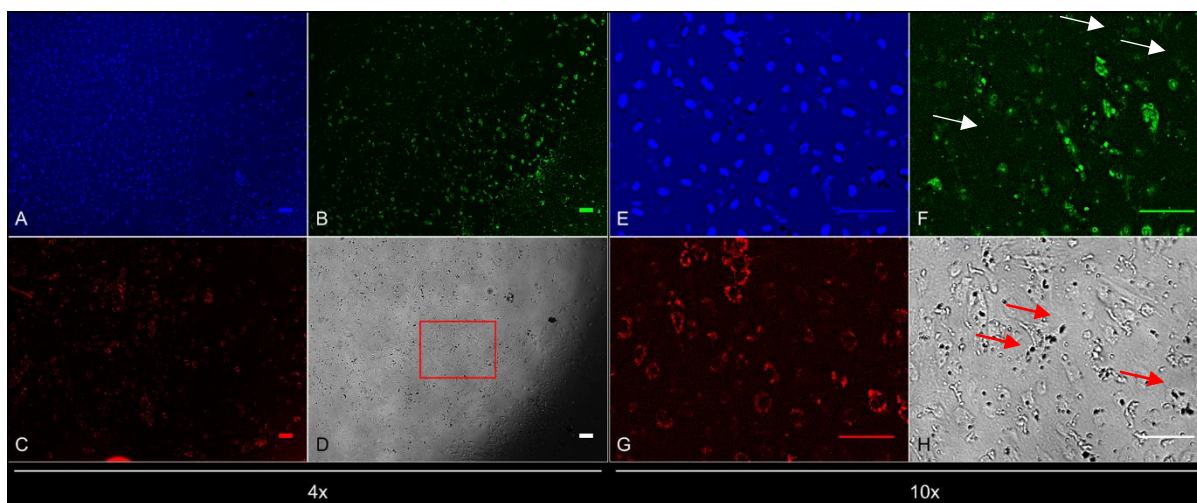


Figure A.101: HCS images of HUVEC cells after 48h exposure to BiFeO₃@asc NPs at 80 $\mu\text{g/mL}$. Panels A and E (blue channels): nuclear staining with Hoechst; Panels B and F (green channels): cell membrane permeability staining; Panels C and G (red channels): lysosomal mass/pH staining; Panels D and H (transmitted light channels).

Left (A-D): 4x objective images. The region highlighted in the Transmitted Light Channel (D) is the area magnified in the right panels (E-H): 10x objective images. The scale bars are 100 μm .

Figure A.101 shows HUVEC cells after 48h of exposure to $\text{BiFeO}_3@asc$ NPs at 80 $\mu\text{g}/\text{mL}$, stained for DNA (blue channels), cell morphology and membrane permeability (green channels) and lysosomal mass/pH changes (red channels). The aggregation and localisation of the $\text{BiFeO}_3@asc$ NPs can be seen in the transmitted light panels (grey channels). As can be seen, after 48h the cells are not confluent, and the particles had aggregated inside the cells (Panels D and H, aggregates are indicated by red arrows in H). In comparison to A549 cells treated in the same way, both the CMP and lysosomal mass/pH staining is more intense and almost every cell is distinctly stained in HUVECs exposed to $\text{BiFeO}_3@asc$ NPs. There is also some extracellular staining in the CMP channel (designated by white arrows in Panel F, Figure A.101) which indicates cell debris.

A3.2.1 Cell count

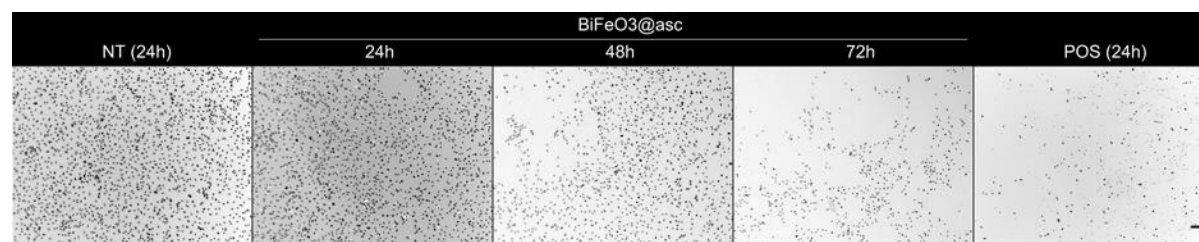


Figure A.102: HUVEC cells exposed to $\text{BiFeO}_3@asc$ NPs, stained for DNA. From left: representative images of untreated cells after 24h, cells exposed to $\text{BiFeO}_3@asc$ NPs at 80 $\mu\text{g}/\text{mL}$ for 24h, 48h, 72h, and cells treated with the positive control (valinomycin, 120 μM) for 24h. Only the Hoechst channel is shown, inverted. The scale bar is 100 μm and is the same for all the images.

HUVEC cells were exposed to $\text{BiFeO}_3@asc$ NPs at three time points and stained for DNA to determine cell count (see Figure A.102). The cells did not reach confluency and cell counts had dropped after 72h. This is borne out by the HCS data below.

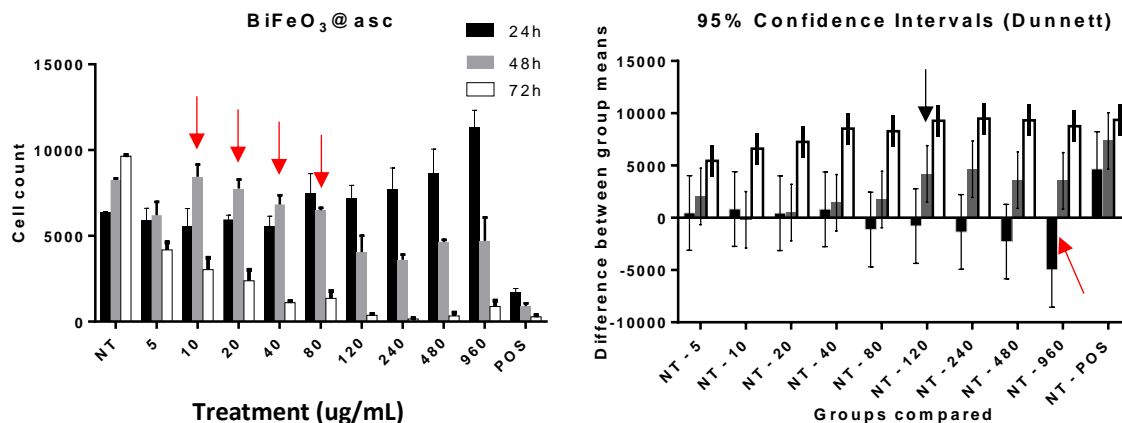


Figure A.103: Cell count of HUVEC cells after treatment with BiFeO₃@asc NPs and the corresponding 95% confidence intervals. Left: Number of cells vs concentration of nanomaterial. Valinomycin was used as positive control. The error bars represent the standard error of the mean of triplicates in three independent experiments. Right: difference between group means relative to the untreated control NT (Dunnett's test for multiple comparisons). The error bars represent the 95% confidence intervals (calculated using ordinary One-Way ANOVA).

Cell count varied significantly at higher concentrations at each time point (Figure A.103, left panel).

The cell number rose with increasing concentration after 24h hours, although the count was only significant when the concentration was 960 µg/mL (indicated by a red arrow in Figure A.103, right panel).

Again, after 48h the trend had reversed; the greater the dose of NPs, the lower the cell number. However, doses below 80 µg/mL appeared to induce an increase in the cell number (indicated by arrows in Figure A.103, left panel), as if the stress response discussed earlier were delayed or mitigated by the adsorbed ascorbic acid. These variations fell within the 95% CI however, and only the reduction in cell number at concentrations from 120 µg/mL were significant (indicated by a black arrow in Figure A.103, right panel).

After 72h, cell count fell more rapidly with increasing concentration than when cells were exposed to BiFeO₃ NPs, approaching the level of the positive control above 120 µg/mL.

A3.2.2 Cell Membrane Permeability

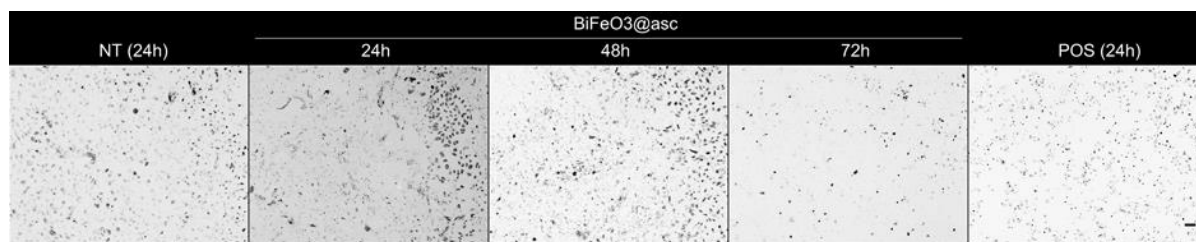


Figure A.104: HUVEC cells exposed to $\text{BiFeO}_3@asc$ NPs, stained for cell membrane permeability. From left: representative images of untreated cells after 24h, cells exposed to $\text{BiFeO}_3@asc$ NPs at $80 \mu\text{g/mL}$ for 24h, 48h, 72h, and cells treated with the positive control (valinomycin, $120 \mu\text{M}$) for 24h. Only the CMP (green) channels are shown, inverted. The scale bar is $100 \mu\text{m}$ and is the same for all the images.

Cell membrane permeability was used to indicate cell viability. Because the images in Figure A.104 are inverted, the number of viable cells in each image is therefore the number of cells in which the intensity of CMP stain surrounding and overlapping the nucleus is below the threshold determined for each plate analysed as described above (see A2.2.2). The data are displayed below (see Figure A.105).

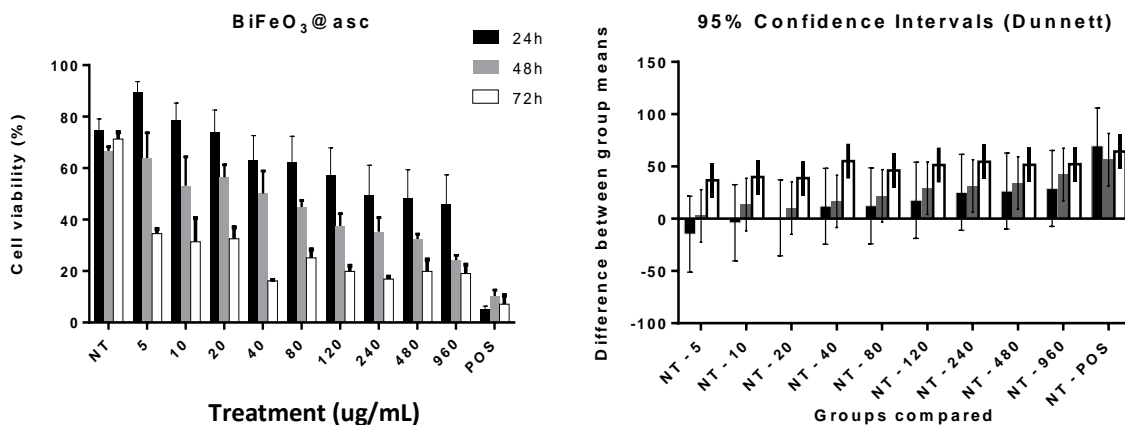


Figure A.105: Cell viability of HUVEC cells after treatment with $\text{BiFeO}_3@asc$ NPs and the corresponding 95% confidence intervals. Left: cell viability vs concentration of nanomaterial. Valinomycin was used as positive control. The error bars represent the standard error of the mean of triplicates in three independent experiments. Right: difference between group means relative to the untreated control NT (Dunnett's test for multiple comparisons). The error bars represent the 95% confidence intervals (calculated using ordinary One-Way ANOVA).

At 24h, there was an apparent increase in cell viability at the lowest dose of $\text{BiFeO}_3@asc$ NP (see left panel, Figure A.105), falling with rising concentration but the variations again all fell within the 95% confidence intervals and are therefore not statistically significant (see right panel, Figure A.105).

Like the cells' response to bare BiFeO_3 NPs, the decreases in viability at 48h fell within the 95% CI at lower concentrations, but decreased significantly with increasing dose from $120 \mu\text{g/mL}$ (indicated by a

black arrow in Figure A.105, right panel). There was greater heterogeneity in the viability after 48h by comparison to the response to bare BiFeO₃, as can be seen in the larger CIs.

Again, after 72h cell viability dropped to approximately 40% at 5 µg/m, falling off as the concentration of BiFeO₃@asc increased to approximately 25%.

Cell viability can only be determined in those cells which have not been removed from the 96-well plate by washing (i.e. those cells whose membranes are not already wholly permeable because such cells die and no longer adhere) so cell count and viability are independent indicators of the response of the cells. Taken together, the drops in cell number and cell viability over time indicate that the BiFeO₃@asc NPs diminish cell viability in HUVEC cells at the concentrations analysed.

Because the same overall pattern was observed for BiFeO₃ and for BiFeO₃@asc NPs, we may conclude that any stress response is induced by the size or morphology of the nanoparticles rather than their surface chemistry.

The initial stimulation of growth seen with bare BiFeO₃ is not observed in the BiFeO₃@asc NPs except at higher concentrations as can be seen in the cell count data. However, this did not mean the overall toxicity of the NPs was lower – the higher the dose, the lower the viability and the 48h and 72h cell counts were lower when the HUVECs were exposed to ascorbic acid coated NPs.

The cells were also examined for changes in lysosomal mass/pH as a last indicator of cytotoxicity.

A3.2.3 Lysosomal mass/pH

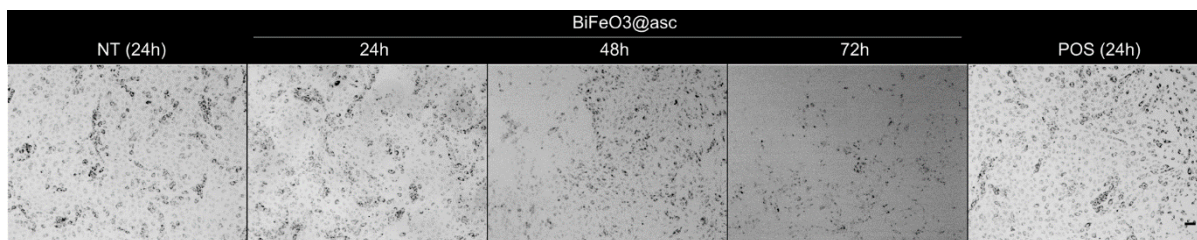


Figure A.106: HUVEC cells exposed to BiFeO₃@asc NPs, stained for lysosomal mass/pH changes. From left: representative images of untreated cells after 24h, cells exposed to BiFeO₃@asc NPs at 80 µg/mL for 24h, 48h, 72h, and cells treated with the positive control (tacrine, 100 µM) for 24h. Only the LysoTracker (red) channels are shown, inverted. The scale bar is 100 µm and is the same for all the images.

LysoTracker™ Red was used to stain for changes in lysosomal mass or pH. Because the images in Figure A.106 are inverted, an increase in the intensity therefore corresponds to a larger mass of lysosomes or decrease in pH, indicating a toxic response to the analyte. These data are displayed below (see Figure A.107).

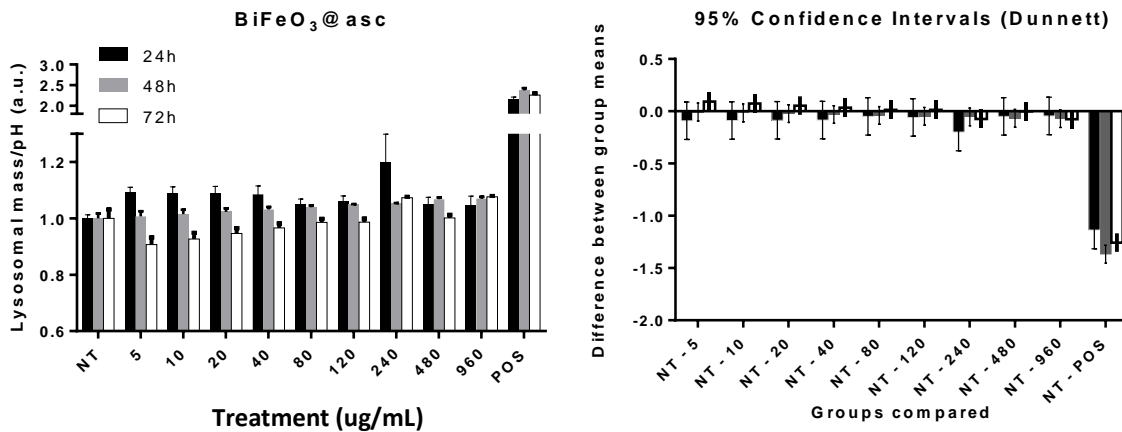


Figure A.107: Lysosomal mass/pH changes in HUVEC cells after treatment with BiFeO₃@asc NPs and the corresponding 95% confidence intervals. Left: Lysosomal mass/pH vs concentration of nanomaterial. Tacrine was used as positive control. The error bars represent the standard error of the mean of triplicates in three independent experiments. Right: difference between group means relative to the untreated control NT (Dunnett's test for multiple comparisons). The error bars represent the 95% confidence intervals (calculated using ordinary One-Way ANOVA).

There are no apparent trends in the lysosomal mass/pH as a function of concentration of BiFeO₃@asc NPs as can be seen in Figure A.107, left panel. Interestingly, the lowest lysosomal mass/pH values are observed at the lowest concentrations after 48 and 72h. This may be due to the adsorbed ascorbic acid (which lowers the pH value) being taken up into lysosomes in the HUVECs (which increases the lysosomal mass). Unlike exposure to bare BiFeO₃-treated cells, there is no significant increase in lysosomal mass/pH at 72h, even at higher concentrations.

A3.3 HUVEC cells treated with BiFeO₃@APTES NPs

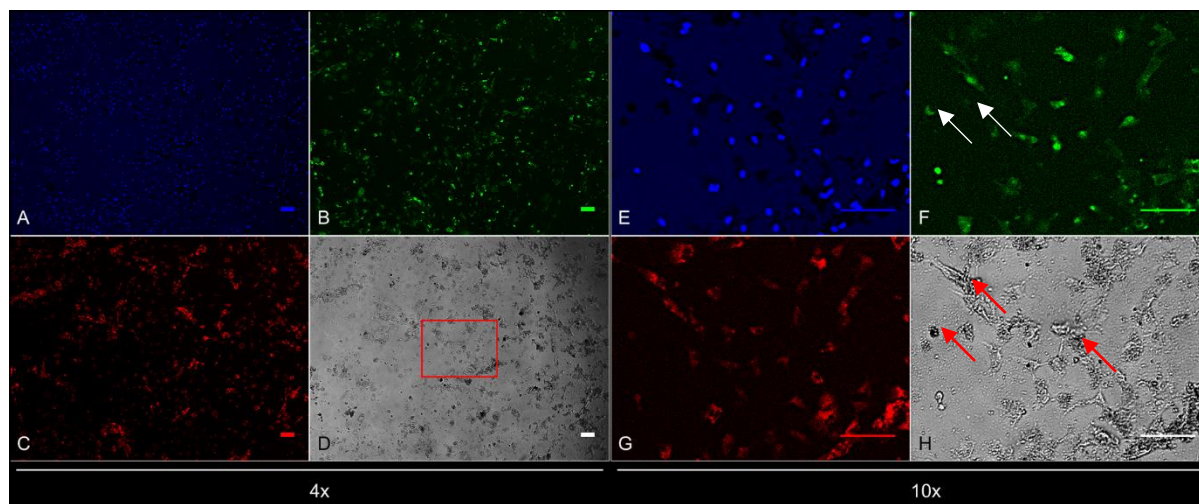


Figure A.108: HCS images of HUVEC cells after 48h exposure to BiFeO₃@APTES NPs at 80 $\mu\text{g/mL}$. Panels A and E (blue channels): nuclear staining with Hoechst; Panels B and F (green channels): cell membrane permeability staining; Panels C and G (red channels): lysosomal mass/pH staining; Panels D and H (transmitted light channels).

Left (A-D): 4x objective images. The region highlighted in the Transmitted Light Channel (D) is the area magnified in the right panels (E-H): 10x objective images. The scale bars are 100 μm .

Figure A.108 shows HUVEC cells after 48h of exposure to $\text{BiFeO}_3\text{@APTES}$ NPs at 80 $\mu\text{g}/\text{mL}$, stained for DNA (blue channels), cell morphology and membrane permeability (green channels) and lysosomal mass/pH changes (red channels). The aggregation and localisation of the $\text{BiFeO}_3\text{@APTES}$ NPs can be seen in the transmitted light panels (grey channels). As can be seen, after 48h the cells are not confluent, and the particles had aggregated inside the cells (Panels D and H, aggregates are indicated by red arrows in H). In comparison to A549 cells treated in the same way, both the CMP and lysosomal mass/pH staining is more intense and almost every cell is distinctly stained in HUVECs exposed to $\text{BiFeO}_3\text{@asc}$ NPs. There is also some extracellular staining in the CMP channel (designated by white arrows in Panel F, Figure A.108) which indicates cell debris.

A3.3.1 Cell count

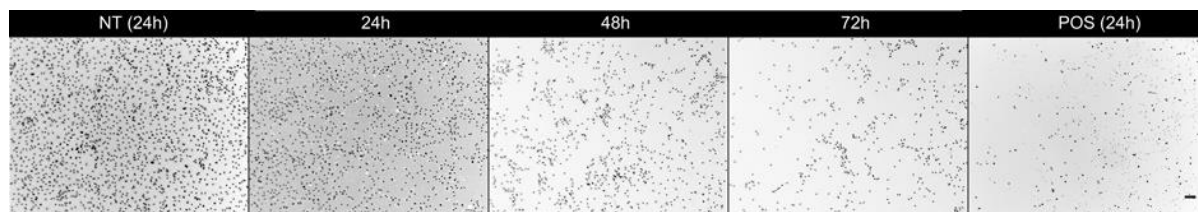


Figure A.109: HUVEC cells exposed to $\text{BiFeO}_3\text{@APTES}$ NPs, stained for DNA. From left: representative images of untreated cells after 24h, cells exposed to $\text{BiFeO}_3\text{@APTES}$ NPs at 80 $\mu\text{g}/\text{mL}$ for 24h, 48h, 72h, and cells treated with the positive control (valinomycin, 120 μM) for 24h. Only the Hoechst channel is shown, inverted. The scale bar is 100 μm and is the same for all the images.

HUVEC cells were exposed to $\text{BiFeO}_3\text{@APTES}$ NPs at three time points and stained for DNA to determine cell count (Figure A.109). Hoechst stains both the nuclear area and cell debris as seen in the positive control. It is for this reason that a minimum area (10 μm^2) is set to automatically identify nuclei prior to the cell count in the HCS analysis software.

As can be seen, the cells did not reach confluency and the population fell after 48 and 72h, as borne out by the HCS data below.

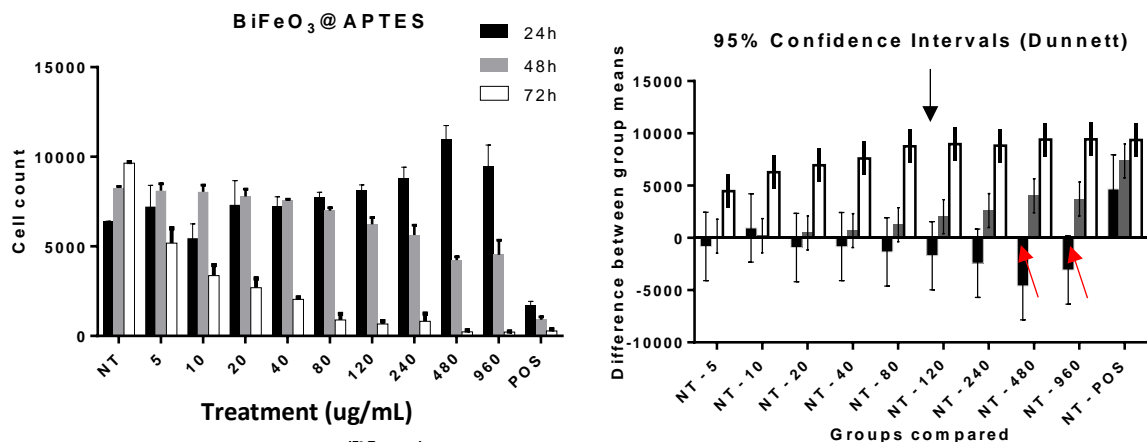


Figure A.110: Cell count of HUVEC cells after treatment with $\text{BiFeO}_3\text{@APTES}$ NPs and the corresponding 95% confidence intervals. Left: Number of cells vs concentration of nanomaterial. Valinomycin was used as positive control. The error bars represent the standard error of the mean of triplicates in three independent experiments. Right: difference between group means relative to the untreated control NT (Dunnett's test for multiple comparisons). The error bars represent the 95% confidence intervals (calculated using ordinary One-Way ANOVA).

Cell count varied significantly at higher concentrations at each time point (Figure A.110, left panel).

In line with the response attributed to stress, the cell number rose with increasing concentration after 24h hours, although the count was only significant when the concentration was above 480 $\mu\text{g}/\text{mL}$ (indicated by red arrows in Figure A.110, right panel).

Again, after 48h the trend had reversed; the greater the dose of NPs, the lower the cell number, with doses above 120 $\mu\text{g}/\text{mL}$ inducing a significant decrease in the cell number (indicated by a black arrow in Figure A.110, right panel).

After 72h, cell count fell more rapidly with increasing concentration than when cells were exposed to bare or ascorbic acid stabilised BiFeO_3 NPs, approaching the level of the positive control from 480 $\mu\text{g}/\text{mL}$.

A3.3.2 Cell Membrane Permeability

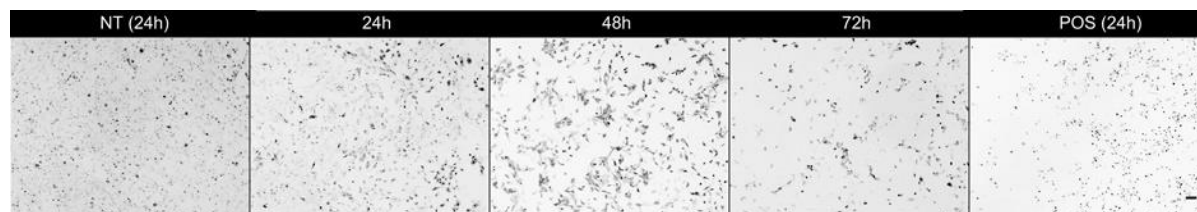


Figure A.111: HUVEC cells exposed to $\text{BiFeO}_3\text{@APTES}$ NPs, stained for cell membrane permeability. From left: representative images of untreated cells after 24h, cells exposed to $\text{BiFeO}_3\text{@APTES}$ NPs at 80 $\mu\text{g}/\text{mL}$ for 24h, 48h, 72h, and cells treated with the positive control (valinomycin, 120 μM) for 24h. Only the CMP (green) channels are shown, inverted. The scale bar is 100 μm and is the same for all the images.

Cell membrane permeability was used to indicate cell viability. Because the images in Figure A.111 are inverted, the number of viable cells in each image is therefore the number of cells in which the intensity of CMP stain surrounding and overlapping the nucleus is below the threshold determined for each plate analysed as described above (see A2.2.2). The data are displayed below (see Figure A.112).

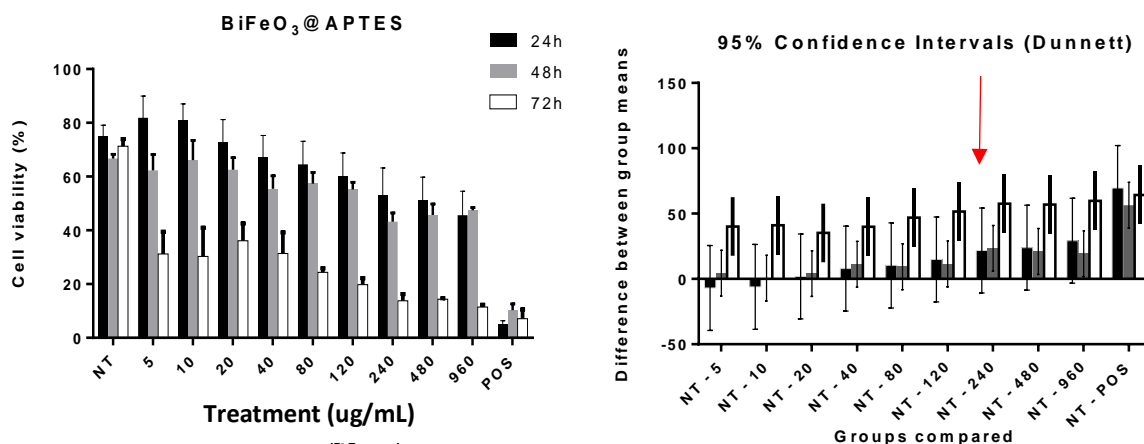


Figure A.112: Cell viability of HUVEC cells after treatment with BiFeO₃@APTES NPs and the corresponding 95% confidence intervals. Left: cell viability vs concentration of nanomaterial. Valinomycin was used as positive control. The error bars represent the standard error of the mean of triplicates in three independent experiments. Right: difference between group means relative to the untreated control NT (Dunnett's test for multiple comparisons). The error bars represent the 95% confidence intervals (calculated using ordinary One-Way ANOVA).

At 24h, the viability values in the concentration-dependent response fall within the 95% confidence intervals and are therefore not statistically significant (see right panel, Figure A.112). This is due in part to the large variability between samples and between experiments resulting in large uncertainty in the measurement.

The same trend was observed after 48h however, and due to the lower heterogeneity between the 48h samples, the decreases in viability as concentration of BiFeO₃@APTES increased was significant from 240 µg/mL and above (indicated by an arrow in the right panel of Figure A.112).

After 72h the fall in cell viability with rising concentration was more pronounced, and all values lay outside of the 95% CI. Furthermore, the viability fell off as the concentration of BiFeO₃@APTES increased, reaching a minimum of approximately 20% above 480 µg/mL.

Taken together, the drops in cell number and cell viability over time indicate that the BiFeO₃@APTES NPs diminish cell viability in cells at the concentrations analysed. This means that the silane layer did not appreciably reduce toxicity in HUVECs. On the other hand, because the initial increases in cell count were much lower, we can also conclude that the stress response of elevated cell proliferation was

mitigated by surface passivation. Finally, because the 72h cell counts of the BiFeO₃@asc and BiFeO₃@APTES were approximately equal at each concentration, this suggests that the toxicity results from the size or morphology of the nanoparticles rather than their chemical composition.

The cells were also examined for changes in lysosomal mass/pH as a final indicator of cytotoxicity.

A3.3.3 Lysosomal mass/pH

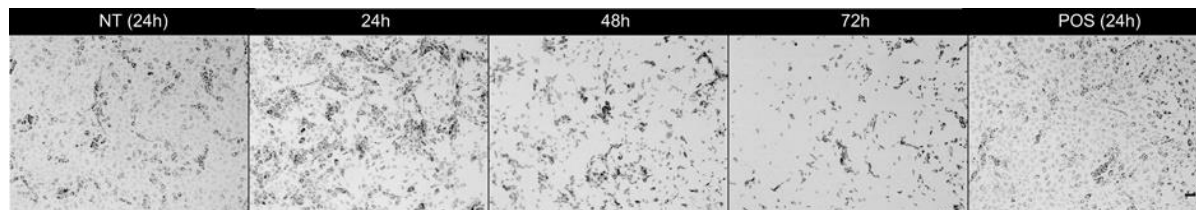


Figure A.113: HUVEC cells exposed to BiFeO₃@APTES NPs, stained for lysosomal mass/pH changes. From left: representative images of untreated cells after 24h, cells exposed to BiFeO₃@APTES NPs at 80 µg/mL for 24h, 48h, 72h, and cells treated with the positive control (tacrine, 100 µM) for 24h. Only the LysoTracker (red) channels are shown, inverted. The scale bar is 100 µm and is the same for all the images.

LysoTracker™ Red was used to stain for changes in lysosomal mass or pH. Because the images in Figure A.113 are inverted, an increase in the intensity therefore corresponds to a larger mass of lysosomes or decrease in pH, indicating a toxic response to the analyte. These data are displayed below (see Figure A.114).

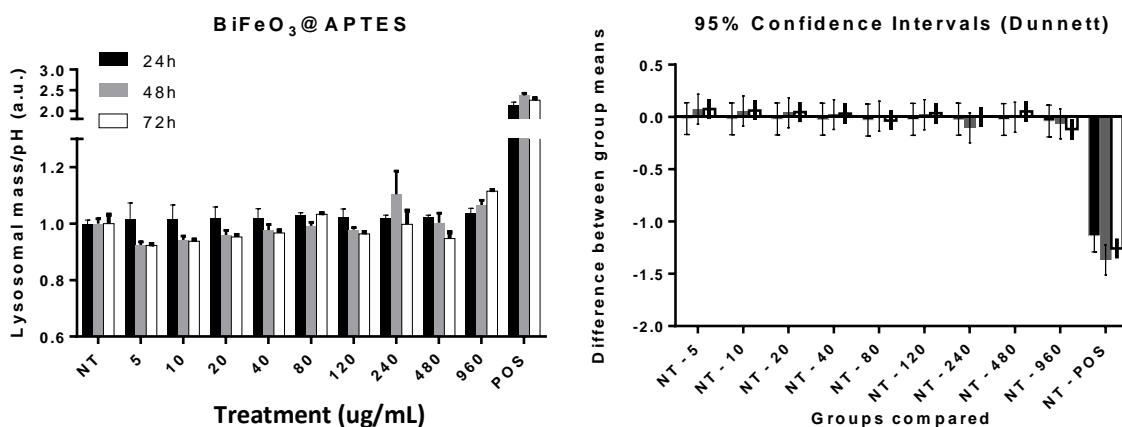


Figure A.114: Lysosomal mass/pH changes in HUVEC cells after treatment with BiFeO₃@APTES NPs and the corresponding 95% confidence intervals. Left: Lysosomal mass/pH vs concentration of nanomaterial. Tacrine was used as positive control. The error bars represent the standard error of the mean of triplicates in three independent experiments. Right: difference between group means relative to the untreated control NT (Dunnett's test for multiple comparisons). The error bars represent the 95% confidence intervals (calculated using ordinary One-Way ANOVA).

While there is an apparent drop in lysosomal mass/pH in cells exposed to BiFeO₃@APTES NPs after 48h and 72h, the response is not dose-dependent (see Figure A.114, left panel) and the variations fall within the respective 95% confidence intervals and are hence not significant (right panel, Figure A.114).

Given the drop in cell count and viability, the lack of significant variation in lysosomal mass/pH suggests that the NPs coated with a silane layer are not being internalised by the HUVECs as efficiently as other NPs or that internalisation is accompanied by a change in pH which counteracts the lysosomal mass increase (see the section on uptake for further information).

A3.4 HUVEC cells treated with BiFeO₃@Fe₃O₄@asc NPs

HUVEC cells were exposed to BiFeO₃@Fe₃O₄@asc NPs at 80 µg/mL for 48h, stained for DNA (blue channels), cell morphology and membrane permeability (green channels) and lysosomal mass/pH changes (red channels) (see Figure A.115).

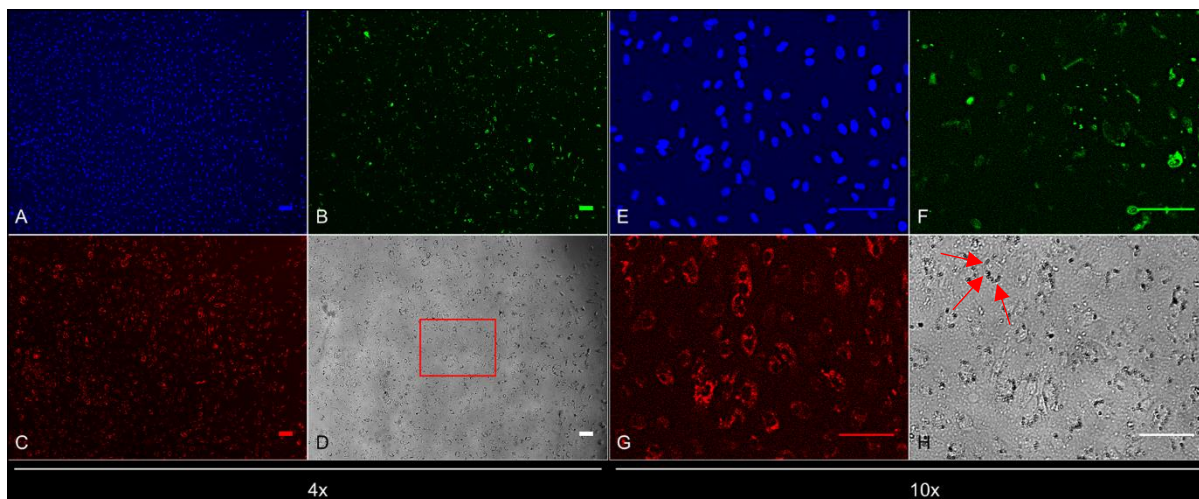


Figure A.115: HCS images of HUVEC cells after 48h exposure to BiFeO₃@Fe₃O₄@asc NPs at 80 µg/mL. Panels A and E (blue channels): nuclear staining with Hoechst; Panels B and F (green channels): cell membrane permeability staining; Panels C and G (red channels): lysosomal mass/pH staining; Panels D and H (transmitted light channels). Left (A-D): 4x objective images. The region highlighted in the Transmitted Light Channel (D) is the area magnified in the right panels (E-H): 10x objective images. The scale bars are 100 µm.

The aggregation and localisation of the BiFeO₃@Fe₃O₄@asc NPs can be seen in the transmitted light panels (grey channels). As can be seen, after 48h the cells are not confluent, and particles had formed small aggregates at the surface of the cells (Panels D and H, aggregates are indicated by red arrows in H), as distinct from previous samples in which NPs were seen inside and around the cells, and formed larger aggregates, especially bare BiFeO₃ and BiFeO₃@APTES. In comparison to A549 cells treated in the same way, both the CMP and lysosomal mass/pH staining is more intense and almost every cell is distinctly stained in HUVECs exposed to BiFeO₃@Fe₃O₄@asc NPs.

A3.4.1 Cell count

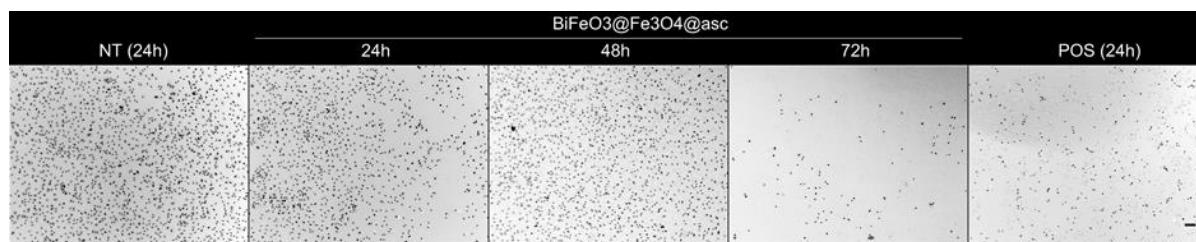


Figure A.116: HUVEC cells exposed to $\text{BiFeO}_3@Fe_3O_4@asc$ NPs, stained for DNA. From left: representative images of untreated cells after 24h, cells exposed to $\text{BiFeO}_3@Fe_3O_4@asc$ NPs at $80 \mu\text{g/mL}$ for 24h, 48h, 72h, and cells treated with the positive control (valinomycin, $120 \mu\text{M}$) for 24h. Only the Hoechst channel is shown, inverted. The scale bar is $100 \mu\text{m}$ and is the same for all the images.

HUVEC cells were exposed to $\text{BiFeO}_3@Fe_3O_4@asc$ NPs at three time points and stained for DNA to determine cell count (Figure A.116). As can be seen, the cells did not reach confluency and the population fell after 48 and 72h, as borne out by the HCS data below.

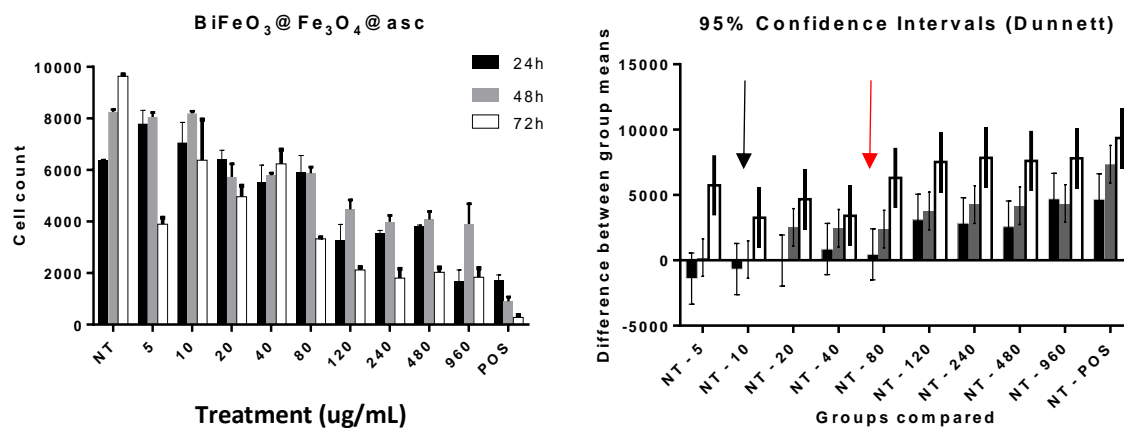


Figure A.117: Cell count of HUVEC cells after treatment with $\text{BiFeO}_3@Fe_3O_4@asc$ NPs and the corresponding 95% confidence intervals. Left: Number of cells vs concentration of nanomaterial. Valinomycin was used as positive control. The error bars represent the standard error of the mean of triplicates in three independent experiments. Right: difference between group means relative to the untreated control NT (Dunnett's test for multiple comparisons). The error bars represent the 95% confidence intervals (calculated using ordinary One-Way ANOVA).

The cell number fell with increasing concentration at each time point (Figure A.117, left panel), although at 24h the decreases in cell count were not significant up to $80 \mu\text{g/mL}$ and at 48h the numbers were not significant up to $10 \mu\text{g/mL}$ (indicated by red and black arrows respectively in Figure A.103, right panel).

Once again, after 48h the trend had reversed; the greater the dose of NPs, the lower the cell number, a trend which endured after 72h. There are obvious parallels with the cell count of HUVECs treated with $\text{BiFeO}_3@asc$ (see Figure A.102), the only distinctions being that the cell count rose in response to

the ascorbic acid coated NPs after 48h at low concentrations and, as a result, the counts after 72h were also lower at those concentrations. Most interestingly however, the variations in cell count after 24 and 48h most closely resemble the response of the cells to the bare BiFeO₃ NPs.

This provides further evidence that the *presence* of NPs, rather than their chemical composition, induces cell proliferation as a stress response.

At the highest concentrations, the 72h cell counts are marginally higher than those of NPs discussed earlier, implying that capping with a stabilising ligand increases the colloidal stability and mitigates the toxic response.

A3.4.2 Cell Membrane Permeability

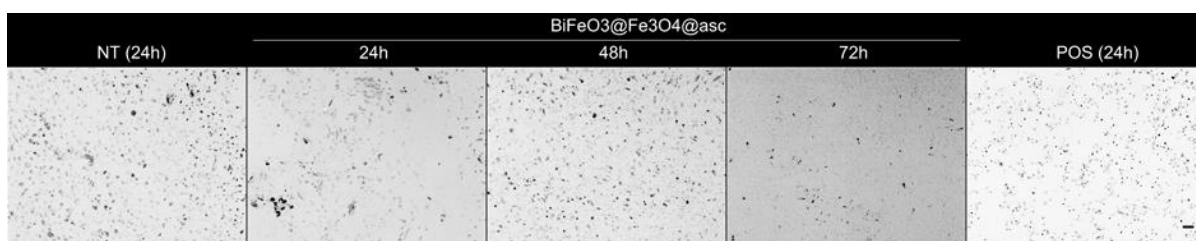


Figure A.118: HUVEC cells exposed to BiFeO₃@Fe₃O₄@asc NPs, stained for cell membrane permeability. From left: representative images of untreated cells after 24h, cells exposed to BiFeO₃@Fe₃O₄@asc NPs at 80 µg/mL for 24h, 48h, 72h, and cells treated with the positive control (valinomycin, 120 µM) for 24h. Only the CMP (green) channels are shown, inverted. The scale bar is 100 µm and is the same for all the images.

Cell membrane permeability was used to indicate cell viability. Because the images in Figure A.118 are inverted, the number of viable cells in each image is therefore the number of cells in which the intensity of CMP stain surrounding and overlapping the nucleus is below the threshold determined for each plate analysed as described above (see A2.2.2). The data are displayed below (see Figure A.119).

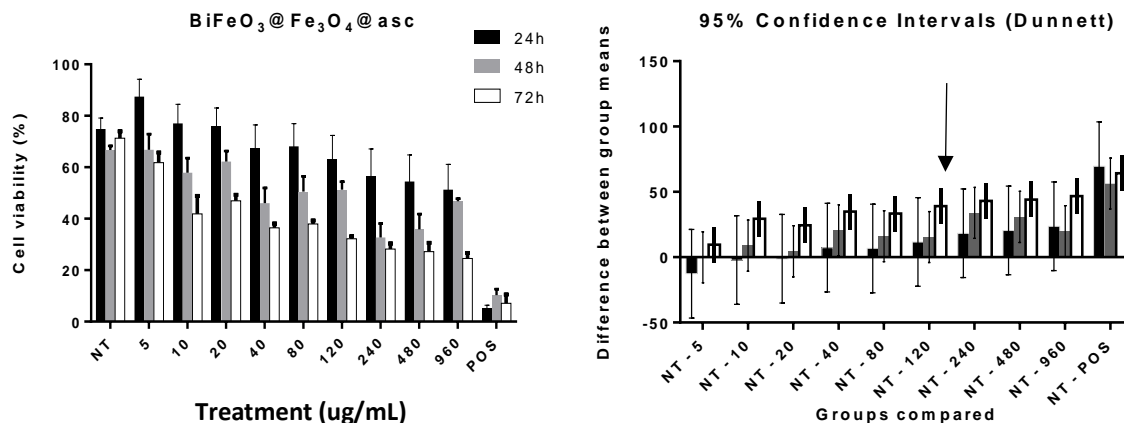


Figure A.119: Cell viability of HUVEC cells after treatment with BiFeO₃@Fe₃O₄@asc NPs and the corresponding 95% confidence intervals. Left: cell viability vs concentration of nanomaterial. Valinomycin was used as positive control. The error bars represent the standard error of the mean of triplicates in three independent experiments. Right: difference between group means relative to the untreated control NT (Dunnett's test for multiple comparisons). The error bars represent the 95% confidence intervals (calculated using ordinary One-Way ANOVA).

After 24h, the viability of HUVECs exposed to BiFeO₃@Fe₃O₄@asc NPs, although initially higher than the untreated control, descended as concentration increased (see left panel, Figure A.119) however, the viabilities fall within the 95% confidence intervals and are therefore not significantly different to the untreated control (see right panel, Figure A.119).

After 48h, cell viability values fell significantly at concentrations of 240 µg/mL and above and exhibited the same downward trend with increasing dose. After 72, the pattern was preserved with viability dropping from approximately 40% on exposure to 10 µg/mL to approximately 20%.

Because the same overall tendencies were observed in the cell count and viabilities on exposure to the BiFeO₃@Fe₃O₄@asc as those NPs discussed previously, this further supports the conclusion that the response is induced by the presence or morphology of the nanoparticles rather than their surface chemistry. The initial concentration-dependent stimulation of growth seen in the cell counts does not mitigate the overall toxicity of the NPs and the proliferation phase was accompanied by a dose-dependent decrease in viability for each of the NPs.

The cells were also examined for changes in lysosomal mass/pH as a final indicator of cytotoxicity.

A3.4.3 Lysosomal mass/pH

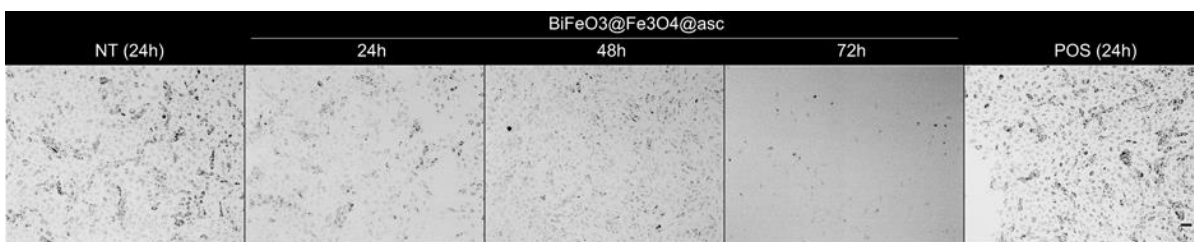


Figure A.120: HUVEC cells exposed to $\text{BiFeO}_3@Fe_3O_4@asc$ NPs, stained for lysosomal mass/pH changes. From left: representative images of untreated cells after 24h, cells exposed to $\text{BiFeO}_3@Fe_3O_4@asc$ NPs at $80 \mu\text{g/mL}$ for 24h, 48h, 72h, and cells treated with the positive control (tacrine, $100 \mu\text{M}$) for 24h. Only the LysoTracker (red) channels are shown, inverted. The scale bar is $100 \mu\text{m}$ and is the same for all the images.

LysoTracker™ Red was used to stain for changes in lysosomal mass or pH. Because the images in Figure A.120 are inverted, an increase in the intensity therefore corresponds to a larger mass of lysosomes or decrease in pH, indicating a toxic response to the analyte. These data are displayed below (see Figure A.121).

For example, the lowest lysosomal mass/pH values are observed at a dose of $5 \mu\text{g/mL}$ after 48 and 72h (indicated by an arrow in Figure A.121, left panel), and the lysosomal mass/pH intensity rose with increasing concentration.

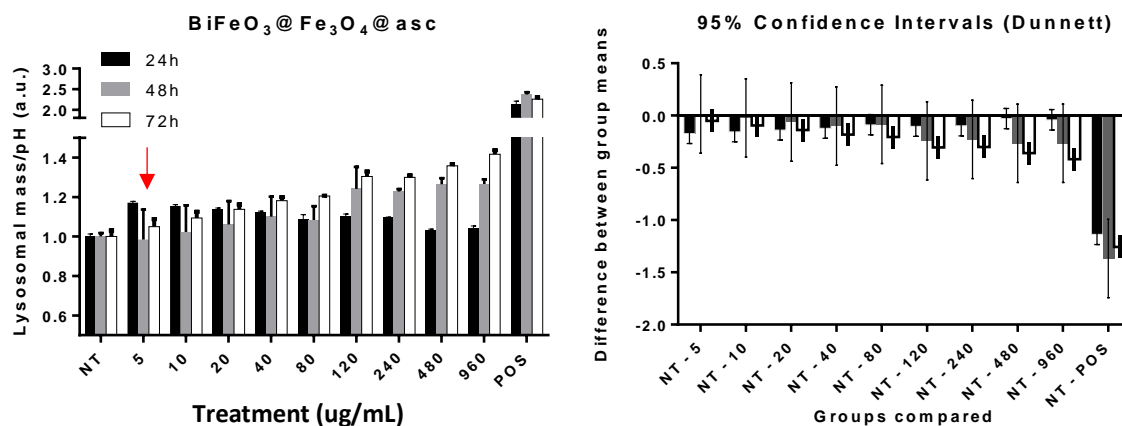


Figure A.121: Lysosomal mass/pH changes in HUVEC cells after treatment with $\text{BiFeO}_3@Fe_3O_4@asc$ NPs and the corresponding 95% confidence intervals. Left: Lysosomal mass/pH vs concentration of nanomaterial. Tacrine was used as positive control. The error bars represent the standard error of the mean of triplicates in three independent experiments. Right: difference between group means relative to the untreated control NT (Dunnett's test for multiple comparisons). The error bars represent the 95% confidence intervals (calculated using ordinary One-Way ANOVA).

As stated previously, this may be due to the adsorbed ascorbic acid. Although free ascorbic acid lowers the pH and increases the intensity of the LMPH stain, adsorption of the ascorbic acid modifies the surface charge. This leads to counter ions being drawn from solution to form the electrical double layer thus decreasing the intensity of the stain. When the cells are then exposed to higher concentrations of NPs which can be taken up into lysosomes, this results in greater lysosomal mass or number, increasing the intensity of the stain with rising dose.

The rise in lysosomal mass/pH can be attributed to the internalisation of NPs by the cells (see the section on uptake for further information).

A3.5 HUVEC cells treated with BiFeO₃@Fe₃O₄@APTES NPs

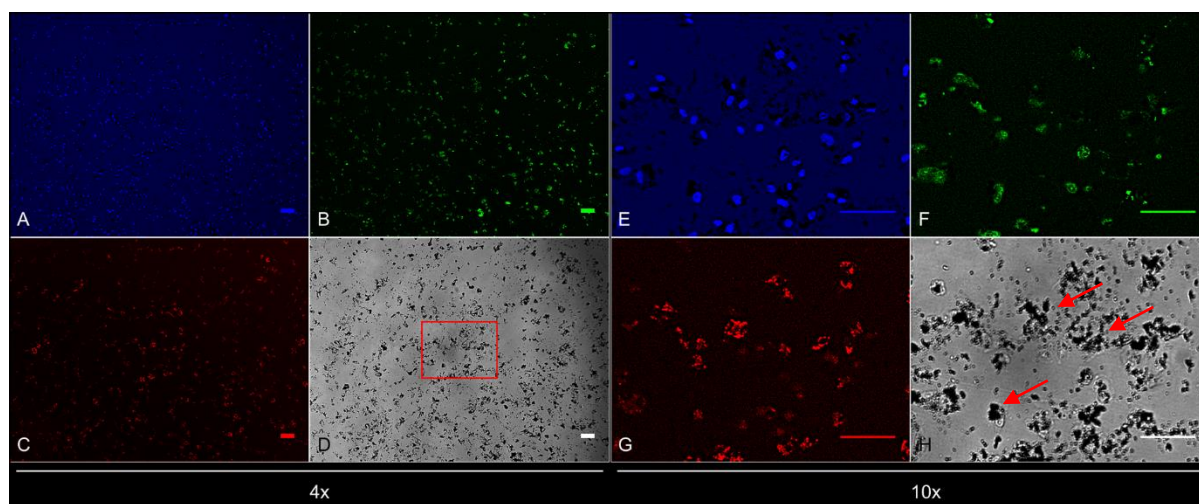


Figure A.122: HCS images of HUVEC cells after 48h exposure to BiFeO₃@Fe₃O₄@APTES NPs at 80 µg/mL. Panels A and E (blue channels): nuclear staining with Hoechst; Panels B and F (green channels): cell membrane permeability staining; Panels C and G (red channels): lysosomal mass/pH staining; Panels D and H (transmitted light channels). Left (A-D): 4x objective images. The region highlighted in the Transmitted Light Channel (D) is the area magnified in the right panels (E-H): 10x objective images. The scale bars are 100 µm.

Figure A.122 shows HUVEC cells after 48h of exposure to BiFeO₃@Fe₃O₄@APTES NPs at 80 µg/mL, stained for DNA (blue channels), cell morphology and membrane permeability (green channels) and lysosomal mass/pH changes (red channels). The aggregation and localisation of the BiFeO₃@Fe₃O₄@APTES NPs can be seen in the transmitted light panels (grey channels).

As can be seen, after 48h the cells are not confluent, and the particles had formed very large aggregates inside and outside the cells (Panels D and H, aggregates indicated by arrows in H). Some of the aggregates visible here are approximately 20 µm, like those seen when cells were treated with BiFeO₃@APTES, which further supports the conclusion that surface passivation with a silane layer lowers the colloidal stability of the NPs in biological media as well as aqueous suspension.

A3.5.1 Cell count

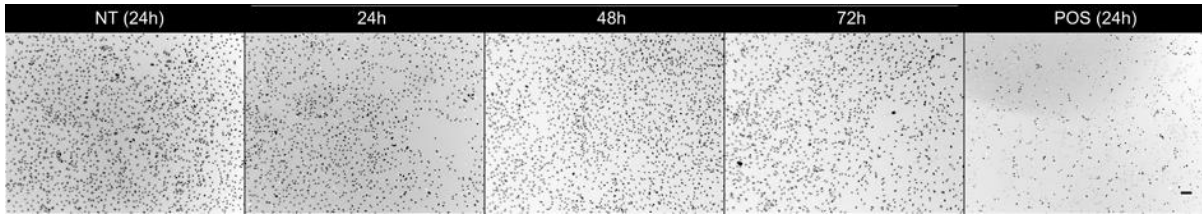


Figure A.123: HUVEC cells exposed to $\text{BiFeO}_3@Fe_3O_4@APTES$ NPs, stained for DNA. From left: representative images of untreated cells after 24h, cells exposed to $\text{BiFeO}_3@Fe_3O_4@APTES$ NPs at $80 \mu\text{g/mL}$ for 24h, 48h, 72h, and cells treated with the positive control (valinomycin, $120 \mu\text{M}$) for 24h. Only the Hoechst channel is shown, inverted. The scale bar is $100 \mu\text{m}$ and is the same for all the images.

HUVEC cells were exposed to $\text{BiFeO}_3@Fe_3O_4@APTES$ NPs at three time points and stained for DNA to determine cell count (see Figure A.123). As can be seen, the cells did not reach confluency and the population fell after 48 and 72h, as borne out by the HCS data below.

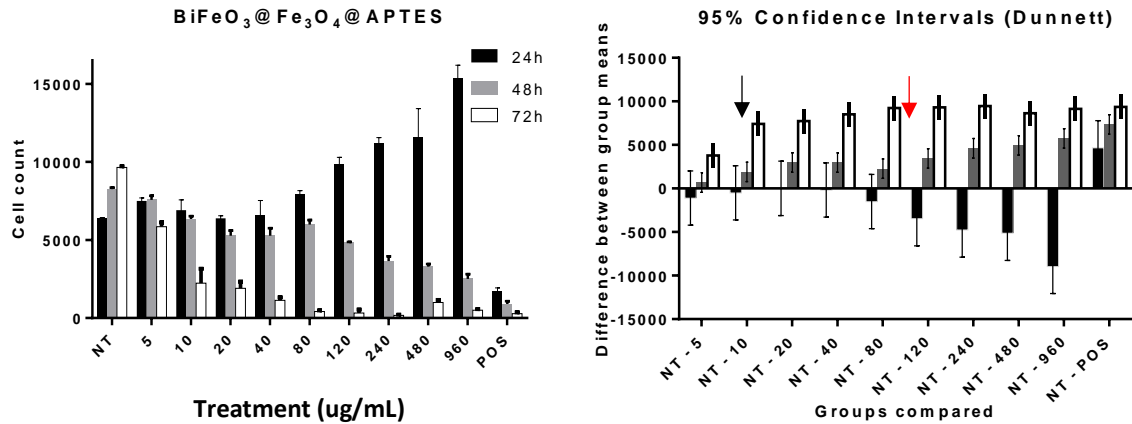


Figure A.124: Cell count of HUVEC cells after treatment with $\text{BiFeO}_3@Fe_3O_4@APTES$ NPs and the corresponding 95% confidence intervals. Left: Number of cells vs concentration of nanomaterial. Valinomycin was used as positive control. The error bars represent the standard error of the mean of triplicates in three independent experiments. Right: difference between group means relative to the untreated control NT (Dunnett's test for multiple comparisons). The error bars represent the 95% confidence intervals (calculated using ordinary One-Way ANOVA).

The response of HUVECs to $\text{BiFeO}_3@Fe_3O_4@APTES$ NPs more closely resembled exposure to bare BiFeO_3 or $\text{BiFeO}_3@APTES$ NPs than to $\text{BiFeO}_3@Fe_3O_4@asc$. At 24h, higher concentrations resulted in elevated cell counts but after 48h and 72h the cell numbers dropped progressively with increasing dose. There are trends in the variation of cell count with concentration of $\text{BiFeO}_3@Fe_3O_4@APTES$ (Figure A.124, left panel), with counts significantly higher than the untreated control when exposed to doses of NPs from $80 \mu\text{g/mL}$ for 24h (indicated by a red arrow in the right panel of Figure A.124), yet lower than the untreated control from $20 \mu\text{g/mL}$ after 48h (indicated by a black arrow) and at all doses after

72h as can be seen from the 95% confidence intervals. This hormesis further supports the conclusion that the cells undergo a phase of rapid proliferation as a stress response.

The general tendency of initially elevated followed by dramatic fall off in cell count suggests that the NPs are toxic to HUVECs.

A3.5.2 Cell Membrane Permeability

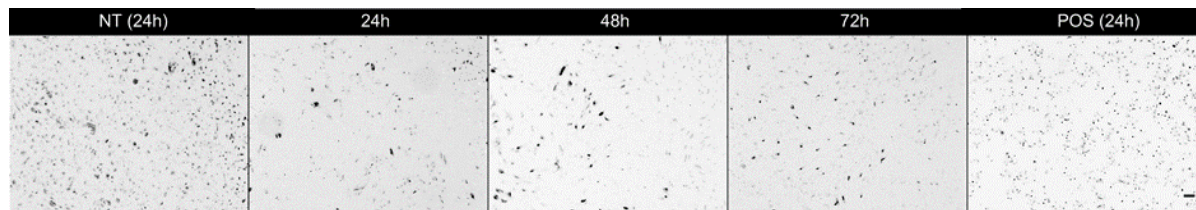


Figure A.125: HUVEC cells exposed to $\text{BiFeO}_3@Fe_3O_4@APTES$ NPs, stained for cell membrane permeability. From left: representative images of untreated cells after 24h, cells exposed to $\text{BiFeO}_3@Fe_3O_4@APTES$ NPs at 80 $\mu\text{g}/\text{mL}$ for 24h, 48h, 72h, and cells treated with the positive control (valinomycin, 120 μM) for 24h. Only the CMP (green) channels are shown, inverted. The scale bar is 100 μm and is the same for all the images.

Cell membrane permeability was used to indicate cell viability. Because the images in Figure A.125 are inverted, the number of viable cells in each image is therefore the number of cells in which the intensity of CMP stain surrounding and overlapping the nucleus is below the threshold determined for each plate analysed as described above (see A2.2.2). The data are displayed below (see Figure A.126).

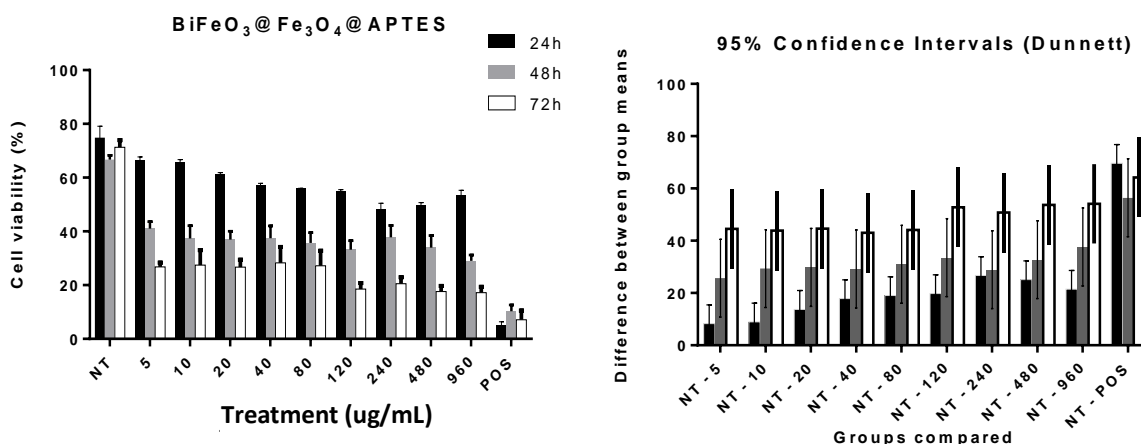


Figure A.126: Cell viability of HUVEC cells after treatment with $\text{BiFeO}_3@Fe_3O_4@APTES$ NPs and the corresponding 95% confidence intervals. Left: cell viability vs concentration of nanomaterial. Valinomycin was used as positive control. The error bars represent the standard error of the mean of triplicates in three independent experiments. Right: difference between group means relative to the untreated control NT (Dunnett's test for multiple comparisons). The error bars represent the 95% confidence intervals (calculated using ordinary One-Way ANOVA).

There are apparent trends in the concentration-dependent response of the cells to the NM (see left panel, Figure A.126). Unlike previously discussed NPs, the variations at each timepoint all fall outside

the 95% confidence intervals and are therefore statistically significant (see right panel, Figure A.126). Cell viability decreased significantly with increasing concentration. Together with the cell count data, this suggests that the NPs are toxic to HUVECs regardless of surface passivation, which in turn supports the conclusion that the toxic effect is associated with the size or morphology of the NPs rather than the chemical composition alone.

The cells were also examined for changes in lysosomal mass/pH as a final indicator of cytotoxicity.

A3.5.3 Lysosomal mass/pH

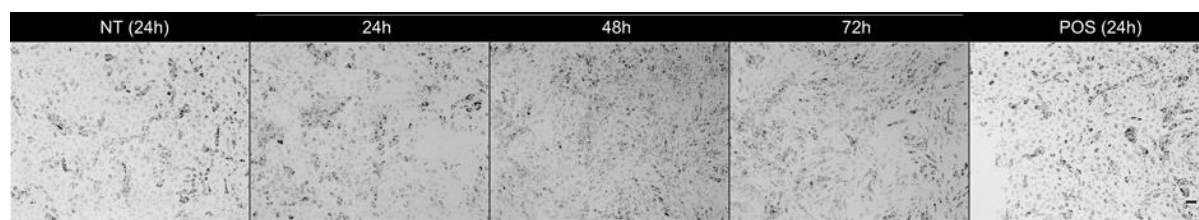


Figure A.127: HUVEC cells exposed to $\text{BiFeO}_3@Fe_3O_4@APTES$ NPs, stained for lysosomal mass/pH changes. From left: representative images of untreated cells after 24h, cells exposed to $\text{BiFeO}_3@Fe_3O_4@APTES$ NPs at $80 \mu\text{g/mL}$ for 24h, 48h, 72h, and cells treated with the positive control (tacrine, $100 \mu\text{M}$) for 24h. Only the LysoTracker (red) channels are shown, inverted. The scale bar is $100 \mu\text{m}$ and is the same for all the images.

LysoTracker™ Red was used to stain for changes in lysosomal mass or pH. Because the images in Figure A.127 are inverted, an increase in the intensity therefore corresponds to a larger mass of lysosomes or decrease in pH, indicating a toxic response to the analyte. These data are displayed below (see Figure A.128).

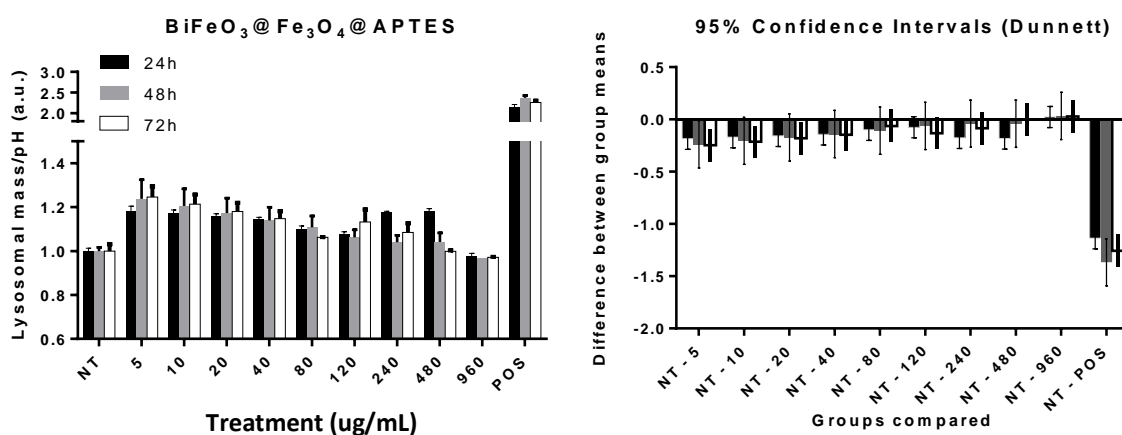


Figure A.128: Lysosomal mass/pH changes in HUVEC cells after treatment with $\text{BiFeO}_3@Fe_3O_4@APTES$ NPs and the corresponding 95% confidence intervals. Left: Lysosomal mass/pH vs concentration of nanomaterial. Tacrine was used as positive control. The error bars represent the standard error of the mean of triplicates in three independent experiments. Right: difference between group means relative to the untreated control NT (Dunnett's test for multiple comparisons). The error bars represent the 95% confidence intervals (calculated using ordinary One-Way ANOVA).

While there is an apparent increase in lysosomal mass/pH in cells exposed to $\text{BiFeO}_3@Fe_3O_4@APTES$ NPs after each of the time-points (see Figure A.128, left panel), at higher concentrations the variations fall within the respective 95% confidence intervals and are hence not significant (right panel, Figure A.128).

Nevertheless, lower concentrations induced a small but significant increase in the LMPH at each time-point.

Given the drop in cell count and viability, the lack of significant increase in lysosomal mass/pH with rising dose suggests that the NPs are not being internalised by the HUVECs, possibly due to the size of the aggregates, or that internalisation is accompanied by a change in pH which counteracts the lysosomal mass increase.

A3.6 HUVEC cells treated with $\text{BiFeO}_3@Fe_2O_3@asc$ NPs

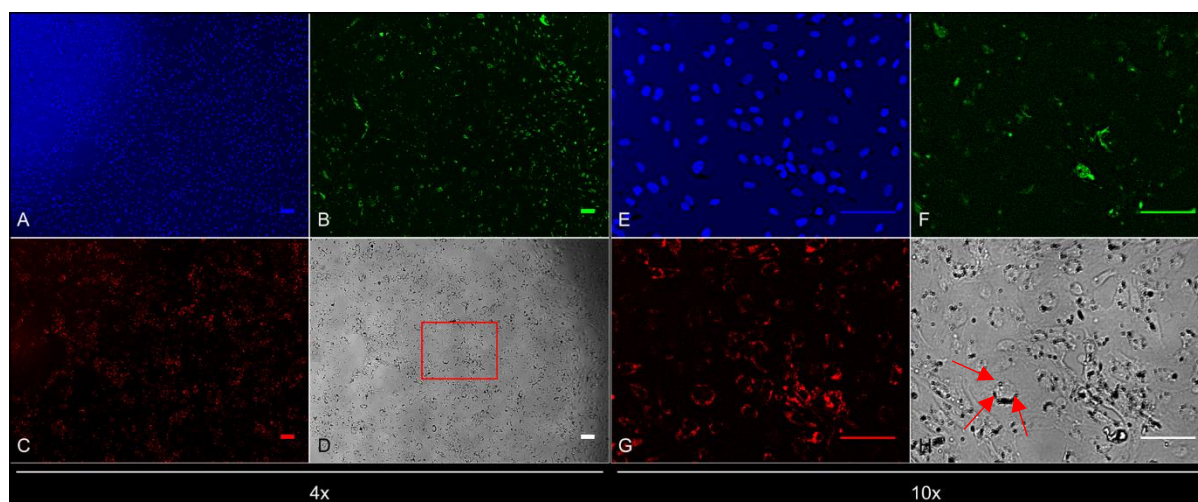


Figure A.129: HCS images of HUVEC cells after 48h exposure to $\text{BiFeO}_3@Fe_2O_3@asc$ NPs at $80 \mu\text{g/mL}$. Panels A and E (blue channels): nuclear staining with Hoechst; Panels B and F (green channels): cell membrane permeability staining; Panels C and G (red channels): lysosomal mass/pH staining; Panels D and H (transmitted light channels). Left (A-D): 4x objective images. The region highlighted in the Transmitted Light Channel (D) is the area magnified in the right panels (E-H): 10x objective images. The scale bars are $100 \mu\text{m}$.

Figure A.129 shows HUVEC cells after 48h of exposure to $\text{BiFeO}_3@Fe_2O_3@asc$ NPs at $80 \mu\text{g/mL}$, stained for DNA (blue channels), cell morphology and membrane permeability (green channels) and lysosomal mass/pH changes (red channels). The aggregation and localisation of the $\text{BiFeO}_3@Fe_2O_3@asc$ NPs can be seen in the transmitted light panels (grey channels). As can be seen, after 48h the cells had reached confluency despite the presence of the NPs and the particles had aggregated inside the cells (Panels D and H). As can be seen, after 48h the cells are not confluent, and particles had formed small aggregates

at the surface of the cells (Panels D and H, aggregates are indicated by red arrows in H), similar to when HUVECs were exposed to other NPs stabilised with ascorbic acid (see $\text{BiFeO}_3@Fe_3O_4@asc$, this).

A3.6.1 Cell count

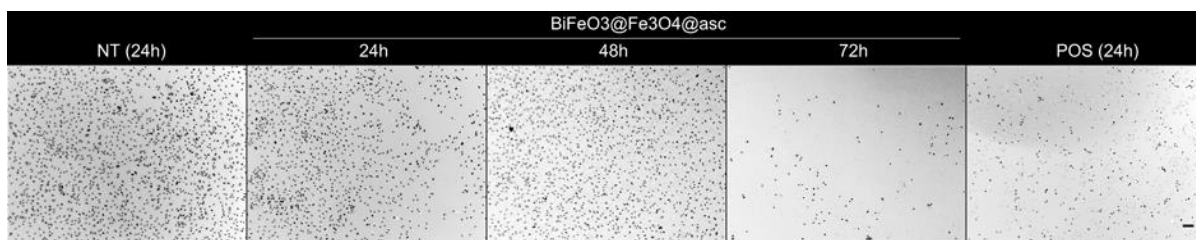


Figure A.130: HUVEC cells exposed to $\text{BiFeO}_3@Fe_2O_3@asc$ NPs, stained for DNA. From left: representative images of untreated cells after 24h, cells exposed to $\text{BiFeO}_3@Fe_2O_3@asc$ NPs at $80 \mu\text{g/mL}$ for 24h, 48h, 72h, and cells treated with the positive control (valinomycin, $120 \mu\text{M}$) for 24h. Only the Hoechst channel is shown, inverted. The scale bar is $100 \mu\text{m}$ and is the same for all the images.

HUVEC cells were exposed to $\text{BiFeO}_3@Fe_2O_3@asc$ NPs at three time points and stained for DNA to determine cell count (Figure A.130). As can be seen, the cells did not reach confluency and the population fell after 48 and 72h, as borne out by the HCS data below.

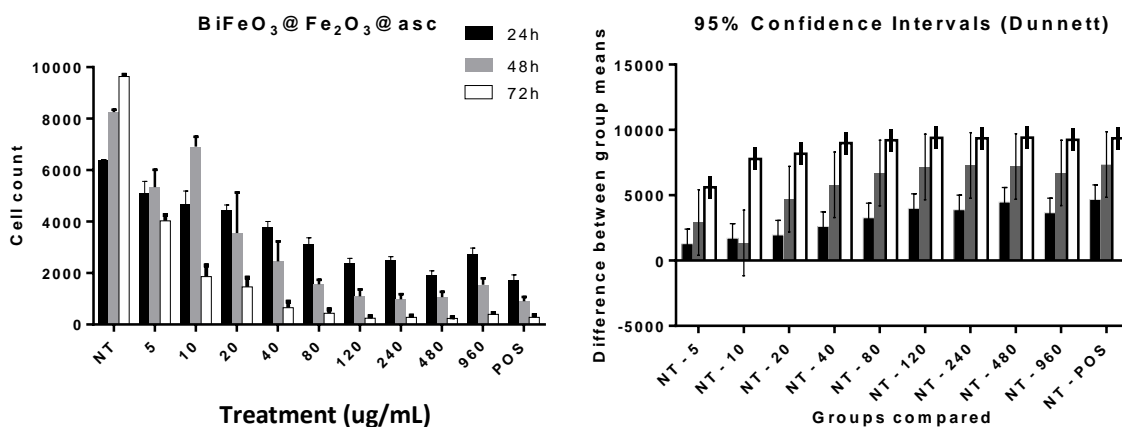


Figure A.131: Cell count of HUVEC cells after treatment with $\text{BiFeO}_3@Fe_2O_3@asc$ NPs and the corresponding 95% confidence intervals. Left: Number of cells vs concentration of nanomaterial. Valinomycin was used as positive control. The error bars represent the standard error of the mean of triplicates in three independent experiments. Right: difference between group means relative to the untreated control NT (Dunnett's test for multiple comparisons). The error bars represent the 95% confidence intervals (calculated using ordinary One-Way ANOVA).

Cell count dropped significantly with increasing dose at each timepoint, albeit with large heterogeneity in the sample after 48h (see Figure A.131, left panel). Importantly, the cell number fell to approximately the level of the positive control on exposure to $240 \mu\text{g/mL}$ at each time-point, clearly indicating a toxic response.

A3.6.2 Cell Membrane Permeability

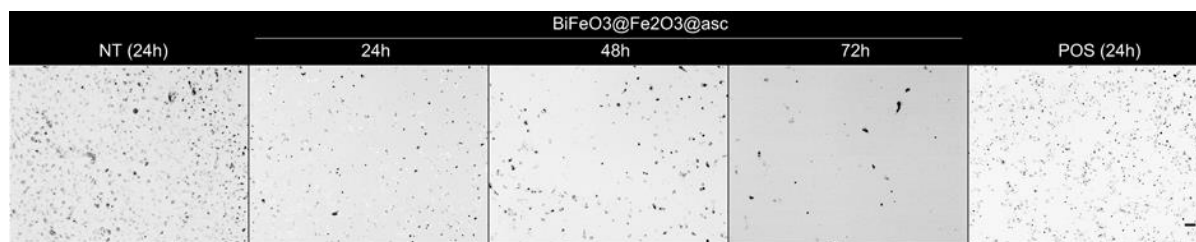


Figure A.132: HUVEC cells exposed to $\text{BiFeO}_3@Fe_2O_3@asc$ NPs, stained for cell membrane permeability. From left: representative images of untreated cells after 24h, cells exposed to $\text{BiFeO}_3@Fe_2O_3@asc$ NPs at 80 $\mu\text{g}/\text{mL}$ for 24h, 48h, 72h, and cells treated with the positive control (valinomycin, 120 μM) for 24h. Only the CMP (green) channels are shown, inverted. The scale bar is 100 μm and is the same for all the images.

Cell membrane permeability was used to indicate cell viability. Because the images in Figure A.132 are inverted, the number of viable cells in each image is therefore the number of cells in which the intensity of CMP stain surrounding and overlapping the nucleus is below the threshold determined for each plate analysed as described above (see A2.2.2). The data are displayed below (see Figure A.133).

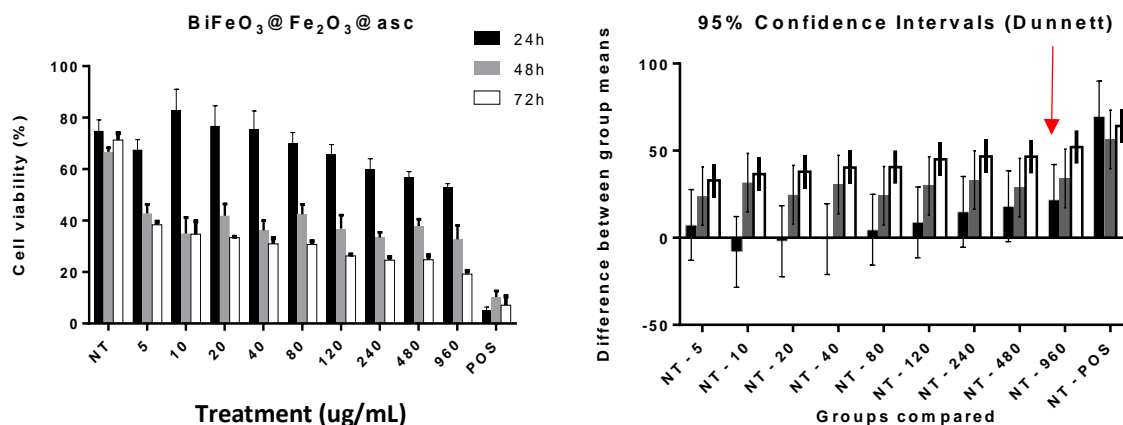


Figure A.133: Cell viability of HUVEC cells after treatment with $\text{BiFeO}_3@Fe_2O_3@asc$ NPs and the corresponding 95% confidence intervals. Left: cell viability vs concentration of nanomaterial. Valinomycin was used as positive control. The error bars represent the standard error of the mean of triplicates in three independent experiments. Right: difference between group means relative to the untreated control NT (Dunnett's test for multiple comparisons). The error bars represent the 95% confidence intervals (calculated using ordinary One-Way ANOVA).

There are apparent trends in the concentration-dependent response of the cells to the NM (see left panel, Figure A.133). At 24h however, the variations all fall within the 95% confidence intervals and are therefore not statistically significant except at a dose of 960 $\mu\text{g}/\text{mL}$ (indicated by an arrow in Figure A.133).

By contrast, the fall in viability recorded at all values of concentration after 48 and 72h lie outside the 95% CI and are therefore significant and we can see a dose-dependent decrease from approximately

40% to 20% after 72h. In conjunction with the cell count data, this supports the conclusion that BiFeO₃@Fe₂O₃@asc NPs accelerate cell death in HUVECs by increasing cell permeability.

The cells were also examined for changes in lysosomal mass/pH as a final indicator of cytotoxicity.

A3.6.3 Lysosomal mass/pH

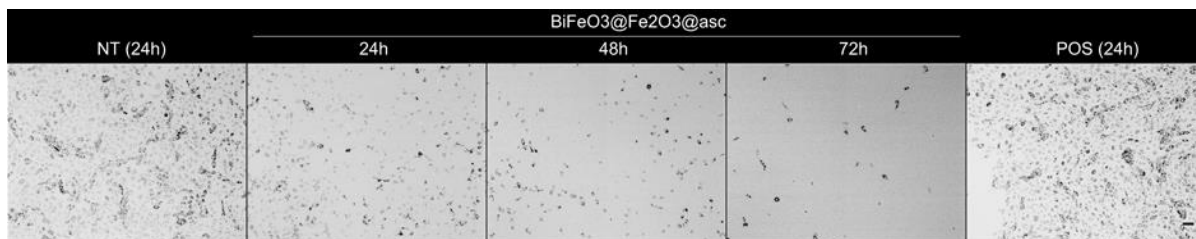


Figure A.134: HUVEC cells exposed to BiFeO₃@Fe₂O₃@asc NPs, stained for lysosomal mass/pH changes. From left: representative images of untreated cells after 24h, cells exposed to BiFeO₃@Fe₂O₃@asc NPs at 80 µg/mL for 24h, 48h, 72h, and cells treated with the positive control (tacrine, 100 µM) for 24h. Only the LysoTracker (red) channels are shown, inverted. The scale bar is 100 µm and is the same for all the images.

LysoTracker™ Red was used to stain for changes in lysosomal mass or pH. Because the images in Figure A.134 are inverted, an increase in the intensity therefore corresponds to a larger mass of lysosomes or decrease in pH, indicating a toxic response to the analyte. These data are displayed below (see Figure A.135).

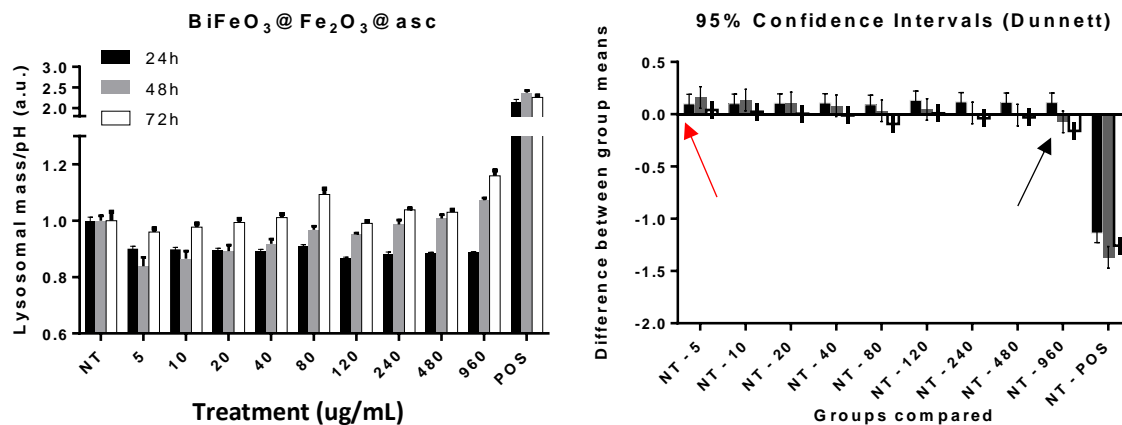


Figure A.135: Lysosomal mass/pH changes in HUVEC cells after treatment with BiFeO₃@Fe₂O₃@asc NPs and the corresponding 95% confidence intervals. Left: Lysosomal mass/pH vs concentration of nanomaterial. Tacrine was used as positive control. The error bars represent the standard error of the mean of triplicates in three independent experiments. Right: difference between group means relative to the untreated control NT (Dunnett's test for multiple comparisons). The error bars represent the 95% confidence intervals (calculated using ordinary One-Way ANOVA).

Like the other ascorbic acid-coated NPs, there is a dose-dependent response in the lysosomal mass/pH as a function of concentration of BiFeO₃@Fe₂O₃@asc NPs as can be seen in Figure A.135, left panel. One unusual feature observed here is the lower LMPH at all doses after 24h.

Lysosomal mass/pH rose with increasing rising concentration after 48h from a low of ~0.85 a.u. on dosing with 5 µg/mL (right panel, Figure A.135). From 40 µg/mL the variations fell within the respective 95% confidence intervals and are hence not significant.

Similarly, the variations in LMPH after 72h fell within the 95% CI except at 960 µg/mL (indicated by a black arrow in the right panel of Figure A.135). The lowest lysosomal mass/pH values resulted from exposure to the lowest dose (5 µg/mL, indicated by a red arrow), and rose with increasing concentration, as with the other ascorbic acid-coated NPs.

As postulated previously, this may be due to the adsorbed ascorbic acid drawing counterions from suspension (which lowers the pH, decreasing the intensity of the LysoTracker stain) being balanced on increasing the concentration by more NPs being taken up into lysosomes in the HUVECs (which raises the number and/or mass of lysosomes, hence increasing the intensity).

A3.7 HUVEC cells treated with SiO₂&BiFeO₃ NWs

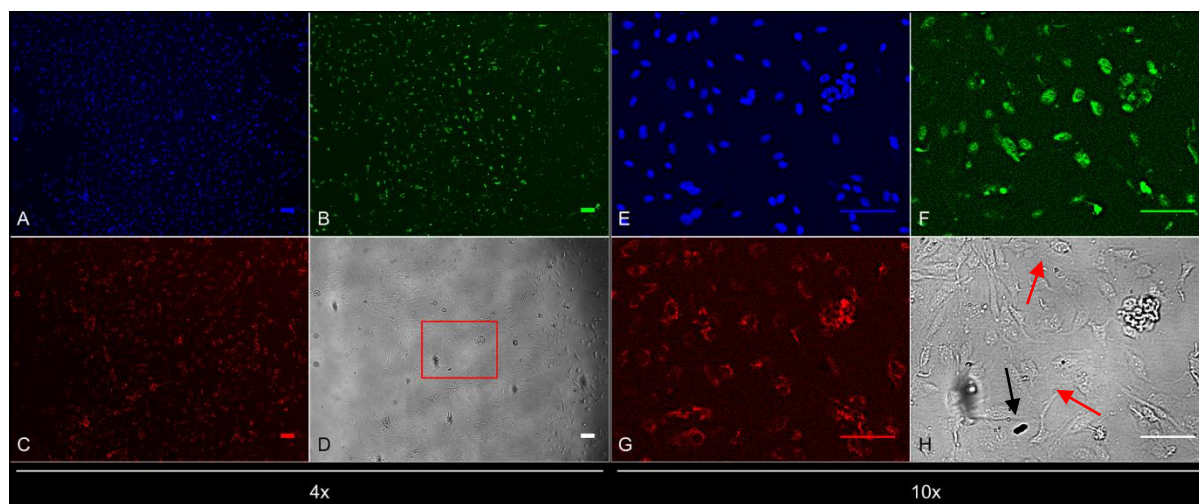


Figure A.136: HCS images of HUVEC cells after 48h exposure to SiO₂ & BiFeO₃ NWs at 80 µg/mL. Panels A and E (blue channels): nuclear staining with Hoechst; Panels B and F (green channels): cell membrane permeability staining; Panels C and G (red channels): lysosomal mass/pH staining; Panels D and H (transmitted light channels). Left (A-D): 4x objective images. The region highlighted in the Transmitted Light Channel (D) is the area magnified in the right panels (E-H): 10x objective images. The scale bars are 100 µm.

Figure A.136 shows HUVEC cells after 48h of exposure to SiO₂ & BiFeO₃ NWs at 80 µg/mL, stained for DNA (blue channels), cell morphology and membrane permeability (green channels) and lysosomal mass/pH changes (red channels). The aggregation and localisation of the SiO₂ & BiFeO₃ NWs can be

seen in the transmitted light panels (grey channels). Because the wires are below the Rayleigh limit (i.e. they are much narrower than the wavelength range of visible light) and the contrast is very low, the wires can only be seen when aggregated into bundles (indicated by red arrows in Panel H). After 48h the cells had not reached confluency and the NWs had amassed inside and around the cells (Panels D and H). Some higher contrast aggregates are also visible which are likely NPs that have been released from the mesoporous nanowires (designated by a black arrow in Panel H).

A3.7.1 Cell count

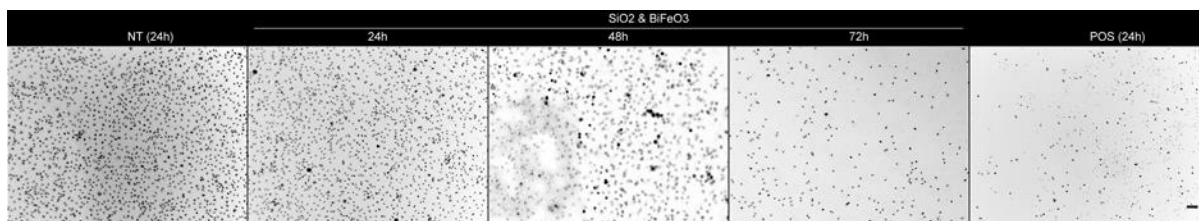


Figure A.137: HUVEC cells exposed to SiO_2 & BiFeO_3 NWs stained for DNA. From left: representative images of untreated cells after 24h, cells exposed to SiO_2 & BiFeO_3 NWs at $80 \mu\text{g/mL}$ for 24h, 48h, 72h, and cells treated with the positive control (valinomycin, $120 \mu\text{M}$) for 24h. Only the Hoechst channel is shown, inverted. The scale bar is $100 \mu\text{m}$ and is the same for all the images.

HUVEC cells were exposed to SiO_2 & BiFeO_3 NWs at three time points and stained for DNA to determine cell count (Figure A.137). As can be seen, the cells did not reach confluency and the population fell after 72h, as borne out by the HCS data below.

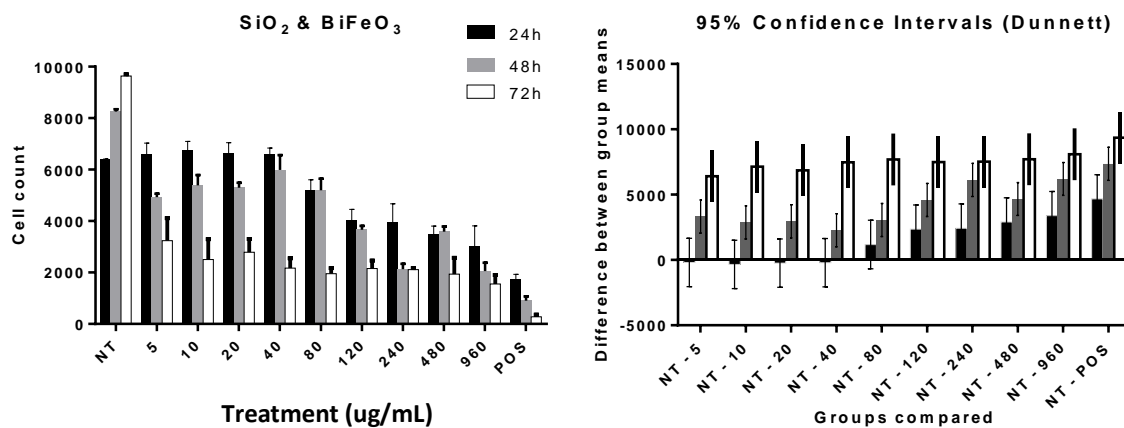


Figure A.138: Cell count of HUVEC cells after treatment with SiO_2 & BiFeO_3 NWs and the corresponding 95% confidence intervals. Left: Number of cells vs concentration of nanomaterial. Valinomycin was used as positive control. The error bars represent the standard error of the mean of triplicates in three independent experiments. Right: difference between group means relative to the untreated control NT (Dunnett's test for multiple comparisons). The error bars represent the 95% confidence intervals (calculated using ordinary One-Way ANOVA).

There are trends in the variation of cell count with concentration of SiO_2 & BiFeO_3 NWs (Figure A.138, left panel), with counts significantly lower than the untreated control when exposed to more than 80

$\mu\text{g}/\text{mL}$ of the NPs for 24h, and at all doses after 48 and 72h as can be seen from the 95% confidence intervals (Figure A.138, right panel). Although the data is somewhat heterogeneous, the general tendency suggests that the NPs are toxic to HUVECs. At the highest concentrations, the 72h cell counts are like those of ascorbic acid-coated NPs discussed earlier. This implies that embedding the NPs in silica has a similar effect on the toxicity as stabilising the NPs, only mitigating the toxic response at lower doses.

A3.7.2 Cell Membrane Permeability

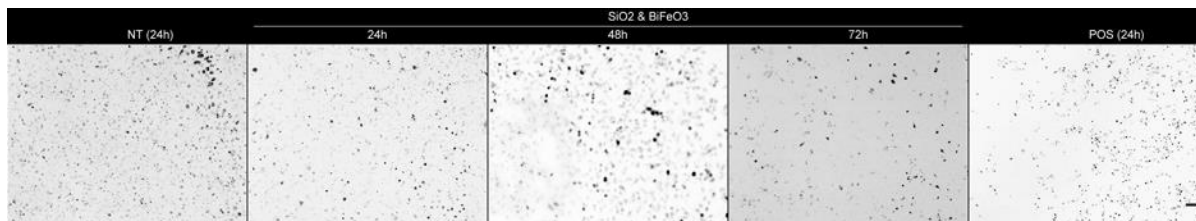


Figure A.139: HUVEC cells exposed to SiO_2 & BiFeO_3 NWs stained for cell membrane permeability. From left: representative images of untreated cells after 24h, cells exposed to SiO_2 & BiFeO_3 NWs at $80 \mu\text{g}/\text{mL}$ for 24h, 48h, 72h, and cells treated with the positive control (valinomycin, $120 \mu\text{M}$) for 24h. Only the CMP (green) channels are shown, inverted. The scale bar is $100 \mu\text{m}$ and is the same for all the images.

Cell membrane permeability was used to indicate cell viability. Because the images in Figure A.139 are inverted, the number of viable cells in each image is therefore the number of cells in which the intensity of CMP stain surrounding and overlapping the nucleus is below the threshold determined for each plate analysed as described above (see A2.2.2). The data are displayed below (see Figure A.140).

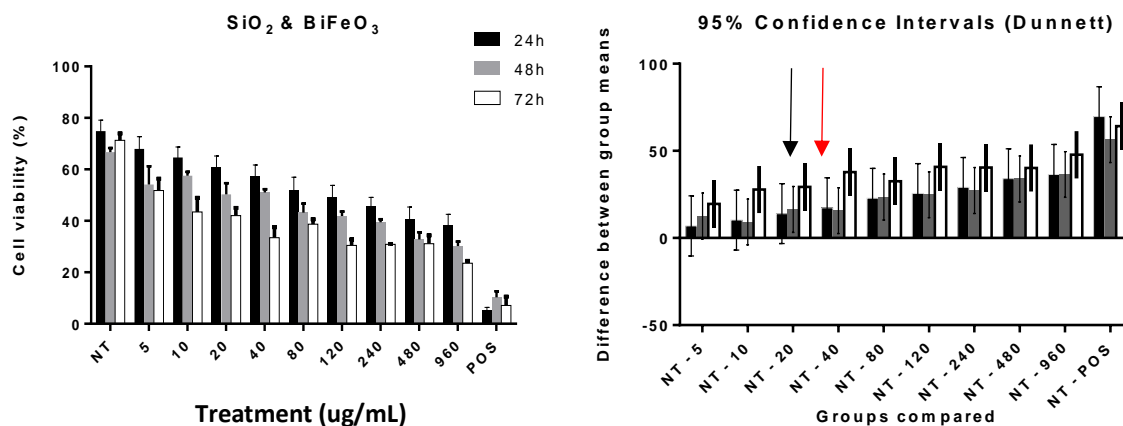


Figure A.140: Cell viability of HUVEC cells after treatment with SiO_2 & BiFeO_3 NWs and the corresponding 95% confidence intervals. Left: cell viability vs concentration of nanomaterial. Valinomycin was used as positive control. The error bars represent the standard error of the mean of triplicates in three independent experiments. Right: difference between group means relative to the untreated control NT (Dunnett's test for multiple comparisons). The error bars represent the 95% confidence intervals (calculated using ordinary One-Way ANOVA).

As with the cell count, there was concentration-dependent decrease in the viability of the cells (see left panel, Figure A.140). However, the variations at the lowest concentrations after 24 and 48h fall within the 95% confidence intervals and are therefore not statistically significant.

After 24h, viabilities dropped significantly from 40 $\mu\text{g}/\text{mL}$ (indicated by a red arrow in Figure A.140, right panel) and fell steadily with increasing dose. The same decline was observed from 20 $\mu\text{g}/\text{mL}$ after 48h (indicated by a black arrow in Figure A.140, right panel).

After 72h the viability changes all fell outside the 95% CI. This supports the conclusion that the SiO_2 & BiFeO_3 NWs impair cell viability and increase cell death in HUVEC cells at the concentrations analysed.

The cells were also examined for changes in lysosomal mass/pH as a final indicator of cytotoxicity.

A3.7.3 Lysosomal mass/pH

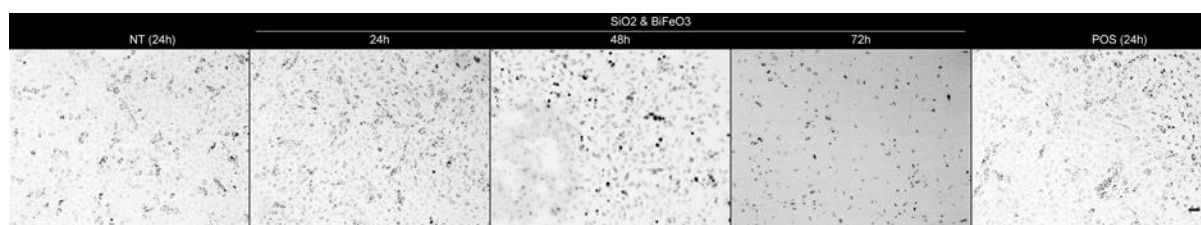


Figure A.141: HUVEC cells exposed to SiO_2 & BiFeO_3 NWs stained for lysosomal mass/pH changes. From left: representative images of untreated cells after 24h, cells exposed to SiO_2 & BiFeO_3 NWs at 80 $\mu\text{g}/\text{mL}$ for 24h, 48h, 72h, and cells treated with the positive control (tacrine, 100 μM) for 24h. Only the LysoTracker (red) channels are shown, inverted. The scale bar is 100 μm and is the same for all the images.

LysoTracker™ Red was used to stain for changes in lysosomal mass or pH. Because the images in Figure A.141 are inverted, an increase in the intensity therefore corresponds to a larger mass of lysosomes or decrease in pH, indicating a toxic response to the analyte. These data are displayed below (see Figure A.142).

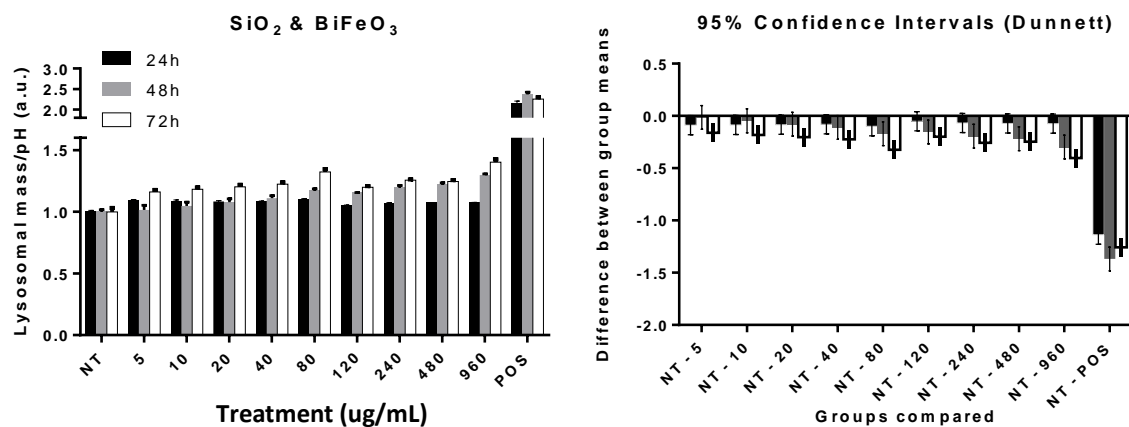


Figure A.142: Lysosomal mass/pH changes in HUVEC cells after treatment with SiO₂ & BiFeO₃ NWs and the corresponding 95% confidence intervals. Left: Lysosomal mass/pH vs concentration of nanomaterial. Tacrine was used as positive control. The error bars represent the standard error of the mean of triplicates in three independent experiments. Right: difference between group means relative to the untreated control NT (Dunnett's test for multiple comparisons). The error bars represent the 95% confidence intervals (calculated using ordinary One-Way ANOVA).

Lysosomal mass/pH fell at all concentrations after 24h exposure to SiO₂ & BiFeO₃ NWs as can be seen in Figure A.142, left panel. A trend of increasing lysosomal mass/pH with rising concentration is observed after 48h and 72h but the variations fall within the respective 95% confidence intervals and are hence not significant except at the highest concentration after 72h (indicated by an arrow, right panel, Figure A.142).

The lack of response after 24h suggests that the nanowires are not immediately internalised, perhaps due to their surface chemistry as discussed in 3.3.2. The concentration-dependent increase in LMPH observed after 48h and 72h may be due to delayed uptake of the nanowires, dissolution of ions from the embedded nanoparticles or to the release of the nanoparticles from the mesoporous silica nanowires.

A3.8 HUVEC cells treated with SiO₂&BiFeO₃@Fe₃O₄ NWs

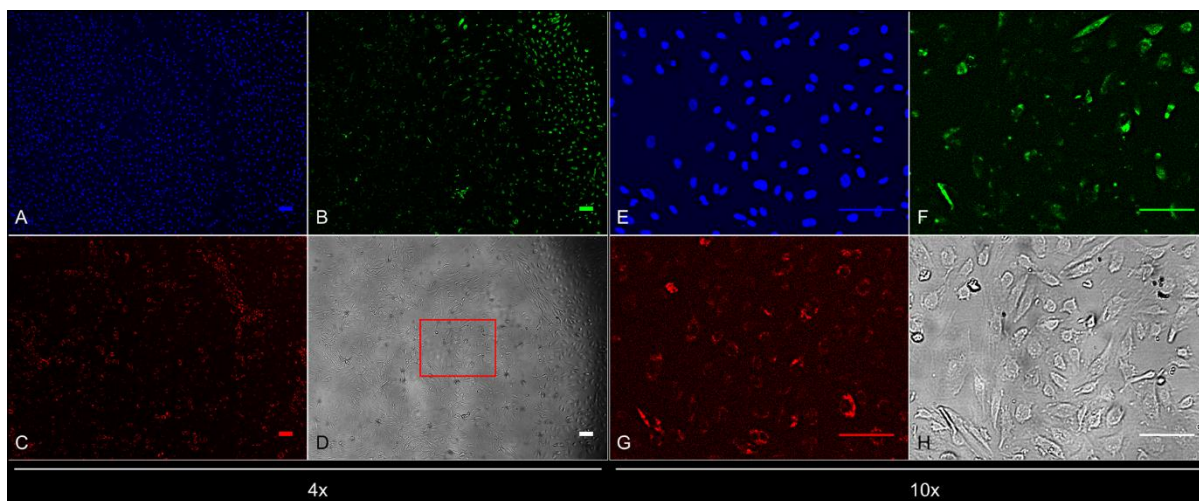


Figure A.143: HCS images of HUVEC cells after 48h exposure to SiO₂ & BiFeO₃@Fe₃O₄ NWs at 80 µg/mL. Panels A and E (blue channels): nuclear staining with Hoechst; Panels B and F (green channels): cell membrane permeability staining; Panels C and G (red channels): lysosomal mass/pH staining; Panels D and H (transmitted light channels). Left (A-D): 4x objective images. The region highlighted in the Transmitted Light Channel (D) is the area magnified in the right panels (E-H): 10x objective images. The scale bars are 100 µm.

Figure A.143 shows HUVEC cells after 48h of exposure to SiO₂ & BiFeO₃@Fe₃O₄ NWs at 80 µg/mL, stained for DNA (blue channels), cell morphology and membrane permeability (green channels) and lysosomal mass/pH changes (red channels). The aggregation and localisation of the SiO₂ & BiFeO₃@Fe₃O₄ NWs can be seen in the transmitted light panels (grey channels). As can be seen, after 48h the cells had reached confluency despite the presence of the NWs and the particles had aggregated inside the cells (Panels D and H).

A3.8.1 Cell count

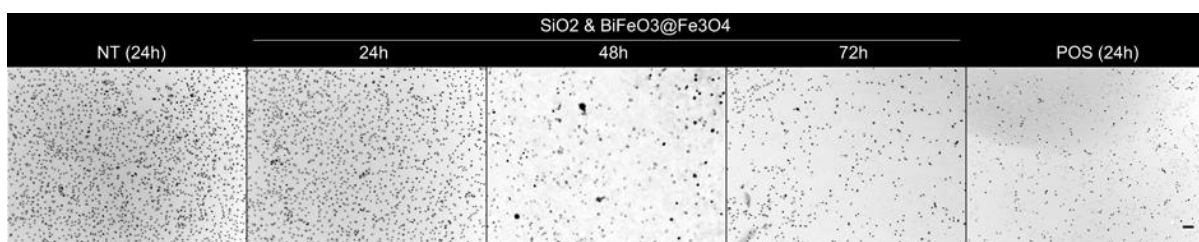


Figure A.144: HUVEC cells exposed to SiO₂ & BiFeO₃@Fe₃O₄ NWs stained for DNA. From left: representative images of untreated cells after 24h, cells exposed to SiO₂ & BiFeO₃@Fe₃O₄ NWs at 80 µg/mL for 24h, 48h, 72h, and cells treated with the positive control (valinomycin, 120 µM) for 24h. Only the Hoechst channel is shown, inverted. The scale bar is 100 µm and is the same for all the images.

HUVEC cells were exposed to SiO₂ & BiFeO₃@Fe₃O₄ NWs at three time points and stained for DNA to determine cell count (Figure A.144). As can be seen, the cells did not reach confluency and the population fell after 48 and 72h, as borne out by the HCS data below.

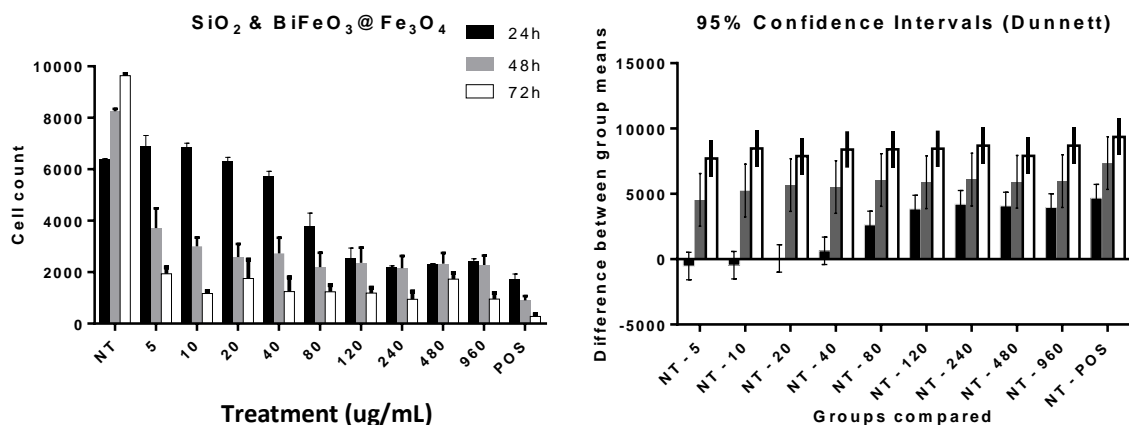


Figure A.145: Cell count of HUVEC cells after treatment with SiO₂ & BiFeO₃@Fe₃O₄ NWs and the corresponding 95% confidence intervals. Left: Number of cells vs concentration of nanomaterial. Valinomycin was used as positive control. The error bars represent the standard error of the mean of triplicates in three independent experiments. Right: difference between group means relative to the untreated control NT (Dunnett's test for multiple comparisons). The error bars represent the 95% confidence intervals (calculated using ordinary One-Way ANOVA).

There are trends in the variation of cell count with concentration of SiO₂ & BiFeO₃@Fe₃O₄ NWs (Figure A.145, left panel), with counts significantly lower than the untreated control when exposed to 80 µg/mL of the NPs or more for 24h, and at all doses after 48 and 72h as can be seen from the 95% confidence intervals (Figure A.145, right panel). The dose-response tendency suggests that the NWs are toxic to HUVECs, though somewhat less toxic than the BiFeO₃@Fe₃O₄@asc NPs: the 72h cell counts are slightly lower than those of APS-coated NPs discussed earlier. This supports the conclusion that embedding the NPs in silica has a similar effect on the toxicity as capping with a silane layer, passivating the surface and mitigating the toxic response.

A3.8.2 Cell Membrane Permeability

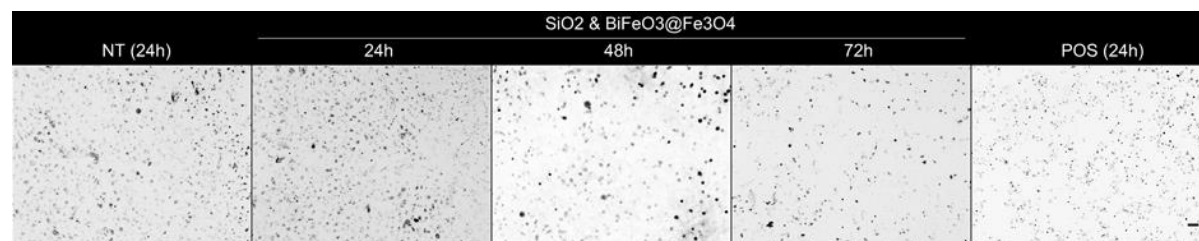


Figure A.146: HUVEC cells exposed to SiO₂ & BiFeO₃@Fe₃O₄ NWs stained for cell membrane permeability. From left: representative images of untreated cells after 24h, cells exposed to SiO₂ & BiFeO₃@Fe₃O₄ NWs at 80 µg/mL for 24h, 48h, 72h, and cells treated with the positive control (valinomycin, 120 µM) for 24h. Only the CMP (green) channels are shown, inverted. The scale bar is 100 µm and is the same for all the images.

Cell membrane permeability was used to indicate cell viability. Because the images in Figure A.146 are inverted, the number of viable cells in each image is therefore the number of cells in which the intensity

of CMP stain surrounding and overlapping the nucleus is below the threshold determined for each plate analysed as described above (see A2.2.2). The data are displayed below (see Figure A.147).

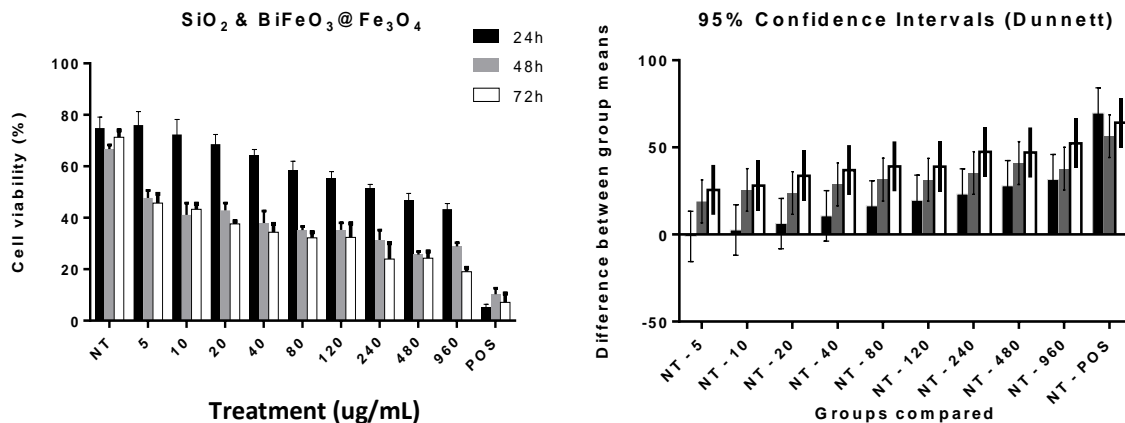


Figure A.147: Cell viability of HUVEC cells after treatment with SiO₂ & BiFeO₃@Fe₃O₄ NWs and the corresponding 95% confidence intervals. Left: cell viability vs concentration of nanomaterial. Valinomycin was used as positive control. The error bars represent the standard error of the mean of triplicates in three independent experiments. Right: difference between group means relative to the untreated control NT (Dunnett's test for multiple comparisons). The error bars represent the 95% confidence intervals (calculated using ordinary One-Way ANOVA).

As with the cell count, there are apparent trends in the concentration-dependent response of the cells to the NM, especially at 24h (see left panel, Figure A.147). However, the variations all fall within the 95% confidence intervals and are therefore not statistically significant.

This supports the conclusion that the SiO₂ & BiFeO₃@Fe₃O₄ NWs do not accelerate cell death in HUVEC cells at the concentrations analysed.

The cells were also examined for changes in lysosomal mass/pH as a final indicator of cytotoxicity.

A3.8.3 Lysosomal mass/pH

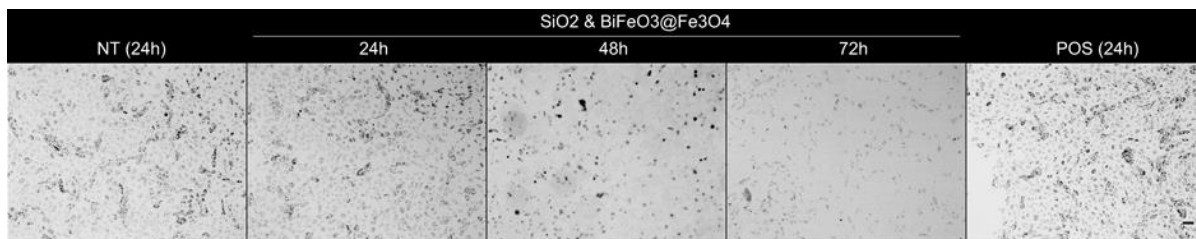


Figure A.148: HUVEC cells exposed to SiO₂ & BiFeO₃@Fe₃O₄ NWs stained for lysosomal mass/pH changes. From left: representative images of untreated cells after 24h, cells exposed to SiO₂ & BiFeO₃@Fe₃O₄ NWs at 80 µg/mL for 24h, 48h, 72h, and cells treated with the positive control (tacrine, 100 µM) for 24h. Only the LysoTracker (red) channels are shown, inverted. The scale bar is 100 µm and is the same for all the images.

LysoTracker™ Red was used to stain for changes in lysosomal mass or pH. Because the images in Figure A.148 are inverted, an increase in the intensity therefore corresponds to a larger mass of lysosomes or decrease in pH, indicating a toxic response to the analyte. These data are displayed below (see Figure A.148).

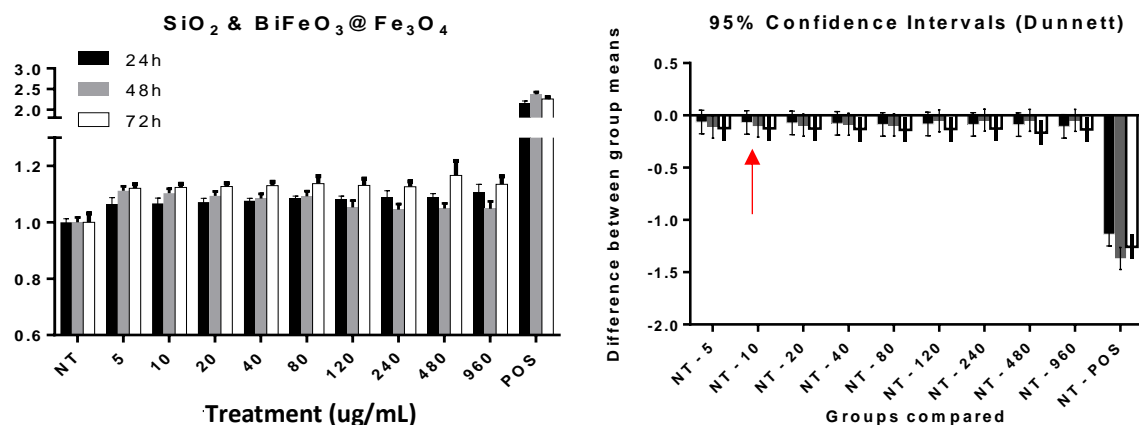


Figure A.149: Lysosomal mass/pH changes in HUVEC cells after treatment with SiO₂ & BiFeO₃@Fe₃O₄ NWs and the corresponding 95% confidence intervals. Left: Lysosomal mass/pH vs concentration of nanomaterial. Tacrine was used as positive control. The error bars represent the standard error of the mean of triplicates in three independent experiments. Right: difference between group means relative to the untreated control NT (Dunnett's test for multiple comparisons). The error bars represent the 95% confidence intervals (calculated using ordinary One-Way ANOVA).

There is an apparent dose-dependent decrease in the lysosomal mass/pH as a function of concentration of SiO₂ & BiFeO₃@Fe₃O₄ NWs after 24h but the variations fall within the 95% confidence interval and are hence not significant (see Figure A.149, left panel). A similar trend of falling lysosomal mass/pH with rising concentration is observed after 48h with LMPH values significantly higher than the untreated control at doses up to 10 µg/mL (indicated by an arrow, right panel, Figure A.149).

After 72h however, there was a small but significant increase at all concentrations, supporting the assertion that the uptake of nanowires is inhibited and that the delayed rise in LMPH may be due to the dissolution of ions into the media and/or the uptake of nanoparticles released from the pores of the nanowires.

A3.9 HUVEC cells treated with SiO₂&BiFeO₃@Fe₂O₃ NWs

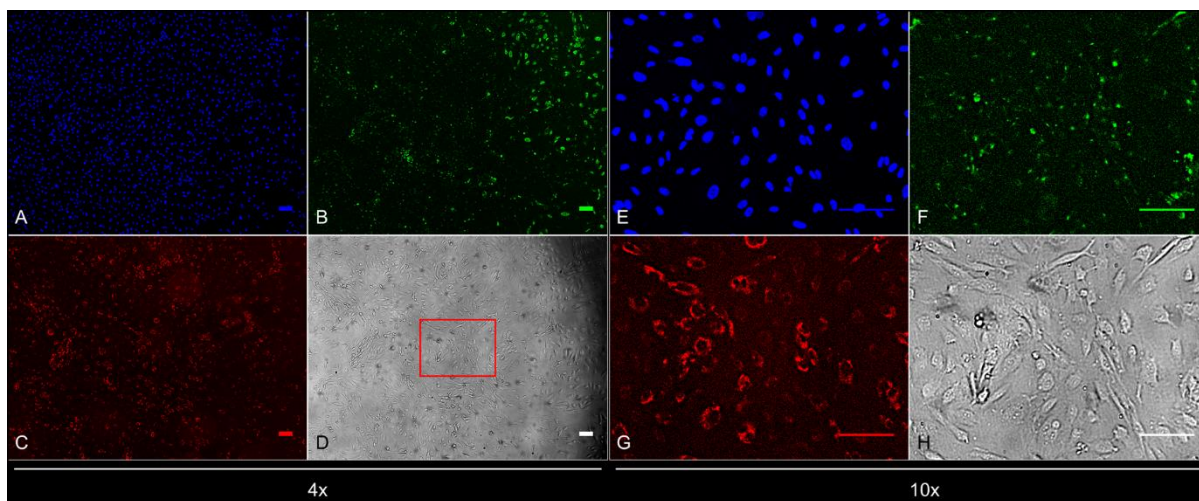


Figure A.150: HCS images of HUVEC cells after 48h exposure to SiO₂ & BiFeO₃@Fe₂O₃ NWs at 80 µg/mL. Panels A and E (blue channels): nuclear staining with Hoechst; Panels B and F (green channels): cell membrane permeability staining; Panels C and G (red channels): lysosomal mass/pH staining; Panels D and H (transmitted light channels). Left (A-D): 4x objective images. The region highlighted in the Transmitted Light Channel (D) is the area magnified in the right panels (E-H): 10x objective images. The scale bars are 100 µm.

Figure A.150 shows HUVEC cells after 48h of exposure to SiO₂ & BiFeO₃@Fe₂O₃ NWs at 80 µg/mL, stained for DNA (blue channels), cell morphology and membrane permeability (green channels) and lysosomal mass/pH changes (red channels). The aggregation and localisation of the SiO₂ & BiFeO₃@Fe₂O₃ NWs can be seen in the transmitted light panels (grey channels). As can be seen, after 48h the cells had reached confluency despite the presence of the NWs and the particles had aggregated inside the cells (Panels D and H).

A3.9.1 Cell count

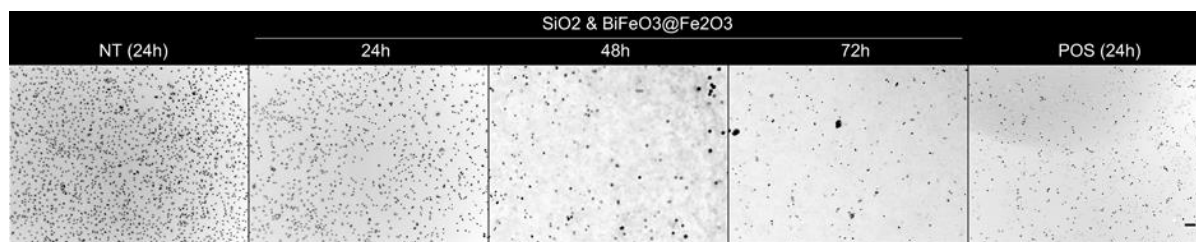


Figure A.151: HUVEC cells exposed to SiO_2 & $\text{BiFeO}_3@Fe_2O_3$ NWs stained for DNA. From left: representative images of untreated cells after 24h, cells exposed to SiO_2 & $\text{BiFeO}_3@Fe_2O_3$ NWs at $80 \mu\text{g}/\text{mL}$ for 24h, 48h, 72h, and cells treated with the positive control (valinomycin, $120 \mu\text{M}$) for 24h. Only the Hoechst channel is shown, inverted. The scale bar is $100 \mu\text{m}$ and is the same for all the images.

HUVEC cells were exposed to SiO_2 & $\text{BiFeO}_3@Fe_2O_3$ NWs at three time points and stained for DNA to determine cell count (Figure A.32). As can be seen, the cells did not reach confluency and the population fell after 48 and 72h, as borne out by the HCS data below.

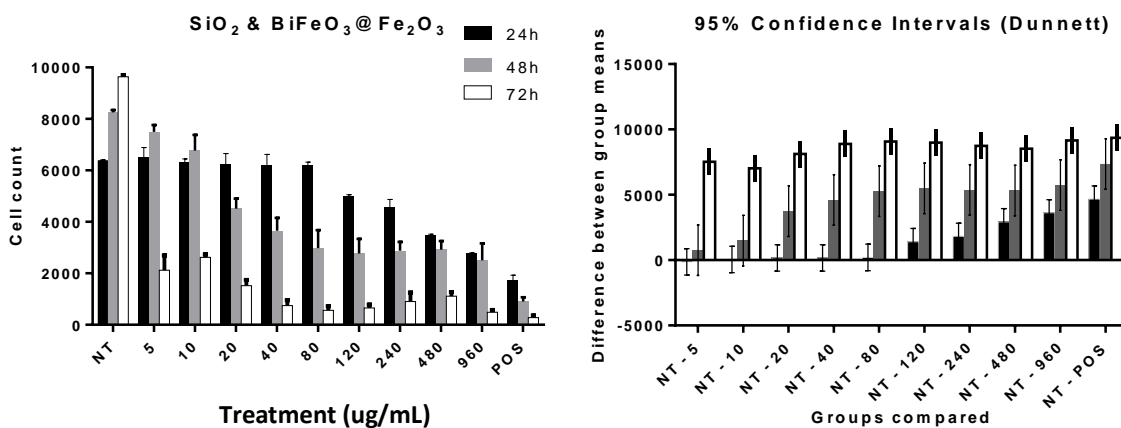


Figure A.152: Cell count of HUVEC cells after treatment with SiO_2 & $\text{BiFeO}_3@Fe_2O_3$ NWs and the corresponding 95% confidence intervals. Left: Number of cells vs concentration of nanomaterial. Valinomycin was used as positive control. The error bars represent the standard error of the mean of triplicates in three independent experiments. Right: difference between group means relative to the untreated control NT (Dunnett's test for multiple comparisons). The error bars represent the 95% confidence intervals (calculated using ordinary One-Way ANOVA).

There are trends in the variation of cell count with concentration of SiO_2 & $\text{BiFeO}_3@Fe_2O_3$ NWs (Figure A.152, left panel), with counts significantly lower than the untreated control when exposed to more than $120 \mu\text{g}/\text{mL}$ of the NWs for 24h, above $20 \mu\text{g}/\text{mL}$ after 48 and at all doses after 72h as can be seen from the 95% confidence intervals (Figure A.152, right panel). The dose-response tendency suggests that the NWs are toxic to HUVECs, though somewhat less toxic than the $\text{BiFeO}_3@Fe_3O_4@asc$ NPs: the 72h cell counts are slightly lower than those of APS-coated NPs discussed earlier. This supports the

conclusion that embedding the NPs in silica has a similar effect on the toxicity as capping with a silane layer, passivating the surface and mitigating the toxic response.

A3.9.2 Cell Membrane Permeability

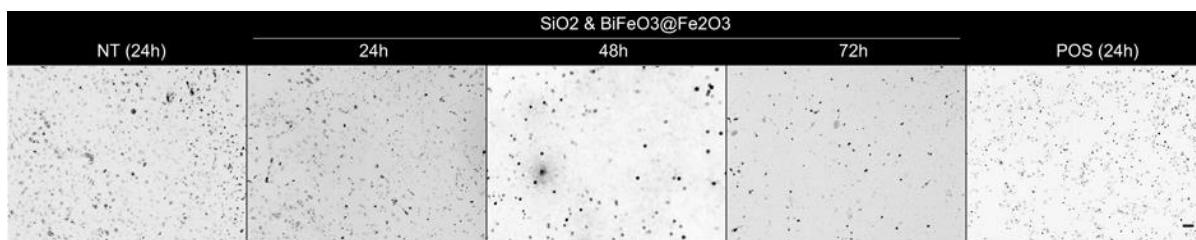


Figure A.153: HUVEC cells exposed to SiO_2 & $\text{BiFeO}_3@Fe_2O_3$ NWs stained for cell membrane permeability. From left: representative images of untreated cells after 24h, cells exposed to SiO_2 & $\text{BiFeO}_3@Fe_2O_3$ NWs at 80 $\mu\text{g/mL}$ for 24h, 48h, 72h, and cells treated with the positive control (valinomycin, 120 μM) for 24h. Only the CMP (green) channels are shown, inverted. The scale bar is 100 μm and is the same for all the images.

Cell membrane permeability was used to indicate cell viability. Because the images in Figure A.153 are inverted, the number of viable cells in each image is therefore the number of cells in which the intensity of CMP stain surrounding and overlapping the nucleus is below the threshold determined for each plate analysed as described above (see A2.2.2). The data are displayed below (see Figure A.154).

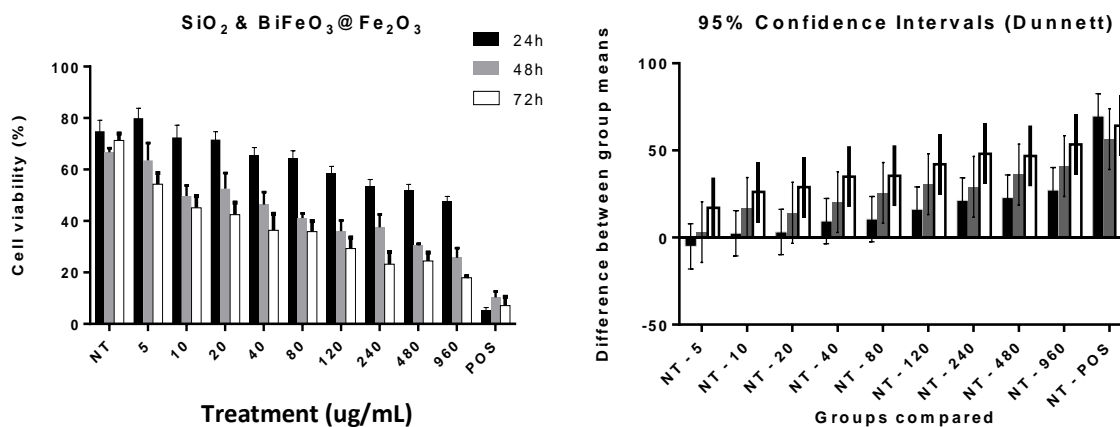


Figure A.154: Cell viability of HUVEC cells after treatment with SiO_2 & $\text{BiFeO}_3@Fe_2O_3$ NWs and the corresponding 95% confidence intervals. Left: cell viability vs concentration of nanomaterial. Valinomycin was used as positive control. The error bars represent the standard error of the mean of triplicates in three independent experiments. Right: difference between group means relative to the untreated control NT (Dunnett's test for multiple comparisons). The error bars represent the 95% confidence intervals (calculated using ordinary One-Way ANOVA).

As with the cell count, there are apparent trends in the concentration-dependent response of the cells to the NM, especially at 24h (see left panel, Figure A.154). However, the variations all fall within the 95% confidence intervals and are therefore not statistically significant.

This supports the conclusion that the SiO_2 & $\text{BiFeO}_3@Fe_2O_3$ NWs do not accelerate cell death in HUVEC cells at the concentrations analysed.

The cells were also examined for changes in lysosomal mass/pH as a final indicator of cytotoxicity.

A3.9.3 Lysosomal mass/pH

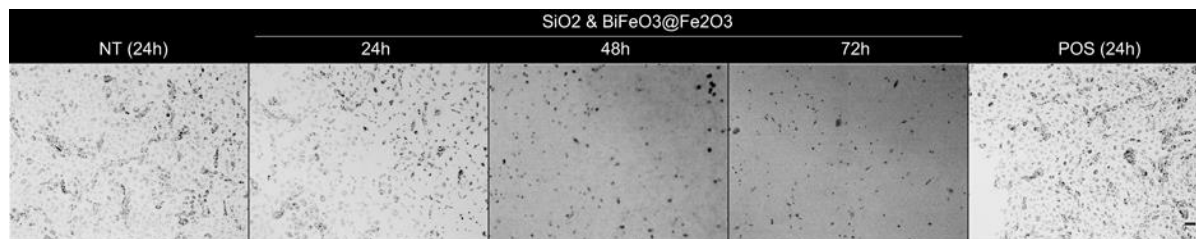


Figure A.155: HUVEC cells exposed to SiO_2 & $\text{BiFeO}_3@Fe_2O_3$ NWs stained for lysosomal mass/pH changes. From left: representative images of untreated cells after 24h, cells exposed to SiO_2 & $\text{BiFeO}_3@Fe_2O_3$ NWs at $80 \mu\text{g}/\text{mL}$ for 24h, 48h, 72h, and cells treated with the positive control (tacrine, $100 \mu\text{M}$) for 24h. Only the LysoTracker (red) channels are shown, inverted. The scale bar is $100 \mu\text{m}$ and is the same for all the images.

LysoTracker™ Red was used to stain for changes in lysosomal mass or pH. Because the images in Figure A.155 are inverted, an increase in the intensity therefore corresponds to a larger mass of lysosomes or decrease in pH, indicating a toxic response to the analyte. These data are displayed below (see Figure A.156).

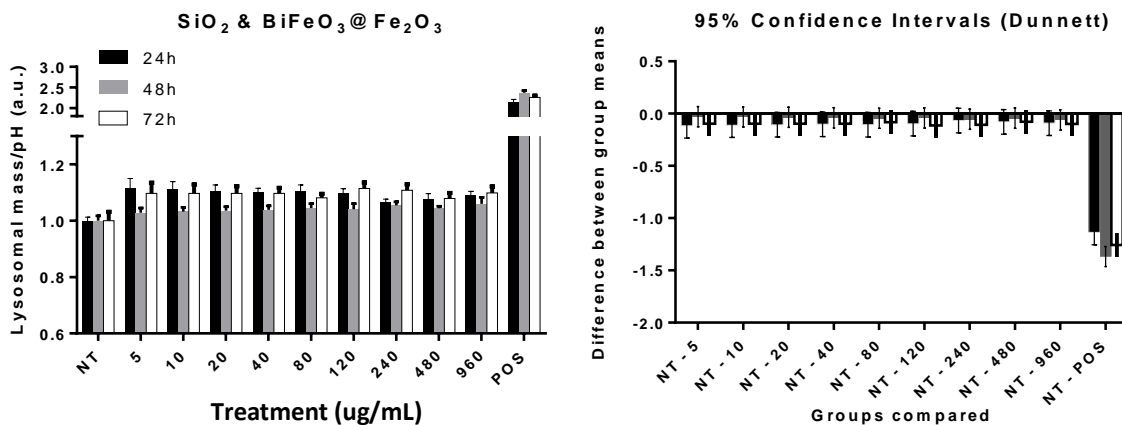


Figure A.156: Lysosomal mass/pH changes in HUVEC cells after treatment with SiO_2 & $\text{BiFeO}_3@Fe_2O_3$ NWs and the corresponding 95% confidence intervals. Left: Lysosomal mass/pH vs concentration of nanomaterial. Tacrine was used as positive control. The error bars represent the standard error of the mean of triplicates in three independent experiments. Right: difference between group means relative to the untreated control NT (Dunnett's test for multiple comparisons). The error bars represent the 95% confidence intervals (calculated using ordinary One-Way ANOVA).

There is no distinct dose-dependent response in the lysosomal mass/pH as a function of concentration of SiO_2 & $\text{BiFeO}_3@Fe_2O_3$ NWs as can be seen in Figure A.156, left panel. Although there is an apparent

increase at the lowest dose after 24h and 72h the variations fall within the respective 95% confidence intervals and are hence not significant (right panel, Figure A.156).

The lack of significant difference in the LMPH indicates that there is diminished uptake of the nanowires or that an increase in uptake is accompanied by a reduction in the pH.